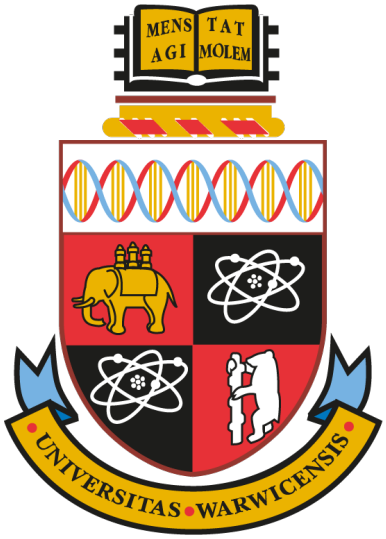


Precise Photometry with a Scientific CMOS camera

by

Ioannis Apergis

Thesis

Submitted to the University of Warwick

for the degree of

Doctor of Philosophy

Department of Physics

May 2026

UNIVERSITY OF WARWICK

Contents

List of Tables vii

List of Figures ix

Acknowledgments xiii

Declarations xvi

Abstract xviii

Abbreviations and quantities xix

Chapter 1 Introduction 1

1.1 Early astronomical detectors . . . 1

1.1.1 The Human eye . . . 2

1.1.2 The Photographic plates . . . 2

1.1.3 The Photomultiplier tubes . . . 4

1.2 Semiconductor digital detectors . . . 5

1.2.1 Band theory . . . 5

1.2.2 Device Fabrication . . . 7

1.2.3 The *p*-*n* junction . . . 8

1.2.4 The Photodiode and Field Effect Transistors . . . 9

1.3 CCD image sensors . . . 12

1.4 CMOS image sensors . . . 17

1.5 Characteristics of CMOS and CCD devices . . . 18

1.5.1 Read Noise . . . 19

1.5.2 Dark Current . . . 19

1.5.3 Non-uniformities . . . 19

1.5.4 Saturation . . . 19

1.5.5 Linearity . . . 19

1.6 Planets and Exoplanets . . . 19

1.6.1 The Solar System . . . 20

1.6.2 Exoplanets . . . 20

1.6.3 Transits via photometry . . . 23

1.6.4 Radial velocity . . . 26

1.6.5 Other detection methods . . . 27
1.7 Photometric transit surveys . . . 31
1.7.1 The Next Generation Transit Survey (NGTS) . . . 34
1.7.2 Transiting Exoplanet Survey Satellite (TESS) . . . 37
1.8 Spectrographs for Follow-Up of Transiting Exoplanet Candidates . . . 40
1.8.1 The High Accuracy Radial Velocity Planet Searcher (HARPS) . . . 40
1.8.2 CORALIE . . . 41
1.9 Thesis overview . . . 42

Chapter 2 Lab testing of the Marana CMOS camera 43
2.1 Introduction . . . 44
2.2 The Marana Camera . . . 46
2.2.1 The Marana 4.2BV-11 Camera . . . 46
2.2.2 Low Gain and High Gain channels . . . 46
2.2.3 High Dynamic Range and Fastest Frame Rate imaging modes . . . 47
2.2.4 Amplifier Glow . . . 48
2.2.5 Spurious Noise Filter . . . 48
2.3 Laboratory Setup . . . 49
2.4 Methods . . . 51
2.4.1 Photon Transfer Curve . . . 51
2.4.2 Bias . . . 51
2.4.3 Row and Column banding . . . 52
2.4.4 Dark . . . 52
2.4.5 Photo Response Non-Uniformity . . . 53
2.4.6 Linearity Testing . . . 53
2.4.7 Quantum Efficiency and Window Transmittance . . . 54
2.5 Results, Analysis and Discussion . . . 55
2.5.1 Photon Transfer Curve Results . . . 55
2.5.2 Bias level, Read Noise and DSNU . . . 58
2.5.3 Row and Column Noise . . . 64
2.5.4 Dark frame structure and Dark level measurement . . . 69
2.5.5 Photo Response Non-Uniformity (PRNU) . . . 72
2.5.6 Linearity Results . . . 75
2.5.7 Quantum Efficiency and Transmission Window Results . . . 76
2.6 Conclusions . . . 79
2.7 Appendix: Bias, Light and temperature stability . . . 82
2.8 Appendix: Quantum Efficiency and Transmission Window calculations . . . 83
2.9 Appendix: Dark signal calculations . . . 84
2.10 Appendix: Dark current calculations . . . 84

Chapter 3 Further characterisation of the Marana Camera 87
3.1 Introduction . . . 87
3.2 High Gain and Low Gain channels . . . 87

3.3 Characterisation Testing of the High Gain and Low Gain channels 90
3.3.1 PTC and Linearities in HG and LG channels 90
3.3.2 Read Noise and Bias level in HG and LG channels 91
3.3.3 Row and Column temporal noise in HG and LG channels 93
3.3.4 Row, Column and pixel spatial noise in HG and LG channels 93
3.3.5 Dark current and non-uniformities in HG and LG channels 96
3.3.6 PRNU and DCNU in HG and LG channels 96
3.3.7 Summary of the HG and LG channel testing 97
3.4 Supply Voltage Adjustments 98
3.4.1 Investigation on the PTC of the LG channel 98
3.4.2 Adjustments of the VDDPIX voltage in HG and LG channels 100
3.4.3 Characterisation of the HDR mode with voltage adjustments 102
3.5 Image Lag 106
3.5.1 Image lag introduction 106
3.5.2 Set up for image lag experiment 107
3.5.3 Methodology 107
3.5.4 Results from the image lag experiments 109
3.5.5 Discussion 122
3.6 Conclusion 124

Chapter 4 On-sky testing of the Marana CMOS and iKon-L CCD cameras 126
4.1 Introduction 127
4.2 Observatory and Instruments 128
4.2.1 The NGTS Facility 128
4.2.2 The iKon-L 936 CCD Camera 130
4.2.3 The Marana CMOS Camera 130
4.3 Methods 132
4.3.1 Installation of the Marana CMOS Camera at NGTS 132
4.3.2 Observations 132
4.3.3 Image reduction and Photometry pipeline 134
4.4 Photometric Noise 136
4.4.1 Detector Noise 136
4.4.2 Sky Background noise 137
4.4.3 Source Noise 137
4.4.4 Total Noise 138
4.4.5 Systematic Noise 138
4.5 Results 138
4.5.1 Noise model comparison 138
4.5.2 Timescale of noise 139
4.5.3 Transit lightcurves 142
4.6 Discussion 144
4.6.1 Fractional Noise 144
4.6.2 Sky Background 147

4.6.3 Camera Efficiency . . . 148
4.6.4 Red Noise . . . 151
4.7 Conclusions . . . 152
4.8 Appendix . . . 153

Chapter 5 Characterisation of Andor Toran 26B CMOS camera 164
5.1 Introduction . . . 165
5.2 The Toran 26B CMOS Camera . . . 165
5.3 Optical bench, Telescope and Observations . . . 166
5.3.1 Laboratory Setup . . . 166
5.3.2 Telescope configuration and Observations . . . 167
5.4 Methods . . . 168
5.4.1 Bias and Dark . . . 168
5.4.2 Photo Response and Linearity . . . 169
5.4.3 Quantum Efficiency and Transmission Window . . . 169
5.4.4 Image reduction and photometry . . . 170
5.4.5 Photometry . . . 171
5.4.6 System Noise . . . 171
5.5 Results, Analysis and Discussion . . . 172
5.5.1 PTC, PRNU and Linearity measurements . . . 172
5.5.2 Bias level Spatial and Temporal Noise . . . 173
5.5.3 Dark frame structure and Dark Current . . . 174
5.5.4 QE and Window Transmittance . . . 179
5.5.5 Noise models from on-sky tests . . . 180
5.5.6 Timescale of noise from on-sky tests . . . 181
5.5.7 Transiting exoplanets from on-sky tests . . . 183
5.6 Conclusions . . . 187
5.7 Extra Material . . . 188

Chapter 6 Discovery of the long period warm Jupiter NGTS-39b 196
6.1 Introduction . . . 197
6.2 Photometry . . . 198
6.2.1 TESS Photometry . . . 198
6.2.2 NGTS Photometry . . . 203
6.2.3 TFOP SG1 Follow-up Photometry . . . 205
6.3 Spectroscopy . . . 207
6.3.1 Radial Velocity monitoring with CORALIE . . . 207
6.3.2 Radial Velocity monitoring with HARPS . . . 208
6.4 Analysis and Results . . . 208
6.4.1 Stellar analysis of the system . . . 208
6.4.2 Global modelling of the NGTS-39 system . . . 209
6.4.3 The NGTS-39 system . . . 213
6.4.4 Sensitivity maps for Companions . . . 216

6.5 Discussion . . . 216
6.5.1 Parameters of NGTS-39 b . . . 216
6.5.2 The atmosphere of NGTS-39 b . . . 216
6.5.3 An outer companion . . . 217
6.6 Conclusion . . . 220
6.7 Appendix: RV dataset . . . 220
6.8 `allesfitter` results tables . . . 220

Chapter 7 Conclusions **224**
7.1 The role of CMOS sensors in astronomy . . . 224
7.2 Ground-based instruments with CMOS . . . 225
7.3 Space-based instruments with CMOS . . . 226
7.4 A Standardised and Universal Method . . . 227
7.5 The future discovery of long period transiting systems . . . 228

List of Tables

1.1 Summary of the observing cycles of TESS. 38

2.1 Specifications of the Andor Marana CMOS camera. 47
2.2 Specifications of the Marana CMOS camera measured in this work in comparison with a deep depleted back-sided iKon-L 936 CCD. 80
2.3 Exposures steps based on the saturation exposure (1.5 seconds. 82
2.4 Best fit from the linear relation of the dark signal as a function of exposure at different temperatures. 86
2.5 Best fit of the logarithmic dark current as a function of temperature at different regions on the images. 86

3.1 Specifications measured for the Marana CMOS camera in HDR LG and HDR HG channels. 98
3.2 Characterisation of VDDPIX LG and HG channels. 101
3.3 Specifications measured for the Marana CMOS camera in HDR mode with VDDPIX 2.0 V and 2.1 V. 105
3.4 Description of the experiments in Image Lag. 109
3.5 Experiment 2: Image lag measurements table. 113

4.1 Specifications of the CCD and CMOS camera 131
4.2 Simultaneous transit observations of bright stars with CMOS and CCD cameras . . 134
4.3 `allesfitter` model priors for the transiting system WASP-4 144
4.14 Percentage ratio of transition pixels within star apertures. 153
4.4 `allesfitter` model priors for the transiting system TOI-905 154
4.5 `allesfitter` model priors for the transiting system WASP-95 155
4.6 `allesfitter` model priors for the transiting system TOI-2109 156
4.7 `allesfitter` model priors for the transiting system KELT-10 157
4.8 `allesfitter` model priors for the transiting system WASP-97 158
4.9 `allesfitter` model priors for the transiting system WASP-97 159
4.10 `allesfitter` model priors for the transiting system WASP-95 160
4.11 `allesfitter` model priors for the transiting system KELT-10 161
4.12 `allesfitter` model priors for the transiting system TOI-4463 162
4.13 `allesfitter` model priors for the transiting system WASP-30 163

5.1 Specifications of the sensor for the Toran 26B camera 166

5.2 Transit observations. 169
5.3 `allesfitter` model priors for the transiting system KELT-16 186
5.4 Specifications of the Andor CMOS camera measured in this work in for the LN and HWC modes. 188
5.5 `allesfitter` model priors for the transiting system KELT-1 192
5.6 `allesfitter` model priors for the transiting system Kepler-41 193
5.7 `allesfitter` model priors for the transiting system Kepler-670 194
5.8 `allesfitter` model priors for the transiting system Kepler-76 195

6.1 NGTS-39 Stellar parameters 200
6.2 A portion of the NGTS photometric data for NGTS-39. 204
6.3 Summary of photometric observations of NGTS-39. 207
6.4 NGTS-39 b properties. 210
6.5 Spectroscopic data for NGTS-39. 221
6.6 Continuation of Table 6.5. 222
6.7 `allesfitter` global fitted values and priors 222
6.8 `allesfitter` global model derived values 223

List of Figures

1.1 The human eye. . . . 2
1.2 The Orion Nebula. . . . 3
1.3 An example of a photomultiplier tube 4
1.4 Band scheme for Solids. . . . 6
1.5 Absorption length as a function of wavelength 7
1.6 Flat images on CCD sensor 9
1.7 The p-n junction 10
1.8 Semiconductor channel devices. . . . 11
1.9 Pinned Photodiode. . . . 12
1.10 Schematic representation of the CCD pixels 14
1.11 An example of a CCD detector. . . . 15
1.12 Schematic illustration of a CCD device sliced perpendicular. . . . 16
1.13 Comparison of QE curves. . . . 16
1.14 CMOS pixel and sensor architecture. . . . 18
1.15 Phase-folded radial velocities. . . . 21
1.16 Population plots from the updated NASA exoplanet archive. . . . 22
1.17 Schematic illustration of an exoplanet transiting a host star. . . . 24
1.18 A schematic illustration of limb darkening. . . . 26
1.19 A schematic illustration of the periodic RV signal. . . . 28
1.20 Direct imaging of the fourth planet in HR 8799 30
1.21 Microlensing event of OGLE-2003-BLG-235/MOA-2003-BLG-53. . . . 32
1.22 The NGTS enclosure. . . . 35
1.23 The theoretical throughput of a typical NGTS telescope. . . . 36
1.24 The Noise model for the NGTS on a no-moon scenario. . . . 37
1.25 The NASA's Transiting Exoplanet Survey Satellite. . . . 38
1.26 The observing strategy of TESS. . . . 39

2.1 Optical bench setup for the Marana camera. . . . 49
2.2 Bias level, light source signal and temperature for the Marana camera over time. . . . 50
2.3 The optical bench of the QE measurement of the Marana CMOS camera. . . . 54
2.4 Photon transfer curves for the Marana camera at -25 °C. . . . 57
2.5 Binary image time series. . . . 59
2.6 Bias frames from Marana camera. . . . 60

2.7 Read noise distribution using 100 consecutive bias frames. 62
2.8 An example sub-frame showing the read noise map for the FFR mode. 63
2.9 Histogram distribution of the DSNU for both readout modes 65
2.10 Row noise distribution using 100 consecutive bias frames. 67
2.11 Column noise distribution using 100 consecutive bias frames. 68
2.12 Marana dark images taken in the HDR mode at a camera temperature of -25° C. . . 69
2.13 Mean dark signal as a function of exposure time over a range of temperatures. . . . 71
2.14 The logarithmic dark current as a function of the inverse temperature. 73
2.15 Histogram distributions of the photo response non-uniformities for both modes. . . 74
2.16 Linearity measurements for the Marana in FFR mode (left) and HDR mode (right). 76
2.17 Linearity zoom-in. 77
2.18 QE results for Marana sCMOS camera at three temperatures. 78
2.19 Normalised QE measurements as a function of wavelength. 79
2.20 Transmission as a function of wavelength. 80
2.21 Bias level, light source signal and temperature for the Marana camera over time. . . 82
2.22 Bias frames from Marana camera recorded at minimum exposure for the FFR mode. 83
2.23 The responsivity of the photodiode used for the QE measurements. 84
2.24 The corresponding QE values of the photodiode as a function of wavelength. 85
2.25 Photodiode measurements as a function of wavelength. 85

3.1 Circuit diagram of a pixel from the GSENSE400BSI sensor. 88
3.2 Photon transfer curves for the Marana camera at +15 °C. 91
3.3 Linearity measurements for the Marana camera at +15 °C. 92
3.4 Bias frames from Marana camera recorded at minimum exposure and at +15 °C. . . 92
3.5 Read noise distribution using 100 consecutive bias frames. 94
3.6 Row noise distribution using 100 consecutive bias frames. 95
3.7 Column noise distribution using 100 consecutive bias frames. 95
3.8 Histogram distribution to estimate the overall DSNU for the HG and LG channels. . 96
3.9 Dark current maps for the Marana camera at -25 °C. 97
3.10 Illuminated frames before saturation for the LG channel at 15 ∘C. 99
3.11 PTC estimated for VDDPIX supply pixel voltage at 2.1 V for the HG and LG channels. 100
3.12 Linearities estimated for VDDPIX supply pixel voltage at 2.1 V for the LG (left) and HG (right) channels. 101
3.13 PTC measurements for the Marana camera at +15 °C for the HDR imaging mode. . 103
3.14 Linearity measurements for the Marana camera at +15 °C for the HDR imaging mode. 103
3.15 Marana dark images taken in the HDR mode, with camera temperature of -25° C. . 104
3.16 Measurements of the FWC, read noise, and dynamic range as a function of VDDPIX. 105
3.17 Example of image lag caused by traps and defects. 106
3.18 Diagram of the image-lag experimental bench. 108
3.19 Schematic illustration of the two types of image lag. 109
3.20 Experiment 1 oscilloscope traces. 110
3.21 Experiment 1: Sequence of images at different light pulse duration. 111
3.22 Experiment 2 oscilloscope traces. 112

3.23 Experiment 2: Sequence of images at four different colours. 112
3.24 Experiment 2: Image lag at -25 °C. 113
3.25 Experiment 3 oscilloscope traces. 114
3.26 Experiment 3: Dark image, bright image, and lag image acquired at 25 °C. 115
3.27 Experiment 3: Lag ratio image at 25 °C. 116
3.28 Experiment 3: Dark image, bright image, and lag image acquired at 25 °C. 116
3.29 Experiment 3: Lag ratio image at -25 °C. 117
3.30 Experiment 3: Lag ratio as a function of signal level from the ratio of the lag image. 118
3.31 Experiment 4 oscilloscope traces. 118
3.32 Experiment 4: Image lag measured for the Marana camera from a sequence of 25 images at a temperature of 25 °C. 119
3.33 Experiment 4: Image lag for the Marana camera at -25 °C 119
3.34 Experiment 5 oscilloscope traces. 120
3.35 Experiment 5: Image lag for the Marana camera with the overlap disabled at different frequencies. 121
3.36 Experiment 5: Image lag for the Marana camera at -25 °C. 121

4.1 QEs of the CCD and CMOS camera 129
4.2 Marana CMOS camera at NGTS 133
4.3 Target pixel frame for CCD and CMOS 136
4.4 Noise models for CCD and CMOS camera 140
4.5 Ratio of CCD and CMOS camera noise 141
4.6 Timescale of noise for CCD and CMOS 143
4.7 Normalised lightcurves for transiting system of WASP-4 145
4.8 CMOS/CCD flux ratio 147
4.9 Sky background as a function of time 149
4.10 Ratio of stellar flux vs effective temperature 150
4.11 Number of transition pixels 151
4.12 Normalised lightcurves for transiting system of TOI-905 154
4.13 Normalised lightcurves for transiting system of WASP-95 155
4.14 Normalised lightcurves for transiting system of TOI-2109 156
4.15 Normalised lightcurves for transiting system of KELT-10 157
4.16 Normalised lightcurves for transiting system of WASP-97 158
4.17 Normalised lightcurves for transiting system of WASP-97 159
4.18 Normalised lightcurves for transiting system of WASP-95 160
4.19 Normalised lightcurves for transiting system of KELT-10 161
4.20 Normalised lightcurves for transiting system of TOI-4463 162
4.21 Normalised lightcurves for transiting system of WASP-30 163

5.1 Optical bench setup for the Toran 26B camera 167
5.2 The TWenty-Inch Survey Telescope 168
5.3 Photon transfer curve for Toran 26B 172
5.4 Linearity for the Toran 26B 173

5.5 PRNU for Toran 26B . . . 174
5.6 Read noise for Toran 26B . . . 175
5.7 Column noise for Toran 26B . . . 176
5.8 Row noise for Toran 26B . . . 177
5.9 DSNU for Toran 26B . . . 178
5.10 Dark images for the Toran 26B . . . 179
5.11 QE plot for Toran 26B . . . 180
5.12 Transmission plot for Toran 26B. . . . 181
5.13 Noise models for Toran 26B with HWC mode. . . . 182
5.14 Noise models for Toran 26B with LN mode. . . . 182
5.15 Noise ratio for Toran 26B for HWC and LN mode. . . . 183
5.16 Timescale of noise for Toran 26B . . . 184
5.17 Normalized lightcurves for the transiting system of KELT-16 . . . 186
5.18 Statistical difference of fitted transit parameters . . . 187
5.19 Dark images for Toran 26B without LDC . . . 189
5.20 Spatial autocorrelation for Toran 26B . . . 189
5.21 Diagnostic output from the photometry. . . . 190
5.22 Noise model for performing relative photometry on a target star. . . . 191
5.23 Normalized lightcurves for the transiting system of KELT-1. . . . 192
5.24 Normalized lightcurves for the transiting system of Kepler-41 . . . 193
5.25 Normalized lightcurves for the transiting system of Kepler-670 . . . 194
5.26 Normalized lightcurves for the transiting system of Kepler-76 . . . 195

6.1 TESS Sector 7 Full-Frame Image cutout (11×11 pixels) of NGTS-39. . . . 201
6.2 TESS Sector detrended and normalised lightcurves for NGTS-39. . . . 202
6.3 NGTS lightcurves from 2023/09/03 to 2024/02/04 for NGTS-39. . . . 205
6.4 Transit lightcurves of NGTS-39, from TESS. . . . 211
6.5 Transit lightcurves of NGTS-39, from NGTS. . . . 212
6.6 Transit lightcurve of NGTS-39, from SG1. . . . 213
6.7 RV measurements of NGTS-39. . . . 214
6.8 O-C diagram for transit NGTS-39 b. . . . 215
6.9 Sensitivity maps for NGTS-39. . . . 217
6.10 Population diagrams showing planetary radius and orbital eccentricity. . . . 218
6.11 Stellar effective temperature, against planetary equilibrium temperature. . . . 219

Acknowledgments

First and foremost, I would like to thank my friends Utkarsh, Qiming, Alin, Maciej, Wellington, and Yuhong for the many reunions, conversations, and the friendship we shared throughout these years.

Going to Greece, I am deeply thankful to my friend Michalakis. Special thanks go to my friend Argyros, whose support helped me through difficult struggles, and whose company and humour made the hardest moments much easier to bear. My sincere thanks also go to my dear friend Jio for the meaningful conversations we shared each time I returned to Greece. My dearest friends Teo, Jim, Q, and Telis deserve special thanks for following me even into the most difficult and unfriendly rocky places for fishing, and for all the wonderful moments we shared over the past years. Moreover, I would also like to thank my friends – Alex, Lefo, Giorgos, Xrhstos, David, and Leonidas – for the endless discussions and shared memories. I am also grateful to Andreas, with whom, although we have not seen each other for a long time, I still fondly remember our many passionate debates about politics. A special mention goes to Stelios, with whom I once spent only 32 hours in Greece just so we could watch Olympiacos win its first European trophy. And to Alexandros, whom I am proud to call a brother after 19 years of friendship: thank you for being by my side through both the difficult times and the moments worth celebrating.

Back in Coventry, I would like to thank Sergio Ramírez Ramírez, Ginger Frame, Anna-Maria Cutolo and Isobel Lockley for their friendship and the moments we shared. I am also especially grateful to Jamie for sharing the office with me, for never complaining about my "five-minute" breaks, and for all the times we passed the football around indoors. To the rock band, the football team, the family – the legendary 442 Charter Avenue: Robert James Scott Airey Disk, Alastair Bryan Claringbold, James Anthony Blake, and Marcelo Aron Fetzner – thank you for the countless hours we spent together and for helping each other get through it all. And finally, to Morgan Mitchell, with whom I've spilled the same blood in the same mud since day one of this journey – thank you.

Moving to Belfast and after nearly eleven months, I am grateful for the people I met and everything I learned. My thanks also go to my friends in Belfast who supported me in difficult times – particularly Conor and Cahal, with whom I spent many weekends in pubs and playing video games.

Now, I would like to begin by thanking James McCormac, without whom my programming skills

would never have developed as they have. Thank you, James, for opening the door to the world of Python and for patiently answering every single one of my (many!) questions. I would also like to thank Paul Chote, whose guidance shaped all of my telescope and operations skills. Thank you for the trips to La Palma, for trusting me with so many instruments, and for always taking the time to answer my questions. My sincere thanks go to Peter J. Wheatley for the countless hours I spent in his office trying to convince him why CMOS cameras are better than CCDs – and for giving me the opportunity to work with NGTS, along with the unforgettable trip to Chile.

I must give a special, heartfelt thanks to my supervisor in Andor, colleague, landlord, flatmate, and above all dear friend Leonidas. Without him, this thesis simply would not have been completed. Thank you, Leonidas.

Finally, I want to thank the person who inspired me throughout my 3.5 years of this PhD and never once declined an unexpected meeting in his office. Thank you, Dan, for trusting me with this work – work that I truly hope I have done justice to – and for shaping me into the more knowledgeable and confident person I am today.

This work is dedicated to my family, whose love, sacrifices, and unwavering belief in me have supported me throughout every step of this journey. To my father Theodore, my mother Mina, my sister Markella, and my brother-in-law Matt and – who else! Thank you for your constant encouragement, patience, and support through every challenge. This thesis would not have been possible without you, and I am forever grateful for your constant support and for standing by me through all challenges.

This thesis is dedicated to my parents.

The one thing I know is that I know nothing.

SOCRATES

Declarations

I declare that this thesis is my own work except where explicitly stated otherwise. This thesis has not been submitted to this or any other academic institution for any other degree or qualification.

This PhD project was undertaken as part of an iCASE studentship in collaboration with Andor Technology. As part of this arrangement, I spent a total of approximately 11 months working with Andor during my PhD in their offices in Belfast, Northern Ireland. The placement provided access to laboratory facilities, camera hardware and software, technical expertise, and practical training relevant to the characterisation of detectors. During this time, my work included laboratory testing and characterisation of Andor camera systems, including measurements of detector performance parameters. These activities were directly relevant to the scientific aims of this thesis and contributed to the development and validation of the methods used throughout the work. Although this project was carried out in collaboration with Andor Technology, the analysis, interpretation, and presentation of the results in this thesis are my own unless otherwise stated. The collaboration provided technical support and access to instrumentation, but the scientific conclusions presented here were derived independently from the data analysis described in the relevant chapters. Where input, advice, hardware access, or technical support from Andor contributed to the work, this has been acknowledged appropriately.

In addition to completing the thesis-related research, my duties at Andor included work with the Research and Development and Optical Engineering teams. This involved supporting the validation and characterisation of camera products, assisting with debugging and investigation of detector or system-level behaviour, and contributing to technical support activities related to customer issues. These duties provided wider industrial context for the thesis work and helped develop practical experience in camera performance evaluation and product validation.

AI tools were also used during the preparation of this thesis. Their use was limited to assistance with writing style, spelling and grammar correction, rephrasing for clarity, and support with coding tasks such as debugging, and code structuring. These tools were not used to generate scientific results independently, and all outputs were reviewed, checked, and edited by the author. The final responsibility for the content, analysis, interpretation, and conclusions of this thesis remains entirely

with the author.

This thesis incorporates material from research that I have published in peer-reviewed academic journals. These are Apergis et al. (2025) presented in chapter 2 and Apergis et al. (2026) presented in chapter 4. The following contributions, resources, or pre-existing facilities were provided by others and were not developed by the author:

- The quantum efficiency testing set out in subsection 2.4.7 and subsection 2.5.7 from chapter 2 used a pre-existing hardware set up at Andor Technologies laboratories.
- The software used to control the camera, mount, telescope and observing schedule tasks for the on-sky tests of the Marana CMOS and the Toran 26B camera in chapter 4 and chapter 5 was made by Dr. Paul Chote (see - `https://rockit-astro.github.io/`).
- chapter 6 incorporates material from the recent submission, in May, in MNRAS of the manuscript entitled "NGTS-39 b: A 58 d transiting warm Jupiter in an eccentric orbit". The stellar analysis for NGTS-39, in chapter 6, particularly in subsection 6.4.1 was conducted and written by the co-authors. Additionally, the radial velocities measurements were conducted by the observers as part of the Warm Jupiter program (program numbers are : 112.261U.002, 112.261U.003, 116.28XG.001, 116.29B6.001), who are also co-authors. Moreover, Figure 6.8 in subsection 6.4.3 was made by Alex Romanec and Figure 6.9 in subsection 6.4.4 was made by Toby Rodel, who are also co-authors.

Abstract

Scientific complementary metal-oxide-semiconductor (CMOS) cameras are increasingly being adopted as competitive alternatives to Charge-Couple Device (CCD) detectors for astrophysical observations. CMOS sensors offer significantly faster readout speeds while achieving performance characteristics comparable to high-quality CCD cameras. In this thesis, a CMOS camera is investigated through extensive laboratory and on-sky characterisation following the EMVA 1288 standard.

Chapter 2 presents the baseline characterisation of the Marana CMOS camera. The results show that the Marana performs comparably to CCD detectors while offering substantially faster readout speeds, however it shows high dark current which displays a noticeable amplifier glow pattern.

Chapter 3 provides an extended characterisation of the camera, focusing on the high dynamic range (HDR) imaging mode, which is produced by two independent gain channels. These channels are analysed separately to study their individual performance, and the camera voltages are tuned to optimise detector performance. Additional investigations include image lag measurements and the impact of temperature and illumination wavelength.

In Chapter 4, the Marana CMOS camera is tested on-sky using the Next Generation Transit Survey (NGTS) telescope and compared with the existing iKon-L CCD detector under identical observing conditions, telescope configuration, and data reduction pipeline. The Marana CMOS achieves similar photometric precision to the CCD, reaching 500 ppm on 30-minute timescales for a T = 10 mag star. Despite the CCD's relatively higher quantum efficiency in the NGTS filter, the CMOS camera's faster readout allows it to collect about 20 % more photons per unit time, giving slightly better performance in the photon-limited regime. Overall, the Marana CMOS is shown to be well suited for astronomical time-series photometry.

Chapter 5 presents the characterisation of the Andor Toran-26B CMOS camera through laboratory and on-sky observations. Laboratory measurements show low dark current and read noise and no detectable amplifier glow. The camera was installed on the TWIST telescope to evaluate its photometric performance. In low noise (LN) mode, the detector is free from significant systematic noise and is primarily limited by sky background and target photon noise. In high well capacity (HWC) mode, the performance for faint targets becomes limited by read noise.

Finally, Chapter 6 presents the discovery and characterisation of NGTS-39 b (TIC 453147896 b), a warm Jupiter-size exoplanet transiting a Sun-like star with an orbital period of 58.2 days and with eccentric orbit ($e = 0.386 \pm 0.019$). The target was first identified by Transiting Exoplanet Survey Satellite (TESS) and later confirmed with NGTS. Follow-up spectroscopic measurements where conducted with HARPS and CORALIE instruments. The planet has a radius of $1.088 \pm 0.012\,R_J$ and a mass of $1.467 \pm 0.081\,M_J$. Its equilibrium temperature is 519^{+6}_{-5} K, placing it between short-period hot Jupiters and colder Jupiter-like gas giants. The radial velocity data show a linear trend of $\dot{\gamma} = -17.75\,\mathrm{m\,s^{-1}\,yr^{-1}}$, which indicates the presence of an outer companion.

Abbreviations and quantities

Abbreviations

ARRAKIHS Analysis of Resolved Remnants of Accreted galaxies as a Key Instrument for Halo Surveys

AO Adaptive Optics

APS Active Pixel Sensor

BJD Barycentric Julian Date

BLS Box-fitting Least Squares

BSI Back-Side Illuminated

CMOS Complementary Metal-Oxide Semiconductor

CoRoT Convection, Rotation, and planetary Transits

CTL Candidate Target List

CTOI Community TESS Object of Interest

DACE Data Analysis Center for Exoplanets

DVR Data Validation Report

EB Eclipsing Binary

ELT Extremely Large Telescope

ESA European Space Agency

ESO European Southern Observatory

ESPRESSO Echelle SPectrograph for Rocky Exoplanets and Stable Spectroscopic Observations

ExoFOP Exoplanet Follow-up Observing Program

FFI Full Frame Image

FSI Front-Side Illuminated

FWHM Full-Width Half Maximum

HARPS High Accuracy Radial velocity Planet Searcher

IAU International Astronomical Union

JWST James Webb Space Telescope

MAGIC Major Atmospheric Gamma Imaging Cherenkov Telescope

MOA Microlensing Observations in Astrophysics

NGTS Next Generation Transit Survey

NIRPS Near-InfraRed Planet Searcher

OGLE Optical Gravitational Lensing Experiment

PDC(SAP) Pre-search Data Conditioning (Simple Aperture Photometry)

PLATO PLAnetary Transits and Oscillations of stars

PPS Passive Pixel Sensor

PSF Point Spread Function

QE Quantum Efficiency

RM Rossiter-McLaughlin effect

RV Radial Velocity

SAP Simple Aperture Photometry

SCExAO Subaru Coronagraphic Extreme Adaptive Optics

SPOC Science Processing Operations Centre

TBJD TESS Barycentric Julian Date

TCE Threshold Crossing Event

TESS Transiting Exoplanet Survey Satellite

TFOP TESS Follow-up Observing Program

TIC TESS Input Catalog

TOI TESS Object of Interest

TPF Target Pixel File

TRIDENT TRopIcal DEep-sea Neutrino Telescope

TSM Transmission Spectroscopy Metric

TTV Transit Timing Variation

VLT Very Large Telescope

WASP Wide-Angle Search for Planets

Quantities

$\mathbf{R}_{\oplus}$ Earth radius: 6371 km

$\mathbf{M}_{\oplus}$ Earth mass: 5.972×10^{24} kg

$\mathbf{R}_{J}$ Jupiter radius: 71,492 km

$\mathbf{M}_{J}$ Jupiter mass: 1.898×10^{27} kg

$\mathbf{R}_{\odot}$ Solar radius: 695,000 km

$\mathbf{M}_{\odot}$ Solar mass: 1.988×10^{30} kg

$\mathbf{L}_{\odot}$ Solar luminosity: 3.846×10^{26} W

$\mathbf{S}_{\odot}$ Solar insolation: 1360 Wm^{-2}

AU Astronomical unit: 1.496×10^{8} km

pc Parsec: 3.086×10^{13} km

Chapter 1

Introduction

"He who must be a creator in good and evil—truly,
he must first be a destroyer and break values. Thus
the highest evil belongs to the highest goodness:
but this is the creative goodness."

'Thus Spoke Zarathustra', Friedrich Nietzsche,
1883

The development of astronomical detectors has been fundamental to the progress of modern astrophysics, transforming the ability of astronomers to observe, measure, and interpret the Universe. From the earliest use of the human eye, to photographic plates, and later to advanced electronic detectors such as Charge-Coupled Device (CCD) and Complementary Metal-Oxide Semiconductor (CMOS) sensors, each technological step has enabled increasingly precise and sensitive observations. The importance of CCD technology was recognised by the 2009 Nobel Prize in Physics, which was awarded in part for the invention of the CCD sensor (Boyle & Smith, 1970). These innovations have not only expanded humanity's view of the cosmos but have also driven many of the most significant discoveries in astronomy. Astronomical digital detectors were key to the observations that led to many Nobel Prizes in Physics, including the discovery of the accelerating Universe via monitoring Type-Ia supernova (Riess et al., 1998; Perlmutter et al., 1998), the discovery of exoplanets (Mayor & Queloz, 1995), and the discovery of the super massive black hole at the centre of the Milky Way (Genzel et al., 2010). Indeed, many landmark achievements in modern astronomy have been made possible by advances in detector technology, underscoring the critical role that instrumentation plays in shaping scientific understanding of the Universe.

1.1 Early astronomical detectors

This section refers to the employment of the first photon detectors in astronomy, starting with the human eye, the earliest instrument used to observe and record the night sky, followed by the introduction of photographic plates, which enabled the permanent capture and quantitative analysis of celestial objects. It then proceeds to the development of photomultiplier tubes, marking a major technological leap by allowing highly sensitive and electronic detection. Together, these

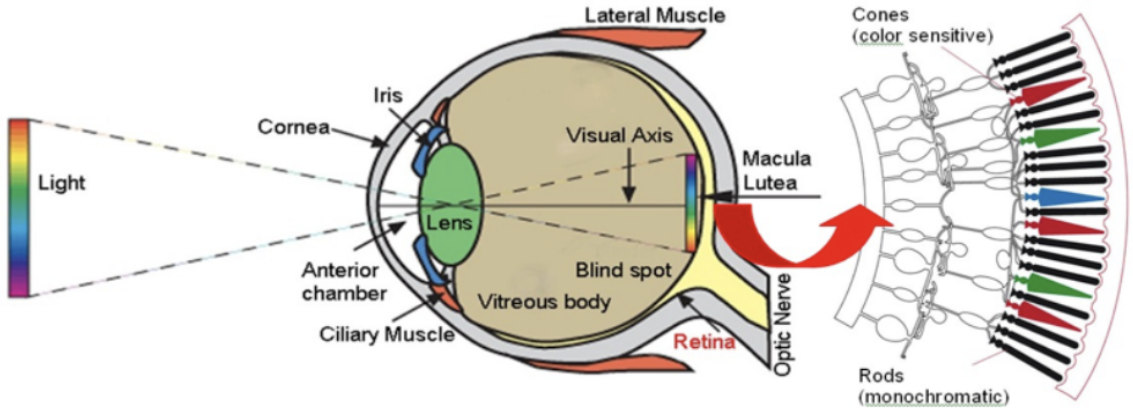


Figure 1.1: Cross-section of the human eye. Image adapted from (Iwert & Delabre, 2010).

advancements illustrate the transition from purely visual observations to increasingly sophisticated, quantitative techniques that laid the foundation for modern astronomical instrumentation.

1.1.1 The Human eye

The first astronomical detector was not invented but is inherent to humans: the eye. It served as the earliest instrument for observing the night sky, enabling astronomers such as Hipparchus to classify stellar brightness on a scale from first to sixth magnitude, with first magnitude corresponding to the brightest stars. The human eye operates as a photon detector, where incoming light is focused by the cornea and lens onto the retina, and converted into electrical signals by photoreceptor cells (rods and cones). Rods are responsible for low-light vision and dominate under dark-adapted conditions, while cones enable colour vision under brighter conditions (Birney et al., 2006). The eye has an effective quantum efficiency (QE) of approximately 10 % (Rose & Weimer, 1989) and it is sensitive in the optical spectral range in the range of 380-750 nm (Schnapf et al., 1987; Cao, 2012) with higher reflectance towards the red wavelengths (Van Norren & Tiemeijer, 1986). An example diagram of the human eye is demonstrated in Figure 1.1.

Its performance is limited by factors such as non-linear response, sensitivity only in the optical regime, low dynamic range, and the inability to integrate or store incoming signals over long periods (Schnapf et al., 1987; Rose & Weimer, 1989; Cao, 2012). Despite these constraints, astronomers in the renaissance and modern era, such as Galileo Galilei, Tycho Brahe, and William and Caroline Herschel relied entirely on visual observations to record the positions, brightness, and motions of celestial objects. The reliance of the human eye on instantaneous perception ultimately highlighted the need for permanent and quantitative recording methods, motivating the development of photographic plates and, later, electronic detectors.

1.1.2 The Photographic plates

Since the human eye could not store information from astronomical observations, and paper-based methods proved difficult and inefficient, the need for a more reliable detector became evident. In the second half of the 19th century, photographic plates were introduced as a solution to this problem, initially as part of the wider search for improved photography (Norman, 1938). The earliest versions



Figure 1.2: Orion Nebula, captured with a 36-inch telescope, taken by Andrew Ainslie Common with 1 h exposure on February 26th 1883.

used glass plates coated with light-sensitive silver halide emulsions suspended in collodion (Ranyard, 1874; Gill, 1887; Stokley Jr, 1923). However, these wet plates had to be prepared and developed immediately and could only be used while still wet, which limited exposure times and made them impractical for astronomical observations (Lankford, 1984). A major breakthrough came in 1871, when collodion was replaced with gelatin as the binding medium for silver halide crystals (Maddox, 1871). This gelatin dry plate process could be prepared in advance and stored until exposure, which made it highly suitable for long astronomical exposures. An example of an image with a photographic plate with long exposures is shown in Figure 1.2. By the late 19th and early 20th centuries, dry gelatin plates had become the standard material for astronomical imaging Lankford (1984); Staubermann (2004).

Photographic plates offered greater sensitivity than the human eye and enabled wide-field imaging and long exposures, leading to major astronomical discoveries such as Phoebe (Pickering, 1899), Pluto (Tombaugh, 1946), the establishment of galaxy classification (Hubble, 1926), the accurate modelling of point-spread functions (Moffat, 1969), and the 1919 solar-eclipse observations that

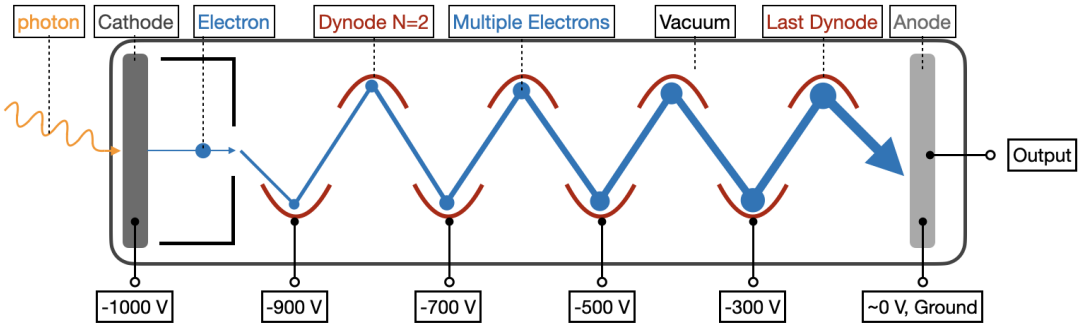


Figure 1.3: An example of a photomultiplier tube. An incoming photon (yellow) strikes the cathode (dark grey), releasing an electron (blue). This electron is successively multiplied as it interacts with the dynodes (red), before ultimately being collected at the anode (light grey). The voltage potential between the dynodes is indicated with values in the lower black rectangles and it is for reference only. The dark dashed lines indicate the label of each element of the photomultiplier.

confirmed Einstein's prediction of the gravitational deflection of light by the Sun (Dyson et al., 1920) However, each exposure required a new plate, making observations time-consuming, and their overall sensitivity was limited by very low QE, which is the which is the ratio of incoming to detected photons, typically ranging from 0.5 % to 1.5 % (Marchant & Millikan, 1965). In addition, the finite depth of the photographic emulsion introduced further complications, as bright stars or stars embedded in bright backgrounds were not always recorded linearly, making precise photometry more difficult (Moffat, 1969).

1.1.3 The Photomultiplier tubes

The need of higher QE and a wider sensitivities across the visible spectrum led engineers to produce Photomultiplier tubes (PMTs) for imaging (Iams & Salzberg, 1935; Zworykin et al., 1936). PMTs became widely used in astronomy during the mid-twentieth century, particularly for photoelectric photometry. Unlike photographic plates, PMTs did not produce images, but provided highly sensitive measurements of stellar brightness (Kitchin, 2020). PMTs were found to be very efficient for photon counting while they have extremely fast response with a sensitivity in the UV and Optical region (Kapusta et al., 2007). The PMT is vacuum shielded. On the one end it has a window to admit photos, and the cathode, while on the other end is the anode along with some electrical pins to supply with voltage. An example of a PMT is shown in Figure 1.3. The cathode is typically a flat metal surface made alkali-based semiconductor that converts the photon into an electron via the photoelectric effect (Einstein, 1905). The electron moves to a positive potential and interacts with an electrode known as dynode. This process continues as a chain process. Every time the electron hits the dynode more electrons are produced and so on. Dynodes are acting as electron multipliers are also made of alkali-based semiconductor and typically they have a potential difference between each other in order to accelerate the generated electrons (Kapusta et al., 2007). The electrons finally end up in the anode. This is the last electrode that collects all the electrons (Chromey, 2010).

Compared to photographic plates, PMTs offer a faster temporal response, on the order of nanosec-

onds, along with much higher sensitivity, with typical QEs in the range of 25 % to 40 % (Kapusta et al., 2007; Ko & Lee, 2015). They can detect faint signals, down to the single-photon level, and their electronic output allows direct digital readout and processing. These measurements, however, come at the cost of spatial information. A PMT is essentially a single-pixel detector, meaning it cannot capture two-dimensional images without mechanical scanning or the use of arrays. Furthermore, PMTs operate at high voltages, which can increase dark current and thereby limit their detectability.

Today, the use of PMTs has become more limited, as most modern astronomical instruments rely primarily on CCD sensors. Nevertheless, PMTs remain essential in specialised applications, such as neutrino detection at the IceCube Neutrino Observatory (IceCube Collaboration, 2013) and the TRopIcal DEep-sea Neutrino Telescope (TRIDENT) experiment (Zhang et al., 2024). They are also employed in gamma-ray astronomy by instruments such as the Major Atmospheric Gamma Imaging Cherenkov Telescope (MAGIC), which uses PMTs to detect very high-energy gamma rays and to search for potential dark matter signals (Bigongiari, 2005; Hahn et al., 2023).

In these observatories, the relevant signal is often a brief flash of light produced when a high energy particle, or the secondary particle shower that it generates, passes through the atmosphere (Bigongiari, 2005; Han & Brandt, 2023), ice (IceCube Collaboration, 2013), or water (Zhang et al., 2024) faster than light can propagate through that medium. This emission, known as Cherenkov radiation (Cerenkov et al., 1934; Frank & Tamm, 1991), can contain only a small number of photons and occurs on nanosecond timescales. Detectors therefore require high internal gain, low noise, single-photon counting, and fast timing response. PMTs are especially valuable in these photon-limited applications because the arrival time and intensity of individual photons can be used to reconstruct the direction, energy, and possible origin of the primary particle.

1.2 Semiconductor digital detectors

Semiconductor physics provide the foundation for modern astronomical detectors. From the photo-electric effect, concepts such as band theory and p–n junctions enable the creation of photodiodes and transistors, which amplify and process these signals Howell (2000). Together, these advances allow the digitisation of astronomical information, forming the basis of CCD and CMOS detectors used in contemporary astronomy.

1.2.1 Band theory

Based on their electronic band structure and electrical conductivity, solid materials are commonly classified as conductors, semiconductors and insulators (Huebener, 2019). Each case represents how feasible it is for the material to generate, sustain, and transport electric current upon the application of an external voltage or exposure to electromagnetic radiation. As show in Figure 1.4, the difference of energy states the electrons can take is presented as the valence and the conduction band. The Fermi level represents the energy of the electrons at absolute zero temperature (T=0 K) and it is defined as the lowest energy the electrons can take in the material.

In metals, the energy bands overlap enabling a large number of free-moving electrons within the structure, which is the primary reason for their high electrical conductivity. Additionally, since these electrons are not bound to specific energy states, they cannot be effectively separated based on

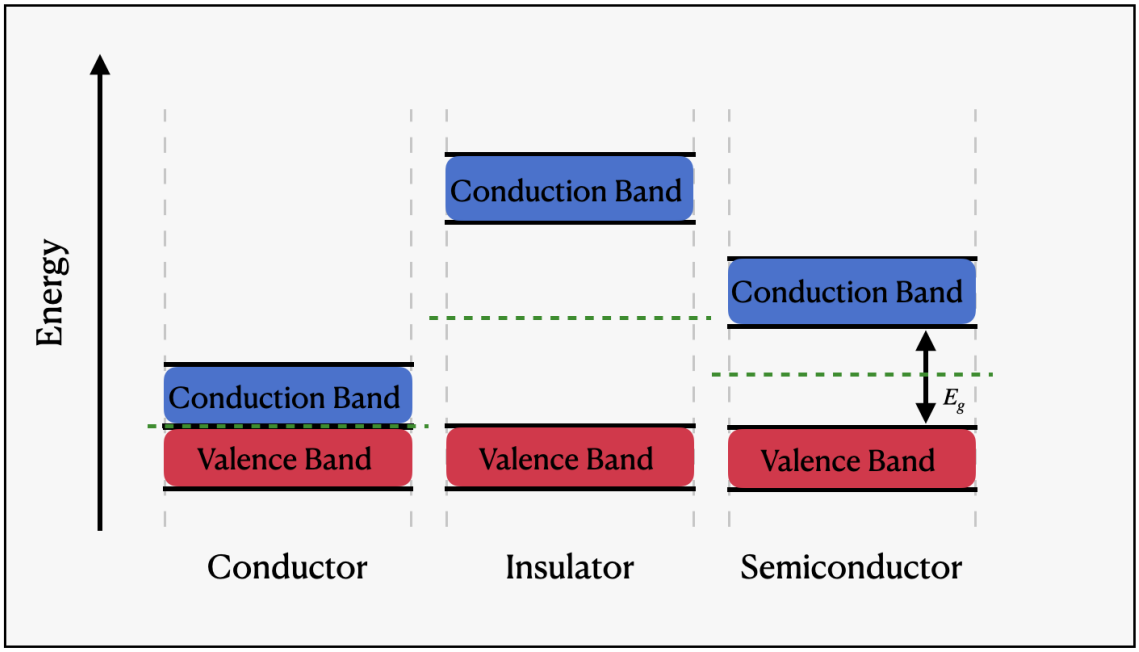


Figure 1.4: Band scheme for Solids. On the **left** is the valance and conductive band for metals, on the **middle** for insulators and on the **right** for semiconductor materials. The Fermi level is marked with the green-dashed line.

charge. Instead, they move freely throughout the material, leading to increased kinetic energy and consequently heat dissipation (Ashcroft & Mermin, 1976; Kittel, 2004).

In contrast, insulators have energy bands that are separated by a wide band gap, representing an energy range where no electrons can exist, the forbidden regions (Kittel, 2004). Electrons can only transition to the conduction band if they receive sufficient external energy to overcome this gap, making insulators poor conductors under normal conditions.

Semiconductors exhibit properties intermediate between metals and insulators, depending on the application. The valence band is filled with electrons that maintain the lattice structure, while the conduction band remains unoccupied. If the band gap is sufficiently small, an external energy source such as incident light, can excite electrons into the conduction band, allowing them to flow and enabling semiconductors to act as conductors. This energy is known as excitation energy (E_g), as indicated for the semiconductor case in Figure 1.4.

Silicon materials have been widely used in astronomy as image sensors thanks to their semiconductive properties. Unlike with the insulators, the band gap is shorter, requiring less energy. This is feasible with heat or with incident light. The excited electrons, known as carriers and therefore free to move, will shift to the conduction band while the empty and unoccupied space left on the valence band known as holes.

For semiconductor detectors, photon energies are commonly expressed in electron-volts (eV), since photo-detection occurs through the generation of electron-hole pairs. In silicon, a photon with energy greater than or equal to the band-gap energy can promote an electron from the valence band to the conduction band. At 300 K, silicon has a band-gap energy of approximately 1.12 eV, corresponding to a long-wavelength cut-off of $\lambda_{\text{cut}} = hc/E_g \simeq 1107$ nm (Strehlow & Cook, 1973; Sze et al., 2021; Stefanov, 2022). For optical photons, a single absorbed photon typically generates

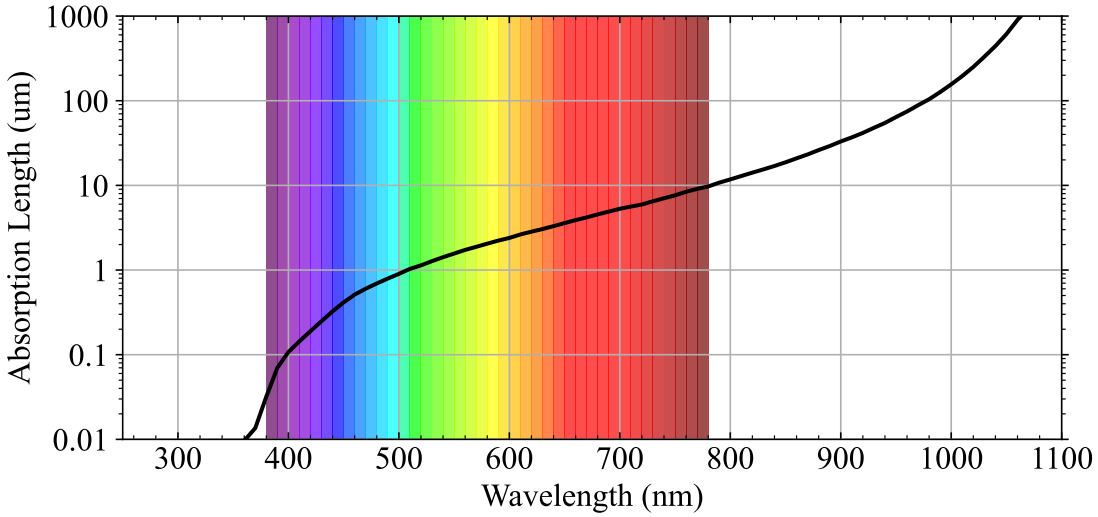


Figure 1.5: Absorption length of incident photons in silicon as a function of wavelength, shown by the black solid line. Visible wavelengths are colour-coded according to their wavelength. The data were adapted from Green (2008).

one electron-hole pair, with any excess energy above the band gap dissipated through thermalisation processes (Scholze et al., 2000; McLean, 2008; Stefanov, 2022). At much higher photon energies, such as in the extreme-ultraviolet or X-ray regimes, a single photon can generate multiple electron-hole pairs, resulting in a non-linear relation between photon number and collected charge. In the optical regime, however, the interaction of photons with silicon is strongly wavelength dependent. Shorter wavelength photons are absorbed close to the silicon surface, while longer wavelength photons penetrate deeper into the detector before being absorbed. This behaviour is described by the absorption length, which represents the characteristic depth over which incident photons are absorbed in silicon. As shown in Figure 1.5, the spectral response of silicon makes it highly sensitive across the visible and near-infrared (NIR) regions, making it well suited for optical astronomical observations.

1.2.2 Device Fabrication

The electrical properties of silicon detectors are further controlled through doping, in which impurity atoms are introduced into the silicon lattice (Pearson & Bardeen, 1949). These impure elements possess either one fewer (trivalent) or one additional (pentavalent) electron in their valence band than silicon does (Streetman & Banerjee, 2015; Sze et al., 2021).

A trivalent dopant has three valence electrons. Examples include boron, aluminium, gallium, and indium. When a trivalent atom replaces a silicon atom in the lattice, it can form only three complete covalent bonds. This leaves one bond effectively short of an electron, creating a hole. These dopants are called acceptors, because they can accept an electron from the lattice. This produces p-type silicon. A pentavalent dopant has five valence electrons. Examples include phosphorus, arsenic, and antimony. When a pentavalent atom replaces a silicon atom, four of its electrons form covalent bonds with neighbouring silicon atoms, while the fifth is only weakly bound. This extra electron can

be easily released into the conduction band. These dopants are called donors, because they donate electrons. This produces n-type silicon (Streetman & Banerjee, 2015; Sze et al., 2021).

The choice of dopant depends on the application. This modification alters the electrical properties of silicon. When free electrons dominate, the material becomes n-type silicon, whereas an abundance of holes results in p-type silicon. In contrast with Figure 1.4, for n-type the Fermi level is close to the conduction band while for p-type the Fermi level is close to the valence band.

The fabrication of n-type and p-type silicon requires advanced semiconductor processing techniques to manufacture integrated circuit devices. This process begins with thermal oxidation, where a layer of silicon dioxide (SiO_2) is grown on the silicon surface to act as an insulator. During this process, the lattice structure is deformed leading to imperfections and defects in the $Si - SiO_2$ interface. These defects can trap and de-trap electrons leading to significant increase of dark current and noise contribution.

Next, lithography is applied to define the desired circuit pattern. This involves coating the wafer, a thin slice of semiconductor material typically made of silicon, with a photoresist material that selectively masks specific regions of the silicon surface (Jaeger, 1987).Following lithography, etching is performed. This technique directs ionised particles onto the silicon substrate with controlled momentum, facilitating a chemical interaction that removes atoms in a precisely defined pattern (Henry et al., 2010). Through etching, specific layers of silicon are stripped away to prepare the surface for doping.

Finally, the electrical properties of the silicon are modified by controlled doping, which may be achieved through diffusion or ion implantation (Sequeda, 1985). Ion implantation (also backside processing, see section 1.3) can introduce lattice damage or non-uniformities, and the wafer is therefore annealed to repair implantation-induced damage and electrically activate the dopants (Sequeda, 1985; Boyd & Wilson, 1980; Poate, 2012). In some thinned, back-illuminated CCDs, non-uniformities associated with the backside laser-annealing process can produce a spatially structured photo-response pattern. This effect is most apparent at blue and near-UV wavelengths, where photons are absorbed close to the detector surface (see Figure 1.5), making the measured response particularly sensitive to surface and backside-processing variations. Such blue-wavelength photo-response non-uniformities, often appearing as diamond- or brick-wall-like patterns in flat-field images, have been reported for astronomical CCDs (Stern et al., 1989). A similar pattern is visible in the left panel of Figure 1.6, which shows a blue flat-field image obtained with the blue-sensitive CCD camera on the Warwick 1 m telescope[1].

1.2.3 The *p*-*n* junction

In an n-type semiconductor, the Fermi level shifts closer to the conduction band, increasing the number of available electron energy states. Since the valence band contains numerous electrons, these energy levels facilitate the excitation of electrons into the conduction band when an external energy source is applied, thereby enabling electrical conductivity. Conversely, in a p-type semiconductor, the Fermi level moves closer to the valence band. This results in an abundance of holes, allowing electrons to move between them, which in turn enables the material to conduct electricity.

[1] Image provided by Morgan Mitchell, private communication.

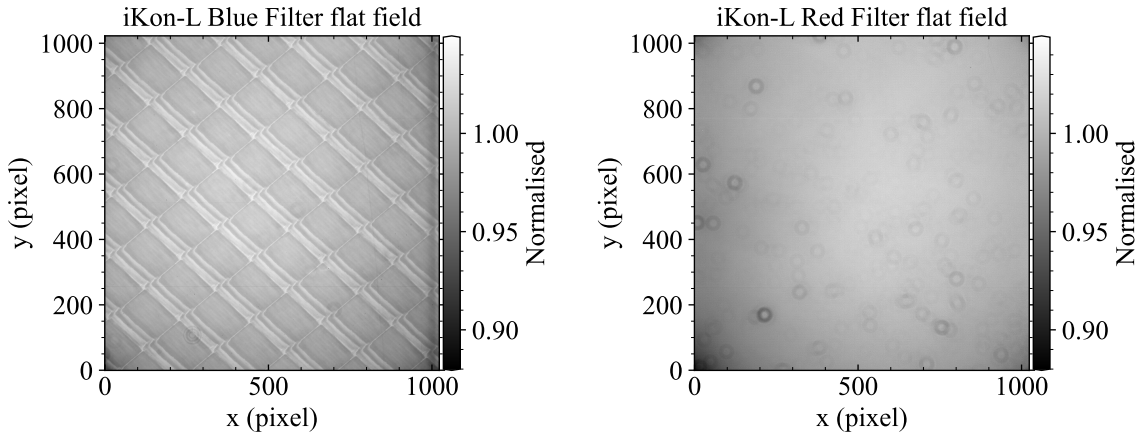


Figure 1.6: A stacked and normalized flat field image captured with an iKon-L CCD blue and red cameras during evening with the Warwick 1 Meter telescope. Images have been binned on-chip by a factor of 2×2. On the **left** flat image with the blue filter and on the **right** flat image with the red filter. Off-focus circles due to dust particles on the optics are also evident on both images.

When n-type and p-type materials are brought into contact, they form a p-n junction. Electrons from the n-type region diffuse into the p-type region, where they recombine with holes. Similarly, holes diffuse from the p-type region into the n-type region and recombine with electrons. This diffusion leaves behind fixed ionised donor atoms on the n-type side and fixed ionised acceptor atoms on the p-type side. As a result, the region near the junction becomes depleted of mobile charge carriers and is known as the depletion region, as shown in grey shaded area in Figure 1.7. The exposed ions create an internal electric field, which opposes further diffusion of charge carriers and establishes equilibrium across the junction.

The formation of the depletion region is also associated with band bending. At equilibrium, the Fermi level becomes constant across the junction, while the conduction and valence bands bend due to the built-in electric potential. If an electron-hole pair is generated within or near the depletion region, the internal electric field separates the carriers: electrons are swept toward the n-type region and holes toward the p-type region. This charge separation is the basic operating principle behind photodiodes and semiconductor imaging detectors (Janesick et al., 1987; Streetman & Banerjee, 2015; Sze et al., 2021).

Since the depletion region is free of charge, any electron captured after the silicon wafer is exposed to light originates (but not solely) from the incident photons and can be accurately collected (Kittel, 2004). The electric field will be generated and can be managed and controlled by applying a voltage. For the purpose of charge collection the additional generated holes will be ignored since the collection time is much slower than electrons (Sze et al., 2021; Stefanov, 2022).

1.2.4 The Photodiode and Field Effect Transistors

To detect photoelectrons, a semiconductor device requires a photosensitive region, known as the photodiode, where the generated charge is initially collected. The structure consists of an electrode (an electrical conductor, also known as gate) positioned above the SiO_2, while the substrate houses the p-n junction. The built-in electric field directs electrons toward the electrode for collection, while holes migrate deeper into the silicon, where they eventually recombine.

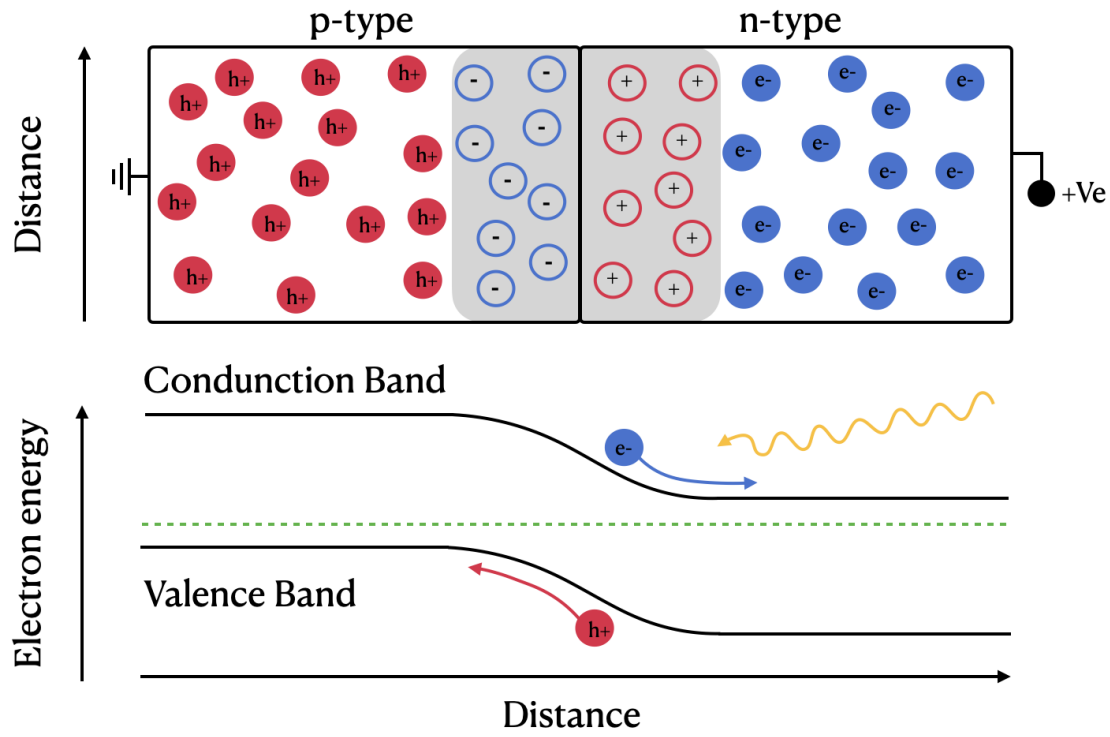


Figure 1.7: A visualisation of a p-n junction when bringing n-type with p-type semiconductors in contact. The diagram on the **top** shows the p-type that has excess of holes while the n-type excess of electrons. The depletion region is created in the middle where only positive and negative ions are in presence. The same diagram but with energy levels shown in the **bottom** with the presence of a photon (yellow) producing an electron-hole pair. The Fermi level shown with the green dashed line.

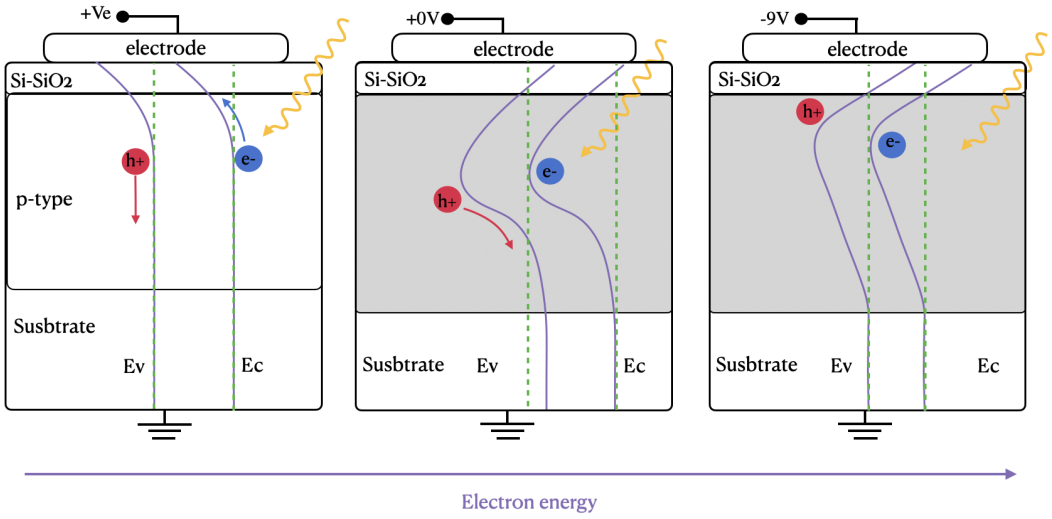


Figure 1.8: Semiconductor channel devices. On the **left** the surface channel device and on the **middle** is the buried channel device, with the deep depletion area coloured with grey. On the **right** is the buried channel but reverse bias The energy band structure is shown with purple. The yellow curly arrow indicates a photon.

Early channel devices collected electrons near the $Si - SiO_2$ interface. By applying a positive voltage to the electrode, a temporary n-type inversion layer was formed, allowing electron accumulation. However, due to significant interface defects, many electrons became trapped and subsequently re-emitted, resulting in increased dark current (Aberle et al., 1992).

To mitigate this issue, the buried channel device was introduced by Boyle & Smith (1970), incorporating an n-type layer beneath the silicon oxide layer. This innovation enabled the formation of a p-n junction (see subsection 1.2.3), allowing photoelectrons to be efficiently detected and collected (Weckler, 1965, 1967). The n-type is connected to a positive voltage in order to attract the electrons. Since electrons will be moved to the positive voltage in the p-n junction, the n-type is acting as a charge storage capacitor as shown in Figure 1.7.

By applying a zero/negative voltage to the electrode, electrons are repelled from the surface, preventing them (but not eliminating the effect completely) from interacting with defect states Walden et al. (1972) due to the potential well created as shown in the right diagram of Figure 1.8 (Emonts & van Dort, 1993). This method also widens the depletion region and creates a potential well beneath the surface. The applied voltage establishes a reverse bias. On the opposite side, if positive voltage is connected to the p-type then the condition is forward bias. Practically, the condition is reversed biased until the n-type and p-type is completely depleted. This buried channel architecture was foundational to the development of the first CCDs, revolutionizing various applications, including astronomical imaging (Boyle & Smith, 1970; Janesick et al., 1987).

Beside the significant contribution to astronomical imaging with CCDs sensors, the buried channel had limitations. For instance, charge was remaining within the photodiode resulting in an incomplete charge transfer (Dyck & Jack, 1974). The effect is known as image lag (see details in section 3.5). In addition, short-wavelength (blue) photons have a small absorption length in the silicon (see Figure 1.5), meaning they are absorbed very close to the surface. In these shallow

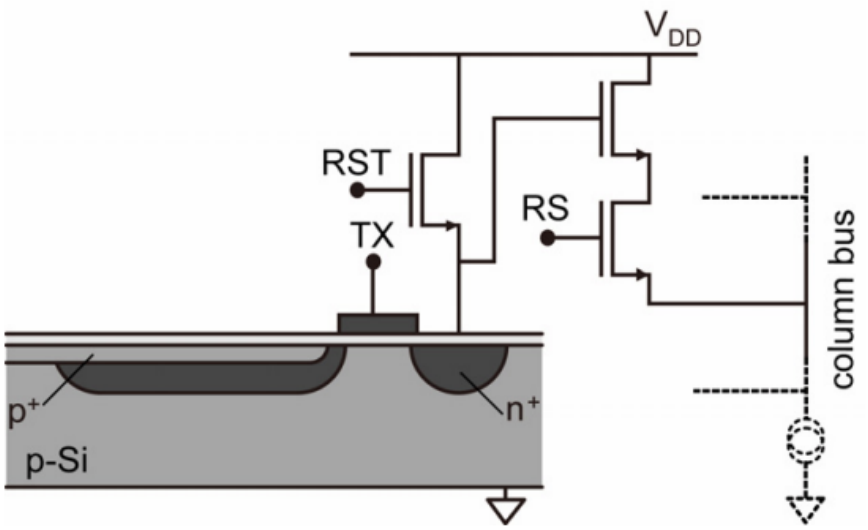


Figure 1.9: Basic configuration of a pinned photodiode, also showing as a single pixel structure. The installation of the p+ is below the surface of the photodiode. The circuit diagram represents the transistor structure (see in Figure 3.1 for details). The schematic is taken from Theuwissen et al. (2006).

regions, the generated electron–hole pairs may recombine before being collected, reducing the QE at blue wavelengths (Fossum & Hondongwa, 2014). Additionally, defects on the SiO_2 interface were impacting the charge transfer process by introducing extra electrons that were de-trapped from the defects contributing as dark current.

The solution that was proposed was an installation of a heavy dopped p+ layer (Teranishi et al., 1982) below the $Si - SiO_2$ layer, decreasing drastically the image lag and trapping of the charge carriers and the generation and recombination of electrons under the Shockley-Read-Hall (SRH) process was minimized (Shockley & Read, 1952; Aberle et al., 1992; Teranishi, 2016). This new structure, as shown in Figure 1.9, is called pinned photodiode (PPD; Burkey et al., 1984). Since its a p-type layer, another p-n junction is created between the p+ and n- layers resulting in higher capacitance (Teranishi et al., 1982). Today, most of the astronomical image sensors are using PPDs as the photosensitive surface in order to detect and capture photons.

1.3 CCD image sensors

In a Charge-Coupled Device (CCD), generating photoelectrons in the photodiode is only the first step. The accumulated charge must be transported across the pixel array to a readout amplifier. This charge transfer is accomplished using clocked metal–oxide–semiconductor field-effect transistor (MOSFET) structures fabricated directly in the silicon. A MOSFET consists of two n-type regions (the source and drain) embedded in p-type silicon. When a voltage is applied to the gate electrode, an electric field induces an inversion layer beneath the oxide, creating a conductive channel. In a CCD, several such gates are arranged in sequence to form a series of potential wells. By clocking the gate voltages in a controlled sequence, these potential wells shift laterally, allowing packets of charge to be passed from one pixel to the next, in a serial fashion, until they reach the output amplifier.

An example of the CCD architecture is shown in Figure 1.10. Once the charge reaches the readout node, it is converted into a voltage signal proportional to the number of electrons collected in each pixel. Since the voltage amplifier is not integrated within the pixel, CCDs are consider passive pixel sensors. This analog voltage is then digitized by an analog-to-digital converter (ADC), producing a discrete digital value for each pixel that can be stored, processed, and analysed. The precision of the ADC, typically defined by its bit depth, sets the dynamic range and quantization noise of the final digital image. For a typical astronomical image this is usually 16-bit depth (Howell, 2000; Chromey, 2010).

With these notable adjustments and the potential for using these devices as solid-state imaging systems, NASA's Jet Propulsion Laboratory (JPL) commissioned a large program to develop CCDs for astronomical applications (Janesick et al., 1987). In 1970's, ground-based observatories started to utilise CCDs as image sensors (Smith, 1976). An example of a modern CCD (model CCD270 (Verhoeve et al., 2016) for the upcoming PLATO mission (Rauer et al., 2025) detector is shown in Figure 1.11.

While a CCD pixel is often depicted as a simple square, it is actually a complex structure consisting of the photodiode, multiple polysilicon gates, clocking electrodes, insulating oxides, and metal interconnects. Only the photodiode area is truly photosensitive; the ratio of this area to the total pixel area is called the fill factor. Detectors where most of the electronics are located on the surface exposed to light are known as front-side illuminated (FSI) detectors. These sensors were initially used in astronomical applications, but their architecture limits the fill factor and, consequently, the QE. Incoming photons must pass through the network of electrodes and metal wiring before reaching the silicon, and some photons may be absorbed or reflected by the electronics and never generate signal electrons. This effect, together with the limited fill factor, constrains the sensitivity of FSI sensors. Over the years, CCD technology has undergone significant improvements to enhance photon collection and overall QE. One of the first major innovations was the integration of microlenses over each pixel, which focus incoming light onto the photodiode while minimizing reflection from the metal wiring (such as the gates), boosting QE to around 70 % (Holst & Lomheim, 2011; Stefanov, 2022; Durnez et al., 2023).

To further increase the sensitivity, CCDs evolved to back-side illuminated (BSI) architectures, in which the silicon substrate is thinned and illuminated from the rear. This design eliminates obstructions from front-side electronics, significantly increasing the fill factor and improving QE.

The production of a BSI sensor requires that the back surface of the CCD be exposed to light. This is achieved by flipping the sensor so that the bulk silicon faces the incident light, while the electronic structures remain on the opposite side and are not exposed. The bulk silicon is then thinned through chemical etching (see details in subsection 1.2.2), progressively removing material until only the depletion region remains. Backside illumination was not common in the earliest CCDs because it required reliable wafer thinning and backside surface passivation, both of which were technically challenging (Hoenk et al., 2009; Fernandez-Moroni et al., 2020) [2]. This is the active region where incoming photons generate electrons (Holland et al., 2007). By eliminating the front-side obstructions, BSI sensors achieve effective fill factors approaching 100 %, allowing light

[2]Early CCDs were therefore typically front illuminated, despite losses from the gate structures, while backside illuminated devices became practical only after fabrication processes improved

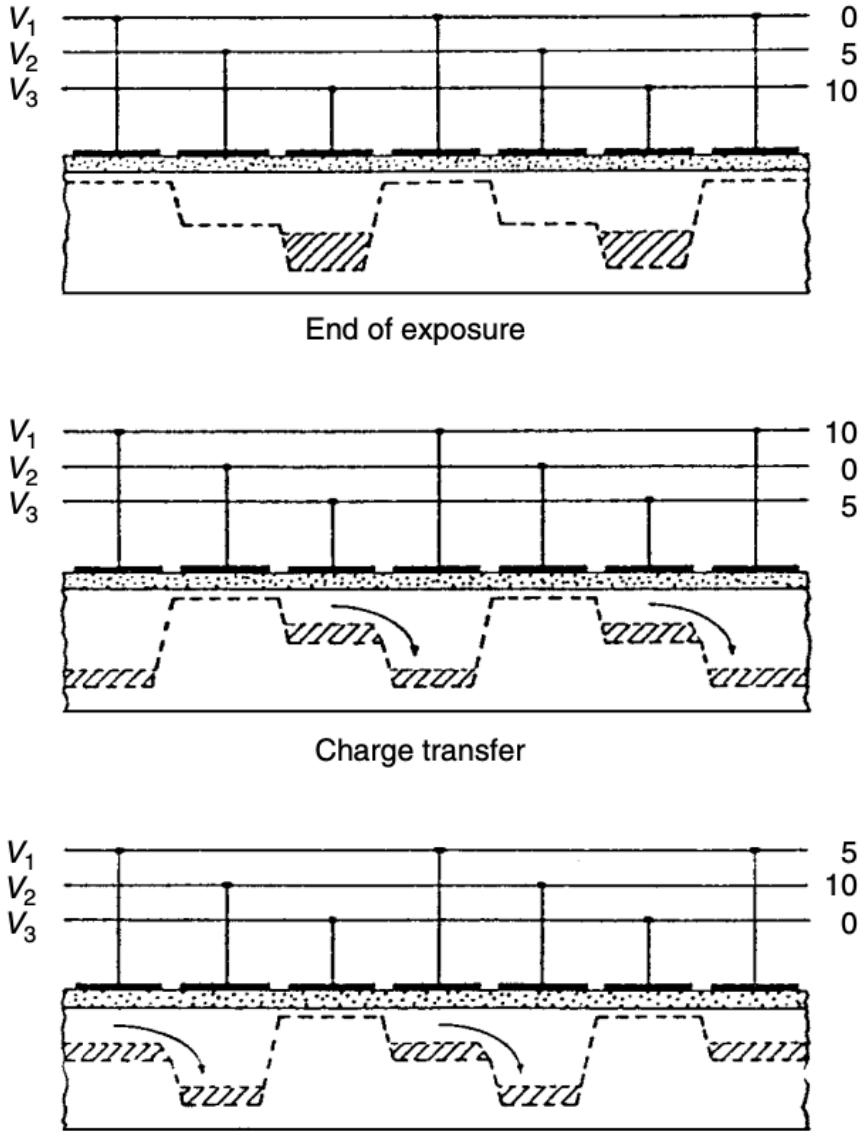


Figure 1.10: Schematic representation of the CCD pixels. Each panel illustrates a different clocking phase applied to the same group of pixels. The electrodes, labelled V_1, V_2, and V_3, are arranged in a repeating three-phase pattern across the CCD columns. During the initial clock cycle (top panel), the photo-generated charge is confined within potential wells beneath one set of electrodes. In the subsequent phase, the applied voltages are changed so that a new potential well is formed under the adjacent electrode (e.g., V_1 held high while V_2 is driven low), causing the charge packet to shift to the neighbouring pixel. By sequentially modulating the electrode potentials, the charge is transferred in a controlled, parallel manner toward the serial register for readout. Image from Walker (1987).

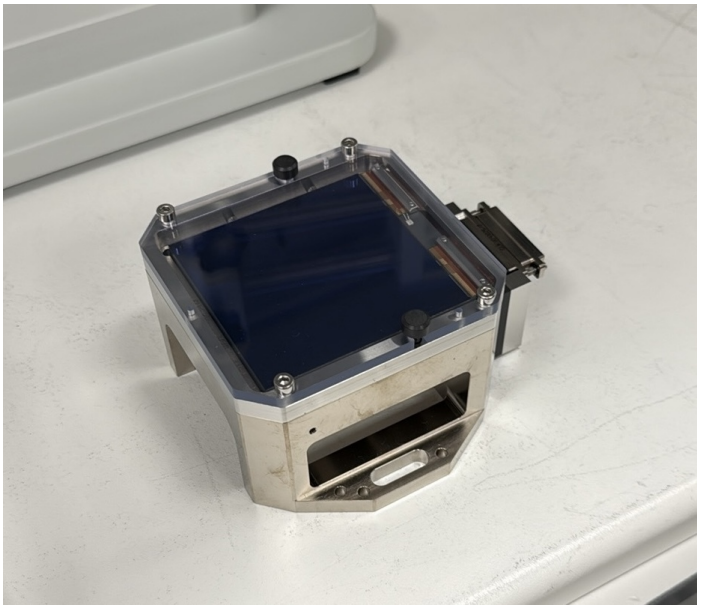


Figure 1.11: An example of a back-side illuminated CCD detector. The model CCD 270-84-2-F15 manufactured from Teledyne e2v, for the upcoming PLATO mission (Rauer et al., 2025). The sensor features a 4510 × 4510 pixels with pixel rate of 4 MHz and with <28 electrons read noise. The sensor has ∼ 95 % QE at 650 nm.

to interact directly with the silicon. The architectural differences between front-side illuminated (FSI) and back-side illuminated sensors are illustrated in Figure 1.12.

In BSI CCDs, the silicon substrate is thinned and illuminated from the reverse side, allowing incident photons to reach the photosensitive region without obstruction from front-side wiring and gate structures. This configuration significantly enhances the QE, particularly at shorter wavelengths where absorption occurs close to the surface. The thickness of the silicon substrate also plays a crucial role in determining spectral response: while thinner devices improve blue sensitivity, increasing the substrate thickness allows photons with longer wavelengths to be absorbed more efficiently, thereby extending sensitivity into the near-infrared and broadening the operational spectral range (Peckerar et al., 1979, 1981; Tsoi et al., 1985; Gimeno et al., 2016). An example is presented in Figure 1.13, which compares the QE curves of a BSI illuminated and a FSI illuminated CMOS detector. The BSI sensor exhibits an increase in QE of approximately 50 % relative to the FSI device. Both cameras employ thinned silicon layers, resulting in high sensitivity in the blue–green spectral region. However, at longer (redder) wavelengths, photons may traverse the thinned silicon without being fully absorbed, leading to a decline in QE toward the near-infrared, which is also evident in Figure 1.13.

The development of CCDs in the early 1970s, and their first successful application to astronomy in the mid-1970s at Mount Lemmon's 154-cm telescope, marked a major turning point in observational astrophysics (Smith, 1976; Janesick et al., 1987; Gunn et al., 1987; Oke et al., 1988). Compared to photographic plates and photomultiplier tubes, CCDs offered significant advantages. Their pixelated architecture forms a two-dimensional array, enabling direct imaging with precise spatial information. Furthermore, CCDs produce digitised data with a high dynamic range, allowing both faint and bright sources to be recorded simultaneously within the same exposure. Continued technological improvements have also broadened their QE, making CCDs highly sensitive across much of the

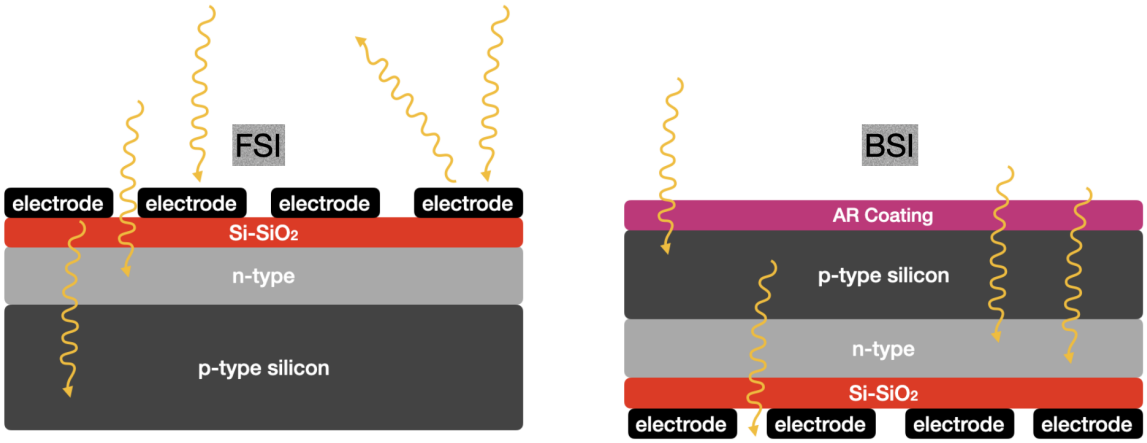


Figure 1.12: Schematic illustration of a CCD device sliced perpendicular. On the left panel is the front side illuminated CCD, and on the right panel is a back-side illuminated CCD. The incoming light is marked with the yellow curved arrow. This demonstration also shows light that interacts directly with the silicon, reflected from the wirings (i.e. electrodes) or not interacting at all.

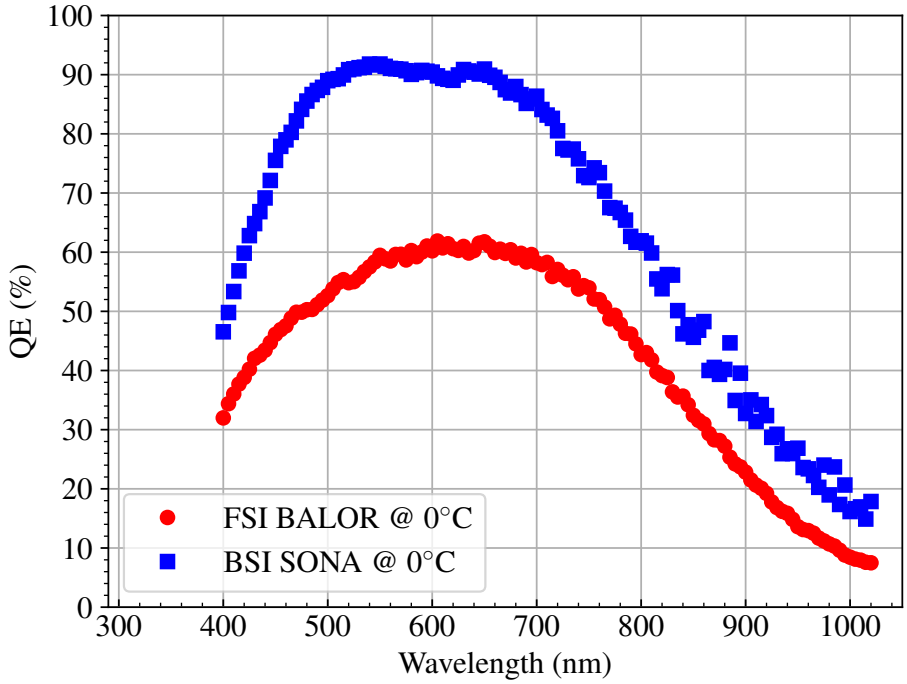


Figure 1.13: Comparison of QE curves for two different sensor architectures. The QE measured at 0 °C of an FSI sensor (blue circles), installed in the Balor camera from Andor Technology, is shown alongside the QE of a BSI sensor (red squares), integrated in the Sona camera from Andor Technology.

optical wavelength range and establishing them as the dominant detectors in modern astronomy.

1.4 CMOS image sensors

Alongside CCD technology, Complementary Metal-Oxide-Semiconductor (CMOS) detectors were also developed. CMOS devices share many similarities with CCDs, as both are fabricated using silicon substrates with doped regions and rely on the same fundamental physical principle, namely the photoelectric effect. Many optimisation techniques originally developed for CCDs over the years have also been successfully implemented in CMOS sensors (i.e. microlenses and BSI architecture, see section 1.3).

The fundamental architecture of a CMOS camera is based on the concept of the active pixel sensor (APS). In contrast to CCDs, where charge is transferred across the chip to a common output node, CMOS sensors integrate most of the readout electronics directly within each pixel. Specifically, every pixel contains a photodiode and a set of transistors, including an in-pixel amplifier that converts the collected charge into a voltage signal locally (see also chapter 2 and chapter 3 for details).

In their early stages, however, CMOS sensors were characterised by relatively large read noise, significant pixel-to-pixel non-uniformities, and crosstalk effects (Tian et al., 1999). As a result, they were initially adopted primarily in the consumer market, driven largely by the rapid expansion of smartphone production over the past decades. Nevertheless, CMOS technology offered important advantages, including low manufacturing cost and reduced power consumption. Subsequent architectural innovations substantially reduced read noise, in some cases to levels below those of typical CCDs (Hynecek, 1997; Teranishi & Mutoh, 1986). Furthermore, the implementation of dual readout channels (Inoue, 1999; Yonemoto et al., 2000; Fossum & Hondongwa, 2014) enabled an extended dynamic range comparable to that of CCD detectors (see also introduction in chapter 2. These performance improvements led to the development of what are now commonly referred to as Scientific CMOS (sCMOS) sensors.[3]

The parallel readout architecture of CMOS sensors is enabled by column-level circuitry. After in-pixel charge-to-voltage conversion, the signal is routed to column-parallel analog-to-digital converters (ADCs) integrated on the sensor. Because amplification occurs within each pixel and digitisation is performed in parallel along the columns, the overall readout process is significantly faster than in CCDs (Inoue, 1999; Yonemoto et al., 2000; Fossum & Hondongwa, 2014). An illustration of a CMOS array is presented in Figure 1.14.

The high readout speed is one of the principal advantages of CMOS cameras over CCDs. This architecture also consumes significantly less power than CCD technology, as it employs multiple amplifiers-typically one per column-allowing signals to be read out in parallel. This eliminates the need to transfer charge sequentially across the entire array, as required in CCDs, thereby reducing power consumption and increasing efficiency (Stefanov, 2022). Modern CMOS sensors achieve very low read noise levels without compromising readout speed, unlike CCDs where lower noise is often obtained at the expense of slower readout. This enhances their sensitivity and makes them well suited for the detection of faint astronomical sources.

Additionally, the integration of transistors within each pixel (see chapter 3) allows flexible readout

[3]In this thesis, the term CMOS refers to Scientific CMOS unless otherwise specified.

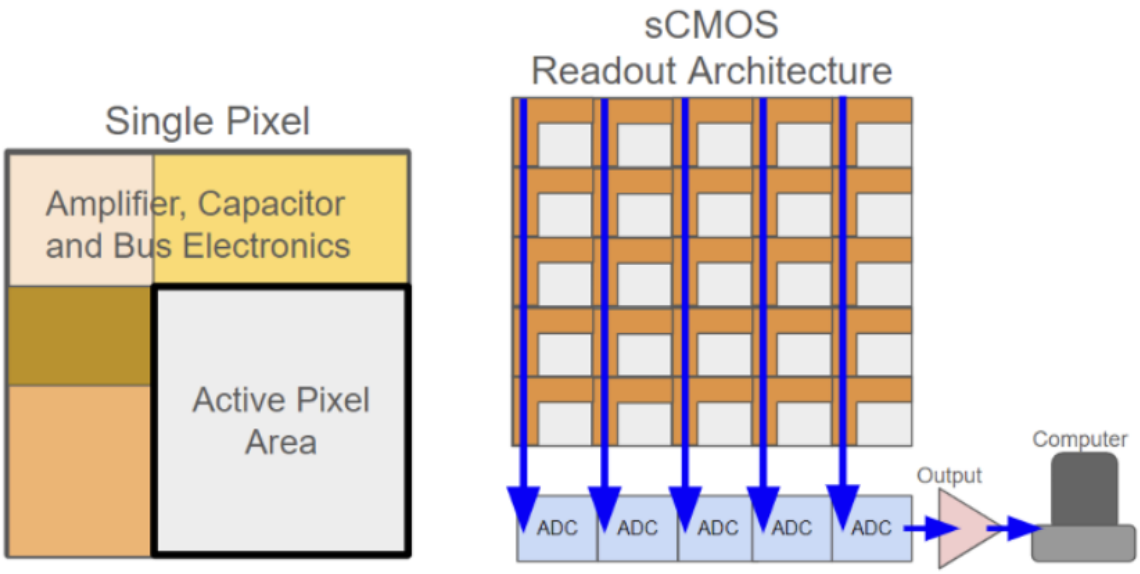


Figure 1.14: Artist's illustration of a CMOS pixel (left) and a CMOS pixel array (right). Each pixel contains a photodiode (active area), an in-pixel amplifier, a capacitor, and the associated transistors responsible for charge transfer and readout. The CMOS architecture enables parallel signal transfer, where pixel signals are routed column-wise to integrated ADCs converters before being fully digitized and transmitted to the computer. Note that this illustration represents a FSI CMOS sensor. Image adopted by Axiom Optics.

schemes, including rolling or global shutter operation, eliminating the need for a mechanical shutter in many applications. In a rolling shutter configuration, the sensor is read out sequentially, typically on a row-by-row basis, such that different parts of the image are exposed at slightly different times. In contrast, a global shutter exposes all pixels simultaneously and then reads out the entire frame, ensuring that the image corresponds to a single instant in time (Lauxtermann et al., 2007).

Currently, CMOS devices are available in both FSI and BSI architectures. In both cases, the depletion region is typically fabricated to be relatively thin, resulting in enhanced sensitivity in the blue-green spectral range. In recent years, efforts have focused on increasing the thickness of the depletion region to improve absorption at longer wavelengths. This development aims to produce CMOS sensors with enhanced red and near-infrared sensitivity, and such deep-depletion CMOS technologies are currently under active development (Rhodes et al., 2009; Lahav et al., 2020; Vici et al., 2020).

1.5 Characteristics of CMOS and CCD devices

To evaluate whether a camera is suitable for scientific applications, particularly in astronomy, it is essential to define the key parameters that influence the quality of the data acquired through a telescope. Both CCD and CMOS detectors are characterised by fundamental instrumental properties that determine their overall performance. For both types of sensors, these fundamental parameters are largely the same, allowing for a direct and meaningful comparison between different camera systems.

1.5.1 Read Noise

Since the collected charge is first amplified, converted into a voltage signal, and subsequently digitized into digital units, the readout process inevitably introduces fluctuations originating from the electronic circuitry. These fluctuations arise primarily from the output amplifier, column amplifiers (in CMOS sensors), and the ADC converter (Howell, 2000). This noise contribution is known as read noise, and it is an intrinsic component of the readout process in all solid-state detectors. Read noise sets the minimum detectable signal of the sensor and therefore defines the noise floor of the system.

1.5.2 Dark Current

During the integration time, thermal energy within the silicon lattice can generate electrons even in the absence of incident photons (Shockley & Read, 1952; Aberle et al., 1992; Stefanov, 2022). This thermally generated signal is referred to as dark current. Dark current accumulates linearly with exposure time and increases strongly with temperature. For this reason, astronomical detectors are typically cooled to reduce thermal electron generation.

1.5.3 Non-uniformities

No detector is perfectly uniform across its pixel array. Variations in fabrication and pixel electronics introduce pixel-to-pixel non-uniformities (Stefanov, 2022). Such non-uniformities introduce fixed-pattern noise, which can be mitigated through calibration procedures such as flat-field and dark-frame corrections (Howell, 2000).

1.5.4 Saturation

Each pixel can store only a finite number of electrons before saturation occurs. This limit is known as the full well capacity (Howell, 2000). Once the pixel reaches this capacity, additional charge cannot be properly stored, leading to saturation and possible blooming. Full well capacity directly impacts the detector's dynamic range. The dynamic range is the ratio of the full well capacity to the read noise.

1.5.5 Linearity

Linearity describes how accurately the detector response is proportional to the number of incident photons. An ideal detector exhibits a linear response over its full operating range (Howell, 2000; Chromey, 2010; Stefanov, 2022). However, near saturation or at very low signal levels, deviations from linearity may occur due to amplifier limitations, charge transfer inefficiencies and image lag (Teranishi et al., 1982; Teranishi, 2016; Stefanov, 2022).

1.6 Planets and Exoplanets

Following the discovery and space exploration of the Solar System, the question naturally arose as to whether planetary systems exist around other stars. The search for such systems has transformed modern astrophysics, leading to the discovery of thousands of exoplanets and revealing a remarkable

diversity in their physical and orbital properties. In this section, I first provide a brief historical overview of the planets in the Solar System. I then discuss the emergence of exoplanet discoveries, with particular emphasis on Jupiter-like exoplanets, and the principal detection techniques currently employed to identify and characterise planets beyond the Solar System.

1.6.1 The Solar System

When observing the night sky under dark conditions, the planets of the Solar System can be readily distinguished from the background stars due to their steady brightness and apparent motion. This was already recognised by ancient Babylonian astronomers, who carefully recorded the movements of these "wandering stars" (Sachs, 1974). Later, ancient Greek scholars identified the planetary nature of Mercury, Venus, Mars, Jupiter, and Saturn, distinguishing them from the fixed stars[4].

The establishment of the heliocentric model by Nicolaus Copernicus in the 16th century provided a revolutionary framework that placed the Sun at the centre of the Solar System, with the planets orbiting around it[5]. This model resolved many inconsistencies of the earlier geocentric system and laid the foundation for modern planetary astronomy.

In 1781, William Herschel discovered Uranus using a refracting telescope, marking the identification of the seventh planet in the Solar System (Pasachoff & Olson, 2011). The final major addition came in 1846, when the mathematical calculations of Urbain Le Verrier predicted the existence of another planet influencing Uranus's orbit. This prediction led to the observational confirmation of Neptune by Johann Galle in 1846 (Galle, 1846). Subsequently, in 1930, Pluto was discovered (later reclassified as a dwarf planet; Soter 2006). Although this discovery was initially considered a confirmation of Percival Lowell's hypothesis of a trans-Neptunian planet (Lowell, 1915), Pluto was later found to be too low in mass to account for the predicted perturbations. Lowell had interpreted these apparent perturbations as evidence for an unknown planet beyond Neptune, but later work showed that they were mainly due to inaccurate observational data and an incorrect estimate of Neptune's mass rather than Pluto's gravitational influence (Standish, 1993).

1.6.2 Exoplanets

Planets that exist outside the Solar System are referred to as exoplanets. According to the International Astronomical Union (IAU), an exoplanet is defined as a body with a true upper mass limit of $13\,M_J$, corresponding to the threshold for deuterium thermonuclear fusion (Lecavelier des Etangs & Lissauer, 2022). Such an object may orbit a star, a brown dwarf, or a stellar remnant. Regardless of its formation mechanism, any object meeting this criterion is classified as an exoplanet (Lecavelier des Etangs & Lissauer, 2022).

It was obvious that since the Solar system contains planets, therefore any other star in space may also accommodate exoplanets. It was not until the end of 20th century where the first exoplanet was detected, orbiting a pulsar star (Wolszczan & Frail, 1992). Pulsars are characterised by the

[4]The Babylonians already recognised and recorded the five naked-eye planets. The Greeks developed the terminology and theoretical interpretation.

[5]Although a heliocentric model had already been proposed by Aristarchus of Samos in the 3rd century BCE, it did not gain traction in the ancient world because it conflicted with the prevailing Aristotelian physics, lacked observable evidence for the expected annual stellar parallax, and did not provide the mathematical predictive power of the established geocentric models.

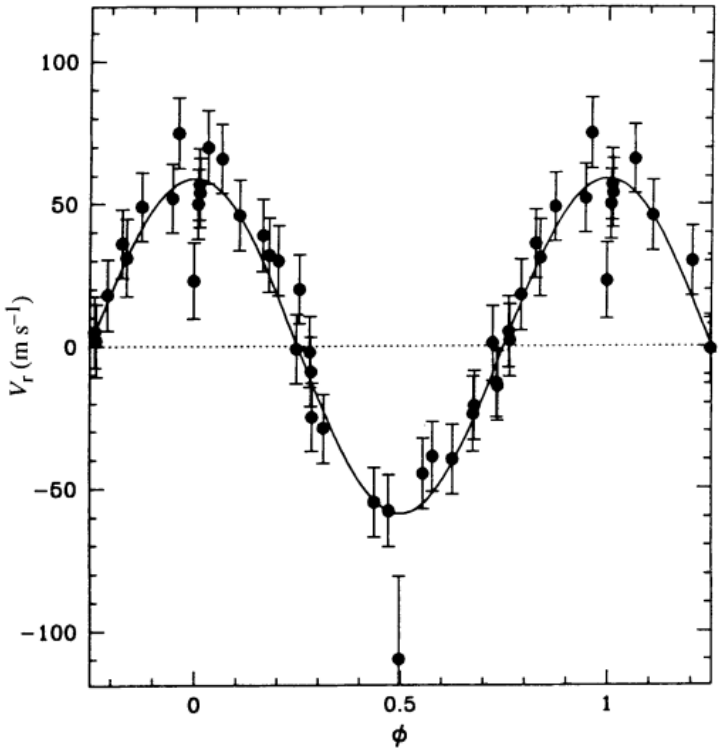


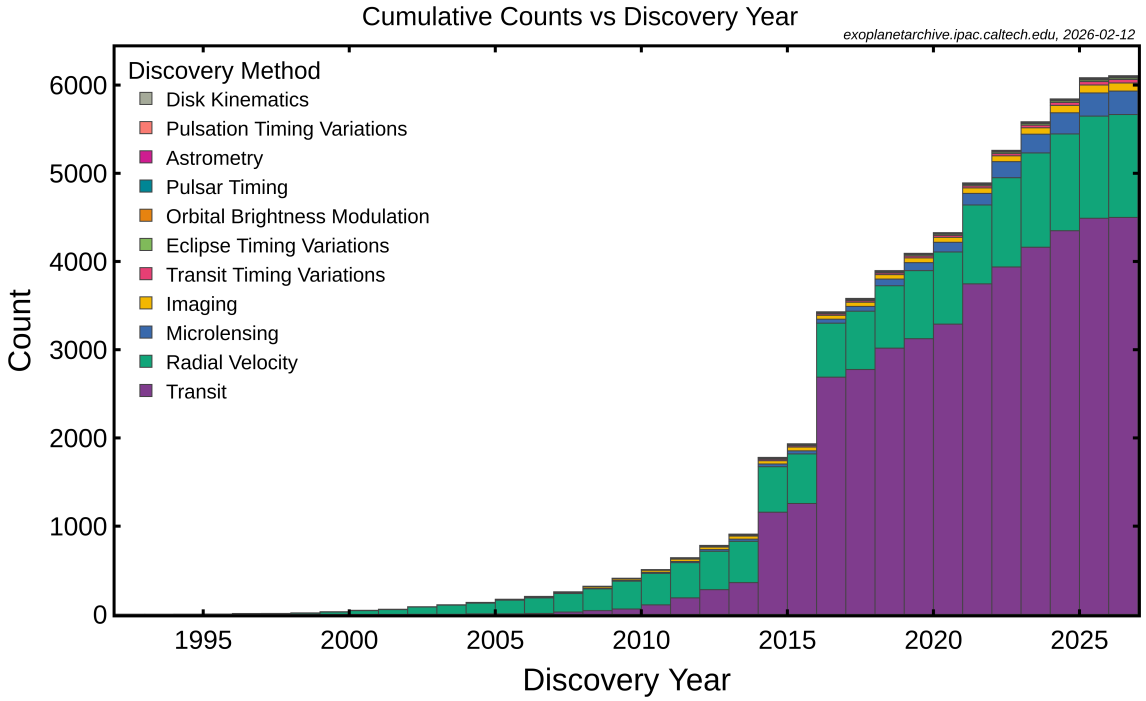
Figure 1.15: Phase-folded radial velocities measurements for the system 51 Pegasi. Figure from (Mayor & Queloz, 1995).

periodic pulses emitted and captured via radio telescope. The exoplanet was detected by measuring the small variations in the periodic arrival times of the pulses indicating the gravitational influence of two orbiting planets. Subsequently, the first exoplanet orbiting a Solar-type star, 51 Pegasi b, was discovered (Mayor & Queloz, 1995). The planet was detected using the Doppler technique, through precise radial velocity measurements (see details in subsection 1.6.4). 51 Pegasi b is a gas giant with an orbital period of 4.23 days and a minimum mass of 0.47 M_J. The corresponding radial velocity curve of the host star is shown in Figure 1.15.

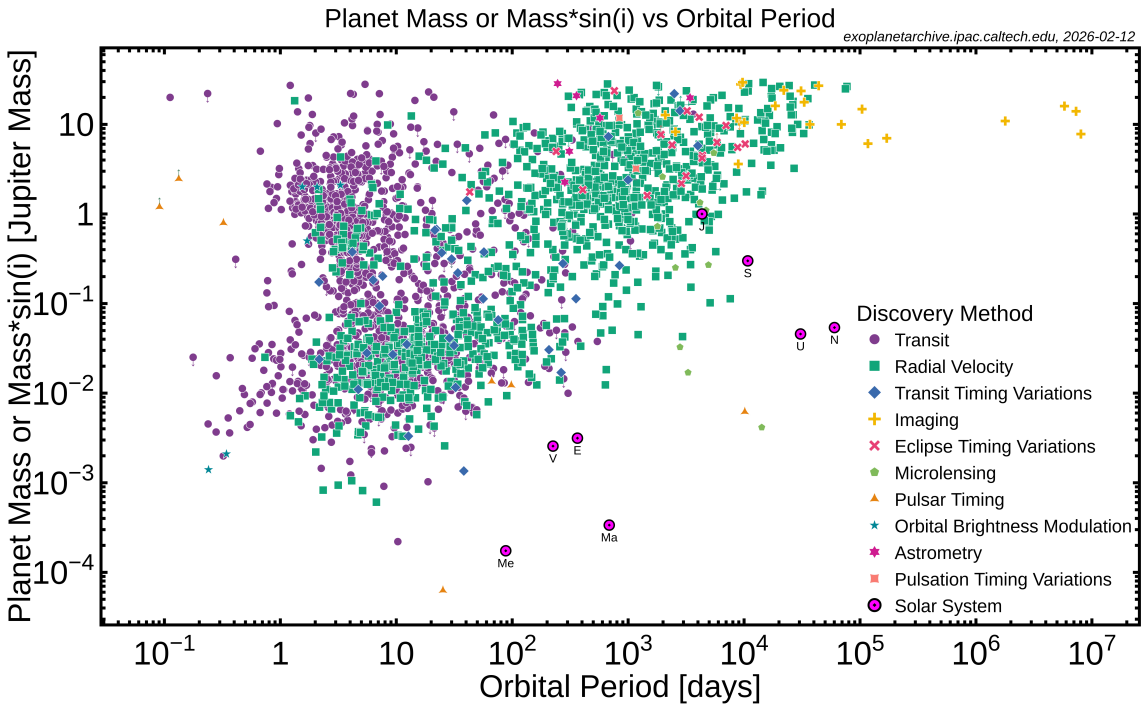
Today, more than 30 years after the first detection, thousands of exoplanetary systems have been discovered, revealing a remarkable diversity of planetary architectures. Advances in optical instrumentation, covering a wide spectral range, have enabled the detection and detailed characterisation of these planets. To date, over 6000 confirmed exoplanets[6] have been identified, and this number continues to grow rapidly, as illustrated in the upper panel of Figure 1.16.

This population is illustrated in the lower panel of Figure 1.16, which shows the distribution of confirmed exoplanets in the mass–orbital period plane, including both measured and minimum masses. It is evident that the majority of these exoplanets occupy regions of parameter space that are very different from the planets of the Solar System. This highlights both the diversity of exoplanetary systems and the importance of continuing to explore these largely uncharted regions, which differ significantly from the architecture of the Solar System. In addition, observational biases-arising from the limitations of current optical instruments and detection methods-also influence the

[6]Based on the NASA Exoplanet Archive, `https://exoplanetarchive.ipac.caltech.edu/`, accessed 2026/02/12



(a) Cumulative histogram of exoplanet detections.



(b) Planetary mass as a function of orbital period for confirmed exoplanets.

Figure 1.16: The population of known exoplanets (or minimum mass) from the updated NASA exoplanet archive (2026-02-12) colour-coded by their detection method (Akeson et al., 2013). The highlighted points indicate the planets of the Solar system.

observed distribution (see details in subsection 1.6.3 and section 1.7).

1.6.3 Transits via photometry

The most widely used method for detecting exoplanets is the transit technique, which is based on the same geometric principle observed in the Solar System during transits of Mercury or Venus. A transit occurs when a planet passes in front of its host star, causing a temporary dip in the star's observed brightness for the duration of the passage.

The first exoplanet detected to transit was HD 209458 b (Charbonneau et al., 2000). To measure these variations in stellar brightness, astronomers use photometry (see details in chapter 4), which quantifies the flux received from a star. In an image, the star appears as a point source, and its light is distributed across pixels on the detector. When performed as a time-series, photometric measurements produce a light curve that reveals the characteristic dips caused by transiting planets (Howell, 2000).

This technique became widely adopted in the early 2000s with the development of ground-based facilities designed to observe wide fields and collect stellar light curves. These observatories made significant contributions to exoplanet discovery, including WASP (Pollacco et al., 2006), KELT (Pepper et al., 2018), HATnet (Bakos et al., 2004) HATSouth (Bakos et al., 2013), and later NGTS (Wheatley et al., 2018). Space-based missions were developed to achieve the same goal with higher photometric precision, free from atmospheric effects. Notable examples include Kepler (Borucki et al., 2010), K2 (Howell et al., 2014), CoRoT (Auvergne et al., 2009), TESS (Ricker et al., 2015) and the upcoming PLATO mission (Rauer et al., 2025).

However, not all exoplanets produce observable transits. This method depends strongly on the system's geometry; the planet's orbit must be aligned such that it passes along the line of sight from Earth. In particular, the orbital inclination must be close to 90 deg (edge-on) so that the planet crosses in front of its host star and blocks a detectable fraction of the starlight. Additionally, the planet must be sufficiently large relative to the star for the resulting dip in brightness to be measurable (this also depends on the precision of the instrument).

Detecting exoplanets via the transit method does not provide a direct measurement of the planet's mass, which is essential for confirming its planetary nature. For this reason, transit photometry is typically combined with other techniques, such as the radial velocity method (see subsection 1.6.4), in order to determine the planet's mass and hence its bulk density.

Despite not yielding the mass, transit observations provide a wealth of valuable information. When the planet begins to cross the stellar disk, the moment at which the stellar brightness first starts to decrease is known as ingress (first contact). Similarly, when the planet finishes crossing the star and the stellar brightness returns to its original level, this stage is called egress (last contact). These phases, along with the rest of the transit geometry, are illustrated schematically in Figure 1.17.

The transit duration is defined as the total time the planet spends passing in front of the star, beginning at ingress and ending at egress. The decrease in stellar flux during the transit, ΔF, is measured relative to the out-of-transit flux, F_0. The ratio is defined as the transit depth, which is directly related to the ratio of the planetary radius to the stellar radius, according to:

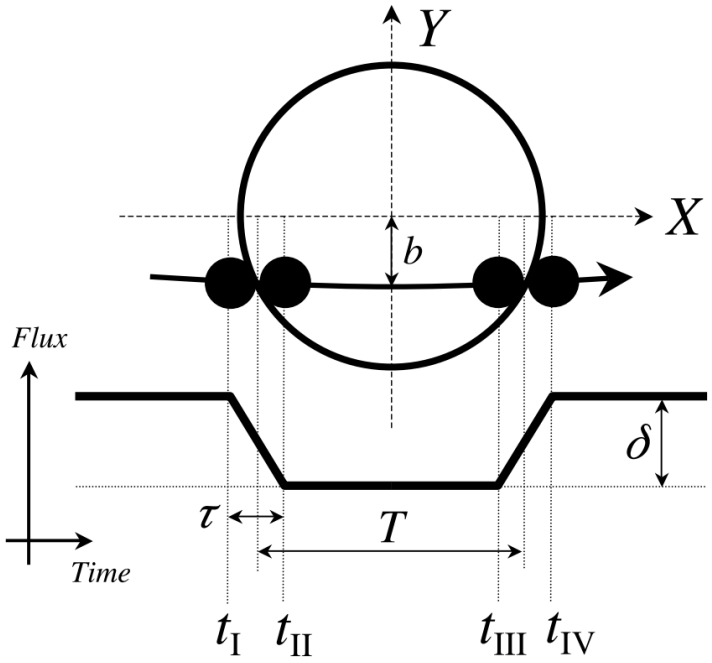


Figure 1.17: Schematic illustration of an exoplanet transiting a host star. The diagram shows the depth δ, impact parameter b, total transit duration between the first contact point of the ingress and the last contact point of the egress, T_{14}, and the full transit duration between the second and third contact, T_{23}. Adapted from Winn (2010).

$$\frac{\Delta F}{F_0} = \left(\frac{R_p}{R_*}\right)^2 . \tag{1.1}$$

Assuming that the stellar parameters are well determined-typically derived from spectral energy distribution (SED) fitting and isochrone modelling-it is then possible to estimate the planetary radius (R_p) from the measured transit depth and the known stellar radius (R_*).

Another important parameter that can be derived from transit observations is the impact parameter b, which describes the transit geometry. In particular, it quantifies how centrally the planet crosses the stellar disk, and therefore depends on the orbital inclination ($\cos i$) of the system. Following the equation described in Winn (2010), the impact parameter is defined as:

$$b = \frac{a \cos i}{R_*} \left(\frac{1 - e^2}{1 + e \sin \omega}\right) \tag{1.2}$$

where the semi-major axis (a) represents the distance between the planet and the host star, e is the orbital eccentricity, and ω is the longitude of periastron. The exact transit condition depends on the ratio of the planetary to stellar radius ($R_p/R_\star$). For $b = 0$, the transit occurs across the centre of the stellar disk, while for $b \approx 1$, the transit occurs near the stellar limb. Only when $b > 1 + \frac{R_p}{R_\star}$ does the planet completely miss the stellar disk and no transit is observed.

For a transit event that repeats periodically, meaning the exoplanet completes a full orbit around its host star between successive events, the orbital period P can be directly determined from the light curve. By measuring the time interval between consecutive mid-transit times (T_c), one obtains

a precise estimate of the planet's orbital period. If multiple transits are observed over a long time baseline, fitting a linear ephemeris as describe in Winn (2010),

$$T_c(n) = T_0 + nP, \tag{1.3}$$

where T_0 represents the time of inferior conjunction, typically corresponding to the mid-time of the first observed transit event. The transit light curve also provides valuable information about the duration of the event. In particular, the full transit duration refers to the time during which the planet is entirely in front of the stellar disk, producing the maximum decrease in stellar brightness and excluding the ingress and egress phases. In contrast, the total transit duration measures the entire event from the first contact, when the planet begins to obscure the star, to the fourth contact, when the planet completely exits the stellar disk. These durations yields the geometric and physical information about the system, allowing constraints on parameters such as the scaled semi-major axis (a/R_*), the impact parameter, the orbital inclination, and, through Kepler's Third Law, even the mean stellar density. Analytic expressions for these relationships are described in Winn (2010), particularly the following

$$b^2 = \frac{(1-\sqrt{\delta})^2 - (T_{23}/T_{14})^2(1+\sqrt{\delta})^2}{1-(T_{23}/T_{14})^2}, \tag{1.4}$$

$$\frac{R_*}{a} = \frac{\pi}{\delta^{1/4}} \frac{\sqrt{T_{14}^2 - T_{23}^2}}{P} \left(\frac{1+e\sin\omega}{\sqrt{1-e^2}} \right). \tag{1.5}$$

While transit photometry alone provides detailed information about the planet, the star's geometry generally offers only limited direct constraints on the orbital eccentricity e. In principle, the combination of the total transit duration (T_{14}), the full transit duration (T_{23}), the orbital period P and the stellar radius R_* can provide some information about e and the argument of periastron ω through the scaling factor $(1 + e\sin\omega)/\sqrt{1-e^2}$ that appears in the expression for R_*/a. However, because the transit shape depends on multiple parameters simultaneously (including the impact parameter b and the radius ratio R_p/R_*), it is generally difficult to disentangle eccentricity from transit photometry alone without additional constraints. To further constrain the eccentricity complementary observations required, particularly radial velocity measurements.

When an exoplanet transits its host star, the observed stellar brightness decreases because the planet blocks a fraction of the star's light. If the stellar surface were perfectly uniform in brightness, the transit would produce a flat-bottomed light curve while the planet fully covers part of the stellar disk. However, observed transits typically show a curved, rather than flat, bottom.

This curvature arises from limb darkening, the phenomenon whereby the outer regions (the limb) of a star appear fainter than its centre. Limb darkening occurs because the effective optical depth depends on the viewing angle. At the centre of the stellar disk, the line of sight probes deeper, hotter, and therefore brighter layers of the stellar atmosphere. In contrast, toward the stellar limb, it intersects higher, cooler, and less dense atmospheric layers, resulting in reduced emergent intensity and a gradual decline in brightness, as illustrated in Figure 1.18.

Moreover, limb darkening is wavelength dependent. At shorter (bluer) wavelengths, the opacity is generally higher than at longer (redder) wavelengths. Consequently, blue light emerges from higher

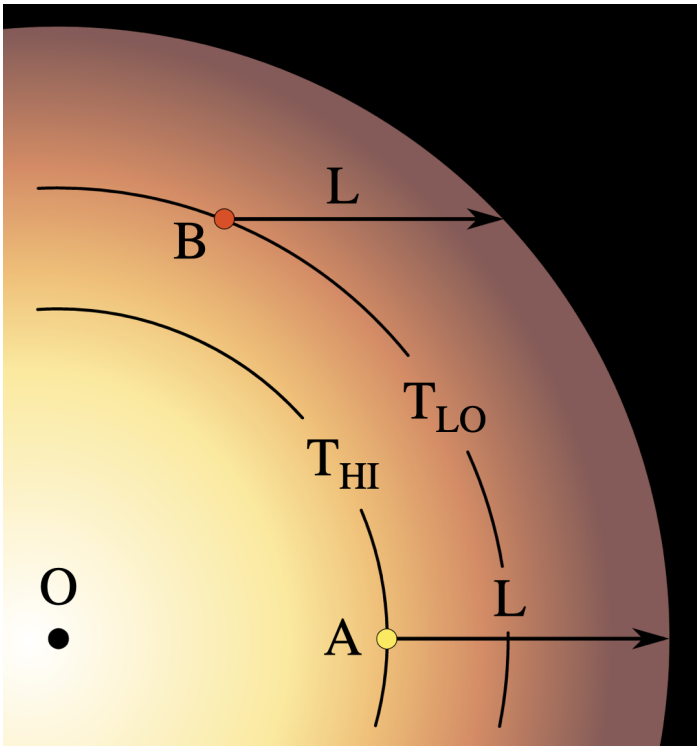


Figure 1.18: A schematic illustration of limb darkening. The radial distance, normalized to unity and labelled L, represents the stellar disk. Photons emerging from point A, located near the centre of the disk (O), originate from deeper, hotter layers of the stellar atmosphere (high temperature, T_{HI}). In contrast, photons emerging from point B, closer to the stellar limb, arise from higher, cooler layers (low temperature, T_{LO}).

and cooler layers of the atmosphere compared to red light. Because these layers are cooler and emit less intensely, limb darkening is typically more pronounced at shorter wavelengths (Hestroffer & Magnan, 1998).

To accurately model the shape of an exoplanet transit light curve, limb darkening must be included through parameterised limb-darkening coefficients based on the characteristics of the host star (Claret & Bloemen, 2011; Parviainen & Aigrain, 2015). These coefficients depend strongly on the wavelength (transit shape is flatter towards red wavelengths) of observation (Hestroffer & Magnan, 1998) and the physical properties of the stellar atmosphere.

1.6.4 Radial velocity

Another widely used technique for detecting exoplanets is the radial velocity (RV) method (Wright, 2018). This method measures variations in the line-of-sight velocity of a star caused by the gravitational influence of an orbiting companion. As the planet and star orbit their common centre of mass, the star exhibits a periodic "wobble" that can be detected as shifts in its spectral lines.

RV measurements are frequently used as complementary observations to photometric transit surveys. While transits provide the planetary radius, RV follow-up enables the determination of the planet's mass. In the absence of inclination information, however, only the minimum mass $M_p \sin i$ can be derived. A landmark example is the first confirmed exoplanet around a Sun-like star, 51 Pegasi b, discovered using RVs (Mayor & Queloz, 1995).

RVs are measured using high-resolution spectrographs, typically mounted on ground-based telescopes, such as CORALIE (Queloz et al., 2001) and HARPS (Pepe et al., 2002) (see further in section 1.8). These instruments disperse the starlight into its constituent wavelengths, producing a spectrum. If the star is moving toward or away from the observer due to the gravitational pull of a planet, its spectral lines experience a Doppler shift. This shift in wavelength is directly related to the star's RV (Sasselov et al., 2020) and forms the basis of the RV detection method. This is expressed as:

$$v_r = \frac{\Delta\lambda}{\lambda} c, \tag{1.6}$$

where the Doppler shift $\Delta\lambda$, the rest wavelength λ and c the speed of light. From this, one can infer other parameters, particularly the periodic modulation of the radial velocity, as well as the semi-amplitude of the radial velocity as shown in Figure 1.19. Those relation are described in Cumming et al. (1999):

$$K = \left(\frac{2\pi G}{P}^{\frac{1}{3}}\right) \frac{M_p \sin i}{(M_* + M_p)^{\frac{2}{3}}} \frac{1}{\sqrt{1-e^2}}, \tag{1.7}$$

where P is the period, G is the gravitational constant, e is the orbital eccentricity, M_p and M_* is the mass of the planet and the star respectively.

Depending on the measured semi-amplitude, RV signals can sometimes correspond to stellar mass companions rather than planetary ones, leading to potential false positives. Large velocity amplitudes are often indicative of binary star systems rather than true exoplanets. However, when RV measurements are combined with photometric transit data, the full set of planetary parameters including mass, radius, and bulk density, can be determined.

1.6.5 Other detection methods

A variety of additional techniques have been developed to detect and characterise exoplanets. In the following section, I briefly describe these additional detection methods.

Astrometry

A method closely related to RV method is astrometry, which measures the orbital motion of a star on the plane of the sky. If the star has a companion, both objects orbit their common centre of mass due to mutual gravitational attraction (Black & Scargle, 1982; Quirrenbach, 2010). Unlike the RV method, which probes motion along the observer's line of sight via the Doppler effect and can be limited by inclination ambiguity, astrometry directly measures the star's positional wobble across the sky, making it a complementary technique. This angular displacement of the star can be expressed as (Sasselov et al., 2020):

$$\alpha = \frac{a}{d}\left(\frac{M_p}{M_*}\right), \tag{1.8}$$

where a is the orbital semi-major axis of the planet, d is the distance to the system, M_p is the planet's mass, and M_* is the stellar mass. Astrometry is particularly sensitive to massive planets

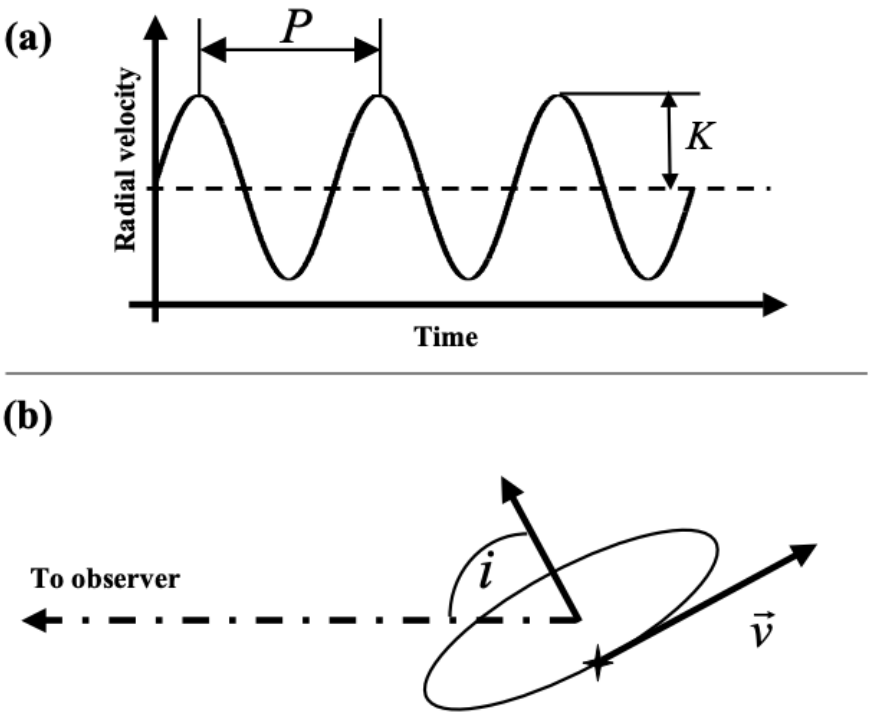


Figure 1.19: A schematic illustration of the periodic RV signal of a star induced by an orbiting planet, shown as a function of time in (a). The sinusoidal variation reflects the orbital period (P) of the planet and the K is the semi-amplitude. Panel (b) presents an illustration of the orbital inclination angle (i). Image adopted from (Sasselov et al., 2020).

on wide orbits around nearby stars, as these produce larger stellar displacements. A key advantage of this method is that, unlike radial velocity, it allows determination of the planet's true mass and orbital inclination, rather than just a lower limit ($M_p \sin i$).

Achieving the precise measurement of a star's angular displacement requires instruments with extremely high astrometric precision. To minimise the effects of atmospheric turbulence and other noise sources, the most effective approach is to use space-based telescopes. As of 3 March 2026, only a small number of systems have been confirmed and detected via astrometry, currently just six systems, namely DENISP J082303.1-491201 b (Sahlmann et al., 2013) that is a sub-stellar companion, GJ 896 A b (Curiel et al., 2022) that is a Saturn-like exoplanet, HIP 66074 b (Sozzetti et al., 2023) that is a Jupiter-like exoplanet, HD 128717 b (Pinamonti et al., 2026) that is a sub-stellar companion, Gaia-4 b (Stefánsson et al., 2025) that is a Jupiter-like exoplanet, Gaia-5 b (Stefánsson et al., 2025) that is a sub-stellar companion. This small number underscores the observational challenges of astrometry.

This limited detection rate primarily reflects the fact that Europeans Space Agency's *Gaia* mission (Gaia Collaboration et al., 2016) is the only space instrument capable of delivering astrometric measurements with the precision needed to detect planetary stellar wobbles[7]. Despite these limitations, Gaia's survey is expected to significantly expand the catalog of astrometrically detected exoplanets, approximately 21000±6000 candidates within a distance of 500 parsec (Perryman et al., 2014; Lammers & Winn, 2026).

Direct imaging

To study the solar corona, Bernard Lyot invented the coronagraph in late 1930s (Lyot, 1939). A coronagraph is an optical instrument designed to block the direct light of the Sun, thereby creating an artificial solar eclipse within a telescope. By suppressing the overwhelming brightness of the solar disk, the much fainter corona becomes observable from the ground.

The same principle, which is suppressing the light of a very bright object to reveal nearby faint sources, was later adapted for exoplanet detection. In direct imaging, a coronagraph is used to block the starlight so that faint planetary companions can be detected in its immediate surroundings (Macintosh et al., 2014; Bowler, 2016).

For this technique to be successful, the planet must typically be located at a relatively wide orbital separation from its host star. Planets that orbit too close to the star are difficult to resolve due to the small angular separation and the extreme contrast in brightness. Direct imaging is therefore most sensitive to young, massive exoplanets in wide orbits, which are still warm and luminous from their formation and emit detectable infrared radiation. One of the first successful detections using this method was a giant planet orbiting the brown dwarf 2MASSW J1207334-393254 (Chauvin et al., 2004). As of 5 March 2026, 94 exoplanets have been confirmed using the direct imaging technique. An example of a direct imaging of the HR 8799 system (Marois et al., 2010) is shown in Figure 1.20.

In addition to coronagraphy, several other developments have improved the effectiveness of the direct imaging technique. Observations at longer wavelengths are often preferred, as they enhance the contrast between the host star and the planet (Toomey & Ftaclas, 2003; Macintosh et al., 2014). Furthermore, atmospheric distortions affecting ground-based observations caused by turbulence in

[7] *Gaia* completed observations on 15 January 2025.

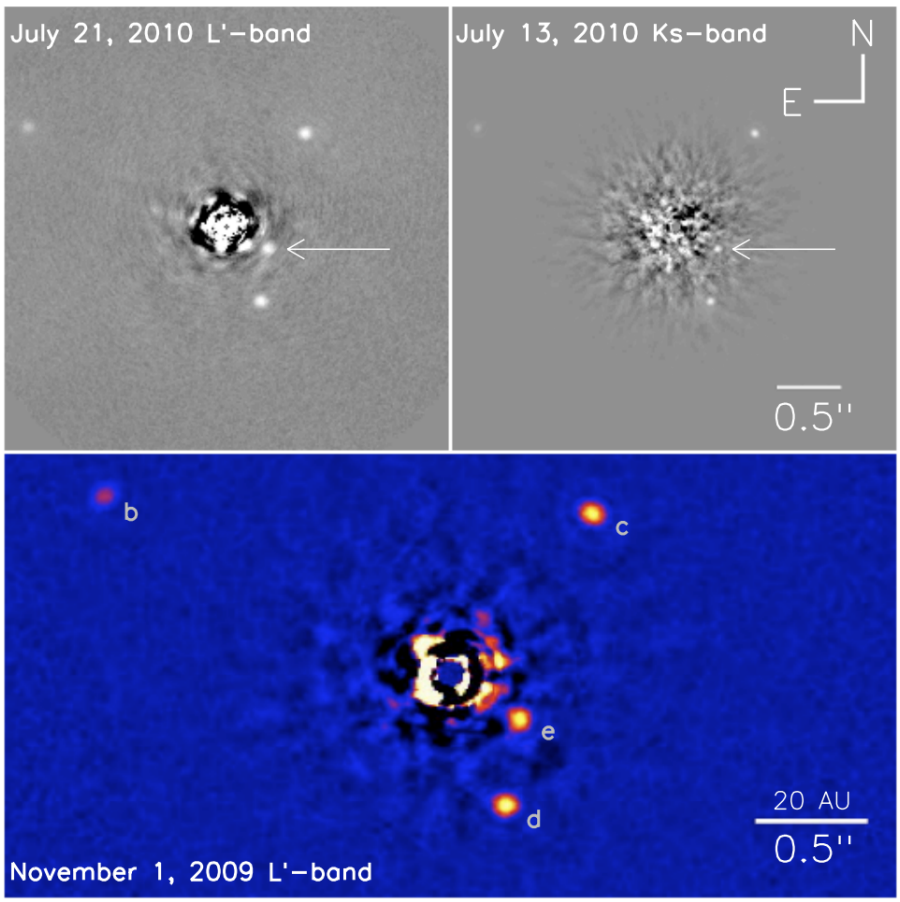


Figure 1.20: Direct imaging of the HR 8799 system. The intense light from the host star is suppressed using a coronagraph, allowing the four orbiting exoplanets to be detected, labelled with b, c, d, e. The observations were obtained in the Ks and L infrared bands. Image from (Marois et al., 2010).

the Earth's atmosphere, can be corrected using adaptive optics systems. These systems employ deformable mirrors that dynamically adjust their shape to compensate for distortions in the incoming wavefronts from the star, thereby improving the spatial resolution and image quality (Lenzen et al., 2003; Rousset et al., 2003; Chauvin et al., 2004).

Gravitational microlensing

Gravitational microlensing is a method for detecting exoplanets based on the effect predicted by the Theory of General Relativity (Einstein, 1916), that mass bends spacetime and therefore deflects light. When a relatively close star (the lens) passes very close to the line of sight between Earth and a more distant background star (the source), the gravitational field of the close star bends the light from the background star. This effect acts like a natural gravitational lens and temporarily magnifies the brightness of the background star (Einstein, 1936; Gaudi & Gould, 1997; Gaudi, 2012).

If the alignment between the foreground lens star and the distant background source star is sufficiently close, the background source star temporarily appears brighter, producing a characteristic symmetric lightcurve. If the lens star hosts a planet, the planet's gravitational field slightly perturbs the lensing configuration, resulting in a small deviation from the otherwise smooth microlensing light curve. An example of the characteristic symmetric curve with the small deviation from the exoplanet is shown in Figure 1.21.

The microlensing method is capable of detecting exoplanets with masses down to that of Earth, as well as planets orbiting very distant stars. However, such events are relatively rare, since they require a precise and temporary geometric alignment between the observer, the lens system, and the background source. In addition, microlensing events are generally non-repeatable once the alignment is lost. As of 5 March 2026, 270 exoplanets have been confirmed using this technique, with the first discovery associated with the microlensing event OGLE-2003-BLG-235/MOA-2003-BLG-53 microlensing event (Bond et al., 2004) using data the Optical Gravitational Lensing Experiment (Udalski et al., 1992, OGLE) and Microlensing Observations in Astrophysics (Bond et al., 2001, MOA) surveys.

1.7 Photometric transit surveys

Photometric transit surveys have been conducted and commissioned across the world with the aim of discovering exoplanets and expanding the parameter space of planetary systems. Several ground-based wide-field surveys have been particularly successful in identifying transiting exoplanets. These surveys typically employ arrays of small-aperture cost-effective telescopes with wide fields of view that continuously monitor thousands to millions of stars. Candidate transit signals identified by these surveys are subsequently followed up with higher-precision photometric and spectroscopic observations to confirm the planetary nature of the detected signals.

The Wide Angle Search for Planets (Pollacco et al., 2006, WASP) was one of the first large-scale sky surveys specifically designed to discover transiting exoplanets. WASP consisted of two facilities to provide nearly full-sky coverage: SuperWASP North, located at the Roque de los Muchachos Observatory on La Palma, Spain, and SuperWASP South, located at the South African Astronomical Observatory (SAAO) in Sutherland, South Africa. Each facility used a single robotic mount equipped

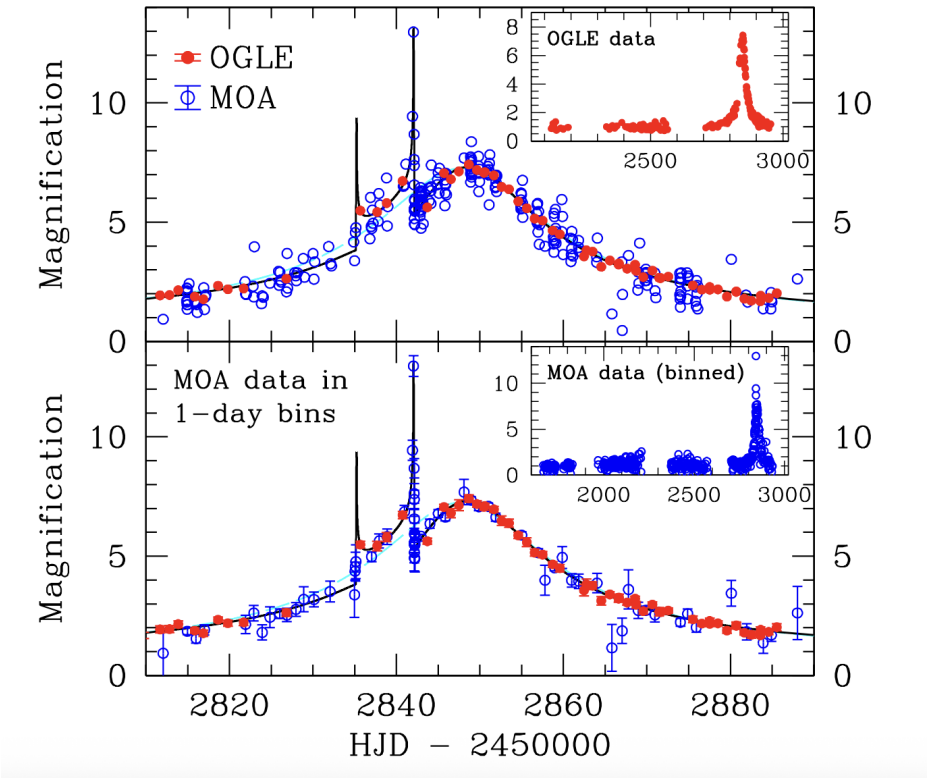


Figure 1.21: Light curve of the microlensing event OGLE-2003-BLG-235/MOA-2003-BLG-53 microlensing event. The photometric measurements are colour-coded for OGLE and MOA surveys. The best-fitting model is shown by the solid black curve. The two peaks superimposed on the otherwise symmetric microlensing lightcurve indicate the presence of a planetary companion. Lower panel represents the top panel but with the MOA dataset binned to 1 days. Image adapted from (Bond et al., 2004).

with eight wide-field CCD cameras (2048 × 2048 pixels, 13.5 µm pixel pitch), coupled to Canon 200 mm $f/1.8$ telephoto lenses. This configuration provided an extremely large total field of view of approximately 482 deg^2, enabling the monitoring of millions of bright stars simultaneously.

During its operational lifetime, WASP successfully confirmed 192 planetary systems, the majority of which orbit relatively bright host stars ($9 < V < 13$ mag), making them ideal targets for follow-up studies. Most discoveries were hot Jupiters, short-period gas giants that produce the largest transit signals.

Many of the hot Jupiters discovered by the WASP survey have become important targets for studying the dynamical and atmospheric properties of close-in exoplanets. Some systems show evidence of orbital decay, where tidal interactions between the planet and the host star gradually shrink the orbit. Examples include WASP-12b (Turner et al., 2021) and WASP-4b (Bouma et al., 2020).

Several WASP planets have also been used as early targets for atmospheric studies with the James Webb Space Telescope (Gardner et al., 2023, JWST), enabling detailed analyses of their atmospheric composition and temperature structure (Ahrer et al., 2023; Mikal-Evans et al., 2023; Ahrer et al., 2025). In addition, some WASP systems were later found to host multiple planets (Neveu-VanMalle et al., 2016; Bryant & Bayliss, 2022). Observations of the Rossiter–McLaughlin effect (Ohta et al., 2005) have also been performed for many WASP planets to measure the alignment between the planetary orbit and the stellar rotation axis (Brown et al., 2012). Furthermore, these systems have been investigated for potential Transit Timing Variations (TTVs), which can reveal additional planetary companions, as studied in systems such as WASP-18 and WASP-126 (Pearson, 2019).

Another prominent ground-based facility is the Hungarian-made Automated Telescope Network (HATNet) (Bakos et al., 2004), a wide-field survey designed to detect transiting exoplanets. HATNet operates from two sites: the Fred Lawrence Whipple Observatory in Arizona and the Mauna Kea Observatory in Hawaii. The network consists of seven small-aperture (11 cm) telescopes, each equipped with a 200-mm $f/1.8$ commercial lens coupled to a front-illuminated CCD with 2048 × 2048 pixels and a 14 µm pixel pitch, providing a total field of view of 8 deg^2 per telescope. The entire system is fully robotic and automated, allowing continuous, unattended monitoring of large areas of the sky.

In total, HATNet has discovered 72 exoplanets, probing a parameter space similar to WASP, with host star magnitudes in the range $9 < V < 14$ mag. Notable discoveries include the short-period hot Jupiter HAT-P-7 b (Pál et al., 2008) and the first Neptune-sized planet detected from the ground via transit, HAT-P-11 b (Bakos et al., 2010).

In the southern hemisphere, the HATSouth network (Bakos et al., 2013) operates across three continents, with facilities located at the Las Campanas Observatory in Chile, the HESS Observatory in Namibia, and the Siding Spring Observatory in Australia. The network comprises 24 telescopes, arranged in four units per mount, and operates fully automatically and robotically. Each telescope has $f/2.8$ focal ratio with a 18 cm aperture primary mirror and is equipped with a front-illuminated CCD of 4096 × 4096 pixels with a 9 µm pixel pitch, providing a combined field of view of 128 deg^2. To date, the HATSouth network has discovered 73 exoplanets. Compared to HATNet, HATSouth primarily targets fainter stars, particularly in the magnitude range $12 < V < 14$ mag. Among

its notable discoveries is HATS-6 b, one of the first giant planets found orbiting an M-dwarf star (Hartman et al., 2015).

1.7.1 The Next Generation Transit Survey (NGTS)

The Next Generation Transit Survey (Wheatley et al., 2018, NGTS) is a ground-based astronomical facility located at the European Southern Observatory's Paranal Observatory in Chile. It is designed as a wide-field photometric survey dedicated to the discovery and characterisation of exoplanets orbiting relatively bright stars, using high-precision ground-based photometry.

NGTS was established with the primary goal of detecting transiting exoplanets ranging from Jupiter-sized planets down to mini-Neptunes. By targeting bright host stars, the survey ensures that its discoveries are well suited for follow up radial velocity measurements, enabling accurate mass determinations and, consequently, estimates of planetary densities and internal compositions.

Furthermore, the NGTS has also been used to follow up targets from the space-based facility such as TESS (Ricker et al., 2015). TESS monitors each field for approximately 27 days before moving to the next, leading to substantial temporal gaps before revisiting the same region. As a result, NGTS is frequently used to observe systems where a single transit event has been identified by TESS, known as monotransits events, with the aim of constraining or determining their orbital periods.

Furthermore, NGTS supports a broad range of scientific programmes led by different working groups. These include the study of mono- and duo-transit events from TESS (Gill et al., 2020a, 2024), as well as long-term monitoring of eclipsing binaries (Casewell et al., 2018), brown dwarfs (Acton et al., 2021), young stellar clusters (Gillen et al., 2020) and white dwarfs.

The NGTS observatory consists of 12 independent small telescopes arranged in an array, each designed with a fast Newtonian optical configuration. Each telescope operates independently on its own mount, allowing for flexible pointing and simultaneous monitoring of multiple fields. The telescopes are housed in a roof-top observatory, which opens during observations to provide an unobstructed view of the sky as presented in Figure 1.22.

The optical tube assembly of each telescope is constructed from custom carbon fiber, providing a lightweight yet rigid structure. The tubes incorporate internal baffles to minimize stray light and reduce scattered light, thereby improving photometric precision. Each telescope features a primary and a secondary mirror, a custom made filter, a CCD camera, a baffle and a mounting and tracking system with an electronic focuser.

The telescope is a fast $f/2.8$ system with a 20 cm primary mirror coated in aluminium and a flat 9 cm secondary mirror, yielding an overall telescope throughput of approximately 80 % (see Figure 1.23). Each telescope is equipped with a custom wide band filter in the range of 520–890 nm, designed for optimal photometric response, ideal for exoplanet detection, particularly for late K and early M dwarf stars (Wheatley et al., 2018). The filter was specifically chosen to match the QE of the cameras. The upper limit of 890 nm was selected on purpose in order to avoid water absorption bands from the atmosphere (in range of 920-1000 nm, see Figure 1.23). The NGTS bandpass exhibits high transmission efficiency across the optical regime, as illustrated in Figure 1.23.

Each telescope incorporates an Andor iKon-L 936 CCD camera, featuring a deep-depleted e2v sensor that enhances sensitivity at red wavelengths. The QE of the sensor peaks at 95 % at 850 nm as illustrated in Figure 1.23. The sensor is housed in a vacuum enclosure and can be cooled to

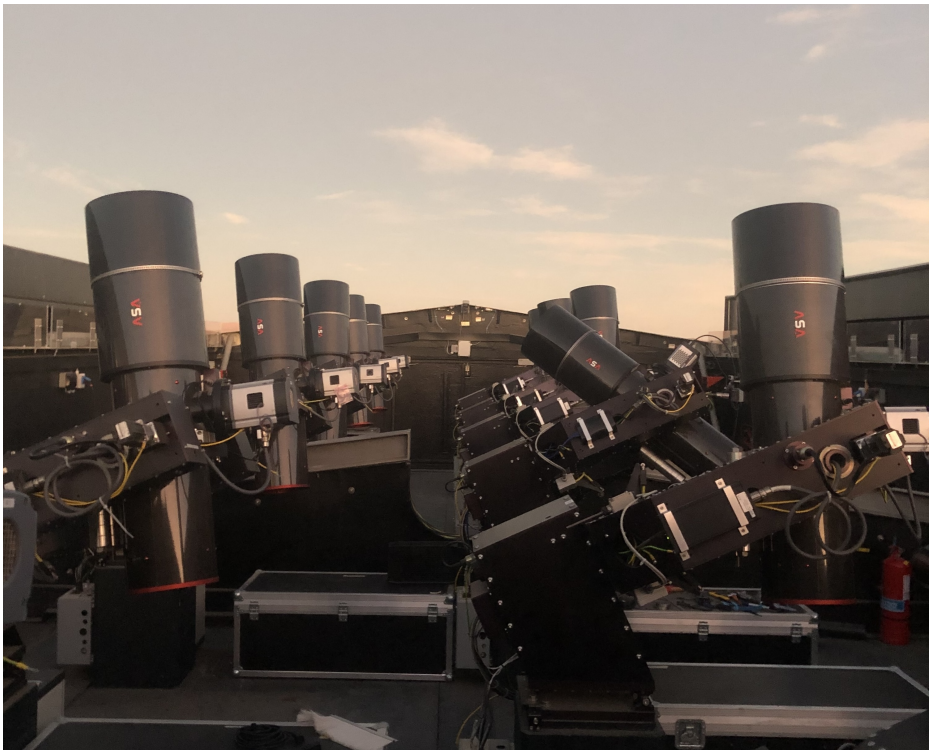


Figure 1.22: The NGTS enclosure and ten of the twelve 20 cm Newtonian telescopes during evening flat-field observations at Paranal Observatory, Chile. The remaining two telescopes are located behind the camera. The telescope observing at relatively different sky coordinates has the CMOS camera mounted.

temperatures as low as –100 °C. It has a 2048 × 2048 useful pixel image array with a relatively large pixel pitch of 13.5 µm, resulting in a diagonal of 39.1 mm. An additional 40 pixels are reserved as a bias offset region. Combined with the telescope optics, this provides a pixel scale of 5 arcsec pixel^{-1} and a field of view of 8 deg^2 per telescope, yielding a total instantaneous sky coverage of 96 deg^2 for all 12 telescopes.

The NGTS is a fully automatic and robotic facility operated remotely from the University of Warwick. Each of the twelve telescopes operates independently through a dedicated control system. The observatory is fully automated, with scheduling software that determines nightly targets based on visibility constraints, weather conditions, and survey strategy. Each telescope is assigned an action label, which records operational information such as image acquisition parameters, target identifiers, focuser positions, and other relevant functions. An advanced autoguiding algorithm, DONUTS (McCormac et al., 2013), is being used for precise tracking ensuring that the target stars will remain on the same pixel during an observing night. The software is capable of achieving sub-pixel guiding precision, thereby minimising pixel drift.

At the beginning of each night, the enclosure roof automatically opens if weather and safety conditions are satisfied. Environmental sensors continuously monitor wind speed, humidity, cloud coverage, and precipitation. During each observing session, calibration frames-including bias, dark, and flat-field images-are acquired both before and after the science observations. These calibration data are subsequently used in the image reduction process to correct the science frames for instrumental effects.

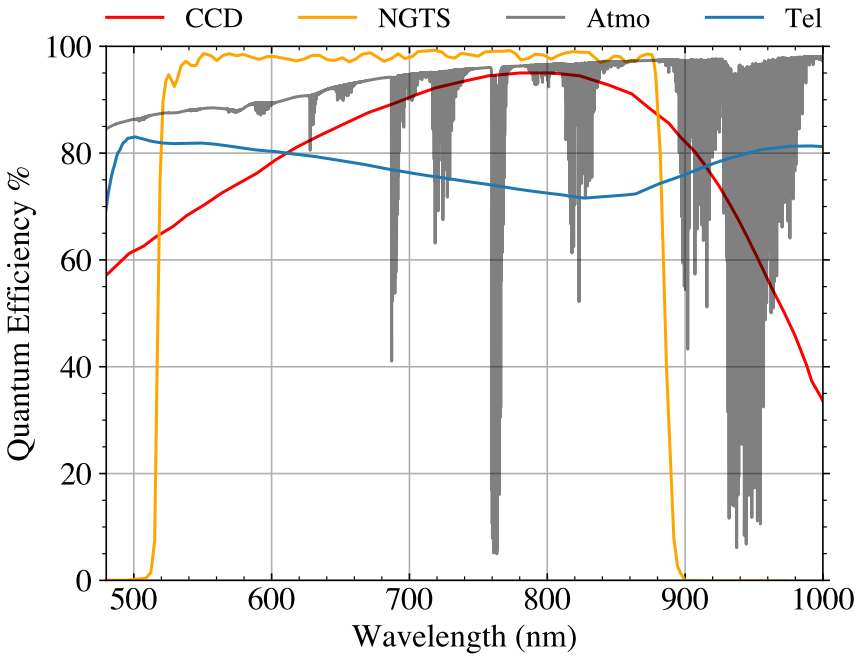


Figure 1.23: The theoretical throughput of a typical NGTS telescope, showing the measured NGTS bandpass in orange, the CCD camera QE in red, the telescope mirror transmission in blue, and with black the atmospheric transmission at Paranal Observatory.

To identify the target sources, the TESS Input Catalog version 8 (Stassun et al., 2018, TIC8) is incorporated, and astrometry is solved for each image using a WCS solution (Lang et al., 2010). An aperture is then defined and positioned on each star to measure the photometric signal from the pixels enclosed within it. Further details of the photometric pipeline and the extraction of the final light-curve products are provided in chapter 4.

As a ground-based facility, NGTS is inherently limited by atmospheric scintillation caused by turbulence in the Earth's atmosphere (Osborn et al., 2015; O'Brien et al., 2022). This effect limits bright stars photometry in the magnitude range of $8 < T < 10.5$ for a typical night. Moreover, thanks to the advanced CCD technology, characterised by low dark current and relatively small read noise, the overall noise budget is never limited by instrumental effects but instead by external contributions such as photon shot noise from the target and the sky background, as illustrated in Figure 1.24. NGTS is capable of detecting transits events with a precision down to 0.5 % for stars with magnitude range of $8 < T < 10.5$ for a single telescope and a typical exposure time of 10 seconds. Furthermore, by binning the light curve, a single NGTS telescope can achieve photometric precision of 0.1 % over a 1-hour timescale for bright stars with magnitudes $I \leq 13$ (Wheatley et al., 2018). To date, NGTS has successfully discovered 38 exoplanets and 8 eclipsing binaries[8]. Notable discoveries include NGTS-4b (West et al., 2019), the shallowest transit ever initially detected from a ground-based observatory; NGTS-14Ab (Smith et al., 2021), an exoplanet located within the Neptunian desert; and NGTS-30b (Battley et al., 2024), a very young, long-period warm Jupiter.

[8] `https://ngtransits.org/pages/tabs/publications_page.html`

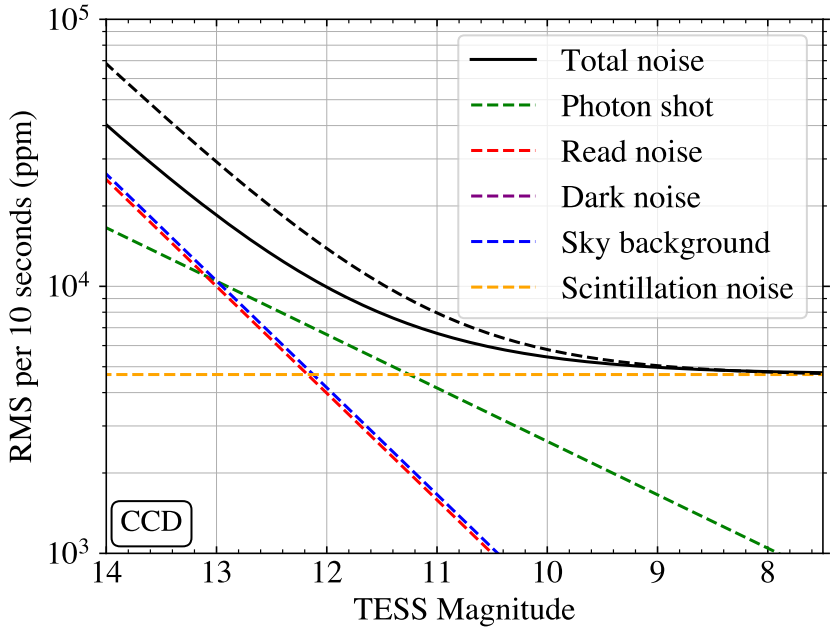


Figure 1.24: The Noise model for the NGTS on a non-moon scenario. The photon shot noise, scintillation noise, read noise and sky background noise are indicated with green, yellow, red and blue dashed lines. The dark current contribution is not visible due to the scale of the plot. The total model for a non-moon case is the black solid line, while on full moon with the black dashed line.

1.7.2 Transiting Exoplanet Survey Satellite (TESS)

The Transiting Exoplanet Survey Satellite (Ricker et al., 2015, TESS) is a space-based telescope designed to conduct a near all-sky survey, with the primary goal of discovering and characterising exoplanets orbiting bright stars through transit photometry (Stassun et al., 2019). To date, TESS has identified thousands of exoplanet candidates and confirmed a large number of planets, while continuing its search for small, rocky worlds. In addition to exoplanet science, the mission also contributes to time-domain astrophysics, including observations of asteroids, pulsating stars, and supernovae in distant galaxies.

TESS consists of four cameras, each featuring a seven-lens optical assembly. The detectors are housed within the instrument along with their associated electronics. Lens hoods are included to minimise stray light and reduce distortion of light from target stars. The payload also includes batteries, propulsion systems, and onboard computers to control operations and transmit data back to Earth via antennas mounted on the spacecraft. Power for its observations is supplied by solar panels attached to the sides of the spacecraft. An illustration of the spacecraft is presented in Figure 1.25.

The spacecraft is currently located in a highly elliptical, high-Earth orbit with a period of 13.7 days. The orbit was specifically chosen to maintain a 2:1 resonance with the Moon, ensuring stability for decades without requiring propulsion. Data are downlinked near perigee to maximise the observing time (Gangestad et al., 2013). The spacecraft launched in 2018, initialising the first year of operation, known as cycle 1. Since then, the mission has successfully completed cycle 7 and the mission is currently operating on the cycle 8. Further details of the cycles are presented in Table 1.1.

The four cameras are equipped with f/1.4 fast lenses, which provides a 24×24 degree wide field

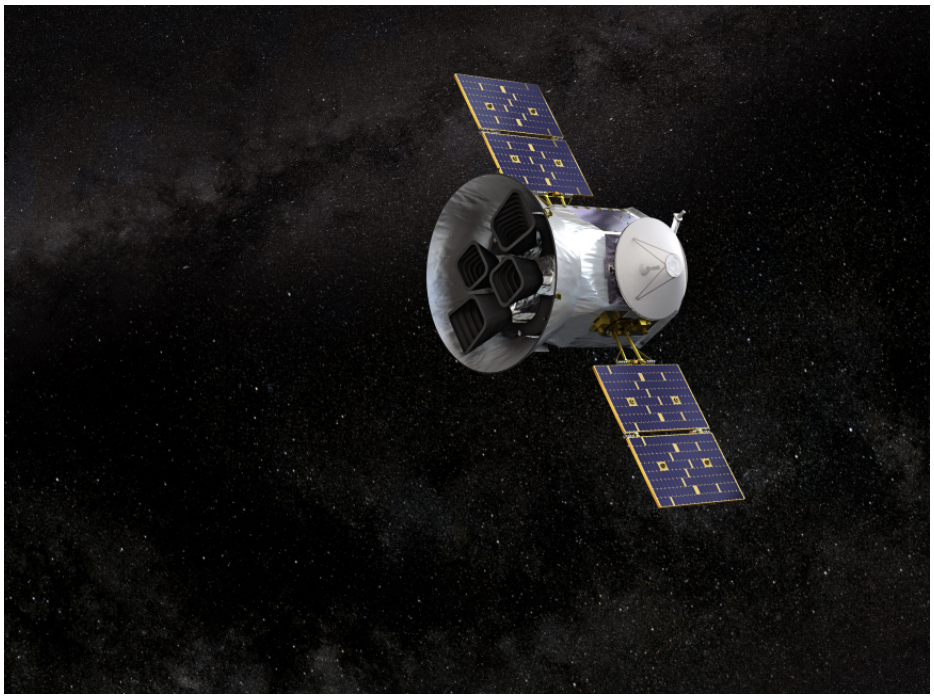


Figure 1.25: Artist's impression of NASA's TESS. Image credit: NASA's Goddard Space Flight Center.

Table 1.1: Summary of the observing cycles of TESS and their corresponding sectors. Note that the values listed for Cycle 8 are provisional and have not yet been confirmed; they remain subject to change.

Cycle number	**Dates**	**Sectors**
Cycle 1	2018/07/25 - 2019/07/17	1-13
Cycle 2	2019/07/18 - 2020/06/04	14-26
Cycle 3	2020/07/05 - 2021/06/24	27-39
Cycle 4	2021/06/24 - 2022/09/01	40-55
Cycle 5	2022/09/01 - 2023/09/20	56-69
Cycle 6	2023/09/20 - 2024/10/01	70-83
Cycle 7	2024/10/01 - 2025/09/15	84-96
Cycle 8	2025/09/15 - 2026/09/07	97-107

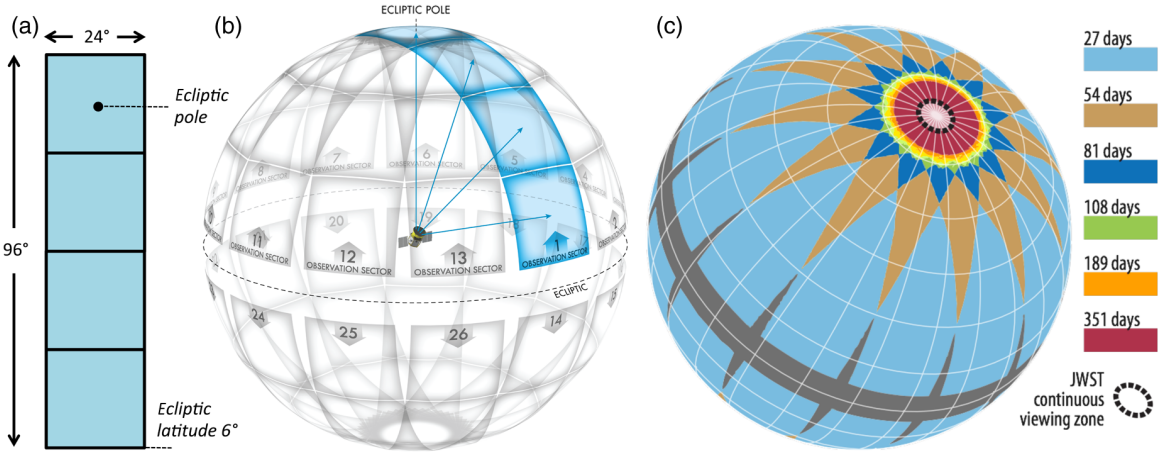


Figure 1.26: The observing strategy of TESS during its primary mission. The figure illustrates the instantaneous field of view of the four TESS cameras and the corresponding mapping of the observing sectors across the sky. The observation durations shown in the right panel (c) are representative of the primary mission. Figure adapted from (Ricker et al., 2015).

of view for each camera. The cameras house CCD detectors, namely the model CCID-80, made by MIT/Lincoln Lab that comes with 4096 × 4096 pixel size with 15 µm pixel pitch, which represents a pixel scale of 21 arcsec pixel^{-1}. The useful image array is also halved since the sensor is using the rest of the sensor to transfer the image and be able to readout. This feature provides a shutterless operation and also rapid readout. The detectors are cooled to -75 °C to minimise the dark current. The camera's sensor features deep depletion fabrication with a silicon layer of 100 µm thickness, providing a sensitive response towards red wavelengths (Woods et al., 2016). Based on that, the TESS custom filter is optimized for a broad red wavelength band from 600–1000 nm, making it particularly well suited for observing late K and M dwarf stars.

The four cameras are aligned vertically to produce a combined 24 × 96 degree field of view on the sky, which represents a sector. Each sector is monitored for in total 27.4 days (see sectors details in Table 1.1). During this period, TESS acquires 2-second exposures. These short exposures are subsequently co-added onboard to generate science data products at longer cadences. Full Frame Images (FFIs) are produced for all pixels in the field, initially at a 30-minute cadence, later improved to 10 minutes, and subsequently to 200 seconds in later mission phases. Moreover, adjacent sectors partially overlap, particularly near the ecliptic poles, resulting in extended temporal coverage in those regions. A schematic representation of the sectors observed is illustrated in Figure 1.26.

TESS produces several types of data products (Stassun et al., 2019). These include the Full Frame Images (FFIs), which contain the complete CCD image arrays recorded at different cadences throughout each observing sector. In addition, TESS provides Target Pixel Files (TPFs), which contain time-series, pixel-level data for pre-selected targets in the form of small postage-stamp images centered on each star.

The photometric light curves are derived from the time-series data in the TPFs by the Science Processing Operations Center pipeline (SPOC; Jenkins et al. 2016). The initial extracted flux, obtained through fixed-aperture photometry, is provided as Simple Aperture Photometry (SAP). After correcting for instrumental systematics, spacecraft trends, and contamination effects, the processed light curves are released as Pre-search Data Conditioning SAP (PDCSAP) flux. Since

TESS operates as an all-sky transit survey, it relies on a stellar catalog known as the TESS Input Catalog (TIC; Stassun et al. 2019), which contains stellar parameters used for target selection. In addition to the SPOC products, alternative light curve data sets are publicly available, including those produced by the Quick-Look Pipeline (QLP; Huang 2020) and the TESS-Gaia Light Curve (TGLC) pipeline (Han & Brandt, 2023).

During data processing, the SPOC pipeline searches the light curves for periodic transit-like signals. Signals that do exceed the predefined detection threshold (7.1 σ) are identified as Threshold Crossing Events (TCEs). These TCEs undergo further automated and manual vetting to assess their astrophysical nature and to eliminate false positives (e.g., eclipsing binaries, instrumental artifacts, asteroids crossing).

Candidates that pass this vetting stage are designated as TESS Objects of Interest (TOIs), representing high-priority planet candidates for follow up observations. In parallel, the broader scientific community can independently identify and vet candidates using publicly available data; such candidates are referred to as Community TOIs (CTOIs). Further analysis on the data products from TESS are also presented in chapter 6.

1.8 Spectrographs for Follow-Up of Transiting Exoplanet Candidates

Many spectrographs have been build in large observational facilities across the world for precise RV measurements. For instance, the high resolution echelle spectrometer (Vogt et al., 1994, HIRES) was mounted on the 10-m Keck I Telescope in Hawaii. It is a high-resolution optical echelle spectrograph designed for precision RV measurements with an accuracy between 4-5 ms^{-1} to 1-2 ms^{-1} (Butler et al., 2017). HIRES achieves a resolving power of $R \sim 67{,}000$, making it ideal for confirming transiting exoplanets and measuring their masses.

Moreover, the Fiber-fed Extended Range Optical Spectrograph (Kaufer et al., 1999, FEROS) is installed on the 2.2-m MPG/ESO Telescope at La Silla Observatory. It was originally installed at the ESO 1.52-metre telescope. Covering a wide optical range of 350–920 nm, FEROS reaches a resolving power of $R \sim 48{,}000$ and a RV precision of roughly 10–20 ms^{-1}. Its broad wavelength coverage and moderate-to-high resolution make it suitable for characterisation of evolved stars and follow-up of transiting exoplanets.

The Echelle SPectrograph for Rocky Exoplanet and Stable Spectroscopic Observations (Pepe et al., 2021, ESPRESSO) operates on the Very Large Telescope (VLT) at Paranal Observatory. ESPRESSO uses either a single VLT unit or the four units simultaneously. It is an ultra-stable optical spectrograph capable of extremely precise RV measurements down to $\sim$10 cms^{-1} over a timespan of 10 years using a single unit telescope. The operates in the optical wavelength covering a range of 380–788 nm with a resolving power of $R \sim 140{,}000$ (in the high resolution mode). ESPRESSO is optimised for detecting Earth-mass planets in the habitable zones of nearby stars and represents the state of the art in high-precision spectroscopy.

1.8.1 The High Accuracy Radial Velocity Planet Searcher (HARPS)

The High Accuracy Radial Velocity Planet Searcher (HARPS; Pepe et al., 2002) is a high-resolution, fiber-fed echelle spectrograph mounted on the ESO 3.6-m telescope at La Silla Observatory in

Chile. HARPS provides a resolving power of $R \sim 115{,}000$ over the visible wavelength range (approximately 380–690 nm) and is specifically optimised for ultra-stable, high-precision radial velocity measurements.

The instrument is installed in a vacuum vessel and operates in a temperature-controlled environment to ensure long-term instrumental stability. The detector installed features 2 mosaic CCDs, one optimised for the blue spectral range and the other for the red, with total of 4k × 4k pixel dimension and 15 µm pixel pitch. HARPS uses a dual-fiber system, allowing simultaneous calibration with a thorium-argon lamp to correct for instrumental drifts. Its optical design, combined with mechanical and thermal stabilisation, and its optical precision of $0.97\,\mathrm{ms}^{-1}$, enables Doppler measurements capable for the detection of low-mass and super-Earth exoplanets (Udry et al., 2007).

RVs are derived through cross-correlation techniques using weighted binary masks matched to stellar spectral types, producing a cross-correlation function (CCF) from which the Doppler shift is measured. Beyond planet detection, HARPS data also provide valuable diagnostics such as line bisectors and activity indicators (e.g., Ca II H &K), which help distinguish planetary signals from stellar activity-induced variations.

Upgrades to the ESO 3.6-m Telescope include the addition of a second spectrograph, designed to operate simultaneously with HARPS, with the aim of extending the wavelength coverage of high-precision spectroscopy. The Near-InfraRed Planet Searcher (Bouchy et al., 2025, NIRPS) is a high-resolution, near-infrared spectrograph equipped with adaptive optics (Blind et al., 2022). This innovative approach both corrects for atmospheric turbulence and concentrates starlight into the fiber, significantly increasing the signal-to-noise ratio for red and faint stars. As a result, NIRPS achieves a high spectral resolving power of $R \sim 90{,}000$ while improving the efficiency of RV measurements, particularly for M-dwarf stars.

1.8.2 CORALIE

The CORALIE instrument (Queloz et al., 2001) is a high resolution fiber-red echelle spectrograph mounted on the *Leonhard Euler* Telescope. The telescope is a 1.2-metre reflecting telescope at ESO's La Silla Observatory site in Chile. The spectrograph operates with a resolving power of $R \sim 60{,}000$ over the visible range (approximately 390–680 nm) and is designed for high-precision RV measurements, achieving measurements down to $\sim$3–6 ms^{-1}, primarily for exoplanet detection and stellar characterisation. The instrument was developed as a successor to the ELODIE spectrograph (Baranne et al., 1996a), which was used in the discovery of the first exoplanet orbiting a Sun-like star, 51 Pegasi b, by Mayor & Queloz (1995).

The instrument employs a dual-fiber system, enabling simultaneous wavelength calibration using a thorium-argon lamp to correct for instrumental drifts. The detector consists of a single large-format CCD with 2k × 2k pixel dimension and 15 µm, optimised for visible wavelengths.

Unlike HARPS, CORALIE is not housed in a vacuum vessel but operates in a temperature-controlled environment to ensure instrumental stability. Radial velocities are derived using the cross-correlation technique with numerical masks matched to stellar spectral types, producing a cross-correlation function (CCF) from which Doppler shifts are measured. Over its operational lifetime, CORALIE has undergone upgrades to improve efficiency and RV precision, significantly contributing to long-term exoplanet surveys in the southern hemisphere.

1.9 Thesis overview

The work presented in the following chapters summarises my research contributions in optical imaging, with particular emphasis on the laboratory testing and characterisation of CMOS image sensors and their ability to achieve photometric precision comparable to that of CCDs in astronomical applications. In addition, this thesis includes efforts toward the detection and characterisation of a long-period exoplanet, contributing to the growing population of these diverse planetary systems.

The first project focuses on the laboratory characterisation of the Marana CMOS camera, investigating its performance through a series of optical and detector-level tests. Chapter 3 presents a more detailed characterisation of the Marana camera, examining the internal functions that define its imaging modes, as well as electronic tuning aimed at optimising its performance. Chapter 4 describes on-sky comparisons between a CCD and the Marana CMOS camera, including multiple tests designed to evaluate photometric precision and observations of well-known exoplanet systems. Chapter 5 introduces a new camera product from Andor Technology, detailing both laboratory characterisation and on-sky testing conducted in La Palma. Chapter 6 presents the discovery of a long-period warm Jupiter initially identified by TESS and subsequently confirmed through follow-up observations with NGTS. Finally, Chapter 7 outlines the conclusions and future work of this research.

Chapter 2

Lab testing of the Marana CMOS camera

"Increscunt animi, virescit volnere virtus"

Aulus Gellius (Noctes Atticae XVIII, XI, IV)

Note

This chapter is a reproduction of the publication 'High-Precision Photometry with a scientific CMOS Camera: I Lab Testing of the Marana Camera' (Apergis et al. 2025), originally published in RAS Techniques and Instruments (RASTI) in October 2025. The writing and analysis of the paper was performed by the author, with comments throughout the paper that came from the co-authors.

Abstract

Scientific CMOS cameras are becoming increasingly prevalent in modern observational astronomy. We assess the ability of CMOS image sensors technology to perform high-precision photometry with a detailed laboratory characterization of the Marana 4.2BV-11 CMOS camera. We characterise the camera in the Fastest Frame Rate (FFR) and High Dynamic Range (HDR) modes. Our evaluation includes read noise, dark current, photo response and dark signal non-uniformities, quantum efficiency and window transmittance. The read noise is found to be 1.577 e^- for the FFR mode. For the HDR mode the read noise floor is measured to be 1.571 e^- for signal levels below approximately 1800 e^-. The bias level shows dark signal non-uniformities with values of 0.318 e^- and 0.232 e^- for FFR and HDR mode, respectively. Pixel well capacity reached 2366 $e^- pix^{-1}$ for the FFR mode and 69026 $e^- pix^{-1}$ with a dynamic range of 93 dB for the HDR mode. The camera demonstrates good linearity, yielding linearity errors of 0.099 % for FFR mode and 0.122 % for HDR mode. The uniformity across the image arrays show a photo response non-uniformity of 0.294 % for the FFR mode and 0.131 % for the HDR mode. The dark current displays a noticeable glow pattern, resulting in mean dark current levels of 1.674 ± 0.011 $e^- pix^{-1} s^{-1}$ for the FFR mode and 1.617 ± 0.008 $e^- pix^{-1} s^{-1}$ for the HDR mode at a constant temperature of -25 °C. We measured the quantum efficiency across

the visible spectrum, with a peak of of >95 % at 560 nm. Our tests indicate that the Marana CMOS camera is potentially capable of performing precise photometry.

2.1 Introduction

Charge-Coupled Devices (CCDs, Boyle & Smith, 1970) are almost universally used for optical astronomical imaging. Examples relating to high precision photometry include the Hubble Space Telescope (Ford et al., 1998, *HST*), *Kepler* (Borucki et al., 2010), Transiting Exoplanet Survey Satellite (Ricker et al., 2015, TESS), *Gaia* (Gaia Collaboration et al., 2016), and PLAnetary Transits and Oscillations (Rauer et al., 2016, PLATO). CCD cameras feature outstanding performance due to their high sensitivity, low read noise, stability, and good pixel-to-pixel uniformities. Additionally, developments in the sensor architecture such as deep depletion sensors (Peckerar et al., 1979, 1981; Tsoi et al., 1985; Gimeno et al., 2016), and back-side illuminated structures, provide exceptional quantum efficiency across a wide range of wavelengths. With thermoelectric or cryogenic cooling, the dark current of CCDs can be reduced to just a few electrons per pixel per hour.

Another type of image sensor developed alongside CCDs over the years is Complementary Metal-Oxide Semiconductor (CMOS). Unlike CCDs with a passive pixel sensor array, CMOS are active pixel sensors, where each pixel contains Field-Effect Transistors (MOSFETs) to convert the charge to voltage on a pixel-by-pixel basis. The individual in-pixel circuitry traditionally resulted to higher noise compared to a CCD with a single amplifier architecture (Tian et al., 1999). Nonetheless, the rapid readout speeds and low power consumption make CMOS sensors ideal for consumer markets. In contrast to CCDs, which are now primarily limited to scientific applications, the significant demand within the commercial market and applications utilizing camera technology has driven manufacturers to develop increasingly advanced CMOS devices by minimizing pixel architectures down to sub-micron level (Vu et al., 2008; Park et al., 2021; Uchiyama et al., 2021). The high production volume of CMOS detectors has made them significantly cheaper and more readily available than CCD detectors. Recent laboratory and on-sky testing results show that CMOS cameras have the potential to compete with CCDs cameras in certain astronomical applications (Jorden et al., 2014; Karpov et al., 2019; Alarcon et al., 2023a; Xiao et al., 2025; Layden et al., 2025).

Today, scientific CMOS (hereafter CMOS; Coates et al., 2009) cameras have found significant usage in astronomy (Qiu et al., 2013; Karpov et al., 2019; Wang et al., 2020; Ardilanov et al., 2021; Qiu et al., 2021; Stefanov, 2022; Townsend-Rose et al., 2023; Alarcon et al., 2023a; Khandelwal et al., 2024) due to their fast readout speed, allowing them to record in short exposures and to maximise the duty cycle. CMOS cameras are also available in large sensor sizes, resulting in a wide field of view that is mandatory for sky surveys, allowing for simultaneous observations of many stars in a single image (Wang et al., 2020; Layden et al., 2025). In contrast to the Analogue-to-Digital Converter (ADC) of CCD cameras, the parallel readout architecture of CMOS cameras, an ADC per column, digitises the voltage signal faster while preserving low power consumption. Thanks to the pinned photodiode pixel architecture and the on-chip amplifier per pixel, CMOS image sensors can achieve low read noise while conserving high frame rates and extended dynamic range (Inoue, 1999; Yonemoto et al., 2000; Fossum & Hondongwa, 2014). The large number of amplifiers and parallel readout path in CMOS sensors allow each pixel to be processed at lower frequencies, resulting in

low read noise. In contrast, CCDs require relatively higher sampling frequencies to process a large number of pixels and therefore lead to higher read noise (Hynecek, 1997; Teranishi & Mutoh, 1986).

Unlike front-illuminated CMOS sensors, recent developments such as back-illuminated sensors (Wuu et al., 2009; Wang et al., 2015), have pushed quantum efficiency values above 90% in visible wavelengths (e.g. Karpov et al., 2019; Alarcon et al., 2023a). CMOS cameras have been proposed for implementation in various astronomical projects such as ATLAS (Tonry et al., 2018); ASTEP (Crouzet et al., 2020), Argus Optical Array (Law et al., 2022) and Mini-MegaTORTORA (Karpov & Beskin, 2022). Under the advanced deployment of optical blocking filters and films, such cameras have also been implemented for X-ray space missions for example in Einstein Probe (e.g the Wide Field X-ray Telescope (WXT) in Yuan et al., 2018) and have also been commissioned for the Earth 2.0 (Ge et al., 2022) and Theseus (McHugh et al., 2020) future missions.

One of the key astronomical applications of large-format digital detectors is time-series photometry. In particular, large-format CCD detectors have been used to simultaneously monitor the brightness of thousands of stars over wide areas of the sky. Surveys such as WASP (Pollacco et al., 2006), Kepler (Borucki et al., 2010), TESS (Ricker et al., 2015) and NGTS (Wheatley et al., 2018) all use large format CCD detectors to achieve high precision time-series photometry in order to discover transiting exoplanets.

In this study, we aim to investigate whether modern CMOS detectors can achieve high precision photometry to a level competitive with CCD detectors. To do this, we characterise and test a modern CMOS camera, the Marana 4.2BV-11 (hereafter Marana) developed by Oxford Instruments Andor[1], under controlled laboratory conditions. In future work, we will extend this characterisation to on-sky observations at the the NGTS facility (Wheatley et al., 2018) at ESO's Paranal Observatory in Chile. The Marana has a low noise floor, high sensitivity, linear response and extended dynamic range. These properties make the Marana a good candidate for high-precision time series photometry. The Marana camera offers several advantages over other CMOS cameras, such as larger dynamic range and pixel size compared to the QHYCCD cameras used in Alarcon et al. (2023a), which is beneficial for photometry of bright stars. Additionally, the Marana delivers lower read noise than typical CCDs while maintaining significantly faster readout speeds at full frame rates.

Three significant studies have examined the performance of the Marana camera. In Karpov et al. (2019), key performance characteristics were evaluated, including photon transfer curves, linearity, dark current, read noise, spatial autocorrelation, random telegraph signal analysis, and on-sky tests. The study by Qiu et al. (2021) compared the Marana with the iKon-L camera across various readout modes, focusing on photon transfer analysis, linearity, read noise, dark current, and on-sky observations. Most recently, Khandelwal et al. (2024) investigated the Sona-11 (a rebranded version of the Marana with the same sensor) along with several other CMOS cameras.

In this work, we evaluate the performance of the Marana camera using a series of established and extended methodologies in a similar manner to Karpov et al. (2019); Qiu et al. (2021); Khandelwal et al. (2024). Specifically, we measure the photon transfer curve, linearity, read noise, and dark current. In addition to the existing literature, we assess the dark signal and photo response non-uniformities (DSNU and PRNU), and analyse the temporal noise characteristics of columns and rows under dark conditions. The dark current and glow are characterized across a range of operating

[1] `https://andor.oxinst.com/`

temperatures. We also present quantum efficiency measurements across a range of temperature of the Marana camera. Finally, to distinguish the sensor quantum efficiency over that of the camera, we report transmission data of the camera optical front window. Additionally, a detailed description of the pixel readout process of the Marana cameras is included.

In this first paper, we perform a thorough characterisation following the latest EMVA-1288 version 4.0 standards (Jähne, 2010). In Section 2.2 we describe the Marana camera and its CMOS sensor. The laboratory set-up is provided in Section 2.3. We explain the techniques and the methods used in Section 2.4. In Section 2.5 we present our results from laboratory testing and the discussion of our findings. Lastly, Section 2.6 outlines our conclusions.

2.2 The Marana Camera

2.2.1 The Marana 4.2BV-11 Camera

The Marana camera[2] is equipped with a thinned backside-illuminated sensor from GPixel[3], specifically the GSENSE400BSI model (Ma et al., 2015). The sensor features a dual-amplifier structure with 4.2 megapixels each 11 µm in size resulting in a 32 mm diagonal. The backside illuminated thinned depletion region results in exceptional quantum efficiency in the visible wavelength range. We have selected the Visible-Near Infrared (VIS-NIR) Enhanced Unwedged window, which provides high transmission at the visible and red wavelengths (see Section 2.4.7). The sensor is enclosed within a vacuum chamber that allows for deep cooling and protects the sensor from condensates. The thermoelectric cooling system ensures effective sensor temperature control, maintaining temperatures down to -25°C for ambient temperatures up to 30°C. Additionally, water cooling allows for the sensor to comfortably cool down to -45°C for ambient temperatures up to 30°C. The Marana weighs 3 kg (6.61 lbs), and an F-mount with a flange focal distance of 46.5 mm and a choke diameter of 43.3 mm is positioned in front of the sensor to maximize the usable field of view of the sensor. This configurations supports beams with f-number of approximately 1.07. Faster beams may cause vignetting. The camera consumes less than 50 W power and comes with USB3 interface, capable of connectivity up to 5 Gbps. For a summary of the specifications of the Marana camera, see Table 2.1.

2.2.2 Low Gain and High Gain channels

The CMOS pixel structure of the Marana camera is based on field effect transistors with functionalities such as amplification and charge transfer. For each integration the charge will be transferred in a sense node of a certain capacitance before it is amplified and readout. Additionally, the sensor is based on a 4 Transistor (4-T) pinned photodiode pixel structure (Ma et al., 2015; Wang et al., 2015). On top of the standard 4-T structure this sensor comprises an additional transistor which is switched off/on in order to enhance the sensitivity for low/high illumination levels, respectively, resulting in a High Gain (HG) and Low Gain (LG) capacitance. When the HG is assigned, the sense node will have a small capacitance leading to high gain and therefore low read noise. On the other hand, the sense node will have a large capacitance when the LG is employed.

[2] https://andor.oxinst.com/products/CMOS-camera-series/marana-CMOS
[3] https://www.gpixel.com/en/index.html

Table 2.1: Specifications of the Andor Marana CMOS camera, as provided on the camera's performance sheet.

Camera	**Andor CMOS**
Model	Marana-4BV11
Chip	GSENSE400BSI
Active pixels	2048×2048
Pixel size	$11 \times 11\,\mu m$
Sensor size	$22.5 \times 22.5\,mm$
Peak QE	95% @570 nm
Readout modes	100MHz @16-bit, 200MHz @12-bit
Shutter type	Rolling shutter*
Gain, e^-/ADU	1.12 @16-bit, 0.63 @12-bit
Pixel Well Depth, e^-	67995 @16-bit, 2679 @12-bit
Linearity	>99.7 %
Read Noise, e^-	1.57 @16-bit, 1.58 @12-bit
Dark current, e^-/pix/s	0.41 @ -45 °C

* Rolling shutter refers to an electronic readout method, not a physical/mechanical shutter.

During the readout sequence, each HG and LG pixel-level pre-amplifiers are read out through HG or LG column amplifiers positioned at the top or bottom of the sensor (Ma et al., 2017). For low light conditions the signal is amplified using the HG pixel-level setting, whereas in brighter light conditions the LG pixel-level setting is used. The HG pixel-level setting is utilized to achieve low read noise (Kawai & Kawahito, 2004), although it comes with a limited full well capacity. The LG pixel-level setting is utilized to achieve an extended full well capacity, but comes at the cost of higher read noise (Ma et al., 2015). To construct an image, the HG and LG channels can be used in two different imaging modes which we describe in the following section.

2.2.3 High Dynamic Range and Fastest Frame Rate imaging modes

The Marana camera offers two distinct imaging modes: the High Dynamic Range (HDR) and the Fastest Frame Rate (FFR). Both modes have been characterised in this study to determine the most suitable one for our imaging requirements.

The HDR mode employs the HG and LG pixel-level pre-amplifiers, to capture an extended dynamic range for the image. Each pixel produces two signals (HG and LG), which are passed to the HG and LG column amplifiers, respectively, and digitised by a dual 12-bit column ADC (Ma & Wang, 2013; Tang et al., 2020; Lou et al., 2023). A selection algorithm is implemented within the camera's Field-Programmable Gate Array (FPGA) to identify the most appropriate channel output for each recorded pixel value, based on the saturation level of the HG channel. The LG pixel values are then scaled to match the gain of the HG channel and the frame is being reconstructed based on the previous selection algorithm resulting in a 16-bit HDR image (Ma et al., 2015). The HDR mode operates at 100 MHz pixel readout rate, resulting in 24 full frames-per-second (fps).

For the FFR mode, the LG column amplifier is being repurposed to operate at the same gain setting as the HG, resulting in two HG column amplifiers. Odd numbered rows are being read using the first HG column amplifier, and even numbered rows are being read using the second HG column amplifier. This results in the readout time being twice as fast as the HDR mode, and therefore the

sensor outputs pixels at a frequency of 200 MHz and 48 full fps. The FFR configuration is also being digitised with 12-bit ADCs, therefore the dynamic range is limited. The specifications of HDR and FFR modes for the Marana camera are shown in Table 2.1, which is based on the technical performance details shipped with the camera.

2.2.4 Amplifier Glow

CMOS cameras exhibit amplifier glow, which may be caused by photons that are emitted by the electronics situated in the periphery of the sensor or from the excess of infrared photons emitted from the Source Follower amplifier (Janesick et al., 1985). Additionally, based on Wang et al. (2015) glow structures can be associated with other electronic circuits. Amplifier glow can be a major issue for certain CMOS devices and can emerge as the primary noise source in low-light imaging, thereby compromising their sensitivity. The impact is particularly notable in various astronomical applications utilizing CMOS sensors, spanning optical (Wang et al., 2020), x-ray (Townsend-Rose et al., 2023), and ultraviolet (Greffe et al., 2022) astronomy. Several approaches have been suggested to address amplifier glow, with one notable method involving the deactivation of electronic amplifiers not in use during exposure (Greffe et al., 2022).

The Marana camera comprises an on-board algorithm to subtract a pre-computed map of the glow from the image. This map is constructed by acquiring a long exposure dark image, in order to capture the glow structure. The dark signal is subtracted from this image leaving behind only the signal from the glow contribution. This reference map is then scaled according to the user requested exposure time and subtracted on a pixel-per-pixel basis. This is known as an Anti-Glow correction. In our testing, we use the Marana camera with and without the Anti-Glow correction. Additionally, strategies to remove the glow pattern have been proposed, including the use of spatially smooth matrices to subtract the effect of amplifier glow during post-acquisition processing (Zhang et al., 2023). In this work, we consider the dark signal as a mixture of the true dark signal and glow because both obey shot noise properties and cannot be distinguished from each other.

2.2.5 Spurious Noise Filter

CMOS detectors can show a number of features that lead to spurious read-out levels at the pixel level. One example is Random Telegraph Signal (RTS, Wang et al., 2006) which can randomly affect any pixel of the sensor. When pixel integration is completed, the charge will be transferred from the photodiode and stored in the sense node capacitor, before amplification and readout occurs.

However, during the fabrication process, defects may arise in the silicon dioxide layer or may get contaminated with impurities that can trap charge carriers (such as electrons) which will either recombine and be lost, or de-trapped by the defects (Le Roch et al., 2019). RTS arises when trapped charge carriers near the source follower channel discretely shift its gain, causing the output voltage to fluctuate between distinct levels. Statistically, RTS is represented as a triple (or more) Gaussian distribution, in which the height of the left/right peaks measures how frequently the event occurs (Martin-Gonthier & Magnan, 2009). When the images are displayed, the pixel which suffers from RTS, blinks through out a sequence of frames. Other examples of noisy pixels include static and persistent events such as hot pixels, which exhibit high dark current compared to normal pixels

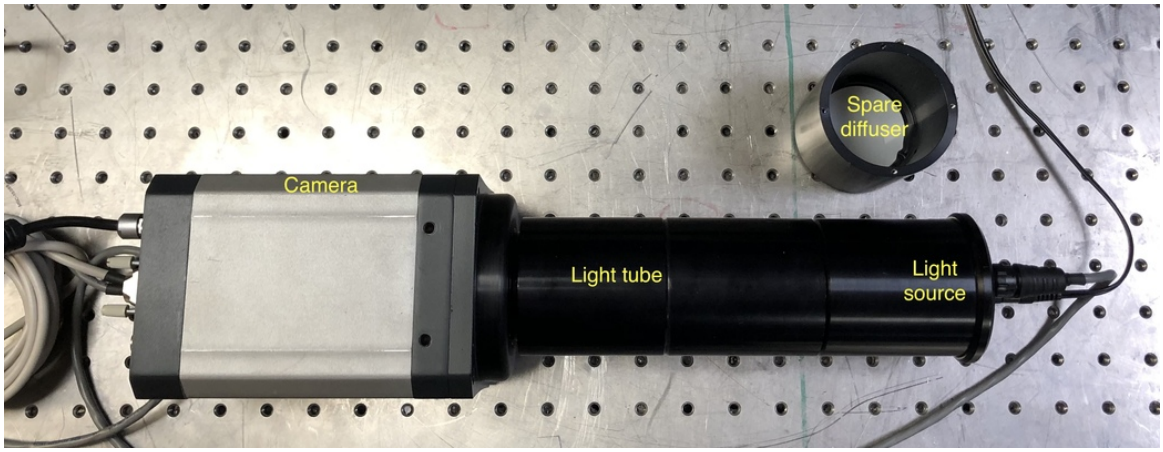


Figure 2.1: Optical bench setup for the Marana camera. The black cylindrical component is the light tube, which houses the light source with a diffuser mounted at the opposite end. A spare diffuser is also visible in the setup.

making them appear brighter than their surroundings (Liu et al., 2023b). Additional cases include unresponsive/black pixels that fail to efficiently collect or transfer charge.

To address the issue with these spurious pixels, the Marana camera uses a spurious pixel filtering algorithm processed by the FPGA in real-time. The FPGA identifies spurious pixels based on a selection algorithm which filters pixels whose values exceed the average value of their neighbouring pixels by a certain percentage. The algorithm corrects these pixels by replacing them with the average value of the non-spurious neighbouring pixels within the 3×3 matrix. The spurious pixel filtering can be turned on or off via the Andor SDK3 software. The spurious pixel filter operates near the bias level and uses a predefined threshold to prevent over-correction. It only targets pixels that significantly deviate from the average bias level. As a result, it is expected not to remove actual objects captured by the camera, such as faint stars.

In this paper, we operate the Marana camera with the spurious pixel filter enabled, excluding it only from the read noise analysis to avoid skewing the true read noise distribution.

2.3 Laboratory Setup

We tested the Marana camera in the laboratory at the University of Warwick. We employed a DC powered light rig equipped with a 9-volt amber 8-LED light array from OSRAM Opto Semiconductors, which provides consistent illumination peaking at 615 nm. The cylindrical-shaped rig contained the light source at the one end, and utilized a 100 mm opal-shaped diffuser to ensure flat illumination. The cylinder rig is at an optimal size to maintain uniform illumination across the sensor area. The diffuser reduces any artefacts that may be caused by small window defects. We covered the internal housing with shielding anti-reflective paper to minimize scattering light, that would normally increase the non-uniformity of the light at the sensor plane. The light tube was securely attached to the front plate of the camera to prevent any stray light from entering the camera as shown in Figure 2.1. Throughout our testing we kept the light source constant and adjusted the exposure time when needed to vary the illumination for an image frame.

To operate the Marana camera, we used the Andor SDK3 software installed on an Intel NUC 11

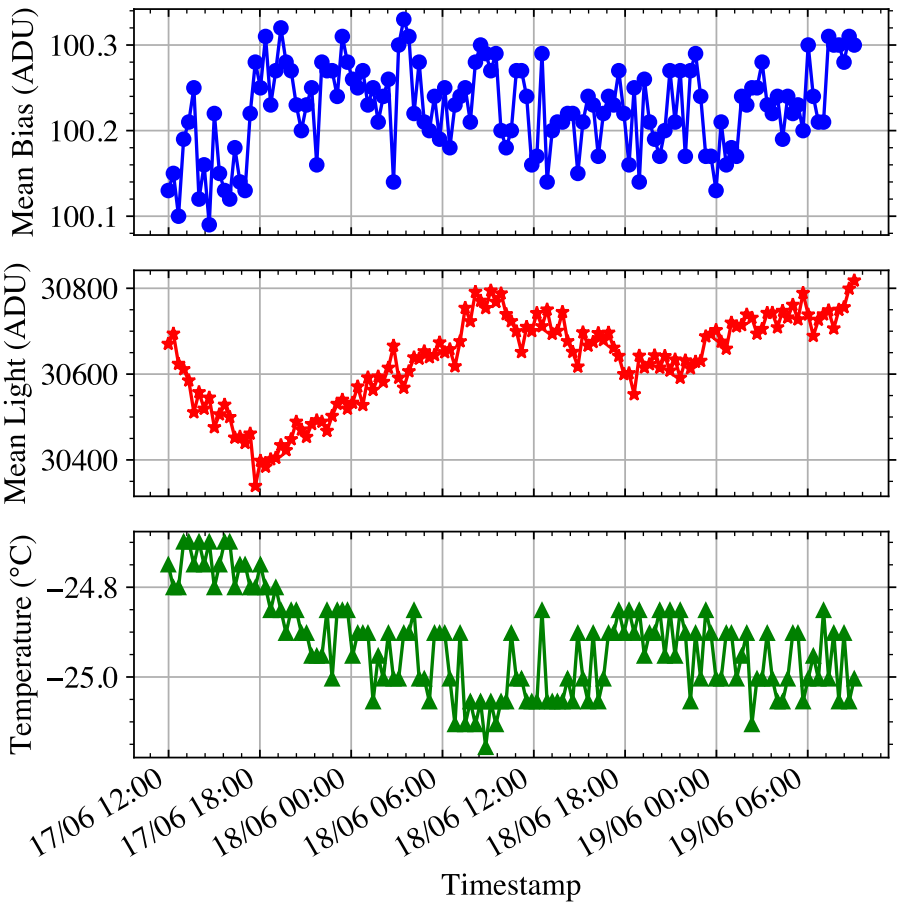


Figure 2.2: Bias level, light source signal and temperature for the Marana camera over time. **Top:** Average bias level value of a series of images at minimum exposure time and at dark environment. **Middle:** Average light source signal of a series images at a fixed exposure time. **Bottom:** Temperature values measured from the camera.

Extreme Kit Core mini computer equipped with an i9 CPU, 32 GB RAM and 4 TB SSD running the Rocky 9 Linux operating system. We controlled the camera using the Andor SDK Version 1.24.0 python wrapper. We integrated the functions of the light rig into the camera control system to directly communicate with the light tube during image acquisition. We configured parameters, including the selection of the Marana camera modes, and the sensor target temperature. To study the stability of the light source signal and the camera sensor temperature, we acquired a set of measurements at 20 minutes interval over the course of 2 days and at a sensor target temperature of -25°C. Our results are shown in the middle and lower panel of Figure 2.2. We monitor the light source stability by acquiring a frame at a fixed exposure that represents the half saturation of the HDR mode (~30000 analog-to-digital units or ADU hereafter). Similar data are shown in Figure 2.21 at 15°C.

Certain of the on-board correction algorithms were activated or deactivated to investigate raw sensor performance. These algorithms are the Anti-glow correction (refer to Section 2.5.4) and the spurious noise filter (refer to Section 2.5.2). All results presented in this paper were taken with the sensor cooled at -25°C unless explicitly mentioned.

Wherever possible, we adhered to the standard set by the European Machine Vision Association

(EMVA), specifically the EMVA-1288[4] latest version (Version 4.0), for Measurement and Presentation of Specifications for Machine Vision Sensors and Cameras, as outlined in Jähne (2010).

2.4 Methods

2.4.1 Photon Transfer Curve

The Photon Transfer Curve (PTC) was introduced in Janesick et al. (1985) and extensively described in Janesick et al. (2007). The PTC is used to extract valuable information on the performance of the camera, such as the conversion gain factor (hereafter gain) and the Full Well Capacity (FWC). The gain value is used to convert pixel values from ADU to the corresponding electrons. We employed this by recording the temporal noise or variance at different signal levels starting from dark conditions until saturation is reached. In order to produce these different signal levels, we used a constant light illumination level and varied the exposure time. (Stefanov, 2022).

We record two consecutive frames per exposure. To optimize computational efficiency and acquisition speed, we extracted a 512×512 central region from the full-frame images and used an increasing exposure time step as the exposure time increases. Thus, more data points are being captured at lower signal levels. We first estimate the maximum exposure to achieve saturation of the sensor and then we set the exposure time steps. In total, 160 pairs of images were recorded. The exposure time steps are summarised in Table 2.3. Bias frames were acquired to correct for the Dark Signal Non-Uniformity (DSNU). The brightness of our light source was kept at a high level to avoid long exposures which could lead to an increase of the noise due to glow and dark current. Given the short acquisition times at various illumination levels, the dark current was negligible; therefore, to further minimize processing time, we did not capture dark frames for each exposure to subtract dark current noise. To distinguish temporal noise (photon shot noise) from spatial noise, the fixed pattern noise, we implemented a technique involving the subtraction of consecutive frames with identical exposures, as outlined in (Janesick et al., 1985).

2.4.2 Bias

Bias is an arbitrary voltage added as an offset to each pixel's value. This is done in order to avoid negative signal values during the readout process which may arise due to random fluctuations of the pixel values (Howell, 2000). To examine the bias level of the Marana camera, we conducted tests in a dark environment with a cap placed over the camera body to ensure that no light reached the detector. The DSNU is a measure of the spatial noise distribution on a per-pixel basis across the image array. The DSNU is a result of the column level amplifier structure of the CMOS sensor and pixel defects created during the fabrication of the sensor (Stefanov, 2022). In this work, we adopt the DSNU parameter from the EMVA Standards (Jähne, 2010) as the pattern noise that only depends on bias levels, to remove any contribution that arises due to dark current noise build up at longer exposures. We choose that way in order to avoid other structures produced on dark images such as glow (see Section 2.2.4). The DSNU represents the fixed-pattern noise in the bias level, which we typically removed during the astronomical image reduction process and does not affect the final

[4] https://www.emva.org/wp-content/uploads/EMVA1288General_4.0Release.pdf

science image. As such, DSNU is generally not considered critical for astronomical applications. However, for the sake of completeness, we include this measurement and report the values, as it may be relevant in other scientific imaging fields.

We defined the temporal variation of pixels in a stack of bias images to be the "readout noise" (Fowler, 2011). The readout noise is a combination of all the noise sources that are not dependent on signal or exposure time. For instance, source follower noise which is a combination of thermal noise, the frequency dependent flicker noise and RTS noise. Additionally, the sense-node reset noise, which arises from thermal (Johnson, 1928) voltage fluctuations when the sense node is reset (Janesick, 2007); systematic noise generated from the on-board electronics, circuits and power supplies (Janesick, 2007) and quantisation noise which arises from the conversion of analog to digital values (Jähne, 2010).

In order to isolate the temporal noise from spatial noise, we studied each pixel individually through a stack of images. For DSNU and readout noise tests, the exposure time is set to "minimum", which is 1.52×10^{-5} s for the FFR mode and 9.48×10^{-6} s for the HDR mode. We captured a stack of 100 images in this mode.

2.4.3 Row and Column banding

Row pattern, also known as row banding, is a characteristic observed with some CMOS cameras. It is mostly noticeable at very low light levels or at bias level and contributes to the overall read noise of the camera (Wang et al., 2014; Karpov et al., 2019; Shao et al., 2024). The effect is mainly produced from the interference of the camera electronic components and the sensor readout circuits (Geurts et al., 2017; Nie et al., 2020) and, typically, the row patterns are much stronger than their column counterparts (Shao et al., 2024). Higher frame rates on CMOS cameras may lead to an increase in sensor power consumption, which in turn could lead to higher power supply fluctuations and voltage dips. These electrical fluctuations may manifest in the output images as row pattern noise (Geurts et al., 2017). Other studies have shown that temporal row banding may affect the accuracy of photometry when acquiring short exposure observations (Shao et al., 2024).

We follow a similar approach as in Section 2.4.2 to study the temporal row-wise and column-wise noise of the Marana camera and report on their contribution to the total read noise of the system.

Advanced methods have been proposed to minimize the row pattern noise such as adding a decoupling capacitor to stabilise the voltage from the row select transistor (Chen et al., 2011). For sensors with additional masked pixels on the periphery, these pixels can be used to subtract the offset and eliminate the row pattern on a per-row basis (Mo & Xu, 2011; Shao et al., 2024).

2.4.4 Dark

The dark current is a signal generated in the absence of light (Stefanov, 2022). Some electrons are excited from the valence band to the conduction band due to thermal effects within the silicon in the same way as electrons are excited from incident light. Additionally, dark current is generated by electron leakage from the photodiode or defects in the semiconductor surface, between the silicon and silicon dioxide (e.g. Shockley & Read, 1952; Aberle et al., 1992). The dark current produced electrons follow the Poisson distribution, and therefore lead to dark shot noise. The dark current

increases linearly with exposure time and can be minimized by cooling the sensor (Metselaar & Oversluizen, 1984; Widenhorn et al., 2002).

We employed tests to measure the dark current in a dark room with the cap on to prevent illumination from background light. The integration time is adjusted to vary from 1 - 10 s in steps of 1 s. We did not subtract the bias level from the dark signal data. The slope of the dark signal as a function of time yields the dark current and the intercept the bias level. The same method was used at different temperatures to investigate the dependence of the dark current with temperature.

2.4.5 Photo Response Non-Uniformity

The Photo Response Non-Uniformity (PRNU) characterizes the variability in pixel responsiveness to uniform light levels. Differences in sensor manufacturing processes can lead to variations in pixel sensitivities, causing some pixels to capture more or less electrons than others (Stefanov, 2022). This results in a spatial structure in the frame, where each pixel exhibits a unique sensitivity profile. Different source followers can produce different conversion gain values for each pixel, that can also significantly contribute to higher PRNU (Jain, 2016).

We characterise the spatial noise under light conditions as fixed pattern noise, which manifests as pixel-to-pixel response variations across the image array. Specifically, we investigate the PRNU, which is defined as the ratio of the fixed pattern noise to the mean level of the signal. It represents the proportionality constant that relates the signal level to the fixed pattern noise amplitude (Janesick et al., 2007).

To quantify the PRNU, we recorded 100 illuminated and bias subtracted images with constant light exposure at a level of approximately half the digitised saturation. We suppressed the photon shot noise components by averaging the 100 images to assess the response of individual pixels across the image (Ye & Lee, 2018).

A potential source of non-uniformity which is unrelated to the sensor itself is the appearance of dust or other debris on the optical window of the camera. To avoid this complication, we ensured the camera window was cleaned before testing using methanol and lens cleaning tissues. During testing, the camera was kept affixed to the light-box, as described in Section 2.3, to prevent any new dust accumulating on the camera window.

2.4.6 Linearity Testing

Linearity defines the relationship between the measured signal and the illumination level or integration time (Stefanov, 2022). It is characterised by a linear correlation between the signal and exposure time. When treating the camera as a black box—where incident photons enter and a digitised signal is output—linearity can be evaluated by either keeping the integration time constant while varying the light source intensity or maintaining a fixed light source while adjusting the integration time.

Measuring linearity in CMOS image sensors, particularly when employing a dual amplifier structure from the HG and LG channels, is crucial due to the presence of various effects that can impact overall linearity. In CMOS sensors with active pixel architecture, additional complications arise during the multiple process stages of the signal processing chain. This includes the linearity of the voltage amplification by the source follower transistor, as well as the linearity of the Analog-to-Digital conversion into ADU (Wang & Theuwissen, 2017). Each stage in this processing chain has

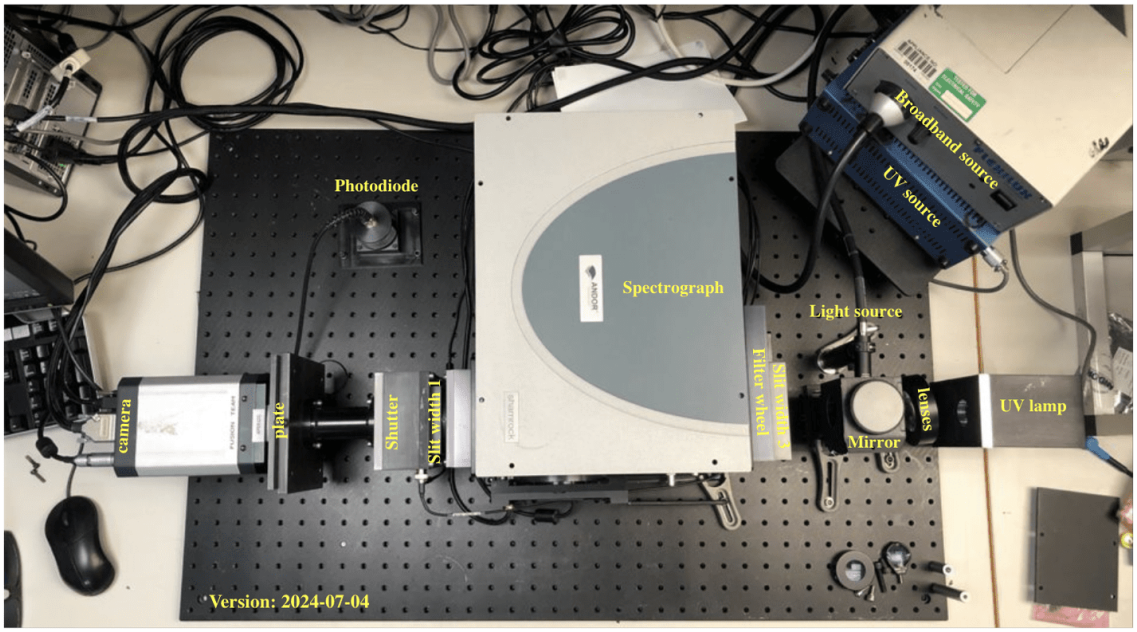


Figure 2.3: The optical bench of the QE measurement of the Marana CMOS camera, including the UV light bulb. Each instrument is labelled with yellow coloured text.

the potential to introduce non-linearities. To mitigate these effects, fabrication techniques for CMOS sensors have been proposed (Wang & Theuwissen, 2017; Wang et al., 2018), effectively improving linearity performance. Additionally, studies have identified a correlation between non-linearity and both the modulation transfer function and pixel noise (Li et al., 2016). Furthermore, compensation techniques and on-chip calibration methods for addressing non-linearities have been reported (Wang et al., 2004, 2018).

We explored how the signal changes relative to exposure time. We used a stable light source fixed while varying the exposure. For this investigation we utilised the same dataset as used in the Photon Transfer Curve (PTC) (see Section 2.4.1).

2.4.7 Quantum Efficiency and Window Transmittance

Many different approaches have been reported in the literature for Quantum Efficiency (QE) measurement (Sperlich & Stolz, 2014; Gill et al., 2022; Shao et al., 2024; Layden et al., 2025). In this work, we set out the methodology and results for our QE testing of the Marana CMOS camera, following the approach of Layden et al. (2025). The QE experiment was conducted at Andor's laboratories. A labelled photograph of the setup is shown in Figure 2.3.

A halogen bulb is used in order to provide constant illumination across the visible spectrum. The light received by the photodiode is converted to electric current and measured with the use of a Keithley picoammeter. To make a measurement at a desired wavelength, Andor's Shamrock SR-303i spectrograph is used as a monochromator. The data acquisition from both the photodiode and camera has been automated using a custom made code. This code establishes communication with the spectrograph in order to set the slits widths, filters, and grating angle and also allows data to be retrieved from the picoammeter through an RS232 protocol.

The wavelength ranges from 400 to 1020 nm in steps of 5 nm. The width for both entrance and

exit slits was set to 1000 μm and was found to be sufficiently wide for enough light to come through while short enough to only allow a small range of wavelengths at the output. By setting the slit width to 1000 μm, the camera exposure time was limited to a range of 0.001 to 0.01 seconds to avoid saturation. We used a combination of filters that are the most sensitive at each wavelength range to eliminate stray light entering the monochromator. First, we measure the photodiode current across the desired wavelength range by mounting it at the exit slit of the monochromator. The photodiode is then replaced by the Marana CMOS camera which is configured at a fixed exposure of 1 ms and the measurement is repeated.

The camera front window consists of a quartz substrate and is covered with an anti-reflection coating which has been specifically chosen to match the sensor's quantum efficiency. This means that the total camera quantum efficiency will be the product of the sensor quantum efficiency and the optical window transmission. Thus, in order to isolate the sensor quantum efficiency, we measured the transmittance of an optical window that is identical to the one used in the Marana camera, with the same glass type, thickness, and anti-reflective coating, using the experimental setup described above. In short, the transmission window is positioned between the entrance slit of the monochromator and the optical fibre connected to the light source with the photodiode mounted at the exit slit in order to record the photodiode current at various wavelengths. The same measurement is then repeated after the window has been removed.

2.5 Results, Analysis and Discussion

2.5.1 Photon Transfer Curve Results

To assess the characteristics of the Marana camera such as the gain and the Full Well Capacity (FWC), we used the Photon Transfer Curve (PTC) technique as described extensively in Janesick et al. (1985). We take two consecutive frames (k=A and k=B) which are used to measure the average signal over all the pixels [m][n], over all rows M and all columns N, using the following equation for each (adopted from Bohndiek et al. (2008)):

$$\mu_y[k] = \frac{1}{MN} \sum_{m=0}^{M-1} \sum_{n=0}^{N-1} y[k][m][n], (k = A, B) \tag{2.1}$$

and the average signal from the two frames is calculated as:

$$\mu_{\mathrm{A,B}} = \frac{1}{2}(\mu_y[A] + \mu_y[B]) \tag{2.2}$$

The temporal variance is not calculated directly from the averaged set. For illuminated images, the main noise sources are the photon shot noise and the fixed pattern noise. The read noise is signal-independent and therefore considered constant. The maximum dark current contribution for the exposure ranges used to construct the PTC curves are 0.022 and 0.26 electrons for the FFR and the HDR mode, respectively. Therefore the read noise and the dark current contribution are considered negligible.

While the fixed pattern noise is the spatial variance of the system, the photon shot noise is the temporal and their expression is given as:

$$\sigma_y^2 + s_y^2 = \frac{1}{NM} \sum_{m=0}^{M-1} \sum_{n=0}^{N-1} (y[k][m][n] - \mu_y[k])^2, (k = A, B) \tag{2.3}$$

where the fixed pattern noise denoted as s_y^2 and the photon shot noise as σ_y^2. To eliminate the fixed pattern noise, one has to subtract two consecutive frames at the same exposure (Janesick et al., 2007). Subtracting two consecutive frames removes the spatial variance associated with the fixed pattern noise and leaves only the temporal noise component as in the following:

$$\sigma_y^2 = \frac{1}{2NM} \sum_{m=0}^{M-1} \sum_{n=0}^{N-1} (y[A][m][n] - \mu_y[A]) - (y[B][m][n] - \mu_y[B]))^2 \tag{2.4}$$

However, when a set of two frames are added or subtracted, the random variance component of the resulted frame increases by a factor of 2. Therefore, Equation 2.4 is divided by this factor to extract the true pixel temporal variance (Janesick et al., 2007).

The PTC curves for both FFR and HDR modes are shown in Figure 2.4. The y-axis indicates the photon shot variance which has been isolated following the method described above. A linear regression is applied in the range of 0-70 % from the saturation, in order to extract the slope of the system which represents the inverse gain G (ADU/e$^-$). This is expressed as:

$$\sigma_y^2 = \frac{\mu_{\mathrm{A,B}}}{G} + \sigma_{\mathrm{RN}}^2 \tag{2.5}$$

Where σ_y^2 is the photon shot variance, σ_{RN}^2 is the read noise variance, $\mu_{\mathrm{A,B}}$ is the mean signal and $1/G$ is the gain which is measured to be $1/G = 0.632 \pm 0.009\,\mathrm{e}^-/\mathrm{ADU}$ for the FFR mode and $1/G = 1.131 \pm 0.008\,\mathrm{e}^-/\mathrm{ADU}$ for the HDR mode. We adopted these gain values for the Marana camera and used them to convert our results to electron units (i.e. read noise and dark current).

The FWC can be extracted from the x-axis for the maximum system variance. The variance decreases while the pixels start becoming saturated, since pixel values reach an identical state, indicative of sense node saturation. The FWC is measured to be 3720 ADU for the FFR and 61031 ADU for the HDR mode. Using the gain values the FWC is measured to be 2351 e^- for the FFR and 69026 e^- for the HDR mode. This was in a good agreement with the FWC in the performance sheet of the camera (see Table 2.1). It is worth noting that we do not calculate the FWC based on the linearity curves, given that the graph only levels off once it reaches the digitisation saturation.

The HDR mode shows a clear transition region at approximately 1800 ADU, which can be seen in the right and zoomed panel of Figure 2.4. The transition is also evident in previous studies reported in Qiu et al. (2021) and Karpov et al. (2019). The transition region under uniform illumination corresponds to the switch from the HG to the LG channel (see Section 2.2.2 and Ma & Wang (2013); Tang et al. (2020) for details). The LG channel has larger read noise (~40 e^-)[5] compared to the HG channel. Since it is a noise component, it contributes directly to the total variance which is shown as a discontinuity in the PTC for the HDR mode in Figure 2.4. When the signal exceeds the HG channel's capacity, excess charge is transferred to the LG channel. To mitigate the gap caused by amplifier gain differences, the amplifier gain ratio could be adjusted to smaller values, however,

[5] A separate analysis of the HG and LG channels confirmed this read noise difference; however, since this work focuses on overall HDR and FFR mode performance, those results are not presented here.

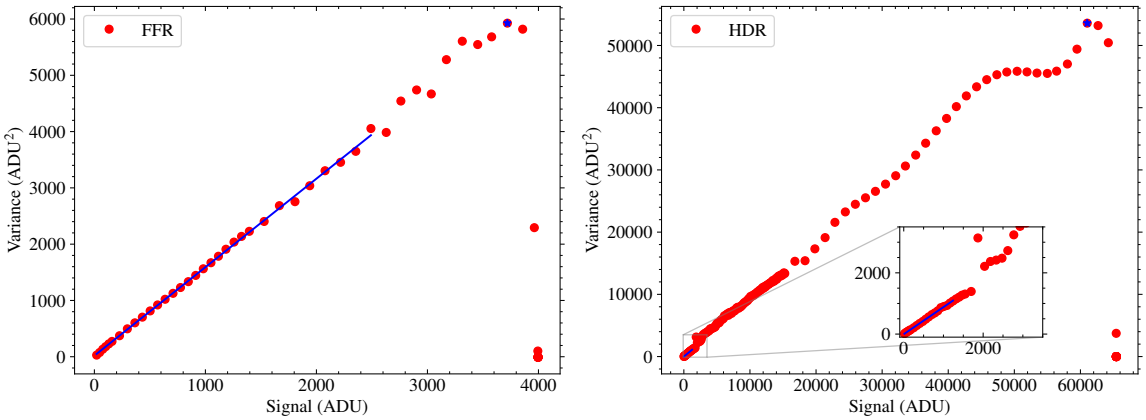


Figure 2.4: Photon transfer curves for the Marana camera at -25 °C. **Left:** The FFR readout mode. **Right:** The HDR readout mode. The solid blue line is a best fit linear model. The data point with the highest variance is marked with a blue star, and indicates the FWC value. A zoom-in panel illustrates the transition region.

this adjustment would lead to either higher read noise (by reducing the HG amplifier gain value) or compromise the maximum FWC by increasing the LG amplifier gain value (see Tang et al. (2020) for details). As a result, linear regression was exclusively applied to low signal values within the range of range 0-70 % for the HG channel, precisely before entering the transition region.

Interestingly, the pixel values on the transition point (~1800 ADU) may be processed by both HG and LG channels. If a pixel is near the transition threshold an increase on its output value can be observed throughout a series for the same exposure and illumination levels. This is because the shot noise sometimes drives the pixel to above or below the transition threshold value. Importantly, this dynamic channel assignment has repercussions when one subtracts frames consecutively, which may lead to higher variance value as shown with an additional spike in the transition in the zoom-in panel of Figure 2.4.

To investigate this, we acquired a set of 150 sub frames (460 × 250) under constant illumination and exposure settings, while applying a gradient in the illumination in the range of 1200-2000 ADU. This range was chosen to isolate pixels operating in distinct amplification modes: at lower signals (<1800 ADU), only the HG amplifier is active, while at higher signals (>1800 ADU), the LG amplifier is used exclusively. In the transition region around 1800 ADU, however, pixel values may be amplified by either the HG or LG channel, depending on the specific pixel behaviour.

We measured the temporal noise of each pixel across the frames. Pixels undergoing a transition between channels are expected to exhibit noise levels exceeding the combined shot and read noise at each signal level. For example, a pixel read out at 1400 ADU using the HG channel should have an expected noise of approximately 37 ADU, while a pixel at 2000 ADU in the LG channel should have expected noise around 60 ADU. Any pixel with noise exceeding these expected values likely experiences additional noise due to the HG–LG channel transition.

To analyse this, we applied a noise threshold of 60 ADU. Pixels exceeding this threshold were flagged, resulting in a binary image, as shown in the top-right panel of Figure 2.5, where only the high noise pixels are highlighted. Additionally, example pixels processed with the HG channel, LG channel and the transition region were selected and plotted as a function of frame number in

Figure 2.5.

The dual amplifier architecture, which constructs an HDR image from HG and LG channel may influence our comparison stars. Specifically, dim stars with low counts will be processed using the HG channel, while bright stars will be processed using the LG channel. Additionally, since the sky background remains considerably low, it will be read out using only the HG channel.

The PTC of the HDR mode exhibits significant non-linear artifacts, particularly dips and jumps at signal levels above the transition point and up to saturation. These effects can potentially be attributed to the non-linear conversion gain of individual pixels. Other studies have also shown that charge transfer inefficiency, also referred to as image lag, can contribute to such behaviour (Stefanov, 2022). This charge spill-back arises from incomplete charge transfer between the photodiode and the sense node, often due to inefficient activation of the transfer gate (Teranishi, 2016). Furthermore, Michelot et al. (2016) demonstrated that this non-linearity in the PTC can be mitigated by maintaining a high reset voltage while keeping the transfer gate low. Image lag can affect photometry results, as residual charge on the photodiode may be lost or accumulate onto the next image during exposures.

2.5.2 Bias level, Read Noise and DSNU

We calculate the mean value (μ_y) of a bias frame (k) by averaging over all of the pixels as:

$$\mu_y[k] = \frac{1}{NM} \sum_{m=0}^{M-1} \sum_{n=0}^{N-1} y[k][m][n]. \tag{2.6}$$

We follow the notation of the EMVA-1288 standards version 4.0 Jähne (2010), where $y[m][n]$ is the value of the pixel in ADU for the mth row and nth column. M and N are the total number of active pixels in the rows and columns of the detector, which in the case of the Marana camera is M=2048 and N=2048.

We find the mean value for the bias level of the Marana camera to be 62.74 e^- (99.26 ADU) with a standard deviation of 1.81 e^- in FFR mode, and 113.65 e^- (100.48 ADU) with a standard deviation of 1.78 e^- in HDR mode. No large scale structures are visible in the bias frames - see Figure 2.6. Some low level (1< e^-) horizontal banding can be seen in both modes. The patterns are slightly more prominent in the FFR mode. The banding is random in nature and cannot be corrected out by means of fixed pattern noise subtraction (Wang et al., 2014; Shao et al., 2024). The bias values are in agreement with the bias values in Karpov et al. (2019). However, Qiu et al. (2021) reported the bias level to be 141 ADU for the HDR and 207 ADU for the FFR mode.

To investigate the pixel-level *temporal* noise in bias frames, we collect a set of K sequential bias images. We organize the bias images into a 3-D array, with the m and n dimensions representing pixel row and column positions on the detector and k representing the image index. This technique ensures that we can study each pixel individually avoiding the dark fixed pattern noise contribution. For each of the 4,194,304 (M=2048 and N=2048) individual pixels across the frames, we calculate the mean as:

$$\mu_{m,n} = \frac{1}{K} \sum_{k=0}^{K-1} y[k][m][n], \tag{2.7}$$

and standard deviation as:

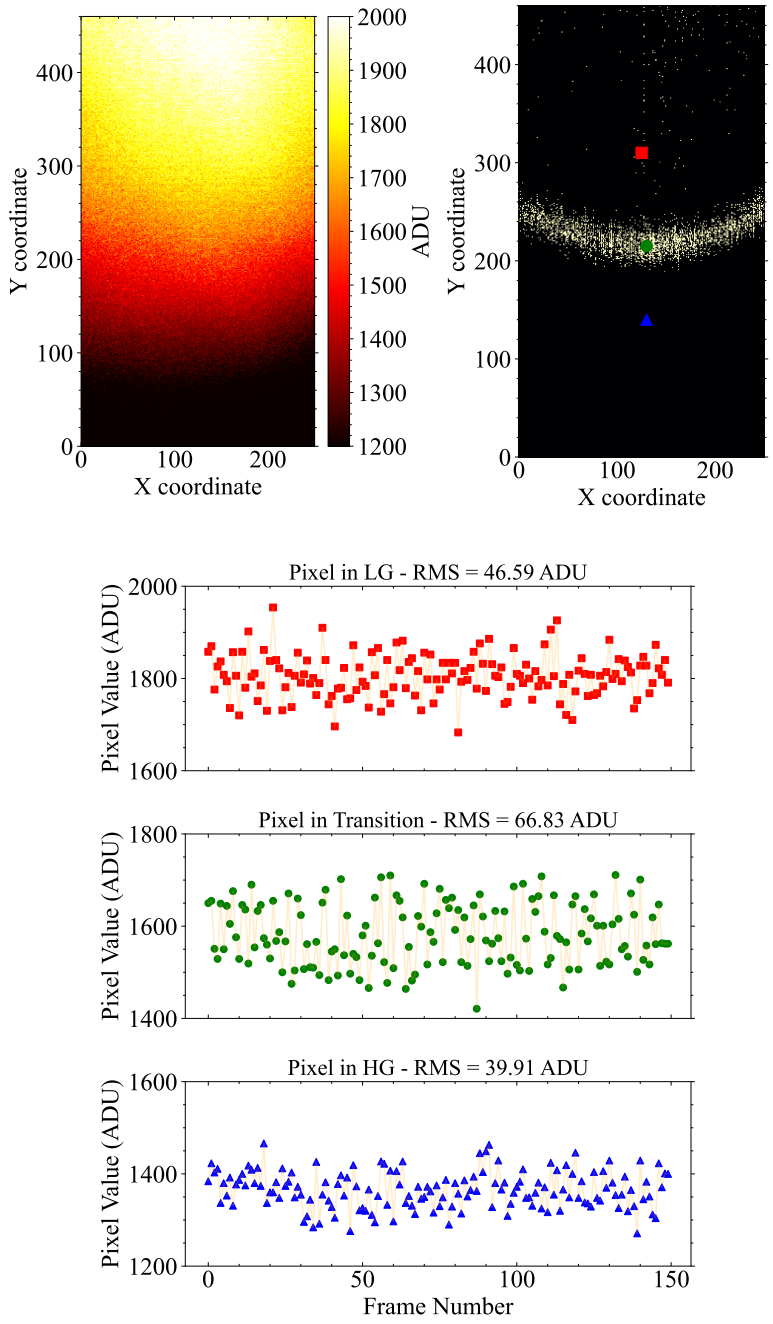


Figure 2.5: **Top left:** An example sub-frame showing the illumination difference across the LG and HG transition region. **Top right:** the binary image is highlighting pixels that exceed the threshold noise value. Also shown are three example pixels processed with the LG, HG channel and in transition, indicated with the red square (Y,X = 310, 125), blue triangle (Y,X = 140, 130) and green circle (Y, X = 215, 130) respectively. **Bottom:** The ADU counts for the three example pixels as a function of frame number, with the RMS calculated for each pixel.

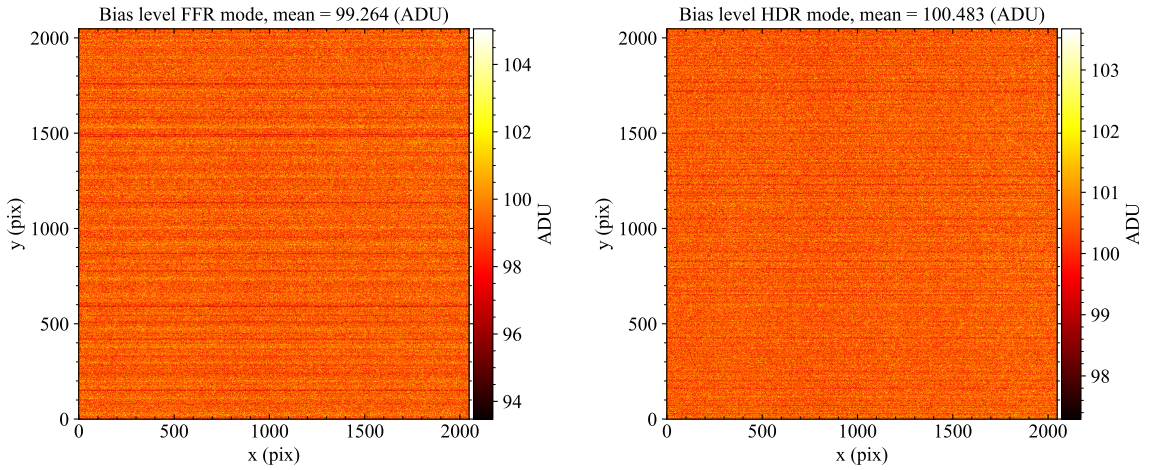


Figure 2.6: Bias frames from Marana camera recorded at minimum exposure for the FFR (**left**) and the HDR (**right**) modes. The camera is operating at temperature of -25° C.

$$\sigma_{m,n} = \sqrt{\frac{1}{K-1}\sum_{k=0}^{K-1}(y[k][m][n] - \mu_{m,n})^2}. \tag{2.8}$$

We carry out this calculation for 100 bias images in the FFR mode and 100 bias images in the HDR mode. The mean values and standard deviations are visualized through the 2-D histograms presented in Figure 2.7. We calculate the mean read noise for the camera ($\mathrm{RN_{mean}}$):

$$\mathrm{RN_{mean}} = \frac{1}{NM}\sum_{m=0}^{M-1}\sum_{n=0}^{N-1}\sigma_{m,n}, \tag{2.9}$$

and the median read noise is found as the middle value after sorting all the $\sigma_{m,n}$ values.

The mean, median and RMS read noise for the Marana camera in FFR mode is 1.71 $\mathrm{e^-}$, 1.577 $\mathrm{e^-}$ and 1.763 $\mathrm{e^-}$ respectively. The mean, median and RMS read noise in HDR mode is 1.697 $\mathrm{e^-}$, 1.571 $\mathrm{e^-}$ and 1.785 $\mathrm{e^-}$ respectively. The median read noise values are in good agreement with the performance metrics provided by Andor. The results are very similar between the two modes, since both utilize the HG channel at low illumination levels. Since the camera operates with the LG channel for high signal levels in HDR mode, the read noise after the transition point at 1800 ADU increases to $\sim 40\,\mathrm{e^-}$. Using a similar pixel-wise method to estimate the read noise, our read noise measurement is approximately half of the values reported in Khandelwal et al. (2024) and in Qiu et al. (2021) with a measured read noise of $3\,\mathrm{e^-}$ and $3.1\,\mathrm{e^-}$ respectively. Moreover, the read noise from the Marana CMOS is lower than comparable CCD cameras such as the iKon-L, which has a read noise of $15\,\mathrm{e^-}$ at 3 MHz speeds (Wheatley et al., 2018). CCDs can also achieve low read noise, however it comes at the expense of reduced readout speeds.

We note that for both readout modes the distribution of the read noise is non-Gaussian, and shows a very long tail of high read noise values (see histograms in Figure 2.7). There are two reasons that contribute to the long read noise tail in Figure 2.7. The first reason is that in the CMOS architecture there are differences in the per-pixel amplifiers and column ADC converters. Therefore each pixel has its own read noise properties, unlike a CCD where pixels are readout through a common amplifier

and ADC converter. This can result in a skewed distribution of read noise if some amplifiers or ADC converters are noisier than others. The second reason is the impact of RTS noise, which have also been reported for the Marana in previous work (Karpov et al., 2019), and forces random pixels towards larger read noise values (Martin-Gonthier & Magnan, 2009) and skew distribution on the histograms in Figure 2.7.

To demonstrate this, we created a binary image as shown in Figure 2.8, using $3\,e^-$ read noise threshold. Pixel values that exceed this threshold are considered noisy. There are various pixels that exceed this threshold, in total 2.64% of the image, most of the spread randomly. However, there are two distinctive column level amplifiers that are noisy. For pixels below the threshold, their bias level at different times are consistent with a Gaussian distribution. In contrast, pixels within the noisy column-level amplifiers show a non-uniform temporal distribution, while pixels outside these columns that exceed the threshold likely display RTS noise, characterized by a multimodal distribution as shown in Figure 2.8.

To further investigate noisy pixels, we used 100 bias images with and without the corrections in order to investigate the number of the corrected pixels. We found that less than 0.02 % of the total pixels on a typical bias frame are flagged as noisy pixels, some of which may also exhibit RTS and are detected by the Spurious Noise Filter on the FFR mode. We did not see any particular difference in the HDR mode. The Spurious Noise Filter operates at very low light signals, approximately to the bias level, and it works by removing noisy pixels referred to as spikes.

To measure the Dark Signal Non-Uniformity (DSNU), we employ the same set of K bias images for the read noise analysis as in Section 2.5.2. As per the EMVA-1288 standard, for modern CMOS sensors, pixels, rows and columns non-uniformities should also be included in the non-uniformity analysis. To suppress the temporal noise (i.e. read noise) we average these frames using the equation:

$$\bar{y}_{\mathrm{k}} = \frac{1}{K} \sum_{k=0}^{K-1} y[k] \tag{2.10}$$

Where $\bar{y}_{\mathrm{k}}$ is the averaged frame. Using the mean value $\mu_{y.\mathrm{bias}}$ of the averaged frame as in Equation 2.6, the spatial variance of the image is calculated using the following:

$$s_{\mathrm{y}}^2 = \frac{1}{MN} \sum_{m=0}^{M-1} \sum_{n=0}^{N-1} (\bar{y}_{\mathrm{k}}[m][n] - \mu_{y.\mathrm{bias}})^2 \tag{2.11}$$

This expression, however, includes a contribution from the temporal variance. To isolate the true spatial variance, we subtract the temporal component:

$$s_{\mathrm{y.k}}^2 = s_{\mathrm{y}}^2 - \frac{\sigma_y^2}{K} \tag{2.12}$$

where $s_{\mathrm{y.k}}^2$ is the spatial variance values for the overall image. To investigate the row and column non-uniform structure, we have to solve for the columns:

$$\mu_y[n] = \frac{1}{M} \sum_{m=0}^{M-1} \bar{y_k}[m][n] \tag{2.13}$$

where $\mu_y[n]$ is the mean value for the columns for the averaged frame. The same approach is

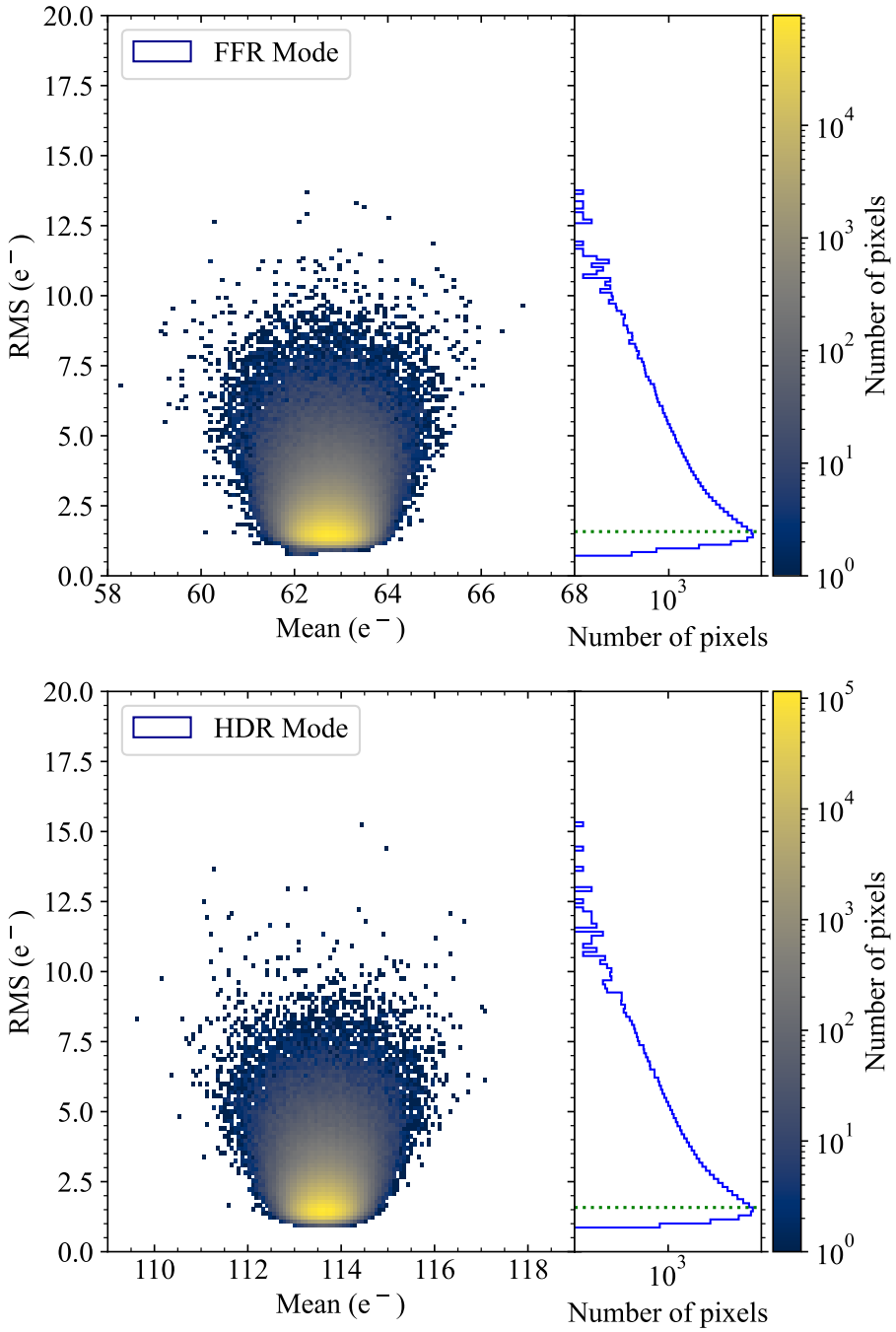


Figure 2.7: Read noise distribution using 100 consecutive bias frames. The 2-D histogram corresponds to temporal noise. The scattered plot shows the mean value of each pixel as measured from these frames while the colour bar indicates the number of pixels. The logarithmic read noise distribution is shown in the blue histograms, with the median value as a green dotted line. **Top:** Median read noise distribution for the FFR mode. **Bottom:** Median read noise distribution for the HDR mode.

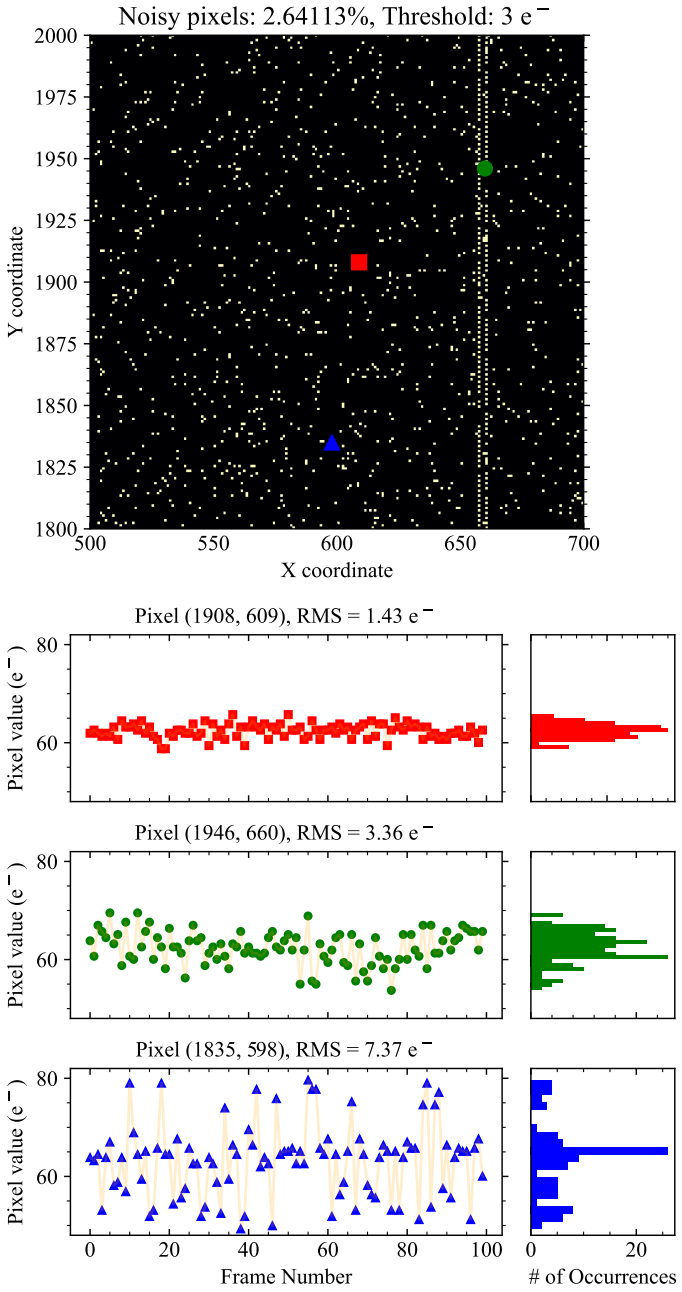


Figure 2.8: An example sub-frame showing the read noise map for the FFR mode. **Top:** Binary image is highlighting pixels that exceed the threshold read noise value. Also shown three example pixels below the threshold, in a noisy column level amplifier and noisy pixel with RTS behaviour, indicated with the red square (Y,X = 1908, 609), green circle (Y,X = 1946, 660) and blue triangle (Y,X = 1835, 598) respectively.**Bottom:** The e^- values for the three example pixels as a function of frame number, with the RMS calculated for each pixel.

done on the rows:

$$\mu_y[m] = \frac{1}{N}\sum_{n=0}^{N-1} \bar{y_k}[m][n] \tag{2.14}$$

where $\mu_y[m]$ is the mean value for the rows for the averaged frame. Again, for both rows and columns we have to remove the temporal variance across rows and columns, respectively (Jähne, 2010):

$$s^2_{y.m} = \frac{1}{M}\sum_{m=0}^{M-1} (\mu_y[m] - \mu_y)^2 - \frac{s^2_{y.pix}}{N} - \frac{\sigma^2_y}{KN} \tag{2.15}$$

$$s^2_{y.n} = \frac{1}{N}\sum_{m=0}^{M-1} (\mu_y[n] - \mu_y)^2 - \frac{s^2_{y.pix}}{M} - \frac{\sigma^2_y}{KM} \tag{2.16}$$

Where $s^2_{y.m}$, $s^2_{y.n}$ and $s^2_{y.pix}$ are the spatial variances for rows, columns and pixel. The total spatial variance is expressed as:

$$s^2_{y,k} = s^2_{y,m} + s^2_{y,n} + s^2_{y,\text{pix}} \tag{2.17}$$

Finally, by solving the matrix with the above three components (Jähne, 2010) the corresponding DSNU values are estimated as:

$$\begin{aligned} s_{\text{DSNU}} &= \sqrt{s^2_{y.k}} \\ s_{\text{DSNU,row}} &= \sqrt{s^2_{y.m}} \\ s_{\text{DSNU,col}} &= \sqrt{s^2_{y.n}} \\ s_{\text{DSNU,pix}} &= \sqrt{s^2_{y.k} - s^2_{y.m} - s^2_{y.n}} \end{aligned} \tag{2.18}$$

All DSNU values are reported in electrons, having been converted from ADU using the gain. Additionally, the averaged frame is normalized by subtracting its mean to aid visualization. The distributions of the normalized averaged frames for both HDR and FFR modes are shown in Figure 2.9. The total, pixel, row and column DSNU was found to be $0.232\,\text{e}^-$, $0.219\,\text{e}^-$, $0.054\,\text{e}^-$ and $0.052\,\text{e}^-$ for the HDR mode and $0.318\,\text{e}^-$, $0.251\,\text{e}^-$, $0.192\,\text{e}^-$ and $0.038\,\text{e}^-$ for the FFR mode.

Overall the DSNU exhibits minimal variation, though it is more pronounced for the FFR mode. Notably, the FFR mode reveals a bimodal distribution in the row DSNU, as shown in Figure 2.9, which is attributed to the odd/even amplifier pattern also observed in Figure 2.10. In FFR mode, row and pixel DSNU are the dominant contributors to the total DSNU, while the column DSNU remains minimal. In contrast, for HDR mode, both row and column DSNU show little variation, with pixel DSNU being the main contributor to the total.

2.5.3 Row and Column Noise

To investigate the pixel level *temporal* row and column noise in bias frames, we used the same set of (K = 100) bias images at minimum exposure time as described in Section 2.5.2. These bias frames form a 3-D data cube, where the dimensions are indexed by k (image index), m (row), and n

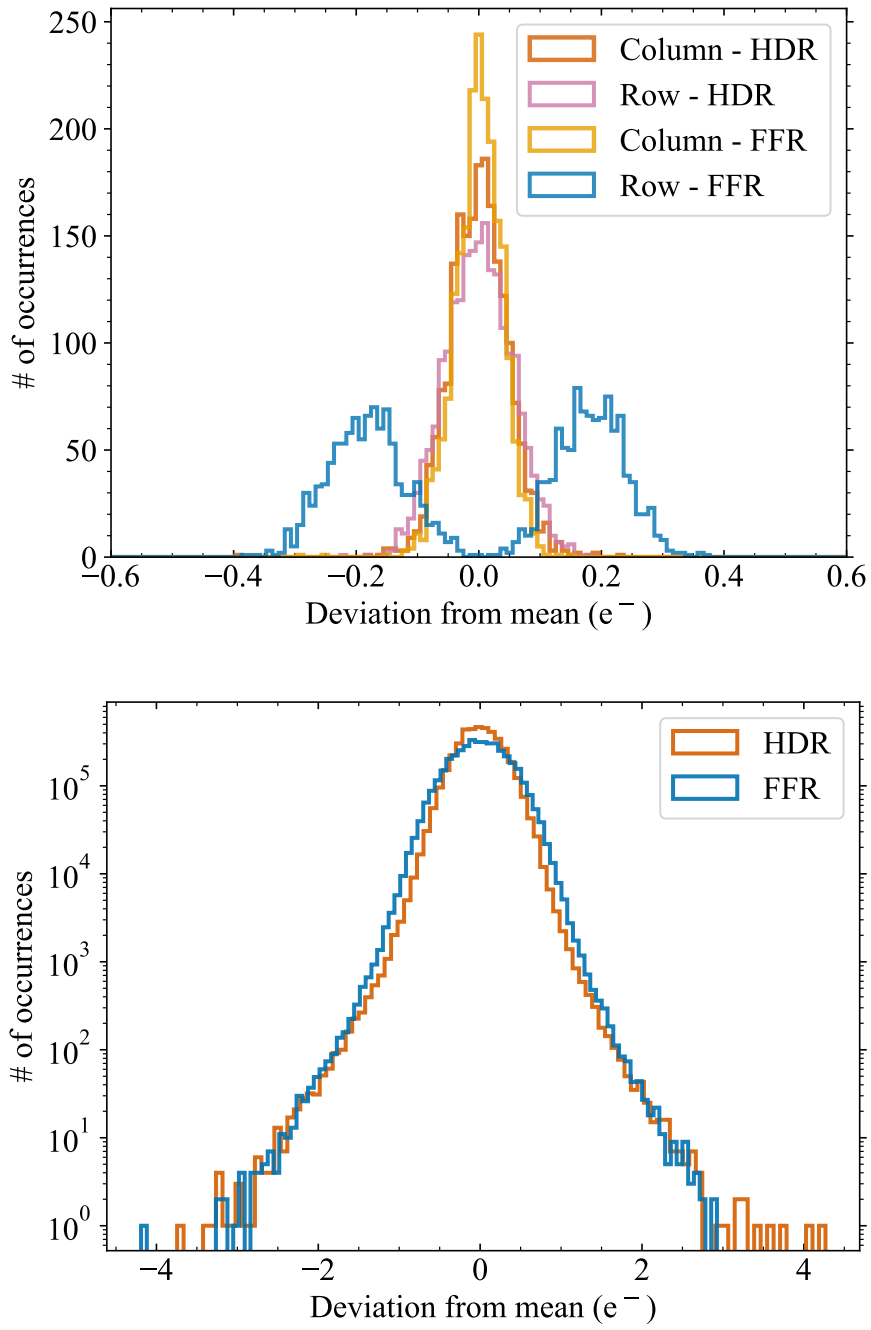


Figure 2.9: Histogram distribution of the mean-subtracted pixel values used to estimate the DSNU for both readout modes. **Top:** Distribution of the row- and column-averaged pixel values after subtracting the spatial mean level. **Bottom:** Distribution of the image-averaged pixel values after subtracting the spatial mean level.

(column). To study the row-wise variation, we compute the average value of all pixels k in each row m:

$$\mu_{k,m} = \frac{1}{N} \sum_{n=0}^{N-1} y[k][m][n], \tag{2.19}$$

where N is the number of columns, and $y[k][m][n]$ is the value of the pixel at a particular image. This creates a list of average values for each row m across the frames. The mean value calculated for each list of a row m is then given by:

$$\bar{\mu}_m = \frac{1}{K} \sum_{k=0}^{K-1} \mu_{k,m}. \tag{2.20}$$

Finally, the standard deviation of each row m across the K images is computed as:

$$\sigma_m = \sqrt{\frac{1}{K-1} \sum_{k=0}^{K-1} \left(\mu_{k,m} - \bar{\mu}_m\right)^2}. \tag{2.21}$$

In this way, for each of the 2048 rows across 100 frames, we quantify the row temporal noise. The same method is applied to evaluate the column-wise noise. In this case, the averaging is performed across rows rather than columns, and the variation is assessed based on the mean values of each column across all images. This way, the standard deviation of the column temporal noise is calculated.

Our results plotted with the same format as the read noise plots shown in Figure 2.10 for the row noise and Figure 2.11 for the column noise in FFR and HDR mode, respectively. For both modes, the column noise is weaker than the row noise. The mean value for the row noise was measured to be 0.467 e^- and 0.438 e^- for the FFR and HDR mode, respectively. The mean value for the column noise was measured to be 0.076 e^- and 0.06 e^- for the FFR and HDR mode, respectively.

Both HDR and FFR modes exhibit Gaussian noise distributions; however, in FFR mode, the 2D histogram (top panel of Figure 2.10) shows two distinct distribution clusters. This separation is not a result of temporal variation due to row banding but is likely a spatial variation due to the readout architecture in FFR mode, where even rows are processed by the first HG channel and odd rows by the second HG channel (see Section 2.2.3). This architecture leads to a noticeable mismatch between the two amplifiers: the first cluster, corresponding to one amplifier, exhibits higher noise of ~0.5 e^- and a lower bias mean signal of 62.35 e^-, while the second cluster shows lower noise of ~0.43 e^- and a higher mean value of 62.78 e^- (99.33 ADU). The HDR mode is consistent with noise of 0.438 e^- and a bias mean signal value of 113.45 e^- (100.3 ADU) since only the HG channel is implemented for both even and odd rows.

We investigated whether applying a row and column banding correction could improve the overall read noise of the camera. For this, we computed the average value of each row after applying sigma-clipping to exclude the contribution of cosmic rays and hot pixels. The row offsets were then subtracted from the image to remove horizontal banding. The same procedure was repeated for columns to correct vertical banding. An example row and column temporal noise removed frame is show in Figure 2.22. Using the row and column noise values, the RMS read noise is expected to be 1.706 e^- for the HDR and 1.721 e^- for the FFR mode. However, our measured RMS values

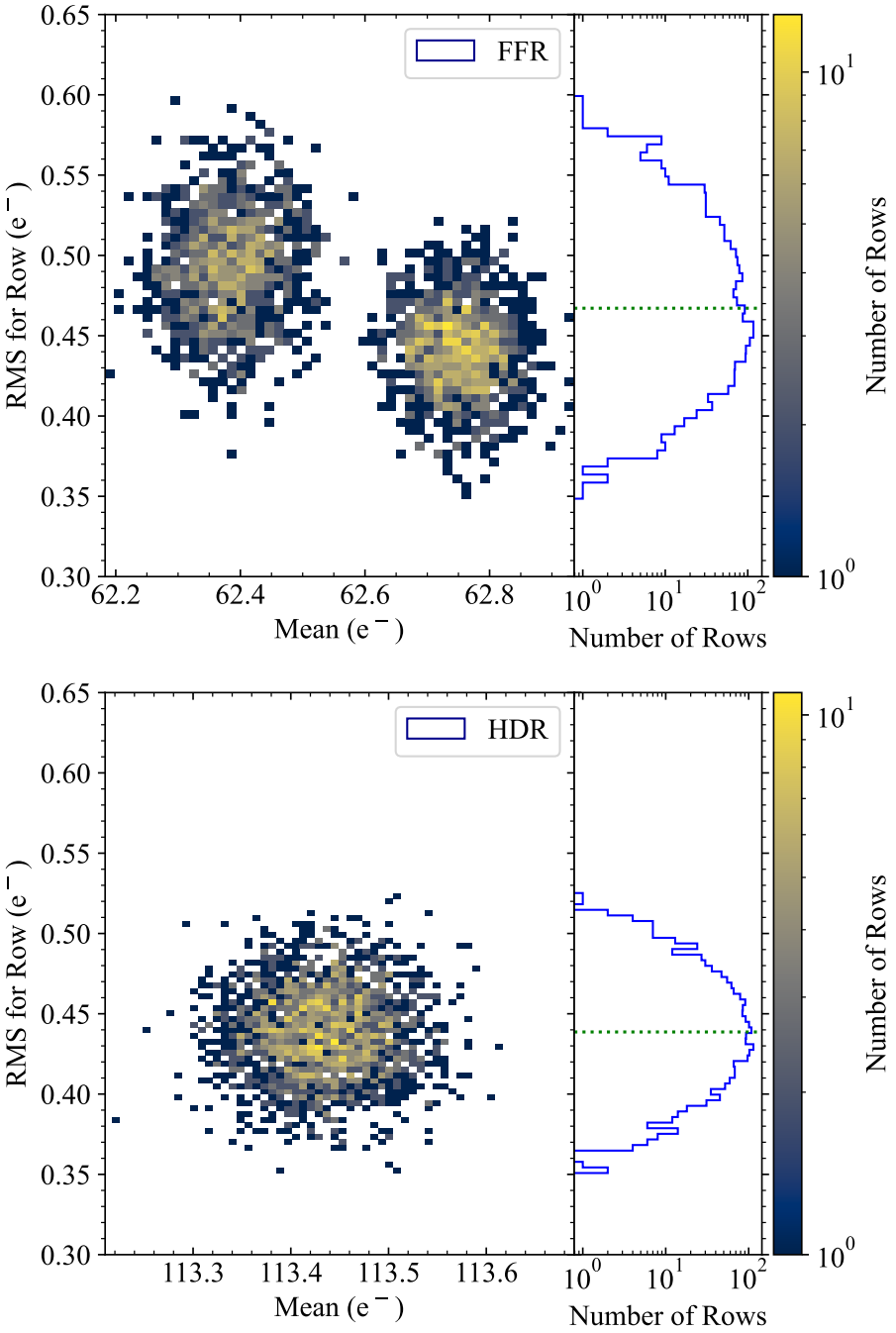


Figure 2.10: Row noise distribution using 100 consecutive bias frames. The 2-D histogram corresponds to row temporal. The scattered plot shows the mean value of each row from these frames while the colour bar indicates the number of rows. The logarithmic row noise distribution is shown in the blue histograms, with the median value as a green dotted line. **Top:** Mean row noise distribution for the FFR mode. **Bottom:** Mean row noise distribution for the HDR mode.

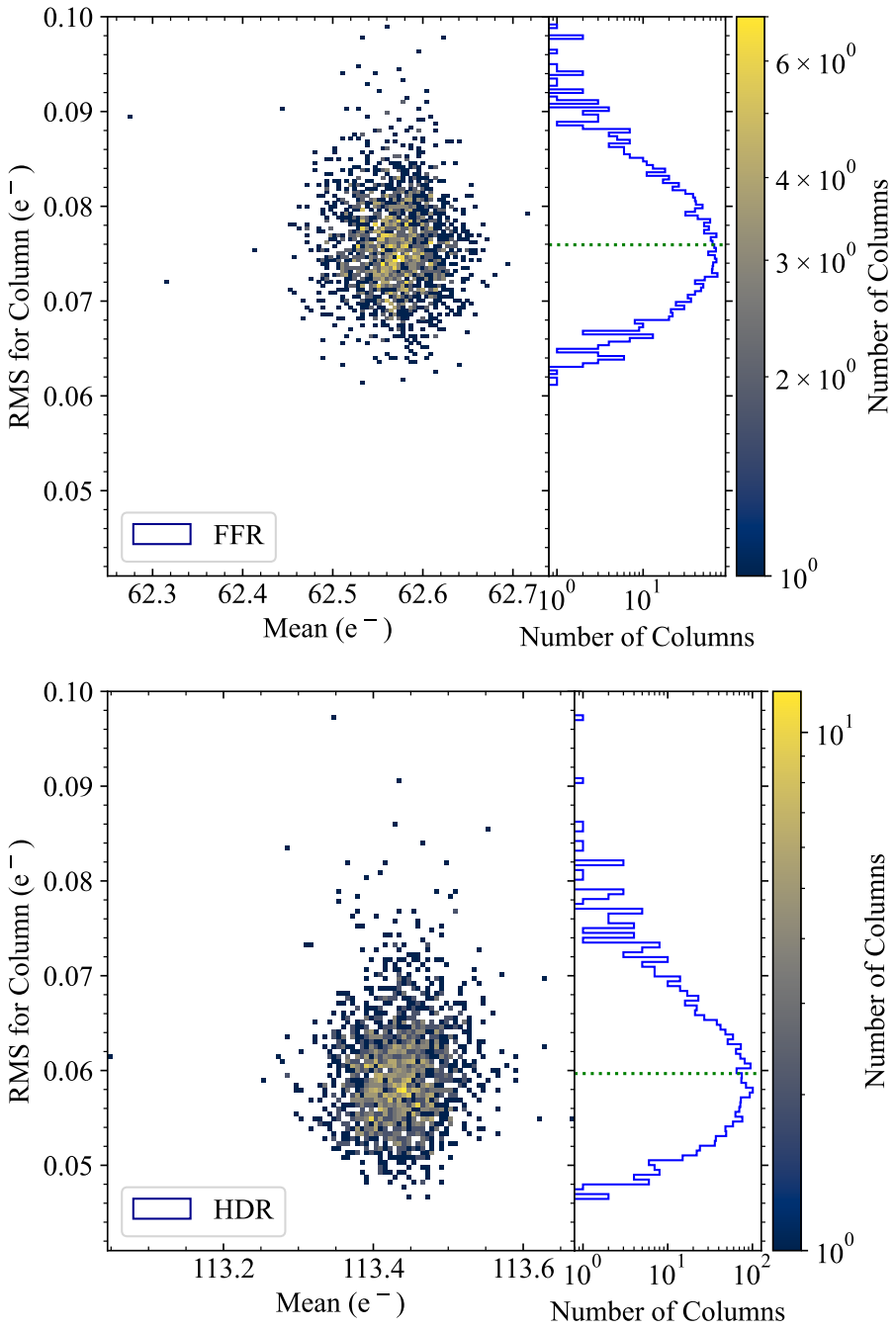


Figure 2.11: Column noise distribution using 100 consecutive bias frames. The 2-D histogram corresponds to column temporal noise. The scattered plot shows the mean value of each column from these frames while the colour bar indicates the number of columns. The logarithmic column noise distribution is shown in the blue histograms, with the median value as a green dotted line. **Top:** Mean column noise distribution for the FFR mode. **Bottom:** Mean column noise distribution for the HDR mode.

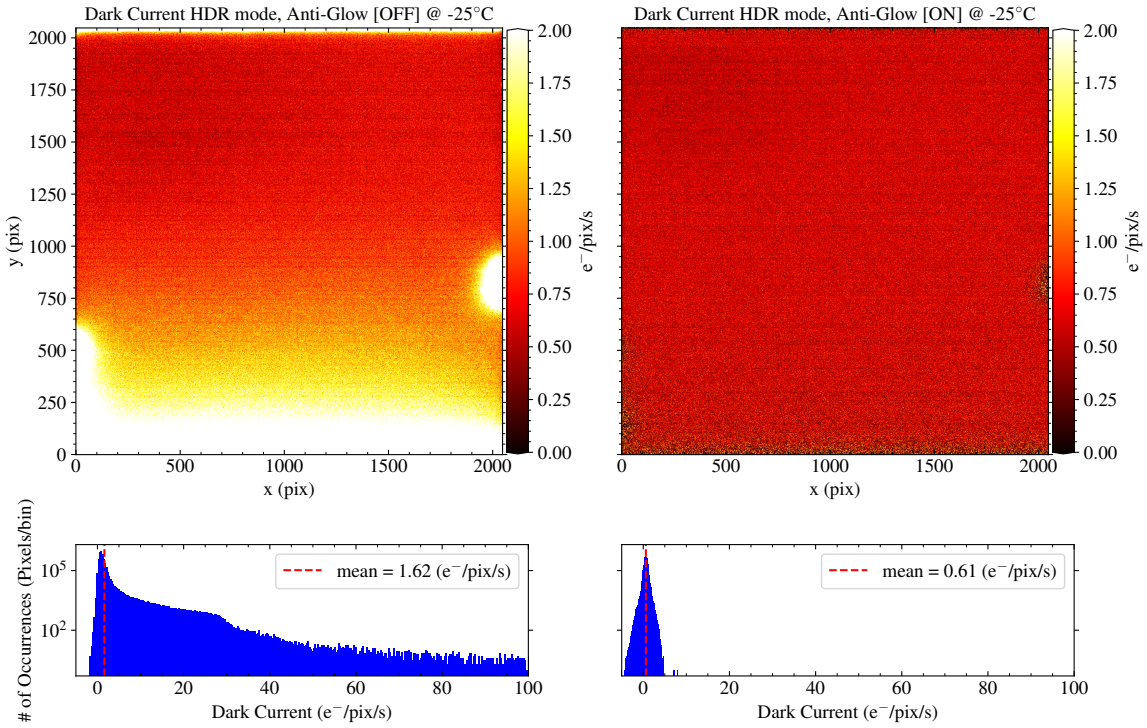


Figure 2.12: Marana dark images taken in the HDR mode at a camera temperature of -25° C. **Left** With the Anti-glow correction OFF. **Right** With the Anti-glow correction ON. Below each we show the histograms of pixel value distributions from each frame, along with the mean (red dotted line).

with correcting the row-column banding were slightly higher at 1.719 e^- for HDR and 1.739 e^- for FFR. This compensation suggests that while banding corrections reduce read noise, additional noise components are present that cannot be removed by this procedure.

2.5.4 Dark frame structure and Dark level measurement

To study the structure in the dark level, we captured two 10 s exposure frames at -25°C: one with the Anti-Glow correction turned ON and one with the Anti-glow correction turned OFF. Exposures were acquired in HDR mode. To isolate the dark signal, we used the 100 bias frames as in Section 2.5.2, to construct a master bias image by averaging the pixel values at each position across all frames (see Equation 2.10). This master bias was then subtracted from each dark frame. To verify that the bias subtraction process did not inadvertently introduce noise, we compared the standard deviation of the dark frames with the Anti-Glow correction turned OFF before and after bias subtraction. The measured standard deviation was 3.291,e^- prior to subtraction and 3.298,e^- afterward, indicating no significant change in noise level. Subsequently, each dark frame is divided by the exposure time to convert it to dark level per unit time in e^- pix^{-1} s^{-1}. The resulting dark level images, along with histograms of pixel value distribution, are shown in Figure 2.12.

The dark image with the Anti-Glow correction OFF shows large scale structure with areas of the image at levels that exceed 2 e^- pix^{-1} s^{-1}. Glow spots are evident at the edges of the array and most prominent in the bottom rows, a strip of rows at the top of the array, and spots in the lower left and centre right of the array. These structures are caused by amplifier glow (see Section 2.2.4). The full frame image has a mean value of 1.62 e^- pix^{-1} s^{-1}. The presence of glow is also clearly evident in

the distribution of the pixels as shown in the histogram of Figure 2.12.

The dark image with the Anti-Glow correction ON is a result of an on-camera master dark frame subtraction for the user requested exposure (see Section 2.2.4). This results in the suppression of the large scale glow structure, although the regions of very high glow can still be in the image. Turning the Anti-Glow ON removes the glow pattern from the frame, but will not remove the shot noise produced from the glow. The mean dark level is reduced 0.61 $e^- pix^{-1} s^{-1}$, and the pixel value distribution is much narrower than the distribution with the Anti-glow correction OFF. An improvement in the reference image used for the Anti-glow correction means that our dark image is much more uniform than the dark frame for the Marana presented in Karpov et al. (2019).

We note that after the anti-glow correction some pixel values are negative. This phenomenon arises from the short exposure time (10 s) employed to capture the dark frame. In these cases, the dark current may not be sufficiently large compared to the bias level to be the dominant noise source in the frame. The Poisson noise after the bias level and the pre-computed dark map subtracted remains in the image. As a result, some pixel values will be positive and some negative, centered around a mean of near zero. The negative values are visibly evident in the histogram distributions in Figure 2.12.

The anti-glow correction proves effective in cosmetically removing the glow from the image. Nonetheless, it is essential to note that this correction is a calibration image for addressing glow in dark current images. As such, it does not eliminate the noise component associated with the dark current signal. The glow noise can be reduced if the amplifiers are set in low power mode during exposure and only initiated during the readout time (Janesick et al., 2007; Wang et al., 2015). This is feasible considering the fast speeds of CMOS cameras, where the amplifiers do not have to operate for a long time on a full integration. This approach minimizes glow, leaving dark current as the primary source of measured noise. Nevertheless, this option is not applicable.

In the HDR mode and at -30 °C, the dark current with the Anti-Glow correction ON is 0.50 $e^- pix^{-1} s^{-1}$, and OFF is 0.80 $e^- pix^{-1} s^{-1}$, which is in agreement with the value reported by Karpov et al. (2019) at temperature -30 °C. We note that Khandelwal et al. (2024) found the dark current for the Sona-11 camera to be 4.5 $e^- pix^{-1} s^{-1}$at -25 °C. However, it is not clear if this is the average value of the full frame image or in cropped regions, that can potentially be affected by glow.

We see from Figure 2.12 that the glow is much more prominent in some regions of the image compared with others. Therefore, one way to mitigate the dark current effect is to avoid placing targets of interest within the areas most affected by glow. For photometry, this includes the target star and also the comparison stars.

To quantify the dark signal for the Marana camera, we measure the mean dark signal as a function of exposure time across a range of temperatures and with the Anti-Glow correction disabled. In order to achieve temperatures below -30 ° C we used a water cooling system. We take exposures ranging from 1 s to 10 s in steps of 1 s. For each frame we calculate the mean frame value. We used this method for both modes. The results are shown in Figure 2.13 for FFR readout mode. For simplicity, we did not plot all the linear fits and only chose to show the fit for three temperatures at +15 °C, -25 °C and -45 °C[6].

[6]These are the customer default temperature settings that the camera has been optimized by Andor for best imaging performance.

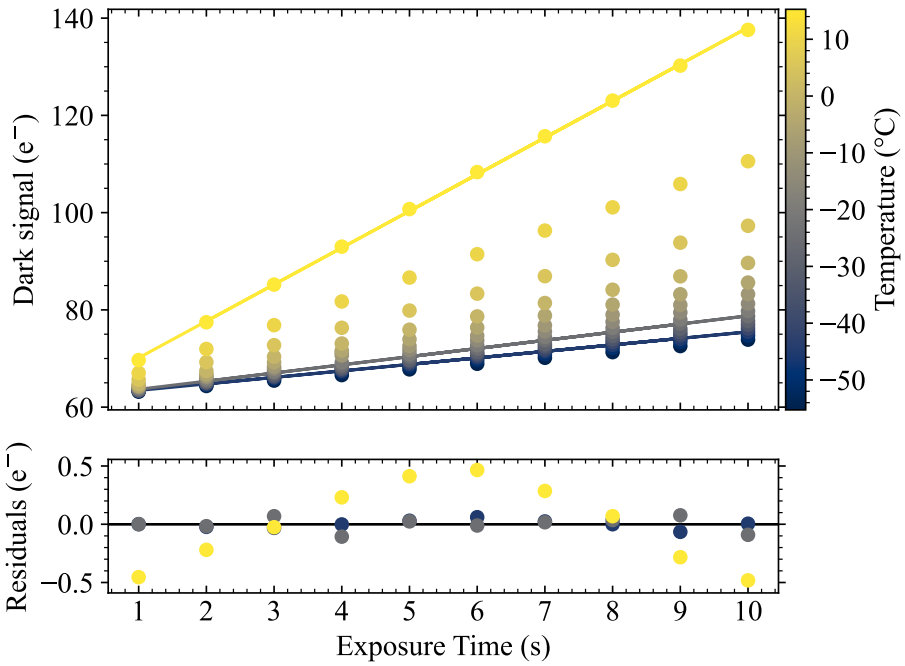


Figure 2.13: Mean dark signal as a function of exposure time over a range of temperatures (color-coded) for the Marana camera in FFR mode. The solid lines represent the slopes at three distinct temperatures at 15 °C, -25 °C and -45 °C. The slope measures the mean dark current of the camera. The intercept indicates the mean bias level of the system. The lower panel shows the residuals from the linear fit from the three temperatures.

The best fit function to the data shows a very good linear relationship between exposure time and mean pixel level, with typical R^2 values for the fit above 0.999 (see Figure 2.13 and Table 2.4). The slopes represents the dark current and the y-axis intercept gives the bias level. It is evident that as temperature increases the slope tends to be steeper and therefore increasing the dark current.

For the FFR mode we find that the dark current (dark signal rate) and bias level at -25 °C to be 0.736 e^- pix^{-1} $s^{-1}$and 98.129 ADU respectively. For the HDR mode, we find the dark current and the bias level at -25 °C to be 0.672 e^- pix^{-1} $s^{-1}$and 99.957 ADU respectively. The bias levels are in agreement with our measurements from Section 2.5.2 yielding an average 98.30±0.11 ADU from the intercepts, which is within 1σ from the measured bias level for the FFR mode in Section 2.5.2. The lower panels of Figure 2.13 display the residuals from the linear fit. In both modes, the Marana CMOS camera shows a considerably higher dark current compared to CCDs.

To investigate the dependence of dark current on camera temperature we used the above analysis for temperature ranging from +15 ° C to -55 ° C in steps of 5 ° C. The slope for each dark signal measurement with the exposures was extracted and plotted in a logarithmic scale Figure 2.14. The predicted dark current (DC) follows the Arrhenius behaviour (Widenhorn et al., 2001) in the form:

$$\mathrm{DC} = D_0 \exp \frac{-\Delta E}{kT}, \tag{2.22}$$

where D_0 is a constant, the ΔE is the activation energy, k is Boltzmann constant and T is the temperature.

As noted by Widenhorn et al. (2001), the dark current can sometimes deviate from a simple

exponential trend as a function of temperature. Our data is best fitted using a two-exponential model for the temperature dependence and at different regions on the images. At lower temperatures, the dark current follows an exponential form that is weakly dependent on temperature. At higher temperatures, the data follows an exponential that is more strongly dependent on temperature. To accurately capture this behaviour, we employ a model that is constructed using the following formula:

$$\mathrm{DC} = D_0 \exp\left(\frac{-A}{T}\right) + D_1 \exp\left(\frac{-B}{T}\right), \tag{2.23}$$

where D_0, D_1, A and B are constants.

For each region the logarithmic dark current differs, with a tendency of larger values in the glow regions, as shown in the middle right, bottom row and middle left labels in Figure 2.14. Overall, our model shows two distinct behaviours with differing dependencies on temperature. At higher temperatures the dark current follows a strong temperature dependency (see values in Table 2.5). At lower temperatures the dark current follows a much weaker temperature dependency (see values in Table 2.5). The strong temperature dependency, is less evident in the first three plots in Figure 2.14, since those regions are dominated by glow. For the average full frame image measurements, the dark current follows a strong temperature dependency with $A = 10.7\,\mathrm{K}$. At lower temperatures, the dark current follows a much weaker temperature dependency of $B = 0.625\,\mathrm{K}$. The overlapping of the two exponential functions occurs at temperature 8.8 °C. The same two-temperature behaviour is observed in all regions, including those with minimal glow. This indicates that the total array is affected by glow, even if the average dark current measured across the full frame is smaller than the values measured directly in the glow dominated regions. For temperatures below 0 °C the dark current is dominated by the amplifier glow, that is weakly dependent on temperature. Only for temperature above 0 °C does the dark current have a significant contribution from the classical thermal noise which is more strongly temperature dependent.

The large dark current signal remains the major drawback of CMOS sensors compared with CCD detectors. For faint objects with low sky background signal, the high dark current from certain CMOS detectors continues to position them as a secondary choice compared to their CCD counterparts. However, some CMOS sensors have significantly less amplifier glow, such as the SONY IMX455, that has demonstrated exceptionally low dark current, even at relatively warm temperatures, reaching as low as $0.018\,\mathrm{e^-\ pix^{-1}\ s^{-1}}$at 0 °C (Alarcon et al., 2023a).

2.5.5 Photo Response Non-Uniformity (PRNU)

To study the PRNU we follow Section 4 of the EMVA-1288 (Jähne, 2010) version 4.0 documentation. The 100 half-saturation images were averaged, and the mean value is calculated as in Section 2.5.2. To measure the spatial variance we used the following:

$$s^2_{y.\mathrm{light}} = \frac{1}{MN} \sum_{m=0}^{M-1} \sum_{n=0}^{N-1} (\bar{y}_{\mathrm{light}}[m][n] - \mu_{y.\mathrm{light}})^2 \tag{2.24}$$

where the spatial variance of the averaged frame is denoted as $s^2_{y.\mathrm{light}}$. However, there is still a temporal variance component included in the value. Therefore, we adjusted the spatial variance by subtracting the residuals of the temporal variance:

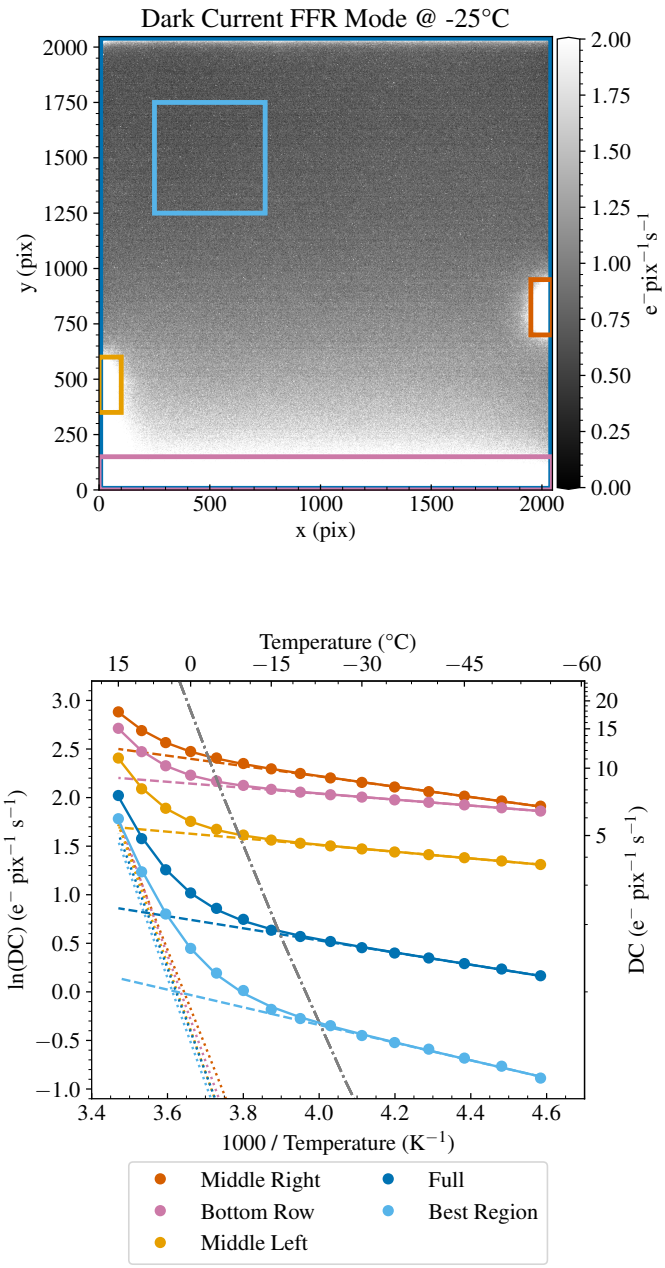


Figure 2.14: The logarithmic dark current as a function of the inverse temperature, following the form of Widenhorn et al. (2001). **Top:** An example dark current image showing the regions of the used for the measurements. **Bottom:** The dark current as a function of temperature for each region. The solid coloured lines represent the best-fit model, which is composed of the sum of two exponential functions (shown as the dotted line and the dashed line). The gray dash-dot line and squares represents the dark current of iKon-L SO Blue Sensitive CCD camera from Andor, as reported in the specification sheet.

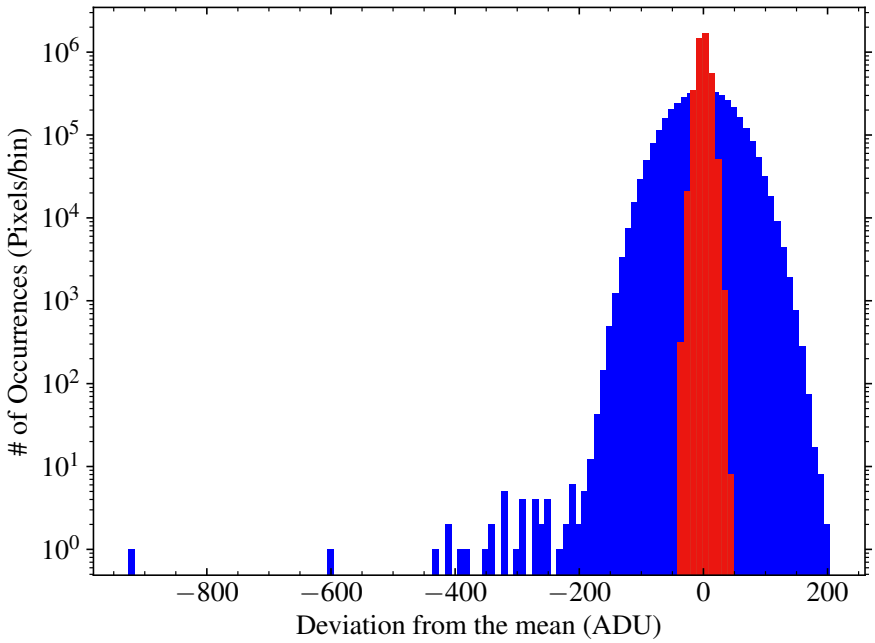


Figure 2.15: Histogram distributions of the photo response non-uniformities for both modes. The red bins indicate the FFR while the blue the HDR mode.

$$s^2_{\text{PRNU}} = s^2_{y.\text{light}} - \frac{\sigma^2_{m,n.\text{light}}}{K} \tag{2.25}$$

where the variance with the temporal noise suppressed s^2_{PRNU}, the variance before the temporal noise subtraction $s^2_{y.\text{light}}$, the temporal variance $\sigma^2_{m,n.\text{light}}$ and K the number of images used. The PRNU is the difference of the variances calculated with and without illumination, and divided by the corrected mean value of the signal at half saturation after subtracting the bias level:

$$\text{PRNU} = \frac{\sqrt{s^2_{\text{PRNU}} - s^2_{\text{DSNU}}}}{\mu_{y.\text{light}} - \mu_{y.\text{bias}}} \tag{2.26}$$

where the variance of the bias level s^2_{DSNU}, the mean value at half saturation $\mu_{y.\text{light}}$ and the mean bias level $\mu_{\text{y.bias}}$. The distribution of the PRNU was plotted as shown in the upper panel of Figure 2.15. The HDR mode exhibits a significantly larger spread compared to the FFR mode. This disparity arises because the half-saturation point for the HDR 16-bit setting is 30000 ADU, whereas for the FFR 12-bit setting, it is only 2000 ADU. Temporal suppression was performed using 100 images; however, in HDR mode, the temporal noise still contributes and therefore leads to a broad distribution. In contrast, this effect is not observed in FFR mode, as the lower half-saturation point of 2000 ADU allows 100 images to sufficiently minimise the spread in the histogram. The results demonstrate that the camera maintains uniform performance, with PRNU values of 0.131 % for HDR mode and 0.294 % for FFR mode.

Since the HDR mode operates using the LG channel at half-saturation, the measured PRNU values suggest that the signal is more uniform in the LG channel, as the PRNU in FFR mode is twice that of HDR mode.

2.5.6 Linearity Results

The linearity is expressed through the linear relationship between the mean pixel signal and the exposure time with a constant light source and at a fixed temperature. This is accomplished by fitting a linear model using weighted least square regression, following the guidelines outlined in EMVA-1288 version 4.0 (Jähne, 2010). The linear model is described as:

$$y[i] = mt_{\text{exp}}[i] + b, \tag{2.27}$$

where $y[i]$ is the mean signal from two consecutive frames and t_{exp} is the exposure time. Since the bias level has been subtracted the residual offset b is zero. For each mean signal level we assign a weight $1/y[i]^2$. The residuals from the linear regression is measured in percentage and calculated as:

$$\delta_y[i] = \frac{\mu_y[i] - (mt_{\text{exp}}[i] + b)}{mt_{\text{exp}}[i] + b} \times 100. \tag{2.28}$$

We quantify the uncertainty in the linearity using the linearity error (LE), which is the average of the absolute values of the deviation of the data points in the range of 5 % to 95 % from the saturation value:

$$LE = \frac{1}{n} \sum_{i=1}^{n} \mid \delta_y[i] \mid, \tag{2.29}$$

where n is the number of the set of images between 5 % and 95 % of saturation value. The results for both FFR and HDR modes are shown in Figure 2.16. The camera demonstrates small non-linearity, yielding linearity errors of 0.066 % and 0.102 % for FFR and HDR mode respectively. These results are consistent with Andor specification for linearities within the range of > 99.7 %.

Over the years, the EMVA-1288 standard has introduced updates to the methods used for measuring camera non-linearity. In this study, we also report results obtained using previous methodologies from release version 3.0 and release version 3.1 candidate 1 and candidate 2. The release version 3.0 follows the same approach as release version 3.1 and calculates residuals from linear regression without incorporating weights. Non-linearity is determined as the average distance between the maximum and minimum residual from the linear regression method.

The release version 3.1 candidate 2 uses the weights on the linear regression to estimate the residuals and two non-linearity values are reported, one for the maximum and one for the minimum residual values. Therefore, the release version 3.0 yields 0.098 % and 0.122 % for the FFR and HDR, and release version 3.1 candidate yields maximum 0.105 %, minimum -0.205 % and maximum 0.277 % and minimum -0.250 % for the FFR and HDR respectively.

We note that the linearity is not evaluated below 5% of saturation when following the EMVA-1288 standard . Since the transition region in HDR mode occurs below this threshold, it is typically excluded from the calculation. Furthermore, this means that for faint stars with brightness below 5% of the saturation, linearity is not guaranteed. To investigate this behaviour, we expand the boundaries of the linearity analysis to include the range from 0.01% to 95% of saturation. The results are presented in the top panel of Figure 2.17, while the bottom panel provides a close-up view of the transition region between the HG and LG channels. The non-linearity was found to be 0.698 %, with

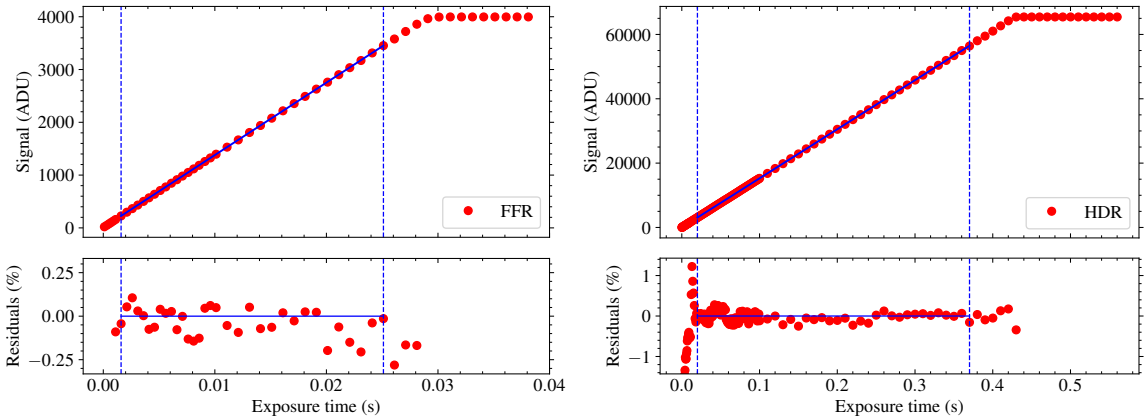


Figure 2.16: Linearity measurements for the Marana in FFR mode (left) and HDR mode (right). The best fit linear model between 5 and 95 % of saturation is plotted with a blue solid line. Residuals to the linear model are shown in the bottom panels. The dashed horizontal blue lines indicate the 5 to 95% boundaries we set to measure fit the linearity.

maximum and minimum residuals of 0.834 % and 1.033 % respectively. Those values are larger than the values reported in the range of 5-95%.

Despite the transition in the two gain channels when sampling signal levels at ~ 1800 ADU, as described in Figure 2.5, the camera demonstrates excellent linearity within the range, consistent with the manufacturer's documentation. The Marana camera show good linearity even when measuring it within a wider range of 0.01 % to 95 %, showing that the sensor is linear in low light signals, despite the ±1 % deviation in the transition region, as shown in Figure 2.17. Our linearity measurement is in agreement with previous works in Qiu et al. (2021) and Khandelwal et al. (2024).

2.5.7 Quantum Efficiency and Transmission Window Results

We measure the photodiode current across a wide range of wavelengths. The responsivity curve of the photodiode, is extracted from the datasheet (see Figure 2.23) and converted to QE values (see Figure 2.24 and Equation 2.39). We measure the camera flux by averaging 10 images of the same exposure after subtracting the bias level in the HDR mode. The absolute QE of the camera is defined as:

$$QE\ (\%) = \frac{G \times S \times q \times \text{PDQE}}{\text{PDC} \times t} \times 100 \tag{2.30}$$

Where G is the gain (e^-/ADU), S is the sum of the signal from all pixels in the averaged frame in ADU, q is the electron charge in Coulomb, PDQE is the QE of the photodiode, PDC is the photodiode current in amperes and t is the exposure time of the images taken with the camera in seconds. The QE was measured at 3 different temperatures; +25 °C, +15 °C and -45 °C as shown in Figure 2.18.

The measured QE is in close agreement with the manufacturer's specifications within the 450–900 nm wavelength range. In the 400–450 nm region, the measured QE is up to 10 % lower than the manufacturer's values, whereas in the 950–1020 nm region, it exceeds the manufacturer's QE by up to 10 %. The Marana camera is most sensitive at ~ 560 nm with a 95 % peak QE. Additionally, the QE curve shows a small increase at higher sensor temperatures and toward the red end of the spectrum when compared against the -45 °C dataset.

Previous studies from Weakliem & Redfield (1979) and Velichko et al. (2019) show that the QE

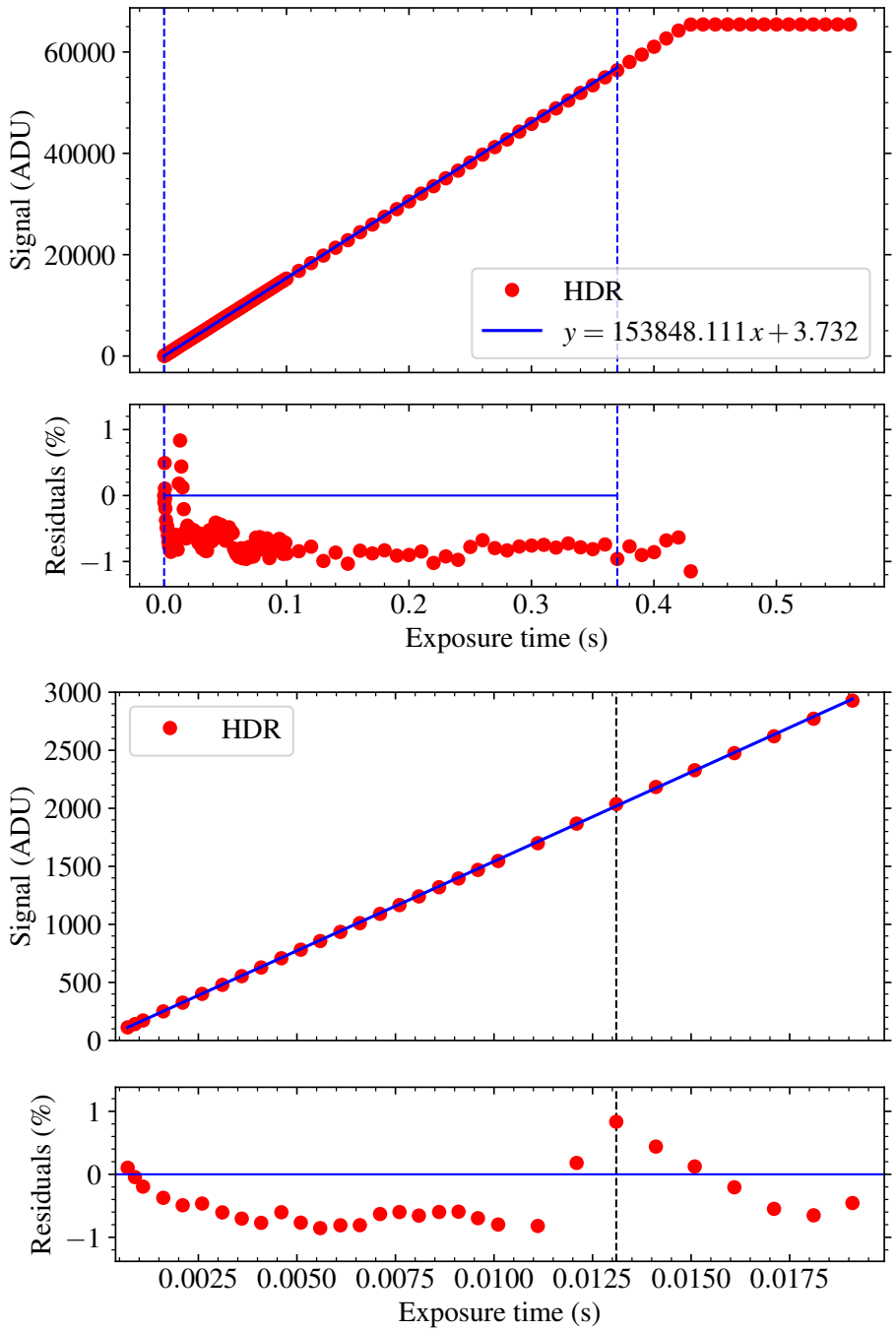


Figure 2.17: **Top:** Linearity measurements for the Marana in the HDR mode. The best fit linear model between 0.01 % and 95 % of saturation is plotted with a blue solid line. Residuals to the linear model are shown in the bottom panels. The dashed vertical blue lines indicate the 0.01 % to 95 % boundaries we set to measure linearity. **Bottom:** Zoom in panel of the linearity in the transition region. The black dashed line indicates the transition region from HG to LG channel.

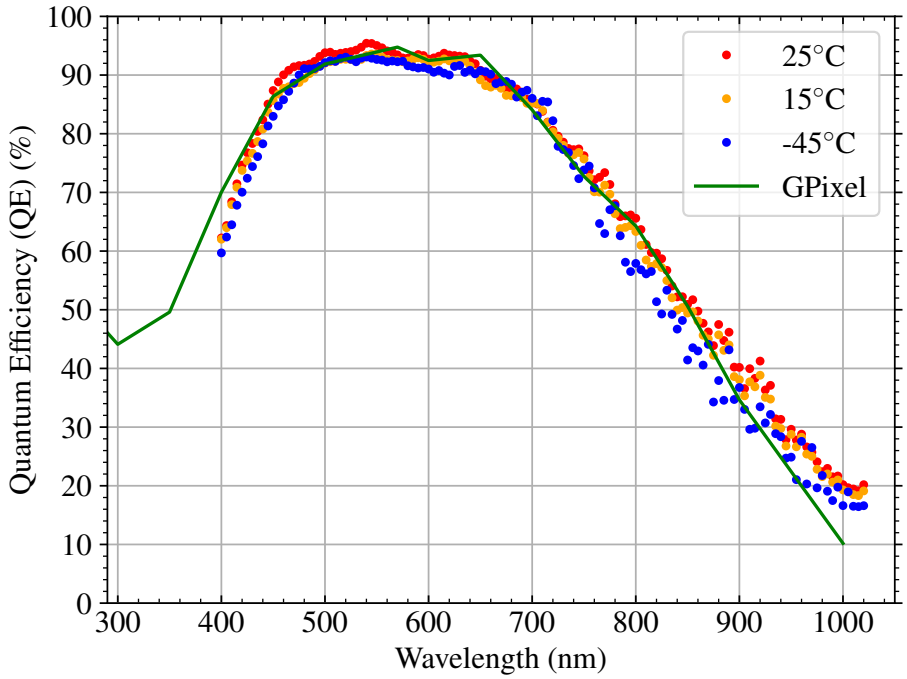


Figure 2.18: QE results for Marana sCMOS camera at three temperatures. With red circles the QE at +25 °C, with orange squares the QE at +15 °C and with blue pentagons the QE at -45 °C. The solid green line represents the QE measured by GPixel.

is red-shifted as the temperature is increasing. This behaviour can likely be explained by the effect of the band gap energy. The band gap energy required to excite an electron on a silicon is 1.12 eV at constant temperature 300 K yielding an upper limit of 1107 nm (cut-off wavelength) (Strehlow & Cook, 1973; Sze et al., 2021; Stefanov, 2022) and producing a single electron-hole pair.

The band gap energy increases slightly at lower temperatures (Bensalem et al., 2017) and therefore the cut-off wavelength is shorter at lower temperatures. Additionally, Green (2008) demonstrated that at lower temperatures the absorption length of the silicon also increases. Consequently, electrons require more energy to transition to the conduction band when incident photons interact with the silicon and therefore fewer electrons are promoted at lower temperatures compared to warmer temperatures. This is expressed as in the following equation from (Bensalem et al., 2017):

$$E_g = E_0 - cT \tag{2.31}$$

where the E_g is the band gap energy for silicon, E_0 is the band gap energy at 0 K, T is the temperature in K and c constant. The effect is more evident at longer wavelengths. This is in agreement with the results in Figure 2.19 showing the normalised QE measurements with respect to the -45 °C QE measurement, where the normalised ratio increases at redder wavelengths for warmer temperatures. The data is being smoothed using the `UnivariateSpline` python package.

To quantify the transmittance of the window, we measured the amount of photons that successfully pass through the camera's optical window for various wavelengths. Transmittance is defined as the ratio of the intensities of the transmitted light and the reference light. This measurement shows which photons are efficiently transmitted and which are partially or fully reflected or absorbed by the window material. This is expressed as the following:

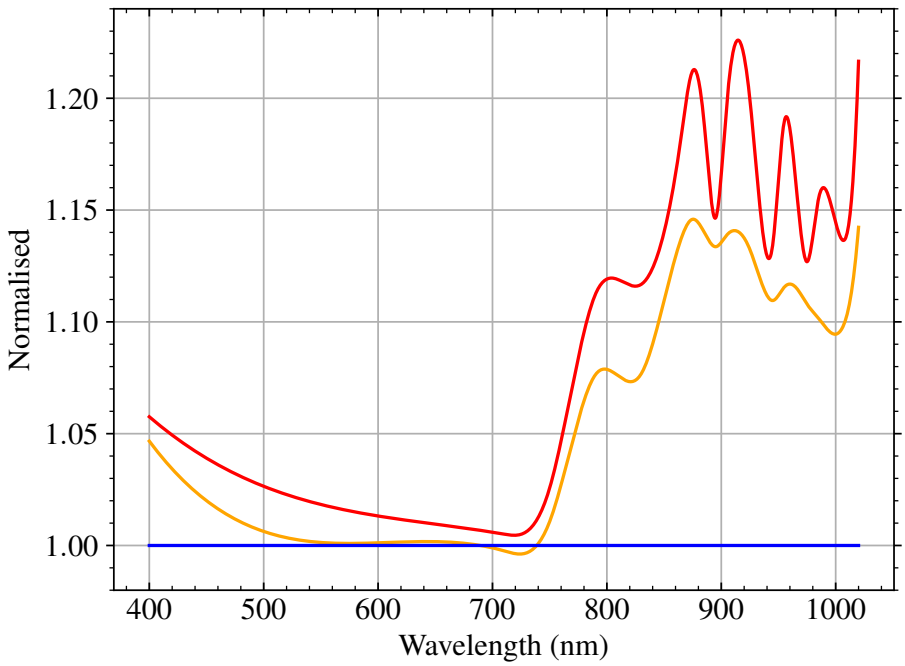


Figure 2.19: Normalised QE measurements as a function of wavelength with respect to the -45 °C QE measurement, showing with the blue line. Orange line indicates the QE measurement for +15 °C while with red line the QE measurement for +25 °C.

$$\text{Tranmission}(\lambda) = \frac{I_t(\lambda)}{I_0(\lambda)} \tag{2.32}$$

where $I_t(\lambda)$ is the photocurrent measured at a specific wavelength with the camera's window in the optical path and $I_0(\lambda)$ is the photocurrent measured with a clear path between the light source and the photodiode for the same wavelength. We recorded 10 current measurements for each wavelength step and estimate the mean and the standard deviation. The ratio of the mean values of these current measurements (see Figure 2.25) was plotted as a percentage figure as shown in Figure 2.20. The transmission curve provided by the window supplier has been included in the same figure for comparison. The results show a slight decrease in transmission to approximately 82 % in the range of 400-500 nm as illustrated in Figure 2.20. Additionally, Andor reported that the steep increase at wavelengths <400 nm is applied to enhance the sensitivity for applications that require observations at shorter wavelengths. Transmission approaches nearly 100 % within the camera's peak sensitivity range and gradually decreases toward redder wavelengths.

2.6 Conclusions

We present a characterisation of the Andor Marana CMOS camera, according to the EMVA-1288 version 4.0 standard. Laboratory tests were conducted in both HDR and FFR modes of the Marana camera. A summary of the Marana camera performance as measured in this work is set out in Table 2.2.

The read noise is low for both modes, and along with the full well depth of the HDR mode, it has good dynamic range. For illumination levels before the transition region, pixels are processed

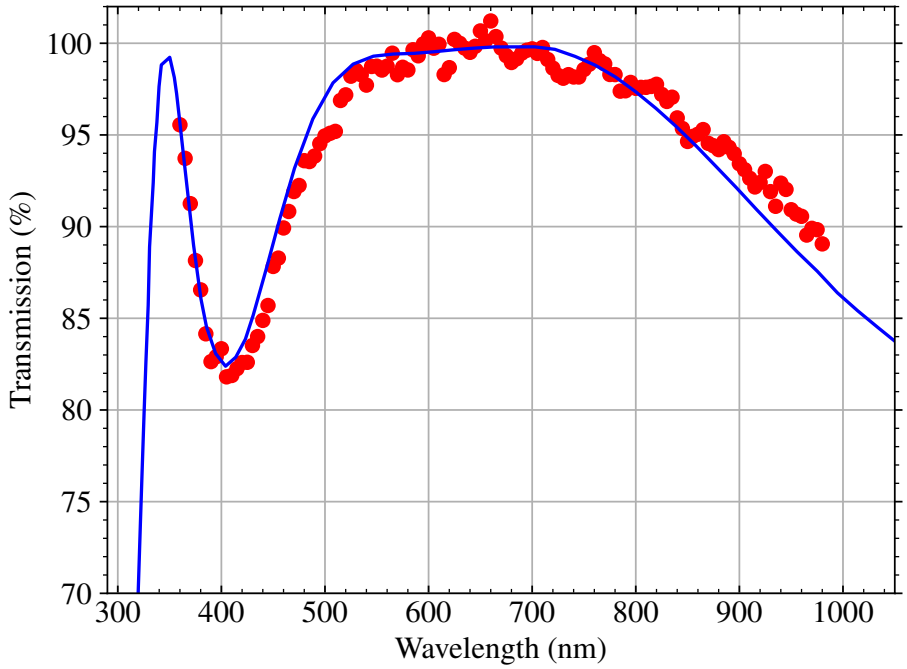


Figure 2.20: Transmission as a function of wavelength for the window which is mounted on the Marana CMOS camera measured as the fractional percentage ratio of the photodiode current measurements from Figure 2.25. The measured data is show with red while for comparison is the transmission curve from Andor with blue solid line. The y-axis is zoomed-in for detailed visualisation.

Table 2.2: Specifications of the Marana CMOS camera measured in this work in comparison with a deep depleted back-sided iKon-L 936 CCD which is currently operating at NGTS telescopes.

Camera mode	**Marana FFR**	**Marana HDR**	**iKon-L**
Digital output	12-bit	16-bit	16-bit
Readout modes	200 MHz	100 MHz	3 MHz
Gain, e^-/ADU	0.632	1.131	1.99
Full Well Capacity, e^-	2351	69026	82000
Non-Linearity, %	0.099	0.122	1*
Read Noise, Median (RMS) e^-	1.577 (1.785)	1.571 (1.763)	12.9
Dark Current Anti-glow ON	0.736 @-25°C	0.672 @-25°C	N/A
Dark Current Anti-glow OFF	1.674 @-25°C	1.617 @-25°C	0.003 @-80°C
PRNU, %	0.294	0.131	1.79
DSNU, e^-	0.318	0.232	3.79
Row Noise, e^-	0.467	0.438	N/A
Column Noise, e^-	0.076	0.06	N/A

[7]The CCD linearity was measured using a different method from that adopted in this work.

with the HG capacitance yielding low read noise. For illumination levels larger than the transition region, the LG capacitance is employed yielding read noise of $40\,e^-$. This read noise change may affect stars with shot noise similar to the read noise. The FFR mode exhibits similar read noise characteristics with the HDR mode, however it has low dynamic range. This limitation becomes critical when observing bright stars, which are more likely to saturate in the FFR mode. The FFR mode is more well suited for fast tracking and high cadence photometry of faint stars where saturation is not achieved early.

Since CMOS sensors employ multiple amplifiers, variations between them can result in significant pixel-to-pixel differences in read noise. In addition, individual pixels may be affected by RTS or inherently noisy amplifiers. This behaviour can have a notable impact on the detection of faint stars, where only a few electrons are collected and may become indistinguishable from RTS induced fluctuations. To mitigate these effects, correction maps should be created or existing solutions, such as spurious noise filter, should be applied.

The Marana camera exhibits a dark current level that is higher than what is typically observed in modern CCD sensors (see Table 2.2, and accompanied by persistently preserved glow spots at the image edges. This contributes significantly to non-uniformities in the frames and the total dark current, creating a blend of dark current and glow. To prevent corruption of the quality of data for high precision photometry, selection of targets near the edges will be avoided as the stars can easily jump out of the frames during tracking. This will result in smaller image format and field of view, which will limited the number of comparison stars for photometry.

Despite the good linearity in the transition region in the HDR mode, faint stars can be affected by the dual amplification from the two channels assuming stars with signal in the same level of the transition. Similar effect for bright stars may occur due to nearby bright pixels in the point-spread function that receive significantly less signal than the star's central pixels, making them more susceptible to the transition level.

The Marana camera offers several advantages for astronomical applications when compared to CCD-based systems such as the iKon-L (see Table 2.2). Its fast readout speeds and low read noise can outperform many standard CCD cameras, making it well-suited for high-cadence time-series photometry where improved temporal resolution is required. The absence of a mechanical shutter further reduces operational complexity and minimizes the need for maintenance or complete shutter replacements. However, like most CMOS sensors, including GSENSE400BSI, deep-depletion technology is not applicable yet. As a result, QE at redder wavelengths remains lower compared to deep-depleted CCDs specifically designed for enhanced red sensitivity. Moreover, the Marana camera provides a dynamic range of 93 dB[8], which is superior to single-channel cameras such as the QHY600, which utilizes Sony's IMX series sensors and typically achieves a dynamic range of around 83 dB (Alarcon et al., 2023a). The GSENSE400BSI sensor used in the Marana also offers a broad QE across the visible spectrum, outperforming the IMX series in this regard and enhancing the camera's sensitivity.

The next step of our study will be to perform time-series photometry using the CMOS Marana camera in real on-sky conditions. To do this, we plan to mount the Marana on an NGTS (Wheatley

[8]For detector dynamic range, it usually describes the ratio between the largest measurable signal and the smallest measurable signal/noise floor, the equation: DR = 20 log10(full well capacity / read noise)

et al., 2018) telescope at the Paranal observatory in Chile. We plan to run the Marana at NGTS simultaneously with one of the existing iKon-L CCDs, providing a direct on-sky comparison between the CMOS and CCD detectors for time-series photometry.

2.7 Appendix: Bias, Light and temperature stability

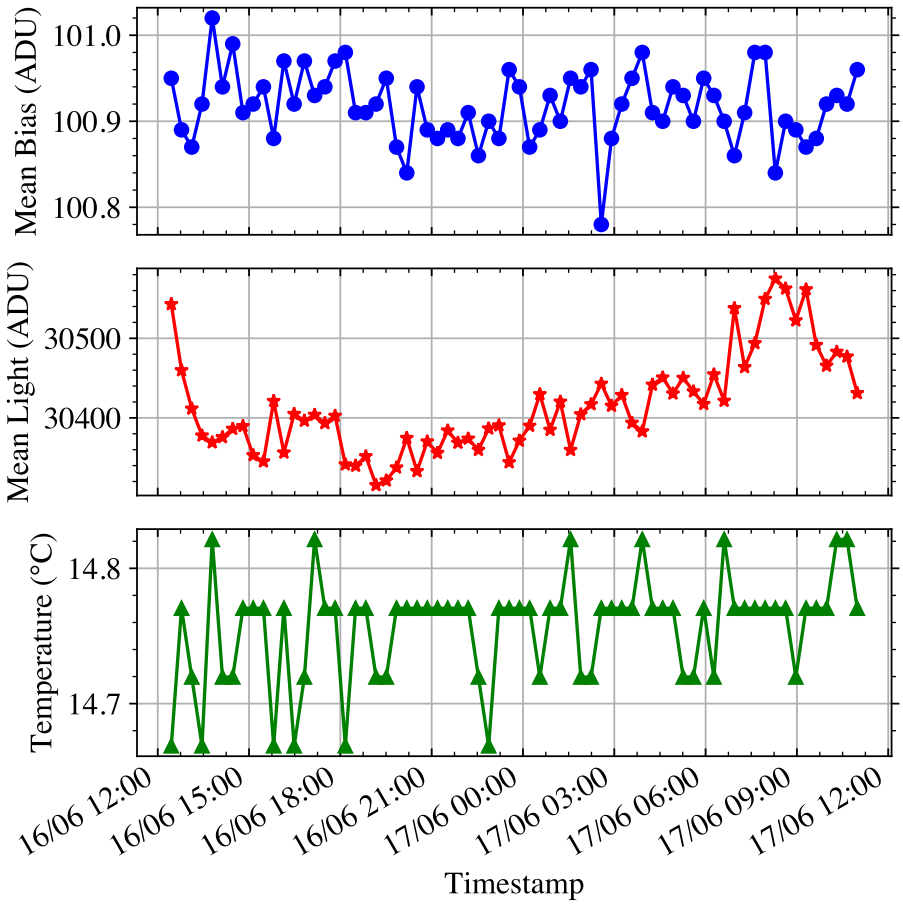


Figure 2.21: Bias level, light source signal and temperature for the Marana camera over time. **Top:** Average bias level value of a series of images at minimum exposure time and at dark environment. **Middle:** Average light source signal of a series images at a fixed exposure time. **Bottom:** Temperature value measured from the camera.

Table 2.3: Exposures steps based on the saturation exposure (1.5 seconds.

Exposure Time	Exposure Step
>= 0.0001 s	0.0002 s
>= 0.001 s	0.0005 s
>= 0.01 s	0.001 s
>= 0.1 s	0.01 s
>= 1 s	0.1 s

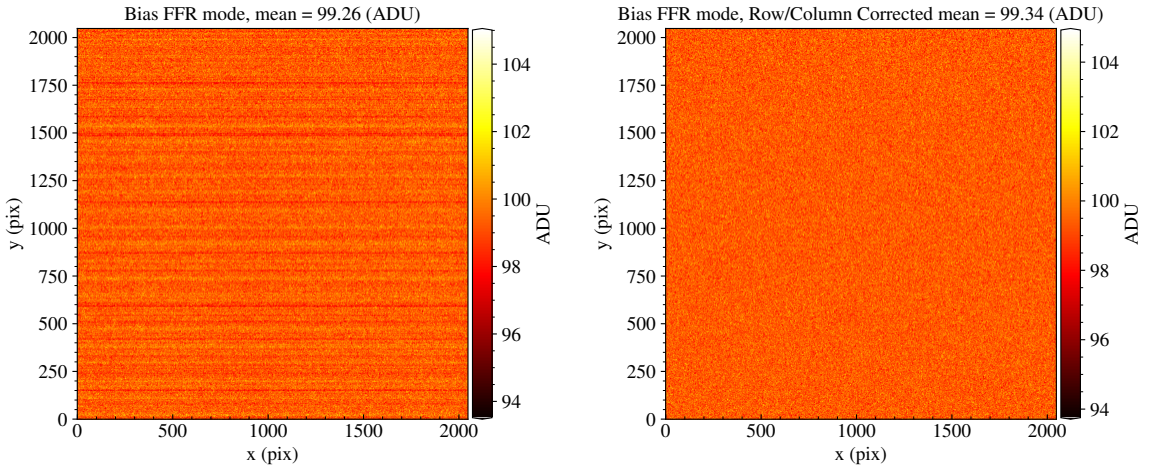


Figure 2.22: Bias frames from Marana camera recorded at minimum exposure for the FFR mode (**left**) and the FFR mode with the row and column temporal noise removed (**right**) . The camera is operating at temperature of -25° C.

2.8 Appendix: Quantum Efficiency and Transmission Window calculations

The QE is expressed by comparing the ratio of the number of electrons with the number of incident photons. This is demonstrated as:

$$\text{QE} = \frac{\text{Number of electrons}}{\text{Number of incident photons}} \tag{2.33}$$

HAMAMATSU provides the responsivity of the photodiode, as shown in Figure 2.23 which quantifies how efficiently it converts optical power into electrical current. However, since the goal is to compare the QE of the camera with that of the photodiode, the responsivity must first be converted to QE for a direct comparison. From Equation 2.33, the number of electrons is approximated as:

$$N_e = \frac{I[A]}{q[C]} \tag{2.34}$$

where the current I, measured in Amps divided by the charge of a single electron q in Coulombs. On the other hand, the number of photons striking the photodiode is the light power and is expressed as:

$$P[J/s] = N_p h[Js] \frac{c[m/s]}{\lambda[nm]} \tag{2.35}$$

Where P is the Power measured in Joules per second, the number of photons N_p, the Plank's constant h in Joules per second, the speed of light c in meters per second and the wavelength λ in nanometres. This equation will take the form:

$$N_p = \frac{P[J/s]\lambda[nm]}{c[m/s]h[Js]} \tag{2.36}$$

Dividing Equation 2.34 with Equation 2.36, yields the QE equation:

$$QE = \frac{\frac{I[A]}{q[C]}}{\frac{P[J/s]\lambda[nm]}{c[m/s]h[Js]}} \tag{2.37}$$

And by doing some dimensional analysis to remove the units, leads to:

$$QE = \frac{\frac{I}{q}}{\frac{P\lambda \times 10e{-}9}{ch}} \tag{2.38}$$

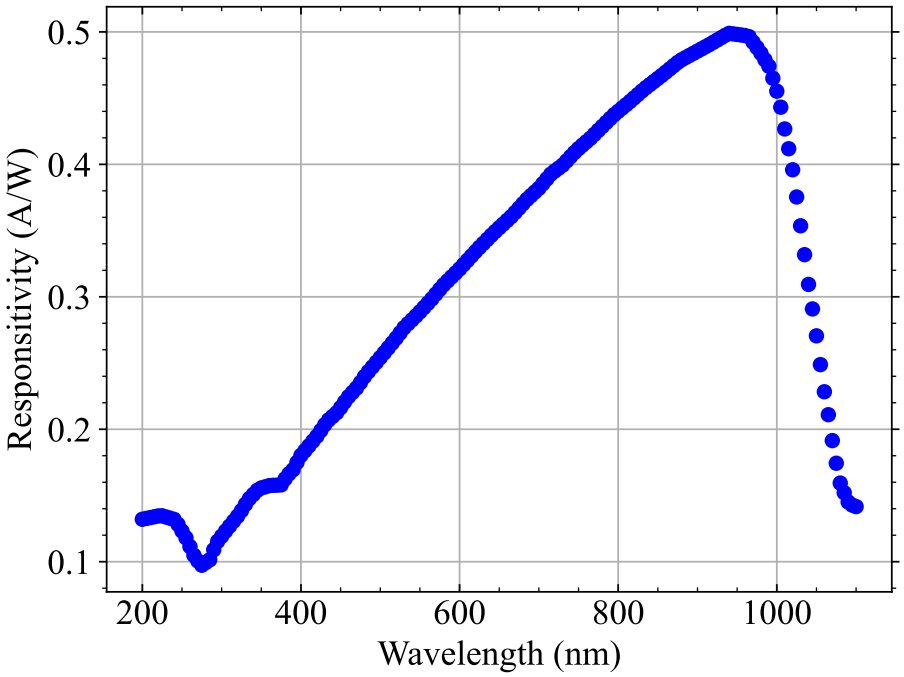


Figure 2.23: The responsivity of the photodiode used for the QE measurements as described in Section 2.5.7 plotted as a function of wavelength.

Solving mathematically the constants and the remaining is the QE of the photodiode:

$$PDQE = 1240\frac{R}{\lambda} \tag{2.39}$$

Where the responsivity of the photodiode R on a particular wavelength. This equation is employed to convert the responsivity values of the photodiode for each wavelength to QE values as shown in Figure 2.24.

2.9 Appendix: Dark signal calculations

2.10 Appendix: Dark current calculations

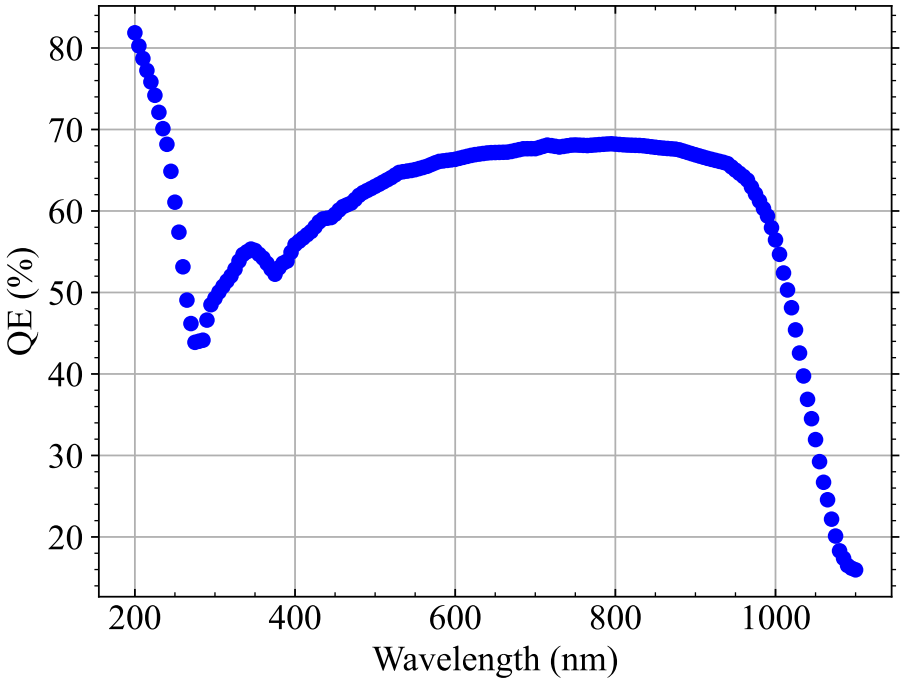


Figure 2.24: The corresponding QE values of the photodiode as a function of wavelength after converting from responsivity using Figure 2.23.

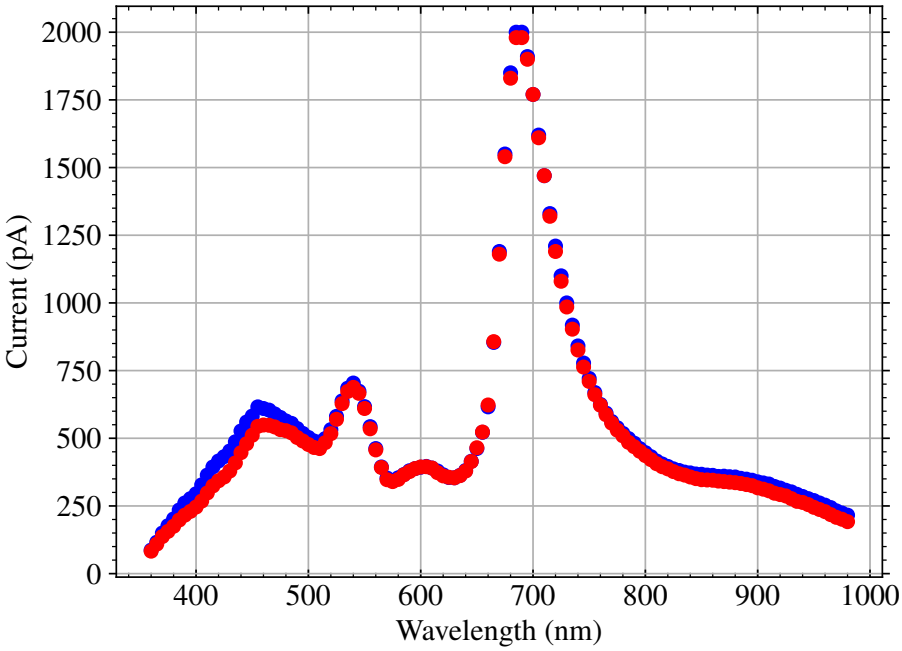


Figure 2.25: Photodiode measurements as a function of wavelength. The current with the transmission window show in red, while with blue current data without the transmission window.

Table 2.4: Best fit from the linear relation of the dark signal as a function of exposure at different temperatures.

Temperature	**Best fit**	R^2	**Intercept**
-55 °C	$1.18059 \pm 0.00875\,e^-\,pix^{-1}\,s^{-1}$	0.99956	97.9789 ADU
-50 °C	$1.26516 \pm 0.00322\,e^-\,pix^{-1}\,s^{-1}$	0.99995	98.2106 ADU
-45 °C	$1.33784 \pm 0.00406\,e^-\,pix^{-1}\,s^{-1}$	0.99993	98.2550 ADU
-40 °C	$1.41730 \pm 0.00370\,e^-\,pix^{-1}\,s^{-1}$	0.99995	98.0159 ADU
-35 °C	$1.49151 \pm 0.00481\,e^-\,pix^{-1}\,s^{-1}$	0.99992	97.9872 ADU
-30 °C	$1.57626 \pm 0.00786\,e^-\,pix^{-1}\,s^{-1}$	0.99980	97.8641 ADU
-25 °C	$1.67426 \pm 0.00705\,e^-\,pix^{-1}\,s^{-1}$	0.99986	97.9353 ADU
-20 °C	$1.76818 \pm 0.00503\,e^-\,pix^{-1}\,s^{-1}$	0.99994	98.0924 ADU
-15 °C	$1.88600 \pm 0.04866\,e^-\,pix^{-1}\,s^{-1}$	0.99470	98.7293 ADU
-10 °C	$2.10966 \pm 0.00749\,e^-\,pix^{-1}\,s^{-1}$	0.99990	98.0786 ADU
-5 °C	$2.36270 \pm 0.01283\,e^-\,pix^{-1}\,s^{-1}$	0.99976	98.1267 ADU
0 °C	$2.76896 \pm 0.00598\,e^-\,pix^{-1}\,s^{-1}$	0.99996	97.9665 ADU
5 °C	$3.51461 \pm 0.00730\,e^-\,pix^{-1}\,s^{-1}$	0.99997	98.3077 ADU
10 °C	$4.84287 \pm 0.01105\,e^-\,pix^{-1}\,s^{-1}$	0.99996	98.4615 ADU
15 °C	$7.54922 \pm 0.04071\,e^-\,pix^{-1}\,s^{-1}$	0.99977	98.8726 ADU

Table 2.5: Best fit of the logarithmic dark current as a function of temperature at different regions on the images.

Region	**Higher Temperature fit**	**Lower Temperature fit**	**Intercept of the fits**
Middle Right	$\ln(5.524 \times 10^{15}) - 9.948\,x$	$\ln(77.30) - 0.532\,x$	22.03°C
Bottom Row	$\ln(1.529 \times 10^{17}) - 10.886\,x$	$\ln(26.20) - 0.306\,x$	18.29°C
Middle Left	$\ln(3.123 \times 10^{17}) - 11.110\,x$	$\ln(17.96) - 0.344\,x$	14.76°C
Full	$\ln(6.828 \times 10^{16}) - 10.700\,x$	$\ln(20.72) - 0.625\,x$	8.80°C
Best Region	$\ln(1.035 \times 10^{17}) - 10.843\,x$	$\ln(27.09) - 0.910\,x$	3.70°C

Chapter 3

Further characterisation of the Marana Camera

"What life? I got no life! I'm in the dark, here! You understand? I'm in the dark!"

'Scent of a Woman', Lt. Col. Frank Slade, 1992

3.1 Introduction

This chapter focuses on the extended characterisation of the Marana CMOS camera not covered in chapter 2. I further explore the dual-amplifier aspect of the Marana camera that allows for high gain and low gain pixel readout (section 3.2). I set out a number of different characterisation tests for each channel (section 3.3) following the same methods as in chapter 2. I test the Marana CMOS camera with different supply voltage values (section 3.4). I also test the image lag in the Marana camera section 3.5. Note, in this work I am using a variant Marana CMOS camera and not the camera characterised in chapter 2. Therefore some parameters may differ slightly between the cameras, such as gain, Full Well Capacity (FWC), linearity and read noise.

3.2 High Gain and Low Gain channels

Dual amplifier readout structure allows for modern CMOS cameras to produce low read noise while capable of storing large numbers of electrons per pixel without saturation (Yadid-Pecht & Fossum, 1997; Doge et al., 2002). The technique involves each pixel being readout twice. One read-out is optimised for low light illumination while the other readout is optimised for high light level illumination. These two readouts are then merged to produce a reconstructed image which is known as a high dynamic range (HDR) image (Ma et al., 2015; Wang et al., 2015; Ma et al., 2017).

Advanced methods have been employed to produce the best HDR image output. These include altering the structure of the pixel design by adding transistors with different capacitance when the charge is transferred from the photodiode (Mizobuchi et al., 2009; Huggett et al., 2009; Wang et al., 2011; Jo et al., 2014), or capturing multiple integration images at low dynamic range to reproduce

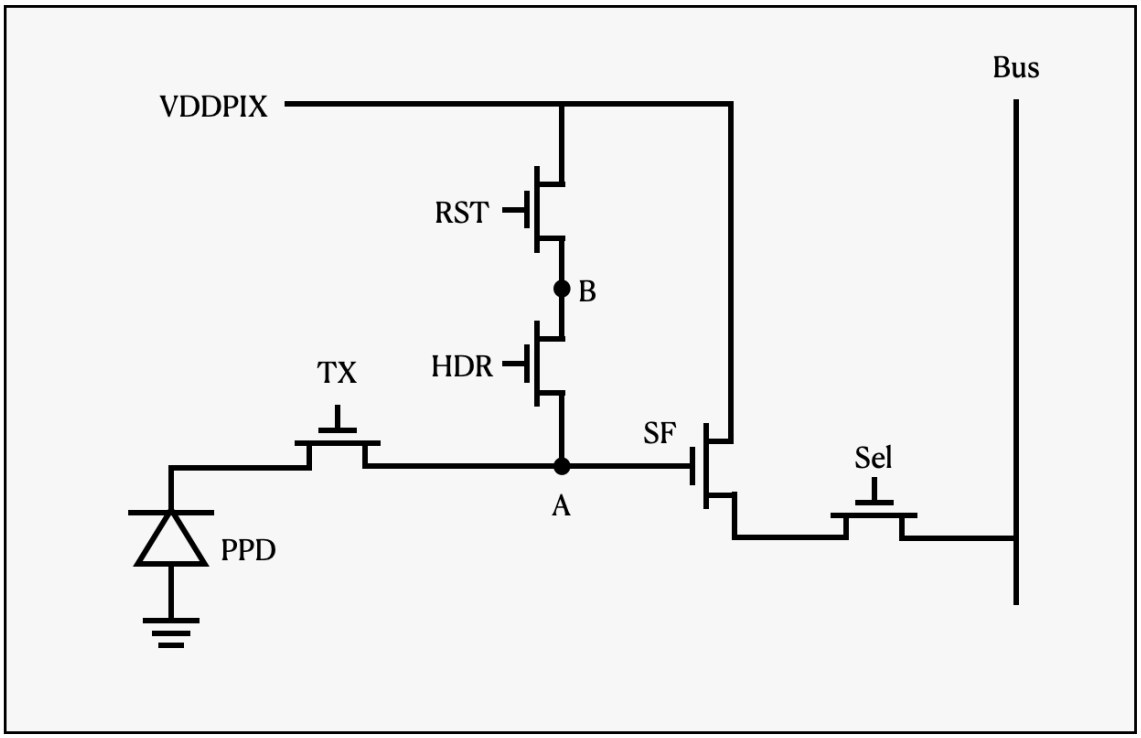


Figure 3.1: Circuit diagram of a pixel from the GSENSE400BSI sensor used in the Marana camera, based on Wang et al. (2015). The integrated charge is collected by the pinned photodiode (PPD). The transfer gate (TX) transfers the charge to either floating diffusion A or B. The HDR transistor (HDR) adjusts the capacitance of the floating diffusion. The reset transistor (RST) provides the reset voltage to the floating diffusion. The charge is buffered by the source follower transistor (SF) and then transferred to the column level for further amplification through the row select transistor (Sel). The VDDPIX voltage supply powers the entire operation of the pixel.

an HDR image (Mann et al., 2012; Jung et al., 2013; Lapray et al., 2016).

The Marana CMOS camera features the GSENSE400BSI sensor which is capable of producing HDR images (see chapter 2). This sensor uses a novel method, based on dual-gain channels, with the addition of the HDR transistor on the pixel architecture. The HDR image is produced by reading the pixel twice, with a High Gain (HG) channel and a Low Gain (LG) channel. The two readouts are digitised with a dual column ADC into 12-bit outputs and combined by the camera's on-board FPGA to produce a 16-bit HDR image (Ma et al., 2015; Wang et al., 2015; Ma et al., 2017).

The GSENSE400BSI sensor contains active pixels and it is based on a 4 complementary metal-oxide semiconductor transistor structure (4-T) with a pinned photodiode (PPD) as the photosensitive surface covers 100 % of the pixel area. The circuit diagram is set out on Figure 3.1.

Each pixel undergoes two phases during imaging: the integration phase and the readout phase. The photodiode serves as the photosensitive area, where electrons accumulate during the integration phase. Before each integration, the photodiode undergoes a cleaning process to remove any residual charge. The pixel is continuously supplied with voltage, referred to as VDDPIX, to enable operation. Initially, the electrons accumulate on the photodiode until the end of the exposure. At the conclusion of the integration phase, the charge is transferred through the transfer gate (TX). The TX transistor drains the charge from the photodiode and dumps it onto the floating diffusion (FD). The FD is a capacitor where the accumulated charge is converted into a voltage. There are two floating

diffusions in the system, labelled A and B, as shown in Figure 3.1. These capacitors serve the same function; however FD B includes an additional HDR capacitor to increase the capacitance. The HDR transistor adjusts the capacitance of the floating diffusion, increasing it when high illumination levels are sampled. The HDR capacitance is associated with FD B in Figure 3.1. When HDR is not active, the charge is transferred to FD A.

The FD is connected to the reset transistor (RST), which applies a known offset voltage to ensure the floating diffusion is reset to the same value each time it is sampled. The Source Follower (SF) transistor buffers the voltage sampled in the floating diffusion. The amplified voltage is then transferred to the column bus via the select transistor (Sel) for further processing.

The GSENSE400BSI sensor readout process works as follows: at the end of the integration phase, the HDR transistor is switched on, and the RST assigns the reset value for the LG sample in FD B. The HDR transistor is then switched off, and the RST assigns the reset value for the HG sample in FD A. The first charge transfer occurs via the TX, and FD A samples the HG signal. A second charge transfer takes place while the HDR transistor is still active. During this transfer, the charge is moved to FD B, which has a larger capacitance due to the addition of the HDR transistor that functions as a capacitor. FD B then samples the LG signal (Ma et al., 2017).

Two pairs of samples are measured: the HG and LG signal voltages, and the HG and LG reset voltages. These pairs are subtracted from each other, specifically the signal from the reset for each pair, to remove Johnson–Nyquist noise (Johnson, 1928) using the Correlated Double Sampling (CDS) method (Enz & Temes, 1996; Xu et al., 2002; Kawai & Kawahito, 2004).

Each column in the pixel array is equipped with two programmable gain amplifiers (PGA), one for the HG signal and one for the LG signal. The PGA amplifiers have been set for the Marana camera to be $\times 1.29$ for the LG channel and $\times 7.25$ for the HG channel. The capacitance is estimated as the number of electrons stored:

$$C = \mathrm{N_e} Q V \tag{3.1}$$

Where the number of electrons $\mathrm{N_e}$, the charge of the electron Q and the potential voltage V. The capacitance of the FD in B which is controlled by the HDR, is compared to the FD in A as the following formula:

$$B = \frac{\mathrm{PGA_{LG}}}{\mathrm{PGA_{HG}}} \times \frac{\mathrm{FWC_{LG}}}{\mathrm{FWC_{HG}}} \tag{3.2}$$

Where the $\mathrm{PGA_{LG}}$ and $\mathrm{PGA_{HG}}$ are the LG and HG amplifier respectively, and the $\mathrm{FWC_{LG}}$ and $\mathrm{FWC_{HG}}$ is the full well capacity of electrons on the pixel for the LG and HG channels respectively.

The signal for each column is amplified twice based on the two PGAs and the CDS technique is performed (Wang et al., 2015). The analogue signal is digitised using the Analogue to Digital (ADC) converter. These two readouts produce two 12-bit image outputs.

The HDR image is constructed upon setting a threshold value to the HG channel signal output. For an integration, if the image has lower signal levels from the threshold then the HDR image will use the HG channel. For higher signal values, however, the LG is implemented as expressed in the equation from Ma et al. (2017):

$$S_{\mathrm{HDR}} = \begin{cases} S_{\mathrm{HG}}, & \text{if } S_{\mathrm{HG}} \leq S_{\mathrm{T}} \\ a \times S_{\mathrm{LG}} + b, & \text{if } S_{\mathrm{HG}} > S_{\mathrm{T}} \end{cases} \tag{3.3}$$

Where the Signal of the HG, S_{HG}, the threshold signal S_T, the signal of the LG, S_{LG}, a is the difference on the sensitivities of the two channels and b is the offset added when changing the channels. The Signal when switching to the LG channel is described by a linear function and therefore, the signal is continuous.

On the other hand, a similar method is used to characterise the noise when switching channels depending on the input signal. The noise sources are the read noise and the shot noise. The HDR image is digitised in 16-bit depth and the switching of channels occurs at low signals (since the HG channel is on 12-bit) the FPN is not significant and therefore can be ignored (Janesick, 2007). The noise sources are following the propagation of errors rules and described as the variance of:

$$\sigma^2_{\mathrm{HDR}} = \begin{cases} \sigma^2_{\mathrm{shot_HG}} + \sigma^2_{\mathrm{read_HG}}, & \text{if } S_{\mathrm{HG}} \leq S_{\mathrm{T}} \\ \sigma^2_{\mathrm{shot_HG}} + \sigma^2_{\mathrm{read_LG}}, & \text{if } S_{\mathrm{HG}} > S_{\mathrm{T}} \end{cases} \tag{3.4}$$

Where $\sigma^2_{\mathrm{shot_HG}}$ and $\sigma^2_{\mathrm{read_HG}}$ is the shot and read noise squared of the HG channel respectively, and $\sigma^2_{\mathrm{read_LG}}$ the read noise of the LG channel.

Since the read noise of the LG is larger than the read noise of the HG channel, their difference producing a discontinuity in the variance (Janesick, 2007; Ma et al., 2017) on the photon transfer curve of the HDR signal (see photon transfer curves for the HDR in Figure 2.4 and Figure 3.14)

To quantify the quality of the Marana CMOS camera in the LG and HG channel, I performed a thorough quality control, measuring the sensitivity, the full well capacity, bias levels, temporal and spatial noise, dark current and photon response non-uniformities. It should be noted that the HG and LG channels do not have on-board preprocessing correction maps applied, and therefore should not be compared directly with the FFR and HDR imaging modes.

3.3 Characterisation Testing of the High Gain and Low Gain channels

In this section I describe the tests performed separately for the High Gain (HG) and Low Gain (LG) channels, treating each operating mode independently. For all experiments, except those measuring dark current, the sensor temperature was maintained at +15 °C.

3.3.1 PTC and Linearities in HG and LG channels

To characterise the response of the camera, I used the same techniques, the equipment and the software to control the camera as in section 2.3 and section 2.4 in chapter 2. I acquired a series of images with constant illumination and varying the exposure time. To remove the FPN from the images, a set of two back-to-back frames were taken and subtracted for each exposure step. The illumination was kept constant for both channel modes. The image outputs from the HG and LG channels have not been processed with correction maps (i.e Anti-Glow map, Spurious Noise Filtering etc, see more details in chapter 2).

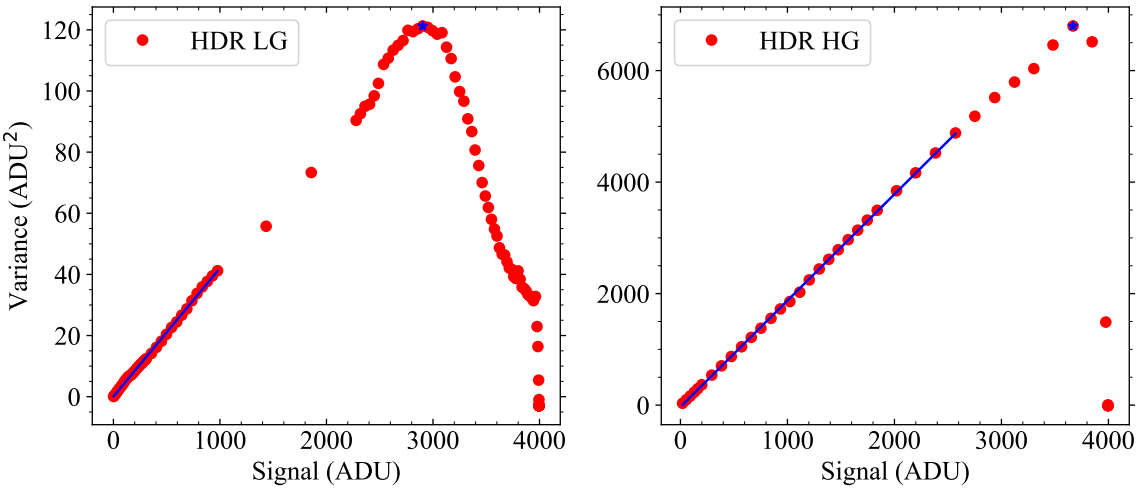


Figure 3.2: Photon transfer curves for the Marana camera at +15 °C. **Left:** The HDR LG channel. **Right:** The HDR HG channel. The solid blue line is a best fit linear model. The data point with the highest variance is marked with a blue star, and indicates the FWC value.

The images are digitised in a 12-bit output and therefore the digitisation saturation occurs at 4096 ADU. The variance and the mean of each image set was measured and the Photon Transfer Curve (PTC) for the HG and LG channel is shown in Figure 3.2.

A fit to the data indicated a sensitivity of 23.81 e^-ADU^{-1} and 0.52 e^-ADU^{-1} for the LG and HG channel respectively. The Full Well Capacity (FWC) was measured as the largest variance and yielded 69137 e^- and 1924 e^- for the LG channel and HG channel respectively.

The same dataset utilised for the PTC is used for the linearity. The linearity is measured between 5 % and 95 % of the saturation, following the EMVA-1288 Version 4.0 standards (Jähne, 2010). To quantify the non-linearity, a linear trend is employed to model the data as shown in Figure 3.3. Since the HG channel is more sensitive to low light levels, the saturation occurs at shorter exposure times when compared to the LG channel. Additionally, the non-linearity of the HG channel is significantly lower than the LG channel as displayed in the residuals plots. The residuals indicated a non-linearity of 0.469 % and 2.544 % for the HG channel and LG channel respectively.

3.3.2 Read Noise and Bias level in HG and LG channels

The bias level of the High Gain (HG) and Low Gain (LG) channel was measured from an average frame of 100 bias images with minimum exposure time, that was found to be 9.48×10^{-6} s for both HG and LG channels. I found the mean value of the LG and the HG averaged bias frame to be 2370 e^- and 28 e^- respectively. The standard deviation for the LG and the HG averaged bias frames was measured to be 38 e^- and 2 e^- respectively. Large-scale structures are evident in both frames, as shown in Figure 3.4. The LG channel bias-averaged frame exhibits a large-scale column-dependent structure rather than discrete individual column patterns, with the bias level varying in blocks of many columns and gradually decreasing from right to left across the frame. In addition, weaker row dependent variations are also present. In contrast, the HG channel bias averaged frame is dominated by distinct column-to-column patterns, while row patterns are present but less pronounced.

The read noise is the temporal noise of the pixels values without the contribution of light and at

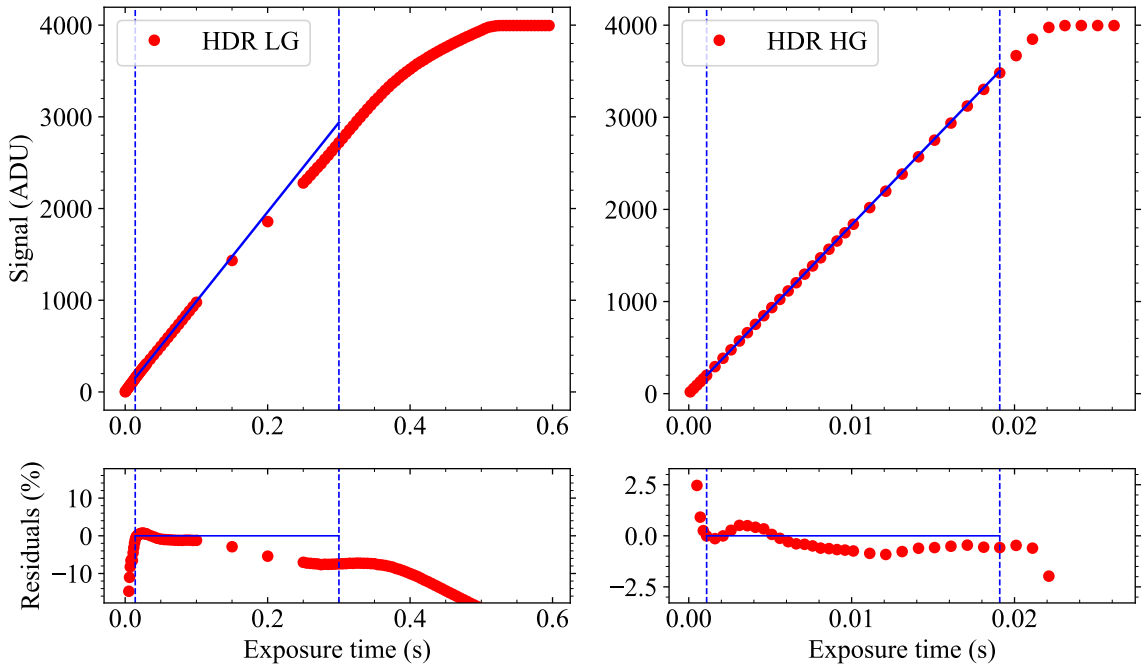


Figure 3.3: Linearity measurements for the Marana camera at +15 °C.**Left:** The HDR LG channel. **Right:** The HDR HG channel. The best fit linear model between 5 and 95 % of saturation is plotted with a blue solid line. Residuals to the linear model are shown in the bottom panels. The dashed horizontal blue lines indicate the 5% to 95% boundaries we set to measure fit the linearity.

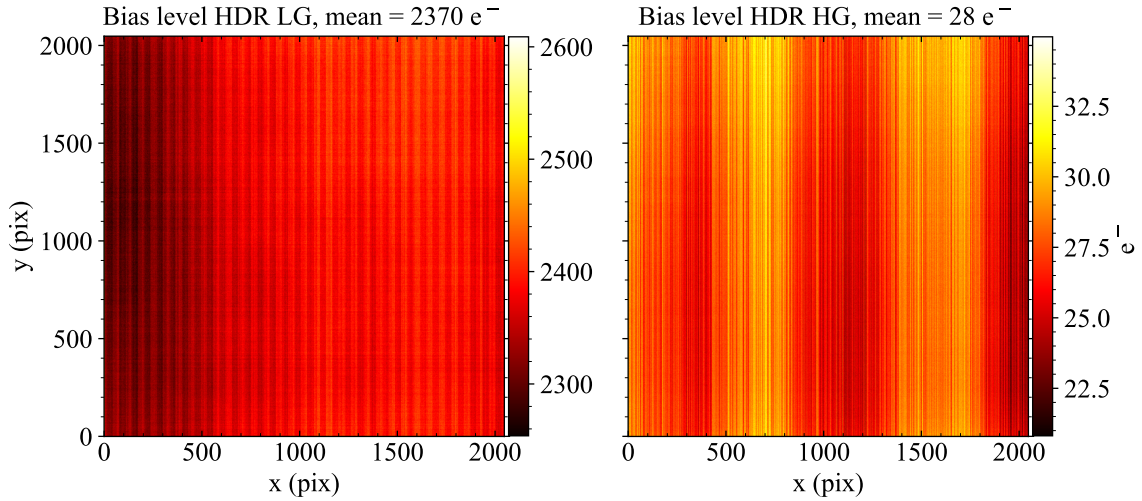


Figure 3.4: Average bias frames from Marana camera recorded at minimum exposure and at +15 °C.**Left:** The HDR LG channel. **Right:** The HDR HG channel.

minimum exposure time. I measured the read noise of 100 bias images for the HG and LG channel. The read noise is visualised on a 2-D histogram in Figure 3.5, which shows the RMS and the mean values of each pixel across 100 bias images.

The median value of the RMS values of each pixel is the read noise of the system. The HG channel is being optimised for the low read noise, yielding mean and median value of $1.67\,e^-$ and $1.56\,e^-$ while the LG channel has larger read noise with mean and median value of $42.69\,e^-$ and $41.08\,e^-$.

The distribution of the read noise is non-Gaussian with a long tail towards large RMS values for HG and LG channel as show in the histograms in Figure 3.5. This is in agreement with the read noise of the FFR and HDR mode as in subsection 2.5.2 in chapter 2. Those noisy pixels exhibiting RTS noise behaviour (Martin-Gonthier & Magnan, 2009), also evident in the HDR and FFR imaging modes subsection 2.5.2.

The 2-D histogram of the LG channel shows a second and less populated cluster of pixels with mean values $\sim 2350\,e^-$. These pixels are not noisier than average, as their RMS is comparable to the bulk population, but they exhibit systematically higher mean levels. Further analysis of the LG channel bias images revealed that the first column consistently appeared brighter than the average, with a mean column value $\sim 2750\,e^-$. Note, that this bright column is not visible in Figure 3.4, as the image contains numerous columns and appears of relatively low quality when visualised.

3.3.3 Row and Column temporal noise in HG and LG channels

To investigate the pixel-level *temporal* row and column noise in bias frames, I used the same set of 100 bias images as in the read noise analysis (see subsection 3.3.2). I followed the same method as described in subsection 2.4.3 in chapter 2. The mean row temporal noise was found to be $16.35\,e^-$ and $0.44\,e^-$ for the Low Gain (LG) and High Gain (HG) channel respectively. The results are illustrated in Figure 3.6. The HG channel exhibits a weak secondary cluster with an average mean value of $28.5\,e^-$.

The mean column temporal noise was found to be $1.72\,e^-$ and $0.064\,e^-$ for the LG and HG respectively. The results are illustrated in Figure 3.7. The LG channel exhibits a weak secondary cluster with an average mean column value of $2315\,e^-$.

3.3.4 Row, Column and pixel spatial noise in HG and LG channels

Since CMOS sensors have a more complex architecture than CCDs, featuring active pixels with additional electronics integrated within each pixel, it is important to quantify the Dark Signal Non-Uniformity (DSNU) across different spatial scales that is row, column, pixel and the overall value, using the same set of 100 bias images as in the read noise analysis (see subsection 3.3.2). For the Low Gain (LG) channel, the DSNU was found to be $8.018\,e^-$, $35.033\,e^-$, $12.789\,e^-$, $38.146\,e^-$ for the row, column, pixel and overall respectively. For the High Gain (HG) channel, the DSNU was found to be $0.523\,e^-$, $2.067\,e^-$, $0.516\,e^-$, $2.193\,e^-$ for the row, column, pixel and overall respectively. The overall DSNU for the HG and LG channel is displayed in Figure 3.8.

The HG channel exhibits a more Gaussian-like distribution, whereas the LG channel shows a wider and less symmetric distribution, primarily due to the large-scale column structure observed in the bias images (Figure 3.4). Additionally, the secondary cluster of the distribution is also visible in the overall DSNU of the LG channel (Figure 3.8) at approximately $350\,e^-$.

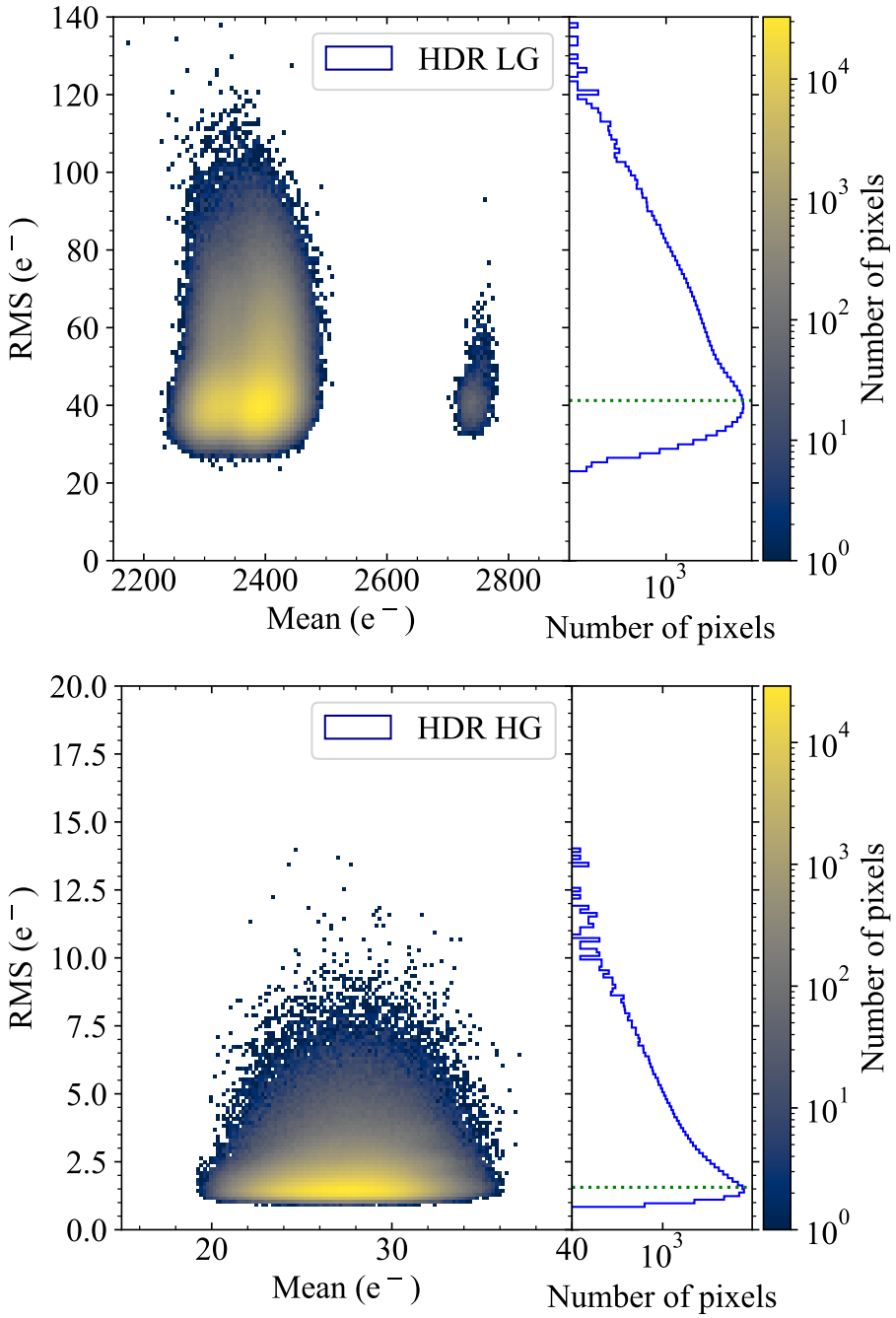


Figure 3.5: Read noise distribution using 100 consecutive bias frames. The 2-D histogram corresponds to temporal noise and the mean of each pixel from these frames while the colour bar indicates the number of pixels. The logarithmic read noise distribution is show in the blue histograms, with the median value as a green dotted line. **Top:** Read noise distribution for the HDR LG channel. **Bottom:** Read noise distribution for the HDR HG channel.

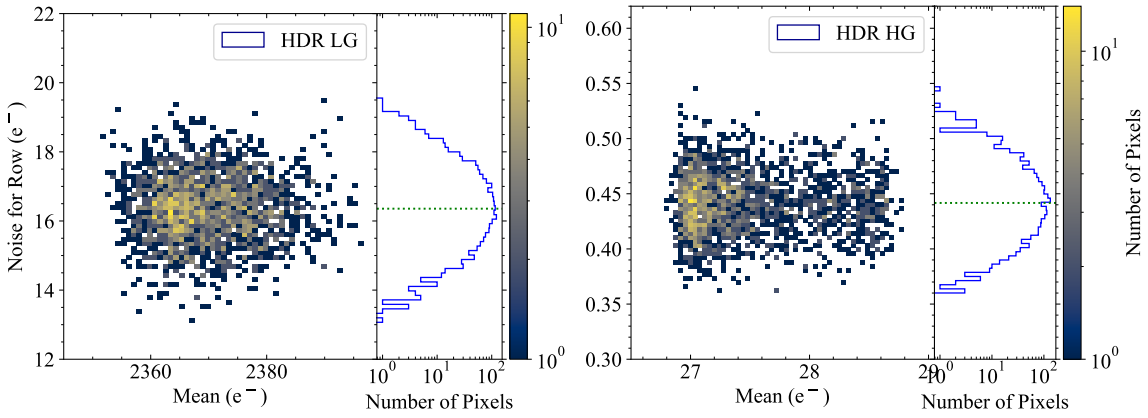


Figure 3.6: Row noise distribution using 100 consecutive bias frames. The 2-D histogram corresponds to temporal row noise and the mean of each pixel from these frames while the colour bar indicates the number of pixels. The logarithmic row noise distribution is show in the blue histograms, with the median value as a green dotted line. **Left:** Row noise distribution for the HDR LG channel. **Right:** Row noise distribution for the HDR HG channel.

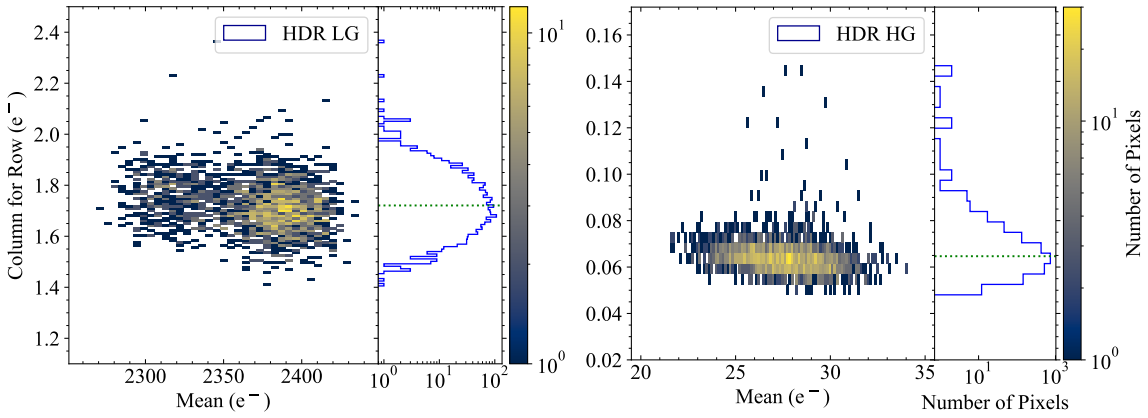


Figure 3.7: Column noise distribution using 100 consecutive bias frames. The 2-D histogram corresponds to temporal column noise and the mean of each pixel from these frames while the colour bar indicates the number of pixels. The logarithmic row noise distribution is show in the blue histograms, with the median value as a green dotted line. **Left:** Column noise distribution for the HDR LG channel. **Right:** Column noise distribution for the HDR HG channel.

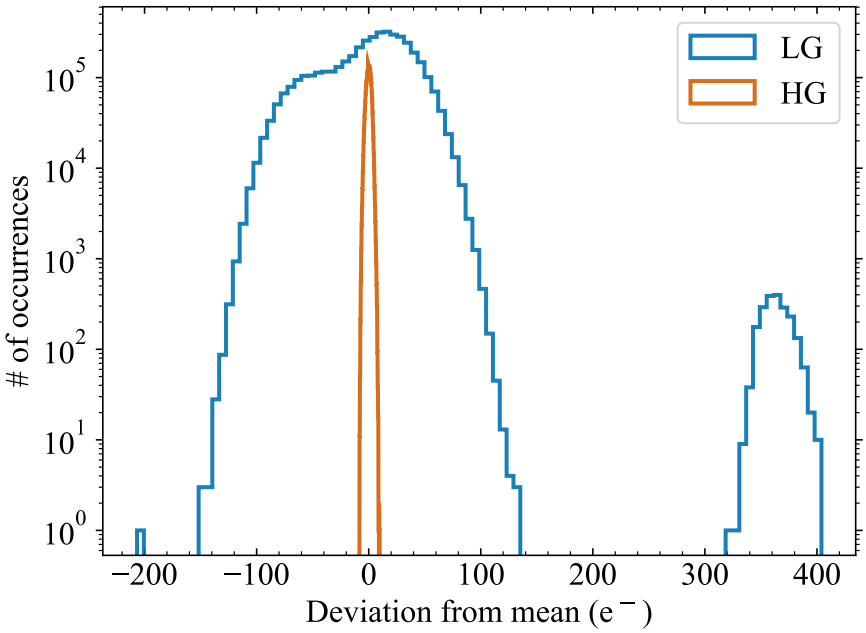


Figure 3.8: Histogram distribution of the mean-subtracted pixel values used to estimate the overall DSNU for the HG and LG channels.

3.3.5 Dark current and non-uniformities in HG and LG channels

To quantify the dark current of the Marana camera, I exposed the sensor for 10 seconds in a dark room for High Gain (HG) and Low Gain (LG) channel at a fixed temperature of -25° C. Each frame has a bias image subtracted and normalised by the exposure time. For each image the median value of the frame was calculated. The maps were converted to electrons using the sensitivities measured in subsection 3.3.1. The results are visualised in Figure 3.9 for the LG channel and HG channel.

The median dark current was measured to be $1.44\,e^-\,pix^{-1}\,s^{-1}$and $2.13\,e^-\,pix^{-1}\,s^{-1}$for the HG and LG channel respectively. The maps indicate the presence of glow on both LG and HG channel, which is evident as spots in the edges of the frame and it is significantly brighter than the rest of the frame. This behaviour also produces a long tail on the histograms as shown in the lower panels of Figure 3.9.

3.3.6 PRNU and DCNU in HG and LG channels

During the quality control tests, only the extracted values are stored in log files, while the image data is not saved to minimise storage usage. As a result, for the Photo Response Non-Uniformity (PRNU), Dark Current Non-Uniformity (DCNU), and Dark Signal Non-Uniformity (DSNU), I will report only the values recorded during the quality control process for each channel.

DCNU is the spatial deviation of a dark current frame. I used the same frames from subsection 3.3.5 to estimate the DCNU on the Low Gain (LG) and High Gain (HG) channel. The DCNU was estimated to be $3.928\,e^-$ and $3.153\,e^-$ for the LG channel and HG channel. The large DCNU values can also be attributed to the presence of glow in the dark current images.

A set of 100 illuminated images at half-saturation recorded for the LG and the HG channels to

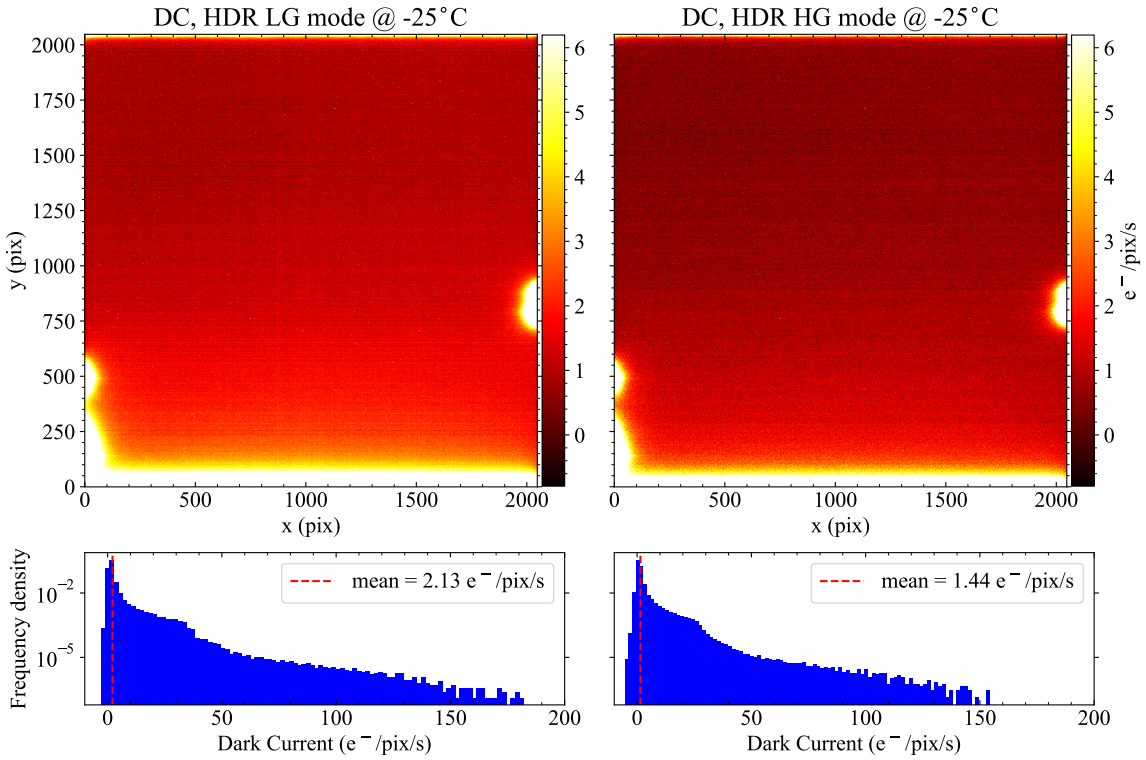


Figure 3.9: Dark current maps for the Marana camera at -25 °C. **Left:** The HDR LG channel. **Right:** The HDR HG channel. Below each map are the histograms of the pixel value distribution from each frame, along with the mean value (red dashed line).

study the PRNU. Both channels maintain uniform performance with PRNU of 0.566 % and 0.862 % for the LG channel and the HG channel.

3.3.7 Summary of the HG and LG channel testing

The results found from characterising the LG channel and the HG channel of the Marana CMOS camera are summarised in Table 3.1.

Using the Full Well Capacity (FWC) values found from the Photon Transfer Curve PTC analysis and Equation 3.2 the capacitance of the of the floating diffusion on B (see Figure 3.1) is changing by a factor of 6.39 in order to store the LG channel. The HDR mode is generated using two 12-bit image outputs from the LG and HG channels. Under low-light illumination, the HG channel is utilised, meaning that the read noise and dark current of the HDR mode are measured from HG channel. The observed differences in measurements arise primarily from the varying sensitivities of the HG channel and HDR mode. Additionally when exposing the sensor in large light illumination the FWC of the LG channel is being used. The FWC of the LG channel and the HDR mode are in agreement. Notably, the LG channel's PTC exhibits a gradual decline in variance prior to saturation, rather than an abrupt drop, suggesting that the LG channel may accommodate additional charge. Further investigation is required to quantify this behaviour (see section 3.4).

The HG channel exhibits a higher PRNU compared to the LG channel, reflecting a greater degree of spatial fixed-pattern structure under uniform illumination. In HDR mode, the PRNU of the LG channel is used; however, it cannot be directly compared to the HDR mode, as half-saturation occurs

Table 3.1: Specifications measured for the Marana CMOS camera in HDR LG and HDR HG channels.

Camera channel	**HDR LG**	**HDR HG**
Digital output	12-bit	12-bit
PGA Amplifier	1.29×	7.25×
Readout modes	100 MHz	100 MHz
Gain, $e^- ADU^{-1}$	23.81	0.52
Full Well Capacity, $e^- pix^{-1}$	69137	1924
Non-Linearity, %	2.544	0.469
Read Noise, e^-	41.084	1.562
Row temporal Noise, e^-	0.064	0.173
Column temporal Noise, e^-	0.023	0.056
Dark Current mean, $e^- pix^{-1} sec^{-1}$	2.13@-25°C	1.44@-25°C
PRNU, %	0.566	0.862
DCNU, e^-	3.928	3.153
DSNU Row, e^-	8.018	0.523
DSNU Column, e^-	35.033	2.067
DSNU Pixel, e^-	12.789	0.516
DSNU Total, e^-	38.146	2.193

at 30000 ADU since the data outputs 16-bit depth.

The bias structure in both channels exhibits pronounced row- and column-dependent patterns, leading to large Dark Signal Non-Uniformity (DSNU) values. The LG channel shows a less symmetric DSNU distribution than the HG channel and additionally displays a secondary cluster at 300–400 e^- (see Figure 3.8), which is caused by the first bright columns in the bias frames. The difference in read noise between the LG and HG channels also marks the transition between the two in HDR mode, appearing as a discontinuity in the variance of the HDR PTC.

In both channels, amplifier glow is evident in the dark current measurements, increasing the Dark Current Non-Uniformity (DCNU). The glow affects the same regions in the LG and HG dark current images as in the HDR and FFR modes in subsection 2.5.4 in chapter 2. Overall, the HG and LG channels exhibit larger variability values for most parameters than the FFR and HDR modes (see Table 3.1 and Table 2.2), indicating that correction maps or processing steps are applied when generating the FFR and HDR imaging modes.

3.4 Supply Voltage Adjustments

In this section, I discuss how tuning the camera's operating voltages during charge integration can enhance the detector's dynamic range, specifically by adjusting the voltages that influence the FWC and read noise.

3.4.1 Investigation on the PTC of the LG channel

To characterise the read noise and Full Well Capacity (FWC) of the High Gain (HG) and Low Gain (LG) channels, the pixel supply voltage (VDDPIX; see Figure 3.1) of the Marana camera was systematically varied. In HDR imaging mode, the FWC is determined by the LG channel. The

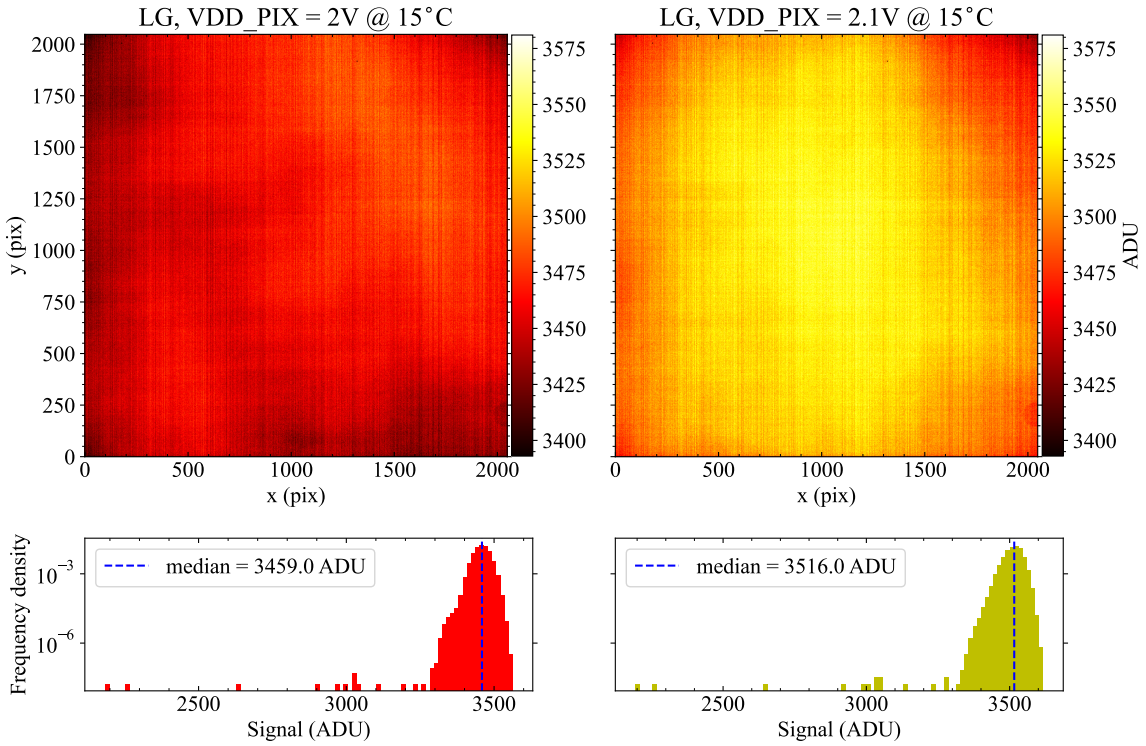


Figure 3.10: Illuminated frames before saturation for the LG channel at 15 °C. **Left:** HDR LG channel with VDDPIX at 2.0 V. **Right:** the HDR LG channel with VDDPIX at 2.1 V. Below each map are the histogram distribution from each frame, along with the median value (blue dashed line).

Photon Transfer Curve (PTC) of the LG channel exhibits an initial decline prior to reaching digital saturation (see Figure 3.2), in contrast to the instant drop observed in the HG channel, motivating the exploration of VDDPIX as an independent control parameter.

In CMOS pixels, VDDPIX sets the reset voltage of the Floating Diffusion (FD) via the reset transistor (RST). During reset, the RST transistor connects the FD to VDDPIX, establishing the initial voltage from which photodiode charge is integrated. Increasing VDDPIX raises the FD node voltage, enabling the integration of a larger number of electrons before saturation and thereby increasing the FWC. This adjustment allows the LG channel in HDR mode to achieve its maximum charge storage within the limits of the FD Stefanov et al. (2022).

The default value of the VDDPIX in the Marana camera is 2.0 V. To change the VDDPIX, I used an internal (not for end-users) tool in Andor Technology using `SOLIS` software. I used the same equipment as in Figure 2.1 from chapter 2.

The VDDPIX was changed to 2.1 V. A new PTC was recorded for the LG channel, focusing on the saturation region, using the same illumination and exposure settings as those employed for the PTC with VDDPIX set to 2.0 V. Images were acquired at the saturation level for the 2.1 V case only, since at this signal level the 2.0 V configuration had already exceeded its saturation point. The resulting images are shown in Figure 3.10.

The 2.1 V case exhibits slightly higher counts at 3516 ADU compared to the 2.0 V configuration, which has already experienced a variance drop at 3459 ADU. The observed difference of approximately 60 ADU may be attributed to shot noise. Additionally, the distribution for the 2.1 V appears to be more symmetric in the image as shown in the right panel of Figure 3.10.

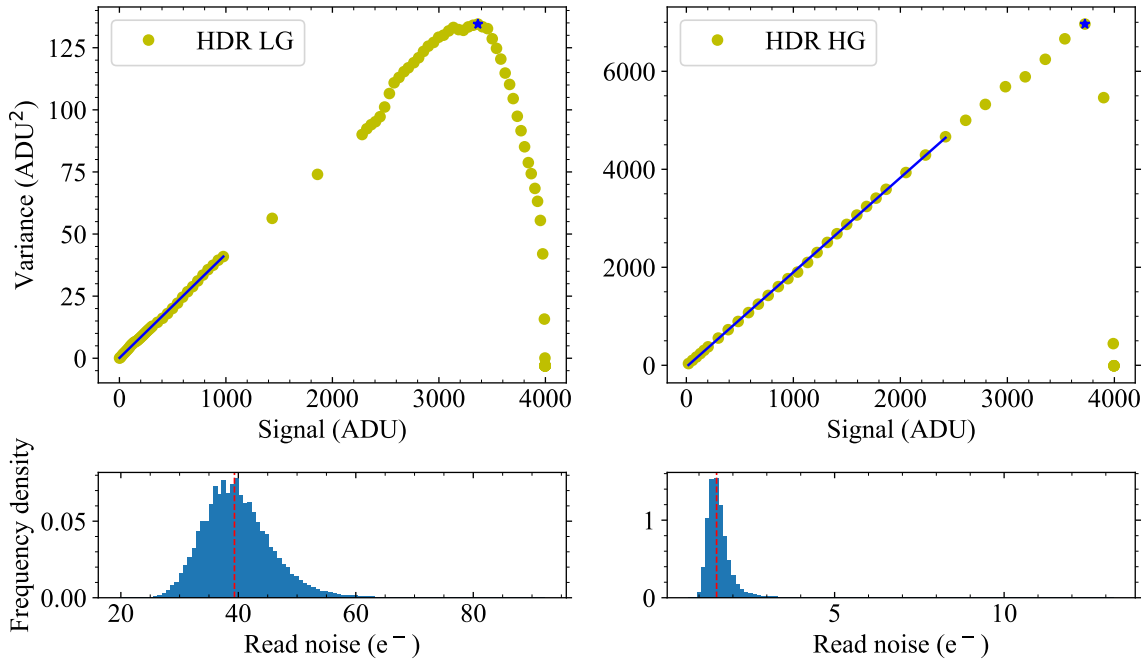


Figure 3.11: PTC estimated for VDDPIX supply pixel voltage at 2.1 V for the HG and LG channels of the Marana camera. All measurements were recorded at a constant temperature of 15 °C. **On the upper left**: is the HG channel. **On the upper right**: is the LG channel. The **lower subplots** represent the corresponding read noise distribution and with red dashed line to be the mean value.

3.4.2 Adjustments of the VDDPIX voltage in HG and LG channels

Characterisation of the High Gain (HG) and Low Gain (LG) channels was performed to evaluate the effect of the increased supply voltages (VDDPIX) value of 2.1 V and to enable a direct comparison with the 2.0 V case. The analysis focused on key parameters including FWC, conversion gain, linearity, and read noise and was achieved with the same way as described in section 2.4 in chapter 2. For all experiments, except those measuring dark current, the sensor temperature was maintained at 15 °C.

The Photon Transfer Curves (PTCs) for the HG and LG channels are shown in Figure 3.11, together with the corresponding read noise distributions. Linear regression of the data yields gains of 23.89 e^- ADU^{-1} (LG) and 0.51 e^- ADU^{-1} (HG), in close agreement with the values obtained at VDDPIX = 2.0 V. The HG Full Well Capacity (FWC) is comparable to the 2.0 V case, while its read noise is slightly reduced. For the LG channel, operating at 2.1 V results in a 16 % increase in FWC relative to 2.0 V, with the read noise remaining essentially unchanged. A summary of the parameter differences between the two VDDPIX settings is provided in Table 3.2.

The PTC data were analysed as a function of exposure time to assess the system linearity, as shown in Figure 3.12. A slight increase in non-linearity is observed for both the HG and LG channels when operating at VDDPIX = 2.1 V. A quantitative comparison between the two operating points is summarised in Table 3.2.

Based on these results, the FWC increases sufficiently without degrading the read noise, resulting in a meaningful enhancement of the system dynamic range. However, the dark current exhibits a substantial increase of approximately 68 % for the LG channel and 78 % for the HG channel

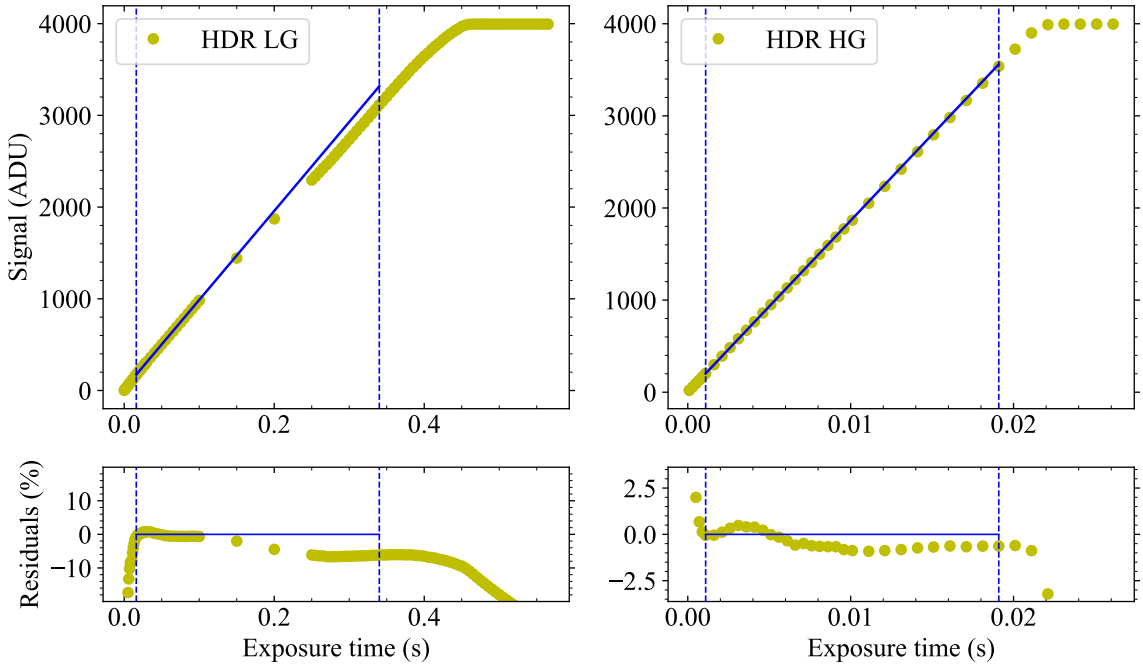


Figure 3.12: Linearities estimated for VDDPIX supply pixel voltage at 2.1 V for the LG (left) and HG (right) channels of the Marana camera. The best fit linear model between 5% and 95% of saturation is plotted with a blue solid line. Residuals to the linear model are shown in the bottom panels. The dashed horizontal blue lines indicate the 5 to 95% boundaries we set to measure fit the linearity.

Table 3.2: Measurements of the VDDPIX at 2.0 V and 2.1 V for LG and HG channel.

Camera channel	**HDR LG, 2.0 V**	**HDR LG, 2.1 V**	**HDR HG, 2.0 V**	**HDR HG, 2.1 V**
Digital output	12-bit	12-bit	12-bit	12-bit
PGA Amplifier	1.29×	1.29×	7.25×	7.25×
Gain, e^- ADU^{-1}	23.89	23.81	0.52	0.51
FWC, e^-	69137	80427	1924	1929
Non-Linearity, %	2.544	2.855	0.469	0.517
Read Noise, e^-	39.270	39.341	1.547	1.519
PRNU, %	0.566	0.569	0.862	0.865
Dark Current mean, e^- pix^{-1} s^{-1}	2.13	3.57	1.44	2.56
DSNU Total, e^-	38.146	40.069	2.193	2.182

when the pixel supply voltage is raised. While this increase may impact applications requiring low-light performance, its effect is mitigated under high-illumination conditions, where shot noise and fixed-pattern noise dominate and the benefit of the increased FWC becomes more significant. The remainder of this analysis focuses on the HDR imaging mode, which combines both HG and LG channels operating at VDDPIX = 2.1 V.

3.4.3 Characterisation of the HDR mode with voltage adjustments

The HDR imaging mode is evaluated with the supply voltage (VDDPIX) set to 2.0 V and then changed to 2.1 V. A comprehensive characterisation of the Marana camera is performed, including measurements of gain, Full Well Capacity (FWC), read noise, dark signal and photo response non-uniformities (DSNU, PRNU), linearity, and dark current. These tests are conducted to assess how variations in the pixel supply voltage impact the overall performance of the HDR imaging mode. This analysis is conducted at a stable temperature of 15 °C. I only vary the dark current measurement that is measured at -25 °C.

The same experimental procedure is applied for both VDDPIX settings using an identical optical bench configuration. From the Photon Transfer Curve (PTC) as illustrated in Figure 3.13, I measure the gain, by extracting the linear regression, to to be $1.07\,e^{-}ADU^{-1}$ with a FWC of $68618\,e^{-}$ at 2.0 V while the gain at 2.1 V is found to be $1.24\,e^{-}ADU^{-1}$ and the FWC is found to be $80005\,e^{-}$. These results indicate a significant change in conversion gain, leading to a measurable increase in the effective FWC, in agreement with the behaviour predicted from the Low Gain (LG) channel analysis (see subsection 3.4.2). The lower panels in Figure 3.13 show the read noise of the system. The mean and median read noise for the 2.0 V are found to be $1.66\,e^{-}$ and $1.58\,e^{-}$. The mean and median read noise for the 2.1 V are found to be $1.67\,e^{-}$ and $1.59\,e^{-}$.

The same dataset for each VDDPIX value was used to measure the linearity of the system. The linearity was measured between the 5 % to 95 % from the saturation signal boundaries. The linearity error for the 2.0 V was found to be 0.141 % while for the 2.1 V it was found to be 0.128 %. Those values indicate a minimal variation and therefore, the linearity is not affected directly from the fact the VDDPIX varied. This is not in agreement with the linearities error found in the High Gain (HG) and LG channels, in which there was a slight increase when the VDDPIX was increased. The results are displayed in Figure 3.14.

Two exposures on a dark environment were captured at 10 s exposures for VDDPIX 2.0 V and 2.1 V respectively. The bias level was subtracted from an average bias frame image. The image array was divided by the exposure and the signal was converted to electrons per second using the gain found from the PTC. The resulted dark current frames are illustrated in Figure 3.15. The Anti-Glow correction (see chapter 2) was enabled during these measurements. The median dark current at 2.0 V is consistent with the value reported in subsection 2.5.4. In contrast, the dark current measured at 2.1 V is approximately twice as high. The elevated dark current more likely reflects an intrinsic increase associated with the higher supply voltage.

Because the dark current of the Marana camera is significantly impacted by amplifier glow and can therefore degrade photometric precision, I decided not to adopt a VDDPIX setting of 2.1 V as the final operating configuration and instead retained 2.0 V. The remaining parameters derived from the characterisation at 2.0 V and 2.1 V are listed in Table 3.3. Based on these results, no other

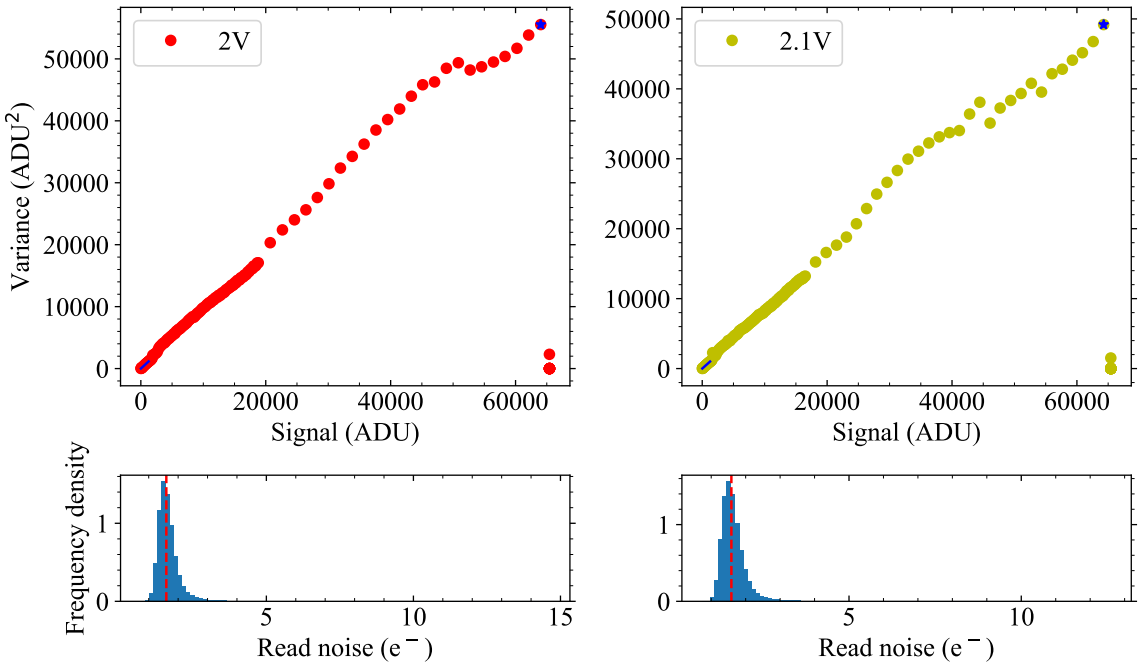


Figure 3.13: PTC measurements for the Marana camera at +15 °C for the HDR imaging mode. **On the upper left**: is HDR with VDDPIX at 2.0 V. **On the upper right**: is the HDR with VDDPIX at 2.1 V. The **lower subplots** represent the corresponding read noise distribution and with red dashed line to be the mean value.

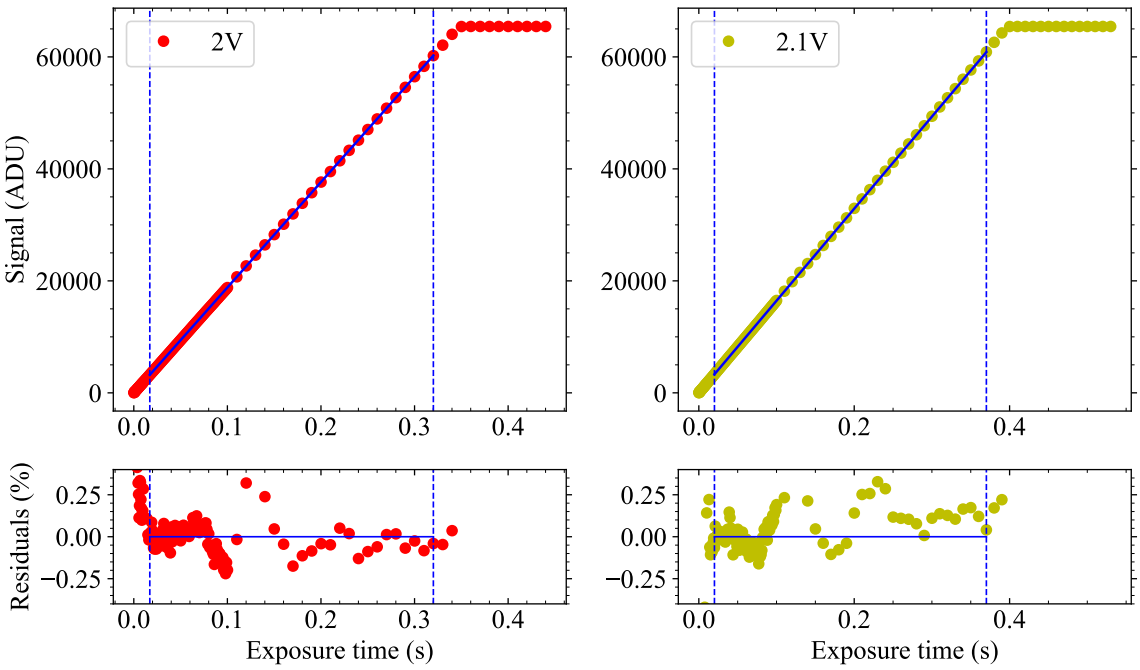


Figure 3.14: Linearity measurements for the Marana camera at +15 °C for the HDR imaging mode. **Left:** The HDR with VDDPIX at 2.0 V. **Right:** The HDR with VDDPIX 2.1 V channel. The best fit linear model between 5 and 95 % of saturation is plotted with a blue solid line. Residuals to the linear model are shown in the bottom panels. The dashed horizontal blue lines indicate the 5 to 95% boundaries we set to measure fit the linearity.

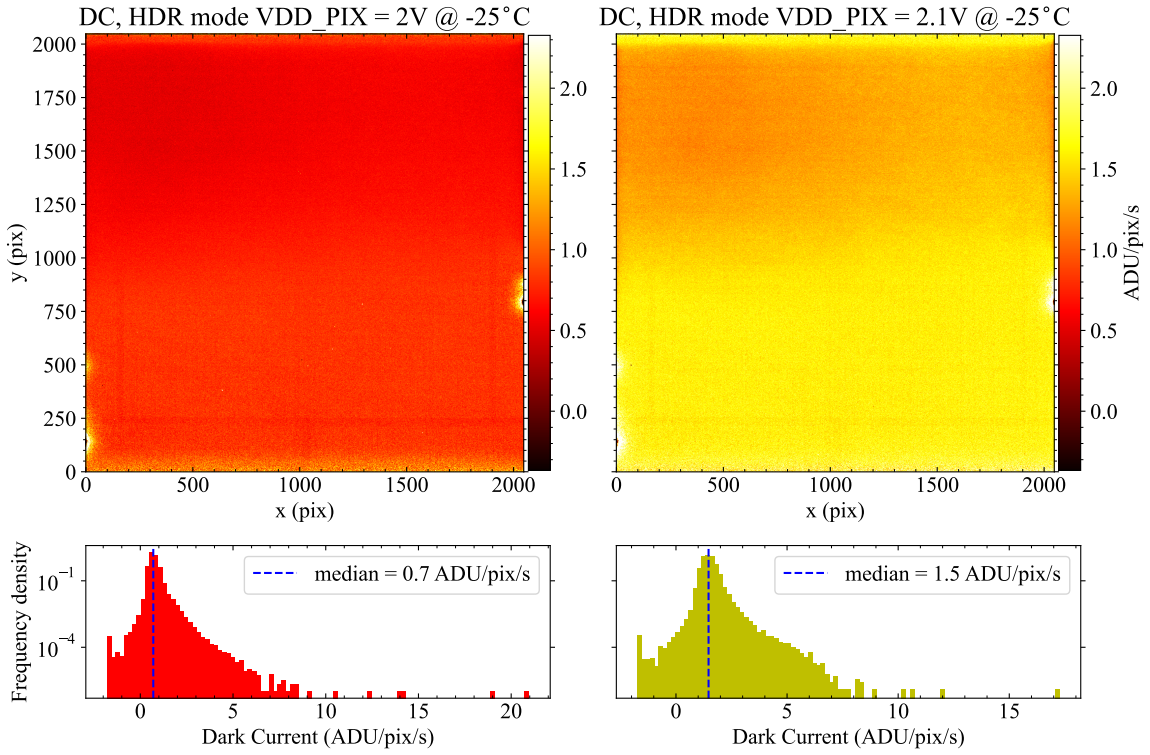


Figure 3.15: Marana dark images taken in the HDR mode, with camera temperature of -25° C and with the Anti-Glow correction ON. **Left** Dark current frame with VDDPIX at 2.0 V. **Right** Dark current frame with VDDPIX at 2.1 V. Below each we show the histograms of pixel value distributions from each frame, along with the median (blue dashed line).

Table 3.3: Specifications measured for the Marana CMOS camera in HDR mode with VDDPIX 2.0 V and 2.1 V.

Camera channel	**2.0 V**	**2.1 V**
Gain, $e^- ADU^{-1}$	1.07	1.24
Full Well Capacity, $e^- pix^{-1}$	68618	80005
Non-Linearity, %	0.141	0.128
Read Noise (Mean), e^-	1.66	1.67
Dark Current mean, e^- pix^{-1} sec^{-1}	0.749@-25°C	1.860@-25°C
PRNU, %	0.114	0.105
DCNU, e^-	0.963	1.041
DSNU, e^-	0.291	0.303

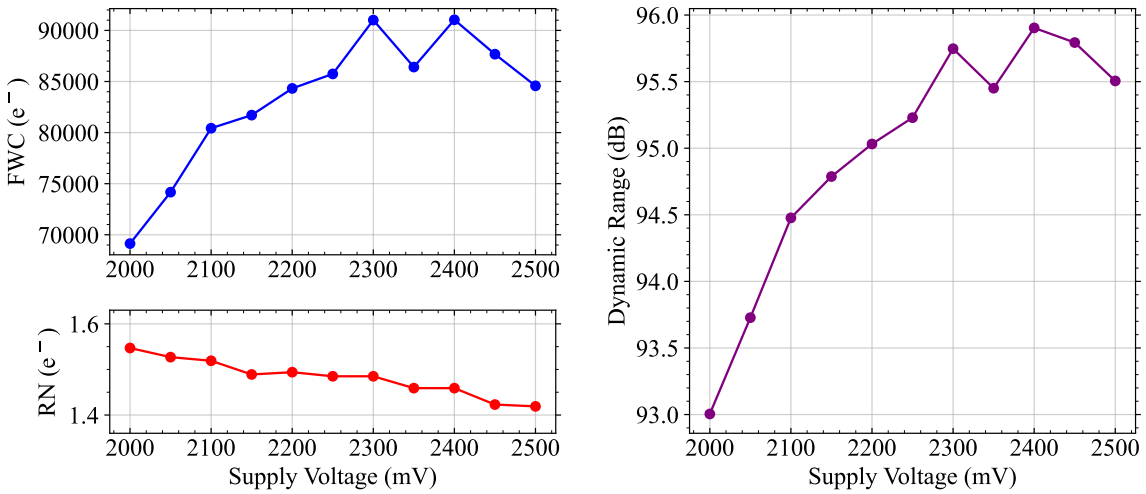


Figure 3.16: Measurements of the FWC, read noise, and dynamic range as a function of VDDPIX from 2.0 V to 2.5 V in steps of 50 mV. The upper-left panel shows the FWC for different supply voltages, the lower-left panel shows the read noise, and the right panel presents the resulting dynamic range computed from the corresponding FWC and read-noise values.

significant differences between the two supply voltages are evident, and most parameters show only minimal variation. The primary changes associated with the voltage adjustment are observed in the read noise, dark current, FWC, and sensitivity.

I also explored a range of VDDPIX values to assess the maximum achievable dynamic range of the camera. For this purpose, the gain, FWC, and read noise were measured at multiple VDDPIX levels, and the corresponding dynamic range of the Marana camera was computed. The VDDPIX was calculated from 2.0 V to 2.5 V in steps of 50 mV. The results are displayed in Figure 3.16.

The FWC increases substantially with increasing VDDPIX, while the read noise decreases more gradually and with weaker sensitivity. Together, these trends lead to an overall increase in dynamic range, as shown in the right panel of Figure 3.16. The FWC reaches a maximum between 2.3 and 2.4 V, where the pixel well saturates at approximately 90000 electrons, which corresponds to the maximum capacity specified by GPixel[1]. A similar peak is observed in the dynamic range at around 2.4 V; beyond this voltage, the dynamic range declines, indicating that 2.4 V represents the maximum achievable dynamic range for this sensor.

[1]GS400BSI Performance sheet, Andor Technology private communication

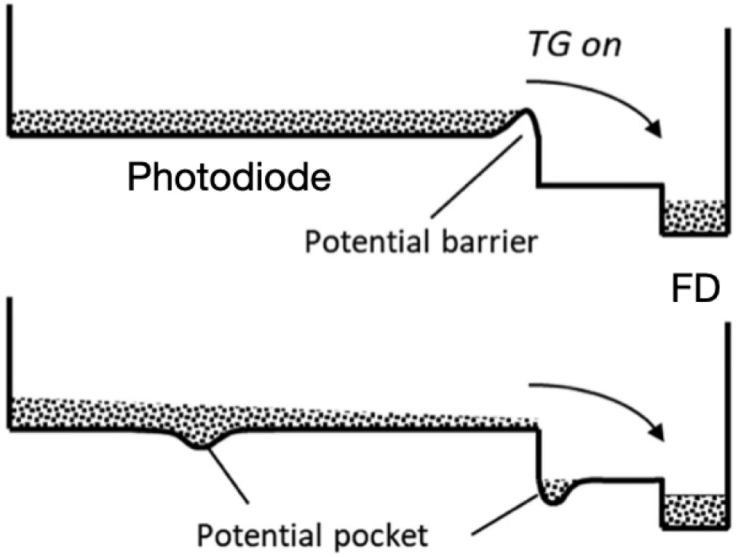


Figure 3.17: Example of image lag caused by traps and defects that create potential barriers. The diagrams illustrate electrons (black dots) being transferred from the photodiode to the floating diffusion when the Transfer Gate (TG) opens. Potential barriers or wells (referred to as pockets) that can trap electrons are labelled accordingly. Image adapted from Stefanov (2022).

3.5 Image Lag

In the following section, I describe the tests conducted at the Andor Technology laboratory to measure the image lag of the GSENSE400BSI sensor mounted in the Marana camera, in order to assess how this effect may impact photometric precision.

3.5.1 Image lag introduction

Each pixel in a CMOS sensor contains dedicated circuitry for amplifying and readout out the signal. During exposure, photoelectrons accumulate in the photodiode. In a 4-transistor (4-T) active pixel structure, such as that used in the Marana camera, the transfer gate opens at the end of the integration period, allowing electrons to move from the photodiode to the floating diffusion, which acts as a capacitor (see Figure 3.1). In some cases, however, not all charge is successfully transferred, and residual electrons remain in the photodiode, giving rise to an effect known as image lag. This phenomenon is also observed in CCD cameras (Thornber, 1974), where it is often discussed in terms of Charge Transfer Efficiency (CTE) or charge persistence (Barrick et al., 2012; Karpov et al., 2020; Lin et al., 2022; Alarcon et al., 2023b).

One source of image lag arises from the transfer gate itself. The transfer gate applies a voltage to move charge from the photodiode to the floating diffusion, but irregularities in the gate transistor can create potential barriers or wells that partially block the charge transfer, trapping electrons. In addition, aspects of the pixel fabrication, such as the physical layout and the distance between the transfer gate and the photodiode, can further increase image lag (Fossum et al., 2003; Xu & Theuwissen, 2013; Stefanov, 2022). This effect is illustrated in Figure 3.17.

Additionally, because electrons move from higher to lower potential by diffusion (i.e., in a field-

free region), the potential difference between the photodiode and the floating diffusion decreases as charge accumulates in the floating diffusion. This reduction in potential difference slows the transfer of electrons, leaving some charge behind in the photodiode, which contributes to image lag (Xu & Theuwissen, 2013; Stefanov, 2022; Teranishi, 2016). Other cases include image lag at high signal levels, in which charge may not fully transfer and can return to the photodiode if the transfer gate potential (i.e., the supply voltage) is insufficient (Fossum et al., 2003; Shafie et al., 2009; Jain, 2016).

In this work, I aim to characterise the image lag that may be present in the Marana CMOS camera. The camera may exhibit this effect as the non-linearities (discontinuities) observed in the Photon Transfer Curve (PTC) for the HDR mode at high signal levels, particularly in the Low Gain (LG) channel (see Figure 2.4 in chapter 2) (Stefanov, 2022). Image lag has been investigated through a series of tests conducted at the Andor Technology laboratory. These tests, referred to as *Experiments* (see further in subsection 3.5.3), systematically vary parameters that may influence image lag, including the light source wavelength, camera temperature, and the duration of the light pulse.

3.5.2 Set up for image lag experiment

On the optical bench, a cylindrical light rig was employed, housing four 4-V LED arrays at one end, covered by a diffuser to provide uniform (flat-field) illumination. The light from the LEDs was collimated, and the camera was mounted at the opposite end of the rig. The entire system was sealed to prevent any unwanted ambient light from entering; therefore, the interior of the rig was considered a dark room. Each LED consists of a unique colour, blue, green, red and infrared with wavelengths at 460±40 nm, 525±50 nm, 640±30 nm, 850±50 nm respectively. For each experiment I used only individual LEDs and not more than one at once.

To achieve precise synchronisation between the camera and the illumination, external triggering was employed for the light source. The trigger box was connected to the light source, while a *Quantum Components* delay generator was connected to both the trigger box and the camera to provide accurate timing control. The delay generator was configured to define the pulse mode (e.g., single-shot), the pulse period, the delay applied to the light pulse, and the pulse width.

An oscilloscope was used to visually verify the timing signals and confirm the measured pulses. The experimental set-up is illustrated in the diagram in Figure 3.18. The camera was operated using the `SOLIS` software provided by Andor Technology, which was used to configure and control the camera operating parameters, including exposure time, frame rate, and acquisition sequencing.

3.5.3 Methodology

To measure image lag, I analyse the signal from both illuminated and dark frames. If a bright image is recorded and image lag is present, some of the charge generated in the photodiode may not be fully transferred to the floating diffusion and readout. This residual charge remains trapped in the photodiode or at defects near the transfer path and can appear in the subsequent frame. If the next frame is a dark image, any detected signal, commonly referred to as a ghosting effect, originates from this leftover charge from the previous bright frame.

Image lag can be categorised into two types: discharging lag and charging lag. In the case of discharging lag, the residual signal from a bright frame appears in the next dark frame; this is often

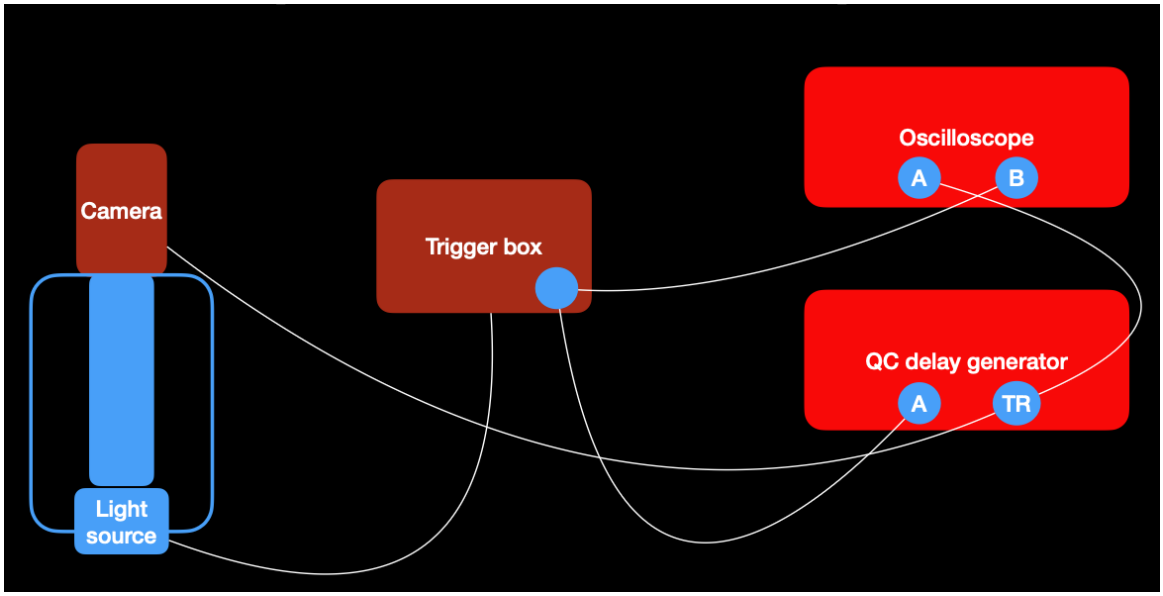


Figure 3.18: Diagram of the image-lag experimental bench. The camera is mounted on one end of the light rig, with the light source located at the opposite end. Both the camera and the light source are externally triggered, and a delay generator is used to control the light pulses. All components are connected using Bayonet Neill-Concelman cables.

referred to as first-image lag (Fossum et al., 2003). Here, trapped electrons in the photodiode are gradually released and eventually transferred to the floating diffusion, producing a delayed signal in the following frame.

Charging lag occurs when a bright frame exhibits a lower signal than subsequent bright frames because some electrons generated by the illumination are temporarily captured by traps within the photodiode or near the transfer gate. These trapped electrons reduce the apparent signal in the first frame, and only in the following frames, as the traps begin to fill or release, does the full expected signal appear. This is illustrated in the following Figure 3.19 adapted from Fossum et al. (2003).

Image lag is quantified as the ratio between the residual (lag) signal measured in the subsequent dark frame and the signal of the corresponding bright (illuminated) frame. The same definition is applied for both charging and discharging lag. Note, this illuminated frame must not be saturated. This definition is expressed by the following equation:

$$\text{Lag}[\%] = \frac{\mu_{\text{lag}}}{\mu_{\text{light}}} \times 100, \tag{3.5}$$

where the mean value of the lag and bright image, μ_{lag}, μ_{light} respectively. For charging lag, the lag image is defined as the first bright frame acquired, while the second bright frame is used as the corresponding light reference image. For discharging lag, the dark frame is defined as the lag image, and the preceding bright frame is used as the light reference image.

Because the experimental setup and equipment are highly technical, I created diagrams based on oscilloscope measurements, referred to as traces, to illustrate the acquisition sequence. These traces depict the timing of each image exposure and the light pulse triggered by the delay generator. They are purely schematic, intended to visually represent the procedure, and do not provide precise quantitative information about pulse durations or signal levels. In these traces, I have omitted to

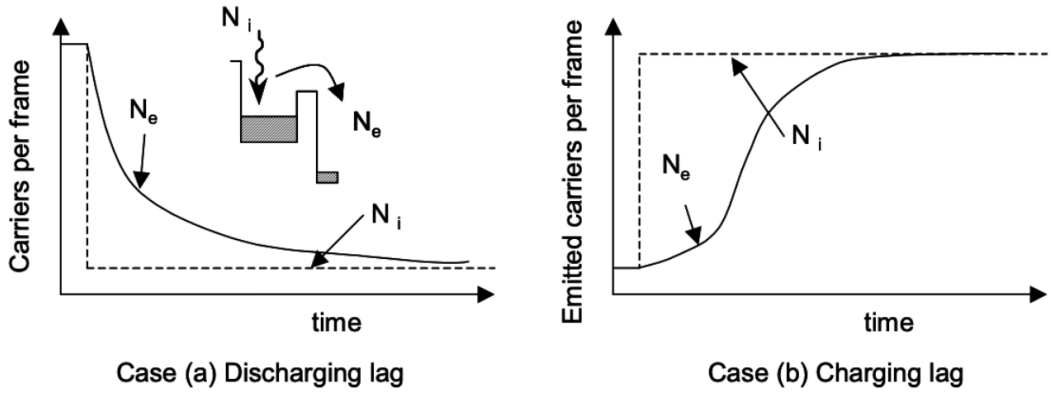


Figure 3.19: Schematic illustration of the two types of image lag. (a) Discharging lag: excess electrons (N_e) are released into subsequent dark frames until the signal relaxes to the expected dark level (N_i). (b) Charging lag: electrons are trapped during the first illuminated exposure (N_e), causing the expected signal to appear in subsequent bright images (N_i). Image adapted from Fossum et al. (2003).

Table 3.4: Description of the Experiments for Image lag.

	Experiment 1	**Experiment 2**	**Experiment 3**	**Experiment 4**	**Experiment 5**
Discharging Lag	-	Measured	Measured	-	-
Charging Lag	-	-	-	Measured	-
Exposure	6.5 ms	0.5 s	0.458 s	0.5 s	0.5 s
Wavelength	Red	Blue, Green, Red, IR	Blue, IR	Blue	Blue
Temperature	25, -25 °C	25, -25 °C	25, -25 °C	25, -25 °C	25, -25 °C
Frame Rate	2.5 Hz	0.5 Hz	2 Hz	1.84, 2 Hz	0.5, 1, 1.5 Hz
Light pulse	50-400 ms (steps 50 ms)	2 s	0.4 s	0.4 s	0.4 s
Imaging mode	HDR	HDR, FFR	HDR	HDR	HDR

show the traces of the camera's sensor reset (known as global clear) and the charge transfer timings. The total readout time shown corresponds to the sum of the global clear and charge transfer intervals which depends on the selected frame rate.

This study was conducted primarily using the HDR imaging mode. The FFR mode is not presented in Experiment 1, as the results from both modes were comparable and effectively identical. In contrast, a comparison between HDR and FFR was performed in Experiment 2, where the results differed significantly. For the remaining experiments, only HDR mode data were recorded and therefore analysed. The description of the Experiments is shown in Table 3.4.

3.5.4 Results from the image lag experiments

In this section, I describe the methodology used to conduct five different experiments, present their results, and analyse the behaviour of image lag under various configurations.

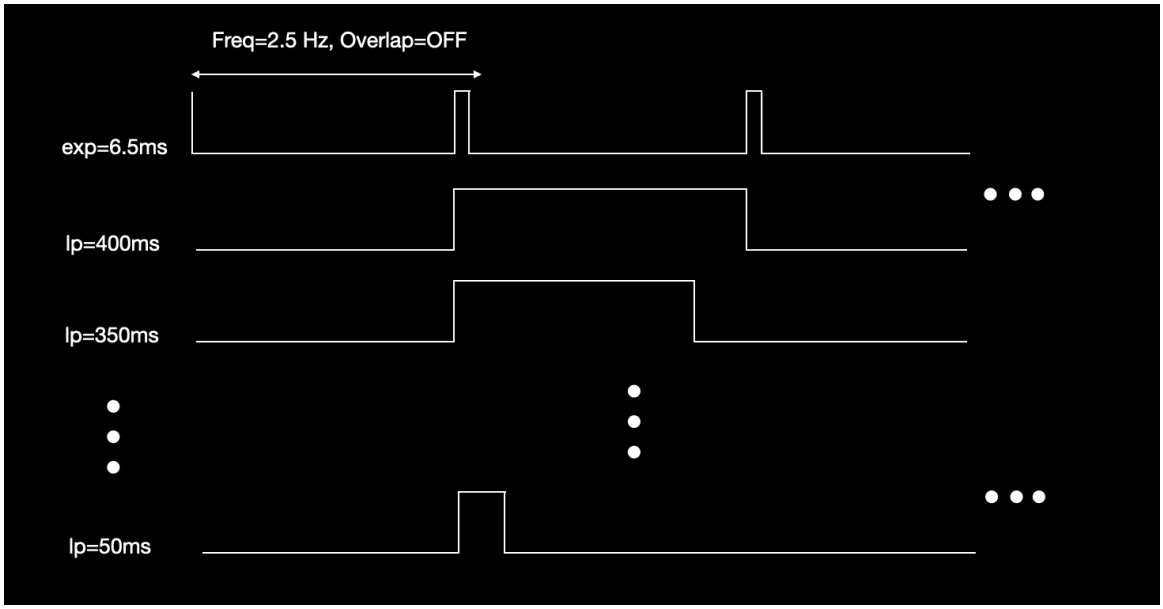


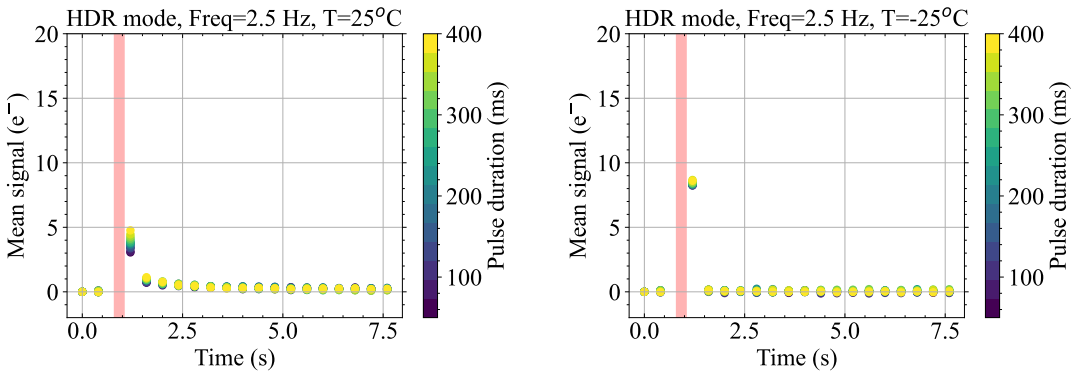
Figure 3.20: Experiment 1: Oscilloscope traces illustrating the timing sequence of the acquisition cycle and the applied light pulse (lp). The camera exposure time (exp) is shown as periodic rectangular pulses corresponding to a fixed 6.5 ms exposure within a 400 ms total frame cycle (2.5 Hz frame rate), indicated by the white arrow. Different durations of the light pulse are also shown.

Experiment 1

In this experiment, the exposure time is kept fixed, while both the pulse duration and the detector temperature are varied. The measurements are performed in both HDR and FFR modes. The frame rate is set to 2.5 Hz, corresponding to a total cycle time (exposure plus readout) of 400 ms, while the exposure time is fixed at 6.5 ms. The exposure time is kept short in order to avoid effects such as the dark current. The initial pulse duration is 50,ms and is subsequently increased in steps of 50 ms. The delay generator is configured to illuminate only the second frame in each sequence. A red light source is used throughout the experiment (see subsection 3.5.2). Note that in this experiment, the image lag cannot be directly estimated from the lag and bright frames, as the bright frame is saturated.

The procedure is as follows: the first frame is acquired in darkness. The light pulse is triggered to coincide with the start of the second exposure, producing a saturated image. All subsequent frames in the sequence are dark images, allowing the residual signal (image lag) to be measured. The experiment is conducted in two distinctive temperatures at 25 °C and -25 °C. This process is described with traces on the diagram illustrated in Figure 3.20. In this experiment, the overlap option is disabled. In overlap mode, the exposure of a given frame begins while the previous frame is still being read out, allowing exposure and readout to occur simultaneously. This configuration automatically fixes the camera operating frequency at the maximum achievable frame rate. However, I choose not to use overlap mode in order to avoid being constrained to the maximum fixed frequency and to maintain full control over the timing parameters. The first dark frame is subtracted from all subsequent images in the sequence. The resulting signal is then converted to electrons to measure any residual charge remaining in the frames acquired after the saturated image.

A sequence of 20 images is recorded, with the third frame being the illuminated and saturated



(a) Image lag at 25 °C.

(b) Image lag at -25 °C.

Figure 3.21: Experiment 1: Sequence of images at different light pulse duration with the third image to be a bright saturated image, shown with the red shaded area.

exposure. The average signal of each image, after bias subtraction and conversion to electrons, is plotted as a function of time for a temperature of 25 °C, as shown in the left panel of Figure 3.21.

The residual charge is clearly visible in the fourth frame (lag frame), immediately following the saturated exposure. The residual signal reaches its maximum when the pulse duration is longest (400 ms) and decreases as the pulse duration is reduced. By the fifth frame, the residuals have diminished further, continuing to decline in subsequent frames.

The same measurement is performed at a temperature of -25 °C, as shown in the right panel of Figure 3.21. The lag frame exhibits roughly twice the residual charge compared to the 25 °C case; however, variations due to different pulse durations are less pronounced. The residual charge drops sharply by the fifth frame, in contrast to the 25 °C case, where it decreases gradually over subsequent frames.

Experiment 2

In this experiment, four different wavelengths are used (see subsection 3.5.2): blue, green, red, and infrared. Measurements are performed in both HDR and FFR modes. The duty-cycle frequency is set to 0.5 Hz, with a camera exposure time of 0.5 s. The delay generator is configured to trigger a 2.0 s light pulse, equal to the duty-cycle period, during the third frame of the sequence. This results in the third frame with an average signal level of half the saturation (30000 ADU for HDR and 2000 ADU for the FFR mode) while the surrounding frames are acquired in darkness to evaluate the residual signal. The experiment is conducted in two temperatures at 25 °C and -25 °C. The overlap mode for this experiment is disabled. The average value of the first two dark images is used to subtract the bias level and quantify the leftover charge and the signal level is converted to electrons. The experimental procedure is illustrated through the traces shown in Figure 3.22.

The light intensity is adjusted for each of the four colours to achieve approximately half-saturation for all light sources. A sequence of 20 images is then recorded at a temperature of 25 °C, repeating the procedure for each colour. The average signal of the image is measured, as shown in Figure 3.23.

In HDR mode, the lag frame exhibits a residual charge of approximately 30,e^-, which gradually decreases in subsequent images. The effect remains noticeable even after 18 images, as the dark

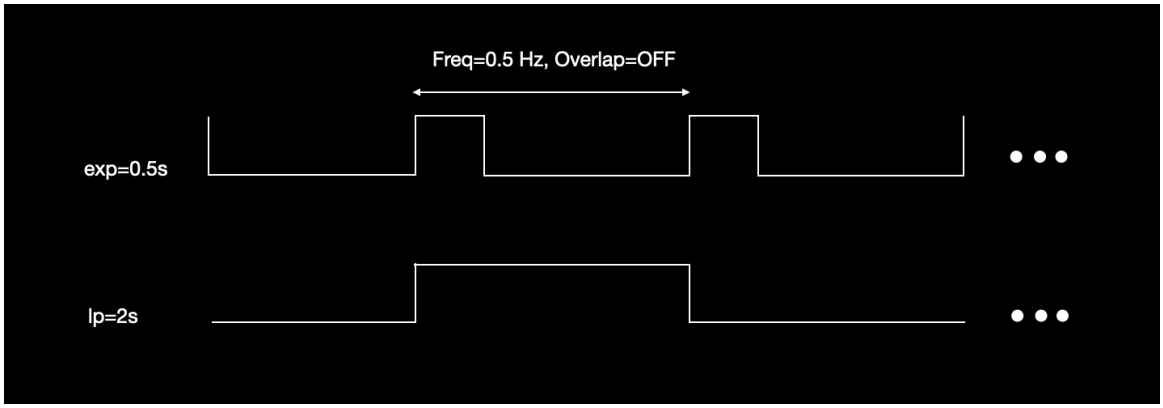
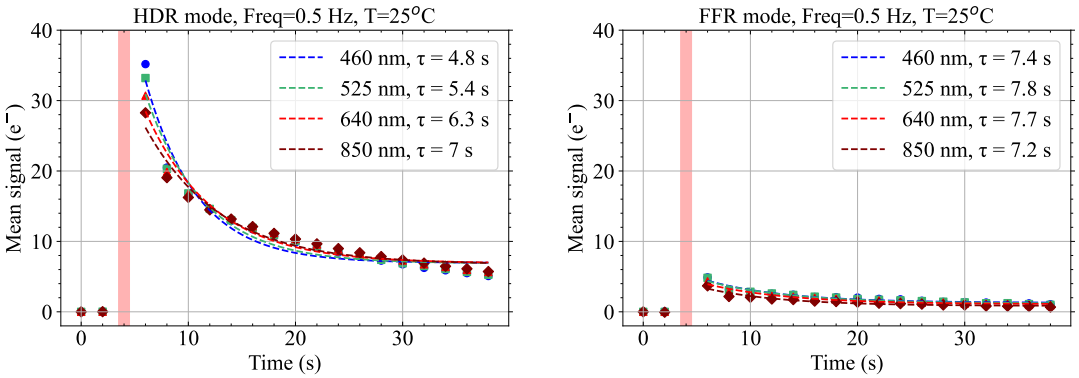


Figure 3.22: Experiment 2: Oscilloscope traces illustrating the timing sequence of the acquisition cycle and the applied light pulse (lp). The camera exposure time (exp) appears as a series of short, periodic rectangular pulses corresponding to the fixed 0.5 s exposure time within a 2.0 s total frame cycle (0.5 Hz frame rate), indicated with the white arrow. The (lp) corresponds to 2.0 s duration.



(a) Image lag at 25 °C with HDR mode.

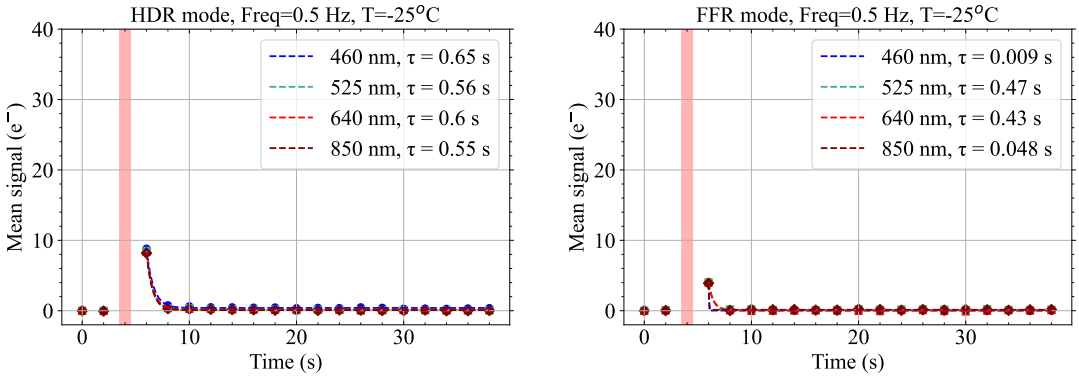
(b) Image lag at 25 °C with FFR mode.

Figure 3.23: Experiment 2: Sequence of images at four different colours marked with circle, square, triangle and diamond for blue, green, red and infrared colours with 2.0 s pulse duration. The third image is a bright non-saturated image, shown with the red shaded area.

images do not return to the same signal level as the initial two dark exposures. In contrast, the lag frame in FFR mode shows a much smaller residual of about 5 e^-. However, a direct comparison between HDR and FFR modes is not strictly appropriate, since the half saturation levels differ due to their different digital outputs.

Regarding wavelength dependence, the HDR mode shows a more pronounced lag for shorter (bluer) wavelengths compared to the infrared, with green and red lying in between. This trend is primarily evident in the lag image itself, while subsequent frames display nearly identical behaviour across all colours. In FFR mode, where the lag is significantly reduced, no clear wavelength dependent differences are observed.

The same procedure is repeated at a constant temperature of -25 °C, as shown in Figure 3.24. In HDR mode (left panel), the lag frame is reduced by nearly a factor of three compared to the 25 °C case, and the wavelength dependence is less pronounced. In the FFR mode (right panel of Figure 3.24), the lag signal is further diminished, and no noticeable colour-dependent differences are observed in the lag frame.



(a) Image lag at -25 °C with HDR mode.

(b) Image lag at -25 °C with FFR mode.

Figure 3.24: Experiment 2: Image lag at -25 °C same as in Figure 3.23.

Table 3.5: Experiment 2: Image lag measurements in blue, green, red and infrared colours for HDR and FFR mode.

Imaging mode	**HDR @ 25 °C**	**FFR @ 25 °C**
lag (%) @ Blue (460 nm)	0.104	0.400
lag (%) @ Green (525 nm)	0.096	0.384
lag (%) @ Red (640 nm)	0.087	0.329
lag (%) @ Infrared (850 nm)	0.069	0.253
Imaging mode	**HDR @ -25 °C**	**FFR @ -25 °C**
lag (%) @ Blue (460 nm)	0.024	0.260
lag (%) @ Green (525 nm)	0.023	0.247
lag (%) @ Red (640 nm)	0.023	0.261
lag (%) @ Infrared (850 nm)	0.021	0.265

The ratio between the lag signal and the bright image is calculated for both imaging modes, temperatures, and wavelengths, and is presented in Table 3.5. In HDR mode at 25 °C, the lag is higher at shorter (bluer) wavelengths and gradually decreases toward longer (redder) wavelengths. This trend disappears when the sensor is cooled to -25 °C, where the lag remains nearly constant across different wavelengths.

A similar behaviour is observed in FFR mode: at 25 °C, the lag is more pronounced at bluer wavelengths, whereas at -25 °C the lag values become comparable across all colours. Overall, the lag effect is significantly less prominent in FFR mode than in HDR mode, where it is approximately an order of magnitude lower.

To quantify the temporal decay of the residual signal, the post-illumination frames were fitted with a single-exponential decay model with a constant offset as described in:

$$S(t) = C + A\exp(-t/\tau), \tag{3.6}$$

where $S(t)$ is the measured residual signal, C is the fitted baseline level, A is the amplitude of the decaying lag component, and τ is the fitted exponential time constant. The fit was applied from the first dark frame following the bright image onward, with time measured relative to the image lag frame.

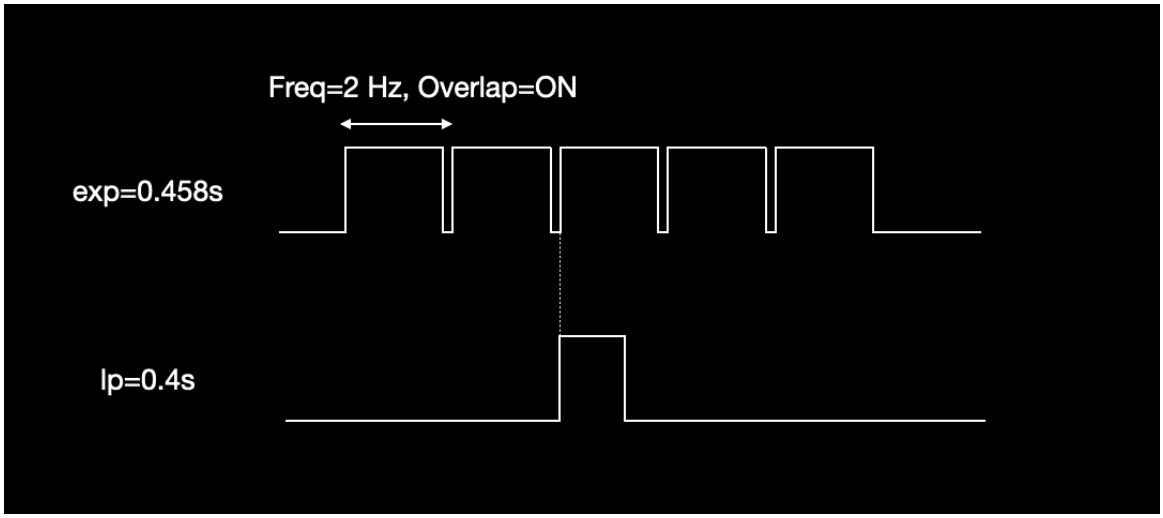


Figure 3.25: Experiment 3: Oscilloscope traces illustrating the timing sequence of the acquisition cycle and the applied light pulse (lp). The camera exposure time (exp) appears as a series of short, periodic rectangular pulses corresponding to the fixed 0.458 s exposure time within a 0.5 s total frame cycle (2 Hz frame rate), indicated with the white arrow. The (lp) corresponds to 0.4 s duration.

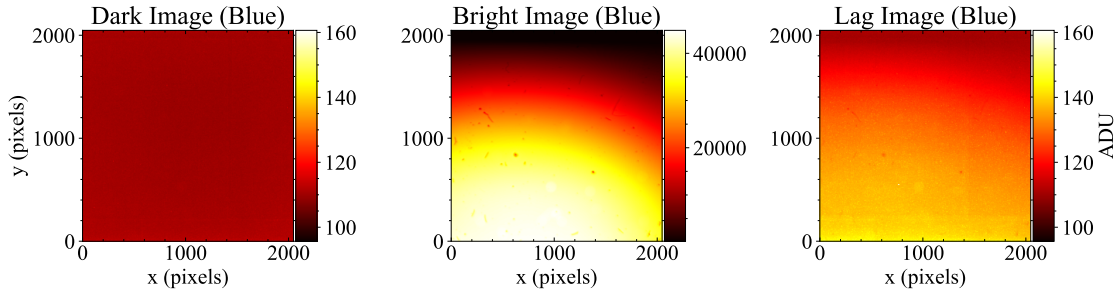
At 25 °C in HDR mode, the fitted time constants were 4.8, 5.4, 6.3, and 7.0 s for blue, green, red, and infrared illumination, respectively. The corresponding values in FFR mode were 7.4, 7.8, 7.7, and 7.2 s. At -25 °C, the fitted time constants were substantially shorter: 0.65, 0.56, 0.60, and 0.55 s in HDR mode, and 0.009, 0.47, 0.43, and 0.048 s in FFR mode for blue, green, red, and infrared illumination, respectively.

Experiment 3

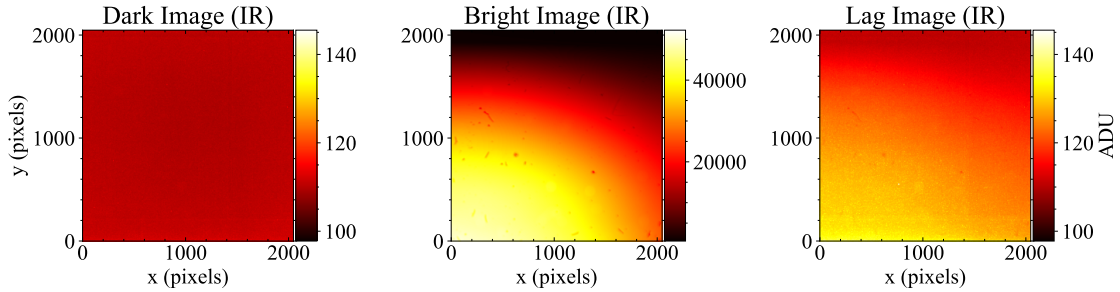
In this experiment, a sequence of five images is acquired in HDR mode with the overlap mode configuration enabled. In this mode, the exposure of a new frame starts while the previous frame is still being read out. Overlap mode is intentionally chosen and enabled because it may amplify the visibility of image lag, as the camera has insufficient time to fully reset during idle periods.

The light pulse duration is set to 0.4 s. The first two frames in each sequence are dark images. The third frame is illuminated, with the signal level gradually increased from low values up to approximately 40-50k ADU. The remaining frames are recorded to evaluate any residual signal. The experiment is conducted at two temperatures, 25 °C and -25 °C, and measurements are performed using the blue and infrared light source. The camera frame rate is set to 2 Hz. To reduce statistical uncertainties, the experiment is repeated 10 times, each time acquiring a five frame sequence. The corresponding frames from each sequence are then stacked (averaged) in the correct order to ensure more robust measurements. The mean value of the first two dark images is subtracted from the sequence and the gain value is used to convert from counts to electrons. On this configuration the exposure time is the cycle time excluding the readout time. Since the readout time is 42 ms for the Marana camera in the HDR mode, the exposure time is set to 0.458 s. The experimental procedure is illustrated through the traces shown in Figure 3.25.

The first three images of the sequence, containing the first dark, the bright and the lag image for both the blue and infrared light sources at 25 °C is illustrated in Figure 3.26. Note that the first and



(a)



(b)

Figure 3.26: Experiment 3: Dark image, bright image, and lag image acquired at 25 °C using the blue (a) and infrared (b) light source. The first and third images are displayed using the same intensity scale for direct comparison.

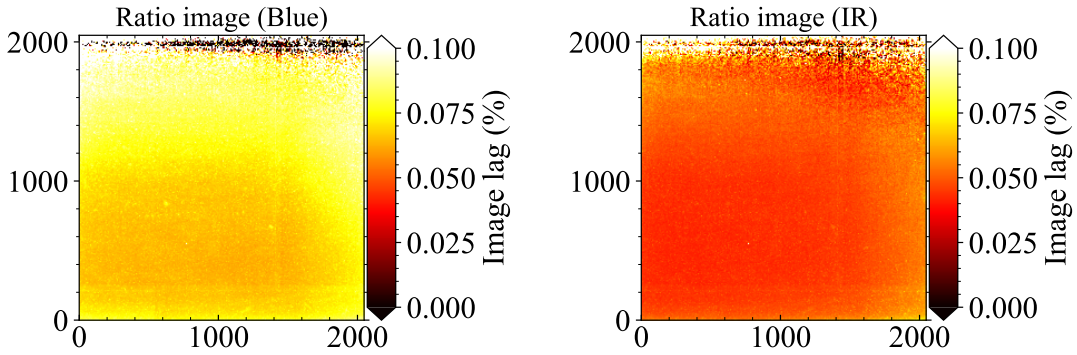
third panels, corresponding to the dark images, are displayed using the same intensity scale, allowing the residual lag charge remaining after the bright exposure to be clearly distinguished.

From Equation 3.5, image lag is estimated as the percentage ratio of the lag image to the bright image. The pixel-by-pixel ratio of the bright and lag frames shown in Figure 3.26 is presented as an image array of identical dimensions in Figure 3.27. Rows near the detector edge, around pixel row 2000, are excluded from the analysis, as the lag signal in this region is minimal and the measured counts are dominated by the bias level and read noise. The lag effect is more pronounced for the blue light source compared to the infrared wavelength.

The same analysis is conducted for temperature at -25 °C and for both light source wavelengths of blue and infrared. The first three frames are displayed in Figure 3.28. Again, the lag frame shows a distinctive pattern from charge residual from the bright image captured before. The pixel by pixel ratio of lag image at temperature of -25 °C is displayed in Figure 3.29. In this case, the lag is very similar between the blue and infrared light source.

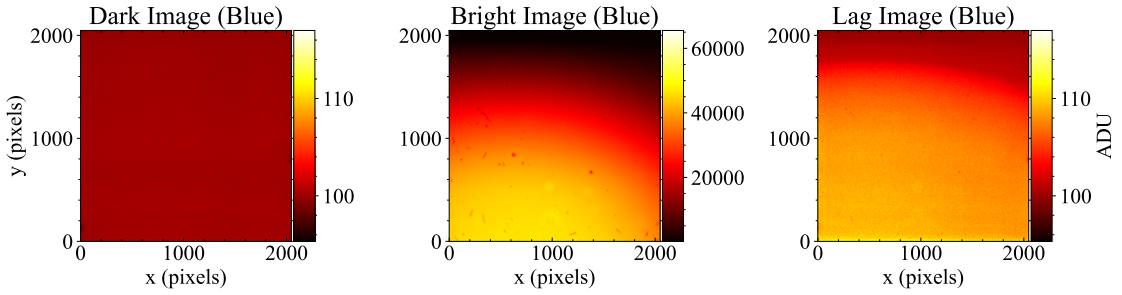
To measure the image lag as a function of signal level, the image array is cropped and divided into subregions in order to compute averaged values. Specifically, the vertical direction (y-pixels) is restricted to rows 1–1800, while the horizontal range (x-pixels) is selected between columns 300 and 700.

Within this region, the image is segmented into consecutive blocks of five rows. For each five-row

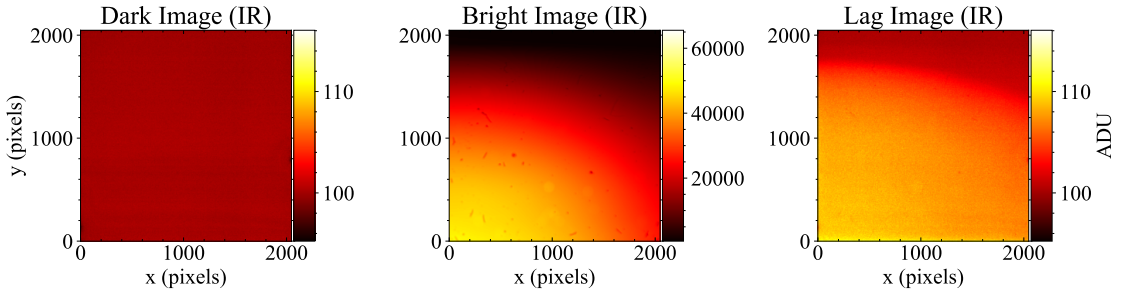


(a) (b) Lag image at 25 °C with infrared colour.

Figure 3.27: Experiment 3: Lag ratio image at 25 °C using the blue (a) and infrared (b) light source from the ratio of the lag image and the bright image in Figure 3.26.

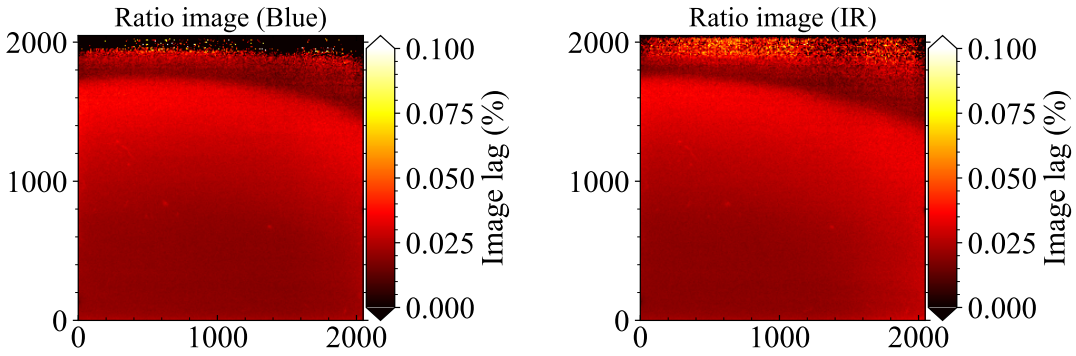


(a)



(b)

Figure 3.28: Experiment 3: Dark image, bright image, and lag image acquired at 25 °C using the blue (a) and infrared (b) light source. The first and third images are displayed using the same intensity scale for direct comparison.



(a) (b)

Figure 3.29: Experiment 3: Lag ratio image at -25 °C using the blue (a) and infrared (b) light source from the ratio of the lag image and the bright image in Figure 3.28.

segment, the mean signal of the bright image and the corresponding lag-to-bright percentage ratio are calculated (after dark subtraction and gain correction). These averaged values are then plotted as a function of signal level, producing the third panel shown in the Figure 3.30.

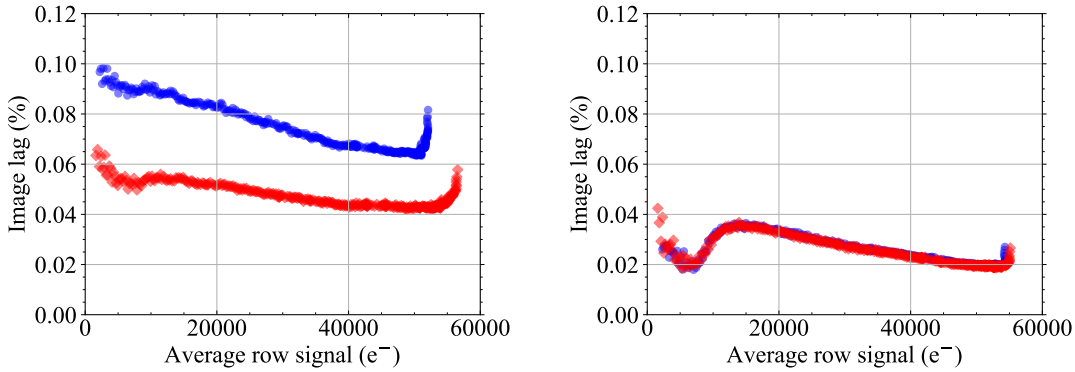
Bluer wavelengths produce a more pronounced image lag in the Marana camera compared to redder wavelengths. This is evident in the left panel of Figure 3.30 at the warmer temperature of 25 °C. However, this wavelength dependence is significantly reduced and, almost identical, when the sensor is cooled to -25 °C, where no strong wavelength trend is observed.

The image lag does not remain constant across the tested signal range. Instead, it is larger at low illumination levels and decreases as the signal level increases, indicating that the measured lag depends on the signal accumulated in the illuminated frame. Furthermore, an increase in lag is observed at signal levels of approximately 55k e^-, where the detector is approaching-though still not reaching-saturation. Moreover, the overall shape of the lag as a function of signal level appears broadly consistent across both wavelengths and remains similar at the two temperatures, suggesting that the dominant behaviour is largely independent of wavelength and only weakly dependent on temperature. Nevertheless, some temperature-dependent differences are observed: the hump is more pronounced at -25 °C, while the subsequent uptick is less pronounced than at the higher temperature.

Experiment 4

In this experiment, I investigate the charging and discharging lag using a sequence of images. A total of 25 frames are recorded in the following order: 5 dark images, 5 illuminated images, 5 dark images, and 5 illuminated images. The camera exposure is set to 0.5 s in HDR mode. The bright images are recorded at approximately 50k ADU. The temperature is set at 25 °C and -25 °C.

The delay generator is configured to deliver a 0.4 s light pulse, with the sequence structured as 5 frames delay, 5 frames with the light on, and 5 frames with the light off. The analysis is performed using only a blue light source, and a comparison is made between having the overlap mode enabled



(a) Lag for signal levels at 25 °C.

(b) Lag for signal levels at -25 °C.

Figure 3.30: Experiment 3: Lag ratio as a function of signal level from the ratio of the lag image and the bright image in Figure 3.28. The blue light source data is indicated with the blue solid circles, while the infrared with the red diamond.

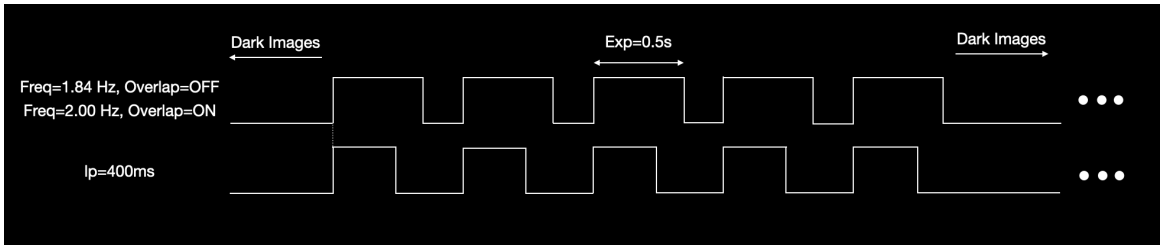


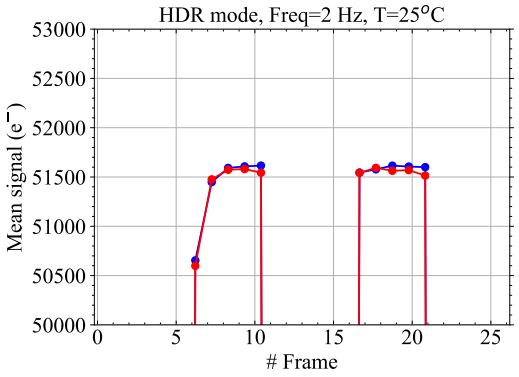
Figure 3.31: Experiment 4: Oscilloscope traces illustrating the timing sequence of the acquisition cycle and the applied light pulse (lp). The camera exposure time (exp) appears as a series of short, periodic rectangular pulses corresponding to the fixed 0.5 s exposure time from total frame cycle of 1.84 Hz and 2 Hz frame rate for overlap ON and OFF respectively. The (lp) corresponds to 0.4 s duration.

versus disabled. The mean value of the first 5 dark images is subtracted from the rest of the sequence to include only the remaining charge. The experimental procedure is schematically illustrated by the traces in Figure 3.31. The duty cycle is set to its maximum for both overlap modes, resulting in a 0.5 s exposure per frame. With overlap enabled, the readout of each frame occurs while the exposure of the previous frame is still in progress.

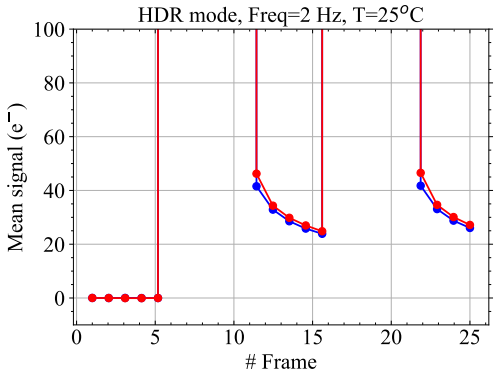
The data are acquired for both overlap configurations, and the mean signal value is extracted from each image. The results are presented in Figure 3.32 for a temperature of 25 °C and in Figure 3.33 for -25 °C. Both plots are a zoom-in representation of the image sequence mean value against frame number in order to observe the charging and discharging lag.

In the left panel of Figure 3.32, the first bright frame exhibits a lower signal level compared to the subsequent bright frames, particularly between frame-6 and frame-7, indicating the presence of charging lag (see Figure 3.19). In contrast, the right panel of Figure 3.32 shows that the dark frames following the illuminated frames (frame-11 to frame-15) retain a residual signal that gradually decreases but does not return to zero before the next bright acquisition begins. This behaviour is characteristic of discharging lag.

The charging lag, calculated using Equation 3.5, is found to be 1.54 % with the overlap mode

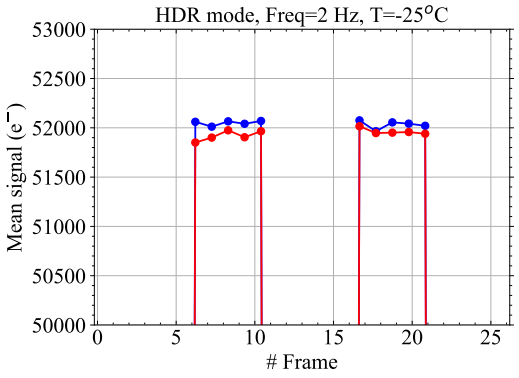


(a) Charging lag.

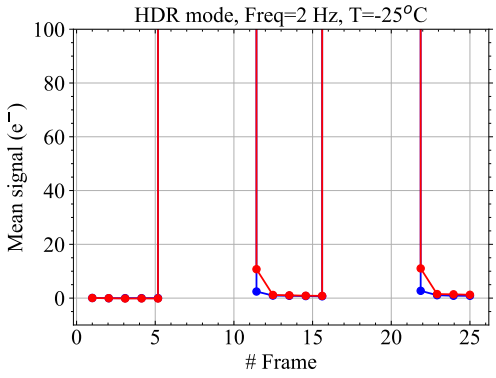


(b) Discharging lag.

Figure 3.32: Experiment 4: Image lag measured for the Marana camera from a sequence of 25 images at a temperature of 25 °C. The plot is zoomed into the highest and lowest signal levels to improve clarity and interpretation. Data acquired with the overlap mode enabled are shown in blue, while data with the overlap mode disabled are shown in red.



(a) Charging lag.



(b) Discharging lag.

Figure 3.33: Experiment 4: Image lag for the Marana camera at -25 °C, same as in Figure 3.32.

enabled and 1.7 % with the overlap mode disabled. The corresponding discharging lag values are 0.08 % and 0.09 % for the overlap mode enabled and disabled, respectively.

This behaviour changes when the sensor is being cooled down at temperature of -25,°C. In particular, in the left panel of Figure 3.33, the first bright image exhibits essentially the same signal level as the subsequent bright images in the sequence (frame-6 and frame-7), resulting in minimal charge lag. Similarly, in the subsequent dark image sequence (frame-11 to frame-15) shown in the right panel of Figure 3.33, the discharging lag is minimal when overlap mode is enabled. When overlap mode is disabled, some residual charge is still present, although it is significantly reduced compared to the case at 25 °C.

The charging and discharging lag is found to be essentially 0 for the overlap mode enabled, while it is measured 0.1 % and 0.02 % for the overlap mode disabled.

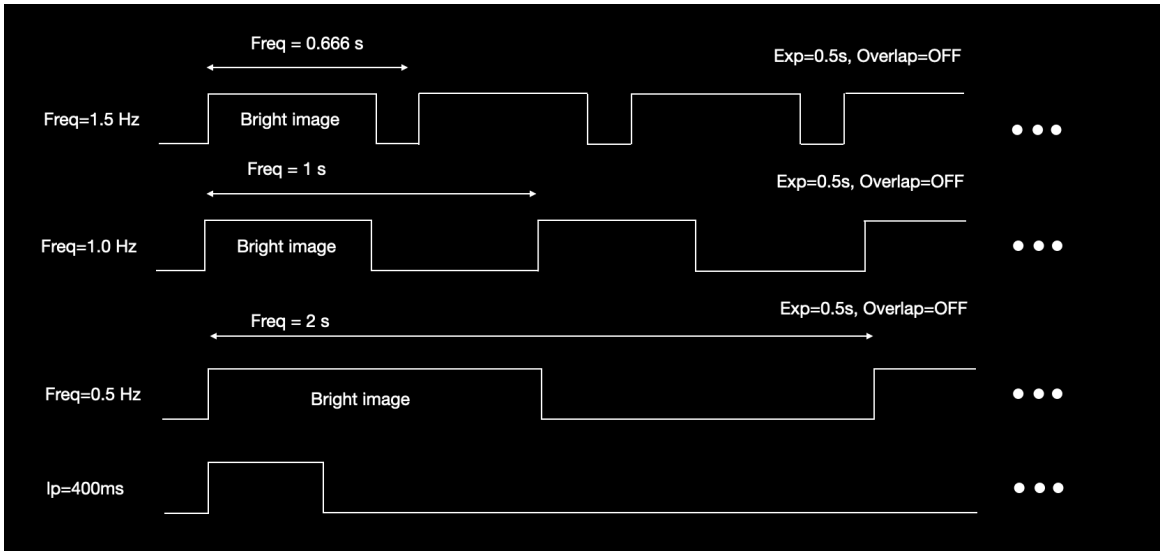


Figure 3.34: Experiment 5: The diagram illustrates the timing sequence between the applied light pulse (lp) and the camera exposure (exp), for 3 different duty cycles. The exposure signal (exp) appears as a series of short, periodic rectangular pulses corresponding to the fixed 0.5 s exposure time within 3 different cases of frame cycle (1.5, 1 and 0.5 Hz frame rate), indicated with the white arrow.

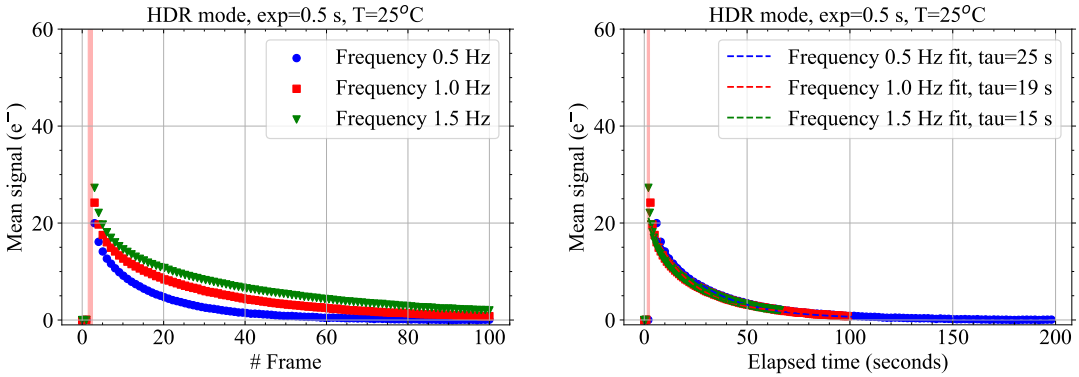
Experiment 5

In this experiment, I study how much the image lag is affected for different frame cycles or from the time elapsed. The overlap mode is disabled and the camera operates in the HDR mode. For this work, 100 images are recorded. The delay generator is configured to deliver a 0.4 s light pulse, with the sequence structured as 2 frames delay. The third image is a bright image with approximately 50k ADU. The exposure is kept fixed at 0.5 s and the light source is blue colour. The mean value of the first two dark images is used to subtract the bias level from the rest of the sequence. The experimental procedure is schematically illustrated by the traces in Figure 3.34.

At constant temperature of 25 °C, 100 dark frames are acquired, with the third frame in the sequence being a bright exposure. The average signal is calculated and plotted as a function of frame number for three different acquisition frequencies of 0.5, 1, and 1.5 Hz, as shown in the left panel of Figure 3.35.

For all frequencies, a residual charge of approximately 30 e^- is observed in the fourth frame, immediately following the bright exposure. The lag then decreases progressively with each subsequent frame until it approaches zero. The rate of decay depends on the applied frequency: at 0.5 Hz the lag dissipates more rapidly than at 1.5 Hz, while the 1 Hz case exhibits intermediate behaviour between the two.

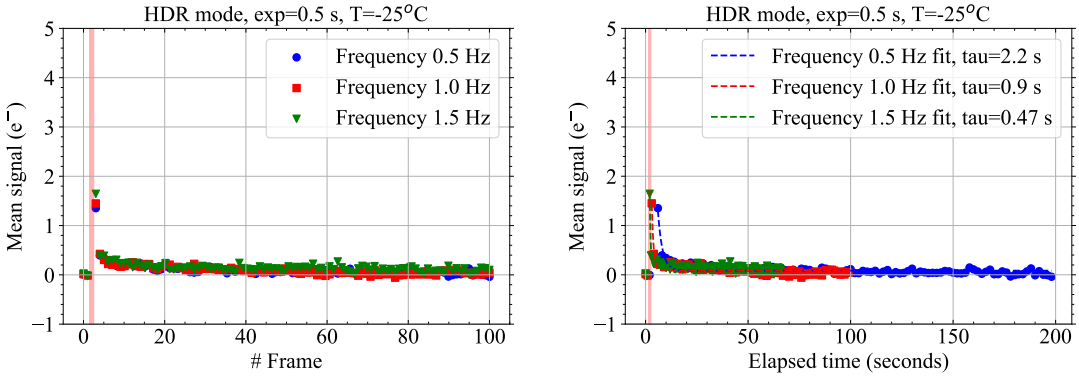
The same dataset is also plotted as a function of elapsed time in order to examine how the behaviour evolves after the bright exposure. In this representation, the three frequencies exhibit nearly identical behaviour, as shown in the right panel of Figure 3.35. If a larger number of frames are acquired for the 1.5 Hz sequence, the subsequent charge dissipation is expected to follow the same trend as observed for the 0.5 Hz case. Similarly, the 1 Hz sequence demonstrates intermediate behaviour between the two.



(a) Image lag as a function of frame number.

(b) Image lag as a function of elapsed time.

Figure 3.35: Experiment 5: Image lag for the Marana camera with the overlap disabled at different frequencies at 0.5, 1 and 1.5 Hz marked with circles, squares and triangles respectively. Data acquired with temperature of 25 °C. The red shaded area represents the bright non-saturated image. The two panels represent the same dataset but plotted as a function of frame (left) and of time (right).



(a) Image lag as a function of frame number.

(b) Image lag as a function of elapsed time.

Figure 3.36: Experiment 5: Image lag for the Marana camera at -25 °C, same as in Figure 3.35.

The same approach is applied at a temperature of -25 °C, as illustrated in the left panel of Figure 3.36, which shows the residual signal as a function of frame number. The residual charge in the frame immediately following the bright exposure is significantly lower than in the -25 °C case. Moreover, the effect dissipates more rapidly, reaching nearly zero by approximately the tenth frame. At this temperature, differences between the acquisition frequencies are difficult to distinguish, as they appear to exhibit nearly identical behaviour. A similar trend is observed when the same data are plotted as a function of elapsed time, as shown in the right panel of Figure 3.36.

The image lag measured on temperature at 25 °C is 0.05, 0.047 and 0.04 % for frequencies 1.5, 1 and 0.5 Hz. At -25 °C, the image lag decreases to 0.003 %, with no significant differences observed between the different frequencies.

To quantify the temporal decay of the residual signal, the image lag decay was fitted as a function of elapsed time using the same single-exponential model from Equation 3.6, described in section 3.5.4. The fitted curves are shown in Figure 3.35 and Figure 3.36. At 25 °C, the decay is well described by an exponential function, with fitted time constants of approximately 25, 19, and 15 s for frame rates of

0.5, 1.0, and 1.5 Hz, respectively. These values indicate that the residual lag decreases more rapidly at higher frame rates, although several time constants are required for the signal to approach the bias level. At -25 °C, the fitted time constants are substantially shorter, decreasing to approximately 2.2, 0.9, and 0.47 s for 0.5, 1.0, and 1.5 Hz, respectively.

3.5.5 Discussion

The Marana camera was thoroughly investigated through a series of experiments aimed at quantifying and characterising the behaviour of image lag. These experiments explored various methods, camera parameters, and configurations, including exposure times, light pulse durations, overlap modes, imaging modes, sensor temperatures, and the wavelengths of the light sources.

In Experiment 1, measurements comparing the FFR and HDR modes showed no significant differences, with both modes producing essentially identical results. Image lag could not be quantified in this experiment because the bright image was saturated. However, at a temperature of 25 °C, it was observed that the duration of the light pulse influenced lag: longer pulses between exposures resulted in increased lag (see Figure 3.21).

In Experiment 2, the measured lag at 25 °C shows a clear wavelength dependence, with larger residual signals at shorter wavelengths and smaller residuals toward the red and infrared (see Figure 3.23). The residual signal also decreases in the frames following the bright exposure, showing that the effect is transient rather than a fixed offset. The exponential fits quantify this behaviour: in HDR mode at 25 °C, the initial lag amplitude decreases from blue to infrared illumination, while the fitted time constant increases. This indicates that shorter- wavelength photons produce a larger immediate residual signal, whereas longer-wavelength photons produce a smaller but more slowly decaying component.

Since the Marana sensor is backside illuminated, this wavelength dependence may be related to the depth at which photons are absorbed in the silicon. Blue photons are absorbed closer to the back surface, farther from the front-side charge-collection and readout structures, where surface effects, trapping sites, or incomplete charge collection may contribute more strongly to persistence. Longer-wavelength photons penetrate deeper into the silicon and may therefore produce a smaller initial residual signal, although the longer fitted time constants suggest that the remaining lag component decays more slowly. This interpretation remains tentative and would require further measurements, ideally comparing otherwise similar backside- and frontside-illuminated sensors.

Cooling the detector to -25 °C significantly reduces both the amplitude and decay time of the residual signal (see Figure 3.24), demonstrating that temperature control is effective in suppressing persistence. At the lower temperature, the wavelength dependence becomes much less pronounced, and the residual signal either decays on a shorter timescale or becomes too small to distinguish from noise and bias variations.

The comparison between HDR and FFR modes is more complex, because the two modes differ in digitisation, full well capacity, and gain-channel readout. FFR uses a 12-bit output with a maximum digitised value of 4095, whereas HDR uses a 16-bit output with a maximum value of 65535. In addition, a non-saturated bright signal of approximately 50,000 electrons in HDR mode is read through the Low Gain channel, while the corresponding FFR signal is limited to approximately 2000 electrons and is read through the High Gain channel (see subsection 3.3.7).

Therefore, the observed mode dependence cannot be attributed to a single factor, but likely reflects the combined effects of digitisation depth, effective full well capacity, and gain- channel readout. Overall, although measurable differences are observed with wavelength, temperature, and acquisition mode, the absolute image lag signal remains small in all cases, with the lowest persistence obtained at reduced temperature and in HDR mode.

In Experiment 3, image lag was measured as a function of signal level for two temperatures and two light sources. At the higher temperature, lag is more pronounced, consistent with the findings of Experiment 2. The effect is stronger at bluer wavelengths and weaker at redder wavelengths (see Figure 3.27a and Figure 3.27b), in agreement with the conclusions from Experiment 2. Image lag for the Marana camera is not constant across signal levels; it is larger at low signals and decreases as the signal increases (see Figure 3.30). At certain signal levels (~5000 and ~55000 e^- in Figure 3.30), lag exhibits a steep increase. A likely explanation is charge spill-back during transfer from the pinned photodiode (PPD) to the Floating Diffusion (FD) (Ivory, 2020). When a large amount of charge is transferred, the FD potential changes as it fills, reducing the driving force for complete charge transfer. Some charge can therefore remain near the transfer gate region instead of being collected fully by the FD. Once the transfer gate is switched off, part of this charge may return to the PPD and be retained until the next readout. This delayed residual charge produces an increased lag signal in the following frame. Despite these variations, the overall shape of the lag curve as a function of signal level is similar across both temperatures and wavelengths, indicating that this behaviour is largely independent of temperature and wavelength.

Image lag in Figure 3.30, was found to be below 0.1 % across most of the dynamic range at a temperature of 25 °C, and below 0.05 % at -25 °C. These values are larger than those reported in Wu et al. (2023b), where the image lag was found to remain below 0.05 % in X-ray observations. Additionally, Wu et al. (2023b) observed that image lag decreases at higher temperatures, which contrasts with the trend found in this work, where lower temperatures result in reduced lag. Furthermore, for a typical 4T CMOS sensor described in Stefanov (2022), the dependence of image lag on signal level exhibits a pattern similar to that observed in Experiment 3. In particular, the lag is relatively high at low signal levels, decreases as the signal increases, and then rises again as the sensor approaches saturation.

In Experiment 4, a sequence of alternating bright and dark images was recorded to quantify both charging and discharging lag at different temperatures and overlap modes. The Marana camera is affected by both types of lag; however, at 25 °C the charging lag is larger than the discharging lag (see Figure 3.32). This effect is substantially reduced when the sensor is cooled to -25 °C (see Figure 3.33). Additionally, no significant difference was observed between measurements taken with overlap enabled and disabled, although the lag appears to be slightly more pronounced when overlap is disabled.

In Experiment 5, we examined the dependency of image lag on both the duty cycle and the elapsed time since the bright exposure. At 25 °C, the results show that for longer frame cycles, the image lag gradually decreases toward the bias level, compared to shorter frame cycles. When the duty cycle is converted into elapsed time, it becomes evident that the lag depends mainly on the time passed since the bright exposure (see Figure 3.35). At the lower temperature of -25 °C, this effect is no longer apparent, as the second frame following the bright image has already returned to the bias

level (see Figure 3.36). Moreover, by applying a single-exponential decay model to the 25 °C data, the residual signal is found to decay on a timescale of 25 s (for the 0.5 Hz where the the lag signal has been completely removed), with fitted time constants of approximately 25 s. This confirms that the observed lag is not a short-lived persistence effect. The absence of a measurable decay tail at -25 °C further indicates that cooling the detector strongly suppresses image lag, both in amplitude and in persistence time. Therefore, the results suggest that the apparent dependence on duty cycle is primarily a time-recovery effect, and that operating the camera at reduced temperature is an effective way to minimise persistence after bright exposures. In general, the fitted time constant decreases with increasing frame rate, indicating that the apparent decay timescale of the residual signal depends on the acquisition cadence (for 0.5, 1 and 1.5 Hz cases). This may reflect differences in trap filling and release under different duty cycles, as well as the fact that a single-exponential model provides an effective description of a potentially more complex persistence process.

The five image lag experiments show that charge persistence in the Marana CMOS camera is generally small. In all cases, the residual signal after illumination represents only a minor fraction of the original signal, indicating that image lag is unlikely to be a significant limitation for most observing conditions. The clearest trend is the benefit of reduced operating temperature: cooling the camera decreases the lag amplitude and also reduces the time over which the residual signal persists. This is particularly important because a small residual signal can still affect precision measurements if it decays slowly. The results therefore suggest that controlling the detector temperature is the most effective practical approach for minimising image lag.

A practical consideration for reproducing these measurements is the time and equipment required. All five experiments used the same laboratory setup, consisting of a programmable delay generator to control the timing of the light pulse, a light tube with the light source, an oscilloscope to verify the trigger and illumination timing, and a simple trigger box containing manual switches. Each experiment required approximately four hours to configure, acquire, and verify, corresponding to a total acquisition time of roughly 20 hours for the full set of measurements, excluding subsequent data reduction and analysis. The financial investment is also relatively modest compared with the cost of the camera itself, but is non-negligible. The light tube used in these experiments cost approximately (~£1000), while a suitable oscilloscope, required only to verify the timing and presence of the trigger pulses, can be obtained for around (~£300). A programmable delay generator suitable for controlling the light-pulse timing is typically of order (~£1000). Including the trigger box, cabling, and other ancillary components, the total cost of the experimental setup is therefore estimated to be of order a few thousand pounds.

3.6 Conclusion

The Marana camera underwent detailed laboratory characterisation. The system operates using two gain channels, High Gain (HG) and Low Gain (LG), from which the FFR and HDR imaging modes are constructed. The characterisation procedures included individual measurements of the HG and LG channels to understand how the HDR and FFR modes are formed. Both channels were characterised in the laboratory following the same experimental procedures and methods described in section 2.4 in chapter 2. The results show that the measured read noise is consistent with that obtained in the HDR

and FFR modes, while the LG channel provides a full well capacity comparable to that measured in the HDR mode. However, in the final implementation of the FFR and HDR imaging modes, the camera applies on-board pre-processing correction maps. As a result, several differences were identified between the standalone channel measurements and the final imaging modes, particularly in terms of linearity and non-uniformity characteristics, including photo response and dark signal non-uniformities (PRNU, DSNU), dark current, and linearity performance.

Adjustments to the electronic configuration of the camera were also investigated. In particular, the VDDPIX pixel supply voltage was treated as a free parameter and the camera was characterised for different voltage settings. The analysis was first performed independently on the HG and LG channels, and subsequently on the HDR imaging mode. The results show that increasing the supply voltage allows the camera to achieve a significantly larger full well capacity, while the read noise remains comparable to the values measured without voltage adjustments. Most other performance characteristics also remain largely unchanged. However, a substantial increase in dark current was observed. Given that dark current and amplifier glow already represent limitations of the Marana CMOS sensor-especially when compared to other CMOS cameras (Gill et al., 2022; Alarcon et al., 2023a) and traditional CCDs-this voltage adjustment was investigated for characterization purposes only and was not implemented during the on-sky tests presented in chapter 4.

Image lag was investigated in the Marana CMOS camera. Overall, the camera exhibits low levels of image lag, although the effect is more pronounced in FFR mode compared to HDR mode. The results indicate that lag depends on the signal level of the illuminated image, the elapsed time since the bright exposure, the sensor temperature, and the wavelength of the illumination source used for the bright image. In particular, cooling the sensor significantly reduces both the amplitude and persistence of the lag. Both charging and discharging lag were measured, with charging lag found to be the more pronounced component. Further measurements are required to confirm the observed wavelength dependence on image lag and to determine whether it is linked to the backside illuminated sensor architecture. A useful follow-up would be to repeat the same procedure on comparable backside- and frontside illuminated cameras.

Chapter 4

On-sky testing of the Marana CMOS and iKon-L CCD cameras

"Leave the gun, take the cannoli"

'The Godfather', Francis Ford Coppola, 1972

Note

This chapter is a reproduction of the publication 'High-Precision Photometry with a scientific CMOS Camera: II On-Sky Testing of the Marana camera at the NGTS facility' (Apergis et al., 2026), originally published in RAS Techniques and Instruments (RASTI) in March 2026. The writing and analysis of the paper was performed by the author, with comments throughout the paper that came from the co-authors.

Abstract

Modern scientific CMOS cameras offer very fast readout speeds and low read noise. In this study, we evaluate the performance of the Andor Marana CMOS camera through on-sky testing carried out at the NGTS facility at the ESO Paranal Observatory in Chile. We mount the Marana camera to an NGTS telescope, and conduct photometric observations of bright stars. In particular, we target transit events around eight known bright exoplanet host stars. Simultaneous observations are carried out using an existing Andor iKon-L CCD camera on a neighbouring NGTS telescope. This allows for a direct comparison of the photometric precision between the CMOS and CCD cameras. We find that the Marana CMOS exhibits a similar level of photometric performance to the CCD camera, achieving 500 ppm at a 30-minute timescale for a T = 10 mag star. Although the CCD has a slightly better quantum efficiency over the NGTS filter range (520-890 nm), we find that the faster readout speed of the CMOS compared to the CCD means that the CMOS camera detects 20 % more photons per unit time for a solar-type star in our standard 10 s exposure time operation mode. This results in the CMOS performing slightly better photometry in the photon-limited regime. We conclude that modern CMOS cameras, such as the Marana, are very well-suited for astronomical time-series

photometry applications.

4.1 Introduction

Charge Coupled Device (CCD) cameras are an essential tool in modern astronomy, being at the heart of almost all astronomical instruments operating at optical wavelengths (Mackay, 1986).

The major space-based exoplanet transit detection missions, such as Kepler (Borucki et al., 2010) and the Transiting Exoplanet Survey Satellite (Ricker et al., 2015, TESS) have been equipped with CCD detectors. The upcoming PLATO mission (Rauer et al., 2025) will also use CCD detectors. Similarly, ground-based transiting exoplanet surveys such as the Wide Angle Search for Planets (Pollacco et al., 2006, WASP) and its successor, the Next Generation Transit Survey (Wheatley et al., 2018, NGTS) have used CCD detectors. However rapid progress in Complementary Metal-Oxide Semiconductor (CMOS) technology, particularly over the past 10 years such as low read noise and extended dynamic range mean that CMOS detectors may now be considered for future transiting exoplanet surveys (Ge et al., 2022).

CMOS cameras provide substantial advantages for dynamic celestial observations requiring rapid data capture and low read noise, such as detecting exoplanet transits (Wheatley et al., 2018), tracking asteroids (Alarcon et al., 2023b), monitoring meteoroids (Kajino et al., 2019), detecting trans-Neptunian objects (Wang et al., 2024) and conducting space situational awareness observations to track and characterise satellites in near-Earth orbit (Zimmer et al., 2016; Blake et al., 2023; Cooke et al., 2023; Airey et al., 2025b; Chote et al., 2025). Recent tests and observational campaigns have demonstrated the capability of CMOS sensors to produce high-quality photometry across a range of applications (Alarcon et al., 2023b; Mu et al., 2024). CMOS cameras can achieve photometric precision comparable to that of CCDs, with accuracies reaching the milli-magnitude level (Xiao et al., 2025). On-sky and detector noise sources measurements have been found to be in agreement with the theoretical noise models (Layden et al., 2025). In particular, modern back-illuminated CMOS detectors do not suffer the strong sub-pixel sensitivity variations associated with front-illuminated detectors (electrode structures, micro-lenses etc). (Karpov et al., 2020).

In this work, we set out to assess the performance of a CMOS camera in this context by deploying one at the NGTS facility, which is situated at a site with exceptional photometric qualities. We utilised a modern CMOS camera, the Marana 4.2BV-11, which has demonstrated great performance in laboratory tests (Karpov et al., 2021; Qiu et al., 2021; Apergis et al., 2025) and is expected to be well-suited for high-precision time-series photometry. By directly comparing the CMOS camera's performance with that of Andor's iKon-L CCD camera that is already installed on the NGTS telescopes, we test if CMOS technology can deliver comparable bright star photometry to the well-tested CCD cameras. This study provides valuable insight into whether CMOS image sensors could potentially compete with CCD image sensors in exoplanet surveys. By evaluating if CMOS devices exhibit similar noise characteristics and performance, we aim to determine their suitability as trusted instruments for precise, stable photometric measurements.

Our first paper (Apergis et al., 2025) evaluated the performance of the Marana CMOS camera under controlled laboratory conditions. We measured the camera's read noise in dark environments and characterized both the temporal and spatial noise patterns across sensor rows and columns. We

examined the behaviour of the dark current and glow at different operating temperatures. Under illuminated conditions, we quantified the photon response non-uniformity and assessed the camera's linearity performance. Additionally, we measured the quantum efficiency of the sensor across multiple wavelengths and determined the transmittance of the front window mounted on the camera. Those results are summarized in Table 4.1. Overall, the performance of the Marana camera demonstrates that it is well suited for high-precision time-series photometry.

In this second paper, we focus on on-sky testing of the Marana CMOS, and making a direct comparison to the iKon-L CCD cameras. To do this, we take observations simultaneously with the CMOS and CCD cameras, with identical hardware configurations for the mount, telescope, filter, and with the same sky conditions. An identical pipeline is used to perform data reduction and photometry routines for both cameras.

This paper reports on on-sky tests of the Marana CMOS with the NGTS facility. It is organised as follows, in Section 4.2 we describe the NGTS facility and the CMOS and CCD cameras. In Section 4.3 we set out the methodology, including the installation of the CMOS camera at NGTS, the on-sky observations made with the CMOS and CCD cameras, and the image reduction and photometry pipeline. In Section 4.4 we discuss the various sources of photometric noise that are present in our CMOS and CCD data. In Section 4.5 we present our photometric results for the CMOS and CCD cameras from the on-sky testing. In Section 4.6 we discuss the results from the CMOS on-sky testing. Lastly, Section 4.7 outlines our conclusions on the suitability of the CMOS camera for bright star photometry.

4.2 Observatory and Instruments

4.2.1 The NGTS Facility

The Next Generation Transit Survey (Wheatley et al., 2018, NGTS) is a ground-based observatory located at ESO's Paranal Observatory in Chile. Inspired by the success of the WASP programme (Pollacco et al., 2006), NGTS was built to provide very high precision time series photometry for bright stars to detect and characterise transiting exoplanets.

NGTS is comprised of 12 Newtonian telescopes, each with $f/2.8$ and 20 cm apertures, manufactured by AstroSysteme Austria[1]. The telescopes are spaced 2 m apart, in two rows of six, in a single enclosure. The optical design of the telescopes include a primary hyperbolic mirror along with a corrector lens. The telescopes are equipped with deep-depleted CCD cameras with high sensitivity in the red spectrum (see Section 4.2.2). These CCD cameras are mounted on a customised focuser with an NGTS-specific filter, designed for the 520-890 nm range. The quantum efficiency of the cameras is shown in Figure 4.1. Further details about the instruments and the operation can be found in Wheatley et al. (2018).

The NGTS facility has successfully discovered 36 exoplanets and 8 eclipsing binaries[2]. Notable discoveries include NGTS-1b (Bayliss et al., 2018), a rare giant planet around a low mass star, NGTS-4b (West et al., 2019), the shallowest ever transit to be initially detected from a ground-based observatory, NGTS-10b (McCormac et al., 2020), a very short-period hot Jupiter, NGTS-14Ab

[1] https://www.astrosysteme.com/references/observatory-paranal-chile/
[2] https://ngtransits.org/pages/tabs/publications_page.html

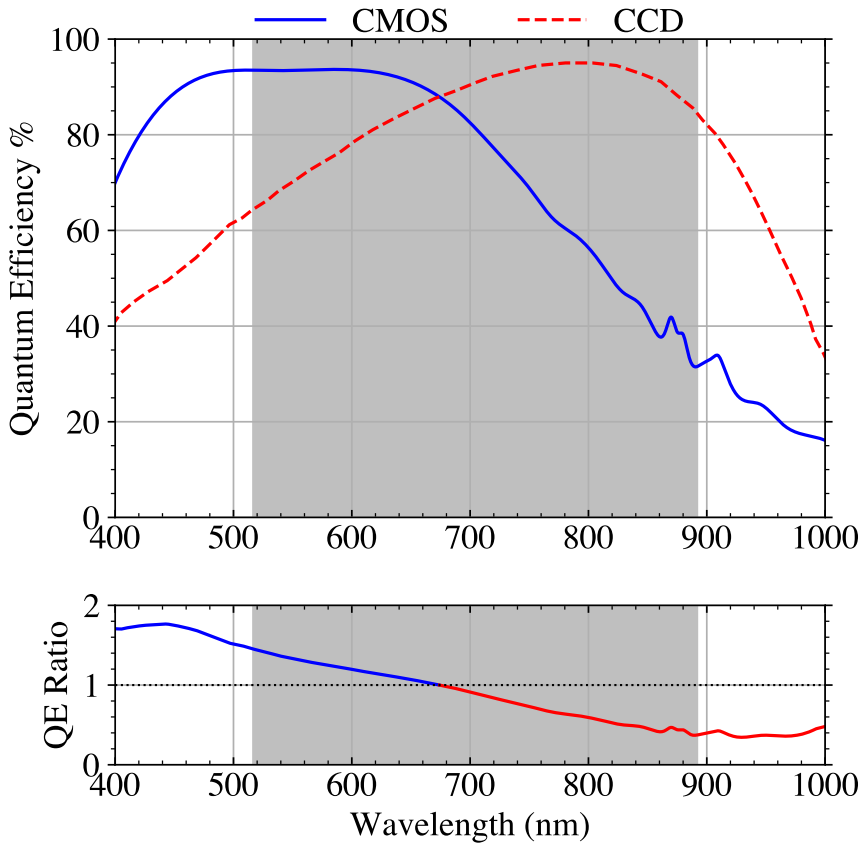


Figure 4.1: **Top:** QEs of the cameras as a function of wavelength. The filled grey area shows the NGTS custom filter. The blue line is the QE for the Marana CMOS camera and the red dashed line is the QE of the iKon-L CCD. **Bottom:** The ratio of the QE (CMOS/CCD).

(Smith et al., 2021), an exoplanet in the Neptunian desert and NGTS-30b (Battley et al., 2024), a very young long-period warm Jupiter. NGTS photometry has been shown to be scintillation limited (O'Brien et al., 2022) for bright stars T < 12 mag. The scintillation noise has been proven to be uncorrelated between the telescopes and therefore NGTS is capable of reaching the precision of TESS for stars of around T = 9 mag (Bryant et al., 2020) when combining data from multiple telescopes.

Currently NGTS is focused primarily on discovering long period transiting exoplanets based on TESS mono-transits or duo-transits (Gill et al., 2020a,c; Ulmer-Moll et al., 2022; Hawthorn et al., 2024). Additionally, NGTS observes targets from a range of science areas, including bright exoplanet host stars (Bayliss et al., 2020, 2022), targeted open cluster surveys (e.g. Gillen et al., 2020), long period eclipsing binaries (e.g. Gill et al., 2020b; Rodel et al., 2025), transiting brown dwarfs (e.g. Henderson et al., 2024) and stellar flares (e.g. Jackman et al., 2023).

4.2.2 The iKon-L 936 CCD Camera

The iKon-L 936 BR-DD is a CCD camera[3] that was developed by Andor Technologies. It features a back-side deep depleted sensor with 2048 × 2048 pixels with pixel dimension 13.5 µm each. The sensor is made by e2v and it is enhanced with fringe suppression and dual anti-reflection coatings.

The iKon-L CCD serves as the primary camera for NGTS, mounted on all NGTS telescopes. It provides high sensitivity in the red wavelengths, achieving QE > 90 % at 750 nm (see Figure 4.1), which is particularly advantageous for observing K and M dwarf stars. Equipped with a five-stage Peltier thermoelectric cooling system, the CCD maintains minimal dark current at operating temperatures as low as -100° C. Additionally, it features vacuum sealing, protecting it from environmental influences and enabling long-term operation without the need for replacement or servicing.

The camera underwent extensive laboratory testing (Wheatley et al., 2018) (see Table 4.1) before NGTS commissioning and successful deployment in 2015. NGTS operates the iKon-L CCD camera in the 3 MHz readout mode and at -70 ° C constant temperature. Typically NGTS uses 10 s exposure time for imaging followed by 1.5 s readout. However, additional delays are introduced due to autoguiding corrections and per-image statistical calculations. Furthermore, the mount requires a short settling period before the shutter can reopen. Altogether, these factors result in a total dead time between the images of approximately 3 s.

4.2.3 The Marana CMOS Camera

The Marana 4.2B-11 Camera[4] is a CMOS device featuring a thinned, back-side illuminated sensor. The sensor has 2048 × 2048 pixels, with pixel dimension 11 µm. It offers low read noise, an extended dynamic range thanks to the high dynamic range (HDR) mode, and high sensitivity across the visible spectrum, with quantum efficiency peaking at 95 % at 550 nm (see Figure 4.1). The sensor is housed within a vacuum chamber, which helps preserve sensor quality by effectively preventing condensation and dust accumulation. The five stage Peltier thermoelectric cooler enables operating temperatures down to -25 ° C air-cooled. The camera also provides fast readout speeds and high frame

[3] https://andor.oxinst.com/products/ikon-xl-and-ikon-large-ccd-series/ikon-l-936
[4] https://andor.oxinst.com/products/scmos-camera-series/marana-scmos

Table 4.1: Specifications of the Marana CMOS camera (Apergis et al., 2025) in comparison with the iKon-L 936 CCD (Wheatley et al., 2018)

Camera	**CMOS**	**CCD**
Model	Marana 4.2B-11	iKon-L 936
Digital output	HDR, 16-bit	16-bit
Readout modes	100 MHz	3MHz
Gain, e^-/ADU	1.131	1.99
Full Well Capacity, $e^- pix^{-1}$	69026	82000
Non-Linearity, %	0.122	1
Read Noise, $e^- pix^{-1}$	1.571	12.9
Dark Current, $e^- pix^{-1} s^{-1}$	1.617@-25°C	0.005@-70°C
PRNU*, %	0.131	1.79
DSNU**, e^-	0.232	3.79
Readout time, s	0.042	1.5
Detector size, mm	22.5×22.5	27.6×27.6
Pixel size, µm	11	13.5
NGTS Pixel scale, arcsec pix^{-1}	4.01	5.01
NGTS Field Of View, deg	2.27×2.27	2.84×2.84
Shutter	Shutterless	45 mm Mechanical
Weight, Kg	3.0	4.6

* Photo Response Non-Uniformity, ** Dark Signal Non-Uniformity

rates, enabling high-cadence monitoring. The performance of the Marana CMOS is summarized in Table 4.1.

For the on-sky testing at NGTS presented in this work, the CMOS camera was operated in High Dynamic Range (HDR) mode. This is the default mode for astronomical applications, offering low read noise and an extended dynamic range. The extended dynamic range and low read noise are achieved through the implementation of two pixel-level pre-amplifiers: a High Gain and a Low Gain. The signal from each pixel is processed simultaneously along both gain paths, with the High Gain channel optimised for low illumination levels and the Low Gain channel for high illumination levels. Each gain channel is digitised using a 12-bit analogue-to-digital converter (Ma & Wang, 2013; Tang et al., 2020; Lou et al., 2023). At the start of an exposure, once the High Gain channel becomes saturated, the system switches to the Low Gain channel (see further discussion in subsection 4.6.3). The final output frame is reconstructed by combining the two gain channels into a single 16-bit image, producing a HDR output (see Apergis et al., 2025, for details).

We operate the camera at a constant temperature of -25 ° C. Based on the temperature information recorded in the image headers, no significant fluctuations were observed, and the detector temperature remained stable at the set point throughout the observations. We set the exposure time to be 10 s in order to match that of the iKon-L CCD camera.

The Marana camera applies internal pre-processing corrections intended to improve image quality. These include Anti-glow correction, which mitigates glow artefacts visible in dark exposures, and the Spurious Noise Filter, which replaces noisy pixels by averaging neighbouring pixels (see Apergis et al., 2025, for details). For the analysis presented here, the Spurious Noise Filter was disabled, while the Anti-glow correction was enabled.

4.3 Methods

4.3.1 Installation of the Marana CMOS Camera at NGTS

In December 2023 we installed a Marana CMOS Camera on one of the NGTS telescopes (telescope ID 06). For this installation we removed the existing iKon-L CCD from the telescope and mounted the Marana CMOS using a custom camera faceplate to achieve the correct telescope back focus distance. As the Marana CMOS is 1.6 kg lighter than the iKon-L CCD camera, the telescope was rebalanced, which was achieved by removing some of its counterweights. Figure 4.2 shows the Marana CMOS camera mounted on the NGTS telescope.

To operate the Marana CMOS camera on NGTS, we installed an Intel NUC 11 Extreme Kit Core control computer in a small cabinet next to the pier of the telescope. This control computer was equipped with an i9 CPU, 32 GB RAM and 4 TB SSD running the `Rocky 9` Linux operating system. The Marana CMOS camera was connected to the control computer via a USB 3.0 connection. This control computer allowed us to operate the Manara CMOS camera independently and without affecting the other eleven NGTS telescopes and cameras.

The control computer operated both telescope and camera using the Robotic Observatory Control kit (`Rockit`)[5], a software package designed for managing ground-based robotic observatories. `Rockit` is also used at the University of Warwick's facilities at the Roque de los Muchachos Observatory (e.g. Airey et al., 2025b; Mitchell et al., 2025). It follows a modular architecture in which background daemons run continuously to handle specific tasks such as telescope control, focusing, instrument management, and overall observatory coordination. These daemons seamlessly interact with each other through a remote procedure call interface, enabling the execution of functions and procedures on remote programs. To facilitate this communication, `Rockit` uses the python library `Pyro4`.

Similarly to NGTS, to maintain the stability of the stars in the images and minimise systematic errors and noise from tracking inaccuracies, we use the `DONUTS` algorithm (McCormac et al., 2013). This innovative python package functions as an autoguiding algorithm, maintaining pixel drift at an accurate sub-pixel level relative to the first image, which serves as the reference frame. This approach meets our high precision photometry requirements and ensures consistent software performance between the CMOS and CCD cameras.

4.3.2 Observations

Observations were conducted from December 2023 to September 2024, during which time the CMOS camera was mounted on one of the NGTS telescopes. We also utilised one of the eleven available CCD cameras on a neighbouring telescope (telescope ID 01) for simultaneous observations. To maintain consistency and ensure photometric stability, the same CCD camera was used for comparison with the CMOS camera throughout the entire campaign. We made observations of well-known transiting exoplanets around bright stars, including WASP (Pollacco et al., 2006) and KELT (Pepper et al., 2018) host stars, as well as confirmed TOI systems. The targets are shown in Table 4.2. For the remainder of the time, the CMOS camera and telescope observed the same fields as the CCD on telescope ID 01, which were primarily TESS monotransit and duotransit candidates monitored as

[5] `https://github.com/rockit-astro`

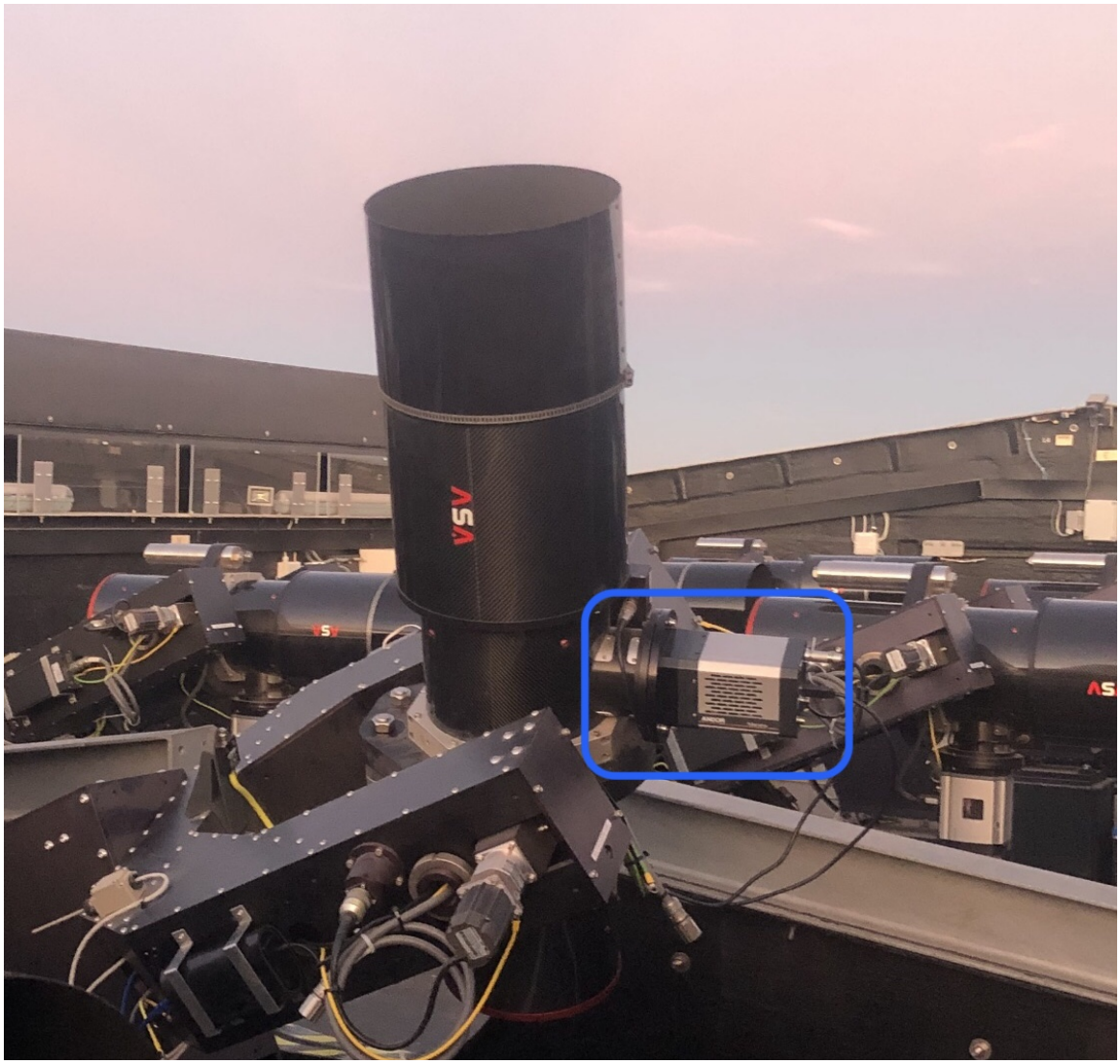


Figure 4.2: The Marana sCMOS camera, highlighted within the blue rectangle, is mounted on one of the NGTS telescopes while capturing flat-field images during evening twilight at Cerro Paranal, Chile.

Table 4.2: Simultaneous transit observations of bright stars with CMOS and CCD cameras.

Target	TIC ID	TESS Magnitude *	Teff (K) *	Observation Date	Observation Duration (hours)	Transit fraction
TOI-905 (Davis et al., 2020)	TIC 261867566	10.57	5380 ± 130	2024-Jul-13	5.7	Full
WASP-95 (Hellier et al., 2014)	TIC 144065872	9.49	5760 ± 130	2024 Jul 14 & Aug 8	7.4 & 8.8	Full
TOI-2109 (Wong et al., 2021)	TIC 392476080	9.78	6650 ± 130	2024 Jul 17	5.5	Full
KELT-10 (Kuhn et al., 2016)	TIC 269217040	10.27	5890 ± 130	2024 Aug 01 & 26	8.3 & 6.5	Ingress
WASP-4 (Wilson et al., 2008)	TIC 402026209	11.82	5500 ± 140	2024 Aug 02	7.4	Full
WASP-97 (Hellier et al., 2014)	TIC 230982885	9.96	5700 ± 130	2024 Aug 04 & 6	5.6 & 5.7	Egress & Full
TOI-4463 (Yee et al., 2023)	TIC 8599009	10.46	5540 ± 140	2024 Aug 27	4.2	Full
WASP-30 (Anderson et al., 2011)	TIC 9725627	10.97	6360 ± 130	2024 Aug 28	7.9	Full

* source: TIC v8.2 (Stassun et al., 2018)

part of the NGTS program to discover long period exoplanet systems from TESS (Hawthorn et al., 2024; Gill et al., 2024).

The nightly schedule for the CCD on Telescope ID 01 was replicated and scheduled in the `Rockit` software to ensure the CMOS camera on Telescope ID 06 observed the exact same field centre as the CCD camera. This setup guaranteed that both cameras monitored the same area of sky simultaneously, although we note the CMOS camera has a smaller field-of-view (see Table 4.1). This strategy maintained consistency in observation duration and coverage between the CMOS and the CCD image sensors which we use for comparisons in this work. The CCD camera operated with an exposure time of 10 seconds and a cadence of 13 seconds. For consistency, the CMOS camera was configured with a 10 second exposure time and a total cadence of 10.042 seconds. NGTS uses a custom filter that covers a wavelength range of 520-890 nm (see Section 4.2 and Figure 4.1). We used this same filter for the observations made using the CMOS camera, although we note the filter is not optimized for the bluer CMOS sensor's quantum efficiency (see Figure 4.1). The images from the Marana CMOS camera were saved as FITS files onto the CMOS control computer. Instrument parameters were saved into the FITS file headers, including the JD timestamps, telescope coordinates, and camera settings.

In this paper we analyse data from nights where known transiting exoplanet systems were observed. We observed eight transiting exoplanets in total, with three of them observed twice. We also analyse two nights of observations taken on a dark night with no moon (2024 July 5) and a bright night with full moon (2024 June 22), both centred on the star TIC-188620407 (R.A.= $23^{h}20^{m}12\overset{s}{.}37$, Dec= $-13°5'56\overset{''}{.}83$, T = 11.57 mag).

4.3.3 Image reduction and Photometry pipeline

For each observation, we execute a custom pipeline daily to extract photometry for each observed field. We solve each image astrometrically using the World Coordinate System (WCS), accounting for the field centre and pixel scale, with the help of *astrometry.net* (Lang et al., 2010). This software solves each image using a simple polynomial model. However, we identify weaknesses in the solution near the image corners, caused by distortions from the telescope's optics. To address this, we incorporate the TESS Input Catalog version 8 (Stassun et al., 2018, TIC8) to identify sources in the field, particularly those brighter than T < 16 mag. Using the initial WCS solution, we iteratively refine the polynomial fit until we achieve sub-pixel accuracy (see Chote et al., 2025, for details) . We

exclude from the dataset any images for which the WCS solution fails; these are typically outliers.

For the selections of stars for photometry, we used TIC8 (Stassun et al., 2018) with an upper cut of T $<$ 14 mag. We apply criteria for blended stars, excluding stars that have a source identified within a 6 pixel radius (24 arcseconds) around the star and a maximum magnitude difference of 2.5 magnitudes for a star to be considered as blended. Additionally, we exclude stars near the edges of the sensor. The same extracted catalog for the CMOS image sensor is used for the CCD image sensor, since the FOV is larger due to the larger pixel scale, ensuring that both fields will contain the same stars.

We acquired dark and bias images when we were on-site, using the telescope cover to prevent external light from reaching the sensor. The properties and the long-term stability of the CMOS camera's bias and dark frames are discussed extensively by Apergis et al. (2025). We record evening and morning flat-field images before and after the science observations. We averaged the dark and bias frames to remove the electronic and thermal signal from each camera, and we create an averaged and normalized flat-field image for flat correction.

For the CCD camera, a flat-field correction was not applied, primarily because the autoguiding system keeps stellar positions stable to within sub-pixel deviations (<0.1 pixel RMS in X and Y positions over a typical observing night), ensuring that the same pixels are used consistently throughout the night (McCormac et al., 2013). The CMOS camera also exhibits sub-pixel positional stability. We performed photometry both with and without applying flat-field corrections for the CMOS data and found no noticeable difference. For a typical sample of stars, we find that omitting flat-field correction results gives an RMS scatter improvement of approximately 0.29 %. Therefore, we adopted the same approach as for the CCD camera and did not apply a flat-field correction.

As part of the pipeline, we also verify that the autoguiding system is performing well by measuring the offsets between images using the `DONUTS` software (McCormac et al., 2013) to ensure that stars remain on the same pixels. We set an upper limit for the x-y positional shifts in the images; any frames exceeding this threshold—such as those affected by satellite trails or guiding lasers from the Very Large Telescope—are excluded from the data. In most cases, the autoguiding performed well within the specified pixel shift threshold.

To perform aperture photometry we extract the position for each star from the catalog. We use the `SEP` python package (Bertin & Arnouts, 1996; Barbary, 2016) with circular apertures of specific radii defined for each camera as set out in Section 4.4. We define a sky background map from the `SEP` option to measure the sky background signal. An example of the target pixel frames for each camera is shown in Figure 4.3.

We perform relative photometry to correct the light curves for atmospheric extinction, color-dependent extinction, and any other systematics common to stars within the image. For each star, we collect its *Gaia* DR3 $G_{BP} - G_{RP}$, TESS magnitude, and TIC ID. We define magnitude and color ranges for selecting comparison stars, with a bright magnitude limit of $T = 9.4$ mag, which usually indicates saturation in a 10 s image.

We establish criteria for the comparison stars by finding the best RMS value for each star within a particular magnitude range. Noisy stars are then excluded (see Section 4.5.3). The remaining comparison stars are combined to produce a master reference star that corrects for the systematics affecting the target star.

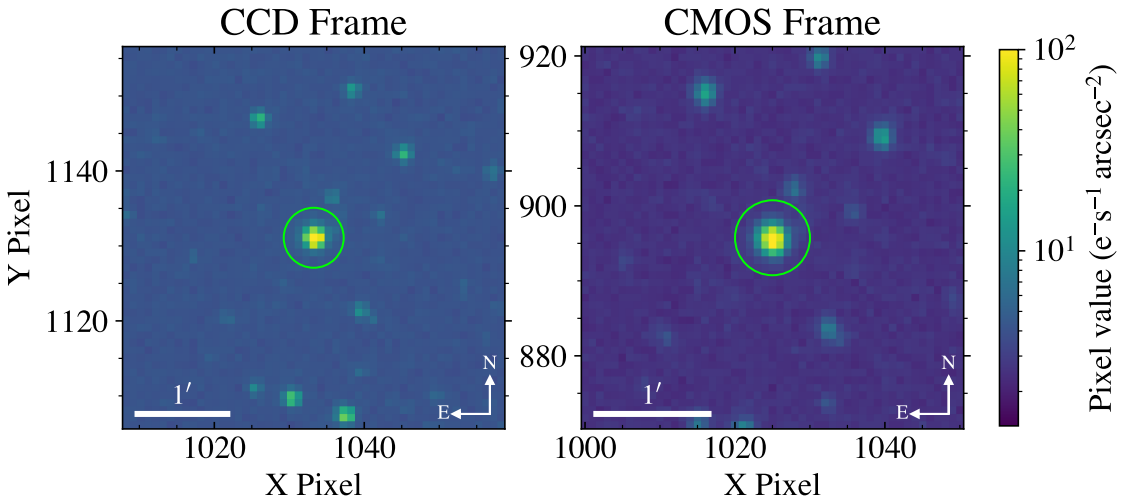


Figure 4.3: Target pixel frame (50 × 50 pixels) for CCD on the left and CMOS on the right. The selected photometric apertures for each camera are shown with green circles for target star KELT-10 (TIC-269217040, T = 10.27 mag) observed on 2024 August 1.

4.4 Photometric Noise

There are several sources of photometric noise that are well known and can be calculated for both the CMOS and CCD cameras. We construct the photometric noise model using the read noise and dark current of each camera (see Table 4.1), the sky background brightness and the target shot noise, and the expected scintillation noise at Paranal Observatory (O'Brien et al., 2022). In order to be able to compare the CMOS and CCD cameras, we express the photometric noise in terms of electrons using the conversion factor (gain) from analog digital units to electrons (see Table 4.1). Since the pixel size is different between the CMOS (11 µm) and the CCD (13.5 µm) image sensors, we calculate the photometric noise for a photometric aperture of a fixed physical radius of almost exactly 55 µm, which equates to a radius of 5 pixels for the CMOS image sensor and 4 pixels for the CCD image sensor. The typical full-width half-maximum (FWHM) of the NGTS point-spread-function is 19 µm, therefore a photometric aperture of 55 µm was found to be optimal for our stars with magnitudes in the range $9 < T < 11$ (Howell, 2000).

4.4.1 Detector Noise

The two major sources of detector noise for digital imaging are read noise and dark current. Read noise is introduced during the process of the charge to voltage conversion and the conversion from analog to digital values. Read noise includes all the noise sources which are independent of the exposure and the incoming signal (Howell, 2000). Traditionally, CMOS image sensors have exhibited higher read noise compared to CCDs, primarily due to the complex circuitry, the large number of amplifiers and their lower quality in earlier designs. However, advancements in CMOS image sensors such as the Marana camera have enabled the achievement of low read noise levels. The median read noise of the Marana camera was found to be 1.57 e^- (Apergis et al., 2025). Furthermore, while CCD image sensors struggle to maintain low read noise at high readout speeds, CMOS active pixel sensors are superior in this regard due to their unique amplifier-per-pixel design. For more details

related to the read noise of the Marana CMOS camera see Apergis et al. (2025).

Dark current is thermal noise produced by the generation of heat within the sensor and it is dependent on the selected exposure time and temperature of the detector (e.g. Shockley & Read, 1952; Aberle et al., 1992). Unlike the passive pixel design of CCDs, CMOS image sensors employ active pixels to amplify the signal on a per-pixel basis (Stefanov, 2022). However, this additional circuitry can emit infrared photons from either the sensor periphery or the pixel amplifier transistor (Janesick et al., 2007; Wang et al., 2015). This glow effect is distinguishable from the dark current at low temperatures, since it exhibits a weaker temperature dependence than the dark current (see Figure 14 in Apergis et al., 2025, for details). Consequently, as the detector temperature decreases, the relative contribution of the glow component becomes more significant. The dark current for the Marana camera was measured to be 1.617 e^- pix^{-1} s^{-1}at constant temperature of -25 ° C. For further details on dark current and glow in the Marana CMOS camera, refer to Apergis et al. (2025).

4.4.2 Sky Background noise

Sky background is a major source of photometric noise in astronomy, especially when monitoring faint objects. Sky background signal consists of all the light entering the photometric aperture other than light from the target object. This may be from scattered light, background astrophysical sources, zodiacal light, and atmospheric effects such as moonlight or air-glow from night-sky emission lines (Maihara et al., 1993; Wüst et al., 2022). The mean sky background signal is subtracted from the photometric aperture during the photometric extraction (see Section 4.3.3). However, the sky background noise will contribute to the Poisson photon noise. The CMOS and CCD cameras show differing amounts of sky background noise largely due to the differences in the quantum efficiency of the cameras over the wavelength range of the NGTS filter (see Figure 4.1).

4.4.3 Source Noise

For ground-based photometric observations, the noise contribution due to light from the target star has two components - Poisson shot noise and scintillation noise. Poisson shot noise from the target star is simply given by the square root of the measured brightness of the star in electrons.

Scintillation noise arises from the fact that incident light from the target star will fluctuate in intensity as it moves through turbulent regions in the Earth's atmosphere (Osborn et al., 2015). This effect causes the star to "twinkle". Scintillation is particularly noticeable for small aperture telescopes observing bright stars (O'Brien et al., 2022), where it becomes a dominant source of noise. We calculate the expected scintillation noise for NGTS using a modified version of Young's formula (Young, 1967; Osborn et al., 2015):

$$\sigma_{\rm sc}^2 = 10^{-5} C_{\rm Y}^2 D^{-4/3} t_{\rm exp}^{-1} \sec^3(z) \exp(-2h_{\rm obs}/H), \tag{4.1}$$

where D is the diameter of the telescope (0.2 m for NGTS), t_{exp} is the exposure time (10 s for our observing), sec(z) denotes the airmass, h_{obs} is elevation above sea level (2433 m for NGTS), and H is the atmospheric scale height (we adopt 8000 m from Osborn et al., 2015). C_Y is an empirical coefficient that quantifies the amplitude of scintillation on a given night. We adopt the median value for Paranal Observatory of $C_Y = 1.54\,m^{2/3}s^{1/2}$ as reported by O'Brien et al. (2022).

Unlike the Poisson shot noise from the star, the fractional scintillation noise is *independent* of the flux from the target star (O'Brien et al., 2022). Thus for bright stars, scintillation noise will form a hard limit to the fractional photometric noise.

4.4.4 Total Noise

The total photometric noise is the quadrature sum of the individual noise sources for a given photometric aperture, as the noise will be statistically independent (Howell, 1989):

$$\sigma_{\text{total}} = \sqrt{\sigma_{\text{flux}}{}^2 + \sigma_{\text{sky}}{}^2 + \sigma_{\text{DC}}{}^2 + \sigma_{\text{RN}}{}^2 + f^2\sigma_{\text{sc}}{}^2}, \tag{4.2}$$

where σ_{flux} is the photon shot noise, σ_{sky} is the background signal noise, σ_{DC} is the dark current noise, σ_{RN} is the read noise, f is the flux from the target star and σ_{sc} is the scintillation noise. In order to calculate the photometric noise expected for a star of a given magnitude, we must convert from flux in electrons (f) to magnitude (m) using the following equation:

$$\text{m} = \text{z}_\text{p} + 2.5\log(\text{G}) - 2.5\log(\frac{f}{\text{t}_\text{exp}}) \tag{4.3}$$

where z_p is the photometric zeropoint, G is the conversion factor from electrons to digital units G ($\text{e}^-\text{ADU}^{-1}$) as listed in Table 4.1, and t_exp the exposure time of the image. The zeropoint for the NGTS filter is determined by measuring the source flux of each star (in electrons) and comparing it to the known TESS magnitude of the star. Using the noise calculations and the conversion from flux to magnitude, we plot both the individual noise components and the total noise model in Figure 4.4.

4.4.5 Systematic Noise

All of the noise sources set out in Section 4.4 produce uncorrelated (white) noise. However it is well known that usually there is some level of systematic noise in the photometry that will give rise to correlated (red) noise (Pont et al., 2006).

To quantify this, we test both cameras for correlated noise as a function of time. We bin the data at different timescales to examine the noise characteristics. McCormac et al. (2017) demonstrated that NGTS photometry using the iKon-M CCDs showed very little red noise, as the majority of its contribution was mitigated by correcting for atmospheric extinction based on the airmass as well as the colour-dependent atmospheric extinction using `SysRem` python software (Tamuz et al., 2005).

We calculate the RMS of the lightcurves from unbinned cadence all the way up to 1800 s binning cadence, and compare the values to the square-root N value expected for purely white noise (see Section 4.5.2).

4.5 Results

4.5.1 Noise model comparison

To assess the on-sky performance of the cameras, we compared measured noise characteristics to the theoretical noise model, which includes read noise, dark current, sky background noise, target shot noise, and scintillation noise (see Section 4.4.4).

Read noise and dark current are calculated using each camera's performance specifications (see Section 4.1). To model the sky background signal, we calculated the median value of all pixels for all bias and dark subtracted images taken on a particular observing night. This provides a good estimate of the sky background for nights when the sky background is not significantly varying. For scintillation noise, we used the average airmass of the total observation and included locational parameters specific to the NGTS observatory (see Section 4.4.3). Finally, we created a synthetic flux array to calculate the shot noise, normalizing all noise parameters with respect to that flux. We measured the zeropoint from the fluxes extracted from photometry and their corresponding TESS magnitudes. The zeropoint was used as in Equation 4.3 in order to convert to synthetic magnitudes. The total noise is the summation in quadrature of all the noise components as shown in Equation 4.2.

For our noise model comparison, we acquired a set of data of the same field (R.A.= $23^{h}20^{m}12\overset{s}{.}37$, Dec= -13°5′56.″83) for a total of 5.5 hours on the night of 2024 June 22 (full moon) and on the night of 2024 July 5 (no moon). Moon conditions were selected in order to assess the performance of each camera with maximum and minimum sky background contribution. We employed relative photometry for stars as described in Section 4.3.3 on a TESS magnitude range of $8 < T < 14$, with the same size physical photometric aperture for each camera (see the introduction of section 4.4). This photometric aperture radius was found to be $\approx 2.9 \times$ FWHM ($1 \times$ FWHM = 19.3 µm), which equates to a radius of 4 pixels for the CCD and 5 pixels for the CMOS (Howell, 2000).

For each star we calculated the fractional RMS from the relative normalized lightcurves. The results for the datasets are shown in the upper panels (no moon) and lower panels (full moon) of Figure 4.4. We colour code the RMS of each star with the *Gaia* DR3 $G_{BP} - G_{RP}$ colour to check RMS for a colour dependence.

The RMS distribution of the stars is in good agreement with the calculated total noise model for both cameras and both datasets. In all cases we see that that reddest stars have a slightly higher RMS than bluer stars. This is likely to be due to the fact that we are plotting the TESS magnitudes for these stars (600-1000 nm), but our photometry is in the NGTS band (520-890 nm). The difference between these bandpasses means that redder stars appear brighter in the TESS filter compared with the NGTS filter, which does not include wavelengths beyond 890 nm. Consequently, in Figure 4.4, the reddest stars would appear brighter using their TESS magnitudes, and fainter for our NGTS photometry. Thus, these redder stars have slightly higher RMS. Our relative photometry and detrending methods are also optimised for the average color star in the field, which will be much bluer than these very red stars. This could also result in systematics in the lightcurves of the redder stars which would produce higher RMS.

To directly compare the RMS for given stars as simultaneously observed in each camera, we plot the ratio of CCD RMS to CMOS RMS for each star, as shown in Figure 4.5. When this RMS ratio exceeds unity, the RMS of the star is lower in the CMOS camera than in the CCD camera - i.e. the CMOS camera shows better precision in the lightcurve. Again we colour-code each star using its *Gaia* DR3 $G_{BP} - G_{RP}$.

4.5.2 Timescale of noise

In order to investigate the presence of red noise in our data from each camera, we calculate the RMS for each lightcurve over a range of binning timescales for the observations taken with no moon (2024

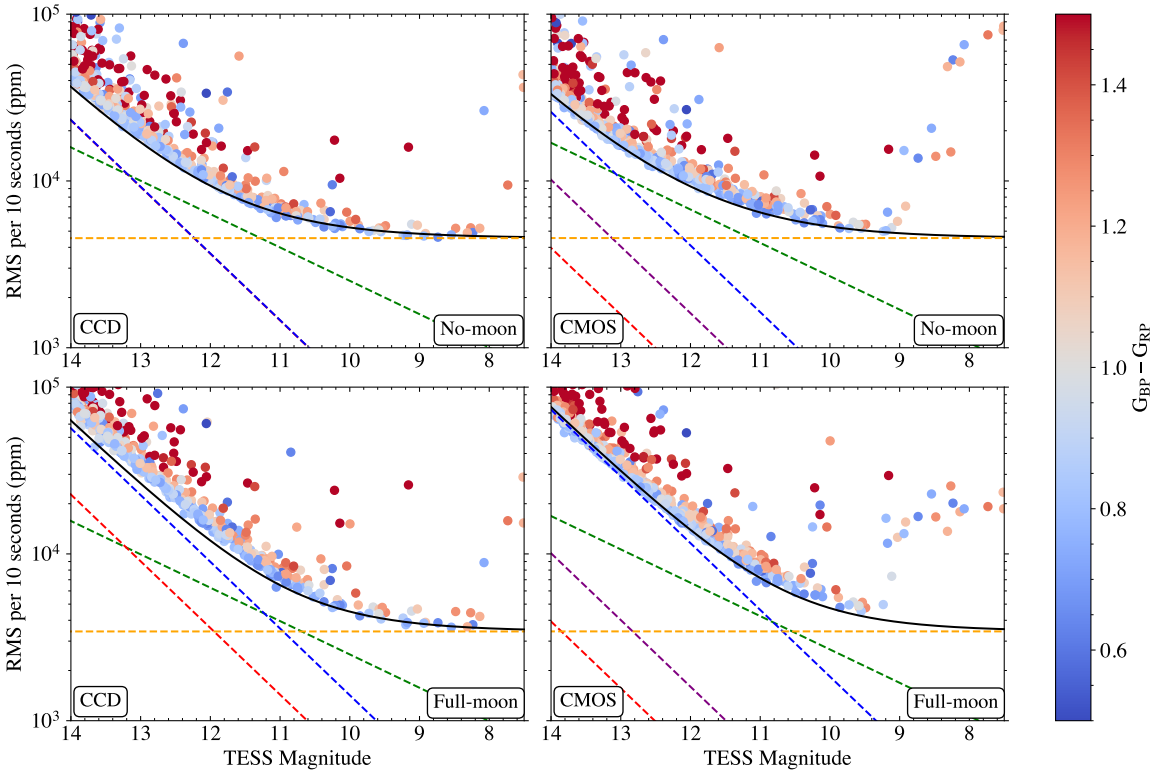


Figure 4.4: Photometric precision as a function of stellar magnitude for 10 seconds exposure predicted by the theoretical model and from observations during the new moon on 5th July 2024 (upper panels) and full moon on 22nd June 2024 (lower panels). The left panels represent data from the CCD, while the right panels correspond to the CMOS. The dark line indicates the total modelled noise, including contributions from scintillation (yellow), photon shot noise (green), dark current noise (purple), sky background noise (blue), and read noise (red). The data points are coloured according to the *Gaia* DR3 $G_{BP} - G_{RP}$ colour and represent the measured noise in the detrended light curves from relative photometry of 746 stars with $8 < T < 14$ in a field centered on TIC-188620407.

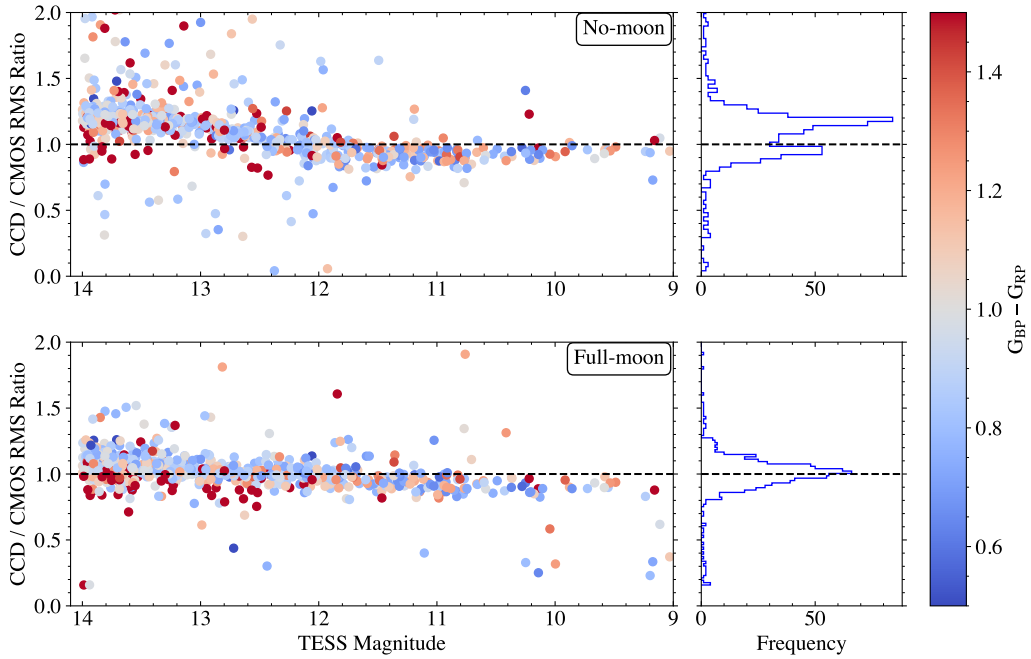


Figure 4.5: Ratio for CCD and CMOS camera noise contribution for different magnitude stars from Figure 4.4. The data points are coloured according to the catalogued *Gaia* DR3 $G_{BP} - G_{RP}$ colour. The black dashed line represents the ratio 1 which is the case where the noise is the same for both cameras. **Top:** The noise ratio for a dark night (no-moon). **Bottom:** The noise ratio for a bright night (full-moon). The panels on the right show the histogram distributions.

July 5). We trim the beginning and end of each night's data to include only observations taken at airmass < 1.7. This helps minimize excess noise associated with high airmass (Bryant et al., 2020), while retaining enough data for effective binning. The total usable data amounted to approximately 4.8 hours. Stars were grouped in 1 TESS magnitude intervals, and their RMS was averaged and plotted for each camera, as illustrated in Figure 4.6. The maximum binning duration applied was 30 minutes. For each magnitude range, 45 stars were randomly selected, and the same set of stars was used for both cameras to ensure consistency. Each bin accounts for both the exposure, read and dead times. The exposure time was 10 s for both cameras, while the readout times differed. For the CMOS camera the readout time is 42 ms and we consider this negligible in our calculations. The CCD has a total of 3 s read and dead time (see Section 4.2.2).

For the first two magnitude ranges, $10 < T < 11$ and $11 < T < 12$, the RMS values for both cameras are comparable, with the CCD camera exhibiting slightly lower noise, as also illustrated in Figure 4.5. In both cases, the RMS decreases similarly with binning time, following the expected trend from the white noise. In the fainter magnitude bins, $12 < T < 13$ and $13 < T < 14$, the initial RMS for the CMOS camera is lower than that of the CCD camera, consistent with the relative performance indicated by the RMS ratio in Figure 4.5.

Some individual detrended lightcurves show excess RMS or residual correlated structure after detrending. This may be caused by intrinsic stellar variability, imperfect removal of systematics, or a sub-optimal choice of comparison stars. Since the RMS shown in each magnitude bin is computed from a finite number of stars, even one object with significant residual red noise can raise the bin-averaged RMS and produce a small departure from the ideal white-noise scaling. This is evident mostly on the CMOS camera within the range of $10 < T < 13$.

4.5.3 Transit lightcurves

A total of 11 successful nights of simultaneous observations of 8 well-known exoplanets transiting bright stars were conducted using the CMOS and CCD cameras, as summarised in Table 5.2. Relative photometry, as outlined in Section 4.3.3, was employed to detrend the light curves from systematic effects. For each target star, an exclusion criterion was applied to remove comparison stars exhibiting high noise levels or significant systematics[6].

We applied additional detrending to all 11 of our target lightcurves using `allesfitter`, a `Python` package (Günther & Daylan, 2019, 2021). To sample the parameters, we employ detrending using Gaussian Process on a covariance function, the Matern 3/2 kernel. The parameters are the characteristic amplitude $\ln(\sigma)$ and length $\ln(\rho)$ of scale.

To model the transits, `allesfitter` package integrates several specialised libraries such as `ellc` (Maxted, 2016) for lightcurve modelling, `dynesty` (Speagle, 2020) for nested sampling (Skilling, 2004; Skilling, 2006) and `celerite` for Gaussian processes (Foreman-Mackey et al., 2017).

The 8 transiting exoplanet systems that we observed have already been extensively observed and characterised with high-precision data from both ground- and space-based instruments. Therefore we chose to fit a photometric model using nested sampling of the initial parameters with their uncertainties adopted from the most up-to-date existing literature as listed on the NASA exoplanet archive for each system (Akeson et al., 2013). We used normal priors for orbital period P, the radius

[6] `https://github.com/EMBryant/bsproc`

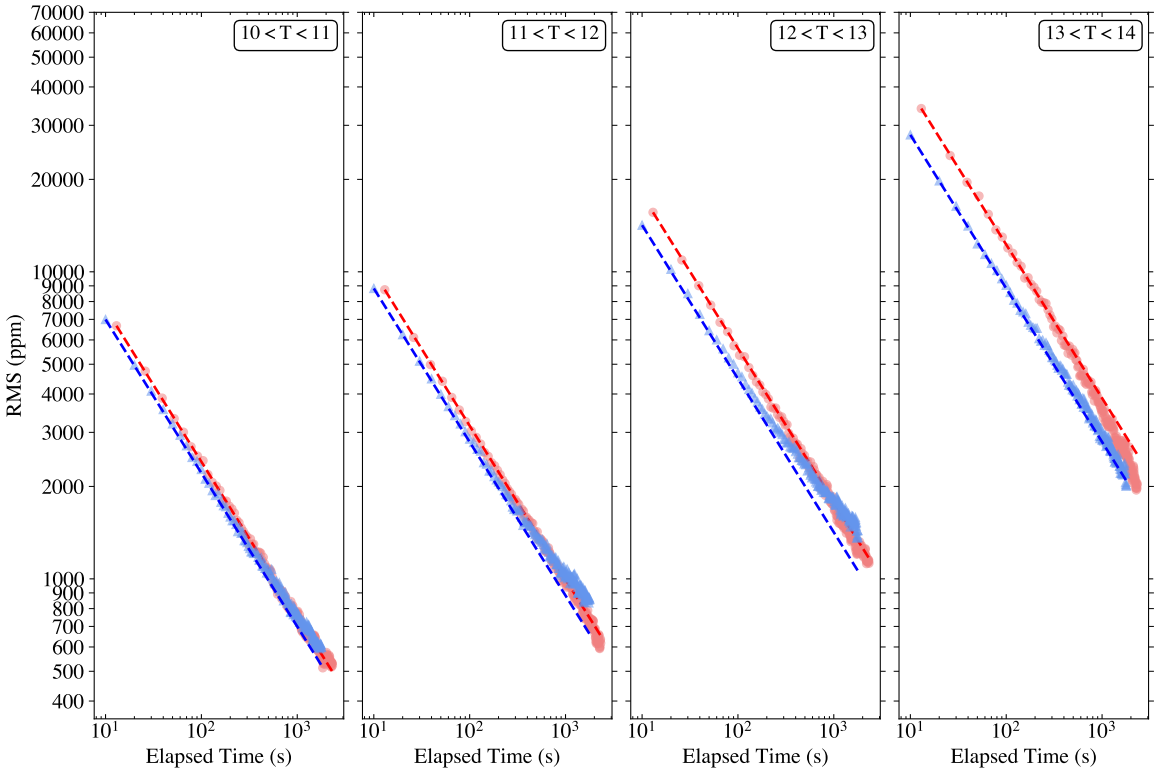


Figure 4.6: Noise levels for CCD (light red circles) and CMOS (light blue triangles) at varying timescales during observations conducted on the no-moon night of 2024 July 5. The data is binned as a function of exposure and readout times. The blue and red dashed lines indicate the white noise model, proportional to $1/\sqrt{n}$ for the CMOS and CCD respectively. The RMS noise was measured from stars that are non-variable and non-saturated. For the CMOS camera, 45 stars were randomly selected and averaged in each magnitude regime, and the same stars were used for the CCD camera.

Table 4.3: `allesfitter` model priors and fitted values. Planetary System properties for the transiting system WASP-4 (TIC 402026209), as shown in Figure 4.7.

Parameter	Initial Guess	Prior	Fitted value CMOS	Fitted value CCD
$R_p/R_\star$	0.15201	$\mathcal{N}(0.15201, 0.00040)$	0.15211 ± 0.00039	0.15215 ± 0.00039
$(R_\star + R_b)/a_b$	0.211339	$\mathcal{N}(0.211339, 0.002017)$	0.2122 ± 0.0016	0.2105 ± 0.0017
$\cos i_b$	0.016405	$\mathcal{N}(0.016405, 0.014657)$	$0.013^{+0.012}_{-0.013}$	$0.016^{+0.013}_{-0.014}$
T_c (BJD)	2455804.515752	$\mathcal{N}(2455804.515752, 0.000019)$	$2460525.796300 \pm 0.000080$	$2460525.796306 \pm 0.000079$
Orbital Period (days)	1.338231466	$\mathcal{N}(1.338231466, 0.000000023)$	$1.338231464 \pm 0.000000023$	$1.338231467 \pm 0.000000023$
q_1	0.385	$\mathcal{N}(0.385, 0.012)$	0.386 ± 0.012	0.387 ± 0.012
q_2	0.400	$\mathcal{N}(0.400, 0.087)$	$0.363^{+0.069}_{-0.075}$	0.419 ± 0.074

ratio (R_B/R_A), semi-major axis ($(R_A + R_B)/a$), the epoch ($T_{0,B}$), orbital inclination ($\cos i_B$) and the quadratic limb darkening coefficients calculated based on the effective temperature, metallicity and the logarithm surface gravity ($\log(g)$ of the host star (Sing, 2010)). The 8 selected exoplanet system were all hot Jupiters with circular orbits reported in the literature. Therefore we set the eccentricity and argument of periastron of the system (implemented as the terms $\sqrt{e}\cos\omega$ and $\sqrt{e}\sin\omega$) as zero. All prior parameters were set to be the same for both the CCD and the CMOS cameras' extracted lightcurves. We did not include a dilution factor, as all the target stars are well isolated from nearby bright objects.

The results for the CCD and CMOS cameras' extracted lightcurves are plotted in Figure 4.7 for WASP-4 with the fitted parameters in Table 4.3 and in Appendix A as Figure 4.12 to Figure 4.21 and Figure 4.4 to Figure 4.13 for all other targets. The upper panels in Figure 4.7 display the normalised lightcurves as extracted from the relative photometry and the detrending fit, the middle panels show the transit fit and the lower panels the residuals from the model. For plotting purposes we bin the detrended and model fitted lightcurves to 5 minutes bins (for both cameras) as shown in Figure 4.7 and also in section 4.8.

4.6 Discussion

4.6.1 Fractional Noise

The RMS precision for lightcurves generated from the CMOS images agree well with our noise model for instrumentation, sky background, and atmospheric scintillation noise (see right-hand panels in Figure 4.4). The CCD data are also in good agreement with the noise model (see left-hand panels in Figure 4.4).

We note that for the CMOS camera, the purely instrumental noise factors (dark current and read noise) are never a significant noise source, even for faint stars on nights with no moon. For the CCD camera, however, the read noise is at the same level as the sky background during no-moon conditions for stars fainter than T>13 mag. This difference is primarily due to the fact that the CCD camera has much higher read noise than the CMOS camera (see Table 4.1). This difference in read noise arises because CMOS pixels are read out in parallel, allowing the amplifiers to process signals at significantly lower frequencies. In contrast, CCD cameras have fewer amplifiers, requiring them to operate at higher frequencies, which leads to larger read noise (Teranishi & Mutoh, 1986; Hynecek, 1997; Apergis et al., 2025).

Although the dark current and amplifier glow contributions for the CMOS image sensors are much

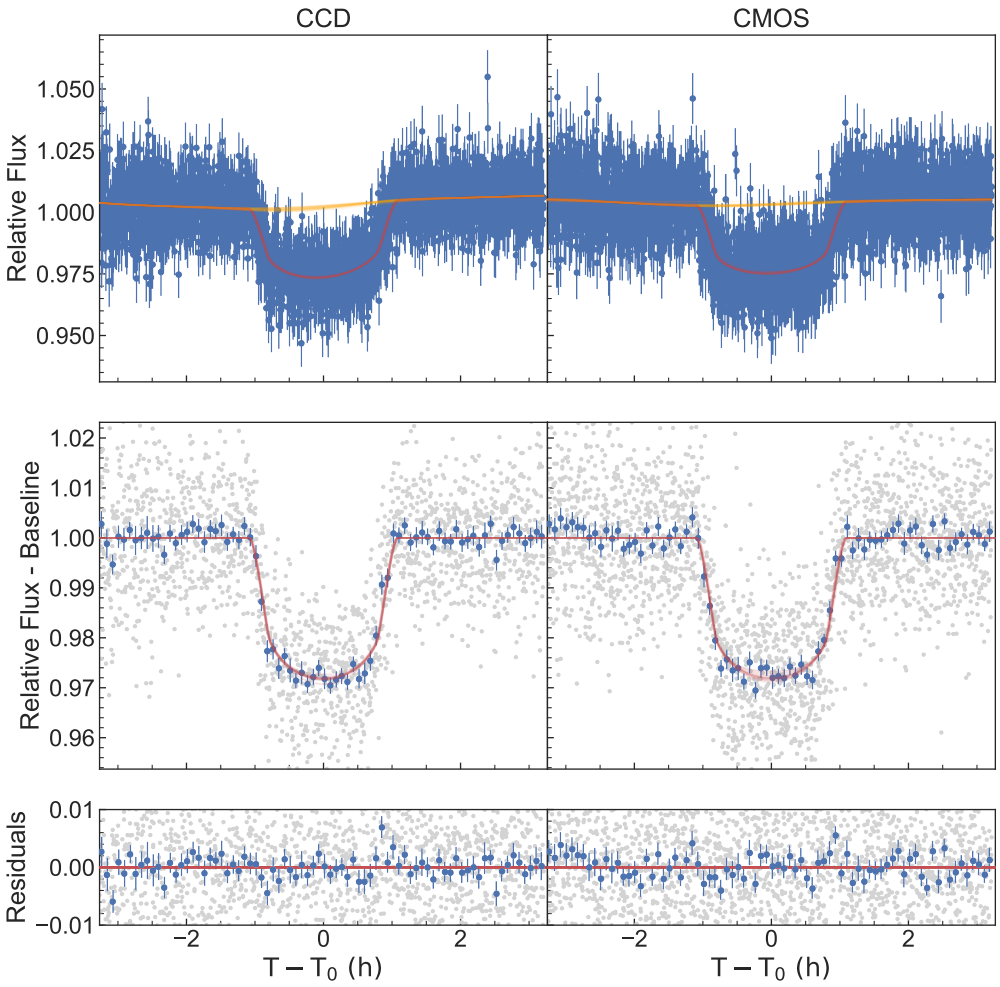


Figure 4.7: Normalized lightcurves for the transiting system of WASP-4 (TIC 402026209) from NGTS on 2024 August 2 for CCD (**left**) and CMOS **right**) cameras.**Top**: Undetrended light curves with the GP detrending function shown as yellow solid line and transit model shown with red solid line. **Middle**: Detrended lightcurve with data binned to 5 minutes (solid blue circles) for clarity. Again the best fit model is shown in red. **Bottom**: Residuals from the best fit.

higher than the CCD image sensors (Karpov et al., 2021; Qiu et al., 2021; Apergis et al., 2025), the dark current is not a significant noise source even for the CMOS camera for this photometry. For the CMOS camera, observations of bright stars under no-moon conditions, we are either limited by atmospheric scintillation or photon shot noise from the target star. For fainter stars, photometric precision is limited by sky background noise, primarily due to the large pixel scale (4 arcsec pix^{-1}) and the point-spread function (FWHM=1.7 pix). This limitation can be mitigated by reducing the photometric aperture size, which helps exclude excess background signal and improves signal-to-noise for fainter stars. We note that if there was a much finer pixel scale and narrower point-spread-function, then the sky contribution would be much less and therefore the dark current would start to become the dominant noise contribution for objects fainter than approximately T= 15 mag. During full-moon conditions, the increased sky background means that all stars with T> 10.5 mag will be limited by sky noise. This is also the case for the CCD camera.

We observed a distinct increase in the RMS for the very brightest stars (T< 9.5 mag) for the CMOS camera, which was less pronounced for the CCD camera (see Figure 4.4). This effect is due to the saturation of the pixel's capacity of the CMOS camera and it is avoided by reducing the exposure time. The CMOS architecture is equipped with transistors within each pixel that amplify and convert charge to voltage. This process involves transferring charge from the photodiode by applying a specific voltage to the gate, which serves as an anti-blooming mechanism, preventing the escape of charge to adjacent pixels (Stefanov, 2022; Apergis et al., 2025). The overall result of this is that charge is not conserved for saturated pixels, hence any relative photometry of a star with a saturated pixel will have a higher RMS proportional to the degree of saturation. A saturated star will not exhibit the same flux–airmass correlation as unsaturated stars, because its recorded counts are clipped by the pixel full well capacity rather than tracking the true incident flux. As a result, standard airmass-based detrending becomes ineffective for such targets, and applying it can introduce additional scatter into the light curve. This is evidenced by the increasing RMS with TESS magnitude for stars with T> 9 mag in Figure 4.4. Although the CCD camera also saturates, the CCD photometry is more precise for these very bright stars. This is due to the sensor architecture of CCD cameras, whereby if a pixel exceeds its full well depth, the excess charge spreads to neighbouring pixels (Janesick et al., 1987). This results in bleeding or smearing artifacts, typically along the direction of charge transfer of the readout (Janesick et al., 1987). For very bright stars, these effects were evident in the CCD frames. In some cases, saturated pixels leaking charge into nearby pixels within the aperture can still be used for photometry, as demonstrated by Pope et al. (2016). Both cameras demonstrate performance that aligns well with the noise model under both no-moon and full-moon sky conditions, achieving scintillation-limited performance for the brightest stars.

Upon analysing the noise ratio comparison shown in Figure 4.5, we find that the CCD camera exhibits lower noise for bright stars (10 < T < 12). In this regime, the photon shot noise from the target stars dominates, and the CCD receives more signal than the CMOS for the same 10-second exposure. This behaviour arises because the NGTS filter is optimised for the CCD's quantum efficiency response. In contrast, the CMOS sensor, which is more sensitive to bluer wavelengths, operates with reduced efficiency since the NGTS filter cuts off much of its most sensitive spectral region (see Figure 4.1). To demonstrate this, we plot the ratio of the average fluxes of catalog stars as a function of stellar effective temperature, as shown in Figure 4.8. In this example, we consider

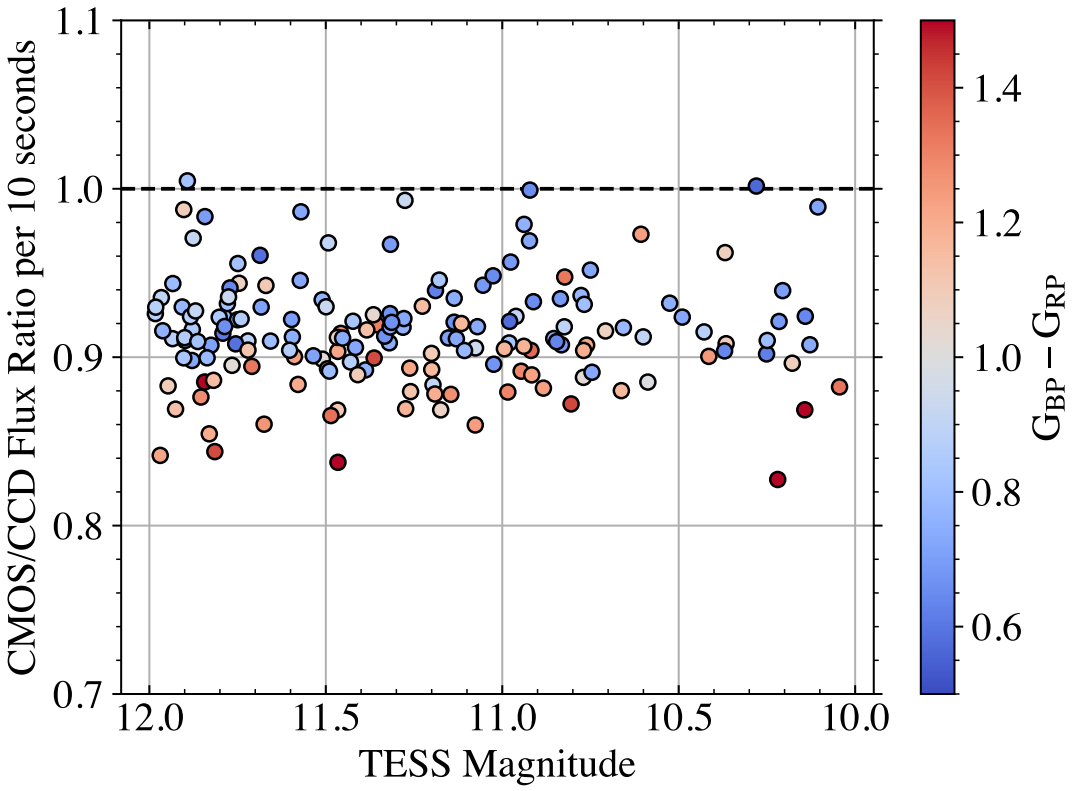


Figure 4.8: The CMOS/CCD flux ratio for a set of stars from the night of 2024 July 5. Flux ratios are represented by circles, colour-coded according to the catalogued *Gaia* DR3 $G_{BP} - G_{RP}$ colour. The dashed line represents the ratio 1 which is the case where the detected flux is equal for both cameras.

only the exposure times and do not account for duty cycles (see Figure 4.10 for the full comparison). We find that the CCD consistently records higher flux values than the CMOS camera, with the mean ratio of CMOS/CCD flux being approximately 0.9. We also see the expected colour dependence, with bluer stars showing a higher flux ratio due to the fact that the CMOS quantum efficiency is more blue sensitive (see Figure 4.1).

A clear transition is observed beyond T > 12 mag, and the CMOS camera achieves better precision. A similar pattern is seen under full-moon conditions (lower panel of Figure 4.5), although the ratio distribution peaks at approximately 0.95. The transition is likely due to the fact that the CCD camera is more sensitive to the sky background signal compared to the CMOS camera (see Figure 4.3 and the discussion of the airglow later in Section 4.6.2). At the bright end (T < 9 mag), direct comparison becomes impractical due to CMOS saturation. It should be noted that the comparisons in Figure 4.4 and Figure 4.5 are made per exposure, without accounting for cadence.

4.6.2 Sky Background

As shown in Figure 4.4, sky-background is the dominant noise source for both our CMOS and CCD photometry for stars with T > 13 mag in no-moon conditions and T > 11 mag in full-moon conditions (using our chosen source aperture size). The CCD camera is deep-depleted, with its quantum efficiency peaking at red wavelengths (see Figure 4.1). This makes the CCD camera more

sensitive to the strong emission lines redwards of 600 nm, such as those from atomic oxygen and OH produced in the mesosphere (Maihara et al., 1993). This phenomenon, commonly referred to as airglow (Noll et al., 2012), remains detectable despite the NGTS having a cut-off at 890 nm. In contrast, the CMOS camera is less sensitive to red wavelengths and therefore less sensitive to airglow. This effect is evident when comparing simultaneous images of the sky background with the CMOS and CCD camera. For example, the target pixel frame in Figure 4.3 shows the CCD camera to have a sky background count of $4.02\,e^-\,s^{-1}\,arcsec^{-2}$, where the CMOS camera's sky background count is only $2.52\,e^-\,s^{-1}\,arcsec^{-2}$.

To examine this effect further, we measured the sky background for both cameras over a 6-hour observation on the no-moon night of 2024 July 5 and on the full-moon night of 2024 June 22. We used the counts from the sky background map. The digital units were converted to electrons and normalised by the exposure time and sky pixel area in $arcsec^{-2}$. The sky background flux in units of $e^-\,pixel^{-1}\,arcsec^{-2}$ is shown in Figure 4.9 as a function of time. The measurements for the no-moon dataset show that although both cameras have a similar trend with time across the observation block, the sky background flux for the CMOS camera is consistently lower than the CCD camera by a factor of approximately 0.5 (see lower panel of Figure 4.9). In contrast, the measurements for the full-moon show the contribution of the moon light which follows the same trend for both cameras while the sky background has increased significantly. The CMOS camera is consistently lower than the CCD camera however the ratio has been increased by a factor of approximately 0.8 (see lower panel of Figure 4.9). Given the only difference is the quantum efficiency of the cameras, the higher sky background for the CCD camera can be attributed to the fact that the sky is brighter in the red wavelengths due to the night sky emission, and therefore the sky background is higher for the more red-sensitive CCD camera.

We note that the overall trend seen for both cameras in Figure 4.9 is due to the fact that the airmass is high (z = 1.91) at the start of the observations. That increase in amplitude just before the end of the observations is primarily due to the fact that we are observing at the astronomical twilight.

4.6.3 Camera Efficiency

We compare the amount of flux collected per unit time for each camera, which takes into account the sum of the exposure times (10 s) and dead times (3 s for the CCD camera and 0.042 s for the CMOS camera). The flux collected is also dependent on the quantum efficiency of each camera (see Figure 4.1), the NGTS bandpass (520-890 nm) and the stellar effective temperature. We assume that the throughput of each NGTS telescope is identical.

We focused only on stars brighter than $T < 12$ mag. Flux measurements for each star were obtained by aperture photometry using a constant physical photometric radius for the CCD and CMOS images (55 µm - 20 arcsec). The duration is determined by the combined exposure and readout times of the respective camera. To evaluate the performance, we computed the ratio of flux in electrons per unit time between the two cameras and compare it to the stellar effective temperature of each observed star, as shown in Figure 4.10.

Overall, the flux ratio between the CMOS and CCD cameras is always greater than unity, which shows that the CMOS camera collects more electrons per unit elapsed time than the CCD camera. This is primarily due to the fact that the CMOS camera reads out approximately 70 times faster than

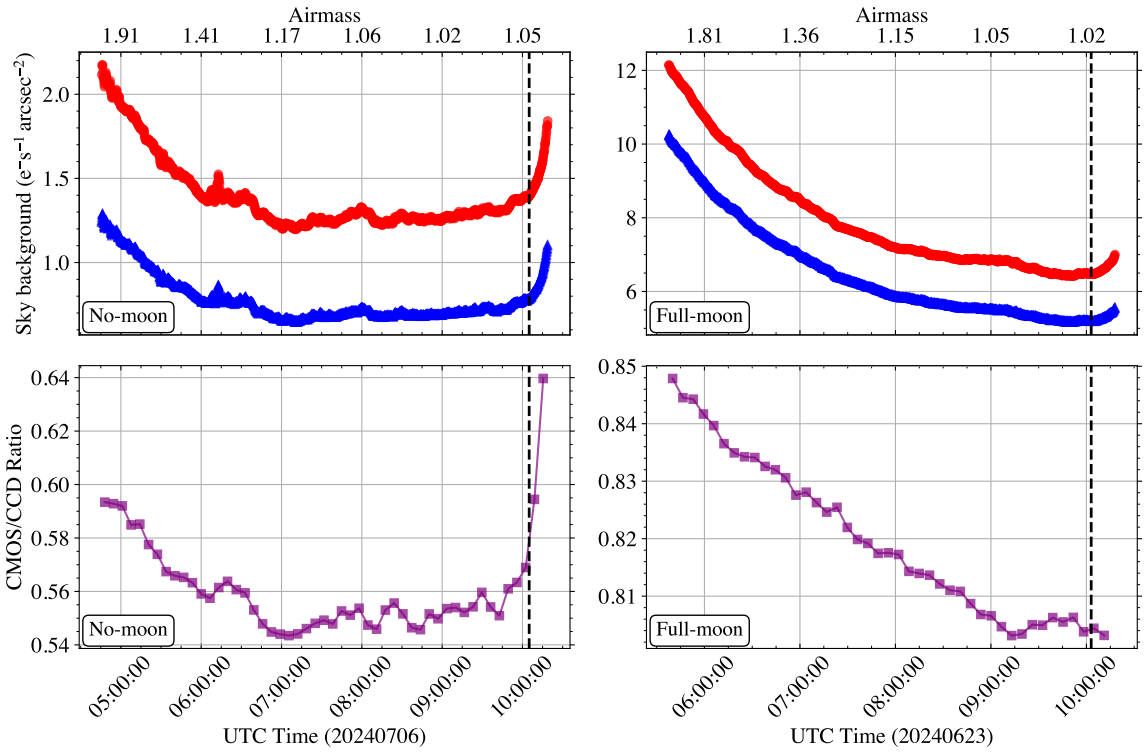


Figure 4.9: **Top:** Sky background flux (e^- pixel^{-1} arcsec^{-2}) as a function of time and airmass from the night of 2024 July 5 (**left**) and the night of 2024 June 22 (**right**) for the CMOS (blue triangles) and CCD (red circles). The dashed vertical line at UT10:05:00 (**left**) and UT10:03:00 (**right**) indicates the start of astronomical twilight. **Bottom:** The CMOS/CCD ratio of the fluxes from the top panel as a function of time.

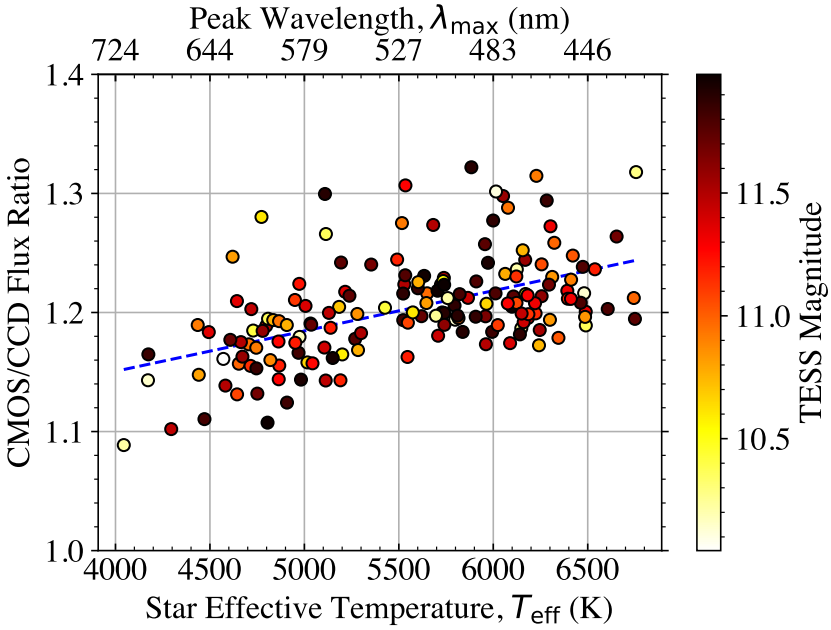


Figure 4.10: Ratio of the flux for bright stars (T < 12 mag), plotted against stellar effective temperature and corresponding peak wavelength, assuming each star behaves as a blackbody, as measured by the CMOS and CCD cameras from the night of 2024 July 5. Flux ratios are represented by circles, colour-coded according to TESS magnitude. The blue dashed line is best-fit linear model the data.

the CCD camera when including the dead times. We find a trend in the flux ratio with the effective temperature of the star derived from the TIC8 (Stassun et al., 2018) catalogue (see Figure 4.10). This trend is due to the fact that the CMOS camera is more blue-sensitive in its quantum efficiency compared to the CCD camera (see Figure 4.1). This means that the CMOS camera performs even better than the CCD camera for the bluest (hottest) stars. We do not detect any trend in the flux ratio with respect to the magnitude of the stars.

The Marana CMOS camera achieves an extended dynamic range through its HDR mode. In our previous work (Apergis et al., 2025), we demonstrated that a transition between the High Gain and Low Gain channels occurs at approximately ~1800 ADU. Pixels with counts in this regime may be processed by either gain channel, thereby introducing additional noise (Apergis et al., 2025, see Figure 9). We investigated which stars are affected by such transition pixels within their photometric apertures. We defined the transition region to be 1600–2000 ADU. For each star, we measured the number of pixels inside the aperture whose values fall within this range, and grouped stars into magnitude bins. This analysis is illustrated in Figure 4.11.

Additionally, we identified stars for which the maximum pixel value inside the aperture, corresponding to the point spread function peak and contributing most significantly to the total flux, lies within the transition region. These stars were found to be in the range 12 < T < 12.8, as indicated by the green shaded region in Figure 4.11. The number of affected stars per magnitude bin, together with the average number of transition pixels per aperture for each star, is presented in Table 4.14. We also analysed the final relative photometry of stars whose point spread functions' contain transition pixels, and compared them with stars whose four highest pixel values do not include any transition

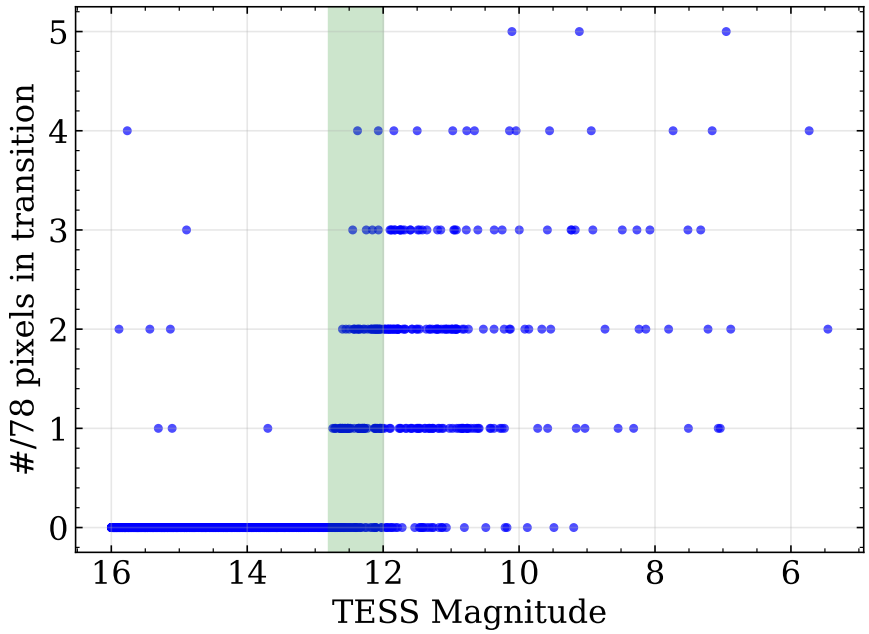


Figure 4.11: Number of transition pixels (1600-2000 ADU) inside the photometric aperture (~78 pixels aperture) for a selection of stars observed with the CMOS camera on the night of 2024 July 5 (new moon conditions). The green shaded area represents the magnitude range in which transition pixels have the maximum value within the photometric aperture.

pixels.

We find that for faint stars (T>13) there are no transition pixels in the photometric aperture. For stars brighter than T~12 there are typically just a few transition pixels, and these pixels are not significantly contributing to the total flux measured for the star. Therefore in both these instances it is unlikely our photometric measurements will be affected by the transition feature of the CMOS detector. The magnitude $12 < T < 12.8$ is at highest risk of the photometry being affected by the CMOS transition from High Gain to Low Gain channels. We do not find a noticeable increase in the of RMS noise of these light curves. However it would be advisable to ensure prime targets of photometric monitoring are not in this region by selecting an appropriate exposure time for observations.

4.6.4 Red Noise

Red-noise is a critical limitation for many applications of bright star photometry - e.g. for detecting exoplanet transits (Pont et al., 2006). Our analysis of the photometric precision for the CMOS and CCD cameras at different timescales (see Section 4.5.2 and Figure 4.6) shows that the noise for both cameras is largely Gaussian (white) noise. This is as expected from previous analysis of NGTS bright star photometry (McCormac et al., 2017; Wheatley et al., 2018; Bryant et al., 2020; Bayliss et al., 2022; O'Brien et al., 2022).

4.7 Conclusions

The Marana CMOS camera was studied extensively on-sky at the Paranal Observatory using an NGTS telescope to test its suitability for high-precision photometry of exoplanet transits. We conducted simultaneous observations using a CCD camera to ensure exactly the same observing conditions and the same targets. The common exposure time was selected to be 10 s. We made sure we accounted for the difference in pixel size between the two cameras (13.5 vs 11 µm for the CCD and CMOS camera respectively). We also considered the differences in the quantum efficiency when reaching our conclusions between the two cameras (Figure 4.1).

The CMOS camera delivered photometry at the precision expected from our noise model, which was scintillation-limited for bright stars (T < 11 mag), and sky background-limited for fainter stars (T > 13 mag). In contrast to the CCD image sensor, the CMOS image sensor was never limited by readout noise. The CMOS camera's dark current noise is much higher than the CCD camera, but this was never a dominant source of noise for our photometry. We see minimal red noise contributions in the photometric precision of the CMOS camera, indicating there are no instrumental red-noise limitations using the CMOS camera for bright star photometry.

The fast readout of the CMOS camera (42 ms) enables a much higher duty cycle than the CCD camera. This effectively enables more flux to be collected over any given observing duration, and hence a better photometric precision. This is even true despite the slightly reduced quantum efficiency of the CMOS image sensor compared with the CCD image sensor, and the fact that the NGTS filter has been optimised to the CCD camera's quantum efficiency response. The transiting exoplanet lightcurves obtained using the CMOS camera are very similar to those obtained with the CCD camera. This result aligns well with other on-sky tests in the literature that show excellent photometric performance for CMOS cameras (Karpov et al., 2021; Alarcon et al., 2023b).

If CMOS cameras were to be adopted across all 12 NGTS telescopes, the upgrade would require more than a direct camera replacement. The results of this work show that CMOS technology can deliver high precision time-series photometry comparable to the existing CCD system, with clear practical advantages from its low read noise, shutterless operation, and much faster readout speeds. These properties would improve the observing duty cycle and reduce the impact of read noise limited performance on dark night, particularly for high cadence monitoring. However, a full NGTS wide implementation would require corresponding changes to the instrument control and data handling infrastructure. The higher cadence would increase the data rate and storage requirements. Exposure time selection would also become more important, both to avoid saturation for bright targets, since it CMOS sensors show anti-blooming behaviour. Because the CMOS quantum efficiency differs from that of the current CCDs, the existing NGTS filter and target selection strategy may not be optimal for all stellar colours. Therefore, while CMOS sensors appear to be a viable and potentially advantageous replacement for the NGTS CCD cameras, their adoption across the full array would require coordinated upgrades to calibration strategy, observing software, hardware, data storage and photometric reduction pipelines.

In conclusion, we find that the Marana CMOS camera is suitable for high-precision time-series photometry. The fast readout speeds and low read noise and shutterless operation often provide a significant advantage over a traditional CCD camera. For applications requiring continuous imaging of rapidly varying astronomical targets, such as satellite tracking and mapping (Blake et al., 2023;

Table 4.14: Percentage ratio of transition pixels within star apertures.

TESS Magnitude bin	Stars affected by transition pixels	Average number of pixels in transition (#/78)
6–7	2/2	3.50
7–8	9/9	2.33
8–9	10/10	2.40
9–10	15/18	2.00
10–11	53/57	1.81
11–12	92/115	1.54
12–13	85/196	0.65
13–14	1/378	0.00
14–15	1/547	0.01
15–16	6/942	0.01

Cooke et al., 2023; Airey et al., 2025b), or near-Earth asteroid monitoring (Larson et al., 2018), CMOS image sensors offer distinct benefits. Furthermore, image degradation caused by saturated stars is mitigated in CMOS cameras due to their anti-blooming pixel architecture, reducing the risk of contamination to nearby targets of interest. As CMOS sensor technology continues to advance, it is likely that these cameras will replace CCDs in most astronomical time-series photometry applications.

4.8 Appendix

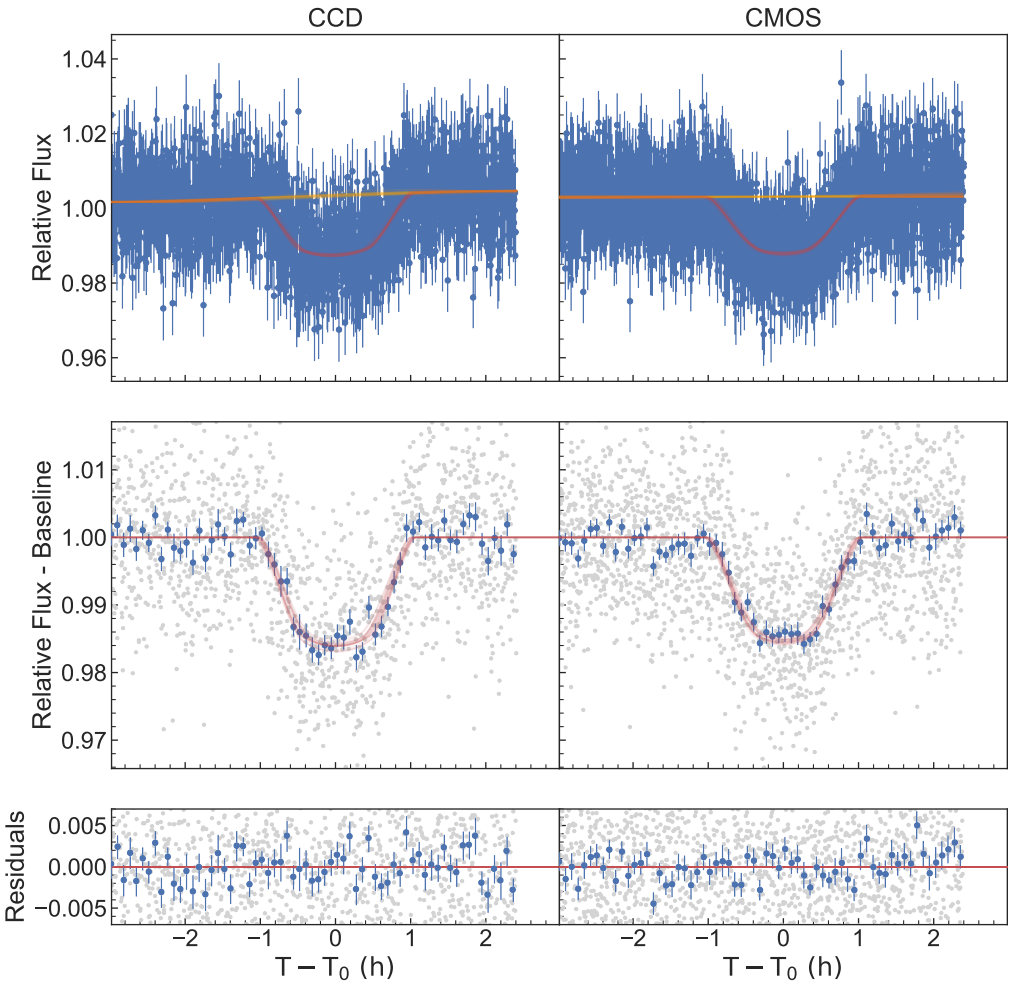


Figure 4.12: Same as in Figure 4.7. Normalized lightcurves for the transiting system of TOI-905 (TIC 261867566) from NGTS on 2024 July 13.

Table 4.4: `allesfitter` model priors. Planetary system properties for the transiting system TOI-905 (TIC 261867566) from NGTS on 2024 July 13.

Parameter	Initial Guess	Prior	Fitted value CMOS	Fitted value CCD
$R_p/R_\star$	0.1311	$\mathcal{N}(0.1311, 0.0012)$	$0.1307^{+0.0011}_{-0.0012}$	0.1310 ± 0.0011
$(R_\star + R_b)/a_b$	0.102827	$\mathcal{N}(0.102827, 0.010844)$	0.1058 ± 0.0034	0.1026 ± 0.0034
$\cos i_b$	0.075327	$\mathcal{N}(0.075327, 0.004524)$	0.0784 ± 0.0032	$0.0734^{+0.0035}_{-0.0037}$
T_c (BJD)	2460505.6096463003	$\mathcal{N}(2460505.6096463, 0.0004719)$	$2460505.61003 \pm 0.00040$	$2460505.60988 \pm 0.00040$
Orbital Period (days)	3.7395671	$\mathcal{N}(3.7395671, 0.0000013)$	$3.7395672^{+0.0000012}_{-0.0000013}$	3.7395670 ± 0.0000013
q_1	0.387	$\mathcal{N}(0.387, 0.015)$	0.389 ± 0.015	$0.388^{+0.014}_{-0.016}$
q_2	0.408	$\mathcal{N}(0.408, 0.099)$	0.447 ± 0.093	0.400 ± 0.097

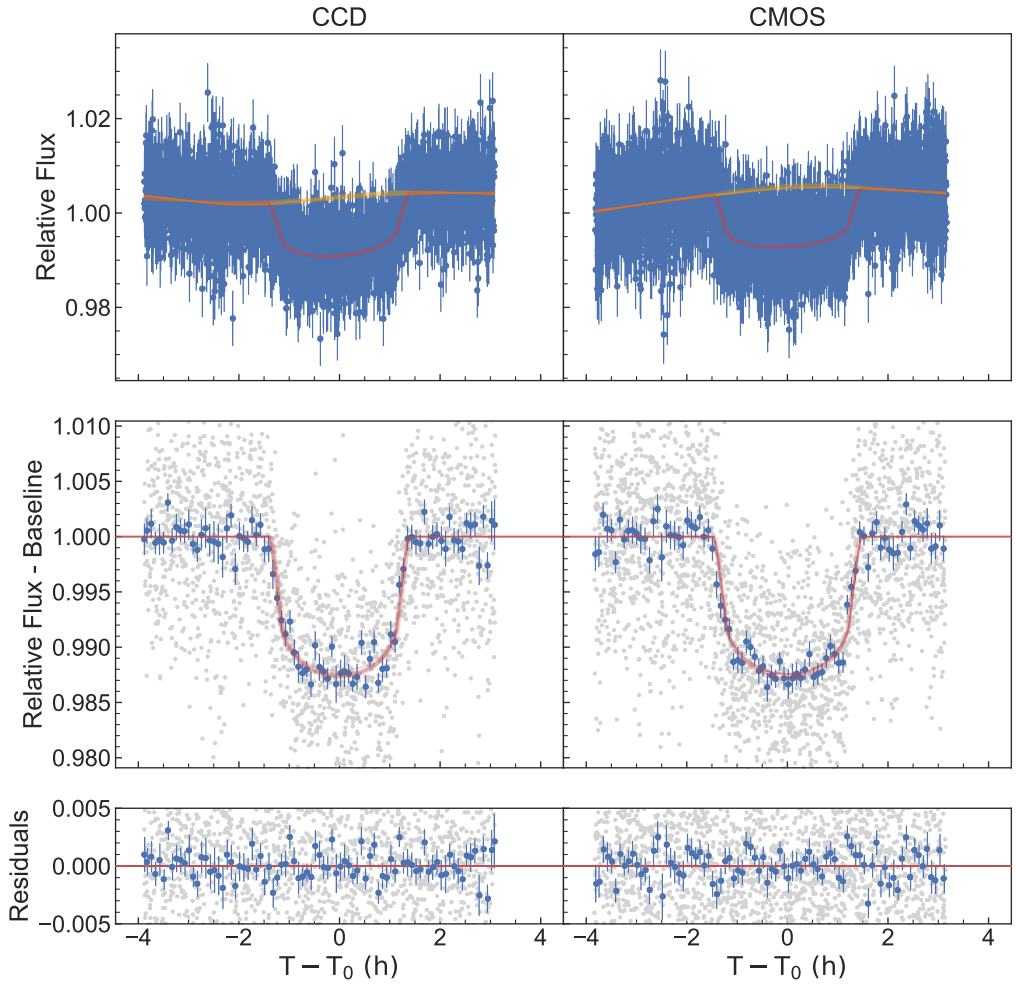


Figure 4.13: Same as in Figure 4.7. Normalized lightcurves for the transiting system of WASP-95 (TIC 144065872) from NGTS on 2024 July 14.

Table 4.5: `allesfitter` model priors. Planetary system properties for the transiting system WASP-95 (TIC 144065872) from NGTS on 2024 July 14.

Parameter	**Initial Guess**	**Prior**	**Fitted value CMOS**	**Fitted value CCD**
$R_p/R_\star$	0.1025	$\mathcal{N}(0.1025, 0.0005)$	0.10231 ± 0.00055	$0.10250^{+0.00047}_{-0.00053}$
$(R_\star + R_b)/a_b$	0.172266	$\mathcal{N}(0.172266, 0.005922)$	$0.1771^{+0.0050}_{-0.0026}$	$0.1732^{+0.0057}_{-0.0048}$
$\cos i_b$	0.027922	$\mathcal{N}(0.027922, 0.036611)$	$0.019^{+0.028}_{-0.039}$	$0.048^{+0.017}_{-0.036}$
T_c (BJD)	2458553.711158	$\mathcal{N}(2458553.711158, 0.000088)$	$2460506.80136 \pm 0.00070$	$2460506.80373 \pm 0.00073$
Orbital Period (days)	2.1846730	$\mathcal{N}(2.1846730, 0.0000014)$	$2.18467329^{+0.0000013}_{-0.0000090}$	$2.1846729^{+0.0000014}_{-0.0000013}$
q_1	0.357	$\mathcal{N}(0.357, 0.012)$	$0.359^{+0.012}_{-0.015}$	0.359 ± 0.011
q_2	0.393	$\mathcal{N}(0.393, 0.089)$	$0.366^{+0.060}_{-0.065}$	0.369 ± 0.079

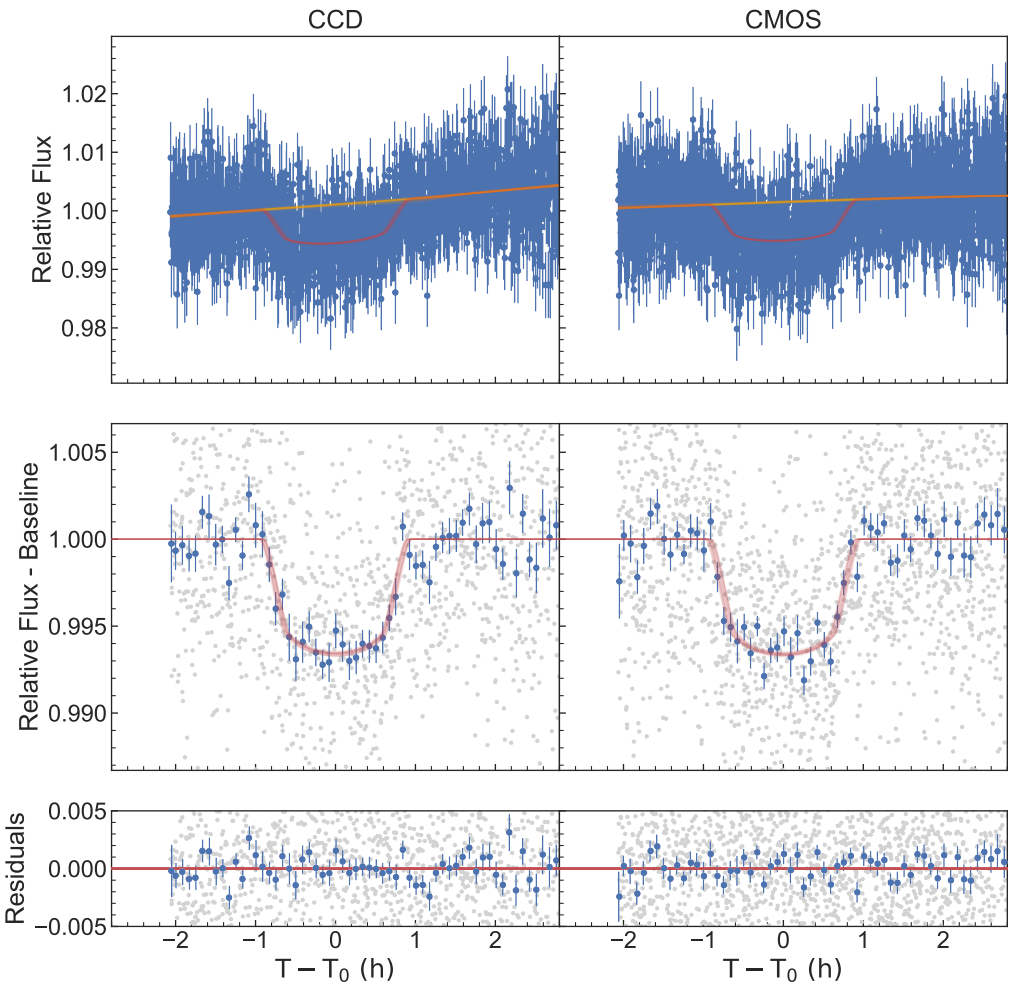


Figure 4.14: Same as in Figure 4.7. Normalized lightcurves for the transiting system of TOI-2109 (TIC 392476080) from NGTS on 2024 July 17.

Table 4.6: `allesfitter` model priors and fitted values. Planetary system properties for the transiting system TOI-2109 (TIC 392476080) from NGTS on 2024 July 17.

Parameter	Initial Guess	Prior	Fitted value CMOS	Fitted value CCD
$R_p/R_\star$	0.08155	$\mathcal{N}(0.08155, 0.00022)$	0.08155 ± 0.00022	0.08155 ± 0.00022
$(R_\star + R_b)/a_b$	0.476874	$\mathcal{N}(0.476874, 0.044155)$	0.4701 ± 0.0073	$0.4649^{+0.0080}_{-0.0076}$
$\cos i_b$	0.329855	$\mathcal{N}(0.329855, 0.006089)$	0.3297 ± 0.0060	0.3299 ± 0.0059
T_c (BJD)	2459378.455370	$\mathcal{N}(2459378.455370, 0.000059)$	$2460509.556868 \pm 0.000074$	$2460509.556874 \pm 0.000074$
Orbital Period (days)	0.672474140	$\mathcal{N}(0.672474140, 0.000000028)$	$0.672474141 \pm 0.000000028$	$0.672474141^{+0.000000027}_{-0.000000029}$
q_1	0.305	$\mathcal{N}(0.305, 0.008)$	0.304 ± 0.008	0.305 ± 0.008
q_2	0.375	$\mathcal{N}(0.375, 0.074)$	0.379 ± 0.074	0.377 ± 0.074

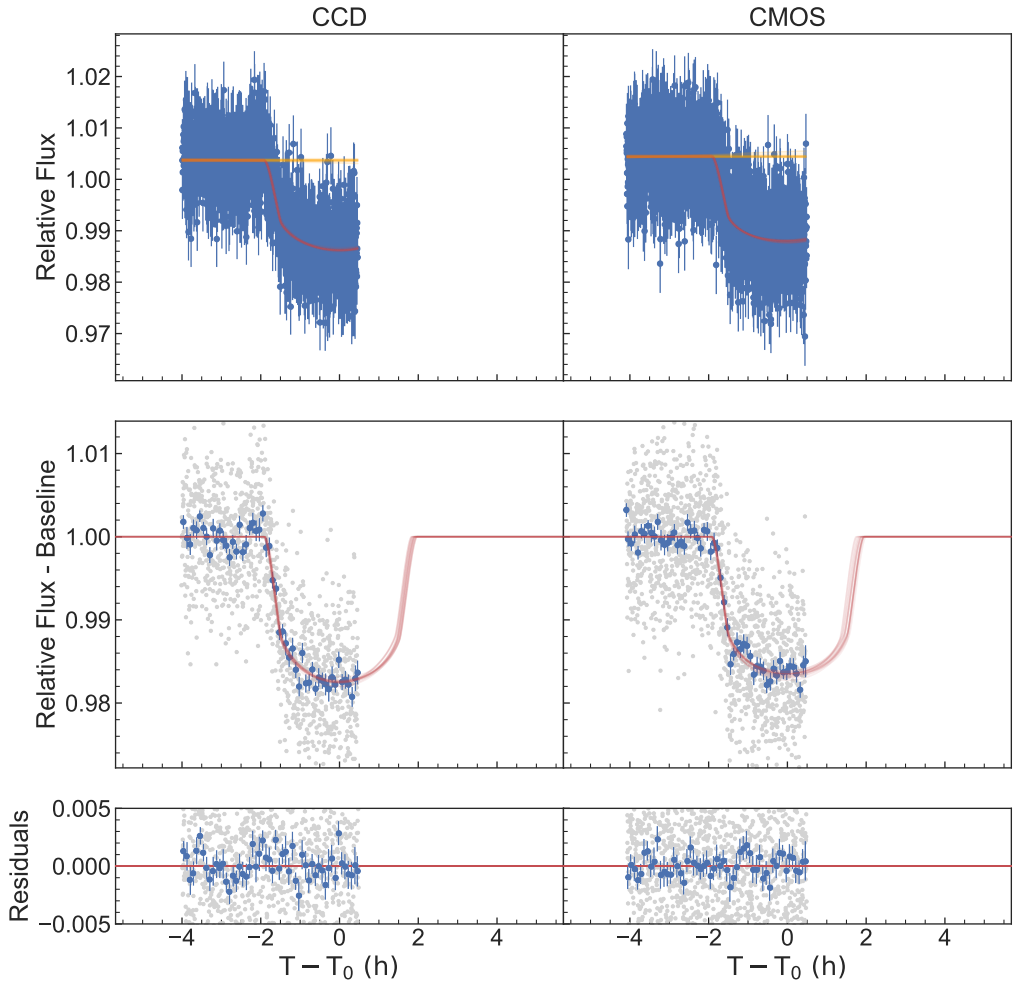


Figure 4.15: Same as in Figure 4.7. Normalized lightcurves for the transiting system of KELT-10 (TIC 269217040) from NGTS on 2024 August 1.

Table 4.7: `allesfitter` model priors and fitted values. Planetary system properties for the transiting system KELT-10 (TIC 269217040) from NGTS on 2024 August 1.

Parameter	**Initial Guess**	**Prior**	**Fitted value CMOS**	**Fitted value CCD**
$R_p/R_\star$	0.1190	$\mathcal{N}(0.1190, 0.0014)$	0.11793 ± 0.0010	0.12013 ± 0.0010
$(R_\star + R_b)/a_b$	0.119807	$\mathcal{N}(0.119807, 0.004107)$	$0.1212^{+0.0028}_{-0.0025}$	$0.1205^{+0.0025}_{-0.0023}$
$\cos i_b$	0.024258	$\mathcal{N}(0.024258, 0.015002)$	$0.021^{+0.011}_{-0.013}$	$0.017^{+0.010}_{-0.012}$
T_c (BJD)	2457612.49947	$\mathcal{N}(2457612.49947, 0.00041)$	2460524.7109 ± 0.0011	$2460524.7110^{+0.0010}_{-0.0011}$
Orbital Period (days)	4.1662541	$\mathcal{N}(4.1662541, 0.0000016)$	4.1662541 ± 0.0000016	4.1662541 ± 0.0000016
q_1	0.350	$\mathcal{N}(0.350, 0.010)$	0.349 ± 0.010	0.351 ± 0.010
q_2	0.385	$\mathcal{N}(0.385, 0.081)$	0.341 ± 0.069	0.416 ± 0.068

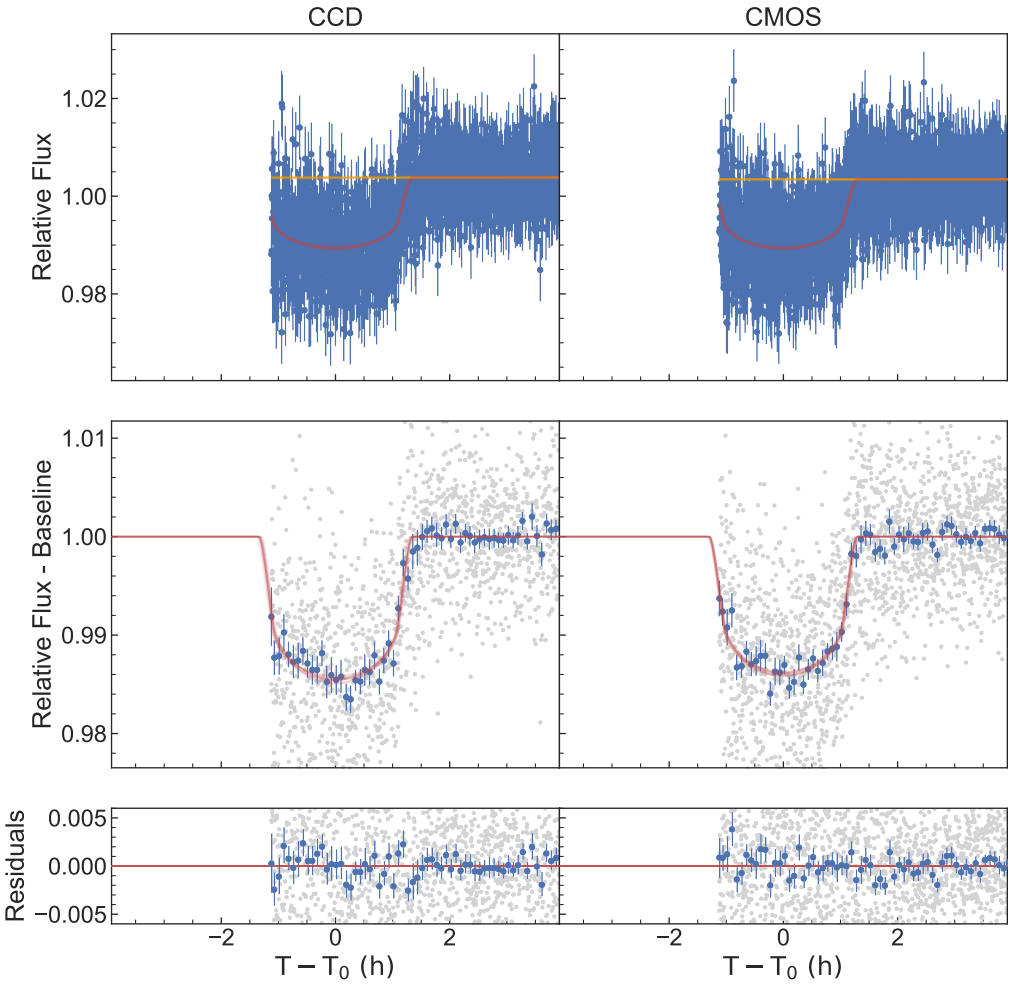


Figure 4.16: Same as in Figure 4.7. Normalized lightcurves for the transiting system of WASP-97 (TIC 230982885) from NGTS on 2024 August 04.

Table 4.8: `allesfitter` model priors and fitted values. Planetary system properties for the transiting system WASP-97 (TIC 230982885) from NGTS on 2024 August 04.

Parameter	**Initial Guess**	**Prior**	**Fitted value CMOS**	**Fitted value CCD**
$R_p/R_\star$	0.1091	$\mathcal{N}(0.1091, 0.0009)$	0.10856 ± 0.00077	0.10913 ± 0.00079
$(R_\star + R_b)/a_b$	0.168300	$\mathcal{N}(0.168300, 0.003833)$	0.1686 ± 0.0035	$0.1699^{+0.0028}_{-0.0026}$
$\cos i_b$	0.034899	$\mathcal{N}(0.034899, 0.022665)$	$0.046^{+0.010}_{-0.013}$	$0.023^{+0.014}_{-0.017}$
T_c (BJD)	2458554.475352	$\mathcal{N}(2458554.475352, 0.000074)$	$2460527.74264 \pm 0.00020$	$2460527.74252 \pm 0.00021$
Orbital Period (days)	2.07275965	$\mathcal{N}(2.07275965, 0.00000021)$	$2.07275967^{+0.00000020}_{-0.00000021}$	$2.07275965 \pm 0.00000021$
q_1	0.369	$\mathcal{N}(0.369, 0.009)$	0.369 ± 0.009	0.369 ± 0.009
q_2	0.400	$\mathcal{N}(0.400, 0.076)$	0.410 ± 0.068	0.389 ± 0.068

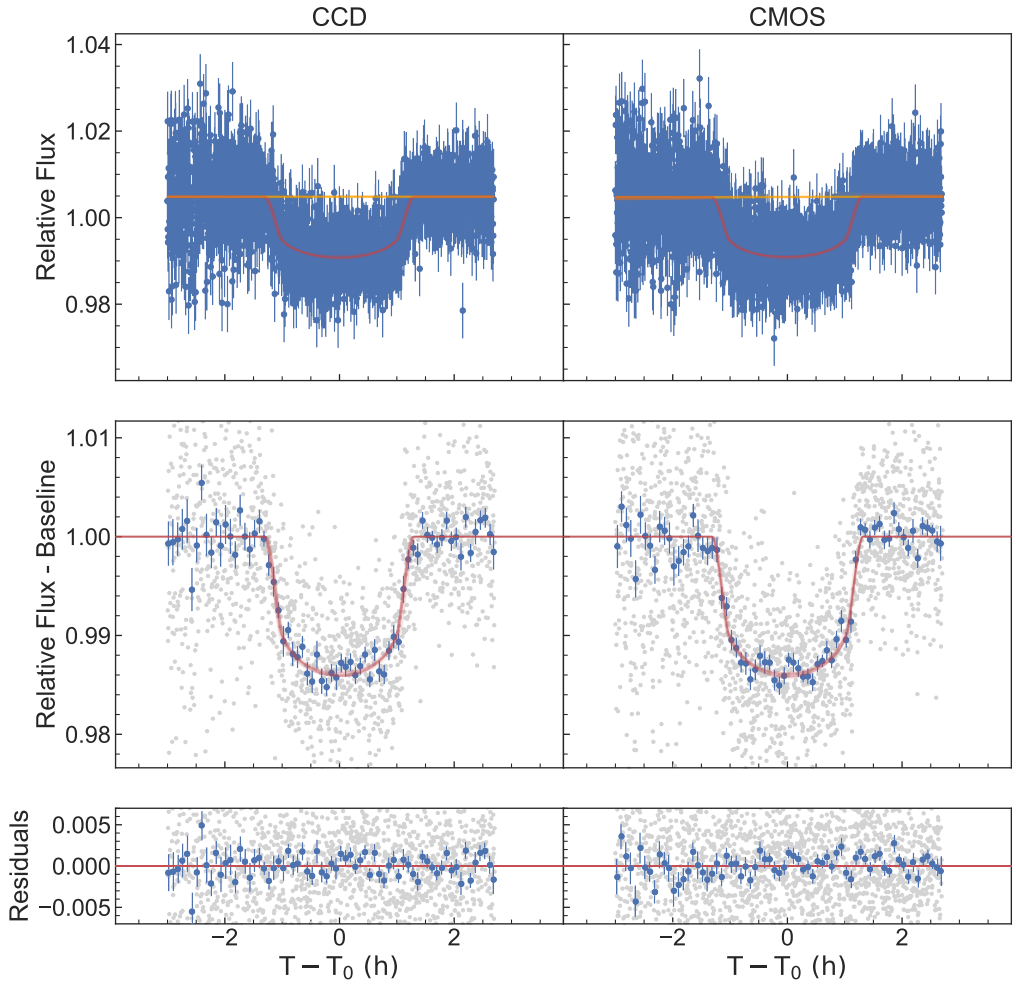


Figure 4.17: Same as in Figure 4.7. Normalized lightcurves for the transiting system of WASP-97 (TIC 230982885) from NGTS on 2024 August 06.

Table 4.9: `allesfitter` model priors and fitted values. Planetary system properties for the transiting system WASP-97 (TIC 230982885) from NGTS on 2024 August 06.

Parameter	**Initial Guess**	**Prior**	**Fitted value CMOS**	**Fitted value CCD**
$R_p/R_\star$	0.1091	$\mathcal{N}(0.1091, 0.0009)$	0.10825 ± 0.00078	0.10865 ± 0.00079
$(R_\star + R_b)/a_b$	0.168300	$\mathcal{N}(0.168300, 0.003833)$	$0.1681^{+0.0033}_{-0.0031}$	0.1681 ± 0.0035
$\cos i_b$	0.034899	$\mathcal{N}(0.034899, 0.022665)$	$0.040^{+0.012}_{-0.016}$	$0.045^{+0.010}_{-0.014}$
T_c (BJD)	2458554.475352	$\mathcal{N}(2458554.475352, 0.000074)$	$2460529.81532 \pm 0.00020$	$2460529.81530^{+0.00019}_{-0.00020}$
Orbital Period (days)	2.07275965	$\mathcal{N}(2.07275965, 0.00000021)$	$2.07275964 \pm 0.00000021$	$2.07275965 \pm 0.00000021$
q_1	0.369	$\mathcal{N}(0.369, 0.009)$	0.369 ± 0.009	0.369 ± 0.009
q_2	0.400	$\mathcal{N}(0.400, 0.076)$	0.385 ± 0.067	0.380 ± 0.070

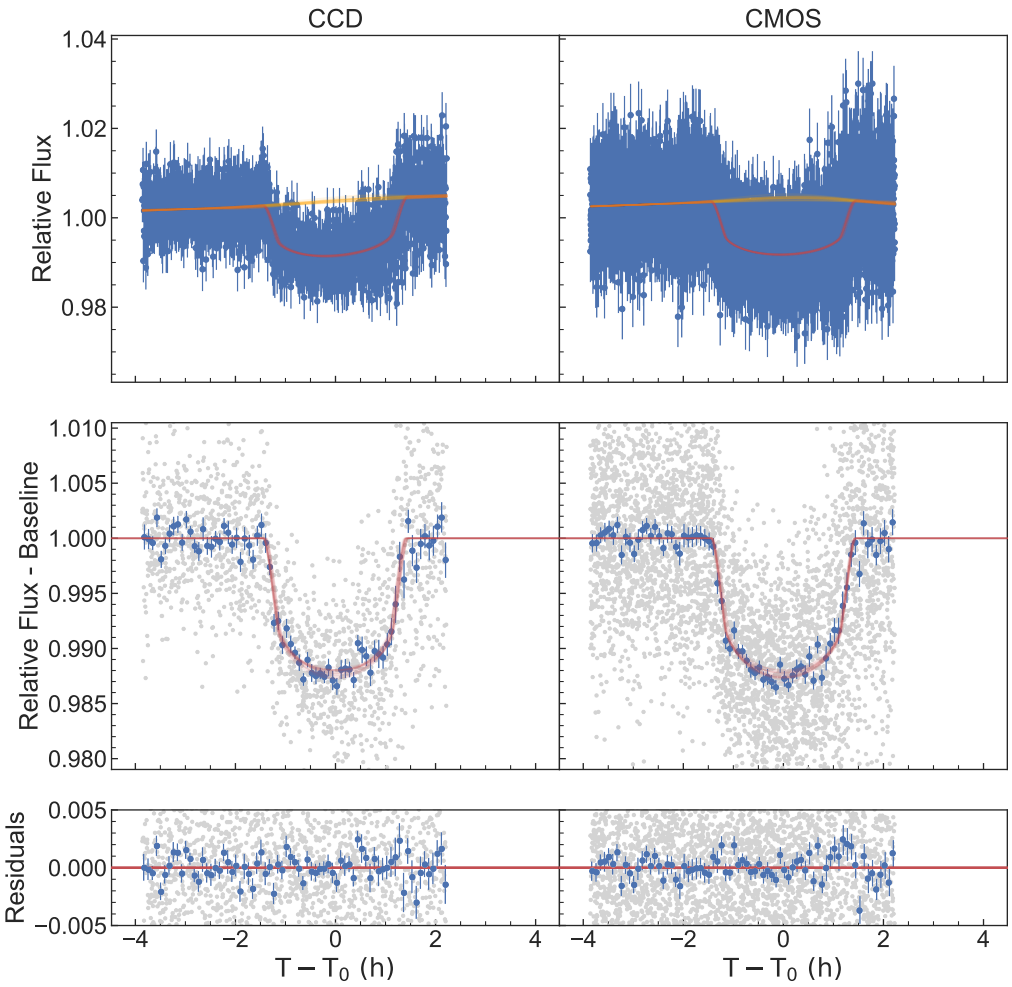


Figure 4.18: Same as in Figure 4.7. Normalized lightcurves for the transiting system of WASP-95 (TIC 144065872) from NGTS on 2024 August 07.

Table 4.10: `allesfitter` model priors and fitted values. Planetary system properties for the transiting system WASP-95 (TIC 144065872) from NGTS on 2024 August 07.

Parameter	**Initial Guess**	**Prior**	**Fitted value CMOS**	**Fitted value CCD**
$R_p/R_\star$	0.1025	$\mathcal{N}(0.1025, 0.0005)$	$0.10251^{+0.00036}_{-0.00059}$	0.10215 ± 0.00048
$(R_\star + R_b)/a_b$	0.172266	$\mathcal{N}(0.172266, 0.005922)$	0.1783 ± 0.0050	$0.1765^{+0.0055}_{-0.0051}$
$\cos i_b$	0.027922	$\mathcal{N}(0.027922, 0.036611)$	$0.031^{+0.029}_{-0.090}$	$0.051^{+0.016}_{-0.038}$
T_c (BJD)	2458553.711158	$\mathcal{N}(2458553.711158, 0.000088)$	$2460530.83412^{+0.00045}_{-0.00050}$	$2460530.83438 \pm 0.00056$
Orbital Period (days)	2.1846730	$\mathcal{N}(2.1846730, 0.0000014)$	$2.1846731^{+0.0000010}_{-0.0000012}$	2.1846729 ± 0.0000014
q_1	0.357	$\mathcal{N}(0.357, 0.012)$	$0.354^{+0.008}_{-0.009}$	0.359 ± 0.012
q_2	0.393	$\mathcal{N}(0.393, 0.089)$	$0.446^{+0.065}_{-0.049}$	0.407 ± 0.079

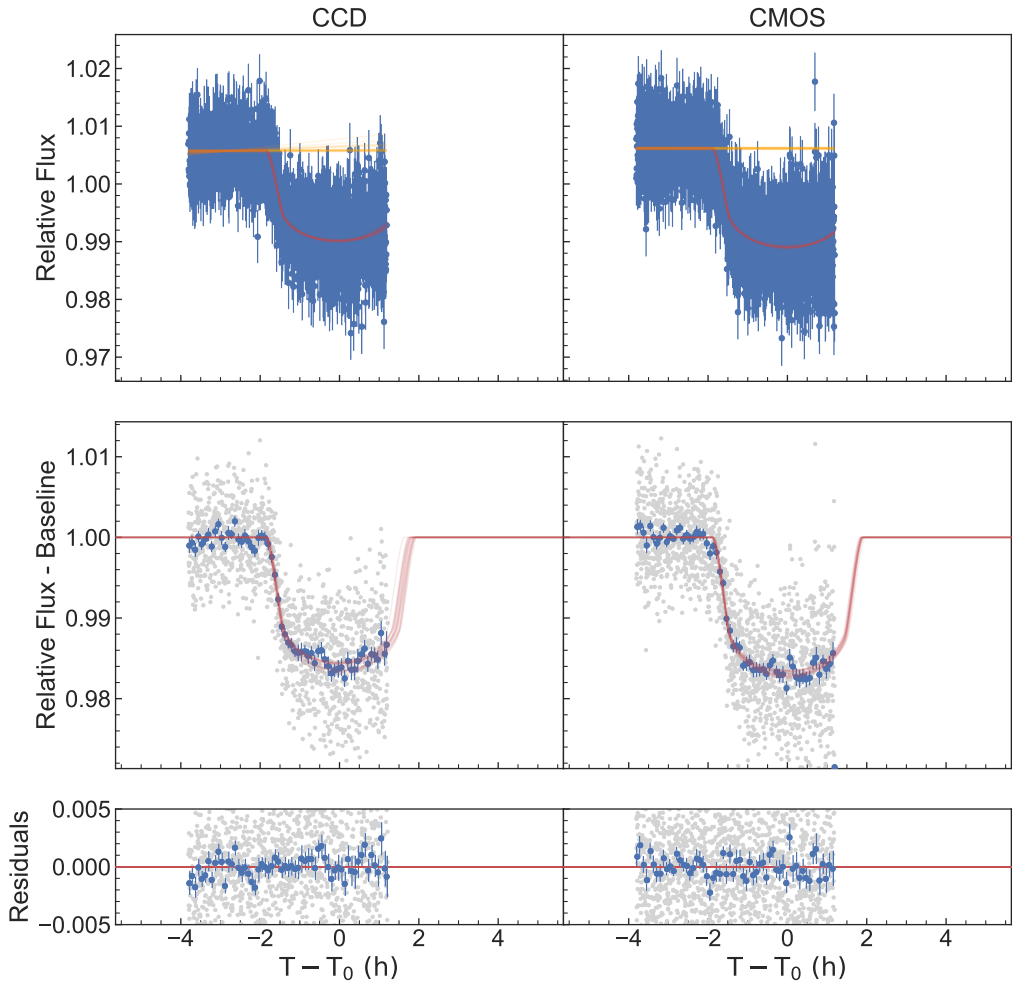


Figure 4.19: Same as in Figure 4.7. Normalized lightcurves for the transiting system of KELT-10 (TIC 269217040) from NGTS on 2024 August 26.

Table 4.11: `allesfitter` model priors and fitted values. Planetary system properties for the transiting system KELT-10 (TIC 269217040) from NGTS on 2024 August 26.

Parameter	**Initial Guess**	**Prior**	**Fitted value CMOS**	**Fitted value CCD**
$R_p/R_\star$	0.1190	$\mathcal{N}(0.1190, 0.0014)$	0.11958 ± 0.00099	$0.1167^{+0.0014}_{-0.0013}$
$(R_\star + R_b)/a_b$	0.119807	$\mathcal{N}(0.119807, 0.004107)$	$0.1204^{+0.0028}_{-0.0025}$	$0.1206^{+0.0033}_{-0.0031}$
$\cos i_b$	0.024258	$\mathcal{N}(0.024258, 0.015002)$	$0.022^{+0.010}_{-0.013}$	$0.0354^{+0.0090}_{-0.013}$
T_c (BJD)	2457612.49947	$\mathcal{N}(2457612.49947, 0.00041)$	$2460549.70892 \pm 0.00099$	2460549.7083 ± 0.0011
Orbital Period (days)	4.1662541	$\mathcal{N}(4.1662541, 0.0000016)$	4.1662541 ± 0.0000016	4.1662541 ± 0.0000015
q_1	0.350	$\mathcal{N}(0.350, 0.010)$	0.350 ± 0.010	$0.350^{+0.010}_{-0.011}$
q_2	0.385	$\mathcal{N}(0.385, 0.081)$	0.358 ± 0.064	0.368 ± 0.072

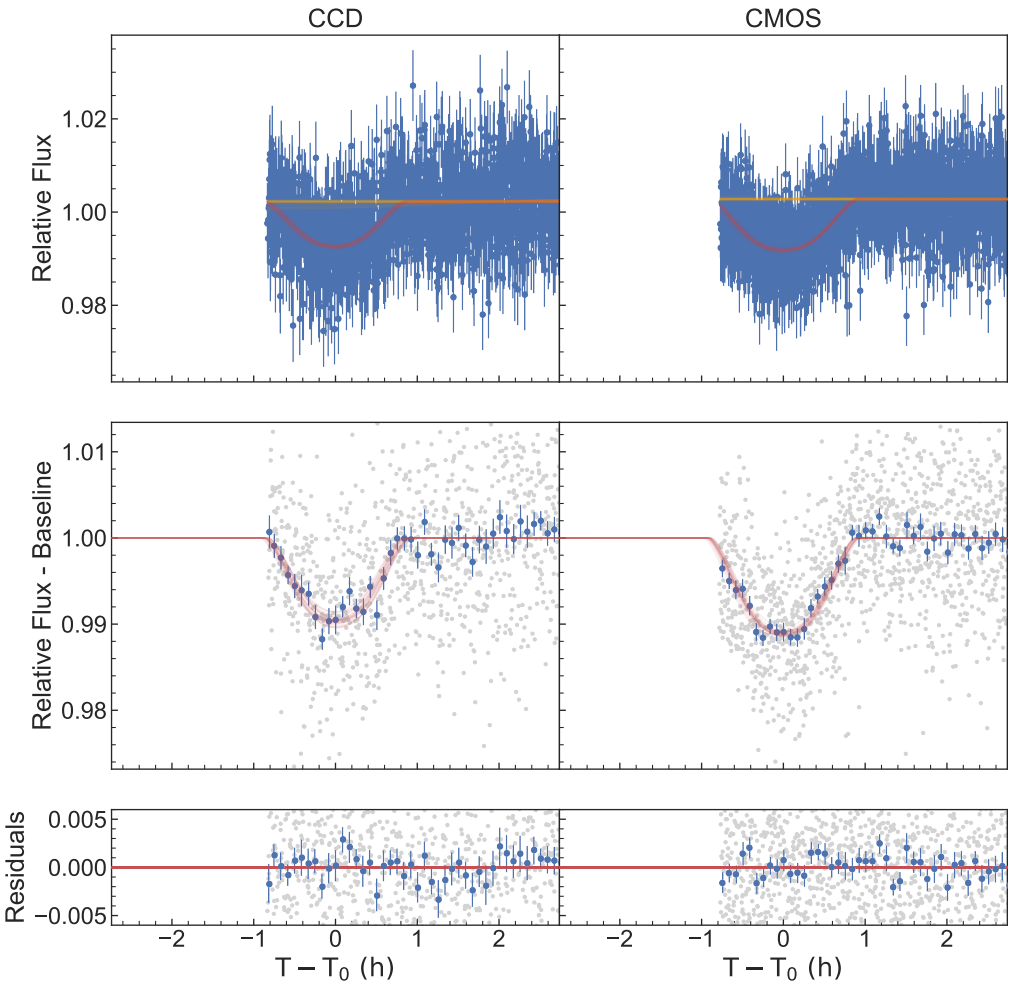


Figure 4.20: Same as in Figure 4.7. Normalized lightcurves for the transiting system of TOI-4463 (TIC 8599009) from NGTS on 2024 August 27.

Table 4.12: `allesfitter` model priors and fitted values. Planetary system properties for the transiting system TOI-4463 (TIC 8599009) from NGTS on 2024 August 27.

Parameter	**Initial Guess**	**Prior**	**Fitted value CMOS**	**Fitted value CCD**
$R_p/R_\star$	0.11449	$\mathcal{N}(0.11449, 0.00397)$	$0.1154^{+0.0032}_{-0.0030}$	0.1133 ± 0.0039
$(R_\star + R_b)/a_b$	0.136414	$\mathcal{N}(0.136414, 0.004037)$	0.1360 ± 0.0029	0.1351 ± 0.0032
$\cos i_b$	0.107652	$\mathcal{N}(0.107652, 0.004857)$	0.1088 ± 0.0027	0.1107 ± 0.0031
T_c (BJD)	2459291.64004	$\mathcal{N}(2459291.64004, 0.00032)$	$2460550.51237 \pm 0.00068$	$2460550.51468 \pm 0.00086$
Orbital Period (days)	2.8807198	$\mathcal{N}(2.8807198, 0.0000028)$	$2.8807197^{+0.0000029}_{-0.0000027}$	2.8807198 ± 0.0000028
q_1	0.372	$\mathcal{N}(0.372, 0.007)$	0.372 ± 0.008	0.372 ± 0.008
q_2	0.400	$\mathcal{N}(0.400, 0.071)$	0.397 ± 0.070	$0.401^{+0.074}_{-0.069}$

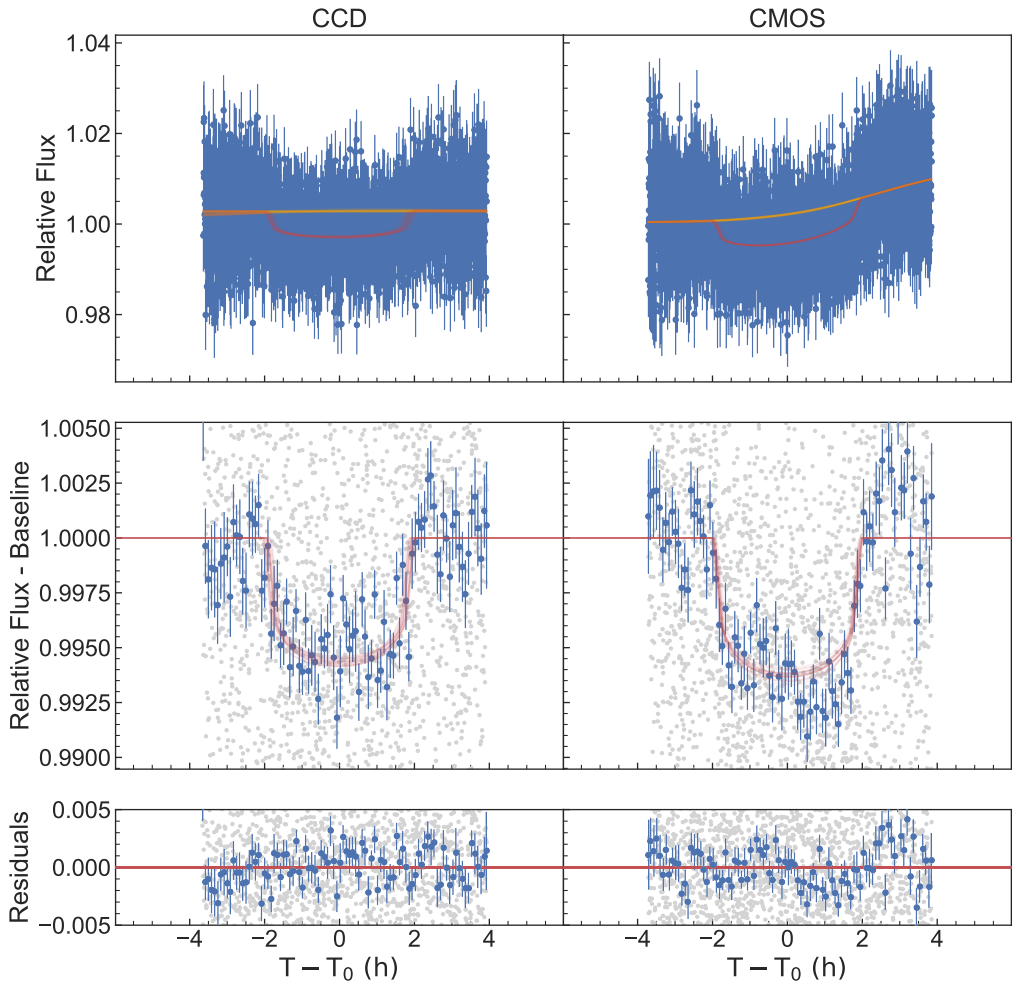


Figure 4.21: Same as in Figure 4.7. Normalized lightcurves for the transiting system of WASP-30 (TIC 9725627) from NGTS on 2024 August 28.

Table 4.13: `allesfitter` model priors and fitted values. Planetary system properties for the transiting system WASP-30 (TIC 9725627) from NGTS on 2024 August 28.

Parameter	**Initial Guess**	**Prior**	**Fitted value CMOS**	**Fitted value CCD**
$R_p/R_\star$	0.0705	$\mathcal{N}(0.0705, 0.0011)$	0.0728 ± 0.0010	0.06924 ± 0.0010
$(R_\star + R_b)/a_b$	0.121078	$\mathcal{N}(0.121078, 0.001989)$	0.1250 ± 0.0015	0.1233 ± 0.0019
$\cos i_b$	0.007505	$\mathcal{N}(0.007505, 0.008202)$	0.0042 ± 0.0063	0.0053 ± 0.0076
T_c (BJD)	2460551.738836	$\mathcal{N}(2460551.738836, 0.0068717)$	2460551.7454 ± 0.0013	2460551.7421 ± 0.0026
Orbital Period (days)	4.156736	$\mathcal{N}(4.156736, 0.00000202)$	4.1567360 ± 0.0000020	4.1567359 ± 0.0000020
q_1	0.330	$\mathcal{N}(0.330, 0.006)$	0.329 ± 0.006	0.329 ± 0.006
q_2	0.373	$\mathcal{N}(0.373, 0.065)$	0.372 ± 0.065	0.350 ± 0.063

Chapter 5

Characterisation of Andor Toran 26B CMOS camera

"Why do we fall, sir? So that we can learn to pick ourselves up."

'Batman Begins', Christopher Nolan, 2005, C. Nolan / J. Nolan / D. S. Goyer

Note

This chapter is based on the manuscript entitled "High-Precision Photometry with a Scientific CMOS Camera: III – Laboratory and Sky Testing of the Andor Toran 26B" (Apergis et al., in preparation), which is being prepared for submission to RAS Techniques and Instruments (RASTI). The writing and analysis of the paper was performed by the author, with comments throughout the paper that came from the co-authors.

Abstract

Scientific CMOS cameras are increasingly used in modern astronomy, offering CCD-like performance with lower power use, faster readout, and reduced cost. We evaluate the photometric precision of the Toran 26B camera, a new CMOS camera from Oxfords Instruments Andor, through laboratory and on-sky tests in its two modes: high well capacity (HWC) and low noise (LN). Key metrics include read noise, dark current, photo and dark signal non-uniformity, quantum efficiency, and window transmittance. The read noise is $1.07\,e^-$ (LN) and $2.79\,e^-$ (HWC). Bias shows minor dark signal non-uniformity: $0.076\,e^-$ (LN), $0.173\,e^-$ (HWC). Pixel well depth reaches $15700\,e^-$ (LN) and $50058\,e^-$ (HWC), with dynamic ranges of 83.39 dB and 85.05 dB, respectively. Linearities are 99.93 % (LN) and 99.82 % (HWC). Photo response non-uniformity is 0.076 % (LN) and 0.05 % (HWC). Dark current at 0 °C is 0.001 $e^-\,pix^{-1}\,s^{-1}$, (LN and HWC). On-sky tests show that the HWC mode can be camera noise limited for specific magnitude ranges, while the LN mode remains free of such limitations, making it the preferred choice.

5.1 Introduction

Charge-Coupled Devices (CCDs) have long been the standard for optical astronomical imaging, particularly in applications requiring high-precision photometry. Notable examples include instruments on *Kepler* (Borucki et al., 2010), Transiting Exoplanet Survey Satellite (Ricker et al., 2015, TESS) and PLAnetary Transits and Oscillations (Rauer et al., 2025, PLATO). CCDs are prized for their high sensitivity, low read noise, minimal dark current, excellent stability, and uniform pixel response. Architectural enhancements, such as deep depletion technology (Peckerar et al., 1979, 1981; Tsoi et al., 1985; Gimeno et al., 2016) and backside illuminated designs, increase their quantum efficiency across a broad spectral range.

Developed in parallel with CCD sensor technology, Complementary Metal-Oxide Semiconductor (CMOS) sensors are based on a fundamentally different architecture. Unlike the passive pixel array of CCD sensors, CMOS sensors use active pixels, with each pixel containing field-effect transistors for performing charge-to-voltage conversion on a per-pixel basis. CMOS sensors have long been favoured in consumer electronics due to their fast readout speeds, low power consumption, and lower cost. Today CMOS image sensors are not only more affordable and accessible than CCD image sensors, but recent lab and on-sky evaluations demonstrate their increasing suitability for scientific imaging (Jorden et al., 2014; Karpov et al., 2019; Alarcon et al., 2023a; Xiao et al., 2025; Layden et al., 2025; Apergis et al., 2025, 2026). CMOS cameras have found significant usage in astronomy (Qiu et al., 2013; Karpov et al., 2019; Wang et al., 2020; Ardilanov et al., 2021; Qiu et al., 2021; Stefanov, 2022; Townsend-Rose et al., 2023; Alarcon et al., 2023a; Khandelwal et al., 2024; Apergis et al., 2025, 2026) due to their ability to operate at high frame rates and short exposure times, maximising the duty cycle.

In this work, we aim to contribute to the growing body of literature evaluating whether modern CMOS detectors can deliver the level of precision required to rival that of traditional CCD detectors. To this end, we conduct a comprehensive characterisation and performance assessment of the Toran 26B CMOS camera, developed by Oxford Instruments Andor[1], through both controlled laboratory experiments and on-sky observations using the TWenty Inch Survey Telescope (TWIST) telescope, a University of Warwick facility located at the Observatorio del Roque de los Muchachos in La Palma, Spain (Mitchell et al., 2025).

This paper is organised as follows: in Section 5.2 we describe the CMOS camera and its capabilities. In Section 5.3 we describe the laboratory set up, the telescope configuration and the observations. Our methodologies of laboratory and on-sky tests are described in Section 5.4. In Section 5.5 we present our results and discussion and in Section 5.6 we set out our conclusions.

5.2 The Toran 26B CMOS Camera

The Toran 26B CMOS camera is equipped with the IMX571 sensor. The camera has 2 imaging modes at different bit depths, referred to the low noise (LN) in 10-bit, 11-bit, 12-bit and 16-bit and the high well capacity (HWC) in 16-bit. For our lab-test and on-sky test applications, which use FITS images format, we primarily operated in 16-bit for both HWC and LN modes. The camera can

[1] `https://andor.oxinst.com/`

Table 5.1: Specifications of the sensor for the Toran 26B camera taken from the manufacturer sheet, and configuration on TWIST telescope.

Parameter	Value/Description
camera	Toran 26B
Sensor Type	CMOS
Model	IMX571 Sony
Active pixels	4176×6252
Pixel size	$3.76 \times 3.76\,\mu m$
Sensor size	15.7×23.5 mm
Peak Response	>90% @500 nm
Bit depths	10-bit, 11-bit, 12-bit, 16-bit
Shutter type	Rolling shutter
TWIST Pixel angular scale	0.225 arcsec pixel^{-1}
TWIST Field Of View	36.1×24.1 arcmin^2

be connected via either a USB 3.2 or a CoaXPress interface.

5.3 Optical bench, Telescope and Observations

5.3.1 Laboratory Setup

A DC-powered light rig, equipped with 4-volt blue 4-LED arrays, positioned in such a way to provide quasi-flat illumination, was used as the light source. This setup provided a stable, constant and collimated light output with a peak wavelength centered at 465 nm. The rig features a cylindrical design, with the light source positioned at one end and the camera mounted at the opposite end. The housing works effectively as a dark room, minimising internal reflections due to its black, anti-reflective paper that was attached in the housing. A diffuser is placed in front of the light source to ensure uniform and flat-field illumination during image acquisition. The full light rig setup, including the Toran 26B camera mounted at the left, is shown in Figure 5.1.

To estimate the quantum efficiency (QE) of the camera and the transmittance of the front window, we used a methodology and optical bench setup similar to that described in chapter 2, with the exception of the light source. We used a calibrated silicon photodiode (model S1337-1010BQ by HAMAMATSU), with sensitivity across the optical range and a peak responsivity at 960 nm. The photodiode current was measured using a Keithley picoammeter connected via an RS232 interface. For wavelength selection, we employed the Andor Shamrock SR-303i spectrograph as a monochromator. Illumination was provided by the CoolLED pe-4000 light source, which is optimised for fluorescence microscopy and delivers broadband light using 16 LEDs spanning wavelengths from 365 nm to 770 nm. The use of the spectrograph allowed us to interpolate between the discrete LED wavelengths, resulting in a finer wavelength sampling and a more accurate QE curve. The total process was controlled and operated via Python using the Andor SDK Python wrapper. The light source was operated manually to select the desired wavelengths during the measurement process.

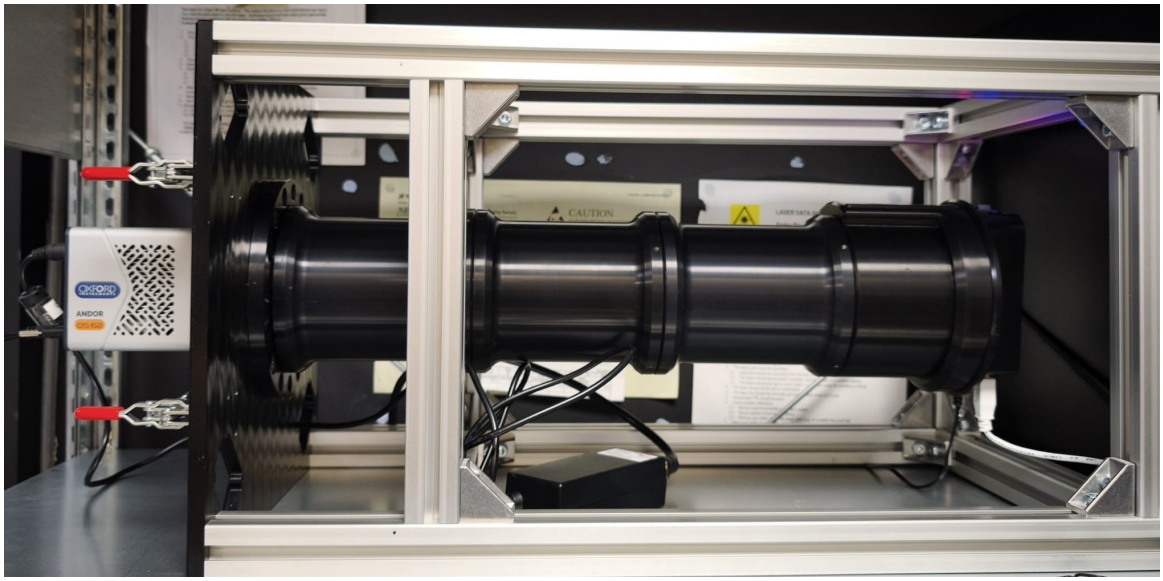


Figure 5.1: Optical bench setup for the Toran 26B camera. The black cylindrical component is the light tube, which accommodates the light source and the diffuser on the right side. The camera is mounted on the left side of the light tube.

5.3.2 Telescope configuration and Observations

After completing the laboratory tests, we installed the Toran 26B camera on the 50 cm aperture TWIST telescope located at the Observatorio del Roque de los Muchachos on La Palma, Canary Islands. The camera was connected to the control computer via a CoaXPress connection. TWIST consists of a PlaneWave Instruments $f/6.8$ CDK20 optical tube assembly (OTA) equatorially mounted on a L500 direct drive mount. The telescope configuration with the camera is shown in Figure 5.2.

Observations were conducted between August and September 2025. We made observations of well-known transiting exoplanets around stars including KELT (Pepper et al., 2018), Kepler host stars (Borucki et al., 2010), as well as confirmed TOI systems (Ricker et al., 2015). The target list is shown in Table 5.2. The telescope and camera were controlled using the `Rockit` observatory control system[2]. For consistency between nightly measurements, the CMOS camera was configured with a 10 second exposure time and a total cadence of 10.147 seconds, with the remaining time accounting for the readout. In our operation we did not employ filters. The images from the CMOS camera were saved as FITS files onto the CMOS control computer. Instrument parameters were saved into the FITS file headers, including the JD timestamps, telescope coordinates, and camera settings. In this paper we analyse data from 5 nights where a known transiting exoplanet system was observed, as show in Table 5.2. We use the field observed for KELT-16 (R.A. = $20^{\mathrm{h}}57^{\mathrm{m}}04\overset{\mathrm{s}}{.}4$, Dec = $+31°39'39\overset{''}{.}$) to analyse the noise performance of the camera. To this end, observations were obtained in both HWC and LN modes during bright nights (2025 August 06 and 08) and dark nights (2025 August 19 and September 21).

[2] `https://rockit-astro.github.io/`



Figure 5.2: The TWenty-Inch Survey Telescope equipped with the Toran 26B camera, shown in its enclosure at La Palma, Canary Islands.

5.4 Methods

5.4.1 Bias and Dark

The bias is measured in analog-to-digital units (ADU) and is intentionally added as an offset during the readout process to prevent negative signal values (Howell, 2000). We define the bias signal as the camera output under dark conditions and with the minimum possible exposure time. For our analysis, we acquired 75 bias frames. These frames were utilized both individually and as averaged stacks for temporal and spatial noise analysis, particularly for evaluating read noise and Dark Signal Non-Uniformity (DSNU). The resulting bias frames were also used to subtract the bias level from dark and illuminated images.

To measure the temporal noise, we adopted a similar approach to that described in chapter 2, analysing pixel-to-pixel variations in the bias frames that are independent of both signal and exposure time (Fowler, 2011). These pixel-to-pixel base fluctuations characterise the read noise. In addition, we examined individual rows and columns across the bias frames to investigate the behaviour of correlated noise arising from electronic interference within the camera circuitry or power supply fluctuations (Geurts et al., 2017). This structured noise, commonly referred to as row banding, is a known artefact in imaging systems (Wang et al., 2014; Karpov et al., 2019; Shao et al., 2024).

To assess the spatial noise, an average bias frame was created by median-stacking the individual bias images. We then assessed the pixel-to-pixel, column-to-column, and row-to-row variations within this averaged frame to quantify non-uniformities Jähne (2010); Apergis et al. (2025). This is know as DSNU. For the DSNU and readout noise measurements, the exposure time was set to its

Table 5.2: Transit observations.

Target	TIC ID	TESS Mag	$T_{\rm eff}$ (K)	Observation Date	Duration (hours)	Transit fraction
KELT-16 (Oberst et al., 2017)	TIC 236445129	11.43	5760 ± 130	2025 Aug 6	8.8	Full
KELT-16 (Oberst et al., 2017)	TIC 236445129	11.43	5760 ± 130	2025 Aug 8	8.9	Full
KELT-16 (Oberst et al., 2017)	TIC 236445129	11.43	5760 ± 130	2025 Aug 19	6.9	Full
KELT-16 (Oberst et al., 2017)	TIC 236445129	11.43	5760 ± 130	2025 Sep 21	6.9	Full
KELT-1 (Siverd et al., 2012)	TIC 432549364	10.22	5540 ± 140	2025 Aug 10	5.5	Full
Kepler-41 (Santerne et al., 2011)	TIC 271042217	13.90	5660 ± 113	2025 Aug 12	7.0	Full
Kepler-670 (Morton et al., 2016)	TIC 27990610	14.48	5530 ± 110	2025 Aug 16	6.0	Full
Kepler-76 (Faigler et al., 2013)	TIC 138644215	12.89	6300 ± 126	2025 Sep 9	6.3	Full

minimum value at 8.35×10^{-5} s for both LN and HWC mode.

We analyse dark frames which are acquired with a certain exposure time under dark conditions. During exposure, the system heats up, generating thermally-induced electrons known as dark current. We investigate the dark current at various temperatures to quantify its level and to identify any additional artefacts or signals, such as sensor glow (Janesick et al., 1985) as has been observed in other CMOS camera models (Karpov et al., 2019; Wang et al., 2020; Qiu et al., 2021; Layden et al., 2025; Apergis et al., 2025).

5.4.2 Photo Response and Linearity

To measure the electron to ADU conversion factor (gain) we produce a photon transfer curve, which is a plot of the flux variance versus the mean flux level, as described by Janesick et al. (2007). We maintained stable illumination and varied the exposure time incrementally, capturing two consecutive frames at each step, ranging from low light levels up to sensor saturation. Each pair of frames was subtracted to eliminate the fixed pattern (or spatial) noise, isolating the temporal noise component.

To evaluate the pixel response uniformity, we estimated the Photo Response Non-Uniformity (PRNU) by acquiring images at approximately half of the sensor's saturation level. Averaging a large number of half-saturation signal level frames helps suppress temporal noise, allowing the fixed-pattern component to be isolated more effectively. Our method follows the procedures outlined in Jähne (2010) and implemented in chapter 2. PRNU is defined as the dimensionless ratio of fixed-pattern noise to the mean signal, and it quantifies the spatial variation in pixel responsivity across the sensor.

To assess the linearity of the sensor, we evaluated how the recorded signal increases with exposure time under constant illumination. Ideally, in a linear system, the signal should scale proportionally with exposure time. Any deviation from this linear relationship indicates non-linearity in the sensor response.

5.4.3 Quantum Efficiency and Transmission Window

To estimate the transmission of the camera window, we first measured the current of a calibrated photodiode across various wavelengths using different filter configurations, including a single spectrograph grating mirror. The spectrograph slit width was set to 400 μm, which was found to be sufficiently wide to transmit enough light while narrow enough to isolate a small wavelength band.

For each selected wavelength, we recorded 25 photodiode current measurements using a Keithley picoammeter and calculated the mean and standard deviation. This measurement procedure was then repeated with the camera window placed in front of the light path. By comparing the photodiode current values with and without the window, we estimated the transmission percentage of the window as a function of wavelength.

To determine the camera's QE, we acquired 10 images at each selected wavelength using an exposure time of 0.01 s, which provided a signal level close to half of the sensor's full-well capacity. The average pixel value across these frames was taken as the camera signal. Additionally, 10 bias frames were acquired and averaged for bias level subtraction. Dark current subtraction was omitted due to the sensor's negligible dark current at short exposure times. We extract the QE of the photodiode thanks to the responsitivity curve from HAMAMATSU website. We compared the signal values of the camera with the current values and the QE of photodiode and extract the QE for the camera. Our method is follows the steps and equations in subsection 2.4.7 in chapter 2 and Layden et al. (2025).

5.4.4 Image reduction and photometry

For each observation, we execute a custom pipeline to extract photometry for each observed field. We solve each image astrometrically using the World Coordinate System (WCS), accounting for the field centre and pixel scale, with the help of *astrometry.net* (Lang et al., 2010). While the software applies a simple polynomial model, we find that the solution can be less reliable near the image corners due to optical distortions. To mitigate this, we cross-match sources with the TESS Input Catalog version 8 (Stassun et al., 2018, TIC8), focusing on stars brighter than $T < 16$ mag. The distortion parameters in the initial WCS solution are iteratively refined until sub-pixel accuracy is reached (Chote et al., 2025). Images for which the WCS solution fails are excluded, typically representing less than 3 % of the night's observations. For our photometric analysis we selected isolated stars from the TIC8 catalogue. Stars with neighbours within 100 pixels and 1 delta magnitude of brightness were flagged as blended and rejected from our analysis. We also exclude stars located near the edges of the sensor.

For each observing run, a set of calibration images was obtained, including bias and flat-field frames. Dark frames were not acquired since the sensor exhibits a negligible dark current (see Section 5.5.3). Bias frames were obtained using the minimum exposure time. We used 21 bias frames and average them to construct the master bias frame. We followed the same procedure for the flat images, however, we also apply a normalisation to the master flat image and subtract the master bias signal. We subtract the master bias and divide the master flat from the science images.

To ensure that autoguiding was operating with sub-pixel accuracy, we used the `DONUTS` algorithm (McCormac et al., 2013) to assess the image alignment throughout the dataset. Given the pixel scale of 0.22 arcsec pixel^{-1}, few pixel shifts were expected under ideal conditions. However, since large photometric apertures were used, we adopted an upper limit of 4 pixels for allowable image shifts. Frames exceeding this threshold were excluded from the analysis, typically accounting for less than 0.6 % of the night's observations.

5.4.5 Photometry

We tested a range of aperture radii from 10 to 50 pixels, in steps of 10. Upon examining the resulting lightcurves, we found that an aperture radius of 30 pixels (6.6 arcsec) produced the lowest RMS scatter. Although this aperture size may not be optimal for faint stars, we adopted it for constructing the noise models for stars with $10 < T < 16$ (see Section 5.5.5). For specific targets, such as exoplanet transits, the aperture size was adjusted to achieve the best RMS scatter in the light curves.

We performed aperture photometry by extracting the stellar positions from the catalog and using the `SEP` Python package (Bertin & Arnouts, 1996; Barbary, 2016). Circular apertures with radii ranging from 10 to 50 pixels in steps of 10 were applied. For each star, an annulus was defined to estimate the local sky background, with the inner and outer radii set to 60 and 65 pixels, respectively, to ensure the background region remained well separated from the largest photometric aperture.

We detrended the light curves from atmospheric effect such as airmass, using comparison stars identified within each target's field. To select suitable comparison stars, we applied constraints on their color index ($G_{BP} - G_{RP}$), magnitude difference relative to the target star, and angular separation from it. The filtered stars were then subjected to an iterative selection process based on their photometric stability, quantified by the RMS scatter. Each candidate star's lightcurve is first corrected for airmass trends and normalised before computing the RMS of its residuals. The RMS values are plotted as a function of magnitude and grouped into magnitude bins. Within each bin, a spline fit is used to model the expected RMS trend as a function of brightness. Stars exhibiting RMS values more than 2σ above the median trend are excluded as outliers. This filtering procedure is repeated ten times to ensure a robust selection, progressively removing any variable or noisy stars, as illustrated in Figure 5.22. The remaining stable comparison stars were then combined to create a master reference lightcurve, which was used to correct systematics in the target star's lightcurve.

The entire process is repeated for different color indices, magnitude difference ranges, and angular separations. For each configuration, the RMS value of the target star is computed. The set of parameters that yields the lowest RMS value is then adopted for the final photometry of the target star.

5.4.6 System Noise

The total photometric noise comprises several components that can influence the quality of the data. As stellar fluxes propagate through the Earth's atmosphere, they experience fluctuations due to atmospheric turbulence (Osborn et al., 2015), introducing scintillation noise into the photometric measurements. We estimated the scintillation contribution following the approach described in (Mitchell et al., 2025), taking into account the scintillation coefficient as well as the telescope and observatory site parameters. The received flux from the source and the sky background follows the Poisson distribution. Instrumental noise components include the read noise and the dark current. The total noise for a given photometric aperture is summarised as (Howell, 1989):

$$\sigma_{\text{total}} = \sqrt{{\sigma_{\text{flux}}}^2 + {\sigma_{\text{sky}}}^2 + {\sigma_{\text{DC}}}^2 + {\sigma_{\text{RN}}}^2 + f^2{\sigma_{\text{sc}}}^2}, \tag{5.1}$$

where f is the flux from the target star, σ_{flux} is the shot noise from the target star, σ_{sky} is the sky background noise, σ_{DC} is the dark current noise, σ_{RN} is the read noise and σ_{sc} is the scintillation

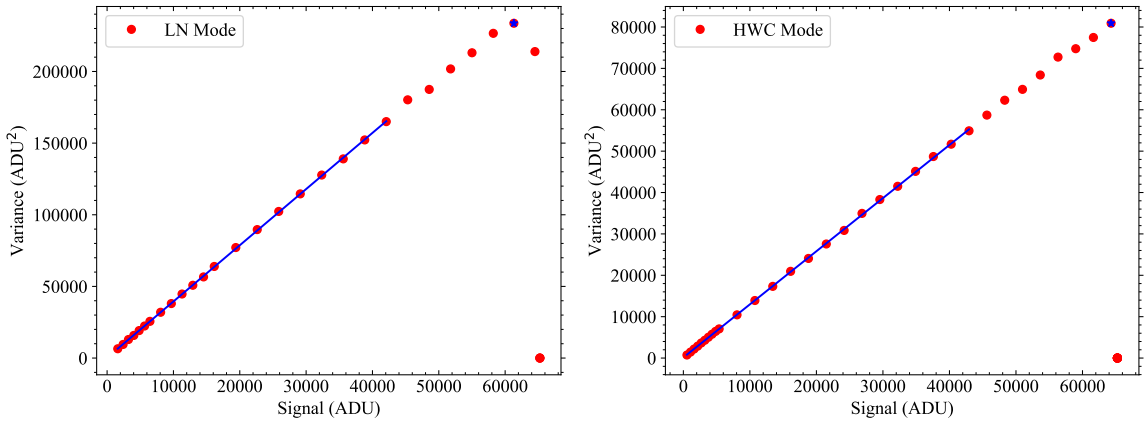


Figure 5.3: Photon transfer curves for the Toran 26B camera at 0 °C. **Left:** The LN image mode. **Right:** The HWC image mode. The solid blue line is a best fit linear model. The data point with the highest variance is marked with a blue star, and indicates the FWC value.

noise.

We examined the photometry of our target stars to assess the presence of correlated (red) noise in the light curves. This was achieved by binning the data as a function of time and analysing how the RMS value of the residuals changes with increasing bin size. For light curves dominated by uncorrelated (white) noise, the RMS is expected to decrease proportionally to the inverse square root of the number of points per bin, following the relation RMS $\propto 1/\sqrt{n}$. In contrast, if the RMS deviates from this white noise trend, by decreasing more slowly with binning, it indicates the presence of time-correlated noise. We apply this method by averaging the RMS values of a sample of stars, randomly selected when possible, at different magnitudes.

5.5 Results, Analysis and Discussion

5.5.1 PTC, PRNU and Linearity measurements

To measure the PTC in HWC mode, we began with an exposure of 0.01 seconds, incrementing by 0.01 seconds up to 0.1 seconds. Beyond this point, the step size was increased to 0.05 seconds until saturation was reached at 1.6 seconds. In LN mode, the sequence also started at 0.01 seconds, but with an initial step size of 0.005 seconds up to 0.1 seconds. From there, the exposure time was incremented by 0.02 seconds until saturation occurred at 0.46 seconds. The mean signal of the consecutive frames and the variance of the subtracted same consecutive frames was plotted for each exposure step as show in Figure 5.3. The PTC appears fairly linear without significant deviations that have been seen in other CMOS camera models (Qiu et al., 2021; Khandelwal et al., 2024; Apergis et al., 2025) that utilise two channels to produce a high dynamic range image.

A linear fit was applied to the photon-transfer curve over the range 0–70 % of the saturation level. The inverse slope of this fit gives the system gain, which was found to be 0.779 e^-/ADU for the HWC mode and 0.255 e^-/ADU for the LN mode. The full well capacity was then estimated from the signal level at the maximum variance point, converted from ADU to electrons using the measured gains. This gave full well capacities of 15,700 e^- for the LN mode and 50,000 e^- for the HWC mode.

The mean signal was analysed as a function of exposure time to assess the system's linearity. A

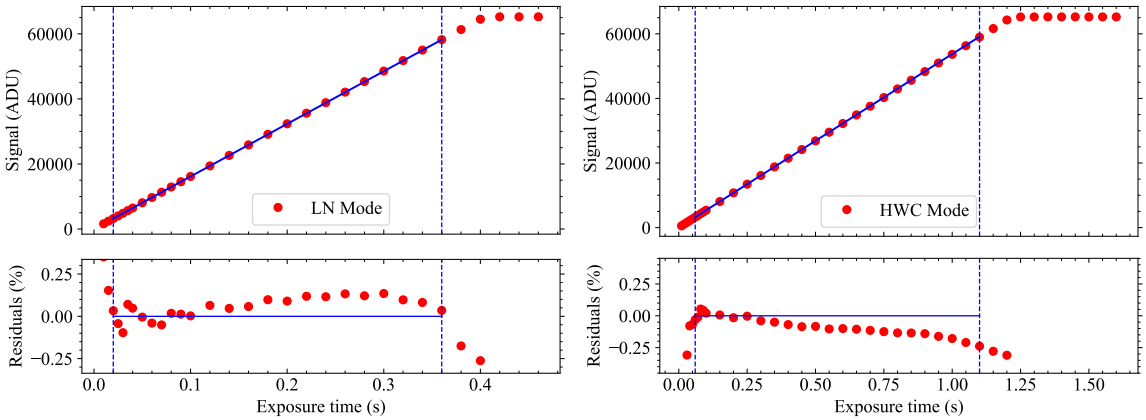


Figure 5.4: Linearity measurements for the Toran 26B camera at 0 °C. **Left:** The LN image mode. **Right:** The HWC image mode. The best fit linear model between 5 and 95 % of saturation is plotted with a blue solid line. Residuals to the linear model are shown in the bottom panels. The dashed horizontal blue lines indicate the 5 to 95% boundaries we set to measure fit the linearity.

linear line was fitted to the measured signal versus exposure, and the residuals were used to quantify the system's non-linearity. The fit employed inverse weighting following the method described in Jähne (2010) and implemented in section 5.4 in chapter 2. The non-linearity was measured within 5 % to 95 % from the saturation as the average absolute deviation of the residuals as show in Figure 5.4. The non-linearity was found to be 0.067 % for the LN mode and 0.09 % for the HWC mode.

To ensure sufficient sampling for estimating the PRNU while avoiding system memory issues, we stacked 500 images in a buffer, following the approach described in Jähne (2010). The measured PRNU was 0.076 % for the LN mode and 0.050 % for the HWC mode. The slightly broader distribution in the LN mode is consistent with its higher PRNU value. The PRNU distribution is shown in Figure 5.5.

5.5.2 Bias level Spatial and Temporal Noise

For each of the 75 bias images, we study pixels individually by reporting the standard deviation and mean values. Our results are illustrated in Figure 5.6. The distribution of the read noise is described with long tail in the histogram, which implies that the pixels are not represented by the same read noise. This feature is a common feature in CMOS sensor since each pixel has its own circuitry. Noisy amplifiers, and Random Telegraph Signal behaviours cause noisy pixels (Tsai et al., 1994; Wang et al., 2006). Nevertheless, the mean and median read noise for the Toran 26B camera was found to be 1.28 e^- and 1.07 e^- for the LN mode and 3.19 e^- and 2.79 e^- for the HWC respectively.

For each of the 75 bias images, we analysed the temporal noise along rows and columns by computing the standard deviation and mean values. The distributions of the column and row temporal noise are shown in Figure 5.7 and Figure 5.8, respectively. The mean column temporal noise was measured to be 0.023 e^- in LN mode and 0.056 e^- in HWC mode. The corresponding mean row temporal noise was 0.064 e^- for LN mode and 0.173 e^- for HWC mode. These values are significantly lower than the overall system read noise, indicating minimal fluctuation in the column-level amplifiers and minimal contribution from the row banding. In contrast, the row temporal

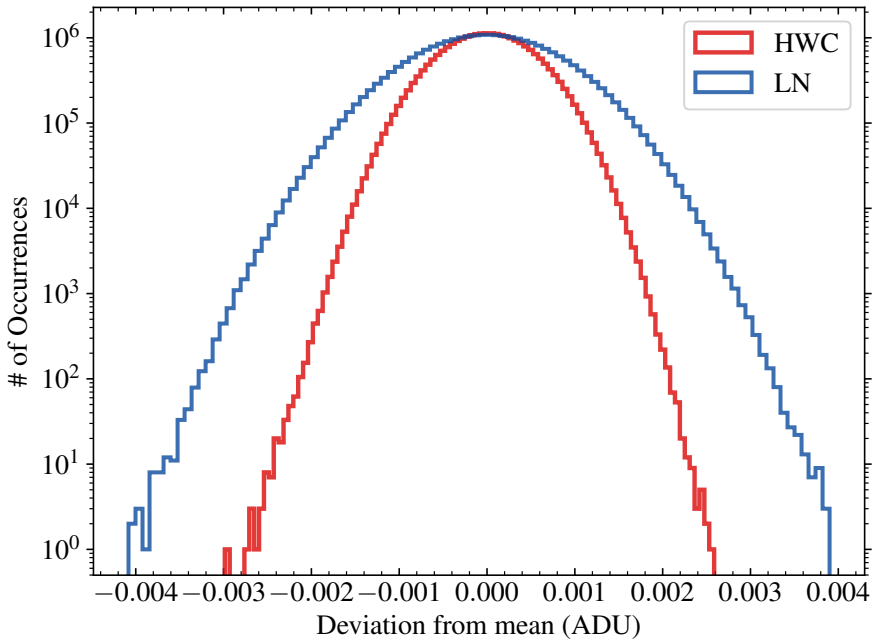


Figure 5.5: Histogram distributions of the photo response non-uniformities for both modes. The red bins indicate the HWC while the blue the LN mode.

noise shows a more pronounced difference between the two modes, suggesting increased row-level variability in HWC mode.

To evaluate the spatial noise distribution across the image, we averaged 75 bias frames by computing the mean value at each pixel position, thereby constructing a representative averaged bias image. Given the use of a CMOS sensor, it is important to investigate the different contributions to the DSNU specifically, the total, pixel, row, and column components, to determine whether the dominant spatial noise arises from pixel-level variation or from fixed patterns from row or column. The results are presented in Figure 5.9, where the mean bias level has been subtracted, and the residuals corresponding to the total, row, and column DSNU are shown. The residual distributions are highly uniform and follow a Gaussian profile. For the LN mode, the distribution is narrower compared to the HWC mode.

Additionally, to investigate potential pixel-to-pixel dependencies, we examined whether correlations exist between neighbouring pixels. Specifically, we analysed the spatial autocorrelation of the bias level using a 20×20 pixel sub-frame, measuring how strongly the central pixel is correlated with its surrounding pixels. No significant spatial correlation was observed in either LN or HWC mode between the central pixel and its neighbours (see Figure 5.20).

5.5.3 Dark frame structure and Dark Current

The IMX571 sensor exhibits remarkably low dark current even at relatively high operating temperatures, outperforming typical CCDs operating at 0 °C (Alarcon et al., 2023a; Ge et al., 2022). The Toran 26B CMOS camera features a low dark current (LDC) mode, which further reduces the dark signal. An example of a one-hour exposure after bias subtraction and normalisation by exposure time, is shown in Figure 5.10. The mean values are 0.001 e^- pix^{-1} $s^{-1}$for the LN mode

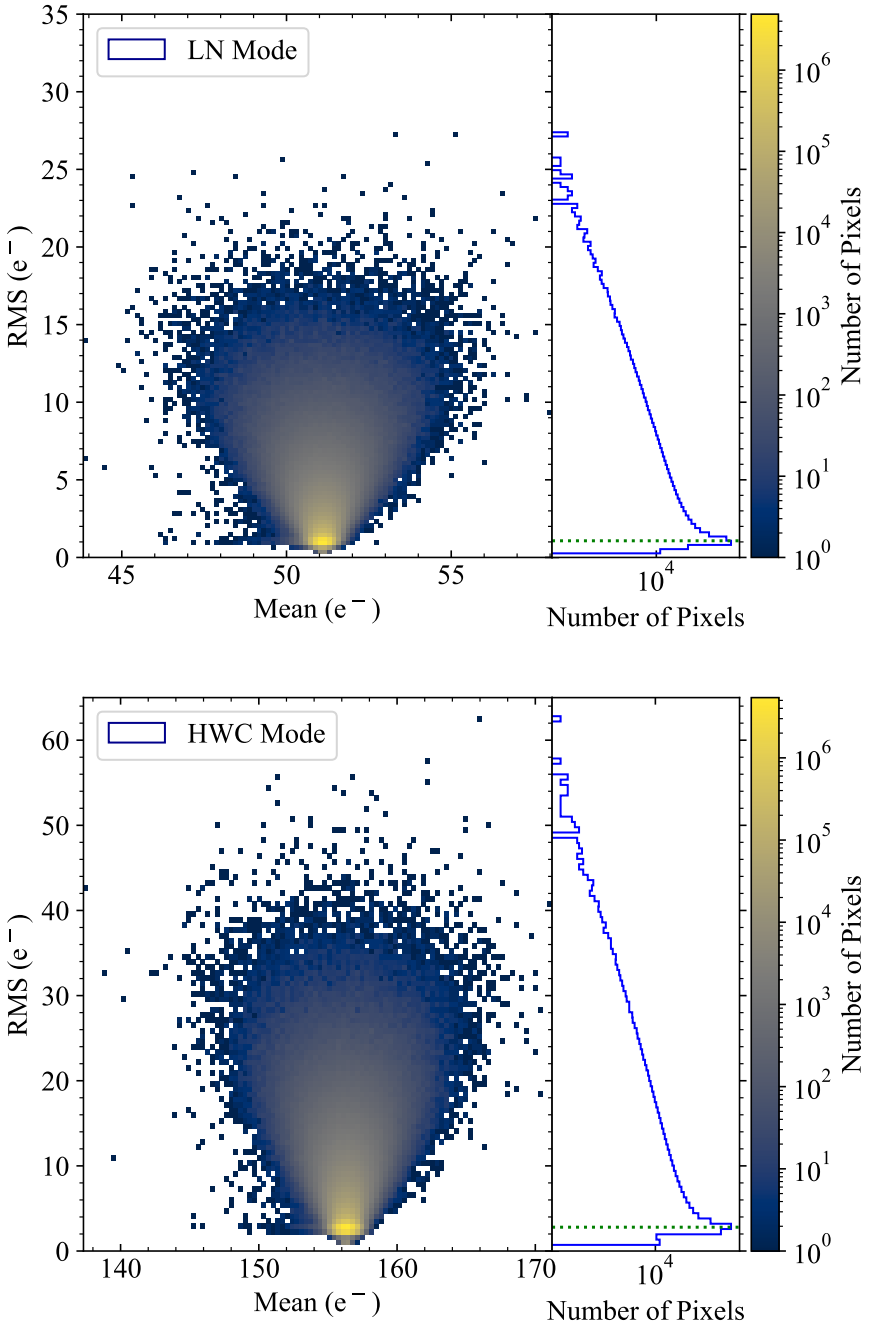


Figure 5.6: Read noise distribution derived from 75 consecutive bias frames. The 2-D histogram represents the temporal noise calculated from the mean and standard deviation of each pixel across all frames, with the colour bar indicating the number of pixels. The blue histograms show the logarithmic distribution of the read noise, with the median value marked by a green dotted line. **Top:** Median read noise distribution for the LN mode. **Bottom:** Median read noise distribution for the HWC mode.

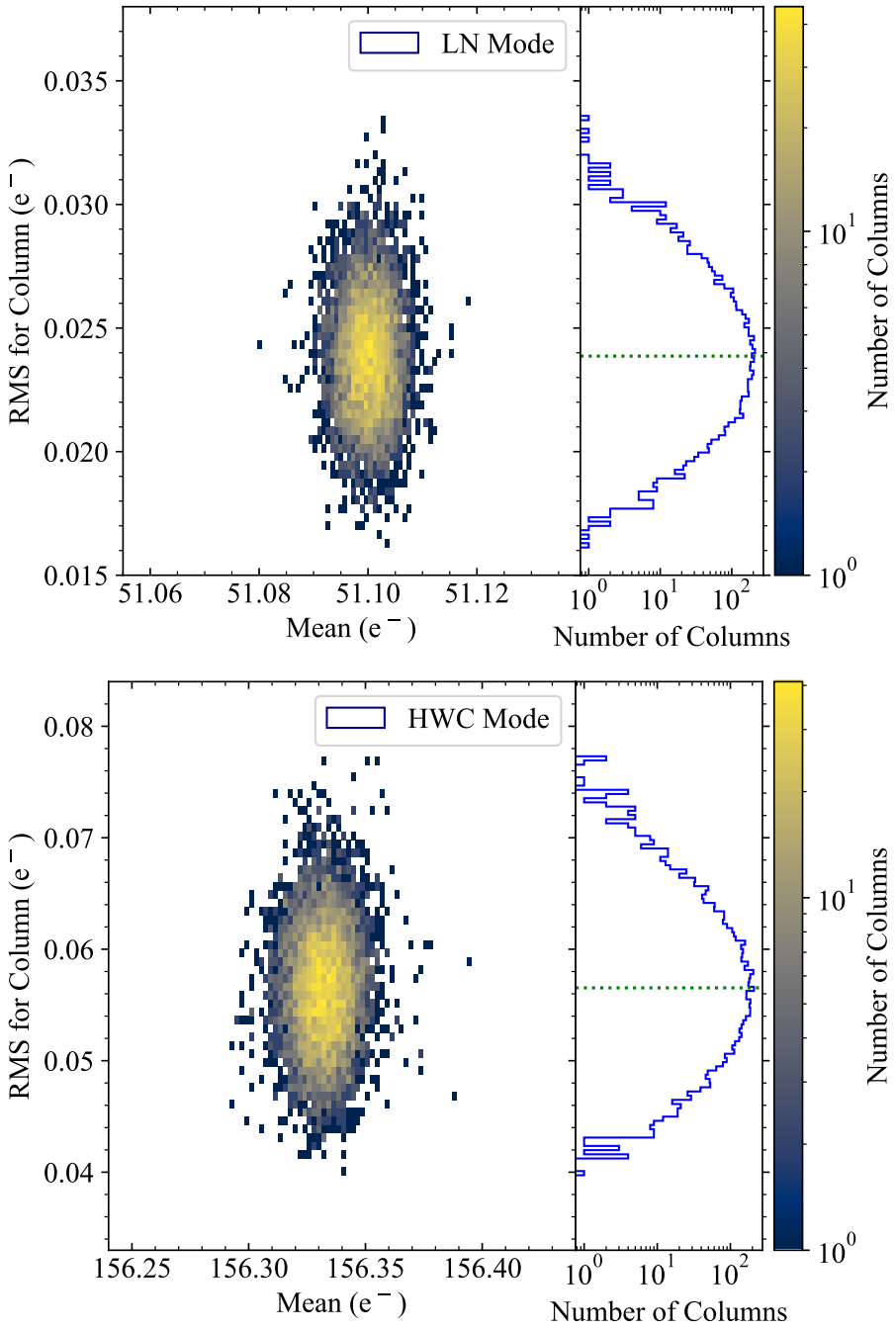


Figure 5.7: Column noise distribution using 75 consecutive bias frames. The 2-D histogram corresponds to row temporal noise and the mean of each row from these frames while the colour bar indicates the number of rows. The logarithmic row noise distribution is show in the blue histograms, with the median value as a green dotted line. **Top:** Mean row noise distribution for the FFR mode. **Bottom:** Mean row noise distribution for the HDR mode.

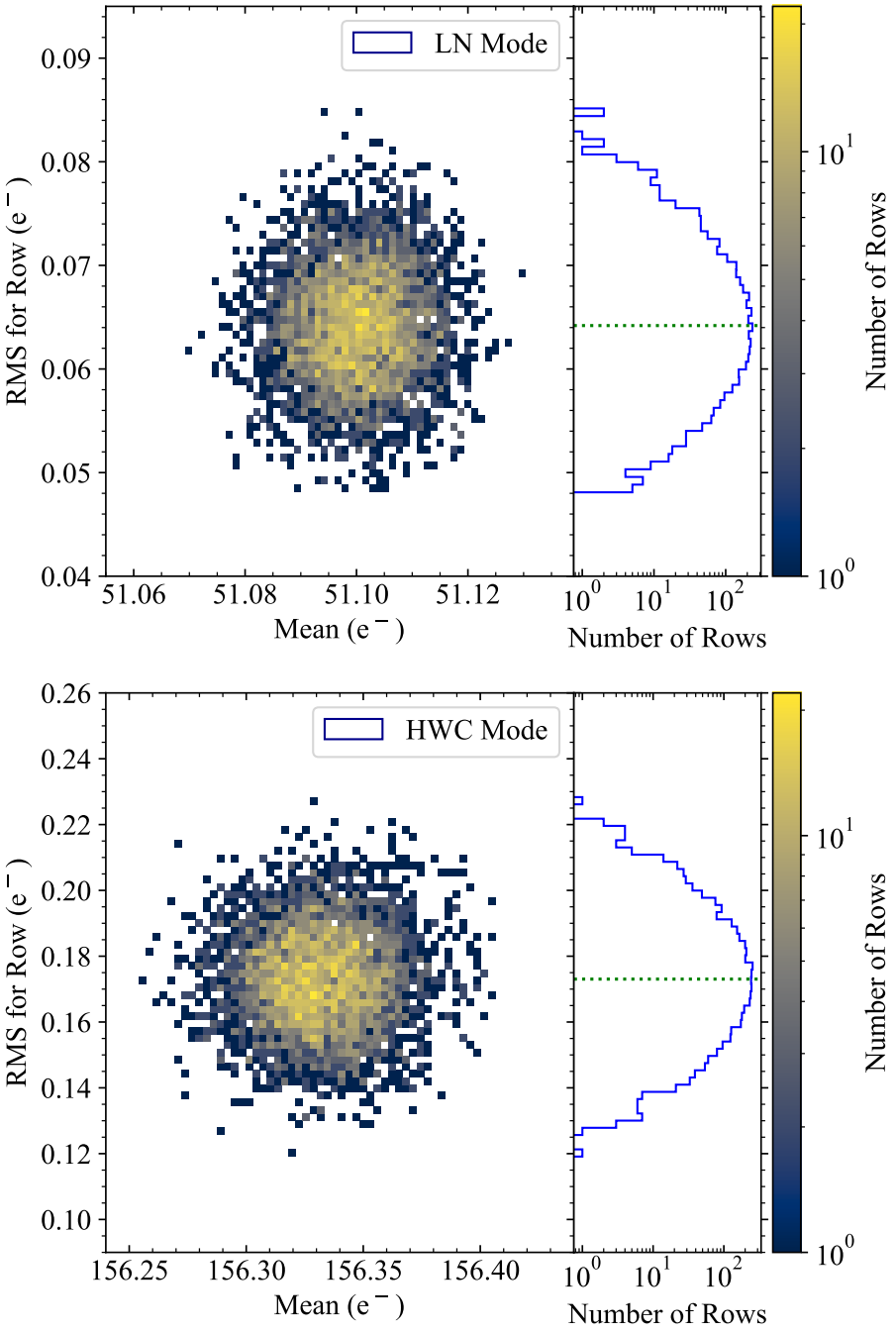


Figure 5.8: Row noise distribution using 75 consecutive bias frames. The 2-D histogram corresponds to row temporal noise and the mean of each row from these frames while the colour bar indicates the number of rows. The logarithmic row noise distribution is show in the blue histograms, with the median value as a green dotted line. **Top:** Mean row noise distribution for the LN mode. **Bottom:** Mean row noise distribution for the HWC mode.

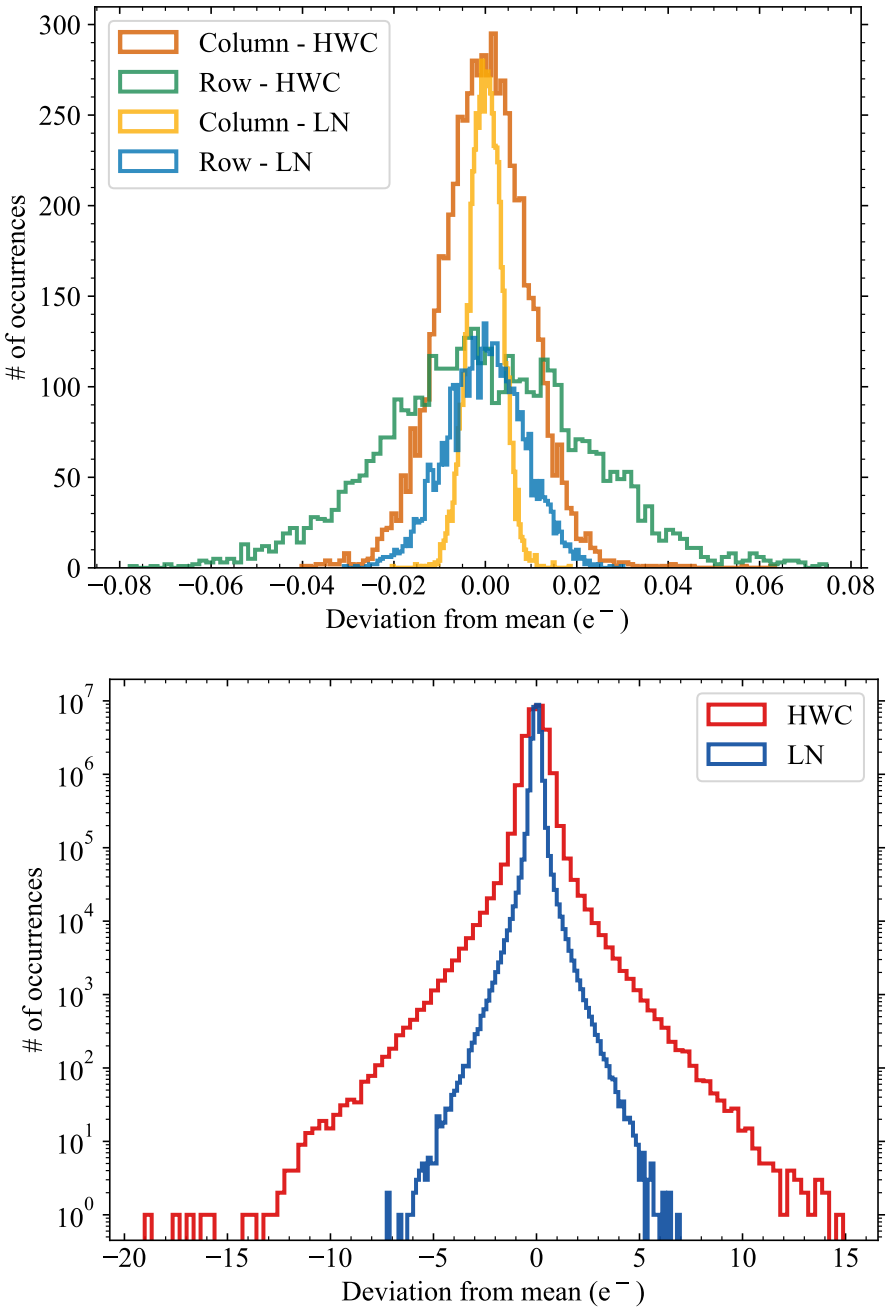


Figure 5.9: Histogram distribution of the DSNU for both modes modes. **The top** panel displays the distribution of row and column DSNU after subtracting the spatial mean level. **The bottom** panel shows the distribution of image DSNU, also after subtracting the spatial mean level.

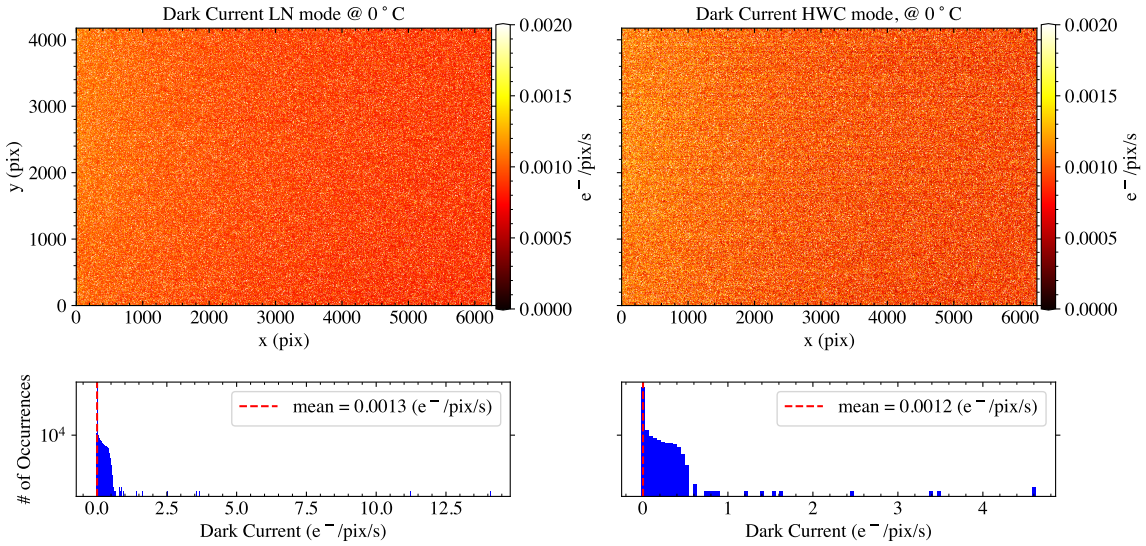


Figure 5.10: Dark images taken for Toran 26B with LDC at temperature of 0 ° C. **Left** is the LN mode. **Right** is the HWC mode. Below each we show the histograms of pixel value distributions from each frame, along with the mean (red dashed line).

and 0.001 e^- pix^{-1} $s^{-1}$for the HWC mode. For comparison, dark current frames acquired without the LDC mode are presented in Figure 5.19 with mean values of 0.009 e^- pix^{-1} $s^{-1}$for both modes demonstrating the effectiveness of the LDC mode. In these images, hot pixels are clearly visible, although the mean signal level remains low. The extended tail observed in the pixel histograms likely originates from noisy pixels, hot pixels, or pixels exhibiting RTS behaviour. Additionally, the images reveal a brighter region on the left side of the sensor array, which may indicate either light leakage accumulated over the one-hour exposure or glow emission from the sensor.

5.5.4 QE and Window Transmittance

QE measurements were performed on two separate days, both conducted at a stable temperature of 0°C, as shown in Figure 5.11. To account for the window transmittance, we measured the current of the photodiode with the window in front of the light source. The measured QE curve exhibits a sharp rise toward the blue end of the spectrum, reaching a prominent peak of 84 % at 500 nm. This behaviour is characteristic of a thinned, back-illuminated sensor architecture. Beyond 550 nm, the QE begins to decline steadily across the green and red portions of the spectrum.

Our results are consistent with previous studies conducted on Sony's IMX455 and IMX411 sensors. For instance, Alarcon et al. (2023a) and Betoule et al. (2023) reported similar QE behaviour, with the IMX411 reaching a peak of 83 % at 490 nm. In the near-infrared region (around 800 nm), our data align with these findings, showing a QE of approximately 20 %. However, Gill et al. (2022) and QHYCCD have reported higher QE values, with peaks near 92 % at 490 nm.

The fractional ratio of the photodiode current measured with and without the camera window is plotted in Figure 5.12, illustrating the transmission curve of the camera's front window. Our measurements generally align with the manufacturer's model, though we observe slightly higher transmission at bluer wavelengths than reported. Due to the lack of data in the ultraviolet range, we cannot confirm whether a significant transmission drop occurs at shorter wavelengths. Nonetheless,

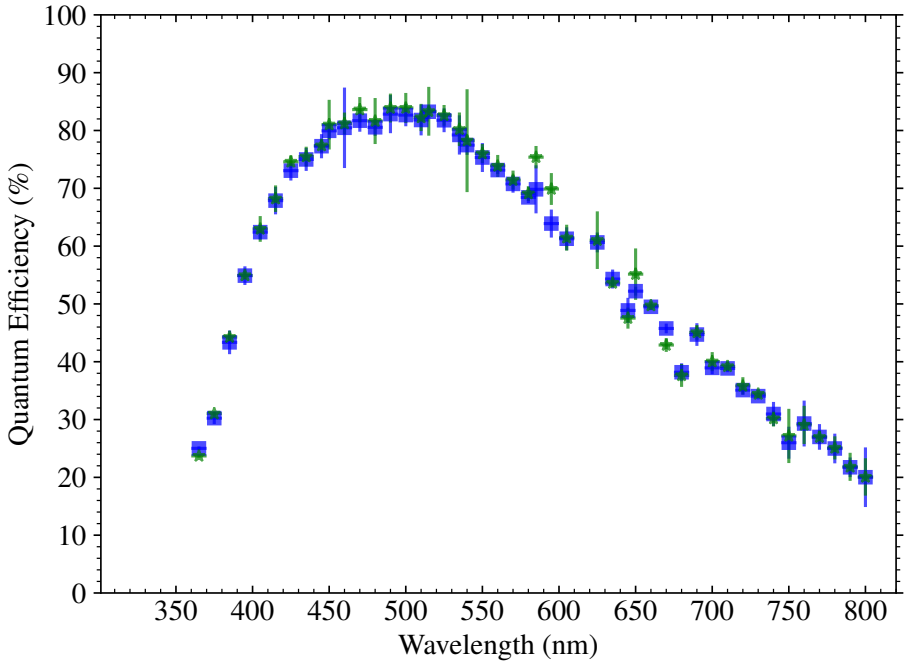


Figure 5.11: QE for the Toran 26B camera at constant temperature of 0 °C. With squares is the first measurement taken and with stars the second measurement taken.

the data suggest that the window is coated to suppress UV and shorter-wavelength light, likely to reduce unwanted signal contributions.

5.5.5 Noise models from on-sky tests

We perform on-sky measurements by comparing the observed stellar noise with the theoretical noise model, which accounts for instrumental contributions such as read noise and dark current, as well as sky background noise, target shot noise, and atmospheric scintillation. We used the read and dark current noise values derived in Sections 5.5.2 and 5.5.3. To model the sky background noise, we extracted the median value of the night's sky level. Parameters specific to the TWIST telescope were incorporated, including the telescope diameter, elevation above sea level, atmospheric scale height, airmass and exposure used. The median empirical coefficient quantifying the scintillation amplitude for each night was adopted from (Osborn et al., 2015) and was set to 1.30. These quantities were applied to a modified version of Young's formula (Young, 1967; Osborn et al., 2015). Finally, all noise components were scaled using a synthetic flux array representing shot noise. The extracted magnitudes were calibrated against TESS magnitudes using the measured zeropoint, and all noise terms were combined to produce the total noise model. Results were obtained for a field centered at KELT-16 star for four observing nights: two using the HWC mode under both bright (moon) and dark (no-moon) night conditions as shown in Figure 5.13, and two using the LN mode under bright and dark night conditions as shown in Figure 5.14.

For the HWC and at the bright night case, the sky background is the dominant noise source for stars fainter than T > 12.5 mag, while scintillation noise becomes the primary contributor for brighter stars. Under dark night conditions, the dominant noise source for faint stars (T > 13.5 mag) is the read noise. In the intermediate magnitude range (11.5 < T < 13.5 mag), shot noise dominates,

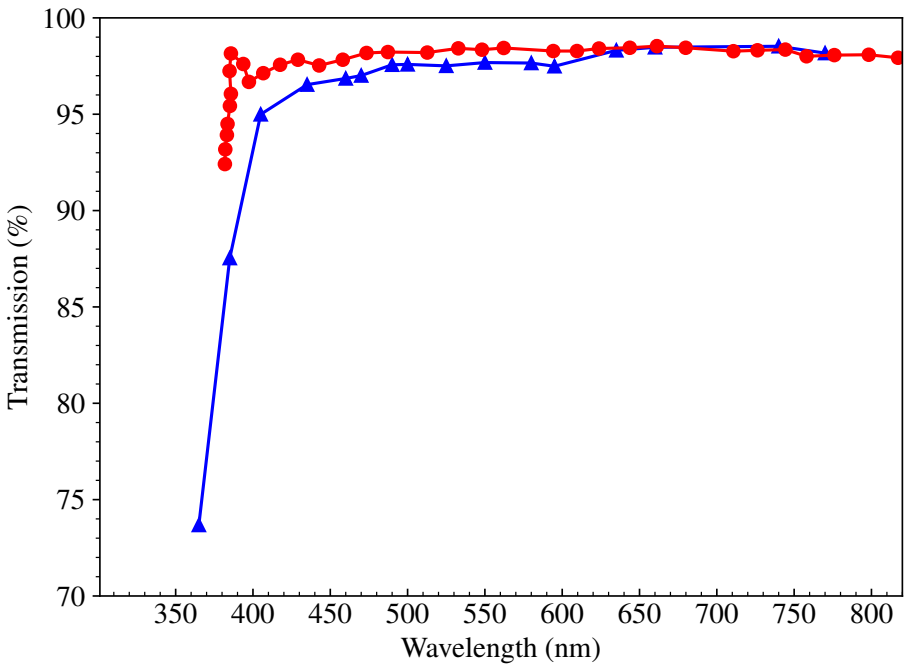


Figure 5.12: Transmission as a function of wavelength for the window which is mounted on the Toran 26B camera measured as the fractional percentage ratio of the photodiode current measurements with and without the window. The measured data is shown with triangles for comparison is the transmission curve from Andor with circles. The y-axis is zoomed-in for detailed visualisation.

and scintillation noise prevails for the brightest stars. Consequently, under certain sky brightness levels and with 10 second exposures, the HWC mode in this telescope configuration can become camera-noise limited.

For the LN mode and at the bright night case, the sky background is the dominant noise source for stars fainter than T > 10.5 mag. In dark night conditions, the sky background dominates for stars fainter than T > 14.5 mag, while shot noise is the main contributor for stars in the range 11.5 < T < 14.5 mag. In both LN cases, scintillation noise is dominant for the brightest stars. Under these conditions and with 10 second exposures, the LN mode is never camera-noise limited in this telescope configuration.

We directly compare the noise models by calculating the ratio of the RMS values of the stars between the two modes for the dark night dataset, as shown in Figure 5.15. Our results indicate that the HWC mode consistently produces higher noise compared to the LN mode. However, this comparison should not be considered definitive, as the datasets were acquired approximately one month apart. It is worth noting that, in the fainter regime (13.5 < T < 16), the LN mode exhibits lower limited noise levels because it is dominated by sky background noise rather than read noise, which is prominent in the HWC mode. Under dark-night conditions, this conclusion remains valid, as the one-month separation between the observations has a negligible effect on this regime.

5.5.6 Timescale of noise from on-sky tests

To evaluate the presence of correlated noise in our light curves, we separate our sample stars into six magnitude regimes. Within each regime, we computed the average RMS of the residuals as a

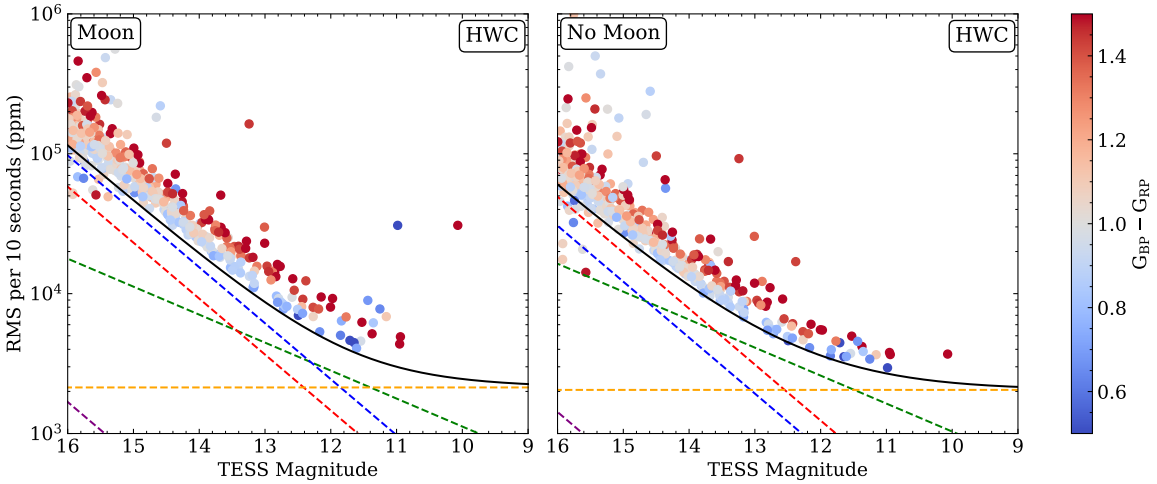


Figure 5.13: Photometric precision as a function of stellar magnitude for 10-second exposures, comparing predictions from the theoretical noise model with observations obtained on a bright night (6 August 2025, left) and a dark night (19 August 2025, right). The data was recorded with with the HWC mode of the camera. The dark line indicates the total modelled noise, including contributions from scintillation (yellow), photon shot noise (green), dark current noise (purple), sky background noise (blue), and read noise (red). Measured noise values, derived from detrended relative photometry light curves of 457 stars with $9 < T < 16$ in a field centered on TIC-236445129 (KELT-16), are plotted as coloured points, where the colour scale represents the *Gaia* DR3 $G_{BP} - G_{RP}$ index.

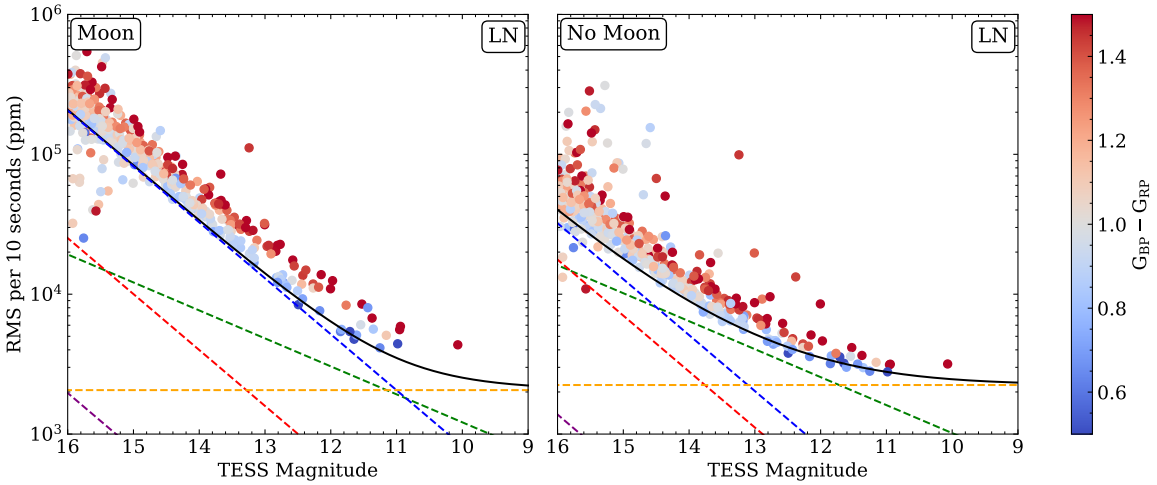


Figure 5.14: Photometric precision as a function of stellar magnitude for 10-second exposures, comparing predictions from the theoretical noise model with observations obtained on a bright night (8 August 2025, left) and a dark night (21 September 2025, right). The data was recorded with with the LN mode of the camera. The dark line indicates the total modelled noise, including contributions from scintillation (yellow), photon shot noise (green), dark current noise (purple), sky background noise (blue), and read noise (red). Measured noise values, derived from detrended relative photometry light curves of 457 stars with $9 < T < 16$ in a field centered on TIC-236445129 (KELT-16), are plotted as coloured points, where the colour scale represents the *Gaia* DR3 $G_{BP} - G_{RP}$ index.

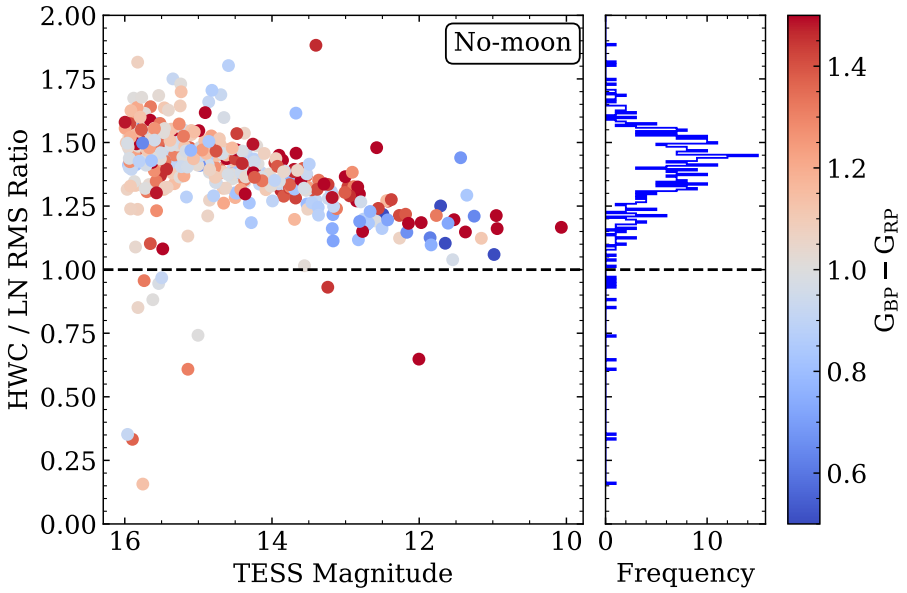


Figure 5.15: Ratio for HWC and LN camera mode of the noise contribution for different magnitude stars from Figure 5.13 and Figure 5.14. The data points are coloured according to the catalogued *Gaia* DR3 $G_{BP} - G_{RP}$ colour. The black dashed line represents the ratio 1 which is the case where the noise is the same for both cameras. The noise ratio for a dark night (no-moon). The right panel show the histogram distribution.

function of binning time, with time bins ranging up to 1800 seconds. This analysis was performed for both the HWC and LN observing modes under dark night conditions, as illustrated in Figure 5.16.

Due to the limited number of bright stars in the range $10 < T < 13$, the sample size in these regimes was smaller than 40 and not randomly selected, since all available stars were used. In these cases, we observed noticeable correlated noise, particularly starting at the 200 seconds binning scale. A few stars in these bright regimes exhibited strong correlated noise contributions, which likely influenced the average noise timescale. Overall, the LN mode showed slightly lower correlated noise levels compared to the HWC mode. Specifically, the minimum RMS at 30-minute binning reached 500 ppm for LN and 700 ppm for HWC.

For the fainter regimes ($13 < T < 16$), we randomly selected 40 stars. In these cases, the RMS as a function of binning time follows the expected white-noise behaviour. The binned RMS values closely follow the theoretical uncorrelated noise trend, with the LN mode again exhibiting slightly lower overall RMS than the HWC mode.

We note that the differences observed between the two modes should not be taken as a rule of thumb, since the observations were conducted approximately a month apart and the sky conditions may have differed between the two epochs.

5.5.7 Transiting exoplanets from on-sky tests

A total of five successful nights of observations were carried out, targeting five well-known transiting exoplanet host stars, as summarised in Table 5.2. All targets are short period gas giants, predominantly classified as hot Jupiters. Relative photometry, described in Section 5.4.5, was applied to correct the

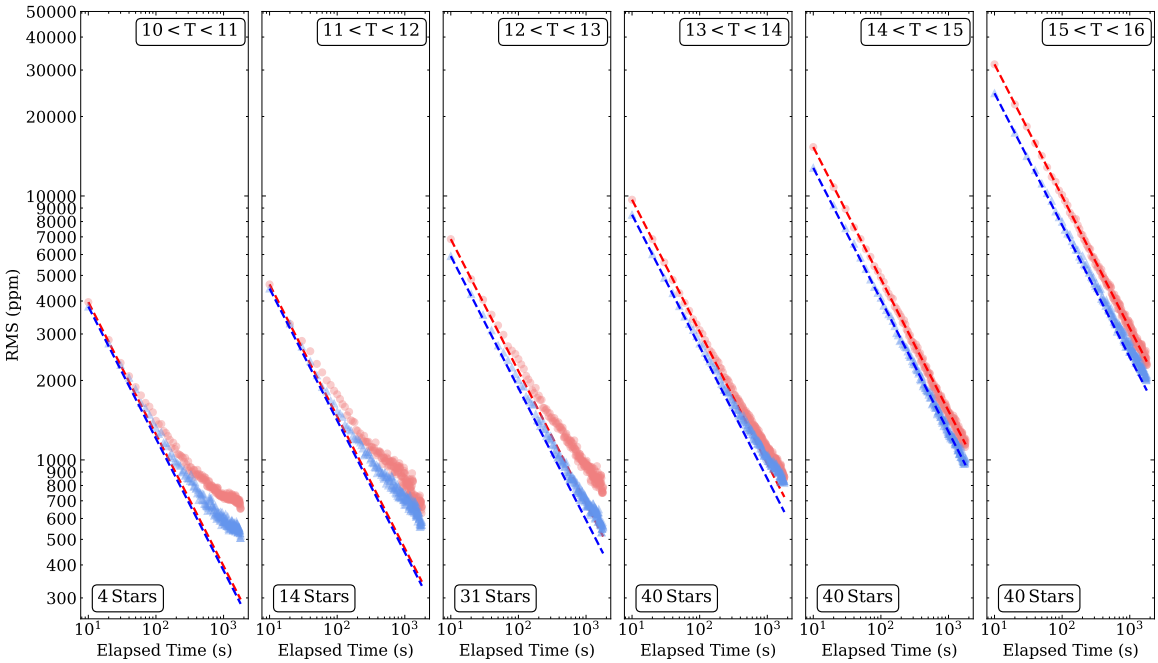


Figure 5.16: Noise levels for Toran 26B camera with the HWC mode (light red circles) and LN mode (light blue triangles) at varying timescales during observations conducted on the dark night of 2025 August 19 and 2025 September 21 respectively. The data is binned as a function of exposure and readout times. The blue and red dashed lines indicate the white noise model, proportional to $1/\sqrt{n}$ for the HWC and LN mode respectively. The RMS noise was measured from stars that are non-variable and non-saturated. The plots also shown the magnitude regimes, and the numbers of stars used.

light curves for systematic effects. As each target star differs in brightness, the photometric aperture was optimised individually to achieve the lowest RMS scatter in the resulting transit lightcurves.

For the transit modelling a similar approach was used as in section 4.3 in chapter 4. We used `allesfitter` package for modelling the transits (Günther & Daylan, 2019, 2021). To sample the model parameters, we applied additional detrending using a Gaussian Process with a Matérn 3/2 covariance kernel. This kernel is described by the logarithmic amplitude, $\ln(\sigma)$, and the logarithmic length scale, $\ln(\rho)$, allowing us to account for time-correlated systematics in the light curves. The transit models were computed with the `ellc` code (Maxted, 2016), which accurately represents the geometry and limb-darkening of transiting systems. Parameter estimation was performed using nested sampling (Skilling, 2004; Skilling, 2006), as implemented in `allesfitter` via the `dynesty` sampler (Speagle, 2020).

For the initial parameters of our five exoplanet systems, we adopted previously published solutions from the literature along with their associated uncertainties (see Table 5.2). These parameters include the orbital period P, planet-to-star radius ratio (R_B/R_A), semi-major axis ($(R_A + R_B)/a$), epoch of mid-transit ($T_{0,B}$), quadratic limb-darkening coefficients, and orbital inclination ($\cos i_B$). Given that these exoplanets are short-period systems, we assumed circular orbits and fixed both the eccentricity and argument of periastron to zero.

An example of a complete transit light curve is shown in Figure 5.17. The upper panel presents the unbinned lightcurve obtained from the relative photometry. Owing to the high quality and low level of systematics in the data, the Gaussian Process contribution was minimal, indicating that only limited detrending was required. The middle panel displays the light curve binned to five minute intervals, while the lower panel shows the residuals of the best fit model. The rest of our sample transiting light curves are provided in section 5.7. For each transiting exoplanet we provide the initial guesses that we used from existed literature to fit for the transit, as shown in Figure 5.3.

To quantify the consistency of the recovered transit parameters with the published literature values, we computed a statistical distance for each fitted parameter. For each system, the posterior median value returned by `allesfitter` was compared with the corresponding literature value used as the initial reference solution. The statistical distance was defined as:

$$\Delta_\sigma = \frac{\theta_{\rm post} - \theta_{\rm lit}}{\sqrt{\sigma_{\rm post}^2 + \sigma_{\rm lit}^2}}, \tag{5.2}$$

where $\theta_{\rm post}$ is the posterior median of the fitted parameter, $\theta_{\rm lit}$ is the literature value, $\sigma_{\rm post}$ is the posterior uncertainty from the fit, and $\sigma_{\rm lit}$ is the published literature uncertainty. For asymmetric posterior uncertainties, we used the posterior uncertainty in the direction of the literature value. For example, if the literature value was larger than the posterior median, the upper posterior uncertainty was used. For the mid-transit time, the literature ephemeris and its uncertainty were propagated to the observed transit epoch before computing Δ_σ, ensuring that the comparison was made at the same orbital cycle. This provides a direct measure of how far the fitted solution lies from the published solution in units of the combined uncertainty. Since each data set contains only a single observed transit, these fits are not expected to improve upon the published system parameters, which are based on multiple transits and longer time baselines. Instead, this comparison provides a consistency check, demonstrating whether the transit parameters recovered from TWIST agree with established

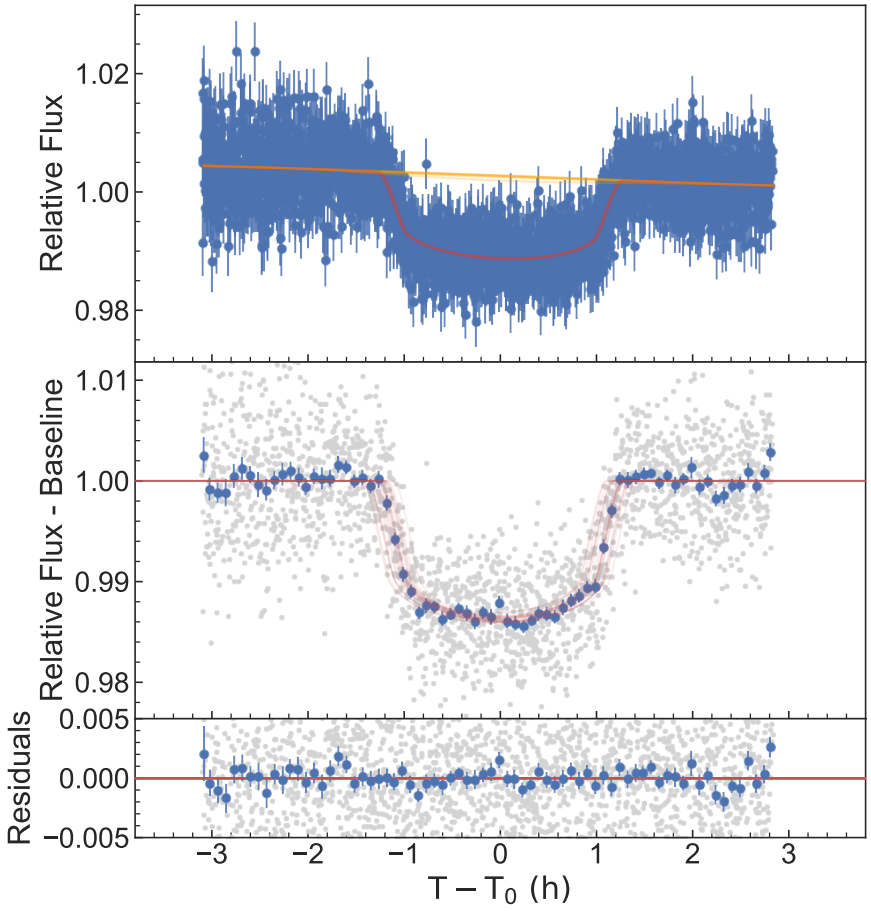


Figure 5.17: Normalized lightcurves for the transiting system of KELT-16 (TIC 236445129) (Oberst et al., 2017) from TWIST on 2025 August 6. **Top**: Undetrended light curves with the GP detrending function shown as yellow solid line and transit model shown with red solid line. **Middle**: Detrended lightcurve with data binned to 5 minutes (solid blue circles) for clarity. Again the best fit model is shown in red. **Bottom**: Residuals from the best fit.

Table 5.3: `allesfitter` model priors from Oberst et al. (2017). Planetary System properties for the transiting system KELT-16 (TIC 236445129), as illustrated in Figure 5.17, at NGTS on 2025 August 6.

Parameter	**Initial Guess**	**Prior**	**Fitted value Toran 26B**
$R_p/R_\star$	0.1070	$\mathcal{U}(0.1, 0.11)$	$0.10905^{+0.00067}_{-0.0013}$
$(R_\star + R_b)/a_b$	0.342724	$\mathcal{U}(0.34, 0.35)$	$0.3475^{+0.0017}_{-0.0021}$
$\cos i_b$	0.097583	$\mathcal{U}(0.097, 0.098)$	$0.09744^{+0.00036}_{-0.00028}$
T_c (BJD)	2458392.587691	$\mathcal{U}(2458392.586, 2458392.589)$	$2460892.5977^{+0.0055}_{-0.0039}$
Orbital Period (days)	0.9689951	$\mathcal{U}(0.965, 0.97)$	$0.9679^{+0.0013}_{-0.0018}$
q_1	0.323	$\mathcal{N}(0.323, 0.003)$	$0.3234^{+0.0033}_{-0.0029}$
q_2	0.376	$\mathcal{N}(0.376, 0.047)$	$0.353^{+0.040}_{-0.037}$

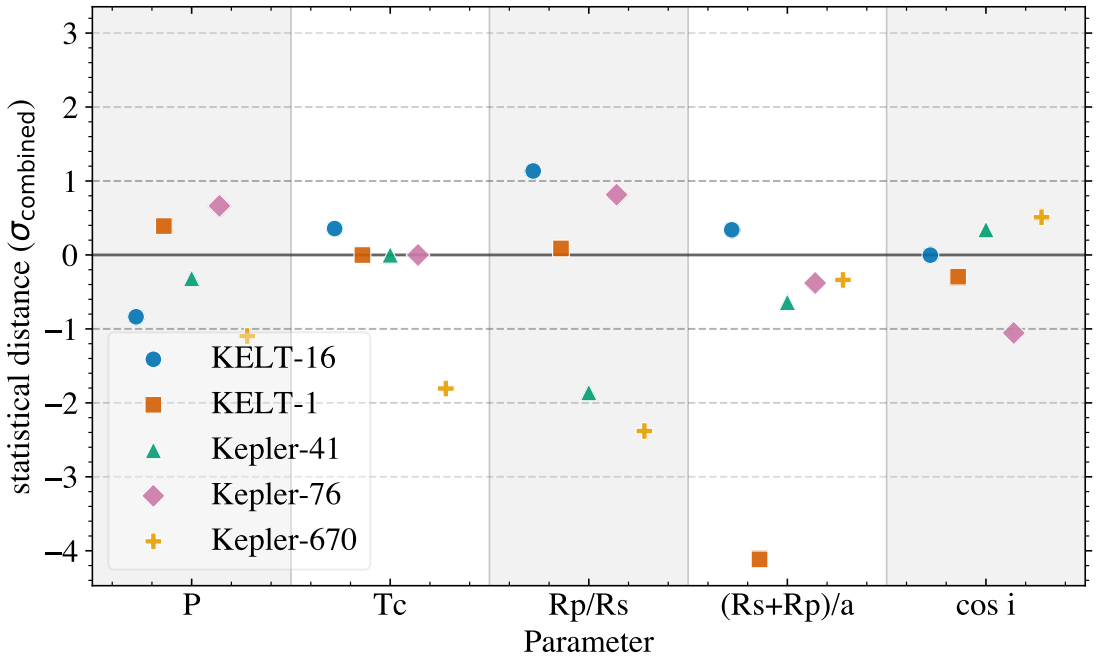


Figure 5.18: Statistical distance between the fitted posterior median values and the corresponding literature values for the transiting systems observed with TWIST. For each parameter, the plotted value is defined as $(\theta_{post} - \theta_{lit})/\sqrt{\sigma^2_{post} + \sigma^2_{lit}}$. Vertical columns separate the fitted parameters, and horizontal dashed lines mark integer sigma offsets from the literature solution.

literature solutions within the combined uncertainties.

5.6 Conclusions

We evaluated the performance of the Toran 26B CMOS camera through both laboratory and on-sky tests. The camera provides two 16-bit operating modes, the LN and HWC, each optimised for different performance characteristics. The HWC produces large well capacity, while the LN produces low read noise. On these combination the dynamic range is similar. In both modes, the read noise exhibited a skewed distribution, indicating that certain pixels are noisier than average, a behaviour commonly observed in many CMOS sensors. The dark current was found to be low and could be considered negligible for short time-series photometry, with no evidence of glow spots in the dark frames. Temporal row and column noise components showed minimal variation. The camera demonstrated good linearity across most of its dynamic range, with only minor non-uniformities detected. The QE measurements of the IMX571 sensor were consistent with previously published results (Alarcon et al., 2023a), though slightly lower than the peak sensitivity reported by some manufacturers. A summary of these results is provided in Table 5.4.

We successfully installed the Toran 26B CMOS camera on the TWIST telescope at the Roque de los Muchachos Observatory in La Palma, where we conducted photometric observations of well-known transiting exoplanets under a range of sky conditions. We estimated the expected photometric noise and compared it with theoretical predictions, finding an agreement between the two. The results

Table 5.4: Specifications of the Andor CMOS camera measured in this work in for the LN and HWC modes.

Camera mode	**LN Mode**	**HWC Mode**
Digital output	16-bit	16-bit
Quantum Efficiency Peak, %	84@500 nm	84@500 nm
Gain, $e^- ADU^{-1}$	0.255	0.779
Full Well Capacity, e^-	15664	50058
Non-Linearity, %	0.067	0.090
Read Noise, e^-	1.07	2.79
Dark Current LDC OFF $e^- pix^{-1} s^{-1}$	0.009@0°C	0.010@0°C
Dark Current LDC ON $e^- pix^{-1} s^{-1}$	0.001@0°C	0.001@0°C
PRNU, %	0.076	0.050
Row temporal Noise, e^-	0.064	0.173
Column temporal Noise, e^-	0.023	0.056
DSNU Row, e^-	0.008	0.021
DSNU Column, e^-	0.002	0.007
DSNU Pixel, e^-	0.075	0.172
DSNU Total, e^-	0.076	0.173
Dynamic Range, dB	83.39	85.05

indicate that the HWC mode is expected to be instrument-noise-limited for faint targets, whereas the LN mode does not reach the instrument-noise limit for this telescope configuration.

An analysis of noise as a function of timescale, performed through data binning, revealed that certain bright stars exhibit persistent correlated noise, while fainter stars are predominantly limited by uncorrelated noise. We successfully observed and modelled the transits of well-known exoplanets, confirming their detections and obtaining results consistent with those reported in the literature.

Overall, the Toran 26B CMOS camera demonstrates performance comparable to that of other Sony sensors based on similar architectures. It is capable of delivering high-precision photometry with minimal influence from instrumental systematics, depending on the selected operating mode. These findings support the growing evidence that modern CMOS detectors can achieve photometric performance on par with high-grade CCD cameras.

5.7 Extra Material

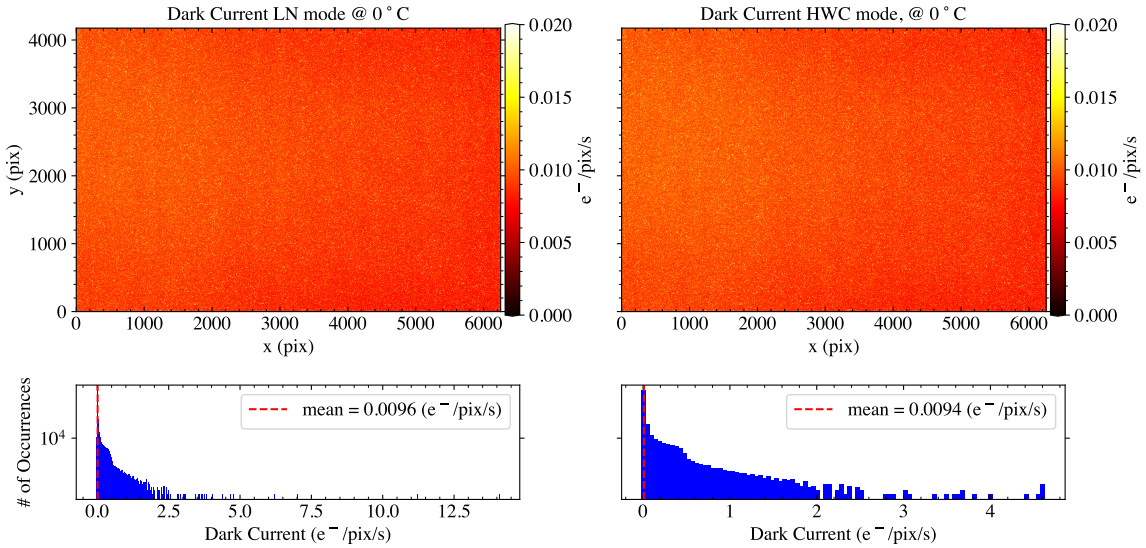


Figure 5.19: Dark images taken for Toran 26B without the LDC at temperature of 0 ° C. **Left** is the LN mode. **Right** is the HWC mode. Below each are the histograms of pixel value distributions from each frame, along with the mean (red dotted line).

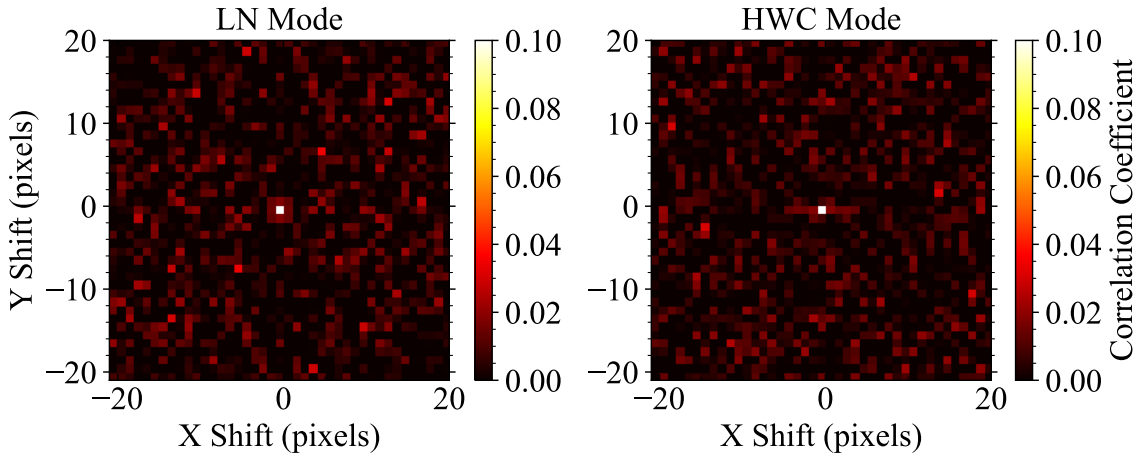


Figure 5.20: Spatial autocorrelation of a 20×20 pixel array extracted from the bias frames, after subtracting the mean bias level. **Left:** LN mode. **Right:** HWC capacity mode. The central white pixel represents the reference pixel; all other values indicate the degree of correlation relative to it.

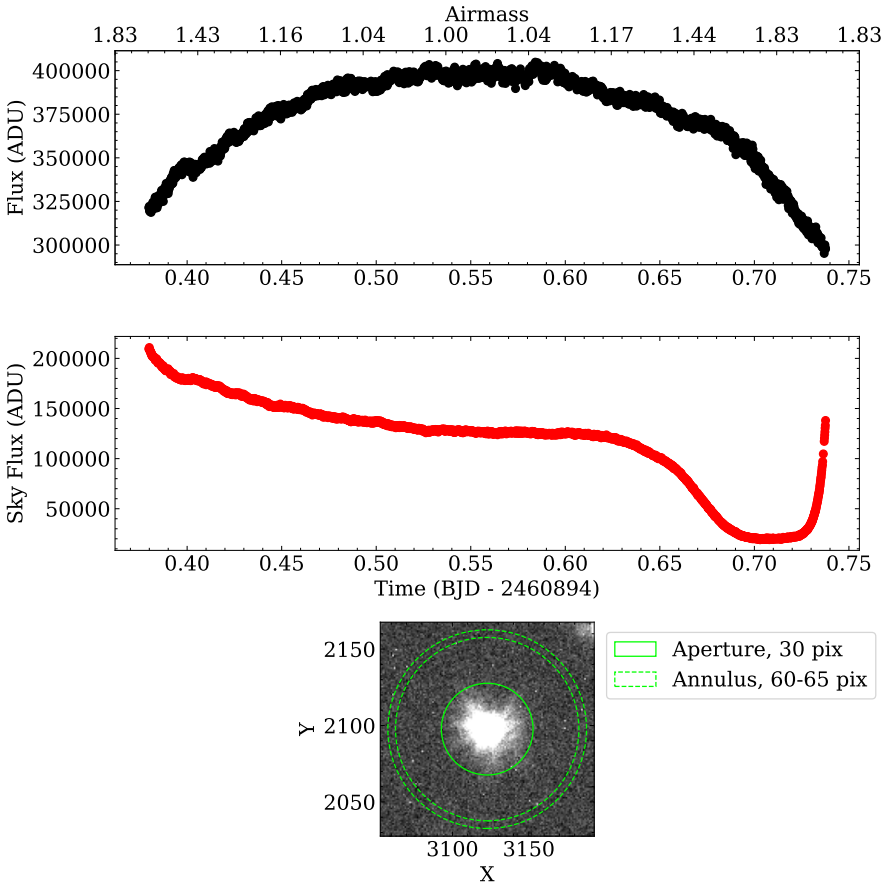


Figure 5.21: Diagnostic output from the photometry. **Upper panel** shows the raw lightcurve for the star KELT-16 in the night of 6 August 2025. **Middle panel** shows the sky background flux. **Lower panel** shows the x-y pixel position of the star with the aperture and annulus radii.

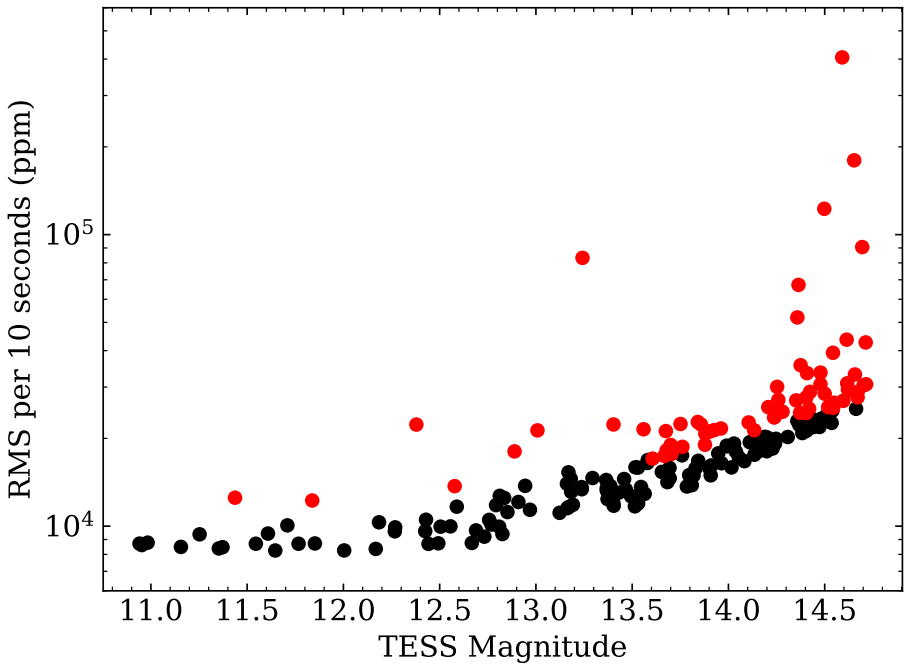


Figure 5.22: Noise model for performing relative photometry on a target star. The RMS noise of the comparison stars is plotted against their magnitude, with the filtering procedure highlighting noisy stars to be removed (red solid points) and stable stars retained for relative photometry (black solid points).

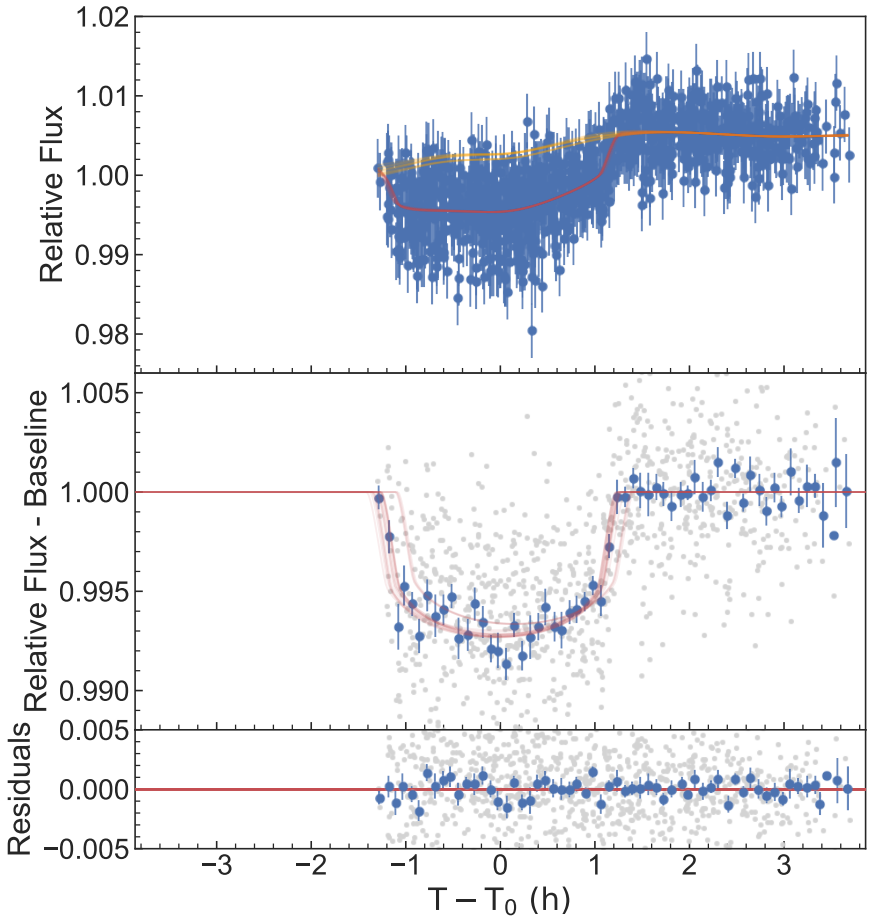


Figure 5.23: Same as in Figure 5.17. Normalized lightcurves for the transiting system of KELT-1 (TIC 432549364) (Siverd et al., 2012) from TWIST on 2025 August 10.

Table 5.5: `allesfitter` model priors from Siverd et al. (2012). Planetary System properties for the transiting system KELT-1 (TIC 432549364), as illustrated in Figure 5.23, at TWIST on 2025 August 10.

Parameter	**Initial Guess**	**Prior**	**Fitted value Toran 26B**
$R_p/R_\star$	0.0771	$\mathcal{U}(0.07, 0.08)$	$0.07732^{+0.00077}_{-0.0024}$
$(R_\star + R_b)/a_b$	0.291897	$\mathcal{U}(0.27, 0.3)$	$0.2732^{+0.0033}_{-0.0011}$
$\cos i_b$	0.055822	$\mathcal{U}(0.04, 0.07)$	$0.0496^{+0.016}_{-0.0081}$
T_c (BJD)	2457727.01162	$\mathcal{U}(2457727.01, 2457727.012)$	$2460894.9301^{+1.2}_{-0.0021}$
Orbital Period (days)	1.21749415	$\mathcal{U}(1.215, 1.219)$	$1.21845^{+0.00051}_{-0.0024}$
q_1	0.318	$\mathcal{N}(0.318, 0.01)$	$0.3263^{+0.0012}_{-0.018}$
q_2	0.369	$\mathcal{N}(0.369, 0.08)$	$0.410^{+0.022}_{-0.027}$

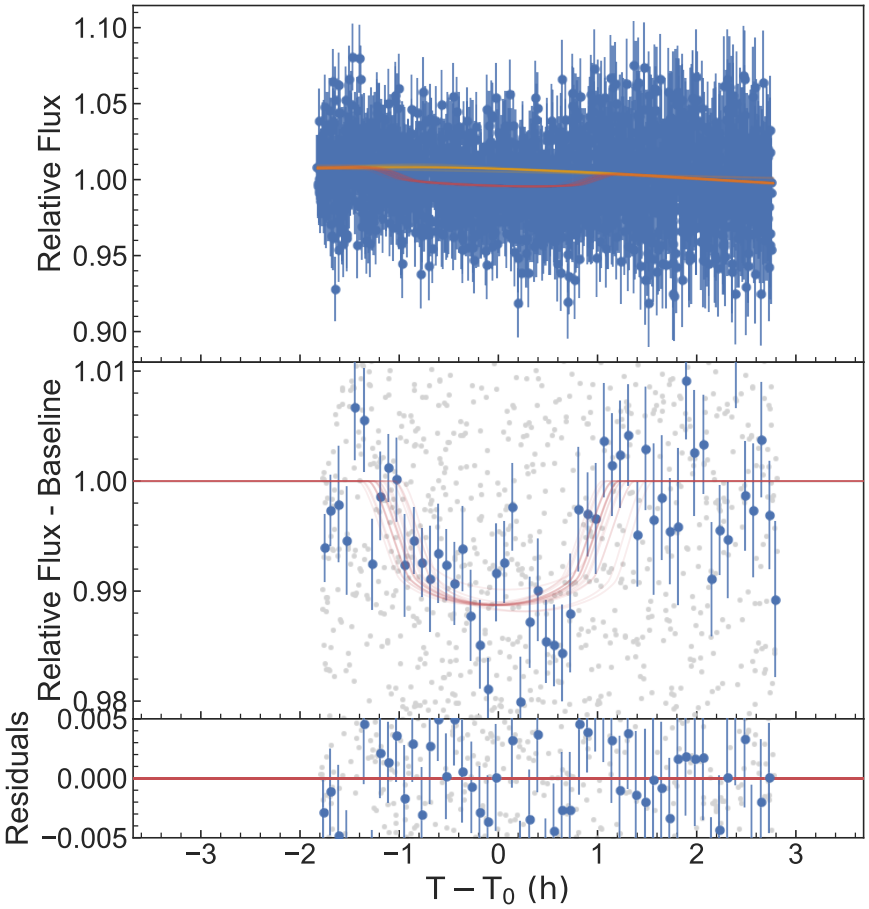


Figure 5.24: Same as in Figure 5.17. Normalized lightcurves for the transiting system of Kepler-41 (TIC 271042217) (Santerne et al., 2011) from TWIST on 2025 August 12.

Table 5.6: `allesfitter` model priors from Santerne et al. (2011). Planetary System properties for the transiting system Kepler-41 (TIC 271042217), as illustrated in Figure 5.24, at TWIST on 2025 August 12.

Parameter	**Initial Guess**	**Prior**	**Fitted value Toran 26B**
$R_p/R_\star$	0.10253	$\mathcal{U}(0.097, 0.107)$	$0.10160^{+0.00026}_{-0.0034}$
$(R_\star + R_b)/a_b$	0.218193	$\mathcal{U}(0.213, 0.223)$	$0.2151^{+0.0048}_{-0.0016}$
$\cos i_b$	0.135473	$\mathcal{U}(0.13, 0.14)$	$0.13789^{+0.00041}_{-0.0069}$
T_c (BJD)	2455664.159537	$\mathcal{U}(2455664.156, 2455664.16)$	$2460893.1^{+5.6}_{-3.7}$
Orbital Period (days)	1.855557555	$\mathcal{U}(1.85, 1.86)$	$1.85368^{+0.0059}_{-0.00020}$
q_1	0.369	$\mathcal{N}(0.369, 0.008)$	$0.3557^{+0.015}_{-0.0035}$
q_2	0.396	$\mathcal{N}(0.396, 0.074)$	$0.4155^{+0.0067}_{-0.058}$

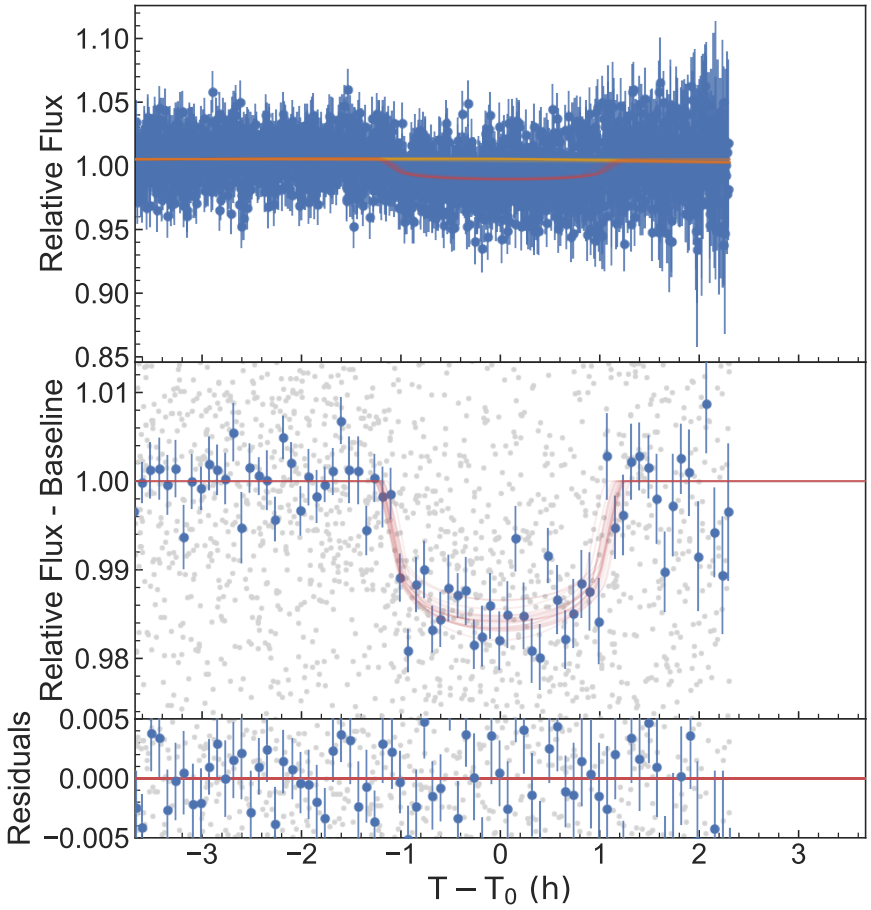


Figure 5.25: Same as in Figure 5.17. Normalized lightcurves for the transiting system of Kepler-670 (TIC 27990610) (Morton et al., 2016) from TWIST on 2025 August 16.

Table 5.7: `allesfitter` model priors from Morton et al. (2016). Planetary System properties for the transiting system Kepler-670 (TIC 27990610), as illustrated in Figure 5.25, at TWIST on 2025 August 16.

Parameter	**Initial Guess**	**Prior**	**Fitted value Toran 26B**
$R_p/R_\star$	0.121703	$\mathcal{U}(0.1, 0.13)$	$0.1150^{+0.0028}_{-0.0054}$
$(R_\star + R_b)/a_b$	0.117198	$\mathcal{U}(0.1, 0.12)$	$0.1146^{+0.0027}_{-0.0050}$
$\cos i_b$	0.010995	$\mathcal{U}(0.005, 0.02)$	$0.0142^{+0.0043}_{-0.0060}$
T_c (BJD)	2455003.96270000	$\mathcal{U}(2455003.96, 2455003.97)$	$2460904.5375^{+0.0016}_{-0.0021}$
Orbital Period (days)	2.816504852	$\mathcal{U}(2.811, 2.818)$	$2.8150^{+0.0013}_{-0.0023}$
q_1	0.382	$\mathcal{N}(0.382, 0.013)$	$0.3809^{+0.012}_{-0.0083}$
q_2	0.393	$\mathcal{N}(0.393, 0.09)$	$0.321^{+0.11}_{-0.065}$

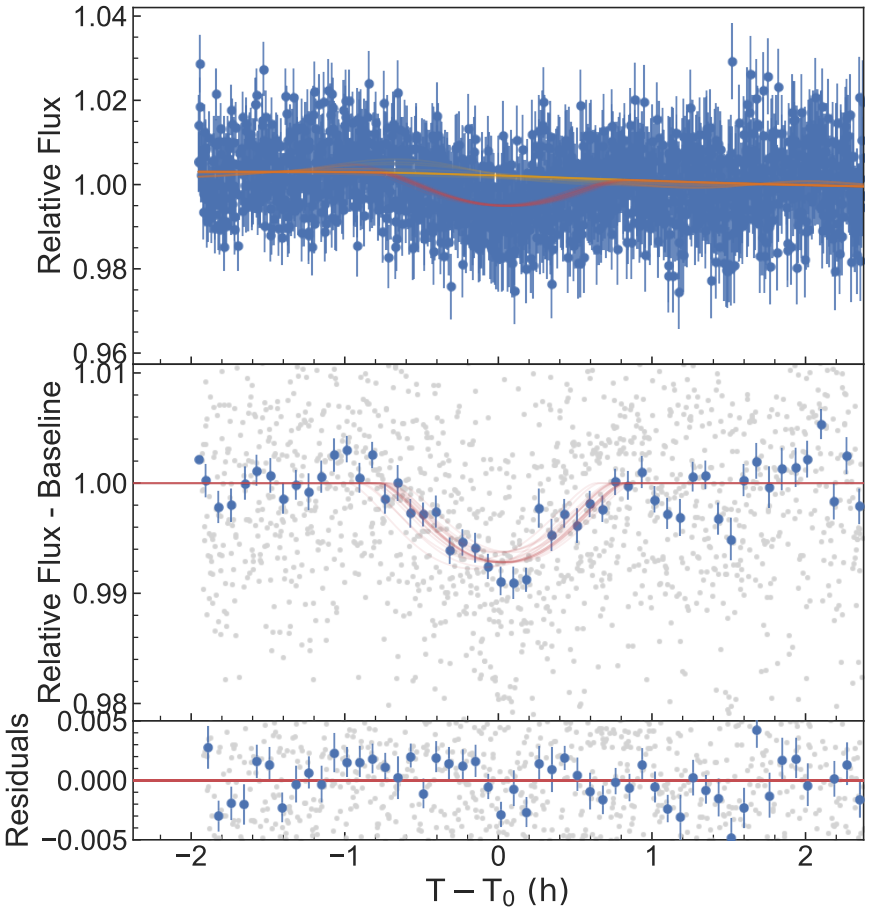


Figure 5.26: Same as in Figure 5.17. Normalized lightcurves for the transiting system of Kepler-76 (TIC 138644215) (Faigler et al., 2013) from TWIST on 2025 September 9.

Table 5.8: `allesfitter` model priors from Faigler et al. (2013). Planetary System properties for the transiting system Kepler-76 (TIC 138644215), as illustrated in Figure 5.26, at TWIST on 2025 September 9.

Parameter	**Initial Guess**	**Prior**	**Fitted value Toran 26B**
$R_p/R_\star$	0.1033	$\mathcal{U}(0.098, 0.108)$	$0.10656^{+0.00025}_{-0.0026}$
$(R_\star + R_b)/a_b$	0.247377	$\mathcal{U}(0.24, 0.25)$	$0.24629^{+0.00015}_{-0.0025}$
$\cos i_b$	0.215588	$\mathcal{U}(0.21, 0.22)$	$0.21193^{+0.00064}_{-0.00050}$
T_c (BJD)	2455654.042121	$\mathcal{U}(2455654.041, 2455654.045)$	$2460934.6^{+1.5}_{-9.3}$
Orbital Period (days)	1.544928884	$\mathcal{U}(1.54, 1.55)$	$1.54583^{+0.00075}_{-0.0014}$
q_1	0.345	$\mathcal{N}(0.345, 0.009)$	$0.35485^{+0.00060}_{-0.0050}$
q_2	0.384	$\mathcal{N}(0.384, 0.08)$	$0.3297^{+0.058}_{-0.0070}$

Chapter 6

Discovery of the long period warm Jupiter NGTS-39b

"To me, it underscores our responsibility to deal more kindly and compassionately with one another and to preserve and cherish that pale blue dot, the only home we've ever known."

Carl Sagan, 1994

Note

This chapter reproduces the manuscript entitled "NGTS-39 b: A 58 d transiting warm Jupiter in an eccentric orbit" (Apergis et al., submitted to Monthly Notices of the Royal Astronomical Society in May 2026). The writing and analysis presented in the paper were carried out by the author, with comments and feedback provided by the co-authors throughout the manuscript. The stellar analysis for NGTS-39, particularly in subsection 6.4.1 was conducted and written by the co-authors. The radial velocities measurements were conducted by the observers as part of the Warm Jupiter program (program numbers are : 112.261U.002, 112.261U.003, 116.28XG.001, 116.29B6.001), who are also co-authors. Moreover, Figure 6.8 in subsection 6.4.3 was made by Alex Romanec and Figure 6.9 in subsection 6.4.4 was made by Toby Rodel, who are also co-authors.

Abstract

We report the discovery and characterisation of NGTS-39 b (TIC 453147896 b), a warm Jupiter transiting a Sun-like star on a 58.2 day, eccentric (e = 0.386 ± 0.019) orbit. NGTS-39 b was first identified from a TESS single transit event, and subsequently confirmed with NGTS photometry and radial velocity measurements from CORALIE and HARPS. The host star is a bright ($T_{\rm mag}$ = 11.02) F9 dwarf with effective temperature of $T_{\rm eff}$= 6053^{+67}_{-30} K. NGTS-39 b is a Jupiter-sized gas giant with a radius of $1.088 \pm 0.012\,R_J$ and a mass of $1.467 \pm 0.081\,M_J$. Its equilibrium temperature is 519^{+6}_{-5} K, placing it between short-period hot Jupiters and cold, Jupiter-like giants. The high orbital

eccentricity and intermediate equilibrium temperature of NGTS-39 b make it a valuable test case for formation and migration models, particularly in the poorly sampled regime of long-period gas giants. The RV data show a linear trend of $\dot{\gamma} = -17.75\,\mathrm{m\,s^{-1}\,yr^{-1}}$, which indicates the presence of an outer companion. The discovery of NGTS-39 b contributes to the small but growing population of transiting warm Jupiters with P>50 days orbiting bright stars.

6.1 Introduction

Long-period transiting exoplanets, typically with orbital periods of several tens to hundreds of days, occupy a unique regime in the study of planetary systems (Uehara et al., 2016; Foreman-Mackey et al., 2016). Unlike short-period hot Jupiters, these planets spend most of their orbits far from their host stars, making transits rare and challenging to detect. Their characterisation often requires long-term photometric monitoring to capture multiple transits and confirm orbital periods.

Space-based missions such as the Transiting Exoplanet Survey Satellite (TESS; Ricker et al., 2015) have substantially expanded the photometric characterisation of Jupiter-like exoplanets, including both newly identified candidates and previously known systems. Owing to their large radii, high geometric transit probabilities, and frequent transits, the most readily detected members of this population are hot Jupiters. While hot Jupiters provide valuable information on planetary formation, evolution, and atmospheric physics (David et al., 2016; Ginzburg & Chiang, 2020), they represent a highly irradiated and dynamically altered population. Their short orbital periods (<10 days) place them in extreme environments dominated by strong stellar irradiation and tidal interactions, which complicates the interpretation of their formation pathways and atmospheric properties (Baraffe & Chabrier, 2010; Laughlin, 2018; Sarkis et al., 2021).

In contrast, warm and cold Jupiter-like planets with orbital periods ranging from tens to hundreds of days offer a much clearer window into planetary system architecture and dynamical history (Petrovich & Tremaine, 2016; Hamers et al., 2017; Anderson et al., 2020; Morgan et al., 2025). These planets reside in environments where their atmospheres are less strongly altered by stellar irradiation, allowing more direct probes of their primordial composition (Madhusudhan, 2019; Komacek et al., 2020; Fortney et al., 2020). Their wider orbits also make them excellent tracers of migration processes: measurements of their masses, eccentricities, and orbital obliquities from ground-based spectroscopic follow-up can provide further evidence for disc-driven migration and high-eccentricity pathways. Moreover, warm Jupiters often coexist with additional planets, making them key to understanding the architecture and long-term evolution of planetary systems (Huang et al., 2016).

Detecting long-period transiting planets is inherently challenging. A single TESS sector provides only ~27 days of continuous coverage, and most fields are not revisited until two years later. Consequently, long-period planets may produce only a single detectable transit (monotransit) in the TESS observing windows (Cooke et al., 2018, 2019, 2021; Villanueva et al., 2019; Rodel et al., 2024), resulting in unknown orbital period solutions.

Ground-based facilities such as the Next Generation Transit Survey (NGTS; Wheatley et al., 2018) have therefore developed dedicated monotransit campaigns to find and observe these TESS candidates (Gill et al., 2020a, 2024). These campaigns follow-up the targets in a blind survey, enabling the

recovery of additional transits in order to determine the true orbital period of the systems.

These efforts allow us to discover exoplanets with longer orbital periods and cooler temperatures than those of typical short-period transiting systems. Such longer-period giant planets provide an important comparison sample because they are less affected by intense stellar irradiation, radius inflation, and tidal evolution than hot Jupiters. Their measured radii and bulk densities can therefore help test whether the diversity in heavy-element enrichment and internal structure seen among giant planets depends on orbital separation and irradiation environment(Dalba et al., 2022; Ulmer-Moll et al., 2022).

In the last few years, photometric and RV follow-up efforts of TESS monotransit candidate led to the discovery and characterisation of transiting long-period exoplanets (e.g. Battley et al., 2024; Gill et al., 2024; Ulmer-Moll et al., 2025). In this work, we report the discovery and detailed characterisation of NGTS-39 b, a long-period giant initially identified in the TESS photometry during the Year 3 extended mission. To constrain its orbital period, we initiated a follow-up campaign with NGTS targeting this monotransit candidate, which successfully observed a second transit three years after the initial TESS monotransit event. Subsequently TESS observed a third transit in the TESS Year 6 extended mission which was consistent with a 58.2 d orbital period. The period was further refined using additional NGTS observations and data from the TESS Follow-up Observing Program Sub Group 1 team (TFOP SG1; Collins et al., 2018). In parallel, high precision radial velocity (RV) measurements from HARPS (Pepe et al., 2002) and CORALIE (Queloz et al., 2001) confirmed the orbital and measure the planetary mass, hence establishing the planetary nature of NGTS-39 b.

We structure this paper as follows. In Section 6.2, we present the TESS and NGTS observations of NGTS-39. Section 6.3 describes the RV monitoring conducted with HARPS and CORALIE. In Section 6.4, we perform a joint modelling of the photometric and spectroscopic datasets to derive the system parameters. We discuss our findings in Section 6.5, and summarise our conclusions in Section 3.6.

6.2 Photometry

6.2.1 TESS Photometry

The TESS mission is a NASA space-based observatory designed to obtain high-precision, wide-field photometry for the detection of transiting exoplanets around bright, nearby stars (Ricker et al., 2015). TESS is equipped with four identical frame-transfer CCD cameras based on the CCID-80 devices developed by MIT/Lincoln Laboratory. These back-illuminated, deep-depleted sensors provide high sensitivity at red optical wavelengths. Each camera comprises a 2048×2048 array of active imaging pixels, with an equal number of storage pixels, and a pixel pitch of 15×15 micron. The plate scale projected on sky is approximately 21 arcsec pixel^{-1}. Each camera covers a field of view of $24^\circ \times 24^\circ$, resulting in a combined instantaneous field of view of $24^\circ \times 96^\circ$. The cameras operate over a broad red-optical bandpass spanning approximately 600-1000 nm and observe the sky in sectors of approximately 27 days. During its prime mission, TESS first observed the southern ecliptic hemisphere in Year 1 and then moved to the northern ecliptic hemisphere in Year 2, thereby completing a nearly all-sky transit survey. This strategy provided near-continuous coverage close to the ecliptic poles, where adjacent sectors overlap, while stars nearer the ecliptic plane were typically

observed for only a single sector.

NGTS-39 (TIC-453147896) is a relatively bright ($T_{\rm mag}$ = 11.02) F9 dwarf star. The full set of stellar properties for NGTS-39 are set out in Table 6.1. For our analysis of NGTS-39, we generate custom light curves directly from the TESS Science Processing Operations Centre (SPOC; Jenkins et al., 2016) Full-Frame images. This was done as the SPOC and Quick Look Pipeline (QLP; Huang, 2020) lightcurves for this star were not always available when we needed them for our analysis. It also allowed us to tailor the photometric aperture and background pixel mask to suit NGTS-39 in each TESS sector. We use the `lightkurve` package (Lightkurve Collaboration et al., 2018) to download the TESS target pixel files for NGTS-39 filtered using the SPOC quality flag QUALITY = 0 (Jenkins et al., 2016; Caldwell et al., 2020). A pixel-level aperture was constructed as a two-tier mask: background pixels were defined as the 30 % lowest-flux pixels in a reference cadence, while target pixels were selected using a threshold mask applied to the summed flux across cadences. An example of our target pixel mask from Sector 7 is shown in Figure 6.1. The target flux was computed by summing all pixels in the target aperture and subtracting the median background flux per pixel multiplied by the number of target pixels. The flux uncertainties were estimated using the median absolute deviation of the simple aperture photometry `SAP` flux, providing robust per-cadence error estimates. To remove long-term trends while preserving transit signals, the lightcurve was split into segments at gaps exceeding 2.4 h, corresponding to spacecraft data downloads and SPOC-flagged regions. Each segment was normalised individually and subsequently smoothed using an iterative Savitzky–Golay filter (five iterations with a 3σ clipping threshold) and a 48 h window size, which efficiently removes stellar activity while setting an upper limit on the duration of detectable transit events (Savitzky & Golay, 1964; Hattori et al., 2022). We present all of the TESS photometry in Figure 6.2.

In total, NGTS-39 has been observed by TESS in Sectors 7, 33, 71, 72, and 87 (see Figure 6.2). Full details of each Sector of TESS observations are set out in Table 6.3.

NGTS-39 was first identified as a monotransit candidate by the NGTS Monotransit working group following the procedure set out in Hawthorn et al. (2024). A transit of duration 4.6 hours and depth 1 % was detected in the TESS Sector 33 lightcurve centered at BJD 2459225.7607 (2021-01-11 06:15 UTC) (see Figure 6.2). Based on this monotransit event, NGTS-39 was scheduled for NGTS follow-up and a second transit was observed (see subsection 6.2.2). NGTS-39 was observed again by TESS in Sectors 71 and 72, although no transits were detected during these Sectors. A subsequent transit was detected in Sector 87, with a depth and duration consistent with the earlier transits detected in Sector 33 and by NGTS.

We note that, based on the orbital period fitted to the TESS data, a transit is expected to occur in Sector 72 (see Figure 6.2), however we could not retrieve the transit. We investigated the availability of alternative data products such as the Quick Look Pipeline (QLP; Huang, 2020). Upon inspection, the QLP light curve is significantly affected by increased scatter similarly to our custom lightcurve product, likely driven by strong stray light. We measured the average sky background during the transit window to be 35 times higher than the average background before the transit. This introduces substantial systematics that degrade the photometric precision. Crucially, the predicted transit occurs immediately prior to a data gap, in a region where the light curve quality is already compromised. As a result, the transit signal cannot be reliably identified or extracted. We also note that the Sector

Table 6.1: NGTS-39 Stellar parameters

Property	Value	Source
Spectral type	F9V	Pecaut & Mamajek (2013)
Identifiers		
2MASS ID	J07194529+0956286	2MASS
Gaia Source ID	3156473342454773248	*Gaia* DR3
TIC ID	453147896	TIC 8
NGTS ID	NGTS-39	This Work
Coordinates		
RA (hh:mm:ss.ss)	07 : 19 : 45.29	*Gaia* DR3
DEC (dd:mm:ss.ss)	+09 : 56 : 28.55	*Gaia* DR3
Proper motion, parallax and systemic velocity		
$\mu_{\rm RA}$ (mas y^{-1})	-10.0423 ± 0.0207	*Gaia* DR3
$\mu_{\rm DEC}$ (mas y^{-1})	-2.9010 ± 0.01538	*Gaia* DR3
Parallax (mas)	$3.584 \pm 0.0.018$	*Gaia* DR3
γ (m s^{-1})	42113.05 ± 2.44	This Work
$\dot{\gamma}$ (m s^{-1} yr^{-1})	-17.75 ± 1.86	This Work
Magnitudes		
V (mag)	11.516 ± 0.048	APASS DR10
B (mag)	12.139 ± 0.044	APASS DR10
G (mag)	11.4221 ± 0.0004	*Gaia* DR3
BP (mag)	11.7190 ± 0.0005	*Gaia* DR3
RP (mag)	10.9675 ± 0.0004	*Gaia* DR3
TESS (mag)	11.025 ± 0.006	TIC 8
J (mag)	10.475 ± 0.024	2MASS
H (mag)	10.187 ± 0.023	2MASS
K (mag)	10.197 ± 0.026	2MASS
W1 (mag)	10.137 ± 0.023	WISE
W2 (mag)	10.178 ± 0.02	WISE
W3 (mag)	10.199 ± 0.076	WISE
Spectral Parameters		
$v \sin i_*$ (km s^{-1})	4.0 ± 0.5	This Work
$T_{\rm eff}$ (K)	6053^{+67}_{-30}	This Work
[Fe/H] ('dex')	0.196 ± 0.023	This Work
$\log g$ (log(cgs))	4.419 ± 0.042	This Work
Derived parameters		
R_* ($R_\odot$)	1.16 ± 0.01	This Work
M_* ($M_\odot$)	1.16 ± 0.05	This Work
Age (Gyr)	2.2 ± 0.8	This Work

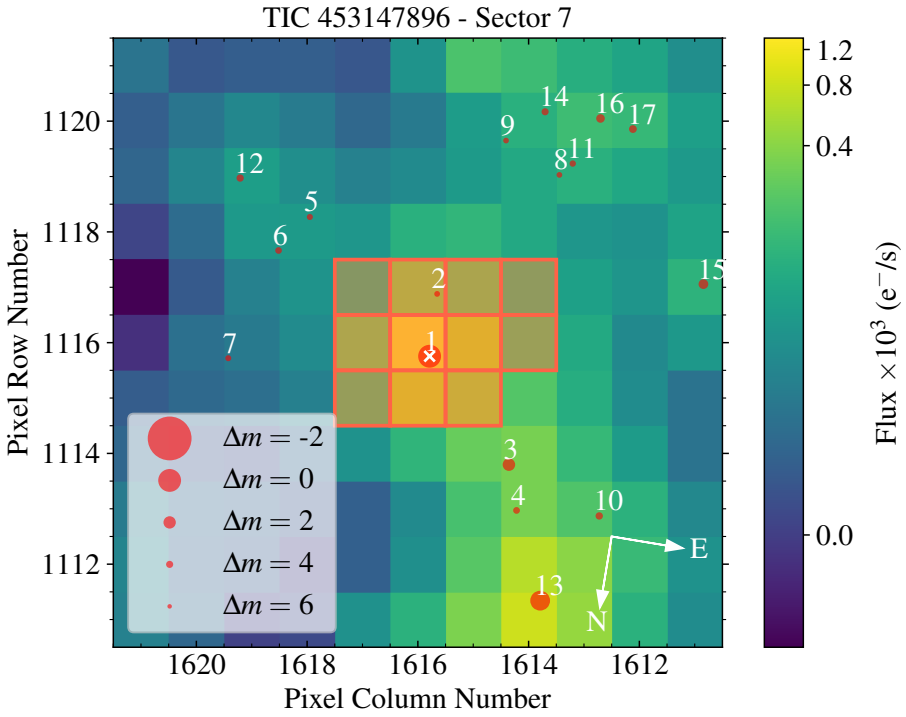


Figure 6.1: TESS Sector 7 Full-Frame Image cutout (11×11 pixels) of NGTS-39 and the surrounding region, generated with `tpfplotter` (Aller et al., 2020). NGTS-39 is shown at the centre, labelled "1" and marked with the white x. The only additional source falling within our adopted aperture is approximately 6 magnitudes fainter than the target, and therefore its flux contribution is expected to be negligible. No significant dilution is therefore expected in the TESS photometry.

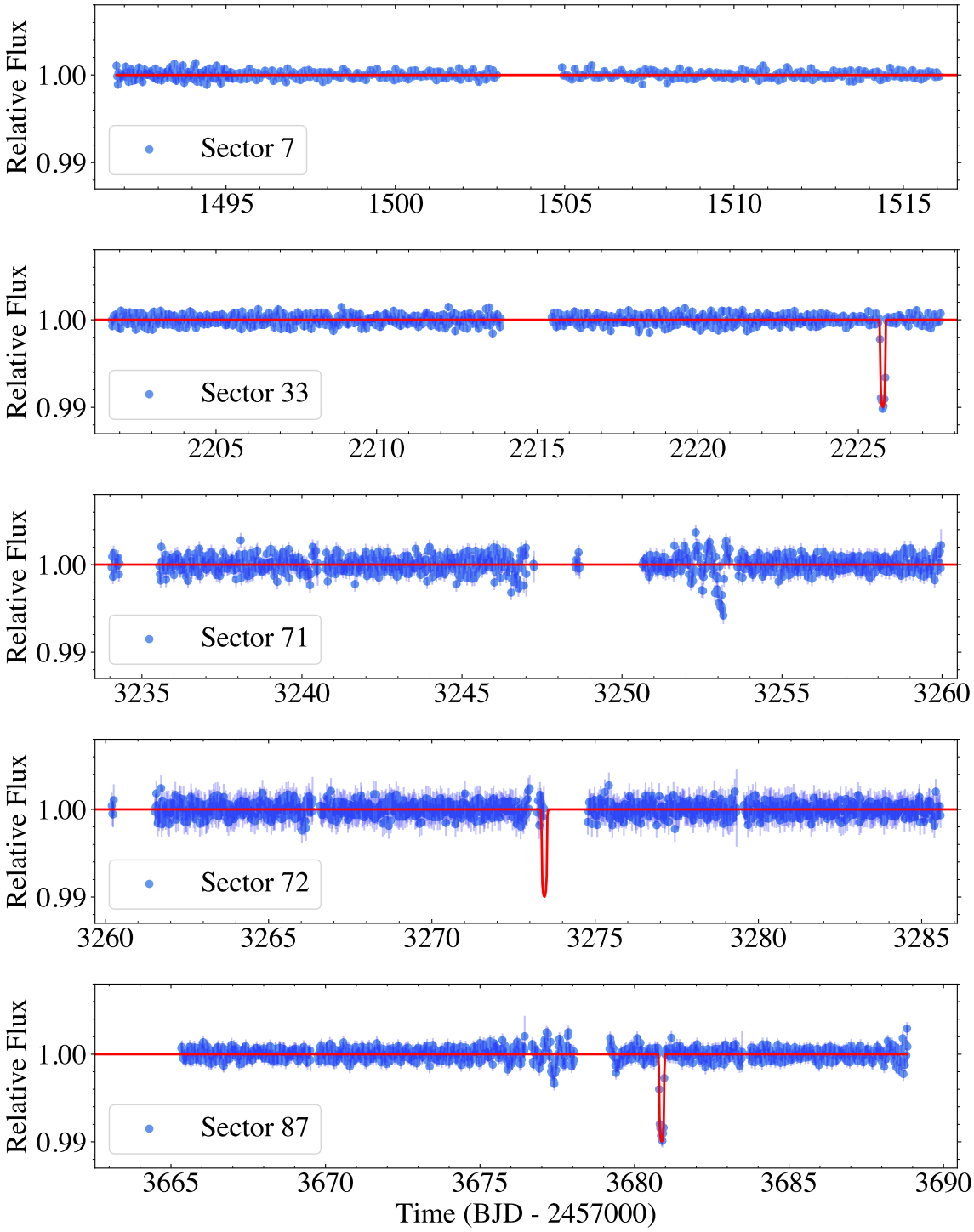


Figure 6.2: TESS Sector detrended and normalised lightcurves zoomed-in for NGTS-39 from TESS full-frame images pipeline. The transit events are marked with red. Transits are detected in Sector 33 and Sector 87. The transit event in Sector 72 was just missed due to the orbit gap in the TESS data. All the data has been binned to 30-minutes for clarity and consistency.

71 light curve shows a flux decrease near 3253 (BJD − 2457000), which could potentially resemble a transit-like event. However this event is most likely a spacecraft systematic, and is immediately prior to a data downlink. The event occurs during a section of poor pointing performance and is common to a large number of stars as evidenced in the data release notes for Sector 71.[1]

6.2.2 NGTS Photometry

NGTS (Wheatley et al., 2018) is an exoplanet-hunting facility located at ESO's Paranal Observatory in Chile. It comprises twelve robotic Newtonian telescopes, each with a 20 cm primary mirror and a $\sim$8 deg^2 field of view. This field of view makes NGTS well suited for high precision photometry of bright stars where a wide field of view is critical for monitoring comparison stars needed for relative photometry.

Each telescope is equipped with a deep-depleted CCD camera featuring 13.5 microns pixel pitch and a 2048 $\times$ 2048 usable sensor with enhanced sensitivity at red wavelengths. Given the NGTS telescope and camera configuration, the plate scale projected on sky is approximately 5 arcsec pixel^{-1}. NGTS uses a custom wide-band filter tailored to the red-sensitive response (520-890 nm) of these detectors. The excellent photometric conditions at Paranal further enhance NGTS's capability for precise photometric observations. Multiple telescopes can observe the same target simultaneously, allowing independent measurements to be combined and improving the overall photometric precision (Bryant et al., 2020). For bright stars, NGTS observations are effectively scintillation-limited without introducing additional correlated noise (O'Brien et al., 2022).

Following the monotransit event identified in the TESS Sector 33 lightcurve, NGTS-39 was targeted as part of the NGTS single-transit program. NGTS observations started in 2023/09/04. The initial monitoring was carried out with a single NGTS telescope using 10 s exposures between 2023/09/04 and 2024/02/04, with observations limited to airmass < 2. In total the NGTS campaign for NGTS-39 lasted for 104 observing nights.

Raw images are astrometrically calibrated using a world coordinate system (WCS) solution via *astrometry.net* (Lang et al., 2010), incorporating field centre, pixel scale, and a low-order polynomial. To improve accuracy near image edges, we cross-match sources with TIC8 (Stassun et al., 2018), selecting stars brighter than $T < 16$ mag, and iteratively refine the fit until sub-pixel precision is reached. Frames lacking a reliable WCS solution are excluded. Stars for photometry are also selected from TIC8 with $T < 16$ mag, avoiding blended sources (neighbours within 6 pixels and $\Delta T < 2.5$ mag) and edge regions (for details see chapter 4). Daily dark and bias frames are obtained, but no flat-field correction is applied, as autoguiding keeps stars on consistent pixels (McCormac et al., 2013; Wheatley et al., 2018). As in chapter 4, we found that omitting flat-field correction improves the RMS scatter by approximately 0.29 % for a typical stellar sample. We therefore consider it safer to omit flat fielding than to apply an imperfect correction. In addition, because the telescopes are very fast (f/2.8), dust on the CCD window is highly out of focus and does not produce strong donut like features. The sealed space between the telescope and CCD window also minimises external dust contamination.

Aperture photometry is performed using SEP (Bertin & Arnouts, 1996; Barbary, 2016) with circular apertures optimised per camera. Background maps are constructed and subtracted prior

[1] `https://archive.stsci.edu/missions/tess/doc/tess_drn/tess_sector_71_drn100_v01.pdf`

Table 6.2: A portion of the NGTS photometric data for NGTS-39. The full table is available online.

Time (BJD -2457000)	Normalised flux	Flux uncertainty
3331.5383449076	1.008609148	0.007050435
3331.5386111111	1.011612138	0.007044304
3331.5387615738	1.006352026	0.007027734
3331.5389004629	1.011517066	0.007022968
3331.5390509260	1.012522132	0.007017232
3331.5392013890	1.018593763	0.007018303
3331.5395023148	1.006691687	0.006990872
3331.5396527778	0.998240140	0.006981137
3331.5398032409	0.988144640	0.006964347
...	...	...

to flux extraction. Relative photometry corrects for atmospheric and instrumental trends using comparison stars. Stars are iteratively filtered based on RMS deviations from magnitude-binned trends, removing variable stars. The remaining stars form a master reference light curve used to correct the target star, and the optimal aperture is chosen to minimise the RMS scatter (see details in Bryant et al. (2020) and the pipeline in `https://github.com/NGTS/bsproc`). An example of the NGTS photometry output is set out in Table 6.2.

We monitored NGTS-39 with the NGTS facility for a total of 104 nights. In total this yielded 82,594 photometric data points. For the present analysis, we excluded nights containing fewer than 200 data points, resulting in the removal of 16 nights. The NGTS photometry from all available observing epochs was combined into a single light curve after restricting the sample to exposures conducted under photometric conditions (i.e. no cloud detected). Non-photometric data, including those affected by cloud, were identified through variations and drops in the photometric zero point. For each exposure, we extracted the barycentric time (BJD_TDB, offset by 2457000), the processed target flux and associated uncertainty, the sky background, and the photometric zero-point. Since observations were made over all moon conditions, the sky background varied greatly over the 104 nights of the campaign. We therefore carried out a simple linear detrend of the photometric flux against the sky background level. We removed 136 photometric data points that we suspected were affected by thin cloud with zero-point magnitudes outside of the the nominal range $-0.06 < \mathrm{zp} < 0.2$. We removed 102 photometric data points via an iterative 4σ clipping with three iterations, which were likely due to effects such as cosmic rays and satellites contaminating the photometry of the target or comparison stars. The resulting lightcurve is set out in Figure 6.3. For illustrative purposes we bin the data into 5-min intervals, requiring at least 20 points per bin.

On the night of BJD 2460331.6503 (2024-01-22 03:35 UTC), we detected an ingress event for NGTS-39 consistent with the transit depth measured by TESS in Sector 33. A second transit was later (after 6 consecutive periods from the transit detected with NGTS) detected in TESS Sector 87 on 2025/01/05, confirming an orbital period of 58.2 days. We therefore scheduled NGTS follow-up for the next visible transit opportunity, which occurred on 2025/10/22. For this campaign, we observed simultaneously with six NGTS telescopes using 10 s exposures. During this night, we again detected a transit ingress, confirming the orbital period of 58.2 days.

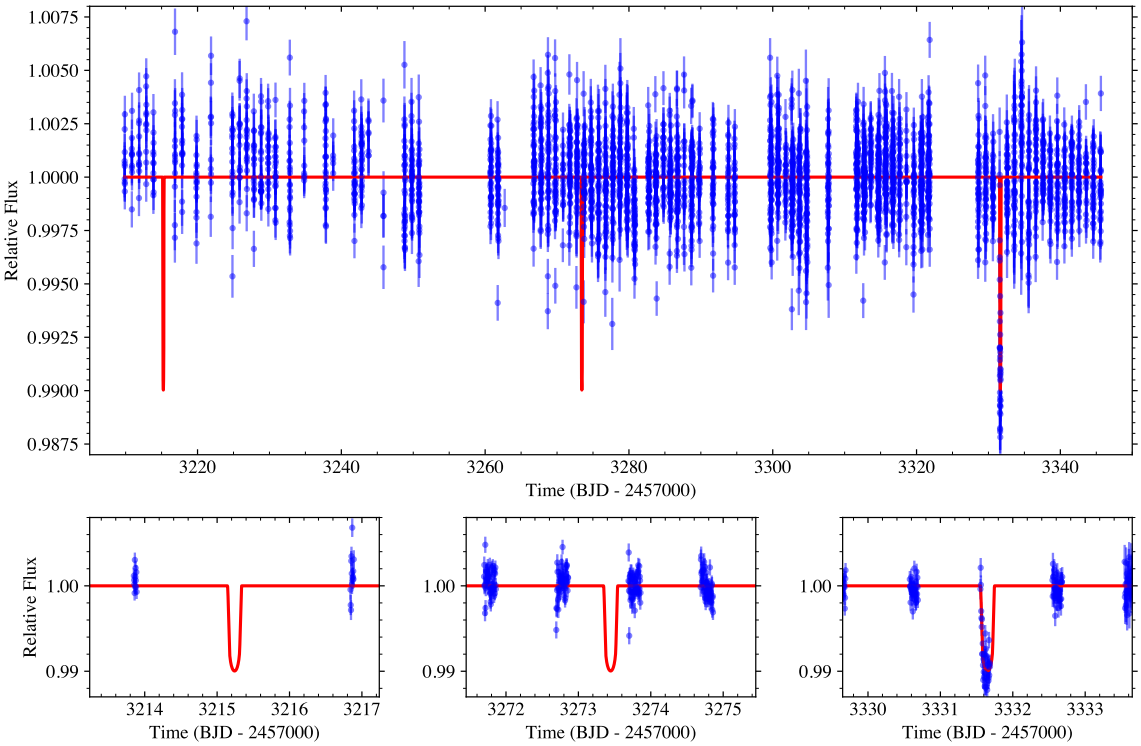


Figure 6.3: NGTS lightcurves from 2023/09/03 to 2024/02/04 for NGTS-39 from the `bsproc` pipeline, normalised and detrended. The transit event is visible in the lower-right panel and was observed on the night of 2024/01/21. For clarity, all data are binned to 5-minute cadence.

6.2.3 TFOP SG1 Follow-up Photometry

In order to monitor the expected transit event on the night of 2025/10/22, we issued an observing alert to the TFOP SG1 team on 2025/10/20. This alert resulted in several observations from SG1 observers around the globe. The data from these observations were reduced with `AstroImageJ` (Collins et al., 2017). We list each SG1 observation in this sub-section. Reduced data from each SG1 observation is available on the corresponding ExoFOP (Christiansen et al., 2025) page.[2]

Acton Sky Portal (0.36 m)

The Acton Sky Portal is a private observatory in Massachusetts, USA. The telescope features a Rowe-Ackermann Schmidt Astrograph (RASA 11) from Celestron with a f/11 focal ratio and a 0.36 m primary mirror. The telescope is equipped with a back-illuminated SBIG Alumna CCD4710 camera, featuring a 1056×1027 pixel sensor and with 13 μm pixel pitch having an image scale of ~ 1 arcsec pixel^{-1}, resulting in a $17.1' \times 17.1'$ full field of view (Mantovan et al., 2024). An egress event of NGTS-39 b was observed on 2025/10/22 using the r' filter and an exposure time of 20 s. An uncontaminated 8″ target aperture was used for photometry, yielding a 10 ppt transit event.

[2] `https://exofop.ipac.caltech.edu/tess/target.php?id=453147896`

LCO-CTIO (0.35 m)

Observations were obtained with a 0.35-meter telescope of the Las Cumbres Observatory Global Telescope (LCOGT; Brown et al., 2013) network, specifically at its Cerro Tololo Inter-American Observatory node in Chile. This instrument is a PlaneWave DeltaRho 350 telescope tube paired with a QHY600 CMOS camera (Harbeck et al., 2024). This configuration yields an image scale of $\sim 0.74\,\mathrm{arcsec\,pixel^{-1}}$ and a $114' \times 72'$ full field of view. Raw images were calibrated using the standard `BANZAI` pipeline (McCully et al., 2018). An ingress event of NGTS-39 b was observed on 2025/10/22 with the r' filter and an exposure time of 60 s. An uncontaminated $7.4''$ target aperture was used for photometry, yielding a 10 ppt transit event.

ULMT (0.6 m)

The University of Louisville Manner Telescope (ULMT) is a 0.6 m Ritchey–Chrétien telescope with an f/8 focal ratio, providing a high-quality, coma-free field of view. The telescope is equipped with a ZWO ASI 6200 CMOS camera, featuring a 9600×6400 pixel sensor with $3.76\,\mu$m pixel pitch. This configuration yields a field of view of approximately $25.9' \times 17.2'$ with a pixel scale of $\sim 0.16\,\mathrm{arcsec\,pixel^{-1}}$, enabling precise time-series photometric observations. An egress event of NGTS-39 b was observed on 2025/10/22 using the r' filter and with exposure time of 60 s. An uncontaminated $5''$ target aperture was used for photometry, yielding a 10 ppt transit event.

Lookout Observatory (0.27 m)

The Lookout Observatory, a private observatory in Carefree, Arizona, USA, operates a 0.27 m primary mirror telescope modified with lens in the secondary, dedicated for wide-field imaging. The telescope is equipped with a ZWO ASI2600 CMOS camera, featuring a 6248×4176 pixel sensor with $3.76\,\mu$m pixel pitch. This configuration provides a field of view of approximately $114' \times 86'$ with a pixel scale of $\sim 2.9\,\mathrm{arcsec\,pixel^{-1}}$ (Thomas & Guan, 2021). An egress event of NGTS-39 b was observed on 2025/10/22 using the r, g, and b filters with 30 s exposures. Photometry was performed with an uncontaminated $30''$ aperture, yielding a transit depth of 10 ppt.

OACC - CAO (0.6 m)

The Campo Catino Austral Observatory (OACC-CAO) is a facility located in El Sauce Observatory in the Atacama desert, in Chile. The telescope features a 0.6 m PlaneWave CDK24 Corrected Dall–Kirkham optical design, delivering a wide, flat, and coma-free field of view. The telescope is fitted with a CMOS detector, specifically in the Moravian C3-61000EC PRO camera. This camera employs a large-format sensor (9576×6388) with 3.76 microns pixel pitch, providing a field of view of approximately $32' \times 21'$ with a pixel scale of $\sim 0.2\,\mathrm{arcsec\,pixel^{-1}}$. The camera is equipped with the $i2$ filter. NGTS-39 b was observed on the night of 2025/10/22 and an ingress event was detected with an exposure time of 120 s. An uncontaminated $12''$ target aperture was used for photometry, yielding a 10 ppt transit event.

Table 6.3: Summary of photometric observations of NGTS-39.

Telescope	Night(s) Observed	N_{images}	Exptime (s)	N_{nights}*	Filter	Sector	Pipeline	Comments
TESS	2019/01/08-2019/02/16	1072	1800	22.33	TESS	7	Custom	No transit
TESS	2020/12/18-2021/01/13	3485	600	24.20	TESS	33	Custom	Transit
TESS	2021/01/14-2021/02/08	8961	200	20.74	TESS	71	Custom	No transit
TESS	2023/01/18-2023/02/12	9577	200	22.17	TESS	72	Custom	No transit
NGTS	2023/09/04-2024/02/04	82594	10	104	NGTS	N/A	`bsproc`	Ingress:2024/01/21
TESS	2024/12/18-2025/01/14	9360	200	21.67	TESS	87	Custom	Transit
NGTS**	2025/10/22	3788	10	1	NGTS	N/A	`bsproc`	Ingress
Acton-Sky-Portal	2025/10/22	762	20	1	r'	N/A	`AstroImageJ`	Ingress
LCO-CTIO	2025/10/22	141	60	1	r'	N/A	`AstroImageJ`	Ingress
ULMT	2025/10/22	77	60	1	r'	N/A	`AstroImageJ`	Egress
Lookout	2025/10/22	551	30	1	OSC	N/A	`AstroImageJ`	Egress
OACC-CAO	2025/10/22	74	120	1	$i2$	N/A	`AstroImageJ`	Ingress
KeplerCam	2025/10/22	305	120	1	i'	N/A	`AstroImageJ`	Egress

* For TESS this is calculated by (Exptime (s) $\times N_{\text{images}}$)/86400 s while for all ground based instruments this is simply the count of nights with observations.
** For NGTS on 2025/10/22, simultaneous observations conducted with 6 telescope units.

KeplerCam (1.2 m)

The Fred Lawrence Whipple Observatory (FLWO) in southern Arizona is equipped with a 1.2 m telescope (Szentgyorgyi et al., 2005). The telescope is fitted with KeplerCam, a conventional CCD imager based on the Fairchild CCD 486 detector. The large-format sensor, comprising 4096×4096 pixels with a pixel pitch of 15 microns, provides a field of view of approximately $23' \times 23'$, making it well suited for high-precision transit photometry. An egress event was detected for the target NGTS-39 b on the night of 2025/10/22, with the i' filter and an exposure time of 120 s. An uncontaminated $12''$ target aperture was used for photometry, yielding a 10 ppt transit event.

6.3 Spectroscopy

6.3.1 Radial Velocity monitoring with CORALIE

RV measurements were taken for NGTS-39 with the CORALIE instrument (Queloz et al., 2001). CORALIE is a high-resolution, fiber-fed echelle spectrograph mounted on the 1.2 m Leonard Euler Swiss Telescope at La Silla Observatory in Chile. It delivers a resolving power of $R \approx 60{,}000$ and operates in the visible wavelength range, yielding an accuracy of approximately 3-5 ms^{-1} (Ségransan et al., 2010; Fontanet et al., 2025). The effective precision depends on the target properties and observing conditions. In total, we collected 43 RV measurements across two observing epochs: 14 data points between 2023/04/16 and 2024/04/09, and 29 data points between 2024/10/28 and 2026/01/29. We excluded in total 4 data points, due to noisy CCF and high airmass (>1.74). An instrument upgrade occurred between the two epochs, introducing an additional RV offset; consequently, we treat CORALIE14 and CORALIE24 as separate instruments throughout our analysis. CORALIE has demonstrated long-term Doppler stability in planet-search programmes spanning more than two decades for suitable targets (Ségransan et al., 2010; Rickman et al., 2019). All observations were acquired with an exposure time of 1500 s. The spectra were reduced using the standard CORALIE reduction pipeline (DRS 3.3.12), and RV measurements derived from standard cross-correlation

techniques with a numerical F9 mask. In our data, the median RV uncertainties of the CORALIE measurements are 23.7 m s^{-1} for CORALIE14 and 21.5 m s^{-1} for CORALIE24. These uncertainties are substantially larger than the intrinsic CORALIE precision. The CORALIE RVs are therefore dominated by photon noise rather than by the instrumental precision floor. The CORALIE data is set out in Table 6.5. These measurements, together with the HARPS data show a signal matching with the photometric period and yielding the mass of the planet.

6.3.2 Radial Velocity monitoring with HARPS

We obtained spectra of NGTS-39 using HARPS (Pepe et al., 2002), the high-resolution, fiber-fed echelle spectrograph mounted on the ESO 3.6-m telescope at La Silla Observatory in Chile. HARPS provides a resolving power of $R \approx 115{,}000$ across the visible band and is optimised for ultra-stable, high-precision RV measurements. In total, we collected 17 RV measurements by the Warm Jupiter program (program numbers are : 112.261U.002, 112.261U.003, 116.28XG.001, 116.29B6.001) using exposure time that varied between 1500 s to 1800 s for each observation. Three measurements were taken between 2024/04/07 and 2024/04/11, seven between 2025/02/19 and 2025/11/21, and four between 2025/10/16 and 2025/10/26. For our HARPS data, the median RV uncertainty is 6.3 m s^{-1}. This is larger than the typical HARPS instrumental accuracy of ~ 1 m s^{-1}. This effective precision depends on the target properties and observing conditions. The HARPS RV uncertainties are therefore dominated by photon noise rather than by the instrumental precision floor.

The data were reduced using the HARPS Data Reduction Software (DRS 3.3.6). Radial velocities were derived via cross-correlation with the F9 mask, providing measurements of the RV, CCF full width at half maximum, bisector span, and associated uncertainties (Baranne et al., 1996b; Pepe et al., 2002). The HARPS data is set out in Table 6.5. These data showed a signal consistent with the CORALIE data indicating a Jupiter-mass exoplanet in a 58 day orbital around NGTS-39. The HARPS spectra of NGTS-39 were also co-added and used for determining the stellar parameters (see subsection 6.4.1).

6.4 Analysis and Results

6.4.1 Stellar analysis of the system

The spectroscopic parameters ($T_{\rm eff}$, $\log g_\star$, [Fe/H]) were estimated using the `ARES+MOOG` method described in Santos et al. 2013; Sousa 2014; Sousa et al. 2021. For this we used the `ARES` code[3] (Sousa et al., 2007, 2015) to measure the equivalent widths (EWs) for the list of Fe I and Fe II lines presented in Sousa et al. (2008). The spectrum analysed was obtained by co-adding the individual exposures performed by HARPS on the target (co-added S/N $\approx$ 110 per pixel at 5500 Å), such that the uncertainty on the derived parameters is not limited by the spectra S/N, but by the intrinsic precision and accuracy of the method instead (for details see Figueira et al. (2025)). The best set of spectroscopic parameters was determined by using a minimization process to find the ionization and excitation equilibrium using a grid of Kurucz model atmospheres (Kurucz, 1993) and the latest version of the radiative transfer code `MOOG` (Sneden, 1973). We also measured $v \sin i_\star$ from isolated

[3]The last version, `ARES` v2, can be downloaded at `https://github.com/sousasag/ARES`

metal lines. Moreover, we derived a more accurate trigonometric surface gravity using Gaia DR3 (Gaia Collaboration et al., 2023) data following the same procedure as described in Sousa et al. (2021), which provides a value consistent with the spectroscopic one.

To determine the stellar radius of NGTS-39, we utilised a Markov chain Monte Carlo (MCMC) modified infrared flux method (IRFM – Blackwell & Shallis, 1977; Schanche et al., 2020). By building a spectral energy distribution from stellar atmosphere models (Castelli & Kurucz, 2003) using our spectroscopically derived stellar parameters, we obtained synthetic photometry that was compared to observed broadband fluxes in the following bandpasses: 2MASS J, H, and K, WISE $W1$ and $W2$, and *Gaia* G, $G_{\rm BP}$, and $G_{\rm RP}$ (Skrutskie et al., 2006; Wright et al., 2010; Gaia Collaboration et al., 2023). This enables us to compute the stellar bolometric flux, from which we obtained the effective temperature and stellar radius when combined with the offset-corrected *Gaia* parallax (Lindegren et al., 2021).

We finally derived the stellar mass and age after inputting $T_{\rm eff}$, [Fe/H], $R_\star$, and $v \sin i_\star$ along with their uncertainties in the isochrone placement routine by Bonfanti et al. (2015, 2016). The algorithm interpolates the input set within pre-computed grids of PARSEC[4] v1.2S (Marigo et al., 2017) isochrones and tracks, further implementing the gyrochronological relation from Barnes (2010) to improve convergence as detailed in Bonfanti et al. (2016). Following Bonfanti et al. (2021), we conservatively inflated the internal uncertainties of the outcomes to account for the isochrone precision and obtained the results listed in Table 6.1.

6.4.2 Global modelling of the NGTS-39 system

We performed global modelling of the NGTS-39 system to determine the physical and orbital parameters of the exoplanet NGTS-39 b. Our analysis combines space-based photometry from TESS, ground-based photometry from NGTS and the SG1 follow-up network, the RV measurements obtained with HARPS and CORALIE, and the stellar parameters derived from the co-added HARPS spectra, and stellar parameters from *Gaia* (Gaia Collaboration et al., 2016).

The modelling was carried out using the `allesfitter` python package (Günther & Daylan, 2019, 2021), which enables the simultaneous analysis of multi-instrument light curves and RV data within a unified Bayesian framework. Transit light curves were modelled using the `ellc` package (Maxted, 2016), while parameter inference was performed using the nested sampling algorithm implemented in `dynesty` (Speagle, 2020), following the formalism of Skilling (2004) and Skilling (2006). The sampling was initialised with 500 live points and used a single bounding strategy to enclose the evolving set of live points. New samples were drawn using a random-walk proposal within the likelihood constraint, providing exploration of the parameter space. The nested sampling run was terminated once the remaining contribution to the Bayesian evidence fell below a tolerance of 1%. For the spectroscopic data, we used the `sample_linear` baseline model for each RV instrument. This accounts for the independent velocity zero-point offsets between HARPS and the two CORALIE datasets, while fitting a common linear RV trend across all three instruments.

We used uniform priors for orbital period P, radius ratio ($R_{\rm p}/R_*$), semi-major axis ($(R_* + R_{\rm p})/a$), epoch of inferior conjuction ($T_{0,{\rm p}}$), orbital inclination ($\cos i_p$). We use normal priors for the quadratic limb darkening coefficients calculated based on the effective temperature, metallicity

[4] *PA*dova and T*R*ieste *S*tellar *E*volutionary *C*ode: `https://stev.oapd.inaf.it/cgi-bin/cmd`

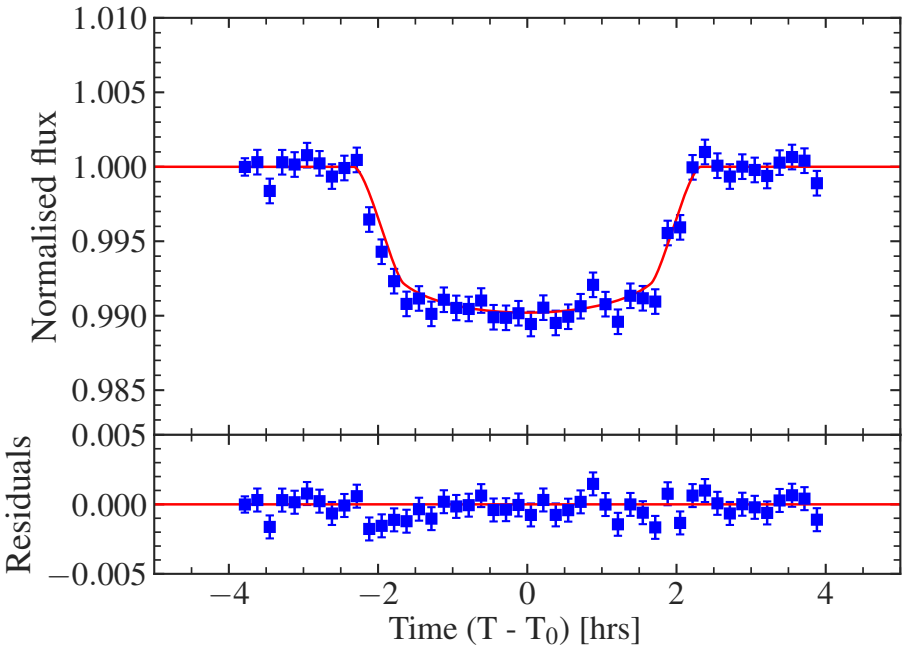
Table 6.4: NGTS-39 b properties.

Parameter	Value*	Source
Period (days)	$58.204720^{+0.000042}_{-0.000038}$	`allesfitter`
Transit Parameters		
T_0 (BJD)	$2460157.03626 \pm 0.00055$	`allesfitter`
R_p/R_*	0.09651 ± 0.00060	`allesfitter`
R_*/a	$0.01751^{+0.00028}_{-0.00026}$	`allesfitter`
b	$0.639^{+0.020}_{-0.023}$	`allesfitter`
T_{14} (hrs)	4.639 ± 0.035	`allesfitter`
T_{23} (hrs)	3.325 ± 0.046	`allesfitter`
RV parameters		
K (km s^{-1})	0.0755 ± 0.0022	`allesfitter`
e	0.386 ± 0.019	`allesfitter`
ω (degrees)	98.3 ± 3.1	`allesfitter`
$\dot{\gamma}$ (m s^{-1} yr^{-1})	-17.75 ± 1.86	This Work (§6.4.3)
Derived parameters		
R_p (R_J)	1.088 ± 0.012	`allesfitter`
M_p (M_J)	1.467 ± 0.081	`allesfitter`
ρ_p (g cm^{-3})	1.411 ± 0.092	`allesfitter`
a (au)	0.3077 ± 0.0055	`allesfitter`
Periapsis	0.189 ± 0.007	$a(1-e)$
Apoapsis	0.426 ± 0.010	$a(1+e)$
$T_{\rm eq}$ (K)	519^{+6}_{-5}	`allesfitter`
g_b (cgs)	3040^{+150}_{-140}	`allesfitter`
$T_{\rm eq;Apastron}$ (K)	441^{+8}_{-7}	This work (§6.4.3)
$T_{\rm eq;Periastron}$ (K)	662^{+18}_{-17}	This Work (§6.4.3)

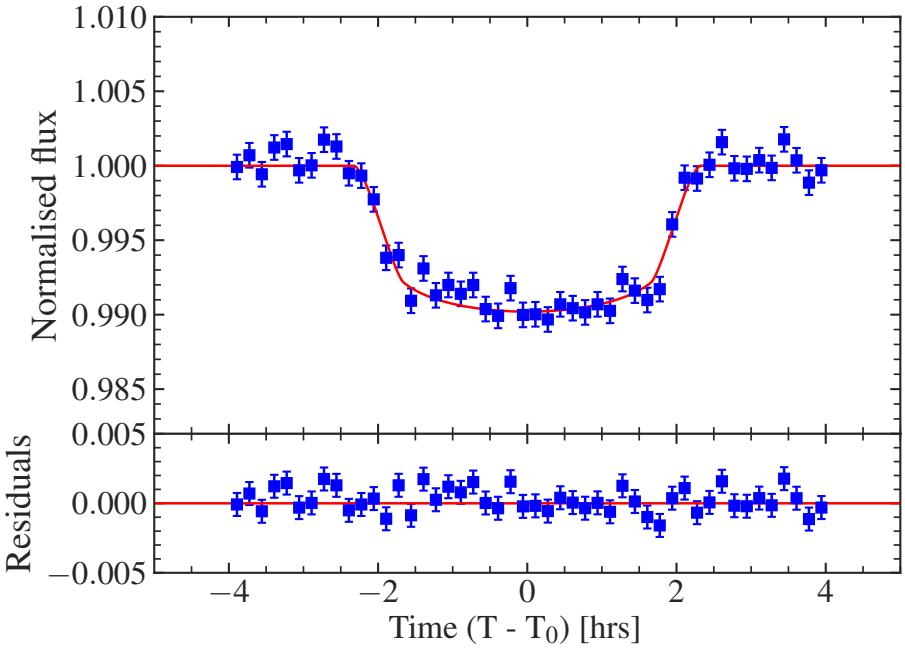
* Those values represent the posterior median values.

and the logarithm surface gravity, $\log g_\star$ of the host star (Sing, 2010). For the treatment of limb darkening, we used the stellar effective temperature, metallicity, and surface gravity, $\log g_\star$, to estimate the quadratic limb-darkening coefficients of the host star (Sing, 2010). This was done using the Limb Darkening Tool Kit (LDTK; Parviainen & Aigrain, 2015), which provides the coefficients in the conventional u_1, u_2 parametrisation. These coefficients were then converted into the triangular q_1, q_2 parametrisation introduced by Kipping (2013), and applied in `allesfitter` as normal priors. We fit the eccentricity and argument of periastron of the system (implemented as the terms $\sqrt{e}\cos\omega$ and $\sqrt{e}\sin\omega$). We also include a dilution factor for the TESS data, as the target star was contaminated by star with number 2 and delta magnitude of 4 within the aperture (see Figure 6.1). We detect an additional linear RV trend. We therefore fit for a linear RV trend in the data. Independent zero point offset for each spectrograph are also fitted to account for absolute instrumental offsets between CORALIE (pre and post upgrade) and HARPS. All of the fitted parameters are set out in Table 6.7.

Our results of the final global model are presented in Table 6.4, and we overplot corresponding median posterior model as a solid red line on our photometric and RV data in Figure 6.4, Figure 6.5, Figure 6.6, and Figure 6.7. The global model derived values of the system are presented in Table 6.8.

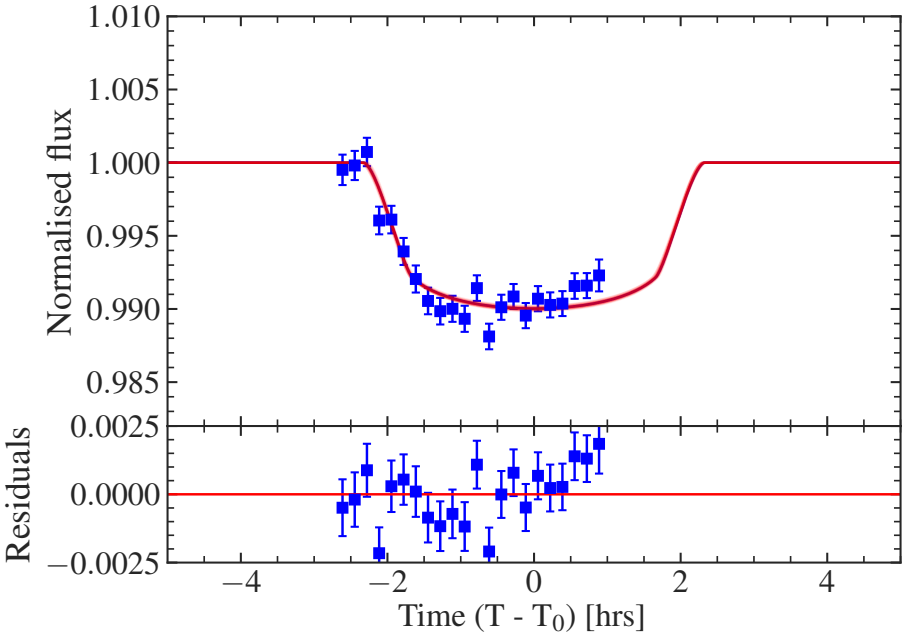


(a) TESS Sector 33 transit.

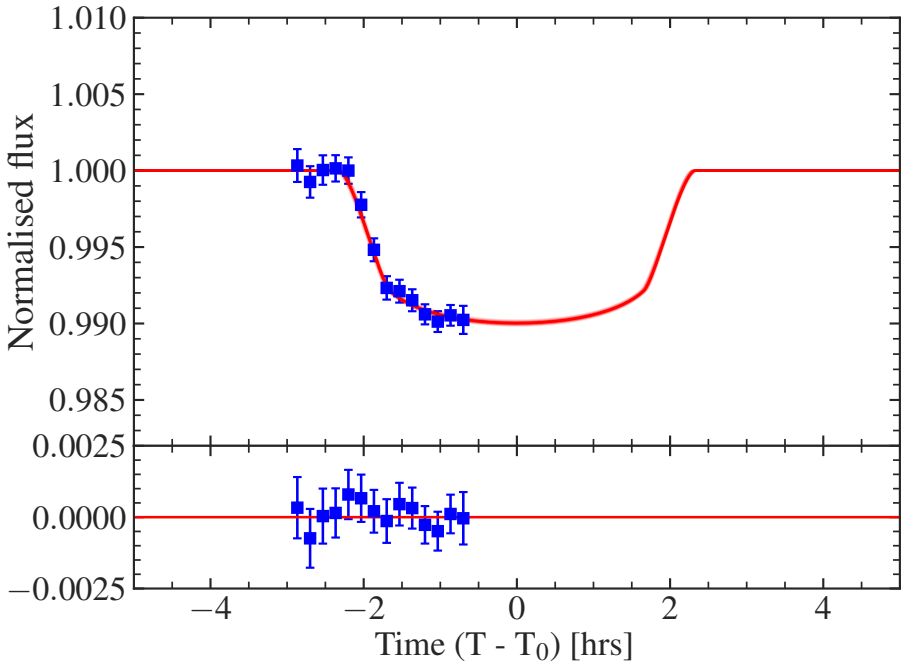


(b) TESS Sector 87 transit.

Figure 6.4: Transit lightcurves for NGTS-39 from TESS. Each panel displays the transit data, depicted by square markers with errors. The data is binned to 10-minutes. The transit model is shown with the solid line. The left panel shows the data from TESS Sector 33 centered on BJD=2459225.7606 recorded with 10 minutes cadence and with the TESS filter. The right panel shows the data from TESS Sector 87 centered on BJD=2460680.8787 recorded with 200 s cadence and with the TESS filter.



(a) NGTS transit with 1 telescope



(b) NGTS transit with 6 telescopes

Figure 6.5: Transit lightcurves for NGTS-39, from NGTS. Each panel displays the transit data, shown as square markers with errors. The data are binned to 10-minutes. The transit model is shown with the solid line. The left panel shows the data from NGTS with 1 telescope unit, with 10 s exposure using the NGTS filter from the observing night of 2024/01/21 centered on BJD=2460331.6503. The right panel shows the data from NGTS with 6 telescope units, with 10 s exposure using the NGTS filter from the observing night of 2025/10/22 centered on BJD=2460971.9023.

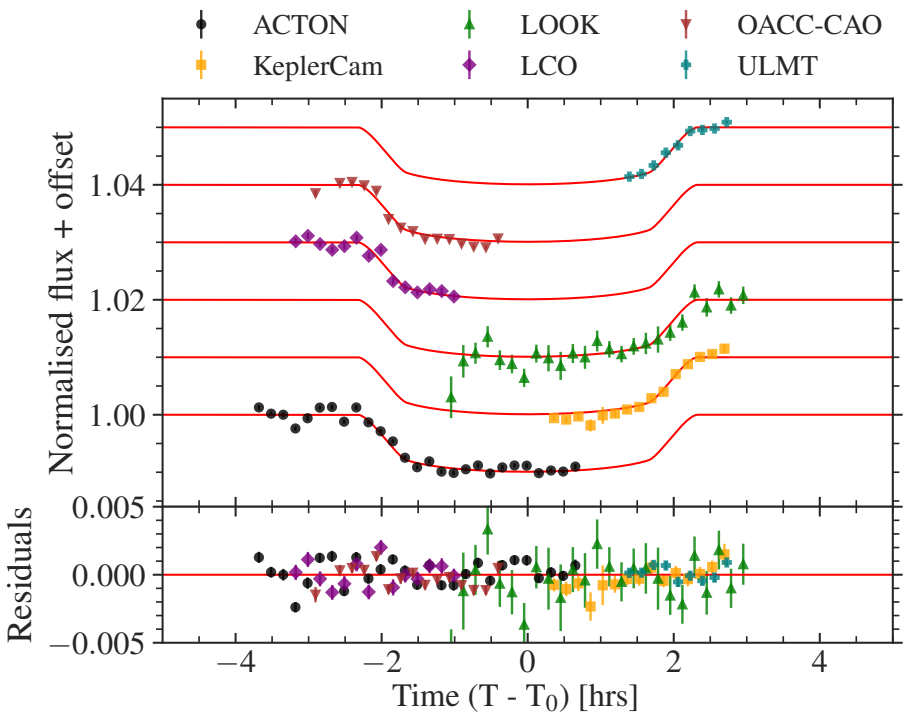


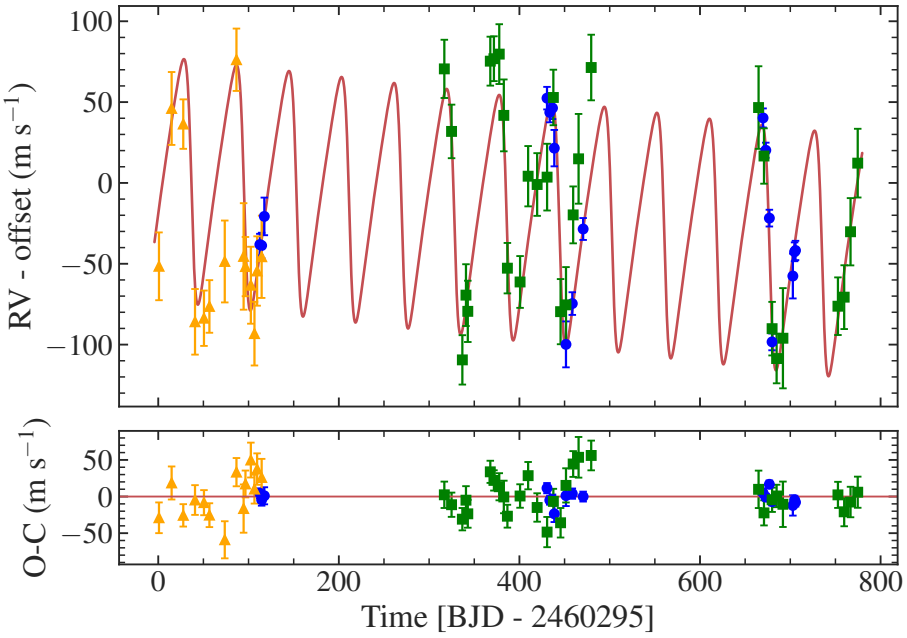
Figure 6.6: Transit lightcurve of NGTS-39 normalised to the out-of-transit flux levels taken with LCO-CTIO, ULMT, Lookout, Acton Sky Portal, KeplerCam and OACC-CAO on 2025/10/22 centered on BJD=2460971.9023. The best fit model is shown in red. The data are binned to 10-minutes for clarity. The panel shows the six individual light curves, each vertically offset for clarity.

6.4.3 The NGTS-39 system

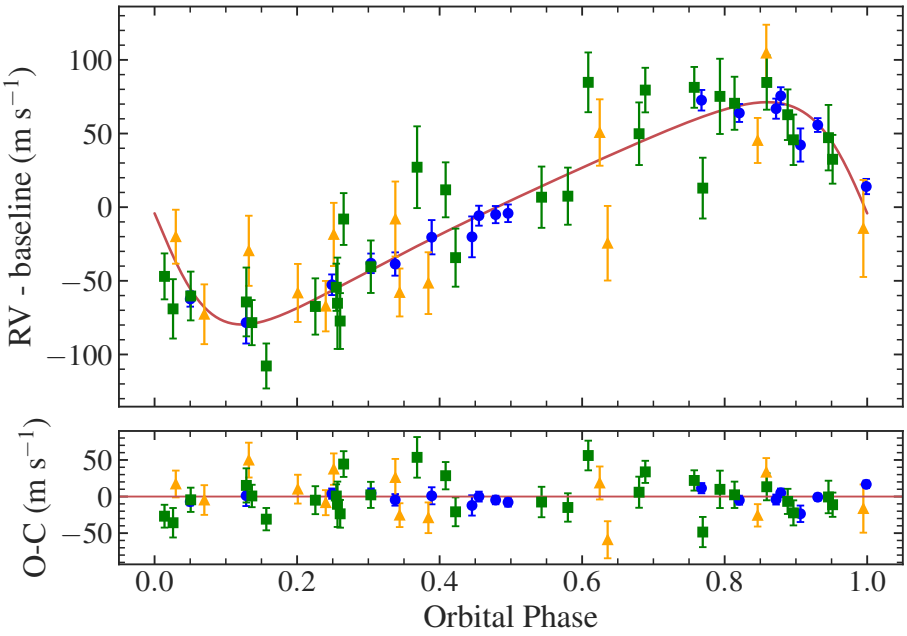
NGTS-39 b is a Jupiter-sized gas giant exoplanet with a radius of $1.088 \pm 0.012\,R_J$ and a mass of $1.467 \pm 0.081\,M_J$, implying a bulk density of $1.411 \pm 0.092\,\mathrm{g\,cm^{-3}}$, which is consistent with a composition dominated by hydrogen and helium, although its density is higher than that of Jupiter and may indicate an enhanced heavy-element content. The planet completes one full orbit every $58.204720^{+0.000042}_{-0.000038}$ days with a semi-major axis of 0.3077 ± 0.0055 AU. Owing to its relatively long orbital period, NGTS-39 b has a moderate mean equilibrium temperature of 519^{+6}_{-5} K, computed assuming a Bond albedo of 0.3, unit emissivity, and full day-night heat redistribution, placing it in the warm Jupiter regime. The planet exhibits a high orbital eccentricity of 0.386 ± 0.019.

The RV data reveals a long-term trend of $\dot{\gamma} = -17.75\,\mathrm{m\,s^{-1}\,yr^{-1}}$, which is evident in Figure 6.7a, over a total RV baseline spanning 2.11 years. This trend indicates the presence of an additional, longer-period companion in the system. To assess whether the trend could instead be caused by stellar activity, for example by long-term magnetic variability, we compared the RV residuals retaining the long-term trend with available activity indicators, namely the FWHM of the cross-correlation function and the H-α index. We find no significant correlation between the RV drift and either diagnostic, supporting the interpretation that the observed long-term RV trend is not due to stellar activity.

In addition to the outer longer-period companion, we also searched to see if NGTS-39 hosts any additional exoplanets. The transit mid-times from the two observed epochs of TESS observations, Sectors 33 and 87, the observed ingress from NGTS and the combined lightcurve of NGTS with



(a) RV versus time of NGTS-39.



(b) Phase folded radial velocities of NGTS-39.

Figure 6.7: RV measurements of NGTS-39. CORALIE data from the first (CORALIE14) and second (CORALIE24) observing cycles are shown as yellow triangles and green squares, respectively, while HARPS measurements are represented by blue circles. The solid line indicates the best-fit RV model. The left panel presents the radial velocities over time along with the residuals from the fit, and the right panel shows the phase-folded radial velocities with their residuals.

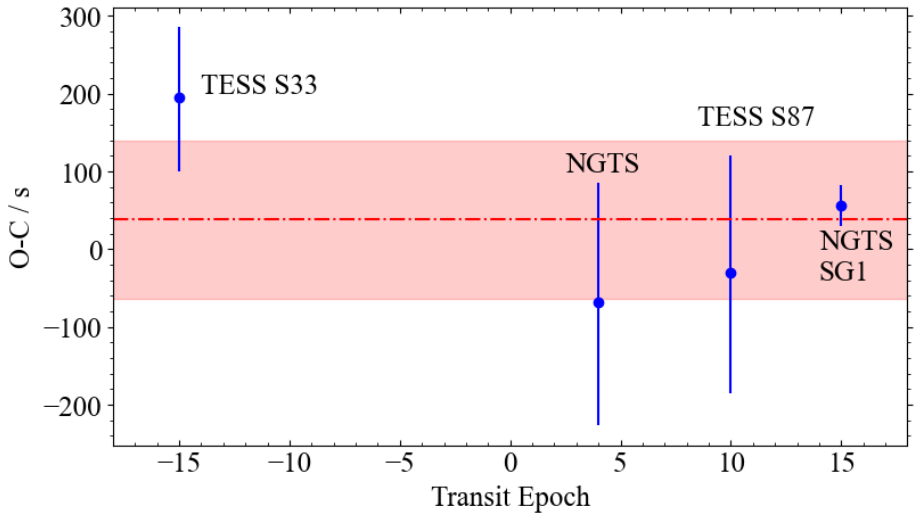


Figure 6.8: O-C diagram for transit NGTS-39 b using TESS data of Sector 33 and 87 (epochs -15 and 10 respectively), NGTS monitoring (epoch 4) and follow-up data from NGTS and the SG1 network (epoch 15). The mean value of the linear model is shown as a red dashed line and the 1-σ RMS with the red shaded area.

6 telescopes and SG1 network were independently fitted to search for deviations from a linear ephemeris, which would indicate transit timing variations (TTVs). A linear fit to the transit times yields an ephemeris consistent with a constant orbital period, with residuals that are consistent with zero within the timing uncertainties. No statistically significant TTV signal is detected across the four transits of NGTS-39 b - see Figure 6.8.

Searches for additional periodic signals in the photometric and RV data did not reveal strong evidence for a second planet. The transit search using all the available photometric data recovered the known signal at $\approx$ 58.2 d, using the Box Least Square method (BLS; Kovács et al., 2002) consistent with the adapted orbital period found from the joint model. Broader period searches were dominated by alias structure. After masking the transit signal and repeating the analysis on the residual lightcurves, the remaining peaks were weak and lacked coherence expected for a robust additional transiting companion. A complementary period search of the RVs likewise recovered the known planet near 58.2 d. Additionally, we found a weaker peak at approximately 29.1 d in the RV periodogram. We note that the absence of corresponding transits (the transits would have been evident in Sector 7 and Sector 71) does not by itself exclude an additional planet, since such a planet could have a non-transiting orbital inclination. We therefore tested whether this signal persists after removing the fitted signal of the known planet. After subtracting the `allesfitter` posterior-median eccentric RV model for the 58.2 d planet, together with the fitted RV baselines, we recomputed the periodogram of the RV residuals. The 29.1 d signal was no longer significant, with a false-alarm probability of 1.0. Since this period is also very close to half of the fitted planet period, $P/2 = 29.102$ d, we interpret the 29.1 d peak as the first harmonic of the eccentric 58.2 d RV signal rather than evidence for an independent planetary signal. We therefore find no statistically evidence for an additional planet in the present photometric and RV data.

6.4.4 Sensitivity maps for Companions

In order to make a quantitative assessment of which potential companion planets are ruled out by our data, and which remain allowed, we assessed the detection limits of the TESS data for NGTS-39 b using the Transit Investigation and Recoverability Application (`TIaRA`; Rodel et al., 2024). We used lightcurve timestamps, contamination values, and the measured photometric precision extracted from the lightcurve `FITS` headers (1-`CROWDSAP` and `CDPP2_0`, respectively) as input for all available sectors. From these inputs, `TIaRA` generates synthetic transiting planet parameters and calculates the expected signal-to-noise ratio and detection probability for a range of orbital periods and planetary radii, producing a sensitivity map shown in Figure 6.9. The resulting map indicates that TESS is most sensitive to large, short-period planets interior to the orbit of NGTS-39 b, where multiple transits are more likely to fall within the observing baseline and the transit signal is correspondingly easier to recover. We note that the sensitivity map in Figure 6.9 does not necessarily reach unity, even for high signal to noise ratio signals, because `TIaRA` converts signal to noise ratio into a recovery probability using incomplete gamma functions that asymptote below unity. This recovery probability is then multiplied by the observing-window probability, further limiting the final sensitivity value (Rodel et al., 2024).

In contrast, the sensitivity decreases toward longer orbital periods, reflecting the reduced probability of observing one or more transits and the lower number of available events from which to build detection significance. Long-period ($P > 100$ d), Jupiter-sized companions are therefore unlikely to be detected by TESS around this star. Likewise, planets with radii smaller than Neptune-sized ($\sim 3.8\,R_\oplus$) are unlikely to be detectable by TESS regardless of their orbital period, so the analysis cannot rule out smaller inner or outer companions. Thus, while the existing TESS data place useful limits on close-in, large- radius companions, they do not exclude lower-radius planets or giant companions on wider orbits.

6.5 Discussion

6.5.1 Parameters of NGTS-39 b

NGTS-39 b is a long-period exoplanet that contributes to the small but growing population of transiting gas giant planets on wide orbits, as illustrated in the period–radius and period–eccentricity diagrams shown in Figure 6.10. In our sample we included only transiting exoplanet systems with P > 10 days and M > 0.5 M_J, resulting in 123 exoplanets. In both parameter spaces, NGTS-39 b occupies a region that is sparsely populated by known exoplanets, highlighting the rarity on detecting of such systems. Its relatively long orbital period places it beyond the bulk of the well-characterised hot Jupiter population, while its high eccentricity further distinguishes it from the predominantly low eccentricity Jupiter-mass planets found at shorter periods.

6.5.2 The atmosphere of NGTS-39 b

Warm Jupiters are particularly valuable targets for atmospheric studies, as they occupy a transitional regime between hot Jupiters and the colder gas giants of the Solar System, where different chemical and physical processes are expected to dominate (Showman et al., 2020; Fortney et al., 2020).

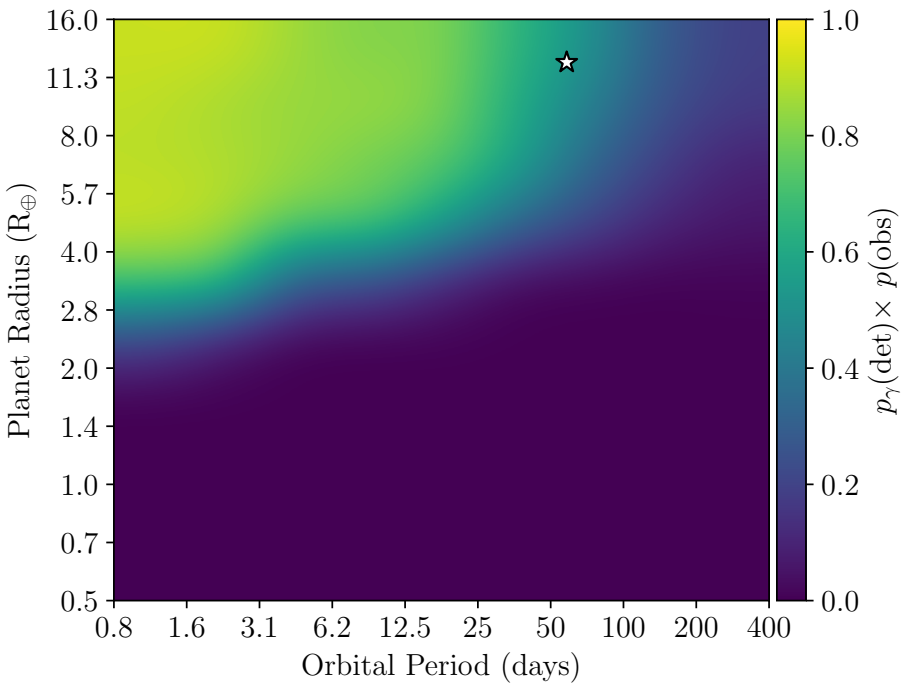


Figure 6.9: Sensitivity maps from `TIaRA` for NGTS-39 in TESS. The target is overplotted as a white star with black borders.

NGTS-39 b is therefore an interesting object for atmospheric characterisation because its relatively moderate equilibrium temperature places it in a sparsely explored chemical regime, while its host star is sufficiently hot and bright to make follow-up observations feasible. To place NGTS-39 b in context, we use the same sample of transiting exoplanets as in subsection 6.5.1, to examine the relationship between the host star's effective temperature and the planet's equilibrium temperature, highlighting the atmospheric regime in which this system resides based on Fortney et al. (2020).

Our results are presented in Figure 6.11. NGTS-39 b lies near the transition between molecular nitrogen (N_2) and ammonia (NH_3), making it an excellent target for follow-up spectroscopic observations aimed at probing atmospheric chemistry in this temperature regime. We note, however, that the N_2-NH_3 transition reported by Fortney et al. (2020) is calculated for a $1\,M_J$ planet, whereas NGTS-39 b has a mass of approximately $1.5\,M_J$. The location of this transition may therefore shift slightly for NGTS-39 b, although we do not expect the effect to be large; if anything, the transition would likely occur at somewhat higher temperature. Additionally, we estimate the planetary temperature variations based on the periastron and apastron distances, taking into account the planet's high orbital eccentricity. We found a periastron temperature of 662^{+18}_{-17},K and an apastron temperature of 441^{+8}_{-7} K. These values suggest that NGTS-39 b lies between the CO–CH_4 and N_2–NH_3 chemical transition boundaries at apastron, while at periastron it falls below the N_2–NH_3 transition.

6.5.3 An outer companion

Since the current RV observations likely cover only a limited fraction of such an outer orbit, the signal appears as an approximately linear acceleration rather than a fully resolved Keplerian signal. Continued RV monitoring is required to detect any curvature in the trend and to constrain the orbital

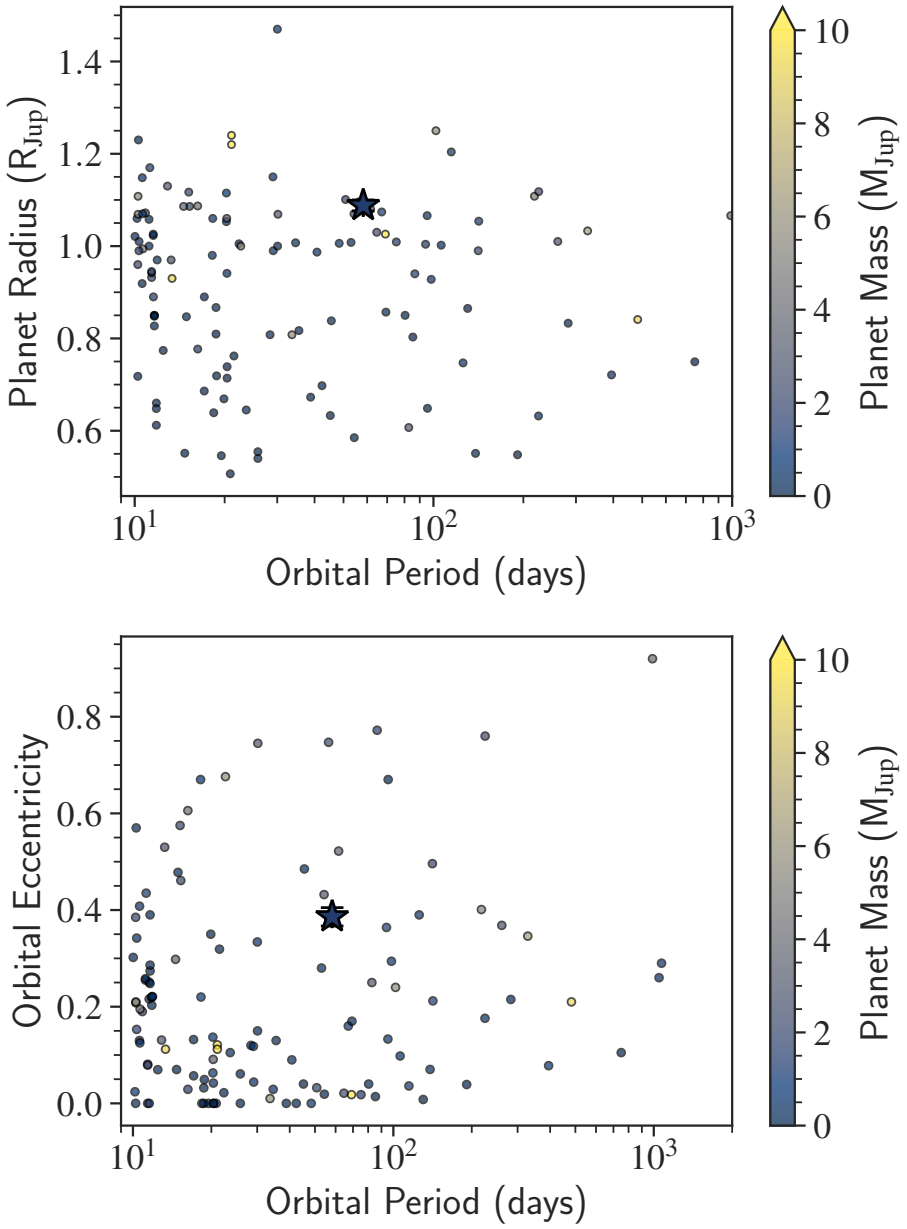


Figure 6.10: Population diagrams showing planetary radius (top) and orbital eccentricity (bottom) as a function of orbital period for exoplanets with period > 10 days and radius > 0.5 R_{Jup}. NGTS-39 b is highlighted as a star marker with a black outline and is colour-coded by its mass, consistent with the rest of the planetary sample.

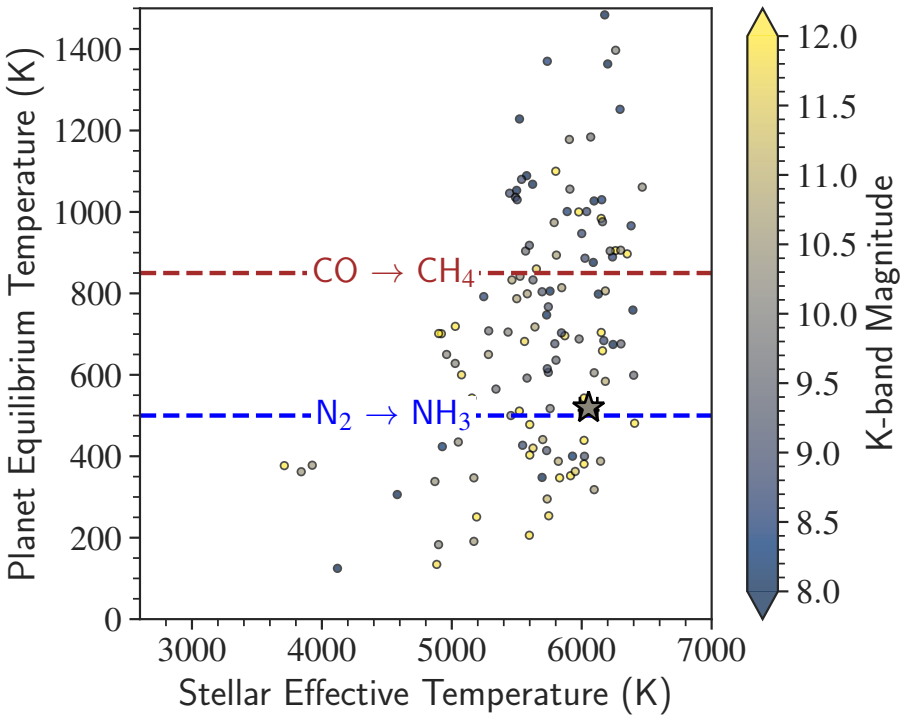


Figure 6.11: Stellar effective temperature, $T_{\rm eff}$, is plotted against planetary equilibrium temperature, $T_{\rm eq}$. NGTS-39 b is highlighted as a star marker with a black outline and is colour-coded by its orbital eccentricity, consistent with the rest of the planetary sample. The horizontal dashed lines at 850 K and 500 K mark the expected CO–CH_4 and N_2–NH_3 chemical transition boundaries, respectively, for a 1 M_J planet (Fortney et al., 2020).

period, eccentricity, and mass of the outer companion.

The Gaia RUWE value of 0.793 indicates a single-star astrometric solution, with no evidence for a significant astrometric signal in the Gaia DR3 data (Castro-Ginard et al., 2024). This disfavours a stellar-companion capable of producing a large astrometric signal. However, it does not rule out a lower-mass companion, such as a massive planet or brown dwarf, nor a companion on an orbit with a period significantly longer than the 34-month Gaia DR3 observing baseline relevant to the RUWE metric (Guerriero et al., 2026).

6.6 Conclusion

In this work, we report the detection and characterisation of NGTS-39 b, a long-period warm Jupiter. A transit was initially observed by TESS in Sector 33. The NGTS follow-up group marked it as a monotransit and initiated an observing campaign for follow-up photometry of NGTS-39 with NGTS. An ingress event of NGTS-39 b was observed and with another transit in Sector 87 the orbital period was constrained. Ground-based follow-up photometry from NGTS was further obtained to better demonstrate the orbital period, with additional photometric observations from the SG1 network further refining the planetary parameters. We also acquired spectroscopic RV measurements with HARPS and CORALIE to confirm the planetary nature of the signal and measure the planetary mass and orbital properties.

A detailed stellar analysis was performed for NGTS-39, which is found to be a main-sequence F9 star. NGTS-39 b is a warm Jupiter with a mass of $1.467 \pm 0.081\,\mathrm{M}_J$ and a radius of $1.088 \pm 0.012\,\mathrm{R}_J$. It completes one orbit every $58.204720^{+0.000042}_{-0.000038}$ days, has an equilibrium temperature of 519 K (assuming a Bond albedo of 0.3), and exhibits a relatively high orbital eccentricity of 0.386 ± 0.019.

This work highlights the importance of systematic follow-up of single-transit events detected by TESS, which are likely to reveal a substantial and previously under-explored population of long-period exoplanets. Such planets provide crucial constraints on planetary formation and migration pathways, particularly in the regime between hot and cold Jupiters. Expanding this sample will help bridge current observational gaps and improve our understanding of the diversity of giant exoplanet architectures. NGTS-39 b is also a valuable target for spectroscopic follow-up being close to the boundary where ammonia is expected to become visible.

Additional RV measurements over a longer time baseline, together with future astrometric constraints, will be required to confirm the nature of the outer companion in the NGTS-39 system.

6.7 Appendix: RV dataset

6.8 `allesfitter` results tables

Table 6.5: Spectroscopic data for NGTS-39.

Instrument	Time (BJD -2400000)	RV ($m\,s^{-1}$)	RV error ($m\,s^{-1}$)	FWHM ($m\,s^{-1}$)	Bisector ($m\,s^{-1}$)	Contrast	H-α	Ca II H K	Na D
CORALIE-14	60295.80997534	42122.52	20.82	9426.90	-107.30	43.15	0.186224	0.245857	0.341326
CORALIE-14	60309.80438275	42220.16	22.41	9332.33	54.11	43.64	0.203109	0.033177	0.358816
CORALIE-14	60322.70379500	42210.49	15.09	9383.14	-52.96	43.22	0.194693	0.124007	0.357653
CORALIE-14	60335.71434432	42088.20	20.14	9291.79	28.43	42.57	0.198576	0.011834	0.365156
CORALIE-14	60345.62997957	42090.41	16.94	9374.09	-25.19	43.39	0.183313	0.193392	0.345591
CORALIE-14	60351.66770422	42097.69	16.08	9333.39	-8.98	43.61	0.191872	0.184797	0.358601
CORALIE-14	60368.65611608	42125.52	25.20	9309.97	3.17	42.35	0.160463	0.237732	0.356916
CORALIE-14	60381.61307386	42250.29	19.13	9345.37	-48.46	43.01	0.182704	0.201045	0.382469
CORALIE-14	60389.54133268	42128.63	32.85	9329.29	-79.17	41.81	0.159824	0.199310	0.364466
CORALIE-14	60391.58859461	42122.35	18.16	9334.37	25.24	43.05	0.190052	0.156512	0.347210
CORALIE-14	60397.55231894	42110.82	23.67	9408.83	49.91	42.73	0.191502	0.049140	0.351448
CORALIE-14	60401.55403324	42080.88	19.54	9266.32	-63.38	42.86	0.175115	0.212246	0.345227
CORALIE-14	60404.48954468	42119.63	21.31	9187.39	-49.41	43.26	0.160620	0.107313	0.338301
CORALIE-14	60409.52064332	42128.42	25.34	9348.32	-20.34	43.22	0.182833	0.138028	0.365810
CORALIE-24	60611.83969783	42216.72	17.84	9339.57	-24.45	43.26	0.198008	0.167301	0.365139
CORALIE-24	60619.84957792	42178.04	16.37	9359.11	-32.96	43.50	0.184750	0.199590	0.354664
CORALIE-24	60631.79977263	42036.72	15.07	9261.17	-20.02	42.96	0.176178	0.140397	0.361714
CORALIE-24	60635.80691002	42076.78	18.94	9310.96	-9.49	43.51	0.182663	0.100758	0.352635
CORALIE-24	60637.83314197	42066.74	18.79	9327.81	-30.63	43.57	0.195988	0.134071	0.351991
CORALIE-24	60662.75537131	42221.50	14.93	9297.96	-52.07	42.54	0.186954	0.156429	0.373003
CORALIE-24	60666.75489358	42223.01	13.63	9308.58	-70.23	43.70	0.187874	0.079251	0.368996
CORALIE-24	60672.67503791	42225.85	18.33	9347.91	20.81	43.64	0.179017	0.201322	0.345683
CORALIE-24	60677.71792751	42187.95	22.08	9258.96	-29.21	43.53	0.187195	0.273395	0.354393
CORALIE-24	60681.69018643	42093.45	15.40	9364.65	-55.30	43.68	0.188171	0.119931	0.354403
CORALIE-24	60695.72248834	42084.92	15.83	9473.43	9.45	43.28	0.166405	0.088115	0.361517
CORALIE-24	60704.65294822	42150.33	18.49	9364.99	-13.09	43.15	0.200977	0.243559	0.362203
CORALIE-24	60714.63558010	42145.20	19.23	9413.86	-16.62	43.42	0.188258	0.064294	0.348071
CORALIE-24	60725.65281709	42149.76	20.49	9347.55	-79.72	43.29	0.179946	0.159661	0.351143
CORALIE-24	60732.58889236	42199.03	17.00	9309.83	-39.47	43.59	0.182394	0.087075	0.359829
CORALIE-24	60740.59269182	42066.56	20.00	9360.40	-30.31	43.20	0.196144	0.189669	0.349143
CORALIE-24	60746.57986256	42070.76	23.22	9415.97	-22.77	42.51	0.196159	0.110846	0.360828
CORALIE-24	60754.52654126	42126.40	17.42	9317.42	-36.01	43.22	0.183655	0.182711	0.350245
CORALIE-24	60760.52503366	42161.09	27.64	9451.71	-102.94	43.19	0.209401	0.155811	0.350728
CORALIE-24	60774.50584590	42217.57	20.14	9304.39	-26.90	42.84	0.212061	0.147045	0.358480
CORALIE-24	60959.87659787	42192.80	25.42	9351.20	-95.18	42.53	0.199527	0.184917	0.403718
CORALIE-24	60965.87765547	42162.82	16.95	9270.30	-95.66	43.58	0.178159	0.129352	0.393471
CORALIE-24	60974.85339112	42056.03	16.38	9418.28	-43.59	42.98	0.189350	0.192727	0.370193
CORALIE-24	60979.84728090	42037.55	15.11	9349.95	14.49	43.12	0.185702	0.109920	0.363239
CORALIE-24	60986.84233893	42050.12	30.90	9176.93	-47.38	43.11	0.200588	0.161048	0.339410
CORALIE-24	61047.76949862	42069.92	17.65	9341.74	-7.98	43.93	0.202864	0.145602	0.340958
CORALIE-24	61054.69166230	42075.52	19.57	9457.04	-41.79	44.20	0.179439	0.131281	0.352853
CORALIE-24	61061.71616546	42115.98	20.65	9355.73	-32.19	44.10	0.186088	0.033686	0.339726
CORALIE-24	61069.68088692	42158.41	21.11	9424.26	13.76	43.94	0.176873	0.080444	0.355464

Table 6.6: Continuation of Table 6.5.

Instrument	Time (BJD -2400000)	RV ($m\,s^{-1}$)	RV error ($m\,s^{-1}$)	FWHM ($m\,s^{-1}$)	Bisector ($m\,s^{-1}$)	Contrast	H-α	Ca II H K	Na D
HARPS	60407.53390987	41980.80	6.15	8757.43	-7.08	53.74	0.203691	0.107009	0.340540
HARPS	60409.50864809	41980.20	7.51	8733.59	-10.50	53.75	0.215756	0.084198	0.339823
HARPS	60412.48923116	41998.21	11.37	8760.99	-21.93	53.41	0.228377	0.045618	0.336937
HARPS	60725.54961517	42071.35	6.52	8723.64	-34.40	54.14	0.222461	0.053107	0.339989
HARPS	60728.63808268	42062.51	5.58	8695.46	-37.23	54.22	0.206239	0.068017	0.339346
HARPS	60731.64197968	42065.24	6.35	8739.46	-14.50	54.15	0.201473	0.059961	0.348973
HARPS	60733.63286984	42040.44	10.98	8778.35	3.42	53.75	0.224288	0.027084	0.358363
HARPS	60746.56373218	41919.05	13.98	8694.36	-33.72	52.92	0.257298	0.054322	0.361998
HARPS	60753.57069333	41944.29	6.56	8746.92	-64.82	53.82	0.209537	0.043312	0.348260
HARPS	60765.57675288	41990.42	6.30	8736.96	-8.24	53.97	0.212411	0.086548	0.351648
HARPS	60964.84191604	42059.11	5.34	8705.22	-15.77	54.03	0.217466	0.105728	0.374481
HARPS	60967.86233549	42039.13	3.97	8742.01	-55.68	53.91	0.205740	0.100019	0.356626
HARPS	60971.82641747	41997.14	4.55	8735.92	-42.63	53.91	0.209265	0.085147	0.365751
HARPS	60974.81643393	41920.59	4.55	8759.67	-30.39	53.82	0.210837	0.075404	0.368474
HARPS	60997.82760728	41961.33	13.63	8685.85	30.97	53.96	0.245599	-0.062214	0.363174
HARPS	60999.76036696	41976.32	5.27	8712.58	-32.39	53.95	0.216451	0.095447	0.354793
HARPS	61000.77443000	41977.14	5.43	8707.87	-32.62	54.09	0.214688	0.072879	0.348836

Table 6.7: `allesfitter` global fitted values and priors

Parameter	Prior	Fitted value	units
$R_b/R_\star$	$\mathcal{U}(0.09, 0.1)$	0.09651 ± 0.00060	
$(R_\star + R_b)/a_b$	$\mathcal{U}(0.01, 0.02)$	$0.01921^{+0.00031}_{-0.00029}$	
$\cos i_b$	$\mathcal{U}(0.002, 0.8)$	0.01812 ± 0.00071	
$T_{0;b}$	$\mathcal{U}(2460680.8, 2460680.9)$	$2460157.03626 \pm 0.00055$	bjd
P_b	$\mathcal{U}(58, 59)$	$58.204720^{+0.000042}_{-0.000038}$	d
$\sqrt{e_b}\cos\omega_b$	$\mathcal{U}(-1, 1)$	-0.090 ± 0.033	
$\sqrt{e_b}\sin\omega_b$	$\mathcal{U}(-1, 1)$	0.614 ± 0.016	
K_b	$\mathcal{U}(0.060, 0.090)$	0.0755 ± 0.0022	$km\,s^{-1}$
$\dot{\gamma}$	$\mathcal{U}(-0.05, 0.05)$	-0.01776 ± 0.001855	$km\,s^{-1}\,yr^{-1}$
γ CORALIE14	$\mathcal{U}(41.50, 42.50)$	42.1741 ± 0.0056	$km\,s^{-1}$
γ CORALIE24	$\mathcal{U}(41.50, 42.50)$	42.1462 ± 0.0036	$km\,s^{-1}$
γ HARPS	$\mathcal{U}(41.50, 42.50)$	42.0189 ± 0.0032	$km\,s^{-1}$
$D_{0;\mathrm{TESS}}$	$\mathcal{U}(0, 0.03)$	$0.0118^{+0.014}_{-0.0084}$	
$q_{1;\mathrm{NGTS}_1}$	$\mathcal{N}(0.3443, 0.0105)$	0.3397 ± 0.010	
$q_{2;\mathrm{NGTS}_1}$	$\mathcal{N}(0.3820, 0.0817)$	0.284 ± 0.070	
$q_{1;\mathrm{NGTS}_6}$	$\mathcal{N}(0.3443, 0.0105)$	0.3397 ± 0.010	
$q_{2;\mathrm{NGTS}_6}$	$\mathcal{N}(0.3820, 0.0817)$	0.284 ± 0.070	
$q_{1;\mathrm{sg1}}$	$\mathcal{N}(0.2879, 0.0084)$	0.2891 ± 0.0083	
$q_{2;\mathrm{sg1}}$	$\mathcal{N}(0.3734, 0.0785)$	0.363 ± 0.069	
$q_{1;\mathrm{TESS}}$	$\mathcal{N}(0.2880, 0.0085)$	0.2871 ± 0.0084	
$q_{2;\mathrm{TESS}}$	$\mathcal{N}(0.3734, 0.0785)$	0.339 ± 0.074	

Table 6.8: `allesfitter` global model derived values

Parameter	Value
$R_\star/a_\mathrm{b}$	$0.01751^{+0.00028}_{-0.00026}$
$a_\mathrm{b}/R_\star$	57.10 ± 0.91
$R_\mathrm{b}/a_\mathrm{b}$	0.001690 ± 0.000031
R_b ($\mathrm{R}_\oplus$)	12.20 ± 0.13
R_b (R_jup)	1.088 ± 0.012
a_b ($\mathrm{R}_\odot$)	66.2 ± 1.2
a_b (AU)	0.3077 ± 0.0055
Inclination b; i_b (deg)	88.961 ± 0.041
e_b	0.386 ± 0.019
w_b (deg)	98.3 ± 3.1
q_b	$0.001212^{+0.000042}_{-0.000040}$
M_b ($\mathrm{M}_\oplus$)	466 ± 26
M_b (M_jup)	1.467 ± 0.081
M_b ($\mathrm{M}_\odot$)	0.001400 ± 0.000078
$b_\mathrm{tra;b}$	$0.639^{+0.020}_{-0.023}$
$T_\mathrm{tot;b}$ (h)	4.639 ± 0.035
$T_\mathrm{full;b}$ (h)	3.325 ± 0.046
$\rho_{\star;\mathrm{b}}$ (cgs)	1.039 ± 0.049
ρ_b (cgs)	1.411 ± 0.092
g_b (cgs)	3040^{+150}_{-140}
$T_\mathrm{eq;b}$ (K)	$519.1^{+6.1}_{-5.3}$
$\delta_\mathrm{tr;undil;b;TESS}$ (ppt)	9.91 ± 0.17
$\delta_\mathrm{tr;dil;b;TESS}$ (ppt)	$9.785^{+0.098}_{-0.14}$
$\delta_{\mathrm{tr;undil;b;NGTS_6}}$ (ppt)	9.976 ± 0.075
$\delta_{\mathrm{tr;dil;b;NGTS_6}}$ (ppt)	9.976 ± 0.075
$\delta_{\mathrm{tr;undil;b;NGTS_1}}$ (ppt)	9.972 ± 0.076
$\delta_{\mathrm{tr;dil;b;NGTS_1}}$ (ppt)	9.972 ± 0.076
$\delta_\mathrm{tr;undil;b;sg1}$ (ppt)	$9.915^{+0.068}_{-0.074}$
$\delta_\mathrm{tr;dil;b;sg1}$ (ppt)	$9.915^{+0.068}_{-0.074}$
$u_\mathrm{1;TESS}$	0.363 ± 0.080
$u_\mathrm{2;TESS}$	0.172 ± 0.080
$u_{\mathrm{1;NGTS_1}}$	0.331 ± 0.082
$u_{\mathrm{2;NGTS_1}}$	0.252 ± 0.082
$u_\mathrm{1;sg1}$	0.390 ± 0.075
$u_\mathrm{2;sg1}$	0.148 ± 0.075
$rho_{\star;\mathrm{combined}}$ (cgs)	1.039 ± 0.049

Chapter 7

Conclusions

"How One Becomes What One Is."

'Ecce Homo', Friedrich Nietzsche, 1888

This thesis presents the characterisation of the Marana CMOS camera (Chapter 2) and a further investigation of its operational performance (Chapter 3). Chapter 4 describes on-sky tests comparing the iKon-L CCD and the Marana camera, including observations of exoplanet transits around bright stars. In Chapter 5, the Andor Toran 26B camera is characterised following a methodology similar to that applied to the Marana camera. Chapter 6 presents the discovery and characterisation of the warm Jupiter NGTS-39 b. Finally, this chapter summarises the main outcomes of this work and discusses their potential impact on future applications.

7.1 The role of CMOS sensors in astronomy

The Marana camera is a high-end scientific CMOS detector whose performance was extensively analysed through laboratory testing. The results demonstrate excellent overall performance. By incorporating two readout channels to produce high dynamic range (HDR) images, the camera can achieve full-well capacities comparable to those of CCD cameras. At the same time, the dual-channel architecture enables significantly lower read noise than a typical CCD without sacrificing frame rate.

Modern CMOS detectors have largely overcome earlier limitations associated with linearity and pixel-to-pixel non-uniformities that arose from their complex pixel architectures. As demonstrated in chapter 2, they can now achieve very low read noise while maintaining stable performance. Furthermore, image lag has been reduced to negligible levels. One remaining issue associated with the complex CMOS architecture is amplifier glow, which can affect measurements at very low light levels and can be difficult to distinguish from dark current. However, newer sensor designs, such as the IMX series discussed in chapter 5, show little to no glow and exhibit dark current levels comparable to those of CCD sensors. These developments demonstrate that modern CMOS sensors can compete with CCDs in terms of performance[1]. In addition, CMOS architectures enable imaging without the need for a mechanical shutter, making them a particularly attractive option

[1] As noted in SPIE Telescopes and Instrumentation 2026 conference, the number of published papers regarding CMOS have been equalised for the first time the number of published papers regarding CCDs.

for observatories operating in isolated and extreme environments, where minimising moving parts reduces maintenance and replacement requirements.

The Marana CMOS camera was also compared on-sky with a typical CCD detector, the iKon-L, using the same telescope configuration, targets, exposure times, and observing conditions. Both cameras produced comparable photometric results, achieving target- and sky-limited precision without being dominated by instrumental noise. However, when comparing duty cycles, the Marana CMOS camera showed improved performance by capturing more stellar photons per observing cycle due to its minimal readout time. Importantly, no additional noise was detected from the dual-channel HDR configuration, particularly during the transition between the HG and LG channels.

7.2 Ground-based instruments with CMOS

CMOS sensors are increasingly becoming valuable tools for high-speed imaging. In addition, because these sensors have been widely adopted in consumer electronics, particularly in smartphone cameras, their cost has decreased significantly, making them substantially cheaper than traditional CCD detectors. This cost advantage has enabled their use in telescope arrays that require multiple cameras operating simultaneously (Law et al., 2022; Airey et al., 2025b).

The affordability of CMOS-based systems has also allowed amateur astronomers to contribute more actively to scientific research. In particular, privately operated observatories are increasingly participating in follow-up observations of exoplanet transits (i.e. Lookout Observatory (Thomas & Guan, 2021), providing valuable complementary data to professional surveys, such as the TESS Follow-up Observing Program Sub Group 1 collaboration (TFOP; Collins et al., 2018).

Furthermore, the high frame rates and minimal readout times of CMOS cameras open new observational opportunities in astrophysics. One important application is space domain awareness, which involves the observation and tracking of satellites. Such objects, particularly those in low Earth orbit, move rapidly across the sky and therefore benefit from detectors capable of fast imaging and high temporal resolution (Zimmer et al., 2016; Cooke et al., 2023, 2025; Airey et al., 2025b,a; Chote et al., 2025). CMOS detectors are also well suited for studies of relatively slower-moving objects in the Solar System, including the tracking of asteroids (Alarcon et al., 2023a), trans-Neptunian objects (Wang et al., 2024), and meteoroids (Kajino et al., 2019). They are also advantageous for observing short-lived events, including supernovae (Jiang et al., 2021), X-ray transient sources (Wu et al., 2022, 2023a; Liu et al., 2023a), and fast optical transients (Karpov et al., 2017).

Upcoming ground-based observational facilities such as the Argus Array (Law et al., 2022) and the Digital Telescope[2] are exploiting the high frame rates of CMOS cameras to introduce new approaches to astronomical observations. In addition, recent technological developments have produced CMOS sensors with increasingly small pixel sizes and large formats, enabling wide-field imaging with high spatial resolution.

The Digital Telescope, in particular, is designed to take advantage of these key CMOS characteristics by operating stationary telescopes that capture images at sub-second cadence, effectively transforming the night sky into a continuous 'video' stream. This approach aims to record astrophysical phenomena in real time, while image stacking techniques can be applied to improve the

[2]Project entitled: Exploring the sky with the Digital Telescope, under the grant number EP/Z534286/1

signal-to-noise ratio. As a result, the system is expected to reach sensitivities of approximately 20–21 magnitudes, allowing the detection of faint astronomical sources.

Furthermore, the high frame rates of CMOS sensors have been used to improve image quality in ground-based facilities by correcting optical aberrations induced by atmospheric turbulence. These corrections are typically achieved through adaptive optics systems, which employ deformable mirrors to compensate for distortions in the incoming stellar wavefront caused by the Earth's atmosphere. To determine the appropriate mirror deformation, the system must first measure the distorted wavefront by acquiring very short, high-cadence exposures prior to the science observation. CMOS cameras are well suited for this task due to their ability to operate at high frame rates with minimal readout time. Such systems are implemented in several current and upcoming large ground-based observatories, including the Extremely Large Telescope (Downing et al., 2016) and the Subaru Coronagraphic Extreme Adaptive Optics (SCExAO) instrument on the Subaru Telescope (Guyon et al., 2010).

Despite these advantages, CMOS technology should not be considered a direct replacement for CCDs in all applications without careful characterisation. CCDs have been used in astronomical instrumentation since the late 1970s (Smith, 1976; Gunn et al., 1987) and have benefited from decades of optimisation, whereas scientific CMOS detectors are still undergoing rapid development. Further improvements are particularly desirable in red and near infrared sensitivity, pixel uniformity, long-term stability, and device-level calibration and fabrication. A key difference is that CMOS sensors contain pixel-level readout electronics, meaning that each pixel can have its own gain, offset, noise, and non-linearity characteristics. This makes detailed calibration especially important for precise and accurate photometry.

At the same time, CMOS detectors introduce practical data-handling challenges. Their high frame rates, large detector formats, and increasingly small pixel sizes can generate very large data volumes, particularly for facilities designed for continuous monitoring or high cadence imaging, like the Argus optical array (Law et al., 2022) and Digital Telescope. Such systems therefore require efficient data storage, real-time reduction, compression strategies, and automated event detection pipelines.

Nevertheless, for new ground-based facilities, CMOS detectors should be strongly considered. They are cheaper, faster, and can operate without mechanical shutters, reducing maintenance requirements and improving reliability, especially for remote robotic observatories. Shutterless operation is particularly valuable for facilities located in isolated sites, where mechanical failures can be costly and difficult to repair. Therefore, while CMOS detectors still require continued technological development and careful calibration, their low cost, high cadence, large formats, and reduced mechanical complexity make them highly attractive for the next generation of ground-based telescope systems.

7.3 Space-based instruments with CMOS

Currently, the primary detectors used in many space astronomy missions are custom CCD sensors. Over several decades, the performance and degradation of CCDs in the space environment have been extensively studied, including the effects of radiation damage, charge-transfer inefficiency, dark-current increase, and hot-pixel formation (Antunes et al., 1993; Kimble et al., 2000; Prod'homme et al., 2012). To deploy CMOS sensors as primary science detectors, it is therefore essential to characterise their behaviour under comparable conditions (Chen et al., 2024; Feng et al., 2026).

CMOS sensors are more complex than CCDs because they contain additional pixel-level and column-level electronics. These components can be affected by radiation damage, single-event effects, random telegraph signal (RTS) noise (Karpov et al., 2019; Apergis et al., 2025), pixel-to-pixel gain variations, and amplifier glow (Apergis et al., 2025). Long-term calibration stability is therefore a key requirement for future space-based CMOS instruments.

Despite these challenges, space missions can benefit significantly from CMOS technology. CMOS detectors generally offer lower power consumption, faster readout speeds, flexible windowing and region-of-interest readout, and high-cadence imaging modes (Eid et al., 2001; Deveaux et al., 2010). These characteristics are particularly attractive for missions requiring rapid time-domain observations, large focal planes, or reduced spacecraft power budgets.

In the coming years, several efforts aim to commission space-based instruments using CMOS sensors as primary science detectors. These missions will provide important tests of CMOS performance in the space environment for astronomical applications. Examples include the Earth 2.0 mission (Ge et al., 2022), which aims to detect and characterise exoplanets using the transit method, and ESA's Analysis of Resolved Remnants of Accreted galaxies as a Key Instrument for Halo Surveys (ARAKIHS) mission, which plans to use CMOS sensors for visible observations to study dark matter and galaxy formation. These developments suggest that CMOS technology is becoming increasingly important for future space astronomy, although further validation is still required before it can replace CCDs in all mission classes.

7.4 A Standardised and Universal Method

The EMVA-1288 standards (Jähne, 2010) has become a fundamental framework for the quantitative characterisation of image sensors, providing a consistent and reproducible methodology for evaluating detector performance. Unlike simpler approaches that treat the sensor as a uniform array, EMVA-1288 enables a more detailed analysis by allowing performance to be assessed at multiple levels, including column-wise, row-wise, and even on a per-pixel basis. This is particularly important for identifying non-uniformities and systematic effects that can significantly impact high-precision astronomical measurements.

Since both CCD and CMOS detectors are predominantly silicon-based, the adoption of uniform calibration procedures and performance metrics is essential for enabling a direct and meaningful comparison between these technologies. A standardised approach ensures that differences in performance arise from the sensor architecture itself, rather than inconsistencies in the measurement methodology.

In addition to metrics such as gain, read noise, dark current, and quantum efficiency, it is important to evaluate the spatial response of the detector system. One quantity in this context is the Modulation Transfer Function (MTF), which describes the ability of the imaging system to preserve contrast as a function of spatial frequency. The MTF provides a comprehensive measure of how fine spatial details are transferred from the object to the recorded image. As such, it serves as a key diagnostic tool for assessing the effective resolution and overall imaging performance of both CMOS and CCD sensors in astronomical applications.

7.5 The future discovery of long period transiting systems

The detection and characterisation of long-period transiting exoplanets remain among the most challenging frontiers in modern exoplanet science. Due to their intrinsically low transit probabilities and the limited temporal baseline of space-based surveys, such systems are often observed only once or, in many cases, only partially. Nevertheless, TESS has demonstrated that even sparse transit detections can provide valuable candidates for further investigation.

Looking ahead, the future of long-period transiting systems with TESS will strongly depend on the synergy between space-based observations and coordinated ground-based follow-up. Extended mission operations, combined with overlapping sectors and improved data reduction pipelines, will increase the likelihood of recovering additional transit events and refining orbital periods. At the same time, targeted photometric campaigns from ground-based facilities will play a crucial role in confirming single-transit events and constraining their ephemerides.

A critical component in the confirmation and characterisation of long-period transiting exoplanets is the synergy with complementary detection techniques. High-precision RV follow-up will continue to play a pivotal role in confirming planetary candidates identified by TESS and in measuring their masses with unprecedented accuracy. This is especially important for long-period systems, where transit observations alone often provide limited constraints on orbital parameters. In parallel, the astrometric capabilities of the Gaia mission (Gaia Collaboration et al., 2016) offer an independent avenue for detecting and characterising planets on wider orbits by measuring the reflex motion of their host stars.

In the case of NGTS-39 b, the RV data already demonstrate the importance of continued long-baseline monitoring. The RVs reveal a long-term linear trend suggesting the presence of an additional, longer-period companion in the system. Since the available RV observations likely sample only a small fraction of the outer companion's orbit, the signal currently appears as an approximately linear acceleration rather than a resolved Keplerian orbit. Further RV monitoring will therefore be required to detect curvature in the trend and constrain the period, eccentricity, and mass of the outer companion. The Gaia astrometric information provides a complementary constraint. The NGTS-39 Gaia DR3 RUWE value of of 0.793 is consistent with a single-star astrometric solution, and therefore shows no evidence for a strong astrometric perturbation. This disfavors a stellar companion producing a large astrometric signal, but does not exclude a lower-mass object, such as a massive planet or brown dwarf, particularly if it lies on an orbit longer than the Gaia DR3 (Gaia Collaboration et al., 2023) observing baseline of 34 months. Future Gaia data releases (Brown, 2025), together with continued RV monitoring, may therefore provide important constraints on the nature of this possible outer companion.

Looking further ahead, the upcoming PLATO mission (Rauer et al., 2025) is expected to significantly enhance this landscape by providing long-baseline, high-precision photometric monitoring, optimised for the detection of Earth-like planets in longer-period orbits. Together, these facilities will establish a powerful, multi-technique framework that will greatly improve the detection efficiency, confirmation rate, and physical characterisation of long-period exoplanetary systems.

Bibliography

Aberle A. G., Glunz S. W., Warta W., 1992, Journal of Applied Physics, 71, 4422

Acton J. S., et al., 2021, MNRAS, 505, 2741

Ahrer E.-M., et al., 2023, Nature, 614, 653

Ahrer E.-M., et al., 2025, MNRAS, 540, 2535

Airey R. J. S., Chote P., Blake J. A., McCormac J., Shrive B., Pollacco D., Cooke B. F., 2025a, RAS Techniques and Instruments, 4, rzaf058

Airey R. J. S., et al., 2025b, Advances in Space Research, 75, 5757

Akeson R. L., et al., 2013, PASP, 125, 989

Alarcon M. R., Licandro J., Serra-ricart M., Joven E., Gaitan V., 2023a, in 2nd NEO and Debris Detection Conference. p. 3

Alarcon M. R., Licandro J., Serra-Ricart M., Joven E., Gaitan V., de Sousa R., 2023b, Publications of the Astronomical Society of the Pacific, 135, 055001

Aller A., Lillo-Box J., Jones D., Miranda L. F., Barceló Forteza S., 2020, A&A, 635, A128

Anderson D. R., et al., 2011, ApJ, 726, L19

Anderson K. R., Lai D., Pu B., 2020, MNRAS, 491, 1369

Antunes A., Burrows D. N., Garmire G. P., Lumb D. H., Nousek J. A., 1993, Experimental Astronomy, 4, 159

Apergis I., et al., 2025, RAS Techniques and Instruments, 4, rzaf049

Apergis I., et al., 2026, RAS Techniques and Instruments, 5, rzag022

Ardilanov V., Murzin V., Afanasyeva I., Ivaschenko N., Pritychenko M., Dodonov S., 2021, Astronomy at the Epoch of Multimessenger Studies, p. 52

Ashcroft N. W., Mermin N. D., 1976, Solid State Physics. Holt-Saunders

Auvergne M., et al., 2009, A&A, 506, 411

Bakos G., Noyes R. W., Kovács G., Stanek K. Z., Sasselov D. D., Domsa I., 2004, PASP, 116, 266

Bakos G. Á., et al., 2010, ApJ, 710, 1724

Bakos G. Á., et al., 2013, PASP, 125, 154

Baraffe I., Chabrier G., 2010, A&A, 521, A44

Baranne A., et al., 1996a, A&AS, 119, 373

Baranne A., et al., 1996b, A&AS, 119, 373

Barbary K., 2016, The Journal of Open Source Software, 1, 58

Barnes S. A., 2010, ApJ, 722, 222

Barrick G. A., Ward J., Cuillandre J.-C., 2012, in High Energy, Optical, and Infrared Detectors for Astronomy V. SPIE, p. 84531K, doi:10.1117/12.926409, https://doi.org/10.1117/12.926409

Battley M. P., et al., 2024, A&A, 686, A230

Bayliss D., et al., 2018, MNRAS, 475, 4467

Bayliss D., et al., 2020, The Messenger, 181, 28

Bayliss D., et al., 2022, in Holland A. D., Beletic J., eds, Society of Photo-Optical Instrumentation Engineers (SPIE) Conference Series Vol. 12191, X-Ray, Optical, and Infrared Detectors for Astronomy X. p. 121911A, doi:10.1117/12.2628966

Bensalem S., Chegaar M., Herguth A., 2017, Current Applied Physics, 17, 55

Bertin E., Arnouts S., 1996, A&AS, 117, 393

Betoule M., et al., 2023, A&A, 670, A119

Bigongiari C., 2005, in Torsten A., et al., eds, International Europhysics Conference on High Energy Physics, HEP2005. p. 20 (arXiv:astro-ph/0512184), doi:10.48550/arXiv.astro-ph/0512184

Birney D. S., Gonzalez G., Oesper D., 2006, Observational astronomy. Cambridge University Press

Black D. C., Scargle J. D., 1982, ApJ, 263, 854

Blackwell D. E., Shallis M. J., 1977, MNRAS, 180, 177

Blake J., et al., 2023, in Ryan S., ed., Proceedings of the Advanced Maui Optical and Space Surveillance (AMOS) Technologies Conference. p. 77

Blind N., et al., 2022, in Evans C. J., Bryant J. J., Motohara K., eds, Society of Photo-Optical Instrumentation Engineers (SPIE) Conference Series Vol. 12184, Ground-based and Airborne Instrumentation for Astronomy IX. p. 121844H (arXiv:2207.14143), doi:10.1117/12.2628321

Bohndiek S. E., Blue A., Clark A. T., Prydderch M. L., Turchetta R., Royle G. J., Speller R. D., 2008, IEEE Sensors Journal, 8, 1734

Bond I. A., et al., 2001, MNRAS, 327, 868

Bond I. A., et al., 2004, ApJ, 606, L155

Bonfanti A., Ortolani S., Piotto G., Nascimbeni V., 2015, A&A, 575, A18

Bonfanti A., Ortolani S., Nascimbeni V., 2016, A&A, 585, A5

Bonfanti A., et al., 2021, A&A, 646, A157

Borucki W. J., et al., 2010, Science, 327, 977

Bouchy F., et al., 2025, A&A, 700, A10

Bouma L. G., Winn J. N., Howard A. W., Howell S. B., Isaacson H., Knutson H., Matson R. A., 2020, ApJ, 893, L29

Bowler B. P., 2016, PASP, 128, 102001

Boyd I., Wilson J., 1980, Nature, 287, 278

Boyle W. S., Smith G. E., 1970, Bell System Technical Journal, 49, 587

Brown A. G. A., 2025, arXiv e-prints, p. arXiv:2503.01533

Brown D. J. A., et al., 2012, MNRAS, 423, 1503

Brown T. M., et al., 2013, PASP, 125, 1031

Bryant E. M., Bayliss D., 2022, AJ, 163, 197

Bryant E. M., et al., 2020, MNRAS, 494, 5872

Burkey B., Chang W., Littlehale J., Lee T., Tredwell T., Lavine J., Trabka E., 1984, in 1984 International Electron Devices Meeting. pp 28–31

Butler R. P., et al., 2017, AJ, 153, 208

Caldwell D. A., et al., 2020, Research Notes of the American Astronomical Society, 4, 201

Cao D., 2012, Retina E-Book: 3 Volume Set, p. 284

Casewell S. L., et al., 2018, MNRAS, 481, 1897

Castelli F., Kurucz R. L., 2003, in Piskunov N., Weiss W. W., Gray D. F., eds, IAU Symposium Vol. 210, Modelling of Stellar Atmospheres. p. A20 (arXiv:astro-ph/0405087)

Castro-Ginard A., et al., 2024, A&A, 688, A1

Cerenkov P., et al., 1934, in Dokl. Akad. Nauk SSSR. pp 451–454

Charbonneau D., Brown T. M., Latham D. W., Mayor M., 2000, ApJ, 529, L45

Chauvin G., Lagrange A.-M., Dumas C., Zuckerman B., Mouillet D., Song I., Beuzit J.-L., Lowrance P., 2004, A&A, 425, L29

Chen Y., Theuwissen A. J., Chae Y., 2011, Procedia Engineering, 25, 1265

Chen M., et al., 2024, arXiv e-prints, p. arXiv:2403.15764

Chote P., et al., 2025, Advances in Space Research, 76, 764

Christiansen J. L., et al., 2025, The Planetary Science Journal, 6, 186

Chromey F. R., 2010, To Measure the Sky. Cambridge University Press

Claret A., Bloemen S., 2011, A&A, 529, A75

Coates C., Fowler B., Holst G., 2009, www. scmos. com. Andor Technology PLC, Fairchild imaging, PCO AG, Belfast, Milpitas, Kehlheim, pp 1–14

Collins K. A., Kielkopf J. F., Stassun K. G., Hessman F. V., 2017, AJ, 153, 77

Collins K., Quinn S. N., Latham D. W., Christiansen J., Ciardi D., Dragomir D., Crossfield I., Seager S., 2018, in American Astronomical Society Meeting Abstracts #231. p. 439.08

Cooke B. F., Pollacco D., West R., McCormac J., Wheatley P. J., 2018, A&A, 619, A175

Cooke B. F., Pollacco D., Bayliss D., 2019, A&A, 631, A83

Cooke B. F., et al., 2021, MNRAS, 500, 5088

Cooke B. F., Chote P., Pollacco D., West R., Blake J. A., McCormac J., Airey R., Shrive B., 2023, Advances in Space Research, 72, 907

Cooke B. F., Pollacco D., Blake J. A., Chote P., Eves S., Feline W., Privett G., 2025, RAS Techniques and Instruments, 4, rzaf016

Crouzet N., et al., 2020, in Evans C. J., Bryant J. J., Motohara K., eds, Society of Photo-Optical Instrumentation Engineers (SPIE) Conference Series Vol. 11447, Ground-based and Airborne Instrumentation for Astronomy VIII. p. 114470O, doi:10.1117/12.2562550

Cumming A., Marcy G. W., Butler R. P., 1999, ApJ, 526, 890

Curiel S., Ortiz-León G. N., Mioduszewski A. J., Sanchez-Bermudez J., 2022, AJ, 164, 93

Dalba P. A., et al., 2022, AJ, 163, 61

David T. J., Hillenbrand L. A., Cody A. M., Carpenter J. M., Howard A. W., 2016, ApJ, 816, 21

Davis A. B., et al., 2020, AJ, 160, 229

Deveaux M., et al., 2010, Nuclear Instruments and Methods in Physics Research A, 624, 428

Doge J., Schonfelder G., Streil G., Konig A., 2002, IEEE Transactions on Circuits and Systems II: Analog and Digital Signal Processing, 49, 155

Downing M., et al., 2016, in Holland A. D., Beletic J., eds, Society of Photo-Optical Instrumentation Engineers (SPIE) Conference Series Vol. 9915, High Energy, Optical, and Infrared Detectors for Astronomy VII. p. 991512, doi:10.1117/12.2231960

Durnez C., et al., 2023, Sensors, 23

Dyck R. H., Jack M. D., 1974, in Proc. Intl. Conf. Tech. And Appl. of Charge-Coupled Devices.

Dyson F. W., Eddington A. S., Davidson C., 1920, Philosophical Transactions of the Royal Society of London Series A, 220, 291

Eid E.-S., Chan T. Y., Fossum E. R., Tsai R. H., Spagnuolo R., Deily J., Byers W. B., Peden J. C., 2001, IEEE Transactions on Nuclear Science, 48, 1796

Einstein A., 1905, Annalen der Physik, 322, 132

Einstein A., 1916, Annalen der Physik, 354, 769

Einstein A., 1936, Science, 84, 506

Emonts P., van Dort M., 1993, PhD thesis, Master's thesis, Eindhoven University of Technology

Enz C. C., Temes G. C., 1996, Proceedings of the IEEE, 84, 1584

Faigler S., Tal-Or L., Mazeh T., Latham D. W., Buchhave L. A., 2013, ApJ, 771, 26

Feng Q., et al., 2026, The Astronomical Journal, 171, 283

Fernandez-Moroni G., Andersson K., Botti A., Estrada J., Rodrigues D., Tiffenberg J., 2020, arXiv e-prints, p. arXiv:2007.04201

Figueira P., et al., 2025, A&A, 700, A174

Fontanet E., et al., 2025, A&A, 699, A38

Ford H. C., et al., 1998, in Bely P. Y., Breckinridge J. B., eds, Society of Photo-Optical Instrumentation Engineers (SPIE) Conference Series Vol. 3356, Space Telescopes and Instruments V. pp 234–248, doi:10.1117/12.324464

Foreman-Mackey D., Morton T. D., Hogg D. W., Agol E., Schölkopf B., 2016, The Astronomical Journal, 152, article no. 206

Foreman-Mackey D., Agol E., Ambikasaran S., Angus R., 2017, AJ, 154, 220

Fortney J. J., Visscher C., Marley M. S., Hood C. E., Line M. R., Thorngren D. P., Freedman R. S., Lupu R., 2020, AJ, 160, 288

Fossum E. R., Hondongwa D. B., 2014, IEEE Journal of the electron devices society

Fossum E. R., et al., 2003, in Proc. 2003 IEEE Workshop on CCDs and Advanced Image Sensors, Elmau, Bavaria, Germany. pp 11–13

Fowler B., 2011, Single-Photon Imaging, pp 159–195

Frank I., Tamm I., 1991, Coherent Visible Radiation of Fast Electrons Passing Through Matter. Springer Berlin Heidelberg, Berlin, Heidelberg, pp 29–35, doi:10.1007/978-3-642-74626-0_2, https://doi.org/10.1007/978-3-642-74626-0_2

Gaia Collaboration et al., 2016, A&A, 595, A1

Gaia Collaboration et al., 2023, A&A, 674, A1

Galle J. G., 1846, MNRAS, 7, 153

Gangestad J. W., Henning G. A., Persinger R. R., Ricker G. R., 2013, arXiv e-prints, p. arXiv:1306.5333

Gardner J. P., et al., 2023, PASP, 135, 068001

Gaudi B. S., 2012, Annual Review of Astronomy and Astrophysics, 50, 411

Gaudi B. S., Gould A., 1997, The Astrophysical Journal, 486, 85

Ge J., et al., 2022, arXiv e-prints, p. arXiv:2206.06693

Genzel R., Eisenhauer F., Gillessen S., 2010, Reviews of Modern Physics, 82, 3121

Geurts T., et al., 2017, Proceedings of the International Image Sensor Worshop, Hiroshima, Japan, 30, 43

Gill D., 1887, The Observatory, Vol. 10, p. 267-272 (1887), 10, 267

Gill S., et al., 2020a, MNRAS, 491, 1548

Gill S., et al., 2020b, MNRAS, 495, 2713

Gill S., et al., 2020c, ApJ, 898, L11

Gill A. S., et al., 2022, in Holland A. D., Beletic J., eds, Proceedings of SPIE Vol. 12191, X-Ray, Optical, and Infrared Detectors for Astronomy X. SPIE, p. 1219114, doi:10.1117/12.2627564, https://doi.org/10.1117/12.2627564

Gill S., et al., 2024, MNRAS, 533, 109

Gillen E., et al., 2020, MNRAS, 492, 1008

Gimeno G., et al., 2016, in Ground-based and Airborne Instrumentation for Astronomy VI. pp 872–885

Ginzburg S., Chiang E., 2020, MNRAS, 498, 680

Green M. A., 2008, Solar Energy Materials and Solar Cells, 92, 1305

Greffe T., Smith R., Sherman M., Harrison F., Earnshaw H., Grefenstette B., Hennessy J., Nikzad S., 2022, in X-Ray, Optical, and Infrared Detectors for Astronomy X. pp 72–112

Guerriero F., Penoyre Z., Brown A. G. A., 2026, MNRAS, 548, stag654

Gunn J., Emory E., Harris F., Oke J., 1987, Publications of the Astronomical Society of the Pacific, 99, 518

Günther M. N., Daylan T., 2019, Allesfitter: Flexible Star and Exoplanet Inference From Photometry and Radial Velocity, Astrophysics Source Code Library (ascl:1903.003)

Günther M. N., Daylan T., 2021, ApJS, 254, 13

Guyon O., Martinache F., Garrel V., Vogt F., Yokochi K., Yoshikawa T., 2010, in Ellerbroek B. L., Hart M., Hubin N., Wizinowich P. L., eds, Society of Photo-Optical Instrumentation Engineers (SPIE) Conference Series Vol. 7736, Adaptive Optics Systems II. p. 773624, doi:10.1117/12.857878

Hahn A., Mirzoyan R., Dettlaff A., Fink D. J., Mazin D., Teshima M., 2023, Nuclear Instruments and Methods in Physics Research A, 1046, 167686

Hamers A. S., Antonini F., Lithwick Y., Perets H. B., Portegies Zwart S. F., 2017, MNRAS, 464, 688

Han T., Brandt T. D., 2023, AJ, 165, 71

Harbeck D.-R., et al., 2024, arXiv e-prints, p. arXiv:2405.10408

Hartman J. D., et al., 2015, AJ, 149, 166

Hattori S., Foreman-Mackey D., Hogg D. W., Montet B. T., Angus R., Pritchard T. A., Curtis J. L., Schölkopf B., 2022, AJ, 163, 284

Hawthorn F., et al., 2024, MNRAS, 528, 1841

Hellier C., et al., 2014, MNRAS, 440, 1982

Henderson B. A., et al., 2024, MNRAS, 530, 318

Henry M., Scherer A., of Technology. Division of Engineering C. I., Science A., 2010, ICP Etching of Silicon for Micro and Nanoscale Devices. CIT theses, California Institute of Technology, https://books.google.co.uk/books?id=hw-I0AEACAAJ

Hestroffer D., Magnan C., 1998, A&A, 333, 338

Hoenk M. E., Jones T. J., Dickie M. R., Greer F., Cunningham T. J., Blazejewski E. R., Nikzad S., 2009, Infrared Systems and Photoelectronic Technology IV, 7419, 187

Holland S. E., Dawson K. S., Palaio N. P., Saha J., Roe N. A., Wang G., 2007, Nuclear Instruments and Methods in Physics Research A, 579, 653

Holst G., Lomheim T., 2011, CMOS/CCD Sensors and Camera Systems, Second Edition. SPIE — The International Society for Optics and Photonics, doi:10.1117/3.2524677

Howell S. B., 1989, PASP, 101, 616

Howell S. B., 2000, Handbook of CCD Astronomy. Cambridge University Press

Howell S. B., et al., 2014, PASP, 126, 398

Huang C. X., 2020, TESS Lightcurves From The MIT Quick-Look Pipeline ("QLP"), doi:10.17909/T9-R086-E880, http://archive.stsci.edu/doi/resolve/resolve.html?doi=10.17909/t9-r086-e880

Huang C., Wu Y., Triaud A. H. M. J., 2016, ApJ, 825, 98

Hubble E. P., 1926, ApJ, 64, 321

Huebener R. P., 2019, Conductors, semiconductors, superconductors. Springer

Huggett A., Silsby C., Cami S., Beck J., 2009, in 2009 IEEE International Solid-State Circuits Conference - Digest of Technical Papers. pp 52–53,53a, doi:10.1109/ISSCC.2009.4977303

Hynecek J., 1997, IEEE Transactions on Electron Devices, 44, 1679

Iams H., Salzberg B., 1935, Proceedings of the Institute of Radio Engineers, 23, 55

IceCube Collaboration 2013, Science, 342, 1242856

Inoue I., 1999, in 1999 Workshop on CCD and AIS. pp 25–28

Ivory J. M., 2020, CMOS sensors for precision astronomy. Open University (United Kingdom)

Iwert O., Delabre B., 2010, in High Energy, Optical, and Infrared Detectors for Astronomy IV. pp 646–654

Jackman J. A. G., Wheatley P. J., West R. G., Gill S., Jenkins J. S., 2023, MNRAS, 525, 1588

Jaeger R. C., 1987, Introduction to microelectronic fabrication. Addison-Wesley Longman Publishing Co., Inc.

Jähne B., 2010, Optik & Photonik, 5, 53

Jain U., 2016, Master's thesis, Delft University of Technology

Janesick J. R., 2007, Photon Transfer: DN to Lambda. SPIE Press Vol. PM170, SPIE Press, Bellingham, WA

Janesick J., Klaasen K., Elliott T., 1985, in Solid state imaging arrays. pp 7–19, doi:10.1117/12.950297

Janesick J. R., Elliott T., Collins S., Blouke M. M., Freeman J., 1987, Optical Engineering, 26, 692

Janesick J., Andrews J., Tower J., Grygon M., Elliott T., Cheng J., Lesser M., Pinter J., 2007, in Grycewicz T. J., Marshall C. J., Warren P. G., eds, Society of Photo-Optical Instrumentation Engineers (SPIE) Conference Series Vol. 6690, Focal Plane Arrays for Space Telescopes III. p. 669003, doi:10.1117/12.740218

Jenkins J. M., et al., 2016, in Chiozzi G., Guzman J. C., eds, Society of Photo-Optical Instrumentation Engineers (SPIE) Conference Series Vol. 9913, Software and Cyberinfrastructure for Astronomy IV. p. 99133E, doi:10.1117/12.2233418

Jiang J.-a., et al., 2021, ApJ, 923, L8

Jo Y.-R., Hong S.-K., Kwon O.-K., 2014, IEEE Transactions on Nuclear Science, 61, 2472

Johnson J. B., 1928, Physical review, 32, 97

Jorden P. R., Jordan D., Jerram P. A., Pratlong J., Swindells I., 2014, in High energy, optical, and infrared detectors for astronomy VI. pp 201–215

Jung C., Yang Y., Jiao L., 2013, Optical Engineering, 52, 102004

Kajino F., et al., 2019, in Proceedings of the 36th International Cosmic Ray Conference (ICRC2019), Madison, WI, USA. p. 525

Kapusta M., Lavoute P., Lherbet F., Rossignol E., Moussant C., Fouche F., 2007, in 2007 IEEE Nuclear Science Symposium Conference Record. pp 73–77, doi:10.1109/NSSMIC.2007.4436290

Karpov S., Beskin G., 2022, in Astronomy at the Epoch of Multimessenger Studies. pp 156–156, doi:10.51194/VAK2021.2022.1.1.047

Karpov S., Beskin G., Biryukov A., Bondar S., Ivanov E., Katkova E., Perkov A., Sasyuk V., 2017, in Proceedings of a Conference held at Special Astrophysical Observatory.

Karpov S., Bajat A., Christov A., Prouza M., 2019, Astronomische Nachrichten, 340, 638

Karpov S., Bajat A., Christov A., Prouza M., Beskin G., 2020, in X-Ray, Optical, and Infrared Detectors for Astronomy IX. pp 86–98

Karpov S., Christov A., Bajat A., Cunniffe R., Prouza M., 2021, in Revista Mexicana de Astronomia y Astrofisica Conference Series. pp 190–197, doi:10.22201/ia.14052059p.2021.53.38

Kaufer A., Stahl O., Tubbesing S., Nørregaard P., Avila G., Francois P., Pasquini L., Pizzella A., 1999, The Messenger, 95, 8

Kawai N., Kawahito S., 2004, IEEE Transactions on Electron Devices, 51, 185

Khandelwal A., et al., 2024, in Holland A. D., Minoglou K., eds, Society of Photo-Optical Instrumentation Engineers (SPIE) Conference Series Vol. 13103, X-Ray, Optical, and Infrared Detectors for Astronomy XI. p. 131030R (arXiv:2409.16449), doi:10.1117/12.3018522

Kimble R. A., Goudfrooij P., Gilliland R. L., 2000, in Breckinridge J. B., Jakobsen P., eds, Society of Photo-Optical Instrumentation Engineers (SPIE) Conference Series Vol. 4013, UV, Optical, and IR Space Telescopes and Instruments. pp 532–544, doi:10.1117/12.393973

Kipping D. M., 2013, MNRAS, 435, 2152

Kitchin C. R., 2020, Astrophysical Techniques. CRC press, doi:10.1201/9780429491139

Kittel C., 2004, Introduction to Solid State Physics, 8 edn. Wiley, http://www.amazon.com/Introduction-Solid-Physics-Charles-Kittel/dp/047141526X/ref=dp_ob_title_bk

Ko G. B., Lee J. S., 2015, Medical Physics, 42, 510

Komacek T. D., Thorngren D. P., Lopez E. D., Ginzburg S., 2020, ApJ, 893, 36

Kovács G., Zucker S., Mazeh T., 2002, A&A, 391, 369

Kuhn R. B., et al., 2016, MNRAS, 459, 4281

Kurucz R. L., 1993, SYNTHE spectrum synthesis programs and line data. Astrophysics Source Code Library

Lahav A., Fenigstein A., Strum A., Rizzolo S., 2020, High Performance Silicon Imaging, pp 95–117

Lammers C., Winn J. N., 2026, AJ, 171, 18

Lang D., Hogg D. W., Mierle K., Blanton M., Roweis S., 2010, AJ, 139, 1782

Lankford J., 1984, The general history of astronomy, 4, 16

Lapray P.-J., Heyrman B., Ginhac D., 2016, Journal of Real-Time Image Processing, 12, 747

Larson S. M., Sims G. R., Christensen E. J., 2018, in Advances in Optical and Mechanical Technologies for Telescopes and Instrumentation III. pp 1116–1121

Laughlin G., 2018, in Deeg H. J., Belmonte J. A., eds, , Handbook of Exoplanets. Springer International Publishing, p. 1, doi:10.1007/978-3-319-55333-7_1

Lauxtermann S., Lee A., Stevens J., Joshi A., 2007, in 2007 international image sensor workshop. p. 8

Law N. M., et al., 2022, PASP, 134, 035003

Layden C., et al., 2025, arXiv e-prints, p. arXiv:2502.00101

Le Roch A., Goiffon V., Marcelot O., Paillet P., Pace F., Belloir J.-M., Magnan P., Virmontois C., 2019, Sensors, 19, 5550

Lecavelier des Etangs A., Lissauer J. J., 2022, New Astronomy Reviews, 94, 101641

Lenzen R., et al., 2003, in Iye M., Moorwood A. F. M., eds, Society of Photo-Optical Instrumentation Engineers (SPIE) Conference Series Vol. 4841, Instrument Design and Performance for Optical/Infrared Ground-based Telescopes. pp 944–952, doi:10.1117/12.460044

Li J.-L., Guo Y.-F., Lan T.-J., et al., 2016, International Journal of Grid and Distributed Computing

Lightkurve Collaboration et al., 2018, Lightkurve: Kepler and TESS time series analysis in Python, Astrophysics Source Code Library (ascl:1812.013)

Lin C.-H., Mandelbaum R., Troxel M. A., Hirata C. M., Jarvis M., 2022, MNRAS, 512, 3312

Lindegren L., et al., 2021, A&A, 649, A4

Liu M., Ling Z., Wu Q., Zhang C., Liu J., Zhang Z., Yuan W., Zhang S.-N., 2023a, Journal of Astronomical Telescopes, Instruments, and Systems, 9, 046003

Liu B., Li Y., Wen L., Zhang X., Guo Q., 2023b, Sensors, 23, 6159

Lou S., et al., 2023, IEEE Transactions on Electron Devices

Lowell P., 1915, Memoirs of the Lowell Observatory. John Wiley & Sons, 1, 1

Lyot B., 1939, MNRAS, 99, 580

Ma C., Wang X., 2013, in Proc. Int. Image Sensor Workshop. pp 129–132

Ma C., Liu Y., Li J., Zhou Q., Chang Y., Wang X., 2015, in Widenhorn R., Dupret A., eds, Society of Photo-Optical Instrumentation Engineers (SPIE) Conference Series Vol. 9403, Image Sensors and Imaging Systems 2015. p. 940305, doi:10.1117/12.2083085

Ma C., Liu Y., Li Y., Zhou Q., Wang X., Chang Y., 2017, IEEE Transactions on Electron Devices, 64, 3199

Macintosh B., et al., 2014, Proceedings of the National Academy of Science, 111, 12661

Mackay C. D., 1986, ARA&A, 24, 255

Maddox R. L., 1871, British journal of photography, 18, 422

Madhusudhan N., 2019, ARA&A, 57, 617

Maihara T., Iwamuro F., Yamashita T., Hall D. N. B., Cowie L. L., Tokunaga A. T., Pickles A., 1993, PASP, 105, 940

Mann S., Lo R. C. H., Ovtcharov K., Gu S., Dai D., Ngan C., Ai T., 2012, in 2012 25th IEEE Canadian Conference on Electrical and Computer Engineering (CCECE). pp 1–6, doi:10.1109/CCECE.2012.6335012

Mantovan G., et al., 2024, A&A, 682, A129

Marchant J. C., Millikan A. G., 1965, J. Opt. Soc. Am., 55, 907

Marigo P., et al., 2017, ApJ, 835, 77

Marois C., Zuckerman B., Konopacky Q. M., Macintosh B., Barman T., 2010, Nature, 468, 1080

Martin-Gonthier P., Magnan P., 2009, in 2009 16th IEEE International Conference on Electronics, Circuits and Systems - (ICECS 2009). pp 928–931, doi:10.1109/ICECS.2009.5410825

Maxted P. F. L., 2016, A&A, 591, A111

Mayor M., Queloz D., 1995, Nature, 378, 355

McCormac J., Pollacco D., Skillen I., Faedi F., Todd I., Watson C. A., 2013, PASP, 125, 548

McCormac J., et al., 2017, PASP, 129, 025002

McCormac J., et al., 2020, MNRAS, 493, 126

McCully C., Volgenau N. H., Harbeck D.-R., Lister T. A., Saunders E. S., Turner M. L., Siiverd R. J., Bowman M., 2018, in Guzman J. C., Ibsen J., eds, Society of Photo-Optical Instrumentation Engineers (SPIE) Conference Series Vol. 10707, Software and Cyberinfrastructure for Astronomy V. p. 107070K (arXiv:1811.04163), doi:10.1117/12.2314340

McHugh M., et al., 2020, in Society of Photo-Optical Instrumentation Engineers (SPIE) Conference Series. p. 114448Y, doi:10.1117/12.2563060

McLean I. S., 2008, Electronic Imaging in Astronomy: Detectors and Instrumentation (Second Edition). Springer, doi:10.1007/978-3-540-76583-7

Metselaar R., Oversluizen G., 1984, Journal of Solid State Chemistry, 55, 320

Michelot J., Moreira A., Monsinjon P., Caranhac S., 2016, in Photon Counting, Low Flux and High Dynamic Range Optoelectronic Detectors Workshop. pp 1–4

Mikal-Evans T., et al., 2023, ApJ, 943, L17

Mitchell M. A., et al., 2025, Monthly Notices of the Royal Astronomical Society, p. staf2100

Mizobuchi K., Adachi S., Akahane N., Sawada H., Ohta K., Oshikubo H., Sugawa S., 2009, in Proc. 2009 International Image Sensor Workshop. pp 235–238

Mo Y., Xu C., 2011, Method and apparatus providing analog row noise correction and hot pixel filtering

Moffat A. F. J., 1969, A&A, 3, 455

Morgan M., Bowler B. P., Tran Q. H., Wittenmyer R. A., Wright D. J., Zhou G., Fairnington T. R., 2025, ApJS, 280, 76

Morton T. D., Bryson S. T., Coughlin J. L., Rowe J. F., Ravichandran G., Petigura E. A., Haas M. R., Batalha N. M., 2016, ApJ, 822, 86

Mu H.-Y., Fan Z., Zhu Y.-N., Zhang Y., Wu H., 2024, Research in Astronomy and Astrophysics, 24, 055009

Neveu-VanMalle M., et al., 2016, A&A, 586, A93

Nie K., Zha W., Shi X., Li J., Xu J., Ma J., 2020, IEEE Transactions on Circuits and Systems I: Regular Papers, 67, 2873

Noll S., Kausch W., Barden M., Jones A. M., Szyszka C., Kimeswenger S., Vinther J., 2012, A&A, 543, A92

Norman D., 1938, Osiris, 5, 560

O'Brien S. M., et al., 2022, MNRAS, 509, 6111

Oberst T. E., et al., 2017, AJ, 153, 97

Ohta Y., Taruya A., Suto Y., 2005, ApJ, 622, 1118

Oke J., Harris F., Oke D., Wang D., 1988, Publications of the Astronomical Society of the Pacific, 100, 116

Osborn J., Föhring D., Dhillon V. S., Wilson R. W., 2015, MNRAS, 452, 1707

Pál A., et al., 2008, ApJ, 680, 1450

Park J., et al., 2021, in 2021 IEEE International Solid-State Circuits Conference (ISSCC). pp 122–124, doi:10.1109/ISSCC42613.2021.9365751

Parviainen H., Aigrain S., 2015, MNRAS, 453, 3821

Pasachoff J. M., Olson R. J. M., 2011, in American Astronomical Society Meeting Abstracts #217. p. 111.01

Pearson K. A., 2019, AJ, 158, 243

Pearson G. L., Bardeen J., 1949, Physical Review, 75, 865

Pecaut M. J., Mamajek E. E., 2013, ApJS, 208, 9

Peckerar M., McCann D., Blaha F., Mend W., Fulton R., 1979, in 1979 International Electron Devices Meeting. pp 144–146, doi:10.1109/IEDM.1979.189563

Peckerar M., McCann D., Yu L., 1981, Applied Physics Letters, 39, 55

Pepe F., et al., 2002, The Messenger, 110, 9

Pepe F., et al., 2021, A&A, 645, A96

Pepper J., Stassun K. G., Gaudi B. S., 2018, in Deeg H. J., Belmonte J. A., eds, , Handbook of Exoplanets. arXiv preprint arXiv:1802.10158, p. 128, doi:10.1007/978-3-319-55333-7_128

Perlmutter S., et al., 1998, Nature, 391, 51

Perryman M., Hartman J., Bakos G. Á., Lindegren L., 2014, ApJ, 797, 14

Petrovich C., Tremaine S., 2016, ApJ, 829, 132

Pickering E. C., 1899, Astronomische Nachrichten, volume 149, Issue 10, p. 189, 149, 189

Pinamonti M., et al., 2026, A&A, 707, A67

Poate J., 2012, Laser annealing of semiconductors. Elsevier

Pollacco D. L., et al., 2006, PASP, 118, 1407

Pont F., Zucker S., Queloz D., 2006, MNRAS, 373, 231

Pope B. J. S., et al., 2016, MNRAS, 455, L36

Prod'homme T., Holl B., Lindegren L., Brown A. G. A., 2012, MNRAS, 419, 2995

Qiu P., Mao Y.-N., Lu X.-M., Xiang E., Jiang X.-J., 2013, Research in Astronomy and Astrophysics, 13, 615

Qiu P., Zhao Y., Zheng J., Wang J.-F., Jiang X.-J., 2021, Research in Astronomy and Astrophysics, 21, 268

Queloz D., et al., 2001, The Messenger, 105, 1

Quirrenbach A., 2010, in Seager S., ed., , Exoplanets. University of Arizona Press, pp 157–174

Ranyard A. C., 1874, Nature, 10, 205

Rauer H., Aerts C., Cabrera J., Team P., et al., 2016, Astronomische Nachrichten, 337, 961

Rauer H., et al., 2025, Experimental Astronomy, 59, 26

Rhodes H., et al., 2009, in International Image Sensor Workshop. pp 27–32

Ricker G. R., et al., 2015, Journal of Astronomical Telescopes, Instruments, and Systems, 1, 014003

Rickman E. L., et al., 2019, A&A, 625, A71

Riess A. G., et al., 1998, AJ, 116, 1009

Rodel T., Bayliss D., Gill S., Hawthorn F., 2024, MNRAS, 529, 715

Rodel T., et al., 2025, MNRAS, 537, 35

Rose A., Weimer P. K., 1989, Physics Today, 42, 24

Rousset G., et al., 2003, in Wizinowich P. L., Bonaccini D., eds, Society of Photo-Optical Instrumentation Engineers (SPIE) Conference Series Vol. 4839, Adaptive Optical System Technologies II. pp 140–149, doi:10.1117/12.459332

Sachs A., 1974, Philosophical Transactions of the Royal Society of London. Series A, Mathematical and Physical Sciences, 276, 43

Sahlmann J., Lazorenko P. F., Ségransan D., Martín E. L., Queloz D., Mayor M., Udry S., 2013, A&A, 556, A133

Santerne A., Bonomo A. S., Hébrard G., Deleuil M., Moutou C., Almenara J. M., Bouchy F., Díaz R. F., 2011, A&A, 536, A70

Santos N. C., et al., 2013, A&A, 556, A150

Sarkis P., Mordasini C., Henning T., Marleau G. D., Mollière P., 2021, A&A, 645, A79

Sasselov D. D., Grotzinger J. P., Sutherland J. D., 2020, Science Advances, 6, eaax3419

Savitzky A., Golay M. J. E., 1964, Analytical Chemistry, 36, 1627

Schanche N., et al., 2020, MNRAS, 499, 428

Schnapf J., Kraft T., Baylor D., 1987, Nature, 325, 439

Scholze F., Henneken H., Kuschnerus P., Rabus H., Richter M., Ulm G., 2000, Nuclear Instruments and Methods in Physics Research Section A: Accelerators, Spectrometers, Detectors and Associated Equipment, 439, 208

Ségransan D., et al., 2010, A&A, 511, A45

Sequeda F. O., 1985, JOM, 37, 43

Shafie S., Kawahito S., Halin I. A., Hasan W. Z. W., 2009, Sensors, 9, 9452

Shao L., Zhan H., Liu C., Chi H., Luo Q., Mu H., Shi W., 2024, Research in Astronomy and Astrophysics, 24, 025021

Shockley W., Read W. T., 1952, Phys. Rev., 87, 835

Showman A. P., Tan X., Parmentier V., 2020, Space Sci. Rev., 216, 139

Sing D. K., 2010, A&A, 510, A21

Siverd R. J., et al., 2012, ApJ, 761, 123

Skilling J., 2004, in Fischer R., Preuss R., Toussaint U. V., eds, American Institute of Physics Conference Series Vol. 735, American Institute of Physics Conference Series. pp 395–405, doi:10.1063/1.1835238

Skilling J., 2006, Bayesian Anal., 1, 833

Skrutskie M. F., et al., 2006, The Astronomical Journal, 131, 1163

Smith B. A., 1976, in Charge-Coupled Device Technology and Applications. pp 135–138

Smith A. M. S., et al., 2021, A&A, 646, A183

Sneden C. A., 1973, PhD thesis, The University of Texas at Austin.

Soter S., 2006, AJ, 132, 2513

Sousa S. G., 2014, ARES + MOOG: A Practical Overview of an Equivalent Width (EW) Method to Derive Stellar Parameters. Springer International Publishing, Cham, pp 297–310, doi:10.1007/978-3-319-06956-2_26, https://doi.org/10.1007/978-3-319-06956-2_26

Sousa S. G., Santos N. C., Israelian G., Mayor M., Monteiro M. J. P. F. G., 2007, A&A, 469, 783

Sousa S. G., et al., 2008, A&A, 487, 373

Sousa S. G., Santos N. C., Adibekyan V., Delgado-Mena E., Israelian G., 2015, A&A, 577, A67

Sousa S. G., et al., 2021, A&A, 656, A53

Sozzetti A., et al., 2023, A&A, 677, L15

Speagle J. S., 2020, MNRAS, 493, 3132

Sperlich K., Stolz H., 2014, Measurement Science and Technology, 25, 015502

Standish E. M., 1993, AJ, 105, 2000

Stassun K. G., et al., 2018, AJ, 156, 102

Stassun K. G., et al., 2019, AJ, 158, 138

Staubermann K., 2004, Journal for the History of Astronomy, 35, 447

Stefanov K. D., 2022, CMOS image sensors. IOP Publishing

Stefanov K. D., et al., 2022, in X-Ray, Optical, and Infrared Detectors for Astronomy X. pp 160–167

Stefánsson G., et al., 2025, AJ, 169, 107

Stern R. A., Whittemore T., Winzenread M., Blouke M. M., 1989, in Blouke M. M., Pophal D., eds, Society of Photo-Optical Instrumentation Engineers (SPIE) Conference Series Vol. 1071, Optical Sensors and Electronic Photography. pp 43–57, doi:10.1117/12.952505

Stokley Jr J., 1923, Popular Astronomy, Vol. 31, p. 373, 31, 373

Streetman B. G., Banerjee S. K., 2015, Solid State Electronic Devices, 7 edn. Pearson

Strehlow W. H., Cook E. L., 1973, Journal of Physical and Chemical Reference Data, 2, 163

Sze S. M., Li Y., Ng K. K., 2021, Physics of semiconductor devices. John wiley & sons

Szentgyorgyi A. H., et al., 2005, in American Astronomical Society Meeting Abstracts. p. 110.10

Tamuz O., Mazeh T., Zucker S., 2005, MNRAS, 356, 1466

Tang X., Qian Y., Kong X., Wang H., 2020, Journal of Real-Time Image Processing, 17, 703

Teranishi N., 2016, IEEE Transactions on Electron Devices, 63, 10

Teranishi N., Mutoh N., 1986, IEEE Transactions on Electron Devices, 33, 1696

Teranishi N., Kohono A., Ishihara Y., Oda E., Arai K., 1982, in 1982 International Electron Devices Meeting. pp 324–327

Theuwissen A. J., Snoeij M. F., Wang X., Rao P. R., Bodegom E., 2006, CMOS Image Sensors for Ambient Intelligence. Springer Netherlands, Dordrecht, pp 125–150, doi:10.1007/1-4020-4198-5_8, https://doi.org/10.1007/1-4020-4198-5_8

Thomas N., Guan C., 2021, Open European Journal on Variable Stars, 214, 1

Thornber K. K., 1974, The Bell System Technical Journal, 53, 1211

Tian H., Fowler B. A., El Gamal A., 1999, in Blouke M. M., Williams G. M., eds, Society of Photo-Optical Instrumentation Engineers (SPIE) Conference Series Vol. 3649, Sensors, Cameras, and Systems for Scientific/Industrial Applications. pp 177–185, doi:10.1117/12.347073

Tombaugh C. W., 1946, Astronomical Society of the Pacific Leaflets, Vol. 5, No. 209, p. 73, 5, 73

Tonry J. L., et al., 2018, PASP, 130, 064505

Toomey D. W., Ftaclas C., 2003, in Iye M., Moorwood A. F. M., eds, Society of Photo-Optical Instrumentation Engineers (SPIE) Conference Series Vol. 4841, Instrument Design and Performance for Optical/Infrared Ground-based Telescopes. pp 889–900, doi:10.1117/12.461099

Townsend-Rose C., Buggey T., Ivory J., Stefanov K. D., Jones L., Hetherington O., Holland A. D., Prod'homme T., 2023, Journal of Astronomical Telescopes, Instruments, and Systems, 9, 046001

Tsai M.-H., Ma T., Hook T., 1994, IEEE Electron Device Letters, 15, 504

Tsoi H. Y., Ellul J. P., King M. I., White J. J., Bradley W. C., 1985, IEEE Transactions on Electron Devices, 32, 1525

Turner J. D., Ridden-Harper A., Jayawardhana R., 2021, AJ, 161, 72

Uchiyama M., et al., 2021, in International Image Sensor Workshop (IISW).

Udalski A., Szymanski M., Kaluzny J., Kubiak M., Mateo M., 1992, Acta Astron., 42, 253

Udry S., et al., 2007, A&A, 469, L43

Uehara S., Kawahara H., Masuda K., Yamada S., Aizawa M., 2016, The Astrophysical Journal, 822, 2

Ulmer-Moll S., et al., 2022, A&A, 666, A46

Ulmer-Moll S., et al., 2025, A&A, 703, A258

Van Norren D., Tiemeijer L., 1986, Vision research, 26, 313

Velichko S., Gravelle B., Tekleab D., Guidash M., Johnson S., Oh M., Chang H. C., 2019, in 2019 International Image Sensor Workshop (IISW).

Verhoeve P., et al., 2016, in Holland A. D., Beletic J., eds, Society of Photo-Optical Instrumentation Engineers (SPIE) Conference Series Vol. 9915, High Energy, Optical, and Infrared Detectors for Astronomy VII. p. 99150Z, doi:10.1117/12.2232336

Vici A., Russo F., Lovisi N., Marchioni A., Casella A., Irrera F., 2020, IEEE Journal of the Electron Devices Society, 8, 765

Villanueva Jr. S., Dragomir D., Gaudi B. S., 2019, AJ, 157, 84

Vogt S. S., et al., 1994, in Crawford D. L., Craine E. R., eds, Society of Photo-Optical Instrumentation Engineers (SPIE) Conference Series Vol. 2198, Instrumentation in Astronomy VIII. p. 362, doi:10.1117/12.176725

Vu P., Fowler B., Liu C., Balicki J., Mims S., Do H., Laxson D., 2008, in High Energy, Optical, and Infrared Detectors for Astronomy III. pp 45–53

Walden R., Krambeck R., Strain R., McKenna J., Schryer N., Smith G., 1972, The Bell System Technical Journal, 51, 1635

Walker G., 1987, Astronomical Observations: an optical perspective. Cambridge University Press

Wang F., Theuwissen A., 2017, Electronic imaging, 29, 84

Wang C., Vaidyanathan M., Larson L. E., 2004, IEEE journal of solid-state circuits, 39, 1927

Wang X., Rao P. R., Mierop A., Theuwissen A. J., 2006, in 2006 International Electron Devices Meeting. pp 1–4, doi:10.1109/IEDM.2006.346973

Wang X., Wolfs B., Meynants G., Bogaerts J., 2011, in Proc. Int. Image Sensor Workshop. pp 248–251

Wang S.-Y., et al., 2014, in Holland A. D., Beletic J., eds, Society of Photo-Optical Instrumentation Engineers (SPIE) Conference Series Vol. 9154, High Energy, Optical, and Infrared Detectors for Astronomy VI. p. 91542I, doi:10.1117/12.2057361

Wang X., Ma C., Liu Y., Li Y., Zhou Q., 2015, in Proceedings of the International Image Sensor Workshop.

Wang F., Han L., Theuwissen A. J., 2018, IEEE Journal of Solid-State Circuits, 53, 2970

Wang S., Ping Y., Men J., Zhang C., Zhao C., 2020, in Kimata M., Shaw J. A., Valenta C. R., eds, Society of Photo-Optical Instrumentation Engineers (SPIE) Conference Series Vol. 11525, SPIE Future Sensing Technologies. p. 115252I, doi:10.1117/12.2583913

Wang S.-Y., et al., 2024, in Bryant J. J., Motohara K., Vernet J. R. D., eds, Society of Photo-Optical Instrumentation Engineers (SPIE) Conference Series Vol. 13096, Ground-based and Airborne Instrumentation for Astronomy X. p. 130962Y, doi:10.1117/12.3018461

Weakliem H. A., Redfield D., 1979, Journal of Applied Physics, 50, 1491

Weckler G., 1965, in 1965 International Electron Devices Meeting. pp 38–39

Weckler G. P., 1967, IEEE Journal of Solid-State Circuits, 2, 65

West R. G., et al., 2019, MNRAS, 486, 5094

Wheatley P. J., et al., 2018, MNRAS, 475, 4476

Widenhorn R., Mündermann L., Rest A., Bodegom E., 2001, Journal of Applied Physics, 89, 8179

Widenhorn R., Blouke M., Weber A., Rest A., Bodegom E., 2002, Proceedings of SPIE - The International Society for Optical Engineering, 4669

Wilson D. M., et al., 2008, ApJ, 675, L113

Winn J. N., 2010, in Seager S., ed., , Exoplanets. arXiv preprint arXiv:1001.2010, pp 55–77, doi:10.48550/arXiv.1001.2010

Wolszczan A., Frail D. A., 1992, Nature, 355, 145

Wong I., et al., 2021, AJ, 162, 256

Woods D. F., et al., 2016, in MacEwen H. A., Fazio G. G., Lystrup M., Batalha N., Siegler N., Tong E. C., eds, Society of Photo-Optical Instrumentation Engineers (SPIE) Conference Series Vol. 9904, Space Telescopes and Instrumentation 2016: Optical, Infrared, and Millimeter Wave. p. 99042C, doi:10.1117/12.2231296

Wright J. T., 2018, Radial Velocities as an Exoplanet Discovery Method. Springer International Publishing, Cham, pp 619–631, doi:10.1007/978-3-319-55333-7_4, https://doi.org/10.1007/978-3-319-55333-7_4

Wright E. L., et al., 2010, AJ, 140, 1868

Wu Q., Jia Z., Wang W., Ling Z., Zhang C., Zhang S., Yuan W., 2022, Publications of the Astronomical Society of the Pacific, 134, 035006

Wu Q., Ling Z., Zhang C., Zhang S.-N., Yuan W., 2023a, Publications of the Astronomical Society of the Pacific, 135, 115002

Wu Q., Ling Z., Zhang C., Zhou Q., Wang X., Yuan W., Zhang S.-N., 2023b, Nuclear Instruments and Methods in Physics Research A, 1050, 168180

Wüst S., Bittner M., Espy P. J., French W. J. R., Mulligan F. J., 2022, Atmospheric Chemistry and Physics Discussions, 2022, 1

Wuu S., et al., 2009, in 2009 International Image Sensor Workshop, Bergen, Norway.

Xiao K., et al., 2025, arXiv e-prints, p. arXiv:2503.12449

Xu Y., Theuwissen A. J., 2013, in Proc. Int. Image Sensor Workshop. pp 153–157

Xu C., Chao S., Chan M., 2002, in Proceedings of the 28th European Solid-State Circuits Conference. pp 117–120

Yadid-Pecht O., Fossum E., 1997, IEEE Transactions on Electron Devices, 44, 1721

Ye C. H., Lee D.-H., 2018, in Optical Data Storage 2018: Industrial Optical Devices and Systems. pp 41–47

Yee S. W., et al., 2023, ApJS, 265, 1

Yonemoto K., Sumi H., Suzuki R., Ueno T., 2000, in 2000 IEEE International Solid-State Circuits Conference. Digest of Technical Papers (Cat. No.00CH37056). pp 102–103, doi:10.1109/ISSCC.2000.839709

Young A. T., 1967, AJ, 72, 747

Yuan W., et al., 2018, in den Herder J.-W. A., Nikzad S., Nakazawa K., eds, Society of Photo-Optical Instrumentation Engineers (SPIE) Conference Series Vol. 10699, Space Telescopes and Instrumentation 2018: Ultraviolet to Gamma Ray. p. 1069925, doi:10.1117/12.2313358

Zhang Y., et al., 2023, Journal of Electronic Imaging, 32, 043012

Zhang F., et al., 2024, Journal of Instrumentation, 19, P05040

Zimmer P., McGraw J., Ackermann M., 2016, in Advanced Maui Optical and Space Surveillance Technologies Conference.

Zworykin V., Morton G., Malter L., 1936, Proceedings of the Institute of Radio Engineers, 24, 351